Université catholique de Louvain
Faculté des Sciences Appliquées
Unité de Génie Civil et Environnemental

Flow modelling in compound channels

Momentum transfer between main channel and prismatic or non-prismatic floodplains

Thesis presented for the degree of
Doctor in Applied Sciences by

Didier BOUSMAR

February 12, 2002

Members of the Jury :
Professor Yves Zech, Unité de Génie Civil et Environnemental, UCL (Supervisor),
Professor Jean-Michel Hiver, Universite Libre de Bruxelles,
Professor Gregoire Winckelmans, Unité de Thermodynamique et turbomachines, UCL (Members of the advisory committee),
Professor Mustafa Altinakar, Ecole Polytechnique Fédérale de Lausanne,
Professor Donald Knight, Birmingham University,
Presided by
Professor André De Herde, Faculty Dean, Faculté des Sciences Appliquées, UCL.

A Florence et Solenne,
mes deux rayons de soleil

Abstract

Flow modelling in a compound channel is a complex matter. Indeed, due to the smaller velocities in the floodplains than in the main channel, shear layers develop at the interfaces between these subsections, and the channel conveyance is affected by a momentum transfer corresponding to this shear layer, but also to possible geometrical changes in a non-prismatic reach.

In this work, a one-dimensional approach, the Exchange Discharge Model (EDM), is proposed for such flows. The EDM accounts for the momentum transfer between channel subsections, estimated as proportional to the velocity gradient and to the discharges exchanged through the interface; where two main processes are identified : (1) the turbulent exchange, due to the shear-layer development; and (2) the geometrical transfer, due to cross-sectional changes. The EDM is successfully validated for discharge prediction, but also for water-profile computation, through comparison with existing laboratory and field measurements.

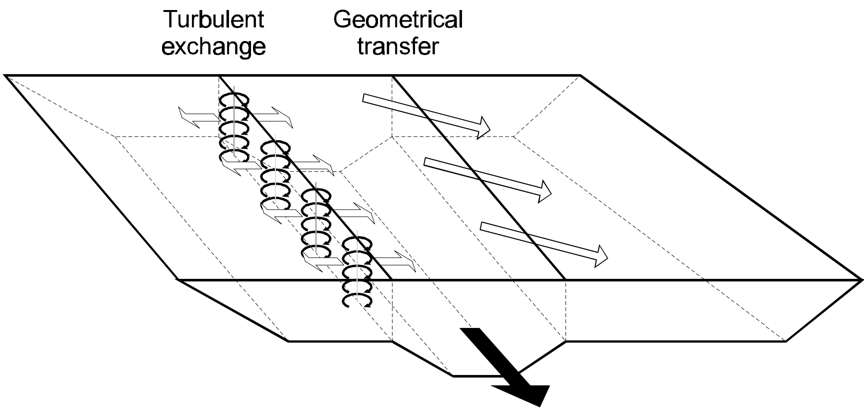

The momentum transfer due to turbulent exchanges is then studied experimentally, theoretically and numerically. At first, new experimental data, obtained by using Particle Tracking Velocimetry techniques, are presented : the periodical vortex structures that develop in the shear layer are clearly identified and characterised. Secondly, a hydrodynamic linear stability analysis enables to predict quite successfully the wave length of some observed vortices. Lastly, an Unsteady-RANS numerical method is used to simulate the perturbation development. The estimated vortex wave lengths agree again with the measurements and the theoretical predictions, although vortices merging occurs in the simulation results, which was actually not observed experimentally. The velocity-profile prediction is found improved when the effect of vortices is considered, thanks to the corresponding additional shearing.

The geometrical transfer is also investigated experimentally and numerically. Novel experiments are designed, with the measurements of the flow in a compound channel with symmetrically narrowing floodplains. The mass transfer and the evolution of the flow distribution along the channel length are clearly observed. A significant additional head loss due to this transfer is measured, in accordance with the EDM hypothesis. Measured water profiles are finally compared successfully with the EDM predictions.

In addition to the EDM development and validation, the so-called Lateral Distribution Method (LDM) is also investigated and the significance of the secondary-currents models proposed by previous authors for this method is discussed. When considering the velocity-profile prediction, the effect of these helical secondary currents is again clearly highlighted, by using dispersion terms in the Saint-Venant equations. However, the actual physical meaning of the related dispersion coefficients remains uncertain. In addition, an extended LDM is also proposed and discussed for non-prismatic flow modelling, using the new narrowing-channel data set.

Résumé

La modélisation des écoulements dans les rivières à plaines inondables est particulièrement complexe. En effet, la vitesse de l'eau étant plus faible sur la plaine d'inondation que dans le lit mineur, une couche de cisaillement se développe à l'interface entre ces sous-sections. La débitance totale de la rivière est dés lors réduite, à cause du transfert de quantité de mouvement qu'occasionne la présence de la couche de cisaillement, mais aussi de part les changements de géométrie qui peuvent se produire dans un lit non-prismatique.

La présente thèse propose, pour la représentation de tels écoulements, une nouvelle approche uni-dimensionnelle dénommée Modèle des Débits d'Echange ("Exchange Discharge Model" – EDM). Le transfert de quantité de mouvement entre les sous-sections de la rivière est pris en compte par l'EDM comme étant proportionnel au gradient de vitesse entre celles-ci et aux débits échangés à travers leur interface. A cette interface, deux phénomènes sont essentiellement présents : (1) un échange turbulent, dû au développement de la couche de cisaillement; et (2) un transfert géométrique, correspondant aux changements de section. L'EDM est validé avec succès pour la prédiction du débit et pour le calcul de lignes d'eau, par comparaison avec des données existantes de laboratoire et de terrain.

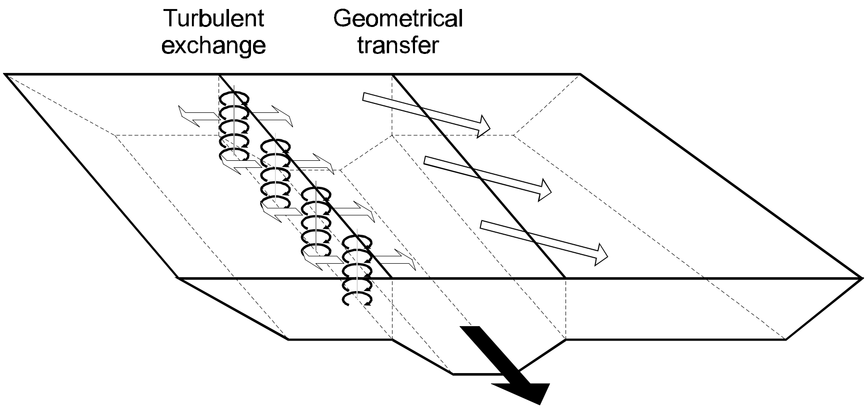

Le transfert de quantité de mouvement dû à l'échange turbulent est ensuite étudié expérimentalement, théoriquement et numériquement. De nouvelles mesures sont obtenues, au moyen d'une technique de vélocimétrie par suivi de particules. Les structures périodiques qui se développent dans la couche de cisaillement sont clairement identifiées et caractérisées. Deuxièmement, une analyse linéaire de stabilité hydrodynamique permet de prédire théoriquement les longueurs d'onde de quelques tourbillons qui ont été observés expérimentalement, et ce avec succès. Enfin, un modèle numérique, de type "Unsteady-RANS", est utilisé pour simuler la croissance des tourbillons dans la couche de cisaillement. Encore une fois, les longueurs d'onde

obtenues correspondent relativement bien avec les valeurs mesurées et prédites théoriquement; bien que les coalescences de tourbillons qui se produisent numériquement n'aient pas été observées expérimentalement. La prédiction des profils de vitesse est améliorée, lorsque l'effet des tourbillons est considéré, grâce à la contrainte de cisaillement additionnelle que ceux-ci génèrent.

Les transferts géométriques sont également explorés expérimentalement et numériquement. Une nouvelle campagne expérimentale a été réalisée, en considérant l'écoulement dans un lit composé symétrique, dont les plaines d'inondation se rétrécissent progressivement. Le transfert de masse entre sous-sections et la redistribution des débits qui lui est associée sont clairement observés au long du canal. Une importante perte de charge additionnelle due à ce transfert est mesurée, en concordance avec les hypothèses de l'EDM. Finalement, les lignes d'eau mesurées sont reproduites avec succès par un calcul utilisant l'EDM.

En complément au développement et à la validation de l'EDM, la "Lateral Distribution Method" (LDM) est également utilisée, avec pour objectif la clarification du rôle des termes de courants secondaires proposés par différents auteurs. Par rapport à la prédiction du profil de vitesse, l'effet de ces courants secondaires est très marqué. Il est ici reproduit en utilisant des termes de dispersion dans les équations de Saint-Venant. Cependant, le sens physique des valeurs des coefficients de dispersion qui doivent être utilisés est discutable. Par ailleurs, une LDM étendue, pour les écoulement en lits non-prismatiques, est proposée et commentée, en utilisant le nouveau jeu de données pour le canal convergent.

Acknowledgements - Remerciements

The present work represents the accomplishment of six years of formation and of research work. This period of my life has been a captivating scientific experience. Beyond the science, it has also been a rich human adventure. I would like therefore to acknowledge here all the people who helped me during this doctorate.

Terminer la rédaction de cette thèse, c'est constater l'aboutissement de près de six années de formation à la recherche. C'est s'arrêter un instant pour contempler le résultat d'une captivante aventure scientifique, ponctuée de découvertes enthousiasmantes, et parfois aussi de moments d'errance et de remise en question.

Terminer la rédaction de cette thèse, c'est aussi, et surtout, prendre le temps d'évoquer la richesse humaine de cette expérience. C'est se remémorer des rencontres, des discussions passionnées, des heures passées à travailler ensemble. C'est prendre une dernière fois la plume, avec plaisir, pour remercier toutes les personnes qui m'ont aidé dans cette entreprise, en me guidant, en me conseillant, en me donnant un coup de main, ou, tout simplement, en m'offrant un petit geste d'encouragement.

Tout d'abord, je voudrais remercier mon promoteur, le Professeur Yves Zech, pour l'opportunité qu'il m'a offerte de réaliser ce doctorat, pour l'encadrement qu'il m'a octroyé, pour les nombreuses occasions qu'il m'a données de participer à des rencontres scientifiques, et pour la confiance qu'il m'a toujours témoignée dans mon travail. Cher Yves, j'ai bien souvent pu apprécier ta disponibilité, même si parfois il fallait faire la file devant ta porte. Outre tes larges compétences scientifiques et ton intérêt pour chacune de mes nouvelles découvertes, je retiendrai ta constante exigence de clarté et de précision dans tous mes développements et mes écrits : je crois que c'est un des apports principaux de la formation que tu m'as apportée, et j'espère que ce souci de rigueur se reflètera dans les pages qui vont suivre. Enfin, au-delà de ces nombreuses qualités scientifiques, ce remerciement serait incomplet si je ne soulignais ton respect de la personne humaine et ton souci permanent d'équité, que j'ai pu apprécier tant dans ce travail que dans les autres activités dont j'ai eu plaisir à m'occuper avec toi depuis mon engagement à l'UCL.

Je voudrais ensuite remercier le Professeur Grégoire Winckelmans, qui a participé à l'encadrement de cette recherche. Les commentaires qu'il a formulé à différentes étapes de mon travail, et tout particulièrement les discussions approfondies de ces dernières semaines, ont certainement contribué à l'amélioration de ma thèse.

Je voudrais aussi remercier le Professeur Jean-Michel Hiver, de l'Université Libre de Bruxelles, qui a également accepté de participer à l'encadrement de mon doctorat. Ses commentaires ont certainement été tout aussi appréciables, tout comme j'ai pu bénéficier de quelques utiles petits coups de pouce logistiques bien utiles, rendus possibles de par sa fonction de Directeur du Laboratoire de Recherches Hydrauliques du Ministère wallon de l'Equipement et des Transports (MET).

Je suis heureux de pouvoir compter parmi les membres de mon jury, le Professeur Mustafa Altinakar, de l'Ecole Polytechnique Fédérale de Lausanne. Cher Mustafa, l'intérêt que tu portes à mes travaux m'honore, et les encouragements que tu m'as transmis à l'occasion de ces dernières semaines de rédaction m'ont particulièrement touché. Enfin, je te suis très reconnaissant pour ton accueil chaleureux à Lausanne, quelques jours avant ma défense privée, ainsi que pour tes nombreux commentaires et remarques sur la première version de ce texte.

I am also honoured that Professor Donald Knight, from the University of Birmingham, accepted to be a member of my jury. Dear Professor Knight, I have appreciated your numerous researches on compound-channel flow modelling, which are many times quoted in the present thesis. Since the first time we met, during a short course in Glasgow in 1996, you expressed an interest in my findings that gave me confidence in pursuing my work. It will therefore be a pleasure for me to discuss the present results with you.

Enfin, je me dois de remercier le Professeur André De Herde qui a accepté de prendre en charge la présidence de mon jury, malgré les nombreuses autres tâches qui lui échoient de par sa fonction de Doyen de la Faculté.

Ce travail s'est bien évidemment réalisé au sein d'une équipe, dans laquelle j'ai pu bénéficier de nombreuses et fructueuses discussions. Je souhaite ici remercier tout d'abord Benoît Spinewine, qui m'a aidé pour la réalisation des mesures par imagerie digitale, et par de nombreux autres coup de main. Un grand merci aussi à Xavier Sillen et Hervé Capart pour les précieux échanges lors des premières années de ce travail. Merci également à Rudy Scherer, Christophe Adriaensen et Marc Poncin, qui ont mis à l'épreuve différentes méthodes que j'ai élaborées dans le cadre de ma recherche. Merci à Jean-François VandenBerghe qui m'a initié au fonctionnement de Labview.

Une pensée toute particulière va à Sandra Soares Frazão qui termine également la rédaction de sa thèse ces jours-ci : outre une saine émulation entre collègues, il était agréable de savoir ne pas être engagé seul dans cette épreuve d'endurance et de pouvoir s'apporter un soutien réciproque.

Je remercie également mes autres collègues et amis de l'équipe d'hydraulique et de l'Unité de Génie Civil et Environnemental : ce travail n'aurait certainement pas été aussi agréable s'il ne régnait entre nous une si bonne ambiance.

Toute la partie expérimentale de ce travail aurait été impossible sans le concours du personnel du Laboratoire du Génie Civil. Parmi ceux-ci, je tiens tout particulièrement à remercier Quintino Renna, qui a réalisé le canal d'essai à lit composé. Outre ses remarquables compétences techniques et son souci du travail bien fait, lors de nombreuses heures passées ensembles au labo, j'ai pu apprécier sa bonne humeur permanente et son incroyable modestie : Cher Tino, il faudra bien un jour que tu reconnaisses que la réussite de ce travail te doit bien plus que tu ne veux l'admettre. Je tiens également à remercier Vincent Forzée qui a brillamment repris le flambeau de Tino, après la retraite de celui-ci, pour les derniers travaux de finition du canal.

L'équipe d'électroniciens du laboratoire est certainement pour beaucoup aussi dans la réussite de cette partie expérimentale. Un tout grand merci à Alex Bertholet, à André Renard et à Bernard Tondeur : pour les nombreux conseils, pour les heures passées à instrumenter le canal, pour les coups de main lors des mesures, pour les innombrables dépannages du WAVO, et pour bien d'autres choses encore…

Parmi les autres membres du personnel du laboratoire, il n'en est probablement pas un que je n'ai mis un jour à contribution pour un service ou un autre. Dans le désordre, merci donc à Stéphane Gorski, Eric Dupuis, Philippe Halloy, Michel Aubecq, Hassan Kamhi, Guy Henriet, René Piérard, Francis Goffin, Eugène Bouchonville, Luc Yung et Pierre Bousman. Merci également à nos secrétaires, Viviane Misson, Marie-Rose Bodart et, aussi, Francine Nowé, toujours prêtes à rendre service et à donner un mot d'encouragement. Merci enfin aux deux directeurs successifs du Laboratoire, Bernard Sine et Albert Mertens de Wilmars, qui, chacun à leur manière, m'ont permis de disposer des ressources nécessaires pour mener à bien ce travail expérimental.

Merci à l'équipe du Centre de Calcul Intensif de l'UCL, où ont été réalisées une partie des simulations numériques présentées dans ce travail, et en particulier à Bernard Van Renterghem, pour ses nombreux conseils et explications.

Durant ces six années, j'ai également eu la chance de pouvoir encadrer plusieurs étudiants qui ont réalisé un travail de fin d'étude consacré à la problématique des écoulements en lits composés. Même s'ils ne se retrouvent pas tous tels quels dans cette thèse, leurs résultats ont certainement contribué à l'avancement de mon travail de recherche. Un grand merci donc à Pierre-Henri Vancaster et Christophe Davreux qui ont développé un premier modèle numérique bi-dimensionnel; à Raphaël Pilate qui a en partie expérimenté la "Lateral Distribution Method"; à Régis Marchal et Benoît Philippe qui ont conçu et supervisé la réalisation du canal d'essai; à Robens Aimable, Tanguy Boucquey, Gaëtan et Vincent De Bloudts qui ont mis au point la plupart des dispositifs de mesure et obtenu quelques beaux résultats; à Thomas Nef qui a réalisé les premières mesures par imagerie; et à Nathalie Wilkin et Jean-Hugues Jacquemart qui ont effectué une superbe campagne d'essais sur les lits convergents.

Several foreign colleagues have also contributed to the success of this research, through valuable discussions or by transmitting me relevant information. I would like therefore to acknowledge : Professor Alan Ervine and Dr Kourosh Babaeyan-Koopaie, University of Glasgow, Dr Joachim von Lukowicz, Technische Hochschule Aachen, Professor Wim Uijttewaal and Bram van Prooijen, Technische Universiteit Delft.

Parmi ces collègues étrangers, j'ai particulièrement apprécié les discussions nombreuses et approfondies avec Sébastien Proust et André Paquier du Cemagref à Lyon, ainsi qu'avec Nicolas Rivière de l'INSA à Lyon. Leur regard toujours pertinent sur mes résultats, et leurs idées relatives aux écoulements en canaux non-prismatiques, ont certainement contribué à l'enrichissement de ce travail, principalement en sa troisième partie.

Guy Bertrand, du Laboratoire de Recherches Hydrauliques du MET, doit sûrement être aussi remercié ici, pour ses résultats, précurseurs de l'"Exchange Discharge Model", et pour ses commentaires intéressants sur mes résultats.

Quelques soutiens institutionnels doivent également être mentionnés : l'Université catholique de Louvain qui, en m'octroyant un poste d'assistant, m'a permis de mener à bien ce travail de recherche; le Fond de la Recherche Fondamentale et Collective qui a, en partie, financé les travaux du canal d'essai; le Fond National de la Recherche Scientifique qui a permis l'acquisition de la sonde acoustique Doppler utilisée dans la seconde partie de ce travail; le Commissariat Général aux Relations Internationales et le programme Tournesol qui ont permis plusieurs échanges et séjours avec nos collègues Lyonnais. Les données relatives à la Sambre, utilisées pour valider l'EDM, ont été gracieusement fournies par le Service d'études hydrologiques (SETHY) du Ministère wallon de l'Equipement et des Transports.

Plusieurs parties de ce texte ont été relues par Florence, par ma mère, par mon père, par Sophie Compère et par Benoît Spinewine. José Flémal a réalisé quelques magnifiques figures. Qu'ils trouvent ici les remerciements qu'ils méritent.

L'aboutissement de ce travail n'aurait sûrement pas été possible sans l'aide et le soutien de plusieurs amis qui, bien que n'ayant pas contribué à son aspect scientifique, m'ont merveilleusement aidé ces derniers temps, soit en me suppléant pour les autres tâches que je n'arrivais plus à assumer seul, soit en m'encourageant de tout leur cœur. Un grand merci donc à mon frère, Eric, et à Sophie; à ma belle-famille, Marie-Thérèse, Angelo et Estelle. Un grand merci également à Isabelle, à Xavier et à Stéphane. Un grand merci enfin à ceux que j'aurais pu oublier dans ces pages et qui, je l'espère, ne m'en tiendront pas rigueur.

Tout ceci n'aurait cependant pas été possible sans mes parents. Ils ont éveillé ma curiosité scientifique, ils m'ont soutenu tout au long de mes études, ils se sont intéressés à mes recherches et m'ont encouragé dans mon doctorat. Enfin, ils ont toujours été à mes côtés dans les moments plus difficiles. Ils m'ont soutenu et aidé tant qu'ils ont pu depuis toujours, et encore plus durant toute la rédaction de cette thèse. Maman, Papa, un immense merci pour tout cela !

Enfin, je n'aurais pas assez de mots pour remercier mon épouse, Florence, et ma fille, Solenne, qui m'ont tant soutenu et encouragé durant ces années et surtout ces derniers mois; et qui ont supporté mes si nombreux moments d'absence, physique ou mentale, la tête perdue dans une équation, certes intéressante, mais tellement hors de propos dans la vie d'une petite famille.

En ce moment, toutes mes pensées vont à Florence, qui a si merveilleusement assumé toutes les choses que j'aurais normalement dû faire avec elle, me forçant même parfois à aller travailler alors que je voulais l'aider. Florence, maintenant que ce doctorat se termine, j'ai tellement hâte de te retrouver pleinement, et d'enfin ne repenser qu'à nous deux !

En ce moment, toutes mes pensées vont aussi à Solenne qui, bien souvent, est arrivée à quatre pattes dans mon bureau pour, d'un air décidé, me faire comprendre que je travaillais depuis trop longtemps et qu'il serait grand temps de jouer avec elle. C'est promis ma puce, maintenant, Papa va prendre un peu plus de temps pour te regarder grandir !

Soignies, le 3 février 2002

Table of contents

Appendices

Introduction

1. Rivers and floods

Rivers have attracted almost every civilisation, as they provide many contributions to human well-being : water for household consumption, irrigation and industry; sustainable energy; convenient transportation links; and valuable wild-life habitat. Human mind is easily captivated by their power, sometimes peaceful in scenic landscapes, sometimes devastating when flooding.

Due to the demographic pressure in the last centuries and to the consequently increased use of rivers, larger settlements have developed on the river floodplains. This has resulted in amplified loss of life and increased economic costs when flooding occurs. Today, flood disasters account for about a third of the losses due to natural disasters throughout the world and are responsible for more than half the fatalities. Trend analyses show that these figures have been increasing significantly in recent years (Berz 2000).

Figure 0.1 : Flood on River Meuse, Belgium, 1993 (Photo MET-SETHY)

River engineers were therefore more and more solicited to mitigate flood impacts. Former responses for flood control first consisted in heavy alleviation works, such as dikes and detention reservoirs. Unfortunately, this possibly overvalued confidence in the ability of man to master nature often resulted in moderate or poor outcome, due among other things to unanticipated morphological responses of the rivers, or in worst cases to dike breaches. Nowadays, more sustainable solutions are preferably adopted : more space is allocated to rivers, respecting or reconstituting their natural floodplains, by withdrawing dikes and abandoning possible settlements areas or using them only seasonally (see e.g. Bhattacharyya and Bora 1997).

The engineer's challenge regarding flood modelling consists thus mainly in predicting maximum water levels and flood propagation speeds, as a function of river bed and watershed topography, either natural or artificially alleviated. On the one hand, hydrological models should provide the actual discharge corresponding to a given rain, but increased difficulty raises from the increased runoff from the watershed due to urbanisation and from the possibly heavier rains due to global climate changes. On the other hand, hydraulic models account for flood propagation in the river bed, for the water levels reached at a given discharge, and for morphological consequences of the floods. This time, the main difficulty – to be investigated in the present work – is probably the complexity of the flow resulting from the complicated cross-section of the river flowing overbank.

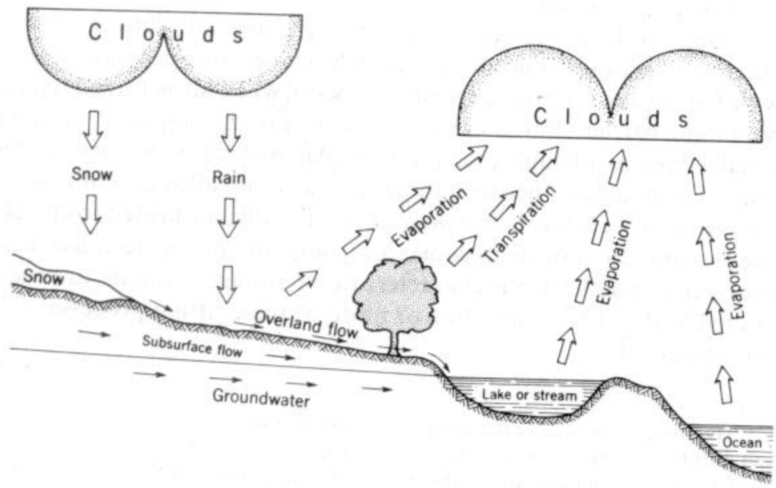

Figure 0.2 : Flood propagation in watershed and river bed : the hydrologic cycle (Linsley and Franzini 1972)

2. Flow in compound channels

Dealing with the hydraulic modelling of flood, the river engineer has to consider the flood propagation along the river; the identification of flooded areas; the design of discharge channels; the dike breaches risk; the morphological effects of the flood; etc. In almost all cases, the stage-discharge relation in a given reach cross-section will be one of the fundamental component of the solution.

Whereas the estimation of the water level corresponding to a given discharge is nowadays an easily handled problem in channels with single cross-section, the problem gets worse when the river enters its floodplains. Indeed, when the floodplains not only serve as detention ponds but also carry part of the discharge, the flow complexity is dramatically increased (Figure 0.3).

The velocity in the floodplains is generally lower than in the main-channel, due to the shallower water level and to the higher roughness in often more vegetation-covered areas. As a result of this velocity gradient, a shear layer is observed at the interface between the main channel and the floodplains. This shear generates large scale turbulent structures, typically large vortices with vertical axis (Figure 0.4), and a consequent momentum transfer from the main-channel to the floodplains : the main-channel conveyance decreases, while the floodplains one increases significantly.

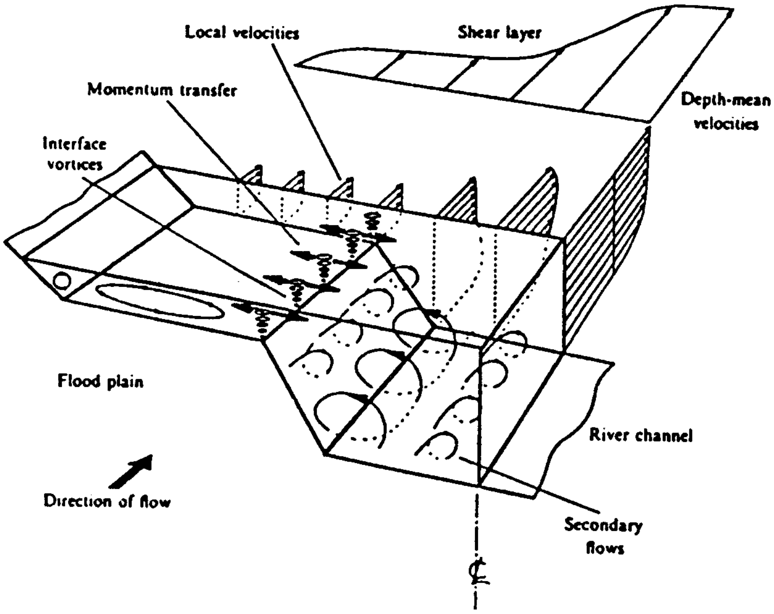

Figure 0.3 : Flow structure in a compound channel (Shiono and Knight 1991)

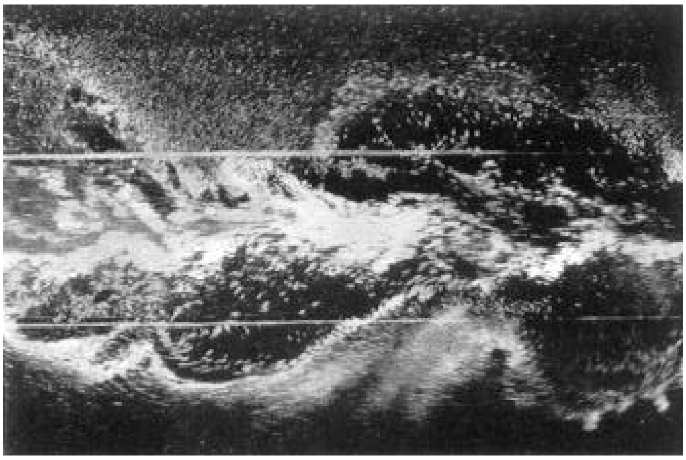

Figure 0.4 : Large vortices observed at the interfaces between the main channel and the floodplains of a compound channel (Sellin 1964)

Although a two-dimensional model could partly take this effect into account, one-dimensional models are usually preferred, due to computational costs, as the reach lengths to be investigated could require huge meshes; and due to data availability, also linked to survey costs. When seeking to estimate the stage-discharge relation in a compound section, as required by a one-dimensional model, the momentum transfer must thus clearly be taken into account.

The problem complexity rises one step more when the river is no longer modelled as a prismatic compound channel, but as a non-prismatic main channel meandering in non-prismatic floodplains, corresponding to actual river geometry as observed in nature. Due to the channel meandering, water flowing in the floodplains now crosses over water flowing in the main channel, resulting in increased interactions and exchanges that should also be considered in the flow modelling (Figure 0.5).

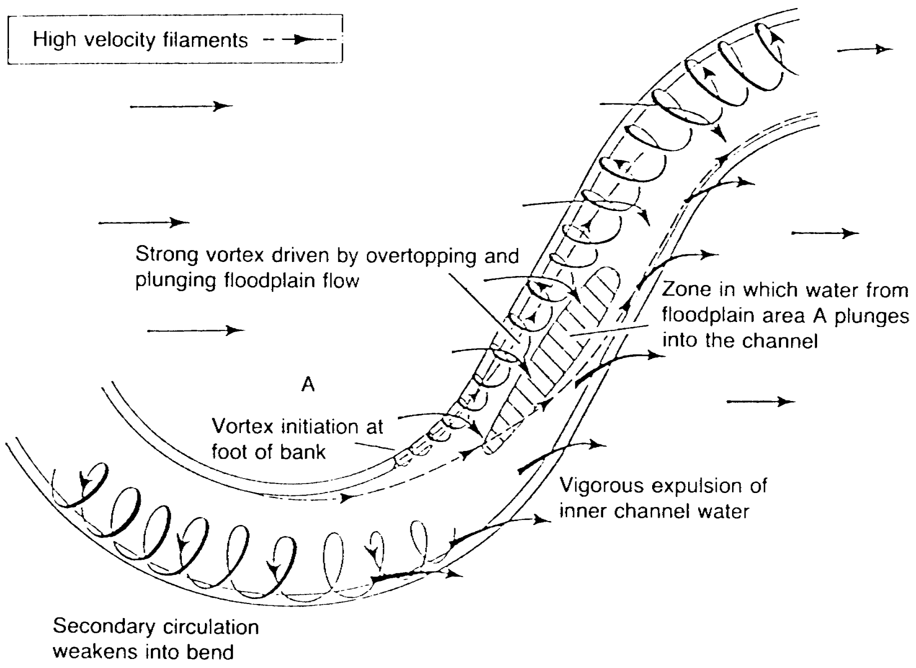

Figure 0.5 : Flow structure in a meandering compound channel (Sellin et al. 1993)

3. Scope of this work

Since the early works by Sellin (1964), many researchers have investigated compound-channel flow and several computational methods have been proposed in order to model the stage-discharge relation. As will be presented in Chapter 1 – State of the art, two recent methods have gained the most credit : the Ackers' method and the various forms of the Lateral Distribution Method (LDM). These methods provide accurate discharge prediction, together, when using the LDM, with the velocity distribution along the cross-section width.

However, both methods are mainly designed for modelling uniform flow in a prismatic channel : using them for non-uniform flow or for a meandering channel could thus reveal hazardous. Some other imperfections make their use not straightforward : the Ackers' method is an empirical method that requires the estimate of several geometrical parameters. Good engineer skills and judgement is necessary when estimating these parameters for a natural geometry, in such a way that this preliminary step of the method could be difficult to automate. On the other hand, the LDM is theoretically well founded. Only the term representing the effects of the secondary currents remains empirically estimated. Unfortunately, part of the LDM accuracy rests on this term whose value could be difficult to extrapolate to natural channels as it is deduced from laboratory experiments and differs for each data set.

Improvement of these methods, or alternative methods development, seems therefore valuable if it tends towards (1) better theoretical background; (2) at least equivalent accuracy; (3) applicability to non-prismatic channels; and (4) easier use in computational programs. The main objective of the present work is to propose such an alternative method.

The proposed Exchange Discharge Model (EDM) accounts for the momentum transfer between the main channel and the floodplains, estimated as proportional to the velocity gradient between both subsections and to the discharges exchanged through the interface. The so-called exchange discharges originate from both a turbulent exchange in uniform flow, i.e. the mass transported by turbulent structures such as the large vortices with vertical axis; and from a net mass transfer due to geometrical changes in non-prismatic channels (Figure 0.6). The EDM equations are then developed in order to express the effects of the momentum transfer as an additional loss to be added to the head loss due to bed friction, for water-profile computation purpose.

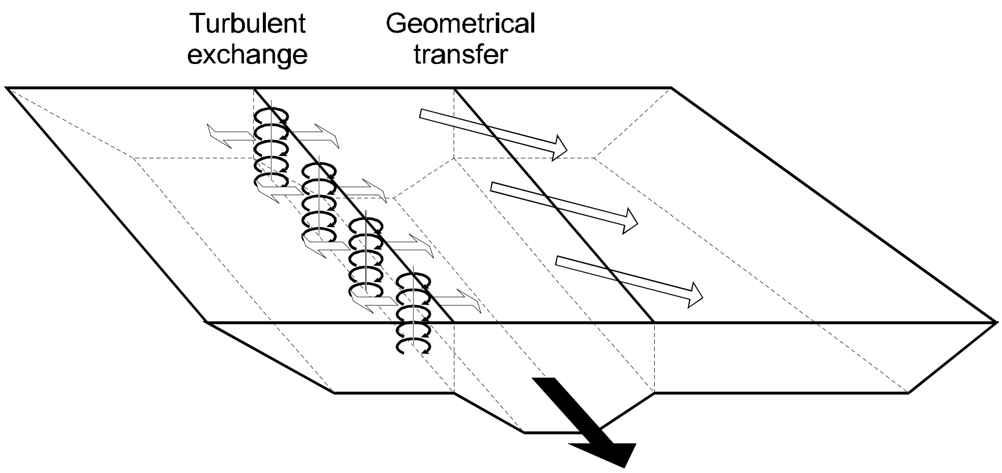

Figure 0.6 : Flow exchanges as modelled by the Exchange Discharge Model

Only two additional coefficients need to be estimated in the EDM formulation. Their values present only little variations when fitted to a large number of data set, in such a way that unique values can be adopted for all applications. With such fixed parameters, the EDM produces accurate discharge predictions for all the prismatic channels tested, with errors of generally less than 5 %. Satisfactory results are also obtained for the non-prismatic geometries investigated, including slightly meandering channels. Although it was not tested in the frame of the present work, it is anticipated that the EDM could also produce good results for meandering channels with higher sinuosity (in the range 1.5), as it is founded on the modelling of a momentum transfer mechanism rather than on an empirical relation.

4. Contents outline

The present work is divided into three main parts : the first one presents the Exchange Discharge Model itself, together with some other fundamental equations; the second part explores tentatively the momentum transfer mechanism associated with the turbulent exchanges; and the third part introduces new experimental measurements attempting to quantify the momentum transfer associated with mass transfer in a non-prismatic geometry.

In the first part, a state-of-the-art chapter reviews some significant contributions to the understanding of the flow behaviour in a compound channel, together with most of the one-dimensional methods proposed up to now. The two-dimensional Saint-Venant equations, or shallow-water equations, are then presented, as they will be used, in the second and third parts, for flow investigations based on two-dimensional modelling. The Lateral Distribution Method is also developed and a tentative clarification of the secondary current term significance, to be tested in the continuation of this work, is proposed. Lastly, the Exchange Discharge Model is developed extensively and significant results are presented.

The momentum transfer due to turbulent exchanges is investigated in the second part of this work. Some new experimental observations using digital imagery techniques are detailed, quantifying the periodical vortex structures due to the shear layer at the interface between the main channel and the floodplains. These periodical structures are also explored through a hydrodynamic stability analysis and through numerical simulations. A tentative model of the momentum transfer due to the horizontal vortices is developed in relation with the Exchange Discharge Model. In addition, the effect of the helical secondary currents on the velocity profile is tentatively modelled, using dispersion term in the Saint-Venant equations, and the results are discussed in relation with the LDM secondary current term.

The mass and momentum transfer due to geometrical changes of non-prismatic channels is finally investigated in the third part. The flow in a compound channel with symmetrically narrowing floodplains is studied experimentally : in such a geometry, the momentum transfer occurs as in meandering channels, although no curvature effect exists, enabling thus an easier comparison with the Exchange Discharge Model. In addition, two-dimensional modelling is performed and a proposed extension of the LDM to non-prismatic flow is tested. Lastly, the flow near the critical depth is experimentally observed : indeed, although the channel remains prismatic, due to the water level variations, this flow is actually non-prismatic and constitutes a final test case for the EDM.

Part I

Fundamental physics and associated equations

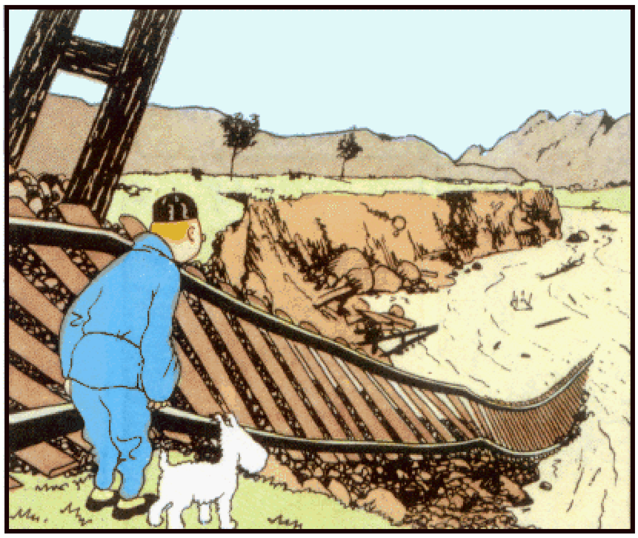

A flood on the Yang-Tse River,
in Hergé (1946), Le Lotus Bleu

Chapter 1
Compound-channel flow and one-dimensional modelling : State of the art

1.1 Introduction

This brief state-of-the-art review intends to present some selected significant contributions to compound channel flow modelling. The available observations concerning compound channel flow structures are summarised; while, according to this work's main objective – the development of a theoretically sound one-dimensional model – the quality of results that can be obtained with one-dimensional formulae are also emphasised. Previous works relative to the modelling of periodical structures and to the mass transfer in non-prismatic geometries will be further investigated in introduction Chapters of Part II and III of this work.

It should be noted that a considerable amount of research papers have been published on the topic, as compound channels have been investigated quite extensively since the early sixties, and as more research is still underway. A complete literature survey is out of the scope of this work. However, the interested reader may refer to the extensive literature search by Hollinrake (1987; 1988; 1989; 1990; 1992) for work prior to '90. For an updated state-of-the-art review, the reader should refer to the IAHR monograph to be published by Knight et al. (2002).

1.2 Pioneer investigations

The estimation of the stage-discharge relation in a given river cross-section has been a challenge for hydraulicians since the early developments of the discipline. Antoine de Chézy, in the year 1775, and Pierre Louis Georges Du Buat, in 1779, were the first to publish algebraical formula for uniform flow calculation (Rouse and Ince 1954). During the 19th century, many empirical formulae were proposed, based on sets of laboratory and fields measurements. Among those pioneer, Manning (1889) proposed two empirical formulae, founded on large amount of data, collected by himself or available in the literature :

$$U = C\sqrt{gR\,S_0}\left[1+\frac{0.22}{\sqrt{mR}}\left(R-0.15\;m\right)\right] \tag{1.1}$$

$$U = C' R^{2/3} S_0^{1/2} \tag{1.2}$$

where U is the flow mean velocity; R is the cross-section hydraulic radius (ratio of the section area A to the wetted perimeter P); S_0 is the channel bed slope; g is the gravity constant; m is the atmospheric pressure, expressed as a column of mercury height (m = 0.76 m, for S.I. units system); and C and C' are two constant, depending of the channel bed and wall composition.

Although Manning preferred the first of these two formulae, only the second one (1.2) has been retained by engineers. It has become one of the most widespread and used friction formula, probably thanks to the good results obtained and to its monomial aspect that makes it easier to use. Most of present textbooks now quote it in the form (e.g. French 1985; Chaudhry 1993) :

$$Q = AU = \frac{AR^{2/3}}{n} S_0^{1/2} \tag{1.3}$$

where Q is the discharge; and n is the so-called Manning roughness coefficient. Tables of Manning coefficient values according to the channel bed material and condition can be found in almost all open channel hydraulic textbooks. It should also be pointed out that this formula is dimensionally non-homogeneous and that the form (1.3) stands for SI units (Yen 1992).

However, the use of the Manning formula (1.3) should be restricted to channels with an almost uniform velocity distribution in the cross-section. The Manning formula must be adapted for application to compound channels, in which the velocity in the main channel is larger than on the floodplains, due to the deeper section and to the generally lower roughness. Indeed, when water starts to flow on the floodplains, the wetted perimeter increases suddenly and the hydraulic radius decreases accordingly, leading to a discharge underestimation. Lotter (1933) has therefore suggested to divide the channel cross-section in subsections where the velocities are more homogeneous (Figure 1.1), namely the main channel and the two floodplains. The discharge is then estimated in each subsection separately, and the whole section discharge Q is obtained by addition of the subsection discharges Q_i. Using the Manning formula (1.3) in each subsection, the following equation is obtained :

$$Q = \sum_i Q_i = \sum_i \frac{A_i R_i^{2/3}}{n_i} S_0^{1/2} \tag{1.4}$$

where subscript i stands for subsection i. This method is nowadays called the Divided Channel Method (DCM); by opposition to the simple application of equation (1.3) to the whole channel, which is called the Single Channel Method (SCM).

Using the DCM, the division limits between the subsections can be either vertical, as suggested by Lotter (Figure 1.1), diagonal or horizontal (Figure 1.2). As discussed below, several authors have investigated which definition of the division lines provides the best results. The most common and practical choice remains nevertheless the vertical ones, that are also easier to implement in a numerical model. The DCM has been therefore widely used in water-profile computational software such as HEC-Ras (HEC 1998).

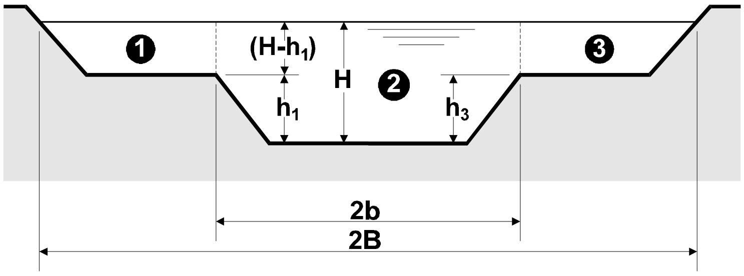

Figure 1.1 : Cross section of a compound channel, division in subsections

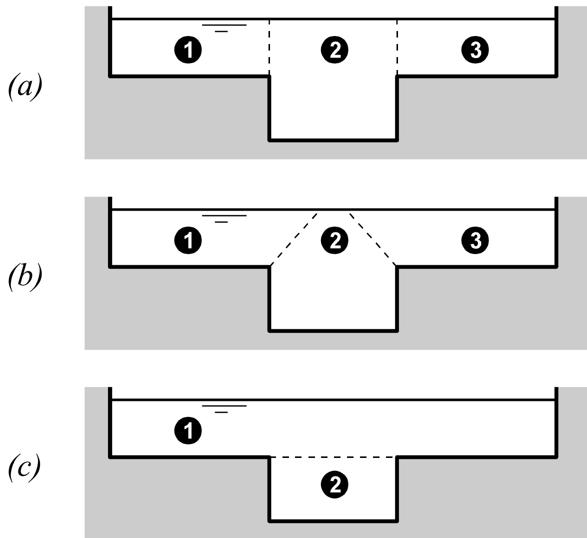

Figure 1.2 : Divided channel method, possible subsection divisions :
(a) vertical; (b) diagonal; and (c) horizontal

Sellin (1964) is one of the first who investigated experimentally the behaviour of the uniform flow in a compound channel. He showed that the DCM overestimates the discharge in a compound channel for a given water depth, and he observed the large vortices with vertical axis located at the interface between the main channel and a floodplain (Figure 0.4). These vortices are due to the shearing between fast and slow moving water in the respective subsections, and they generate a momentum transfer from the main channel to the floodplain. As a result, the velocity decreases in the main channel and increases in the floodplain, resulting in a global conveyance reduction.

Further works have thus attempted to improve or correct the DCM; and some alternative methods were also proposed. Some of these works are described below.

1.3 Shear layer analysis

One of the first investigation on the influence of the division lines choice using DCM is due to Posey (1967). Using experimental data of flow in a compound channel, SCM was compared to the DCM, with vertical (Figure 1.2a) or diagonal (Figure 1.2b) division lines. In this particular case, the SCM was found better for the lower discharges while the DCM with vertical division lines provided the best results for higher overbank flow. Yen and Overton (1973) suggested that the best division line would be a division line where the shear-stress equals zero. On the basis of velocity distribution measurements, they identified such lines, found almost diagonal. Unfortunately, these lines have to be adapted for each given discharge or water depth.

Several authors began to investigate the bed shear stress τ_b distribution in a compound section, in relation to the stage-discharge curve : the shear stress is found to present locally a maximum value on the floodplain, near the interface with the main channel, as a consequence of the local velocity acceleration due to the momentum transfer (Ghosh and Jena 1971; Myers and Elsawy 1975). The observation of a local minimum τ_b value in the main-channel centre line, with two adjacent local maximum, indicated the presence of counter-rotative helical secondary-currents (Knight and Hamed 1984).

On the basis of such bed shear-stress measurements, Myers (1978) performed a momentum balance analysis of each subsection as defined by the DCM, and defined the apparent shear stress τ_a, acting on the vertical division lines and expressing the momentum transfer between main channel and floodplain. For the lower relative depth H_r (ratio of the depth on the floodplains H-h to the depth in the main channel H, see Figure 1.1), this apparent shear stress was found to be as great as 25 % of the main-channel subsection weight component and as 200 % of the floodplain weight component, clearly discarding the DCM approach.

Various empirical relations linking the apparent shear-stress to the cross-section parameter were proposed, as summarised in Table 1.1. Expressing the apparent shear stress as a Reynolds stress $\tau_a = \rho\,\overline{u'v'}$, and using a model similar to the Prandtl mixing length concept, Ervine and Baird (1982) suggested that the apparent shear stress is proportional to the square of the velocity gradient ΔU between main channel and floodplains. The other formulae quoted in Table 1.1 are mainly based on dimensional analysis. All of them enable the correction of the DCM and the estimation of the actual discharge. However, it should be pointed that, although referring to almost the same geometrical parameters, the numerical coefficients of all these formulae present a large scattering. Indeed, each formula refers to one particular tested geometry and is therefore difficult to apply to other data (Knight and Shiono 1996).

Some alternative methods, again based on the DCM, were also developed during the same period. Nicollet and Uan (1979) proposed the DEBORD method, on the basis of an empirical correction of the subsection conveyances. This method is still widely used in France. Dracos and Hardegger (1987) proposed an empirical correction of the

Manning roughness coefficient to be used with the DCM in order to get the actual discharge. Unfortunately, such a correction discards the relation between the actual velocity U and the bed shear stress τ_b, although the latter is also of interest when sediment transport is under consideration. Smart (1992) proposed another empirical roughness correction formula; but also highlighted the discontinuity in the staged-discharge curve just above bank level : for small relative depth H_r, the discharge is sometimes lower than the bankfull discharge, due to the momentum transfer. Lambert and Myers (1998) proposed to use a weighted addition of the discharges computed by the DCM with vertical (Figure 1.2a) and horizontal (Figure 1.2c) division lines. Lastly, it should be pointed out that Wormleaton and Hadjipanos (1985) also showed that, even if the total discharge is roughly approximated by the DCM, the error on the estimated subsection discharges Q_i can be up to 60 %.

Table 1.1 : Some empirical apparent shear stress formulae

Authors	Formula	
Ervine and Baird 1982	$\tau_a = \dfrac{50}{N_f}(\Delta U)^2$	(1.5)
Wormleaton et al. 1982	$\tau_a = 13.84\,(\Delta U)^{0.882}\left(\dfrac{H}{h}\right)^{-3.123}\left(\dfrac{B}{b}\right)^{-0.727}$	(1.6)
Knight and Demetriou 1983	$\tau_a = \dfrac{H}{2H^*\,B/b + 2h} - f(B/b, H_r)$	(1.7)
Prinos and Townsend 1984	$\tau_a = 0.874\,(\Delta U)^{0.92}\left(\dfrac{H-h}{H}\right)^{-1.129}\left(\dfrac{B}{b}\right)^{-0.514}$	(1.8)
Wormleaton and Merrett 1990	$\tau_a = 3.325\,(\Delta U)^{1.451}(H-h)^{-0.354}(B-b)^{0.519}$	(1.9)

where ΔU is the velocity difference between main channel and floodplain; N_f is the number of floodplains; H and h are respectively the main-channel and bankfull depth; B and b are respectively the whole channel and the main-channel width (Figure 1.1)

The study of compound channels has not been restricted to one-dimensional modelling. Krishnappan and Lau (1986) used a tri-dimensional simulation with a k-ε turbulence model, while Keller and Rodi (1988) used a depth-averaged two-dimensional k-ε model. Both study produced satisfactory results for both the velocity and the bed shear-stress predictions.

1.4 The Flood Channel Facility experiments

1.4.1 Experimental campaign

Prior to the mid-'80, almost all experiments on compound channel flow were performed in small- or medium-scale university facilities. Intending to perform such experiments at a larger scale and for higher Reynolds numbers, the U.K. Science and Engineering Research Council founded the building of a large scale Flood Channel Facility (FCF), settled at H.R. Wallingford (Knight and Sellin 1987). The whole FCF is 56-m long and 10-m wide, with a bed slope $S_0 = 1 \times 10^{-3}$ and a maximum discharge of 1.08 m^3/s (Figure 1.3). In a first stage (Series A), various straight channel geometries were tested, involving variation of (1) the floodplain width; (2) the main-channel bank transverse slope; (3) the number of floodplains; and (4) the floodplain roughness (smooth cement finishing or rough, using vertical rods). All the data obtained during this first series have been edited by Knight (1992). Some significant results of the research teams associated to this program are presented hereafter. Some results from the further experimental series concerning meandering channels (Series B) and mobile beds channels (Series C) will be discussed in a next paragraph.

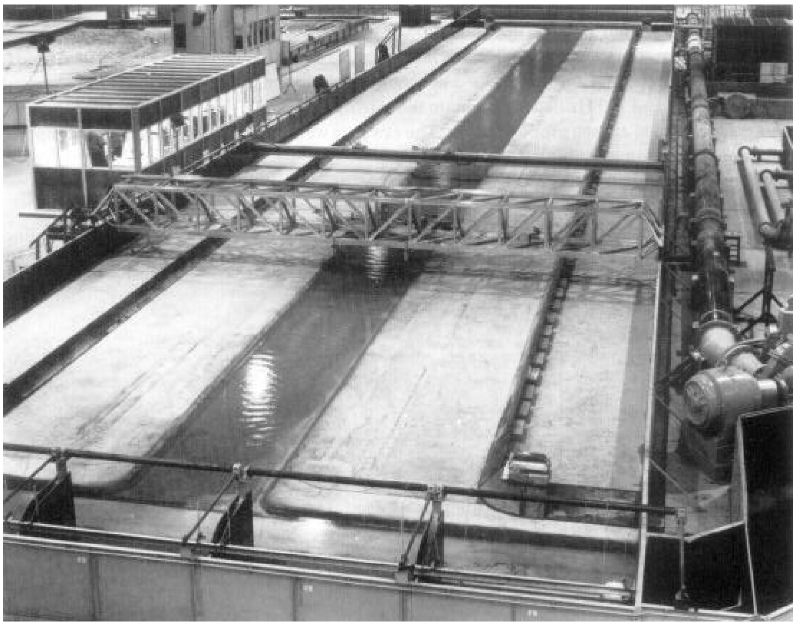

Figure 1.3 : General view of the Flood Channel Facility at H.R. Wallingford (Knight and Shiono 1990)

Wormleaton and Merrett (1990) investigated the bed shear stress distribution and developed the apparent shear stress formula (1.9) quoted above. The roughness coefficient variation was explored by Myers and Brennan (1990) who showed that, as already observed in previous studies, the roughness coefficient estimated for the whole channel presents a sudden increase when the river begins to flow overbank. The estimated main-channel roughness increases, while the floodplain one decreases, as a result of the momentum transfer.

The local velocity distribution, the velocity turbulent fluctuations and the Reynolds stresses were measured by Knight and Shiono (1990), using a Laser Doppler Anemometer (LDA). The vertical distribution of the shear stress τ_{zx} was found to be highly non-linear in the interface zone, indicating strong secondary currents development. The transverse velocity component fluctuations v' in this area revealed periodical oscillations, confirming the presence of the large vortices with vertical axis already observed by Sellin (1964), although no frequency analysis has been provided up to now. Except at the interface area, the vertical velocity profiles are close to the classical logarithmic profile; and, from velocity and bed shear-stress measurements, it is found that the friction coefficient is almost constant in each channel subsection.

Complementary experiments were performed for a main channel skewed to the floodplains (Elliott and Sellin 1990). These experiments in the FCF were also repeated at a smaller scale by Jasem (1990). Both investigations revealed the stronger interactions that will be observed in meandering channel : when the floodplain flow crosses over the main-channel flow, a strong interaction occurs and helical secondary currents are driven within the main channel. This interaction generates a channel discharge reduction up to 10 % (Sellin 1995).

1.4.2 Ackers empirical method

Analysing the new data sets, Ackers (1992, 1993) defined two adimensional parameters : (1) the coherence COH, equal to the ratio between SCM- and DCM-computed channel conveyance; and (2) the discharge adjustment factor DISADF, equal to the ratio between the actual discharge and the discharge estimated by the DCM. The coherence is a measure of the degree of interaction to be expected in a compound channel : a small coherence value indicates large floodplains and a probably intensive interaction, while a coherence value close to the unity indicates a single channel behaviour, with a low interaction. The discharge adjustment factor shows the accuracy of the discharge estimation by the DCM. It is also an indication on how to correct the DCM in order to improve its results.

Figure 1.4 gives a typical plot of the DISADF variation with the relative depth $H_r = (H - h) / H$, i.e. the ratio between floodplain and main-channel depths. Ackers identified four distinct behaviour for four distinct water level regions. Using the FCF data and additional data from previously published works, he developed four empirical equations correcting the DCM in each given region. These empirical equations are function of several parameters such as the relative water depth H_r, the main-channel and floodplain width b and B, the bank slope, the bank level, etc. A sequence of tests enables selection of the appropriate formula.

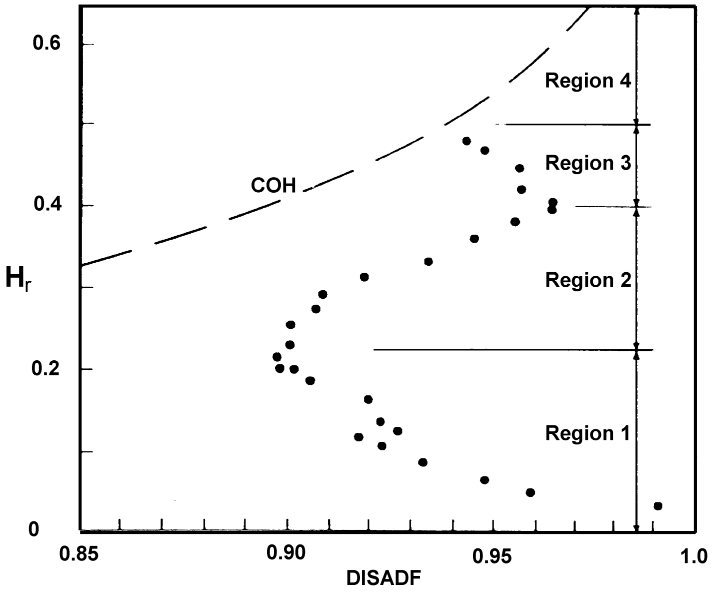

Figure 1.4 : Ackers' method, DISADF values for the FCF 02 series (Ackers 1993)

The Ackers' method produces accurate discharge predictions and has been successfully applied to natural rivers. This method is now recommended by the U.K. National River Authority. One should however remember this method is an empirical one. Moreover, the determination of the geometrical parameters involved in the Ackers' formulae is sometimes tedious, for example when dealing with non-symmetrical geometries having different bank levels on both main-channel sides, and requires some engineer skills and judgement (Wark et al. 1994).

1.4.3 Lateral distribution method

Alternative methods, based on a two-dimensional approach, have also been developed by several researchers of the FCF party (Wormleaton 1988, Knight et al. 1989, Wark et al. 1990). These methods assume a uniform steady flow in a prismatic channel, resulting, by depth averaging the Navier-Stokes equations, in a one-dimensional relation defining the longitudinal velocity. The distribution of the latter may thus be determined along the cross-section, together with the bed shear stress. These so-called Lateral Distribution Method (LDM) incorporates eddy viscosity and, sometimes, also includes secondary currents effects.

The roughness is estimated either by a Manning coefficient (e.g. Wark et al. 1990) or by a Darcy-Weisbach friction factor (e.g. Knight et al. 1989). The eddy viscosity is either assumed proportional to the shear velocity U^* (e.g. Knight et al. 1989) or estimated using a mixing length model (Lambert and Sellin 1996). The effects of secondary currents can be modelled by some constant parameter (Shiono and Knight 1991) or as proportional to the square of the longitudinal velocity (Ervine et al. 2000). No all authors account for this effect which is sometimes modelled through an artificially increased eddy viscosity coefficient (Wark et al. 1990), producing accurate discharge prediction but lower quality velocity profiles. An increase of the roughness coefficient is also possible for that purpose, but this discards the relation between the velocity and the bed shear stress (Shiono and Knight 1991).

These Lateral Distribution Methods will be further discussed in Chapter 3, where a tentative clarification of the significance of the secondary current term is also proposed.

1.5 Recent progress

1.5.1 Tri-dimensional modelling

Parallel to the attempts for developing stage-discharge formulae, several authors investigated further the tri-dimensional structure of the flow in a compound channel, experimentally and numerically.

Quite simultaneously to the FCF experiments, Tominaga and Nezu (1991) performed detailed measurements of the tri-dimensional flow structure in a compound channel, using a LDA system. The helical secondary currents in the main channel and on the floodplains were clearly depicted, and the influence of the corner between the main-channel bank and the floodplain on the structure of these currents was highlighted (Figure 1.5). Using a 3D algebraic stress model, Naot et al. (1993a-b) reproduced quite successfully these observations, with a rather good representation of the longitudinal velocity distribution and of the secondary current pattern.

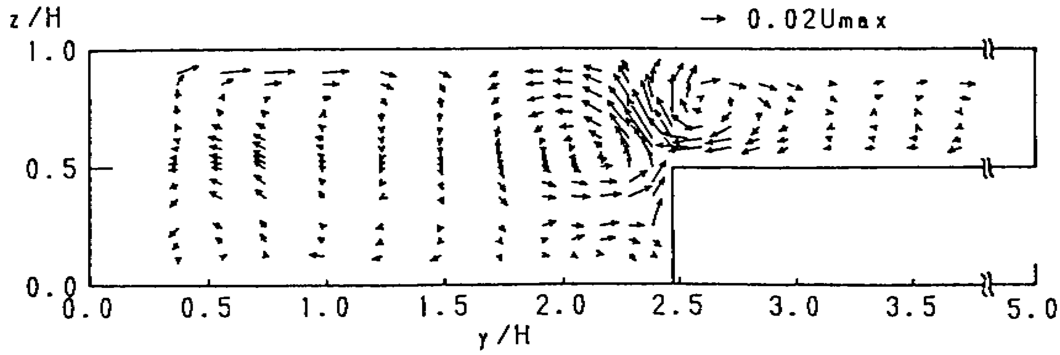

Figure 1.5 : Measured secondary currents in a compound-channel section (Tominaga and Nezu 1991)

Using a 3D Large Eddy Simulation model, Thomas and Williams (1995) computed the flow in an asymmetric compound channel. When compared with the measurements of Tominaga and Nezu, the time-averaged velocity distribution proved to be satisfactorily modelled. However, although they were using a LES model, Thomas and Williams did not provide information on their results regarding the velocity fluctuations and related turbulence structure, such as periodical vortices.

Hosoda et al. (1998) used a non-linear k-ε model to reproduce the turbulence structures development in an asymmetric channel. Modelling a sufficiently long channel, they observed the growth of horizontal vortices and the formation of helical secondary currents, corresponding, at least qualitatively, with the experimental observations.

1.5.2 Flow in meandering channels

Toebes and Sooky (1967) investigated the flow in a meandering compound channel and the subsequent reduction in conveyance. Later, considerable information was gathered from the FCF series B experiments. Sellin et al. (1993) gave a complete description of the flow structure in a meandering channel (Figure 0.5), in which a strong interaction takes place due to the floodplain flow crossing over the main-channel flow. Between the main-channel meander apex, floodplain flow plunges into the channel, generating a strong helical secondary current. As a result, the helical secondary current in the meandering apex is found rotating in the opposite direction at it would have been if only driven by centrifugal forces as in an inbank flow; and part of the water flowing in the main channel is ejected on the floodplain when leaving the apex. These observations were later confirmed with detailed LDA measurements by Shiono and Muto (1998).

Several stage-discharge modelling attempts were produced, using FCF results, together with additional data sets. Ervine et al. (1993) investigated the value of the ratio F^* between the actual measured discharge and a modified DCM evaluated discharge. For this purpose, they used a DCM with a horizontal division line (Figure 1.2c), which corresponds to the plane where the main shear occurs. The floodplain area was divided in two subsections : the first one including the whole meandering belt, the second one for the outside zones. Ervine et al. (1993) found that the ratio F^* is significantly lower than unity, indicating the strong influence of the interaction process when compared to the bed friction. The ratio F^* value reduces when channel sinuosity increases, when the main-channel aspect ratio reduces (width to depth ratio) and when the meander belt width increases compared to the total floodway width. Greenhill and Sellin (1993) developed and validated a computational model, based on the same modified DCM. In order to take into account additional shearing between subsections, they calculated the subsection wetted perimeter by taking into account a part of the division lines.

Researches regarding meandering channels will be further reviewed in Chapter 11, introducing Part III of this work, that deals with flow in non-prismatic channels.

1.5.3 Mobile bed experiments

Further experimental series in FCF, and in other university facilities, are now concerned with sediment transport in compound channels. It has already been observed that the main-channel bed forms are deeply affected when the river flows overbank, and that the sediment coming out of the main channel can settle on the floodplains (Benson et al. 1997). The bed load rate also increases when water reaches the bank level, due to stronger secondary currents (Ervine et al. 1997).

Cassells et al. (2001) recently studied the influence of the mobile bed on the stage-discharge relation in straight compound channels, while Lyness et al. (2001) performed similar investigations for meandering compound channels. They found that, due to deep bed forms, the main-channel roughness can be higher than the floodplain one, resulting in a modified momentum transfer mechanism. However, this latter point may be questionable when considering natural rivers, as the grain size of the sediment used for the experiments is rather coarse when compared to the model scale.

1.5.4 Unsteady flow experiments

Unsteady flow modelling in a compound channel is also of interest and the steady flow formulae should be tested in such extended conditions. Stephenson and Kolovopoulos (1990) performed comparison between the DCM and several corrected methods such as the apparent shear stress equation (1.8) by Prinos and Townsend. Although their study shows clear discrepancies between various methods, the lack of experimental data did not permit to identify the most appropriate one. Using some experimental data, Abida and Townsend (1994) showed that the DCM produced accurate results, only if some momentum transfer correction was included.

New experimental measurements of unsteady flow in a straight compound channel were obtained by both Tominaga et al. (1994, 1995) and Jayaratne et al. (1995). Detailed velocity measurements were achieved in small-scale flume, with rather steep discharge hydrograph. Jayaratne et al. showed that, logically, when water-depth increases, main-channel water flows through the floodplains, while when water-depth decreases, floodplain water flows into the main channel. This effect resulted into a strong hysteresis in the stage-discharge curve, as depicted by Tominaga et al.

Recently, results from similar experiments in meandering compound channels were reported by Watanabe and Fukuoka (2001), showing similar hysteresis.

1.6 Perspectives for the present work

From this brief state-of-the-art review, one will retain that the most accurate stage-discharge prediction methods for compound channels are currently the Ackers method and the LDM. However, the Ackers method is empirical and do not really reflect the actual flow processes occurring in compound channels. Its parameters are also sometimes difficult to define for natural channels. On the other hand, the LDM has a theoretical basis and provides accurate stage-discharge and velocity profile prediction, as far as an suitable parameter calibration is provided. This parameter calibration may sometimes reveals tedious when the secondary-current term is considered, as this term remains partly empirical.

Both this methods were designed for prismatic compound channels and their extension to non-prismatic channels can be hazardous, mainly for an empirical method such as Ackers' one. Methods specific to meandering compound channels are also available.

Unfortunately, up to now, such methods are still empirical. Moreover, their formulation do not enable a smooth transition from prismatic to non-prismatic channel modelling : for example, Greenhill and Sellin method for meandering compound channels is a DCM with an horizontal division line, while Ackers method is founded on a correction of the DCM with vertical division lines.

The review of the previous work briefly presented here highlighted the need for a better model, preferably physically founded rather than empirically built, which could produce accurate stage-discharge prediction and should enable the modelling of non-prismatic compound channels in the same way as for prismatic channels. The Exchange Discharge Model (EDM : Bousmar and Zech 1999a), to be developed in Chapter 4 and investigated further through all this work, attempts to meet these objectives.

The EDM is partly founded on works by Yen et al. (1985), who first considered the momentum transfer due to mass transfer between subsections in a non-prismatic flow; and by Bertrand (1994), who defined an exchange discharge through the interface. This exchange discharge, modelling the turbulent flow exchanges due to the large horizontal vortices, is assumed to be proportional to the velocity difference between main channel and floodplain and to the interface area. A momentum transfer equal to the product of this exchange discharge by the velocity difference is estimated by Bertrand, and enables a correction of the DCM.

Chapter 2
The Saint-Venant equations

2.1 Introduction

The Saint-Venant equations – also called shallow-water equations – describe the behaviour of a two-dimensional flow with a free surface, using depth-averaged values of the velocity components and assuming an hydrostatic pressure distribution along a vertical. Although one of this work main purpose is to develop a one-dimensional model, two-dimensional numerical simulations will be used as a numerical laboratory in Parts II and III, completing the experimental observations. Being easier to solve numerically, these two-dimensional equations are preferred to solving the full three-dimensional Navier-Stokes equations. Indeed, even if only the depth-averaged velocity field is computed, the results obtained from those simulations will prove to be sufficient in most of the cases.

However, the effects of the discrepancies between the depth-averaged and the local values of the velocities are occasionally suspected to have an influence on the computed depth-averaged velocity profile, mostly in the presence of strong helical secondary-currents. Such secondary currents will be encountered in the second part of this work, dedicated to the turbulent exchanges in a uniform flow. Therefore, for some computations, dispersion terms, taking into account these discrepancies, will be added to the Saint-Venant equations. The dispersions terms will also be significant when dealing with the Lateral Distribution Method, in Chapter 3. Since the inclusion of the dispersion terms in the Saint-Venant equations is not common, the complete derivation of these equations, including the additional terms, will be given here. A new model will also be proposed for the evaluation of these dispersion terms.

The Saint-Venant equations can be obtained either by depth-averaging the Navier-Stokes equations, or by writing the mass and momentum balances for a control volume. Although the latter is more intuitive, it is based on already depth-averaged velocities and the dispersion terms can not be derived through this approach. The depth-averaging approach will thus be used in this Chapter, following Yulistiyanto (1997) and Liggett (1994), while the momentum balance approach will be used in Chapter 4, for developing the one-dimensional Saint-Venant equations to be used by the Exchange Discharge Model.

2.2 Depth-averaging of the Navier-Stokes equations

2.2.1 Definitions, boundary conditions

The Navier-Stokes equations to be depth-averaged are the following (see e.g. Rodi 1980) :

$$\frac{\partial \bar{u}}{\partial x}+\frac{\partial \bar{v}}{\partial y}+\frac{\partial \bar{w}}{\partial z}=0 \tag{2.1a}$$

$$\begin{aligned}\frac{\partial \bar{u}}{\partial t}+\frac{\partial}{\partial x}\left(\bar{u}\,\bar{u}\right)+\frac{\partial}{\partial y}\left(\bar{u}\,\bar{v}\right)+\frac{\partial}{\partial z}\left(\bar{u}\,\bar{w}\right)=&-\frac{1}{\rho}\frac{\partial \bar{p}}{\partial x}+\upsilon\,\nabla^2\bar{u}\\ &-\left(\frac{\partial}{\partial x}\overline{u'u'}+\frac{\partial}{\partial y}\overline{u'v'}+\frac{\partial}{\partial z}\overline{u'w'}\right)\end{aligned} \tag{2.1b}$$

$$\begin{aligned}\frac{\partial \bar{v}}{\partial t}+\frac{\partial}{\partial x}\left(\bar{v}\,\bar{u}\right)+\frac{\partial}{\partial y}\left(\bar{v}\,\bar{v}\right)+\frac{\partial}{\partial z}\left(\bar{v}\,\bar{w}\right)=&-\frac{1}{\rho}\frac{\partial \bar{p}}{\partial y}+\upsilon\,\nabla^2\bar{v}\\ &-\left(\frac{\partial}{\partial x}\overline{v'u'}+\frac{\partial}{\partial y}\overline{v'v'}+\frac{\partial}{\partial z}\overline{v'w'}\right)\end{aligned} \tag{2.1c}$$

$$\begin{aligned}\frac{\partial \bar{w}}{\partial t}+\frac{\partial}{\partial x}\left(\bar{w}\,\bar{u}\right)+\frac{\partial}{\partial y}\left(\bar{w}\,\bar{v}\right)+\frac{\partial}{\partial z}\left(\bar{w}\,\bar{w}\right)=&-\frac{1}{\rho}\frac{\partial \bar{p}}{\partial z}-g+\upsilon\,\nabla^2\bar{w}\\ &-\left(\frac{\partial}{\partial x}\overline{w'u'}+\frac{\partial}{\partial y}\overline{w'v'}+\frac{\partial}{\partial z}\overline{w'w'}\right)\end{aligned} \tag{2.1d}$$

where x, y and z are respectively the longitudinal, transverse and vertical directions; u, v and w are the local velocity components, respectively in the x-, y- and z-directions (see Figure 2.1); p is the pressure; ρ is the density of water; g is the gravity constant; and υ is the molecular viscosity. A Reynolds averaging of the local velocity components has been used, where $\bar{u}$, $\bar{v}$ and $\bar{w}$ are the Reynolds averaged velocities; and u', v' and w' are their turbulent fluctuations, whose products define Reynolds turbulent stresses. In the present work, the shear stresses due to molecular viscosity will be neglected compared to the Reynolds stresses, as they are usually several order of magnitude smaller.

The depth-averaging will be performed along the z-direction, between the bed level z_b and the free-surface water level z_w. The depth-averaged longitudinal U and transverse V velocity components are thus defined as :

$$U=\frac{1}{H}\int_{z_b}^{z_w}\bar{u}\,dz \quad \text{and} \quad V=\frac{1}{H}\int_{z_b}^{z_w}\bar{v}\,dz \tag{2.2}$$

where $H = z_w - z_b$ is the water depth (see Figure 2.1).

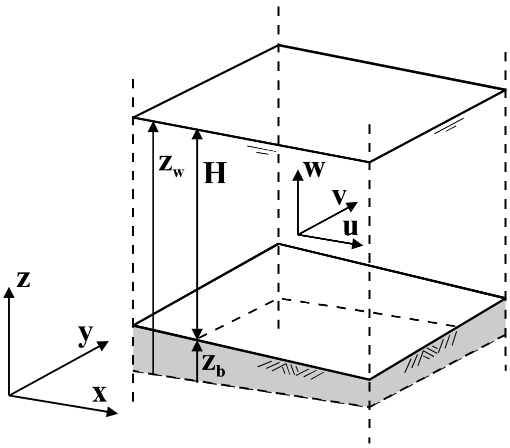

Figure 2.1 : Definition sketch of the axis directions and velocity components

The free-surface boundary condition is defined by assuming that a particle present on the surface at a given time will remain on it (Liggett 1994). The free-surface is thus defined by

$$S(x, y, z, t) = z_w(x, y, t) - z = 0 \tag{2.3}$$

simply expressing that the variable z gets the value z_w defining the free-surface. The substantial derivative D/Dt of this equation (2.3) equals zero, which means that a particle on the free-surface remains on the surface, giving thus

$$\begin{aligned}\frac{DS}{Dt} &= \frac{\partial}{\partial t}(z_w - z) + \overline{u_w}\frac{\partial}{\partial x}(z_w - z) + \overline{v_w}\frac{\partial}{\partial y}(z_w - z) + \overline{w_w}\frac{\partial}{\partial z}(z_w - z) \\ &= \frac{\partial z_w}{\partial t} + \overline{u_w}\frac{\partial z_w}{\partial x} + \overline{v_w}\frac{\partial z_w}{\partial y} - \overline{w_w} = 0\end{aligned} \tag{2.4}$$

where subscript w stands for free-surface values.

The bed boundary condition is obtained similarly :

$$\overline{u_b}\frac{\partial z_b}{\partial x} + \overline{v_b}\frac{\partial z_b}{\partial y} - \overline{w_b} = 0 \tag{2.5}$$

where subscript b stands for bed values, and where the temporal derivative of z_b equals zero, as a fix bed hypothesis is used.

Furthermore, a hydrostatic pressure distribution is assumed. This implies that, in the vertical momentum equation (2.1d), the vertical accelerations and the shear stresses are neglected compared to the pressure term. The equation is then simplified as

$$-\frac{1}{\rho}\frac{\partial \overline{p}}{\partial z} - g = 0 \tag{2.6}$$

and, by integrating over the depth, one obtains

$$\overline{p} = \rho g(z_w - z) + p_a \tag{2.7}$$

where the pressure p_a at the free-surface is set equal to zero.

2.2.2 Continuity equation

Integrating the continuity equation (2.1a) along the depth gives

$$\int_{z_b}^{z_w} \left(\frac{\partial \overline{u}}{\partial x} + \frac{\partial \overline{v}}{\partial y} + \frac{\partial \overline{w}}{\partial z} \right) dz = 0 \tag{2.8}$$

where the integration and differentiation operators have to be inverted using the Leibnitz rule :

$$\frac{\partial}{\partial t} \int_{a(y,t)}^{b(y,t)} f(x,y,t)\, dx = \int_{a(y,t)}^{b(y,t)} \frac{\partial f}{\partial t} dx - f(a,y,t) \frac{\partial a}{\partial t} + f(b,y,t) \frac{\partial b}{\partial t} \tag{2.9}$$

The three terms in the left-hand side of (2.8) are thus written as

$$\int_{z_b}^{z_w} \frac{\partial \overline{u}}{\partial x} dz = \frac{\partial}{\partial x} \int_{z_b}^{z_w} \overline{u}\, dz - \overline{u_w} \frac{\partial z_w}{\partial x} + \overline{u_b} \frac{\partial z_b}{\partial x} \tag{2.10a}$$

$$\int_{z_b}^{z_w} \frac{\partial \overline{v}}{\partial y} dz = \frac{\partial}{\partial y} \int_{z_b}^{z_w} \overline{v}\, dz - \overline{v_w} \frac{\partial z_w}{\partial y} + \overline{v_b} \frac{\partial z_b}{\partial y} \tag{2.10b}$$

$$\int_{z_b}^{z_w} \frac{\partial \overline{w}}{\partial z} dz = \overline{w_w} - \overline{w_b} \tag{2.10c}$$

Grouping again those three terms, and using the definitions of depth-averaged velocities U and V given by (2.2), the continuity equation becomes

$$\begin{aligned} \frac{\partial}{\partial x}(UH) + \frac{\partial}{\partial y}(VH) - \left(\overline{u_w} \frac{\partial z_w}{\partial x} + \overline{v_w} \frac{\partial z_w}{\partial y} - \overline{w_w} \right) \\ + \left(\overline{u_b} \frac{\partial z_b}{\partial x} + \overline{v_b} \frac{\partial z_b}{\partial y} - \overline{w_b} \right) = 0 \end{aligned} \tag{2.11}$$

Using the boundary conditions (2.4) and (2.5), one finally gets :

$$\frac{\partial H}{\partial t} + \frac{\partial}{\partial x}(UH) + \frac{\partial}{\partial y}(VH) = 0 \tag{2.12}$$

where the temporal derivative of the free-surface level z_w is replaced by the temporal derivative of the water depth H, as the bed level z_b remains fixed.

2.2.3 Momentum equation in the *x*-direction

When the momentum equation in the x-direction (2.1b) is integrated along the depth z, one obtains

$$\begin{aligned}\int_{z_b}^{z_w}\left(\frac{\partial \overline{u}}{\partial t}+\frac{\partial}{\partial x}\left(\overline{u}\,\overline{u}\right)+\frac{\partial}{\partial y}\left(\overline{u}\,\overline{v}\right)+\frac{\partial}{\partial z}\left(\overline{u}\,\overline{w}\right)\right)dz &= -\frac{1}{\rho}\int_{z_b}^{z_w}\frac{\partial \overline{p}}{\partial x}dz \\ &-\int_{z_b}^{z_w}\left(\frac{\partial}{\partial x}\overline{u'u'}+\frac{\partial}{\partial y}\overline{u'v'}+\frac{\partial}{\partial z}\overline{u'w'}\right)dz\end{aligned} \tag{2.13}$$

As for the continuity equation, the Leibnitz rule is used to invert the integration and derivation operators. Using the fixed bed hypothesis and the definition of depth-averaged longitudinal velocity U (2.2), the acceleration term – the first term in the left-hand side of (2.13) – gives

$$\int_{z_b}^{z_w}\frac{\partial \overline{u}}{\partial t}dz=\frac{\partial}{\partial t}\int_{z_b}^{z_w}\overline{u}\,dz-\overline{u_w}\frac{\partial z_w}{\partial t}+\overline{u_b}\frac{\partial z_b}{\partial t}=\frac{\partial}{\partial t}(UH)-\overline{u_w}\frac{\partial z_w}{\partial t} \tag{2.14}$$

The first convection term – the second term in the left-hand side of (2.13) – gives

$$\int_{z_b}^{z_w}\frac{\partial \overline{u}^2}{\partial x}dz=\frac{\partial}{\partial x}\int_{z_b}^{z_w}\overline{u}^2\,dz-\overline{u_w}^2\frac{\partial z_w}{\partial x}+\overline{u_b}^2\frac{\partial z_b}{\partial x} \tag{2.15}$$

The integration of the velocity product $\overline{u}^2$ in the first term of the right-hand side of (2.15) will generate the first dispersion term. Indeed, one expects to express this term as a function of the depth-averaged longitudinal velocity U. The local velocity $\overline{u}$ varies along the depth z (Figure 2.2). The depth-integration of its squared value is thus different from the square of the depth-averaged velocity U. Several authors suggest to use the so-called Boussinesq coefficient β in order to take into account this difference (Yen 1973; Liggett 1994) :

$$\int_{z_b}^{z_w}\overline{u}^2\,dz=\beta U^2 h \tag{2.16}$$

However, most of these authors then assume that this Boussinesq coefficient equals $\beta = 1$, neglecting thus the dispersion effect. In the present approach, the dispersion terms will rather be developed explicitly. Therefore, one uses the identity

$$\overline{u}=U+\left(\overline{u}-U\right) \tag{2.17}$$

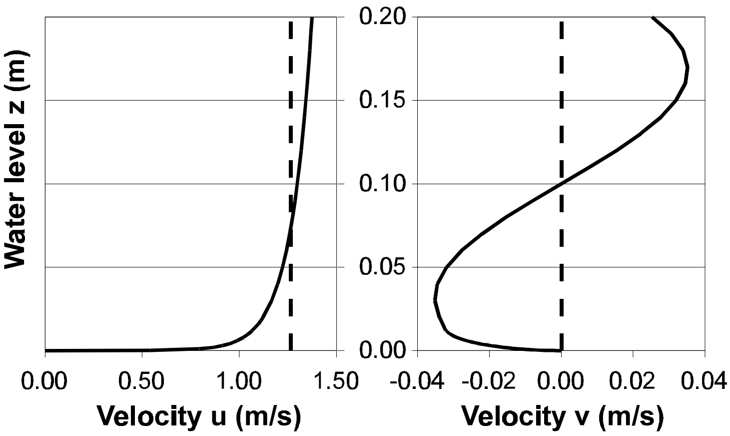

Figure 2.2 : Typical vertical velocity profiles

The integration of the square of $\bar{u}$ in (2.15) can be written as :

$$\int_{z_b}^{z_w} \bar{u}^2 \, dz = \int_{z_b}^{z_w} U^2 \, dz + 2\int_{z_b}^{z_w} \left(\bar{u}-U\right)U \, dz + \int_{z_b}^{z_w} \left(\bar{u}-U\right)^2 \, dz \tag{2.18}$$

where the second term in the right-hand side equals zero, as the integration of $\bar{u}$ along the depth equals U; and the third term is the so-called dispersion term. Equation (2.15) finally gives

$$\int_{z_b}^{z_w} \frac{\partial \bar{u}^2}{\partial x} dz = \frac{\partial}{\partial x} U^2 H + \frac{\partial}{\partial x} \int_{z_b}^{z_w} \left(\bar{u}-U\right)^2 dz - \overline{u_w}^2 \frac{\partial z_w}{\partial x} + \overline{u_b}^2 \frac{\partial z_b}{\partial x} \tag{2.19}$$

In the same way, the second convection term in (2.13) becomes

$$\int_{z_b}^{z_w} \frac{\partial}{\partial y}\left(\bar{u}\,\bar{v}\right) dz = \frac{\partial}{\partial y}\left(UVH\right) + \frac{\partial}{\partial y} \int_{z_b}^{z_w} \left(\bar{u}-U\right)\left(\bar{v}-V\right) dz - \bar{u}_w \bar{v}_w \frac{\partial z_w}{\partial y} + \bar{u}_b \bar{v}_b \frac{\partial z_b}{\partial y} \tag{2.20}$$

and the third convection term of (2.13) simplifies to

$$\int_{z_b}^{z_w} \frac{\partial \bar{u}\,\bar{w}}{\partial z} dz = \bar{u}_w \bar{w}_w - \bar{u}_b \bar{w}_b \tag{2.21}$$

The Leibnitz rule applied to the pressure term in (2.13) – first term in the right-hand side – gives :

$$\frac{1}{\rho} \int_{z_b}^{z_w} \frac{\partial \bar{p}}{\partial x} dz = \frac{1}{\rho} \frac{\partial}{\partial x} \int_{z_b}^{z_w} \bar{p} \, dz - \frac{\overline{p_w}}{\rho} \frac{\partial z_w}{\partial x} + \frac{\overline{p_b}}{\rho} \frac{\partial z_b}{\partial x} \tag{2.22}$$

Using the hydrostatic pressure distribution (2.7), this term becomes

$$
\begin{aligned}
\frac{1}{\rho}\int_{z_b}^{z_w}\frac{\partial \overline{p}}{\partial x}dz &= \frac{1}{\rho}\frac{\partial}{\partial x}\int_{z_b}^{z_w}\rho g(z_w - z)dz - \frac{\rho g(z_w - z_w)}{\rho}\frac{\partial z_w}{\partial x} + \frac{\rho g(z_w - z_b)}{\rho}\frac{\partial z_b}{\partial x} \\
&= g\frac{\partial}{\partial x}\left(z_w(z_w - z_b) - \frac{1}{2}\left(z_w^2 - z_b^2\right)\right) + gH\frac{\partial z_b}{\partial x} \\
&= g\frac{\partial}{\partial x}\tfrac{1}{2}H^2 + gH\frac{\partial z_b}{\partial x}
\end{aligned}
\tag{2.23}
$$

where the x-direction (longitudinal) channel bed slope can be defined as

$$
S_{0x} = -\frac{\partial z_b}{\partial x} \tag{2.24}
$$

Lastly, using again the Leibnitz rule, the shear-stress terms become :

$$
\begin{aligned}
\int_{z_b}^{z_w}\left(\frac{\partial}{\partial x}\overline{u'u'} + \frac{\partial}{\partial y}\overline{u'v'} + \frac{\partial}{\partial z}\overline{u'w'}\right)dz &= \frac{\partial}{\partial x}\int_{z_b}^{z_w}\overline{u'u'}\,dz - \left(\overline{u'u'}\right)_w\frac{\partial z_w}{\partial x} + \left(\overline{u'u'}\right)_b\frac{\partial z_b}{\partial x} \\
&\quad + \frac{\partial}{\partial y}\int_{z_b}^{z_w}\overline{u'v'}\,dz - \left(\overline{u'v'}\right)_w\frac{\partial z_w}{\partial y} + \left(\overline{u'v'}\right)_b\frac{\partial z_b}{\partial y} \\
&\quad + \left(\overline{u'w'}\right)_w - \left(\overline{u'w'}\right)_b
\end{aligned}
\tag{2.25}
$$

It is then assumed that the shear stress at the free-surface is negligible. The second, fifth and seventh term in the right-hand side of (2.25) equal thus zero. On the other hand, regarding the shear stresses at the bed, the third and sixth terms (stresses along vertical planes) will be assumed negligible compared to the eightieth term (stress along the horizontal plane). The shear stress terms (2.25) reduce thus to

$$
\begin{aligned}
\int_{z_b}^{z_w}\left(\frac{\partial}{\partial x}\overline{u'u'} + \frac{\partial}{\partial y}\overline{u'v'} + \frac{\partial}{\partial z}\overline{u'w'}\right)dz &= \frac{\partial}{\partial x}\int_{z_b}^{z_w}\overline{u'u'}\,dz + \frac{\partial}{\partial y}\int_{z_b}^{z_w}\overline{u'v'}\,dz - \left(\overline{u'w'}\right)_b \\
&= \frac{\partial}{\partial x}\int_{z_b}^{z_w}\overline{u'u'}\,dz + \frac{\partial}{\partial y}\int_{z_b}^{z_w}\overline{u'v'}\,dz + \frac{\tau_b}{\rho}
\end{aligned}
\tag{2.26}
$$

where the bed shear stress τ_b is also expressed as

$$
\frac{\tau_b}{\rho} = g\,H\,S_{fx} \tag{2.27}
$$

defining S_{fx} as the head slope in the x-direction.

The depth-averaged x-wise momentum equation (2.13) is obtained by the addition of (2.14), (2.19), (2.20), (2.21), (2.23) and (2.26) :

$$\begin{aligned}
&\frac{\partial}{\partial t}(UH)+\frac{\partial}{\partial x}\left(U^2H\right)+\frac{\partial}{\partial y}(UVH)+\frac{\partial}{\partial x}\int_{z_b}^{z_w}\left(\overline{u}-U\right)^2\,dz+\frac{\partial}{\partial y}\int_{z_b}^{z_w}\left(\overline{u}-U\right)\left(\overline{v}-V\right)dz\\
&-\overline{u_w}\left(\frac{\partial z_w}{\partial t}+\overline{u_w}\frac{\partial z_w}{\partial x}+\overline{v_w}\frac{\partial z_w}{\partial y}-\overline{w_w}\right)+\overline{u_b}\left(\overline{u_b}\frac{\partial z_b}{\partial x}+\overline{v_b}\frac{\partial z_b}{\partial y}-\overline{w_b}\right)\\
&=-g\frac{\partial}{\partial x}\tfrac{1}{2}H^2-gH\frac{\partial z_b}{\partial x}-\frac{\partial}{\partial x}\int_{z_b}^{z_w}\overline{u'u'}\,dz-\frac{\partial}{\partial y}\int_{z_b}^{z_w}\overline{u'v'}\,dz-\frac{\tau_b}{\rho}
\end{aligned}\tag{2.28}$$

where the two last terms of the left-hand side equal zero, due to the boundary conditions at the free surface (2.4) and the bed (2.5). Using the definitions (2.24) of the bed slope S_{0x} and (2.27) of energy slope S_{fx}, and grouping the x-derivatives, one obtains

$$\begin{aligned}
&\frac{\partial}{\partial t}(UH)+\frac{\partial}{\partial x}\left(U^2H+\tfrac{1}{2}gH^2\right)+\frac{\partial}{\partial y}(UVH)=gH\left(S_{0x}-S_{fx}\right)\\
&-\frac{\partial}{\partial x}\int_{z_b}^{z_w}\overline{u'u'}\,dz-\frac{\partial}{\partial y}\int_{z_b}^{z_w}\overline{u'v'}\,dz-\frac{\partial}{\partial x}\int_{z_b}^{z_w}\left(\overline{u}-U\right)^2\,dz-\frac{\partial}{\partial y}\int_{z_b}^{z_w}\left(\overline{u}-U\right)\left(\overline{v}-V\right)dz
\end{aligned}\tag{2.29}$$

The so-called "non-conservative" form of (2.29) is obtained by subtracting the continuity equation (2.12) multiplied by U, and by dividing the resulting equation by H :

$$\begin{aligned}
\frac{\partial U}{\partial t}+U\frac{\partial U}{\partial x}+V\frac{\partial U}{\partial y}&=g\left(S_{0x}-S_{fx}\right)-g\frac{\partial H}{\partial x}\\
&-\frac{1}{H}\frac{\partial}{\partial x}\int_{z_b}^{z_w}\overline{u'u'}\,dz-\frac{1}{H}\frac{\partial}{\partial y}\int_{z_b}^{z_w}\overline{u'v'}\,dz\\
&-\frac{1}{H}\frac{\partial}{\partial x}\int_{z_b}^{z_w}\left(\overline{u}-U\right)^2\,dz-\frac{1}{H}\frac{\partial}{\partial y}\int_{z_b}^{z_w}\left(\overline{u}-U\right)\left(\overline{v}-V\right)dz
\end{aligned}\tag{2.30}$$

Depth-averaged shear stresses τ_{xx} and τ_{xy} can be defined as :

$$\frac{\tau_{xx}}{\rho}=-\frac{1}{H}\int_{z_b}^{z_w}\overline{u'u'}\,dz\quad\text{and}\quad\frac{\tau_{xy}}{\rho}=-\frac{1}{H}\int_{z_b}^{z_w}\overline{u'v'}\,dz\tag{2.31}$$

Writing back the bed slope S_{0x} as a function of z_b, one gets at last

$$\begin{aligned}
\frac{\partial U}{\partial t}+U\frac{\partial U}{\partial x}+V\frac{\partial U}{\partial y}&=-g\frac{\partial z_w}{\partial x}-gS_{fx}+\frac{1}{H}\frac{\partial}{\partial x}\left(H\frac{\tau_{xx}}{\rho}\right)+\frac{1}{H}\frac{\partial}{\partial y}\left(H\frac{\tau_{xy}}{\rho}\right)\\
&-\frac{1}{H}\frac{\partial}{\partial x}\int_{z_b}^{z_w}\left(\overline{u}-U\right)^2\,dz-\frac{1}{H}\frac{\partial}{\partial y}\int_{z_b}^{z_w}\left(\overline{u}-U\right)\left(\overline{v}-V\right)dz
\end{aligned}\tag{2.32}$$

2.2.4 Synthesis

As a result, the Saint-Venant equations can be summarised as (Yulistianto 1997) :

$$\frac{\partial H}{\partial t}+\frac{\partial}{\partial x}(UH)+\frac{\partial}{\partial y}(VH)=0 \tag{2.33a}$$

$$\begin{aligned}\frac{\partial U}{\partial t}+U\frac{\partial U}{\partial x}+V\frac{\partial U}{\partial y}=-g\frac{\partial z_w}{\partial x}-gS_{fx}+\frac{1}{H}\frac{\partial}{\partial x}\left(H\frac{\tau_{xx}}{\rho}\right)+\frac{1}{H}\frac{\partial}{\partial y}\left(H\frac{\tau_{xy}}{\rho}\right)\\ -\frac{1}{H}\frac{\partial}{\partial x}\int_{z_b}^{z_w}\left(\bar{u}-U\right)^2 dz-\frac{1}{H}\frac{\partial}{\partial y}\int_{z_b}^{z_w}\left(\bar{u}-U\right)\left(\bar{v}-V\right)dz\end{aligned} \tag{2.33b}$$

$$\begin{aligned}\frac{\partial V}{\partial t}+U\frac{\partial V}{\partial x}+V\frac{\partial V}{\partial y}=-g\frac{\partial z_w}{\partial y}-gS_{fy}+\frac{1}{H}\frac{\partial}{\partial x}\left(H\frac{\tau_{yx}}{\rho}\right)+\frac{1}{H}\frac{\partial}{\partial y}\left(H\frac{\tau_{yy}}{\rho}\right)\\ -\frac{1}{H}\frac{\partial}{\partial x}\int_{z_b}^{z_w}\left(\bar{u}-U\right)\left(\bar{v}-V\right)dz-\frac{1}{H}\frac{\partial}{\partial y}\int_{z_b}^{z_w}\left(\bar{v}-V\right)^2 dz\end{aligned} \tag{2.33c}$$

where (2.33a) is the continuity equation (2.12); (2.33b) is the x-wise momentum equation (2.32); and (2.33c) is the y-wise momentum equation, obtained similarly to (2.32).

The same equations are given by Rodi (1980), including the dispersion terms, but with an opposite sign than in (2.33). As the dispersion terms development is not given, one can presume that the sign given by Rodi is erroneous. However, Rodi then assumes that those terms can be neglected in most cases, concurring thus with the authors who present a Boussinesq coefficient β (2.16) then taken equal to 1, as already pointed out (Yen 1973; Liggett 1994).

The next paragraphs of this chapter present the models that will be used for the bed friction terms S_{fx} and S_{fy}; for the turbulent shear stresses τ_{xx}, τ_{xy}, τ_{yx} and τ_{yy}; and for the dispersion terms.

2.3 Bed friction modelling

Several models of the head losses due to bed friction, expressed as energy slope S_{fx} and S_{fy} (2.27), have been proposed. Two of them will be used in the present work : the Manning equation and the Darcy-Weisbach equation. The Manning equation, developed empirically and of easy use (Manning 1889), is widely used by practitioners. Extensive tables of Manning-coefficient values are provided. It should nevertheless be pointed out that Manning equation is strictly valid only for rough flow, and that, in some cases, the Manning coefficient can be found to vary with water depth. On the other hand, the Darcy-Weisbach equation reflects more clearly the relation between roughness and turbulence regime, as it has been developed from simple pipe flow experiments (French

1985). As this work intends to meet practical concerns, the Manning equation will be preferred. However, the Darcy-Weisbach equation will sometimes be used concurrently, for comparison purposes, as it was also used by several authors.

For a uniform flow (i.e. water surface parallel to the bed, i.e. energy slope S_{fx} is equal to the bed slope S_0), the one-dimensional Manning formula (1.3) is written as :

$$U = \frac{R^{2/3}}{n} S_0^{1/2} \tag{2.34}$$

where U is, in this case, the mean section velocity (total discharge Q divided by the cross-section area A); R is the cross-section hydraulic radius (ratio between cross-section area A and wetted perimeter P); and n is the Manning roughness coefficient.

For non-uniform flow, it is classically assumed that the energy slope S_f equals the bed slope S_0 of a channel in which a uniform flow occurs at the same discharge and with the same cross-section area (French 1985).

For two-dimensional modelling, the hydraulic radius in a given zone can be estimated as equal to the local water-depth H, as far as the transverse bed slope remains small. Separating both x-wise and y-wise components of the friction slope, the Manning equation can be written as :

$$S_{fx} = \frac{n^2 U \sqrt{U^2 + V^2}}{H^{4/3}} \quad \text{and} \quad S_{fy} = \frac{n^2 V \sqrt{U^2 + V^2}}{H^{4/3}} \tag{2.35}$$

where U and V stand now again for the depth-averaged velocities.

The Darcy-Weisbach equation is given as :

$$U = \sqrt{\frac{8g}{f}} R^{1/2} S_0^{1/2} \tag{2.36}$$

where f is the dimensionless Darcy-Weisbach friction coefficient. For two-dimensional flow, one writes similarly :

$$S_{fx} = \frac{f U \sqrt{U^2 + V^2}}{8gH} \quad \text{and} \quad S_{fy} = \frac{f V \sqrt{U^2 + V^2}}{8gH} \tag{2.37}$$

Besides the energy slope, the bed shear velocity U^* should also be estimated using the friction models. Indeed, the value of U^* is required by the turbulence models presented in the next subsection. The shear velocity is defined as a function of the bed shear stress τ_b (2.27) :

$$U^* = \sqrt{\frac{\tau_b}{\rho}} = \sqrt{gRS_0} \tag{2.38}$$

It can also be expressed as

$$U^* = \sqrt{c_f\left(U^2 + V^2\right)} \tag{2.39}$$

where c_f is a friction factor, to be estimated either by the Manning equation (2.35) or by the Darcy-Weisbach equation (2.37) :

$$c_f = \frac{gn^2}{H^{1/3}} = \frac{f}{8} \tag{2.40}$$

2.4 Turbulent shear stress modelling

2.4.1 Boussinesq eddy viscosity

The depth-averaged Reynolds shear stress terms in the Saint-Venant equations (2.33) are modelled using the Boussinesq eddy viscosity concept. In analogy with molecular viscosity, the shear stresses are assumed to be proportional to the Reynolds-averaged velocity gradients (Rodi 1980) :

$$\frac{\tau_{ij}}{\rho} = -\overline{u_i' u_j'} = \upsilon_t\left(\frac{\partial \overline{u_i}}{\partial x_j} + \frac{\partial \overline{u_j}}{\partial x_i}\right) - \frac{2}{3}\delta_{ij}k \tag{2.41}$$

where υ_t is the eddy viscosity; δ_{ij} is the Kronecker symbol ($\delta_{ij} = 1$ for i = j; and $\delta_{ij} = 0$ for i ≠ j); and k is the kinetic turbulent energy.

For the depth-averaged shear stresses, the Boussinesq assumption is written as :

$$\frac{\tau_{xx}}{\rho} = 2\upsilon_t\left(\frac{\partial U}{\partial x}\right) - \frac{2}{3}k\,;\quad \frac{\tau_{xy}}{\rho} = \frac{\tau_{yx}}{\rho} = \upsilon_t\left(\frac{\partial U}{\partial y} + \frac{\partial V}{\partial x}\right)$$

$$\text{and}\quad \frac{\tau_{yy}}{\rho} = 2\upsilon_t\left(\frac{\partial V}{\partial y}\right) - \frac{2}{3}k \tag{2.42}$$

The eddy viscosity υ_t is either assumed constant; or estimated by an algebraic equation or by a one- or two-equations model. Such models are presented next, according to Rodi (1980).

2.4.2 Algebraic models

The easiest eddy viscosity model would be the constant eddy viscosity model. However, it is expected that this constant eddy viscosity will vary with the flow conditions : a different value has to be estimated for each location and time. Such a model has thus only a limited application range. It has only been used in the first stage of the numerical program testing, but not in practical computations.

For a shallow-water flow, the bed friction may be the main source of turbulence. In this case, a widely used turbulence model for depth-averaged modelling assumes that the eddy-viscosity is proportional to this bed friction, estimated through the shear velocity U^* (2.38), and to the water-depth H :

$$\upsilon_t = \lambda U^* H \tag{2.43}$$

where λ is an adimensional eddy-viscosity factor ($\lambda \approx 0.135$ for wide laboratory flumes, according to Rodi 1980; $\lambda \approx 0.16$ for laboratory flumes, $\lambda = 0.6$ .. 2.0 in natural rivers, according to Wark *et al.* 1990)

If the main turbulence source to be considered is the transverse shearing, the Prandtl mixing length concept may be used, for example in its simplified form :

$$\upsilon_t = l_m^2 \left| \frac{\partial U}{\partial y} \right| \tag{2.44}$$

where l_m is the mixing length. This mixing length equation will not be used in the two-dimensional computations presented in this work, but it will be referred to in both Chapter 3 and Chapter 4, regarding respectively the LDM and the Exchange Discharge Model development.

2.4.3 One- and two-equation models (*k-l* and *k*-e)

Rastogi and Rodi (1978) propose a depth-averaged version of the classical tri-dimensional k-ε model by Launder and Spalding (1974). In this model, the turbulent kinetic energy k is related to the large-scale turbulent motion and to the turbulence velocity-scale, while the dissipation ε is related to the turbulence length-scale. The latter corresponds to the smaller scale where dissipation due to molecular viscosity occurs, controlling thus the whole energy dissipation process.

The eddy viscosity is estimated by

$$\upsilon_t = c_\mu \frac{k^2}{\varepsilon} \tag{2.45}$$

where $c_\mu = 0.09$ is a constant. The depth-averaged kinetic energy k and dissipation ε are estimated through two semi-empirical transport equations :

$$\frac{\partial k}{\partial t}+U\frac{\partial k}{\partial x}+V\frac{\partial k}{\partial y}=\frac{1}{H}\frac{\partial}{\partial x}\left(H\frac{\upsilon_t}{\sigma_k}\frac{\partial k}{\partial x}\right)+\frac{1}{H}\frac{\partial}{\partial y}\left(H\frac{\upsilon_t}{\sigma_k}\frac{\partial k}{\partial y}\right)+P_h+P_{kv}-\varepsilon \tag{2.46a}$$

$$\frac{\partial \varepsilon}{\partial t}+U\frac{\partial \varepsilon}{\partial x}+V\frac{\partial \varepsilon}{\partial y}=\frac{1}{H}\frac{\partial}{\partial x}\left(H\frac{\upsilon_t}{\sigma_\varepsilon}\frac{\partial \varepsilon}{\partial x}\right)+\frac{1}{H}\frac{\partial}{\partial y}\left(H\frac{\upsilon_t}{\sigma_\varepsilon}\frac{\partial \varepsilon}{\partial y}\right)+c_{1\varepsilon}\frac{\varepsilon}{k}P_h+P_{\varepsilon v}-c_{2\varepsilon}\frac{\varepsilon^2}{k} \tag{2.46b}$$

where σ_k, σ_ε, $c_{1\varepsilon}$ and $c_{2\varepsilon}$ are constants, whose values are given in Table 2.1. The significance of the terms in both (2.46a) and (2.46b) can be described as follows (Rodi 1980) : the left-hand side terms stand for the temporal variation and for the transport by convection of the variables k and ε. The two first terms in the right-hand side of the equations stand for the turbulent diffusion of the variables. The P_h term corresponds to the turbulent kinetic energy production, due to the interaction between the turbulent shear stress and the depth-averaged velocity gradient :

$$P_h=\upsilon_t\left[2\left(\frac{\partial U}{\partial x}\right)^2+2\left(\frac{\partial V}{\partial y}\right)^2+\left(\frac{\partial U}{\partial y}+\frac{\partial V}{\partial x}\right)^2\right] \tag{2.47}$$

The terms P_{kv} and $P_{\varepsilon v}$ are source terms, who absorb all the secondary terms originating from non-uniformity of vertical profiles. The main contribution to these terms arises from significant vertical velocity gradients near the bed : they express therefore the turbulent kinetic energy production due to bed friction; and Rastogi and Rodi (1978) assume they are related to the shear velocity U^* (2.38) :

$$P_{kv}=c_k\frac{U^{*3}}{H}\quad\text{with}\quad c_k=\frac{1}{\sqrt{c_f}} \tag{2.48a}$$

$$P_{\varepsilon v}=c_\varepsilon\frac{U^{*4}}{H^2}\quad\text{with}\quad c_\varepsilon=3.6\frac{c_{2\varepsilon}}{c_f^{3/4}}\sqrt{c_\mu} \tag{2.48b}$$

where c_f is the friction coefficient as defined by (2.40); and $c_{2\varepsilon}$ and c_μ are the constants introduced in (2.45) and (2.46).

Table 2.1 : Values of the constants in the depth-averaged k-ε model (Rodi 1980)

c_μ	σ_k	σ_ε	$c_{1\varepsilon}$	$c_{2\varepsilon}$
0.09	1.0	1.3	1.44	1.92

Nadaoka et Yagi (1998) developed a depth-averaged modelling of periodical turbulent structures, that will be presented and used in Chapter 8. Their computation is founded on a one-equation model, which is a simplification of the complete k-ε model. The turbulent kinetic energy k is estimated through the transport equation (2.46a); while the turbulence length-scale l_d is defined algebraically. This length-scale is assumed to be proportional to the water depth h, as the bed friction is the main turbulence source :

$$l_d = \xi\, H \tag{2.49}$$

where ξ is a constant. Nadaoka and Yagi suggest a value around $\xi = 0.1$. The dissipation ε, whose value is to be given in (2.46a), is estimated as :

$$\varepsilon = c_d \frac{k^{3/2}}{l_d} \tag{2.50}$$

where $c_d = 0.17$ is a constant. Using (2.50) in the eddy viscosity υ_t definition (2.45), the latter can be directly related to the kinetic energy k and to the length-scale l_d :

$$\upsilon_t = \frac{c_\mu}{c_d} k^{1/2} l_d = c'_d\, k^{1/2} l_d \tag{2.51}$$

where $c'_d = c_\mu / c_d = 0.17/0.09$ is a constant.

2.5 Dispersion terms modelling

The dispersion terms that appear in the Saint-Venant equations (2.33) take into account the effect of non-uniformity of the vertical profiles of local velocity components u and v (Figure 2.2). This non-uniformity results from the bed friction effect for the longitudinal velocity component u; and from the secondary currents development for the transverse velocity component v. The process of generation of secondary currents will be browsed further in Chapter 9, dedicated to the effect of the dispersion terms on the computed velocity profile. However, it can already be pointed out that two main sources of secondary currents are identified (Nezu and Nakagawa 1993). The so-called secondary currents of Prandtl's first kind are driven by centrifugal force and are observed in non-uniform flow, mostly in curved channels (Figure 2.3a); while secondary currents of Prandtl's second kind are turbulence-driven secondary currents : they are observed even in uniform flow and are due to non-homogeneity and anisotropy of turbulence (Figure 2.3b).

Yulistianto (1997; Yulistianto et al. 1998) developed a dispersion-term model dedicated to curved flow around a cylinder, thus relevant for secondary currents of first kind. In this model, the dispersion terms are written as diffusion terms, and are thus proportional to derivatives of the depth-averaged velocities U and V. In the present study, only secondary currents of second kind will be considered, because the flow is uniform and the depth-averaged transverse velocity V equals zero. This discards thus Yulistianto's expressions.

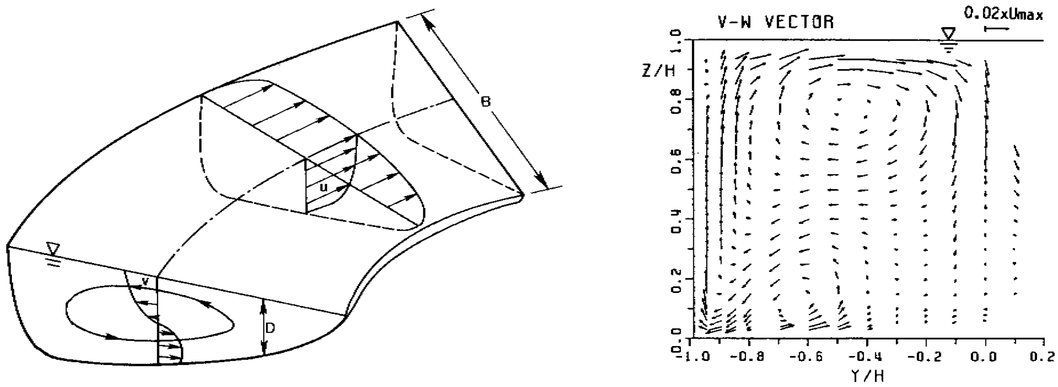

(a) *(b)*

Figure 2.3 : Secondary currents (a) of first kind, in a curved channel (Chang, 1988); (b) of second kind for a uniform flow (Nezu et Nakagawa, 1993)

A new dispersion model is thus proposed. On one hand, a proportionality relation clearly exists between the local velocities u and the depth-averaged velocity U. On the other hand, as discussed in Chapter 9, the turbulence non-homogeneity, that generates secondary currents of second kind, mainly depends on the longitudinal velocity U. The intensity of secondary currents and, as a consequence, the transverse velocity v value, will both be proportional to this longitudinal velocity U (Bousmar and Zech 2001a).

As a result, it is suggested to estimate the dispersion terms as a function of the square of this depth-averaged longitudinal velocity U, by defining three proportionality factors :

$$\int_{z_b}^{z_w} \left(\bar{u} - U\right)^2 dz = \chi_{uu} U^2 H \tag{2.52a}$$

$$\int_{z_b}^{z_w} \left(\bar{u} - U\right)\left(\bar{v} - V\right) dz = \chi_{uv} U^2 H \tag{2.52b}$$

$$\int_{z_b}^{z_w} \left(\bar{v} - V\right)^2 dz = \chi_{vv} U^2 H \tag{2.52c}$$

where the proportionality factors χ_{uu}, χ_{uv} and χ_{vv} will be called dispersion coefficients.

Using this dispersion term model, the Saint-Venant equations (2.33) are finally written as :

$$\frac{\partial H}{\partial t} + \frac{\partial}{\partial x}(UH) + \frac{\partial}{\partial y}(VH) = 0 \tag{2.53a}$$

$$\frac{\partial U}{\partial t}+U\frac{\partial U}{\partial x}+V\frac{\partial U}{\partial y}=-g\frac{\partial z}{\partial x}-gS_{fx}+\frac{1}{H}\frac{\partial}{\partial x}\left(H\frac{\tau_{xx}}{\rho}\right)+\frac{1}{H}\frac{\partial}{\partial y}\left(H\frac{\tau_{xy}}{\rho}\right)$$
$$-\frac{1}{H}\frac{\partial}{\partial x}\left(\chi_{uu}U^{2}H\right)-\frac{1}{H}\frac{\partial}{\partial y}\left(\chi_{uv}U^{2}H\right) \tag{2.53b}$$

$$\frac{\partial V}{\partial t}+U\frac{\partial V}{\partial x}+V\frac{\partial V}{\partial y}=-g\frac{\partial z}{\partial y}-gS_{fy}+\frac{1}{H}\frac{\partial}{\partial x}\left(H\frac{\tau_{yx}}{\rho}\right)+\frac{1}{H}\frac{\partial}{\partial y}\left(H\frac{\tau_{yy}}{\rho}\right)$$
$$-\frac{1}{H}\frac{\partial}{\partial x}\left(\chi_{uv}U^{2}H\right)-\frac{1}{H}\frac{\partial}{\partial y}\left(\chi_{vv}U^{2}H\right) \tag{2.53c}$$

2.6 Numerical modelling

Two numerical models will be used to solve the Saint-Venant equations. Both are classical finite differences models, based on a Mac-Cormack integration scheme, insuring second order precision in both space and time.

The first one is written for a staggered grid, insuring a very good mass and momentum conservation during the resolution. Such a condition is required for the uniform flow modelling with cyclic boundary condition, to be performed in the second part of this work. The second model is written for a curvilinear collocated grid. As the mesh is collocated, some continuity and surface instability problems will be faced. However, the curvilinear grid is required in order to perform computations with boundary fitted mesh for the non-prismatic geometries investigated in the third part of this work. Indeed, it turned out to be too difficult to build this curvilinear grid using a staggered mesh and finite differences, at least within the frame of this work. The discretisation of the equations, together with additional details on the numerical models are provided in Appendix 1.

Chapter 3
The Lateral Distribution Method

3.1 Introduction

The transverse distribution of the depth-averaged longitudinal velocity U is of primary interest when modelling compound channel flow. This distribution can be obtained from the two-dimensional Saint-Venant equations developed in the previous Chapter. However, this can be costly as it requires the complete resolution of a set of partial derivative equations. For cases where only the transverse distribution of velocity is needed, instead of the whole two-dimensional velocity field, several authors suggested to use a simplified method aimed solely at the determination of this distribution. The so-called Lateral Distribution Method (LDM) is derived from a depth-averaging of the Navier-Stokes momentum-conservation equation in the streamwise direction. Assuming a permanent uniform flow, this equation reduces to a single ordinary differential equation, which is easier to solve (Wormleaton 1988, Knight et al. 1989, Wark et al. 1990).

As quoted in Chapter 1 – State of the art, the basic LDM equation takes into account the effects of bed friction and of lateral turbulent friction. Shiono and Knight (1990) proposed an extended equation, considering also the helical secondary-currents effect, resulting in a better prediction of the bed shear-stress distribution. Ervine et al. (2000) recently suggested a secondary-current term formulation also adapted for flow in non-prismatic channels. Unfortunately, none of the proposed secondary-current terms has a clear physical meaning. Their calibration rests thus on partly empirical formulations and can sometimes be tedious.

In the present chapter, a new extension of the LDM to non-prismatic compound channels is proposed, where the physical meaning of the secondary current term is tentatively clarified. The classical LDM is first derived from the depth-averaging of simplified Navier-Stokes equations. The proposed extended LDM is then obtained by directly simplifying the Saint-Venant equations with dispersion terms, as obtained in the previous Chapter. The possible significance of several terms due to the non-prismaticity is highlighted.

The secondary current term significance in prismatic flow will be further discussed in Chapter 9, where secondary-currents effect in uniform flow is modelled through dispersion terms. The proposed extended LDM will be tested in Chapter 13, by using new data from experiments in non-prismatic channels.

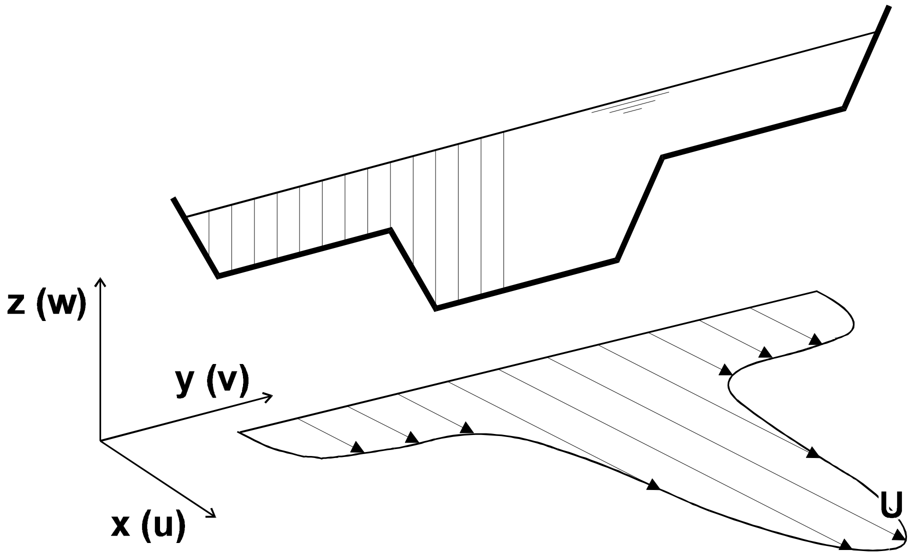

Figure 3.1 : Lateral Distribution Method : reference and variable definition

3.2 Derivation of the Lateral Distribution Method

3.2.1 Simplification and depth-averaging of the Navier-Stokes equations

One of the first LDM presented is due to Knight et al. (1989), who developed it on the basis of the streamwise momentum Navier-Stokes equation (2.1b), rewritten with z normal to the bed rather than vertical :

$$\rho\left(\frac{\partial \bar{u}}{\partial t}+\frac{\partial}{\partial x}\bar{u}^2+\frac{\partial}{\partial y}\left(\bar{u}\,\bar{v}\right)+\frac{\partial}{\partial z}\left(\bar{u}\,\bar{w}\right)\right)=\rho X-\frac{\partial \bar{p}}{\partial x}+\rho\upsilon\,\nabla^2\bar{u}$$
$$-\rho\left(\frac{\partial}{\partial x}\overline{u'u'}+\frac{\partial}{\partial y}\overline{u'v'}+\frac{\partial}{\partial z}\overline{u'w'}\right) \qquad (3.1)$$

where ($\bar{u}$, $\bar{v}$, $\bar{w}$) are Reynolds averaged local velocity components, respectively in the x- (streamwise, parallel to the bed), y- (lateral) and z- (normal to bed) directions (Figure 3.1); ρ is the density of water; X is the x-wise component of gravitational forces which equals the longitudinal bed slope S_{0x} time the gravity constant g; p is the pressure; υ is the molecular viscosity; and ($-\rho\overline{u'u'}$, $-\rho\overline{u'v'}$, $-\rho\overline{u'w'}$) are the Reynolds turbulent shear stresses.

This momentum equation (3.1) is then simplified by assuming a permanent ($\partial/\partial t=0$) and uniform ($\partial/\partial x=0$) flow; and by neglecting the viscous friction $\left(\upsilon\nabla^2\bar{u}\right)$ in regard of the Reynolds stresses :

$$\rho\left(\frac{\partial}{\partial y}\left(\overline{u}\,\overline{v}\right)+\frac{\partial}{\partial z}\left(\overline{u}\,\overline{w}\right)\right)=\rho g S_{0x}+\frac{\partial}{\partial y}\left(-\rho\,\overline{u'v'}\right)+\frac{\partial}{\partial z}\left(-\rho\,\overline{u'w'}\right) \tag{3.2}$$

This simplified equation (3.2) expresses the balance between gravitational driving force and momentum transfer resulting from both secondary currents (left-hand side) and turbulent exchanges (Reynolds stresses in the right-hand side).

This equation (3.2) is now depth-averaged, by integration in the normal direction z, over the water depth H, between the bed level z_b and the free-surface water level z_w. The bed level z_b can vary across the channel width; while the water level is assumed to be horizontal in the transverse direction ($\partial z_w/\partial y = 0$), as a consequence of a one-dimensional flow hypothesis.

For the depth-integration of the first convection term (left-hand side of 3.2), the differentiation and integral operators are inverted using the Leibnitz rule (2.9) :

$$\int_{z_b(y)}^{z_w(y)} \rho\,\frac{\partial}{\partial y}\left(\overline{u}\,\overline{v}\right)dz=\frac{\partial}{\partial y}\int_{z_b(y)}^{z_w(y)}\rho\,\overline{u}\,\overline{v}\,dz-\rho\left(\overline{u}\,\overline{v}\right)_{(z_w,y)}\frac{\partial z_w}{\partial y}+\rho\left(\overline{u}\,\overline{v}\right)_{(z_b,y)}\frac{\partial z_b}{\partial y} \tag{3.3}$$

where the two last terms equal zero, as the velocity on the bed is supposed null ($(\overline{u}\,\overline{v})_{z_b}=0$) and as the water surface is assumed horizontal in the transverse direction ($\partial z_w/\partial y = 0$).

The second convection term in the left-hand side of (3.2) equals zero, as the vertical component of the velocity w is null on both the channel bed and the water surface :

$$\int_{z_b}^{z_w}\frac{\partial}{\partial z}\left(\overline{u}\,\overline{w}\right)dz=\left(\overline{u}\,\overline{w}\right)_{z_w}-\left(\overline{u}\,\overline{w}\right)_{z_b}=0 \tag{3.4}$$

The first Reynolds stress (second term in the right-hand side of 3.2) is also handled with the Leibnitz rule, assuming a zero-velocity on the bed and a horizontal water surface :

$$\int_{z_b(y)}^{z_w(y)}\frac{\partial}{\partial y}\left(-\rho\,\overline{u'v'}\right)dz=\frac{\partial}{\partial y}\int_{z_b}^{z_w}\left(-\rho\,\overline{u'v'}\right)dz=\frac{\partial}{\partial y}\left(H\,\tau_{xy}\right) \tag{3.5}$$

where τ_{xy} is the depth-averaged Reynolds shear stress, as defined by (2.31).

Finally, the second Reynolds stress is depth-integrated :

$$\int_{z_b}^{z_w}\frac{\partial}{\partial z}(-\rho\,\overline{u'w'})\,dz=\tau_{surf}-\tau_{bed}=-\tau_b\sqrt{1+S_{0y}^2} \tag{3.6}$$

where τ_{bed} and τ_{surf} are horizontal projections of respectively the bed and the surface shear stresses. The surface shear stress τ_{surf}, corresponding between others to wind effects, is neglected. The horizontal projection of the bed shear stress τ_{bed} is replaced by the actual bed shear-stress value τ_b, times the ratio between the actual bed perimeter $\sqrt{1+S_{0y}^2}\,\Delta y$ and its horizontal projection Δy, in order to take into account the transverse bed slope S_{0y} due to river banks (Figure 3.2).

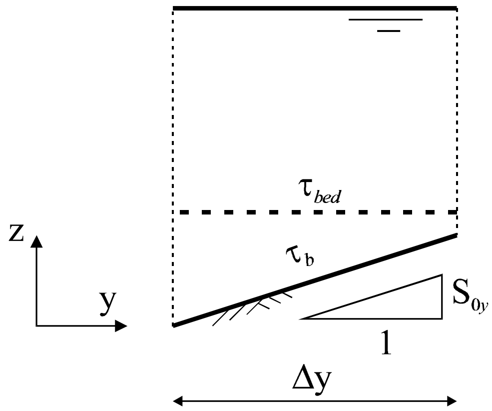

Figure 3.2 : Projection of the actual bed shear stress τ_b on an horizontal plane

Using (3.3) to (3.6), the simplified x-wise momentum Navier-Stokes equation (3.2) finally writes, when depth averaged :

$$\rho g H S_{0x} + \frac{\partial}{\partial y} H \tau_{xy} - \tau_b \sqrt{1+S_{0y}^2} = \frac{\partial}{\partial y} \int_{z_b}^{z_w} \rho\, \overline{u}\, \overline{v}\, dz \tag{3.7}$$

where the right hand term is the so-called secondary current term and corresponds to the effect of the secondary circulation in the channel. It is generally replaced by a depth-averaged value $\left(\rho \overline{u}\,\overline{v}\right)_d$:

$$\rho g H S_{0x} + \frac{\partial}{\partial y} H\, \tau_{xy} - \tau_b \sqrt{1+S_{0y}^2} = \frac{\partial}{\partial y} \left\{ H \left(\rho \overline{u}\,\overline{v}\right)_d \right\} \tag{3.8}$$

Using models of the bed friction τ_b, of the turbulent shear stress τ_{xy} and of the secondary currents, as a function of the depth-averaged longitudinal velocity U, this general LDM equation (3.8) will reduce to an ordinary differential equation, whose solution will give the velocity U distribution along the transverse direction y.

3.2.2 Bed friction and turbulent shear stress modelling

Knight et al. (1989) used a Boussinesq eddy viscosity model for t_{xy} and assumed an eddy viscosity υ_t proportional to the water depth H and to the shear velocity U^* (2.43) :

$$\tau_{xy} = \rho \upsilon_t \frac{\partial U}{\partial y} = \rho \lambda H U^* \frac{\partial U}{\partial y} \tag{3.9}$$

where λ is the adimensional eddy viscosity. Using the Darcy-Weisbach friction law (2.36) to express the value of the bed shear stress τ_b and of the shear velocity U^*; and neglecting at this stage the secondary-current term, the LDM equation is finally given by :

$$\rho g H S_{0x} + \frac{\partial}{\partial y}\left(\rho\lambda\sqrt{\frac{f}{8}}H^2 U \frac{\partial U}{\partial y}\right) - \frac{\rho f}{8}\sqrt{1+S_{0y}^2}\,U^2 = 0 \tag{3.10}$$

where f is the Darcy-Weisbach friction factor. This equation can be solved numerically, and Knight et al. also proposed an analytical solution. The parameter calibration was relatively straightforward, and reasonably close estimates of longitudinal velocities and total channel discharge were obtained for a natural river test-case, using values of the adimensional eddy viscosity in the range $\lambda = 0.2 ... 3.0$.

Wark et al. (1990) developed an equation similar to (3.10), but in terms of the longitudinal unit flow $q = UH$, and using the Manning friction law (2.34) instead of the Darcy-Weisbach law :

$$\rho g H S_{0x} + \frac{\partial}{\partial y}\left(\upsilon_t \frac{\partial q}{\partial y}\right) - \frac{\rho g n^2}{H^{1/3}}\sqrt{1+S_{0y}^2}\,\frac{q^2}{H^2} = 0 \tag{3.11}$$

where n is the Manning friction factor. Good estimates of the velocity profiles were obtained for small-scale laboratory flumes, for the large-scale Flood Channel Facility at Wallingford (FCF), and for a natural river, using realistic values of the friction coefficient and values of the adimensional eddy viscosity that are allowed to vary in the range $\lambda = 0 ... 0.24$, with different values on main-channel and floodplain,.

A last version of the LDM without secondary-current term was proposed by Lambert and Sellin (1996), using the Prandtl mixing length model (2.44) for estimating the eddy viscosity, and assuming that the mixing length l_m is proportional to the local water depth H :

$$\upsilon_t = l_m^2\left|\frac{\partial U}{\partial y}\right| = C_{ml}^2 H^2\left|\frac{\partial U}{\partial y}\right| \tag{3.12}$$

where C_{ml} is a proportionality constant, taken equal to $C_{ml} = 0.6$. Using an appropriate value of the friction factor, good estimates of the velocity profile are obtained for the FCF experiments, without further parameter adjustment.

3.2.3 Modelling of secondary currents

Wormleaton (1988) proposed an almost empirical way of modelling the effect of secondary currents by considering an additional eddy viscosity in the interface area :

$$\upsilon_t = \lambda U^* h + \lambda_s U_s l_s \tag{3.13}$$

where λ_s is a parameter; U_s is an appropriate velocity-scale; and l_s is a length scale representing the shear layer width. This additional eddy viscosity stands for velocity-gradient generated turbulence, while the first part of the eddy viscosity stands for bed-friction generated turbulence.

Although the velocity profiles are accurately reproduced by all of the above methods, Shiono and Knight (1990) showed that this was achieved at the detriment of the bed shear-stress profile prediction. Indeed, if the effect of secondary currents is neglected, additional bed and/or turbulent friction have to be added in order to obtain the true velocity profile. This additional bed friction jeopardises the relation between the depth-averaged velocity and the bed shear stress; in such a way it becomes impossible to get both profiles predicted accurately at the same time.

Shiono and Knight (1990) proposed thus a secondary current model in order to improve the LDM results. The depth-averaged product in the right hand term of the general LDM equation (3.8) is assumed to present linear variations in the y-direction on the floodplain and on the main-channel, in such a way that its derivative can be replaced by one constant on the floodplain and by another constant on the main-channel. This linearity assumption was verified by Shiono and Knight (1991), who estimated the left-hand part of (3.8) from the FCF data, as the direct estimation of the quoted depth-averaged product induced to too much inaccuracies. The LDM now writes :

$$\rho g H S_{0x} + \frac{\partial}{\partial y}\left(\rho\lambda\sqrt{\frac{f}{8}}H^2 U\frac{\partial U}{\partial y}\right) - \frac{\rho f}{8}\sqrt{1+S_{0y}^2}\,U^2 = \Gamma \tag{3.14}$$

where Γ is the secondary-current term, corresponding to helical-current effect. It is assumed to be constant in each channel sub-section.

Shiono and Knight (1991) developed an analytical solution of (3.14) and obtained accurate estimates for both velocity and bed shear-stress profiles, compared to some of the FCF experiments. Knight and Abril (1996), using a numerical solution of (3.14), investigated more FCF results. They found that the dimensionless eddy viscosity value λ can remain constant along the whole channel width, and that it has a low influence when compared to the secondary current term Γ. They also proposed empirical relations enabling the calibration of all the parameters f, λ and Γ, for the investigated FCF cases. These relations were not applied to calibrate the LDM for another channel geometry than the tested ones, and it seems their extrapolation could be hazardous.

Ervine et al. (2000) proposed a new expression for the secondary current term of the LDM, aimed at the modelling of both uniform and non-prismatic flow. They assume that both the local velocities $\bar{u}$ and $\bar{v}$ are proportional to the depth-averaged longitudinal velocity U. The depth-averaged product in the secondary current term of (3.8) is thus proportional to the square of the depth-averaged velocity U, similarly to the dispersion terms, as suggested in the previous Chapter. This new version of the LDM is written as :

$$\rho g H S_{0x} + \frac{\partial}{\partial y}\left(\rho\lambda\sqrt{\frac{f}{8}}H^2 U \frac{\partial U}{\partial y}\right) - \frac{\rho f}{8}\sqrt{1+S_{0y}^2}\,U^2 = \frac{\partial}{\partial y}\left(\rho H K U^2\right) \tag{3.15}$$

where K is a proportionality factor.

Ervine et al. (2000) proposed an analytical solution of their new LDM (3.15). They obtained good agreement for the velocity profile for several FCF straight channel cases, with values of the proportionality factor K_c = 0.25 % on the main-channel, and K_f = 0 on the floodplains, but without indicating if they used the actual roughness coefficient or a fitted value (no information on the bed shear stress results is available). For meandering geometries, also investigated in the FCF, accurate estimates of the velocity profiles are obtained, with values of the secondary current parameter in the range K_c = 1 … 5.5 % on the main-channel, and K_f = 0 … 2 %; the bed shear stress results are presented for one case and show good agreement with the measured data. Although the K values are greater for meandering cases than for prismatic ones, no clearer link is established between the parameter K and the channel geometry.

Discussing Ervine et al. paper, Bousmar and Zech (2001b) suggested that the secondary current term could be separated in two parts, corresponding respectively to a dispersion term in uniform flow (helical secondary currents) and to a transverse convection term (mass transfer due to non-prismaticity). In the next part of this Chapter, an extended version of the LDM is derived directly from the depth-averaged Saint-Venant equations, in order to clarify this distinction, and to investigate the weight of all the terms, including those that are neglected in the classical LDM.

3.3 Extended Lateral distribution method

3.3.1 Simplification of the two-dimensional equations

As developed in Chapter 2, the x-wise Saint-Venant momentum equation (2.33b) is written as :

$$\begin{aligned}\rho H\frac{\partial U}{\partial t} + \rho U H\frac{\partial U}{\partial x} + \rho g H\frac{\partial H}{\partial x} + \rho V H\frac{\partial U}{\partial y} &= \rho g H S_{0x} - \rho g H S_{fx} \\ &+ \frac{\partial}{\partial x}H\tau_{xx} + \frac{\partial}{\partial y}H\tau_{xy} - \rho\frac{\partial}{\partial x}\int_{z_b}^{z_w}\left(\bar{u}-U\right)^2 dz - \rho\frac{\partial}{\partial y}\int_{z_b}^{z_w}\left(\bar{u}-U\right)\left(\bar{v}-V\right)dz\end{aligned} \tag{3.16}$$

where both sides have been multiplied by ρH, in order to get a form similar to the classical LDM.

Assuming a permanent uniform flow, the x-direction momentum equation (3.16) reduces to a form similar to the LDM (3.7) :

$$\rho g H S_{0x} + \frac{\partial}{\partial y} H\,\tau_{xy} - \rho g H S_{fx} = \rho \frac{\partial}{\partial y} \int_{z_b}^{z_w} \left(\bar{u} - U\right)\left(\bar{v} - V\right) dz + \rho V H \frac{\partial U}{\partial y} \tag{3.17}$$

The last term of the right hand side has been written in (3.17) as it arise from the depth-averaging of the $\bar{u}\,\bar{v}$ product in the right hand side of (3.7) – see the term development (2.20). For uniform flow, this term will be null, as the transverse velocity component V equals zero; while, in non-uniform flow, it corresponds to the mass transfer occurring between main-channel and floodplains. The remaining dispersion term corresponds thus clearly to the secondary-current term developed by Shiono and Knight (1990). The secondary-current term of Ervine et al. (2000) corresponds to both terms of the right hand part of (3.17), as it is used also in non-prismatic flow, where V differs from zero.

Nevertheless, using (3.17) or similar LDM equations for non-prismatic flows seems a rather crude assumption, as other terms of (3.16) could be non-negligible : at least the acceleration term ($\rho U H\,\partial U/\partial x$) and the pressure term ($\rho g H\,\partial H/\partial x$) should be taken into account; while the streamwise turbulent friction and dispersion terms are expected to remain small when the flow is gradually varied.

3.3.2 Extension to non-prismatic flow

To obtain the extended LDM equation, the acceleration and pressure terms in (3.16) are grouped with the bottom slope term, in order to define the energy slope S_e :

$$S_e = S_{0x} - \frac{\partial H}{\partial x} - \frac{U}{g}\frac{\partial U}{\partial x} = -\frac{\partial}{\partial x}\left(\frac{U^2}{2g} + z_w\right) \tag{3.18}$$

With this definition, and neglecting the streamwise turbulent friction and dispersion terms, the x-direction momentum equation (3.16) reduces to the proposed extended form of the LDM :

$$\rho g H S_e + \frac{\partial}{\partial y} H\,\tau_{xy} - \rho g H S_{fx} = \rho \frac{\partial}{\partial y} \int_{z_b}^{z_w} \left(\bar{u} - U\right)\left(\bar{v} - V\right) dz + \rho V H \frac{\partial U}{\partial y} \tag{3.19}$$

This new expression differs from (3.17) as the bed slope is replaced by the actual energy slope, which is no more equal to the bed slope in the non-uniform flow case. This modification of the LDM can be paralleled with the classical assumption used for one-dimensional modelling, specifying that the head loss for a given reach is equal to the head loss in the reach for a uniform flow having the same hydraulic radius and average velocity (French 1985). It should be quoted that Lyness et al. (1997) used a similar assumption, but without formally extending the LDM equation, when they used the Wark et al. LDM equation (3.11) to compute conveyance tables to be used for a flood routing simulation.

As for the general LDM equation (3.7), the extended LDM (3.19) requires some further assumptions, in order to express all its terms as function of the main unknown U. In this case, the friction slope is estimated using the Manning friction law; the turbulent friction is modelled using the Boussinesq assumption, with the eddy viscosity proportional to the shearing velocity U^*; while, in a first stage, the energy slope S_e will be estimated on the basis of one-dimensional measurements (see Chapter 13) and will thus be written S_{e1D}.

For the non-prismatic flow modelling, the dispersion term is estimated using the Shiono and Knight secondary current term Γ. Indeed, the mass transfer between subsections, due to the non-prismaticity, is expected to restrain the helical secondary current development on the floodplain and to control their behaviour in the main-channel (see experimental data in Chapter 12). It is thus expected that the secondary-current Γ term will have no influence on the floodplains, and will have a lower influence than the mass transfer in the main-channel. It will therefore be neglected in most of the simulations.

The mass-transfer secondary-current term requires an estimate of the transverse velocity V that will be gathered from the continuity equation (2.33a) : indeed, for non-prismatic channels, as already suggested by Ervine et al. (2000), it is expected that the ratio $\kappa = V/U$ between the transverse and longitudinal depth-averaged velocity components will be a constant depending mainly of the channel geometry. The extended LDM to be tested in Chapter 13 writes thus finally :

$$\rho g H S_e + \frac{\partial}{\partial y}\left(\rho\lambda\sqrt{\frac{gn^2}{H^{1/3}}}H^2 U\frac{\partial U}{\partial y}\right) - \frac{\rho g n^2}{H^{1/3}}\sqrt{1+S_{0y}^2}\,U^2 = \Gamma + \rho\kappa H U\frac{\partial U}{\partial y} \qquad (3.20)$$

It should be observed that the last term of the right-hand part of (3.20), corresponding to the mass-transfer current, differs from the Ervine et al. expression (3.15), as the parameter κ is outside the derivative, and as it is expected to have a value explicitly linked with the non-prismatic channel geometry.

3.4 Numerical solution of the LDM

As already quoted, analytical solutions of the LDM equation have been proposed, at least for the Shiono and Knight (3.14) and for the Ervine et al. (3.15) versions. However, such analytical solutions have not been proposed for all version of LDM. Moreover, the use of an analytical solution is generally not easy when dealing with a natural geometry. A numerical solution can therefore be preferred, as it fits easily to almost every geometry and, as its adaptation for a modified equation is quite straightforward.

In the present work, the LDM numerical solution is obtained by writing the differential equation in a discrete form, using the finite differences method (Figure 3.3). This reduces the LDM equation to a set of quadratic algebraic equations linking together the velocities U_i at each node of the mesh. At the boundaries, a no-slip condition is used by setting the velocity equal to zero along the walls. The so-defined set of equation is solved either by a Newton-Raphson method, or by any other appropriate method.

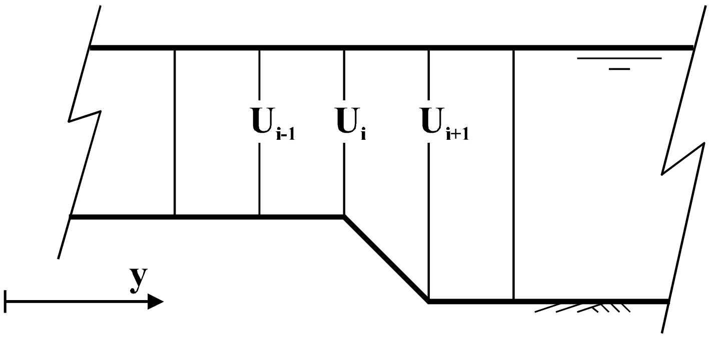

Figure 3.3 : Discrete mesh for the LDM numerical solving

When the U^*H model is used for the eddy viscosity, a more efficient solution can even be found, by using the identity

$$U\frac{\partial U}{\partial y}=\frac{1}{2}\frac{\partial U^2}{\partial y} \tag{3.21}$$

in the LDM equation (3.14), as suggested by Abril (1995). As the friction term is also proportional to the square of U, all the equation can be rewritten as a function of U^2 rather of U. When expressed in discrete form, the LDM reduces now to a set of linear equations linking the square of velocities U_i^2. As the matrix corresponding to this set of equation is tridiagonal, its inversion is almost trivial.

In order to achieve sufficient precision, a high density mesh can be used with, typically, 1000 nodes in a cross-section (Lyness et al. 1997). However, some numerical tests reveals that similar precision is already obtained with less than 100 nodes. On the other hand, it should be noted that internal vertical walls can not be modelled in such a solution. In fact, the same problem also occurs with the analytical solutions. Such internal vertical walls are therefore usually replaced by steep oblique walls, as done by Keller and Rodi (1988) in their two-dimensional model.

Chapter 4
The Exchange Discharge Model

4.1 Introduction

As explained in the general introduction, the main objective of the present work is the development of a new one-dimensional method aimed at estimating the stage-discharge relation in a compound channel, founded on theoretical rather than empirical basis. It is intended that the Exchange Discharge Model (EDM) proposed in this chapter will meet this objective.

The EDM (Bousmar and Zech 1999a) improves the classical Divided Channel Method (DCM, 1.4) by taking into account the effects of the momentum transfers through the interface. Discharges through the interface between main channel and floodplain are considered, which can be due to both turbulent exchange and geometrical transfer. The momentum transfer is assumed to be proportional to these exchange discharges and to the velocity difference between the main channel and the floodplain. Accurate stage-discharge estimations are obtained; while the momentum correction enables the use of actual roughness coefficients, corresponding to the actual river bed material.

Both the turbulent exchange and the geometrical transfer defined by the EDM will be further studied, respectively in Part II and Part III of this work.

An additional feature of the EDM is its formulation in term of an additional head loss, to be summed with the DCM-estimated friction losses. Indeed, although the estimation of the stage-discharge relation is the main focus of such a method, its use in water-profile computation models is also of some concern. Such programs usually solve the Bernoulli equation (for example by the standard step method) between consecutive cross-sections, requiring thus an estimate of the head loss S_f between those sections, as a function of actual discharge, water depth, bed roughness and geometry.

It is traditionally assumed that the head loss for a specific reach is equal to the head loss in the reach for a uniform flow having the same hydraulic radius and average velocity (French 1985). Using, for example, the Single Channel Method (SCM) with the Manning formula (1.3), the head loss S_f writes

$$S_f = \left(\frac{Q}{AR^{2/3}/n} \right)^2 = \left(\frac{Q}{K} \right)^2 \tag{4.1}$$

where Q is the discharge; A and R are the cross-section area and hydraulic radius, depending on the water depth H; n is the roughness coefficient; and K is defined as the conveyance of the cross-section.

Such a head loss equation can also be expressed for the DCM (1.4), by isolating the bed slope S_0 in the left-hand side of the equation. Using the Ackers' method or the LDM, the bed slope can not be isolated so easily. Conveyance K tables are thus used (see e.g. Lyness 1997) : such a table is obtained from a stage-discharge table, computed for a given bed slope, and then divided by this bed slope square root. However, such a method is less straightforward; and, when using the LDM with Shiono and Knight's Γ secondary current term (3.14), it can be shown that the result will not be independent of the initial bed slope value. In the case of the EDM, the additional loss formulation will enable to avoid this conveyance-table calculation.

The EDM was primarily developed for steady flow modelling. The extension to unsteady flow could be straightforward, using the classical assumption that the head loss in unsteady flow equals the head loss computed for steady flow. However, when compound channels are considered, the unsteadiness of the water level generates extra mass transfer between subsections, as pointed out by Jayaratne et al. (1995). In order to investigate the significance of this effect on the water profile predictions, the EDM has been tentatively extended to unsteady flow, by taking into account this new exchange discharge in the momentum transfer estimation (Bousmar et al. 1998). Some results of this extended EDM are discussed at the end of this chapter.

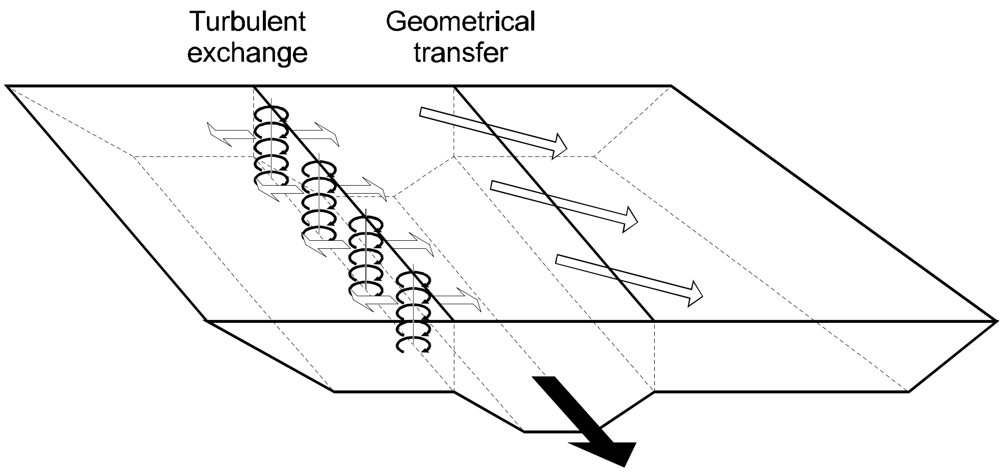

Figure 4.1 : Flow exchange at the interfaces between main channel and floodplains

4.2 Exchange Discharge Model development

As seen in Chapter 1, in straight compound channels, due to the shear layer at the interface between main channel and floodplain, large scale vortices and strong secondary currents appear. These vortices and currents can be seen as a turbulent exchange discharge through the interface (Figure 4.1). Rather than giving an estimate of an apparent shear stress, Bertrand (1994) proposed to model the momentum transfer between subsections by the product of the mass of water flowing through the interface by the velocity gradient at this interface.

This model is then easy to extend to non-uniform and/or non-prismatic flows where a lateral discharge occurs through the interface due to a modification of flow distribution in the subsections (Yen et al. 1985). This geometrical transfer discharge (Figure 4.1) can be added to the turbulent exchange to get a global estimation of the momentum transfer. Up to now, the model does not take into consideration channel sinuosity and the associated secondary currents.

4.2.1 Governing equations

In this paragraph, the one-dimensional Saint-Venant equation are developed on the basis of a momentum equilibrium rather than on the depth-averaging of the Navier-Stokes equations, as in Chapter 2. Indeed, dealing now with a whole channel or a channel subsection, the main focus is on the global exchange processes rather than on the local influence of non-uniformity of the velocity vertical profiles, as it was the case when developing the dispersion terms.

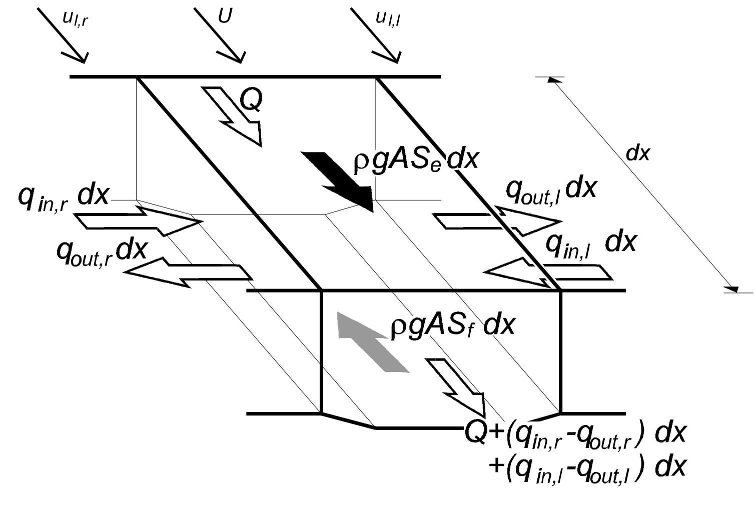

Figure 4.2 : Momentum equilibrium for a compound-channel subsection

For this development purpose, let thus consider that each subsection of a compound channel acts as a channel submitted to a lateral flow per unit length q_L, which is decomposed into an inflow component q_{in} and an outflow component q_{out}, in such a way that conservation of mass may be written :

$$\frac{\partial A}{\partial t} + \frac{\partial Q}{\partial x} = q_L = q_{in} - q_{out} \tag{4.2}$$

where A is the cross-section area; and Q is the discharge. Inflow and outflow are locally mutually exclusive for geometrical transfer (in the same way as for tributary inflow). For turbulent transfer, however, both incoming and exiting flow components are simultaneously considered, yielding a resultant mass transfer equal to zero, but a momentum transfer which is not, as will be developed below.

Using the principle of conservation of momentum which states that the net rate of momentum flux into a control volume plus the sum of the forces (gravity, friction, pressure) acting on the control volume is equal to the rate of accumulation of momentum within the control volume, the momentum equation can be derived for a unit length (Figure 4.2) :

$$\frac{\partial}{\partial t}(\rho AU) = -\frac{\partial}{\partial x}\left(\rho AU^2\right) + \rho q_{in} u_L - \rho q_{out} U + \rho g A\left(S_0 - S_f\right) - \rho g A \frac{\partial H}{\partial x} \tag{4.3}$$

where ρ is the density of water; g is the gravity constant; S_0 and S_f are respectively the bottom and the friction slope, the later estimated for example by (4.1); $U = Q/A$ is the mean velocity in the considered section; H is the water depth; and u_L is the velocity of the lateral inflow in the direction of the main flow. In (4.3), the lateral flows q_{in} and q_{out} stand for the sum of the left and the right components, which will be considered separately later in the development. It is noticeable that inflow and outflow convey different momentum since their initial velocities are not the same. Developing (4.3), it can be obtained :

$$A\frac{\partial U}{\partial t} + U\frac{\partial A}{\partial t} + AU\frac{\partial U}{\partial x} + U\frac{\partial AU}{\partial x} + gA\frac{\partial H}{\partial x} - gAS_0 = q_{in}u_L - q_{out}U - gAS_f \tag{4.4}$$

Because

$$\frac{\partial H}{\partial x} - S_0 = \frac{\partial z}{\partial x} \tag{4.5}$$

where z is the water level, equation (4.4) may be simplified, subtracting to (4.4) the continuity equation (4.2) multiplied by U :

$$A\frac{\partial U}{\partial t} + gA\frac{\partial}{\partial x}\left(z + \frac{U^2}{2g}\right) = q_{in}\left(u_L - U\right) - gAS_f \tag{4.6}$$

showing that only the lateral inflow influences the momentum, whereas the outflow effect is implicitly included in the kinetic head variation. Such a result is given by Chaudhry (1979, page 443), but without demonstration. The equation (4.6) is also in agreement with the developments by Yen (1973) and by Lai (1986), at least if only inflow occurs. An important consequence of this asymmetry between in- and outflow effect is therefore that momentum transfer due to turbulence exists even if the average mass transfer is equal to zero.

In the case of steady flow, the first term of (4.6) disappears, and the partial derivative in the second term, with an opposite sign, may be defined as a head loss per unit length S_e :

$$S_e = -\frac{\partial}{\partial x}\left(z + \frac{U^2}{2g} \right) = S_f + \frac{q_{in,r}\left(U - u_{L,r}\right) + q_{in,l}\left(U - u_{L,l}\right)}{gA} = S_f + S_a \tag{4.7}$$

where the lateral inflow has now been divided into right side r and left side l inflow (Figure 4.2), for further application to a compound channel subsection. For a floodplain, only one side inflow will exist (i.e. flowing from the main channel); but for the main channel, both inflows can be present. The slope S_a is defined as the additional head loss due to the exchange discharges at the interface, to be added to the friction slope, in the given subsection. We can define the ratio $\chi = S_a / S_f$ of this additional loss to the friction loss, so that the above equation becomes :

$$S_e = S_f \ (1 + \chi) \tag{4.8}$$

and

$$\chi = \frac{q_{in,r}\left(U - u_{L,r}\right) + q_{in,l}\left(U - u_{L,l}\right)}{gAS_f} \tag{4.9}$$

In a compound channel, an additional loss ratio and a friction slope will be defined in each subsection i, namely χ_i and S_{fi}. However, the total energy slope S_e is the same in all subsections, as we suppose a one-dimensional modelling. This assumption means that the river adjusts its energy budget in such a way that no more difference in head subsists between adjacent subsections.

For its evaluation, the exchange discharge q is divided in two parts : the first, q^t, is related to turbulent momentum flux, the second, q^g, is associated to the mass transfer due to changes in geometry.

4.2.2 Turbulent momentum flux

The turbulent exchange discharge has to be estimated by a turbulence model. A model analogous to a mixing length model in the horizontal plane was selected because it is simple enough to lead to a global development of the relation between stage, discharge and energy slope presented later. Such a model presents similarities with, for example, Ervine and Baird (1982) apparent shear stress formula (1.5) and Lambert and Sellin (1996) LDM (3.12). Although this model is simple, when compared with experimental data, it will prove to give better results than classical methods and, anyway, accurate enough for water profile computations in natural rivers, in regard to the other inaccuracies involved in the problem.

Both lateral inflows q^t_{cf} and q^t_{fc}, respectively from the main channel to a floodplain and from this floodplain to the main channel, are assumed to be equal to the product of the depth-averaged turbulent part of the transverse velocity $\overline{|v'|}$ by the interface area per unit length (H-h_f), where H and h_f are the water and the bank levels above the main-channel bottom (Figure 1.1). The transverse velocity $\overline{|v'|}$ is assumed to be proportional to the absolute value of the longitudinal velocity difference between subsections $|U_c - U_f|$ (Bertrand 1994) :

$$q^t_{cf} = q^t_{fc} = \overline{|v'|}\left(H - h_f\right) = \psi^t \left|U_c - U_f\right| \left(H - h_f\right) \tag{4.10}$$

where ψ^t is the proportionality factor. The turbulent exchange q^t_{cf} being an oscillating discharge, it is assumed to be equal to the dual exchange q^t_{fc} through the same interface.

It should be noted that the turbulent interaction for the straight channels [see (4.7) and (4.10)] developed using the turbulent exchange discharge can be shown equivalent to the one developed using the apparent shear stress concept with a mixing length model (Ervine and Baird 1982; Smart 1992). Furthermore, the exchange discharge model is more complete as it also takes into account the geometrical transfer discharges in order to model non-uniform or non-prismatic flows.

4.2.3 Exchange discharge due to change in geometry

Let us now consider a floodplain subsection *f*. Due to changes in geometry, the conveyance in the floodplain increases or decreases in such a way that the floodplain discharge also varies, forcing through the interface a geometrical transfer discharge q^g_{cf} or q^g_{fc} equal to this variation (Yen et al. 1985).

For an increasing floodplain conveyance, we have for a unit length :

$$q^g_{fc} = 0 \quad \text{and} \quad q^g_{cf} = \frac{dQ_f}{dx} = \frac{dK_f}{dx} S^{1/2}_{ff} \tag{4.11a}$$

and for decreasing floodplain conveyance :

$$q^g_{fc} = -\frac{dQ_f}{dx} = -\frac{dK_f}{dx} S^{1/2}_{ff} \quad \text{and} \quad q^g_{cf} = 0 \tag{4.11b}$$

where the S_{ff} variation is neglected on the interval where dK_f/dx is evaluated. We can generalise in the form :

$$q^g_{fc} = \psi^g \kappa_{fc} \frac{dK_f}{dx} S^{1/2}_{ff} \quad \text{and} \quad q^g_{cf} = \psi^g \kappa_{cf} \frac{dK_f}{dx} S^{1/2}_{ff} \tag{4.12}$$

where κ_{fc} and κ_{cf} take the appropriate values, respectively (0, 1) for $dK_f/dx > 0$ and (-1, 0) for $dK_f/dx < 0$. A proportionality factor ψ^g has also been included.

The geometrical transfer discharge corresponds to the additional secondary currents experimentally observed in channels where such mass transfer occurs (Elliott and Sellin

1990) : the shear stress increases when water is flowing from floodplain to main channel, and reduces when water is flowing from main channel to floodplain. An appropriate calibration of the proportionality factor ψ^g will take this effect into account.

4.3 Practical evaluation of the flow

Two main practical problems can be solved by the exchange discharge model : (1) Given a channel bottom slope and a water level in a known cross-section, estimate the discharge for rating curve computation; and (2) given a discharge and a water level in a known cross-section, estimate the corresponding energy slope for water-profile computation. Assuming a friction law and using equation (4.8), it is possible to answer those two problems. Manning's equation has been chosen as it is the most widely used in practical cases. This links the discharge Q_i to the friction slope S_{fi} in each subsection i and then to the energy slope S_e for the whole cross-section, using equation (4.8) and the definition of the ratio χ_i :

$$Q_i = A_i U_i = \frac{A_i R_i^{2/3}}{n_i} S_{fi}^{1/2} = K_i S_{fi}^{1/2} = K_i \left(\frac{S_e}{1+\chi_i} \right)^{1/2} \tag{4.13}$$

By this equation, the subsections velocities U_i can be evaluated and a complete expression of the ratio χ_i can be derived from equations (4.8), (4.9), (4.10) and (4.12). This expression is particularised to the three subsections of a compound channel (Figure 1.1), assuming that main-channel velocity is greater than floodplain one. After simplification, it gives :

$$\begin{aligned}\chi_1 = \frac{1}{gA_1} & \left[\psi^t \,(H - h_1) \left(\frac{R_2^{2/3}}{n_2} \left(\frac{1+\chi_1}{1+\chi_2} \right)^{1/2} - \frac{R_1^{2/3}}{n_1} \right) + \psi^g \kappa_{21} \frac{dK_1}{dx} \right] \\ & \cdot \left[\frac{R_1^{2/3}}{n_1} - \frac{R_2^{2/3}}{n_2} \left(\frac{1+\chi_1}{1+\chi_2} \right)^{1/2} \right]\end{aligned} \tag{4.14a}$$

$$\begin{aligned}\chi_2 = \frac{1}{gA_2} & \left\{ \left[\psi^t \,(H - h_1) \left(\frac{R_2^{2/3}}{n_2} \left(\frac{1+\chi_1}{1+\chi_2} \right)^{1/2} - \frac{R_1^{2/3}}{n_1} \right) + \psi^g \kappa_{12} \frac{dK_1}{dx} \right] \right. \\ & \cdot \left[\frac{R_2^{2/3}}{n_2} \left(\frac{1+\chi_1}{1+\chi_2} \right)^{1/2} - \frac{R_1^{2/3}}{n_1} \right] \left(\frac{1+\chi_2}{1+\chi_1} \right) \\ & + \left[\psi^t \,(H - h_3) \left(\frac{R_2^{2/3}}{n_2} \left(\frac{1+\chi_3}{1+\chi_2} \right)^{1/2} - \frac{R_3^{2/3}}{n_3} \right) + \psi^g \kappa_{32} \frac{dK_3}{dx} \right] \\ & \left. \cdot \left[\frac{R_2^{2/3}}{n_2} \left(\frac{1+\chi_3}{1+\chi_2} \right)^{1/2} - \frac{R_3^{2/3}}{n_3} \right] \left(\frac{1+\chi_2}{1+\chi_3} \right) \right\}\end{aligned} \tag{4.14b}$$

$$\chi_3 = \frac{1}{g A_3}\left[\psi^t\,(H - h_3)\left(\frac{R_2^{2/3}}{n_2}\left(\frac{1+\chi_3}{1+\chi_2}\right)^{1/2} - \frac{R_3^{2/3}}{n_3}\right) + \psi^g\,\kappa_{23}\,\frac{dK_3}{dx}\right] \cdot \left[\frac{R_3^{2/3}}{n_3} - \frac{R_2^{2/3}}{n_2}\left(\frac{1+\chi_3}{1+\chi_2}\right)^{1/2}\right] \tag{4.14c}$$

where subscript 2 stands for the main channel and subscripts 1 and 3 for the floodplains.

This system defines the values of the ratios χ_i as a function only of water depth, cross-section geometry and roughness and thus, independently of the discharge value. Bertrand (1994) calculates ratios similar to χ_i using equation (4.9) with velocities evaluated from DCM. Due to the fact that the resulting velocity corrections are sometimes higher than 50 % for flow on floodplains with low water depth, this method may be inaccurate. Equations (4.14), written in implicit form, avoid such a problem. When the channel is a straight symmetrical one with uniform flow, this non-linear system of 3 equations with 3 variables simplifies and an analytical solution can also be found : this particular solution is detailed in Appendix 2, together with a numerical solution procedure for the general problem.

Given the values of χ_i, it is possible to compute the subsection discharges Q_i by the corrected Manning equation (4.13) for an assumed uniform flow at a given water depth H with an energy slope S_e postulated equal to the channel bottom slope S_0 if the latter may be defined. The total discharge Q in the cross-section is the sum of the corrected subsection discharges :

$$Q = \sum_i Q_i = \sum_i K_i \left(\frac{S_e}{1+\chi_i}\right)^{1/2} = \sum_i \left(\frac{K_i}{\left(1+\chi_i\right)^{1/2}}\right) S_e^{1/2} \tag{4.15}$$

In fact, the discharge is now computed in a similar way as the Divided Channel Method, but with corrected conveyance K_i^* in each subsection :

$$K_i^* = \frac{K_i}{\left(1+\chi_i\right)^{1/2}} \tag{4.16}$$

Equation (4.15) also leads to a direct computation of the energy slope for a given discharge, a given water level and the associate cross-section geometry. For practical water profile computation, one can either use a corrected cross-section conveyance table using equation (4.16), or develop another equation giving a global correction χ for the whole cross-section as a global exchange discharge additional loss S_a to be added to the friction slope S_f computed from the Divided Channel Method :

$$
\begin{aligned}
S_e &= S_f + S_a = S_f\,(1+\chi) \\
&= \left(Q \Big/ \sum_i K_i \right)^2 (1+\chi)
\end{aligned}
\tag{4.17}
$$

where $\chi = S_a / S_f$ is the corresponding global ratio.

Introducing the discharge Q from (4.15) into (4.17), a value of the ratio χ can be found as a function of the subsection ratios χ_i and conveyances K_i :

$$
\chi = \left(\frac{\sum_i K_i}{\sum_i \left(K_i \big/ (1+\chi_i)^{1/2} \right)} \right)^2 - 1 \tag{4.18}
$$

Even if this last expression is less efficient from a computational point of view than the conveyance tables, as it leads to extra algebra, it can be useful for analysis as it allows to separate the head loss due to compound channel interaction from the one due to bed friction. It is also more consistent if other additional losses have to be added (minor loss at a bridge, for example).

4.4 Calibration of the turbulent exchange parameter ψ^t

The presented Exchange Discharge Model (EDM) involves only two parameters which have to be characterised : the parameter ψ^t which is the proportionality factor for turbulent exchanges at the interface, and ψ^g which is a correction factor for the geometrical transfer discharge.

The value of the factor ψ^t was evaluated from published experimental data in straight prismatic channels, where no geometrical transfers occur. The first data set used for calibration is the Flood Channel Facility (FCF) one (Knight 1992), which is one of the most complete and accurate available in the literature. Nine different geometries were tested investigating the influence of four parameters : (1) Floodplain to main-channel width ratio B/b; (2) Number of floodplains N_f; (3) Main channel bank slope s_c; and (4) Floodplain roughness (see Table 4.1).

For each of the nine tested geometries, a stage-discharge curve was computed using the EDM with some assumed values of the ψ^t factor, and with a roughness value of $n = 0.010$ s/m$^{1/3}$. This roughness coefficient was estimated from FCF Series 04 single channel experiments, using the Manning formula (1.3). The EDM results were compared to the measured data and the ψ^t factor adjusted for minimising the discrepancy. For this purpose, an unbiased error indicator was used, expressed as the sum of the squared deviation between measured and computed discharges for each water level, following Khatibi et al. (1997). Figure 4.3 shows that the model produces very good results with a value of the ψ^t factor constant for all the water depths in a given geometry. Table 4.1 gives the adjusted ψ^t factor value for each of the 9 geometries, showing also that the mean deviation between data and computed values is generally less than 3 %. The discharge reduction compared to the DCM is in the range 5 to 15 % for the smooth floodplains and in the range 5 to 40 % for the rough ones.

Table 4.1 : Wallingford FCF data : geometrical data and optimal ψ^t values for EDM calculations.

Series	B/b	N_f	s_c	Floodplains roughness	Optimal ψ^t	Mean deviation
01	5.56	2	1	smooth	0.179	1.4 %
02	3.50	2	1	smooth	0.113	2.2 %
03	1.83	2	1	smooth	0.122	2.8 %
06	3.50	1	1	smooth	0.266	4.0 %
07	3.50	2	1	rough	0.093	2.5 %
08	4.00	2	0	smooth	0.267	3.0 %
09	4.00	2	0	rough	0.118	2.0 %
10	3.14	2	2	smooth	0.162	2.4 %
11	3.14	2	2	rough	0.093	2.7 %

When the geometry change, a variation of the ψ^t value is possible as it is a proportionality factor for this particular geometry : Table 4.1 shows that the optimised values of ψ^t are in the range 0.09 to 0.27. As the optimal ψ^t variation does not seem to be correlated with geometrical parameters, the mean value of ψ^t through the 9 series is finally adopted, giving $\psi^t = 0.16$.

Nevertheless, for prismatic channels, a low sensitivity of the EDM discharge prediction to ψ^t is observed around the optimal value, so that this rather rough estimation does not jeopardise the model accuracy, even when compared, for example, with Ackers' method (see next paragraph). A low sensitivity to the ψ^t value around its optimal value will also be observed below, for water profile computation performed for a field case, where the channel is meandering.

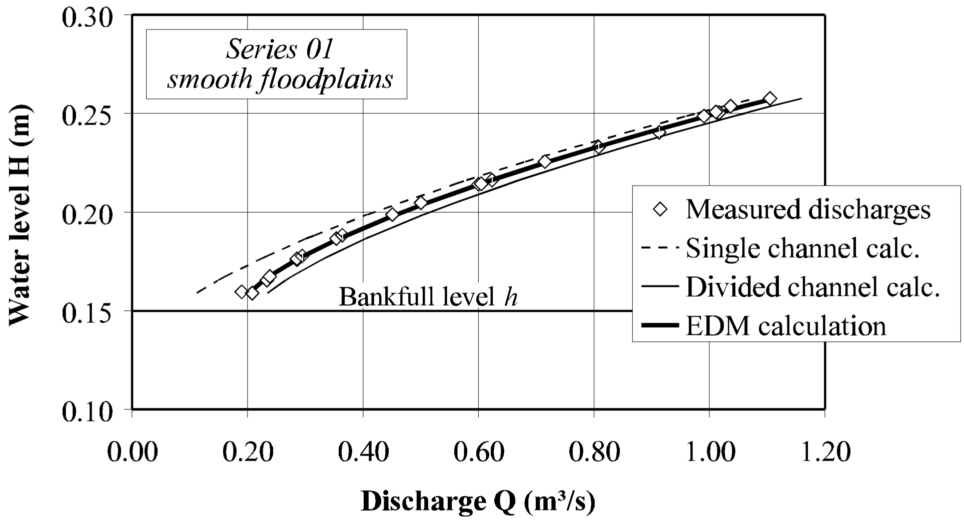

Figure 4.3 : Uniform-flow discharge : calculation against Wallingford FCF data. EDM used with optimal ψ^t values as defined in Table 4.1

4.5 Uniform flow in prismatic channels

4.5.1 Stage-discharge relation

With the adopted averaged value of ψ^t, the stage-discharge curves are computed once again for the Flood Channel Facility experiments, but also for four new sets of data, used here to validate the model (Ghosh and Jena 1971; Wormleaton et al. 1982; Knight and Hamed 1984; Asano et al. 1985). These sets were not previously used for calibration as the experiments were performed at smaller scale, presenting more data dispersion and thus a less dependable fitting.

Table 4.2 : Data sets used for EDM validation

Authors	Nbr of geometry	b/H	B/b	N_f	s_c	n_f/n_c
FCF (Knight 1992)	9	5.0 .. 7.0	1.8 .. 5.6	1 .. 2	0 .. 2	1.0 .. 4.0
Ghosh and Jena 1971	1	2.0	1.4	2	0	1.0
Wormleaton et al. 1982	4	1.2	4.2	2	0	1.0 .. 2.0
Knight and Hamed 1984	8	1.0	2.0 .. 4.0	2	0	1.1 .. 3.3
Asano et al. 1985	6	5.0 .. 15.2	1.4 .. 3.3	2	0	1.0

Stage-discharge curves were also computed using the Single Channel, Divided Channel, Ackers and Lateral Distribution methods as presented above. Absolute values of the relative errors are computed for the various geometries and water levels, using the four methods. Figure 4.4 presents the mean values of these errors for each geometry. The SCM gives mean relative errors between 10 and 30 %, while the DCM errors are between 5 and 50 %. The Ackers method yields errors that are generally less than 5 % but isolated data sets can give errors up to 20 %.

The LDM is used in Wark's formulation (3.11), with Manning roughness and a value of 0.16 for the non-dimensional eddy viscosity. For the tested cases, it produces quite inaccurate results compared to the published ones (Wark et al. 1990), with errors greater than Ackers' results but smaller than the DCM ones. This is probably due to the use of a constant roughness according to water depth, which was assumed in order to be in similar conditions for all the tested methods.

The EDM results present errors between 5 and 10%. Both the Ackers and EDM methods lead to improved agreement for each data set. The errors are sometimes reduced to a tenth of their SCM or DCM values. Finally, comparison between the Ackers and EDM methods indicates that the accuracy of both methods is of the same order of magnitude. However, it should be pointed out that Ackers' method is empirical, and used all the above data for calibration (Ackers 1992), excepted the Ghosh's data; moreover, each data set was used to fit one of the parameters, in such a way that high accuracy could be expected for this method.

The flow distribution between main channel and floodplain was also investigated. Figure 4.5 shows results for Wallingford Flood Channel series 03. Compared to DCM computation, the EDM leads to a reduction of the main channel discharge to 85-90 %, and an increase of the floodplains one to 120 % for high water levels, and up to 200 % for the lowest ones. It can be seen that, even if perfectible, the proposed method gives thus better results than the classical DCM.

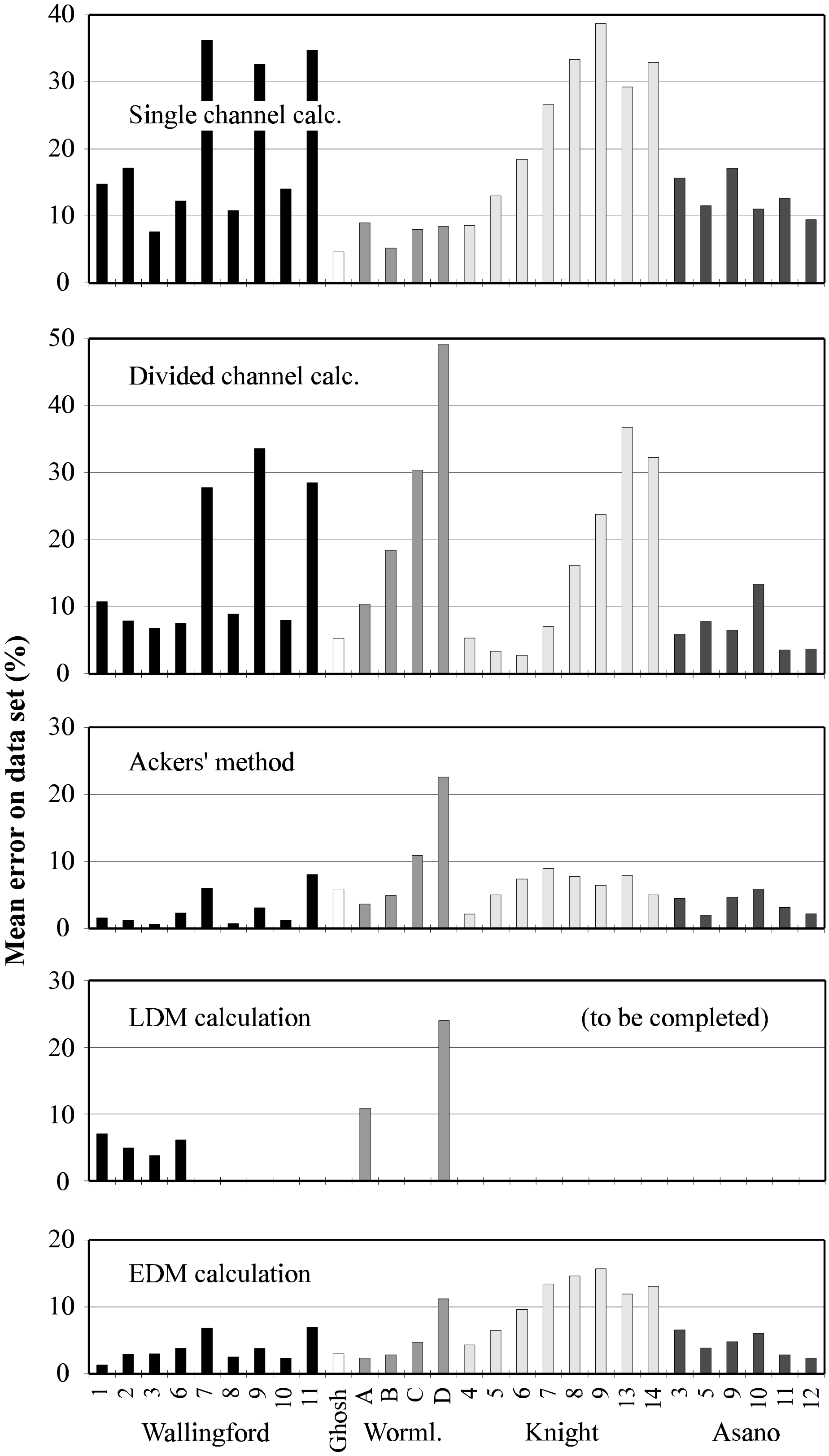

Figure 4.4 : Mean errors on discharges estimation for a given data set with SCM, DCM, Ackers and EDM ($\psi^t = 0.16$) *methods*

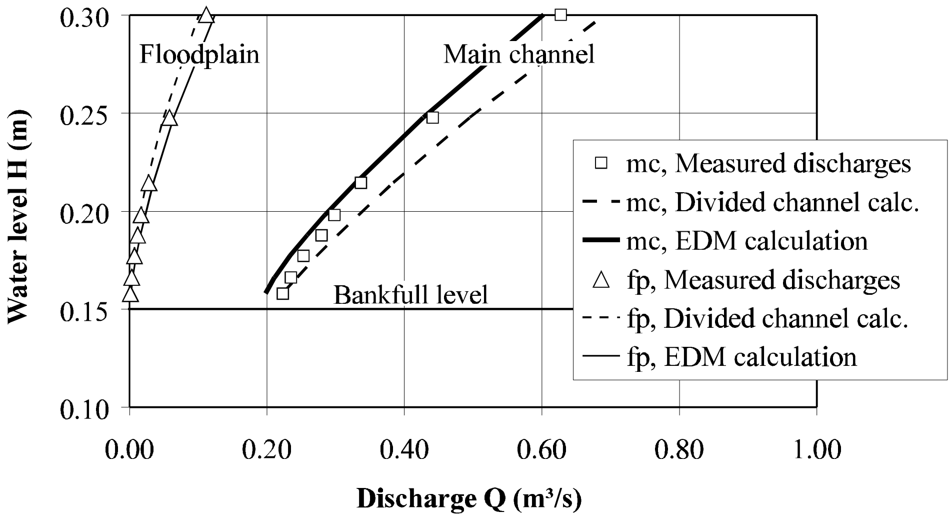

Figure 4.5 : Flow distribution between main channel (mc) and floodplain (fp) : calculation against FCF Series 03 data

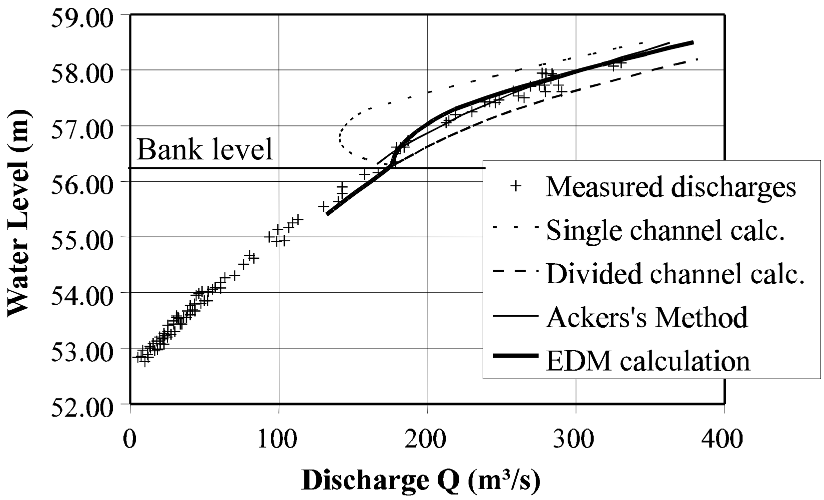

Figure 4.6 : Validation against field observations : River Severn at Montford Bridge, U.K., computed stage-discharge curves for $n_c = 0.0307$ and $n_f = 0.0338$

A last stage-discharge comparison was performed using a natural stream cross-section : the River Severn at Montford Bridge (Knight et al. 1989). The Manning roughness coefficients used are those obtained by Ackers (1992) for a best fitting of his method to the data. Figure 4.6 shows that the EDM gives again better results than the SCM and the DCM as it leads to a DCM correction of up to 16 %. The obtained agreement is equivalent respectively to that resulting from Ackers' Method which gives a mean error of 0.3 % with a 2.7 % standard deviation (Ackers 1992), and to that resulting from LDM which gives a mean error of 2.7 % with a 2.3 % standard deviation, while EDM mean error is 2.7 % with a 4.4 % standard deviation. Moreover, it should be noted that no specific parameters fitting (ψ^t or roughness) was carried out for this calculation which demonstrates the robustness of the new model.

4.5.2 Bed shear stress distribu tion

In addition to the calculation of the stage-discharge relation, information regarding the bed shear stress τ_b distribution is also of interest, when sediment transport mechanisms are considered. Although the EDM do not compute the transverse velocity distribution but only subsection discharges and mean velocities, bed shear stress estimates can be obtained from these mean velocities and compared to measurements.

The bed shear stress distribution, measured along the cross-section with a Preston tube, is given by Figure 4.7 for one of the FCF series 02 tests (Knight 1992). Comparison are then performed with this actual distribution, rather than with subsection-averaged values of the measurements. Indeed, one has to keep in mind that extreme shear stresses are generally more significant regarding the mobilisation of sediments.

From Figure 4.7, it is clear that the EDM underestimates the shear stress in the main channel ($0.00 < y < 0.90$ m), whereas the DCM gives a greater value. In the floodplain ($0.90 < y < 3.15$ m), the EDM lightly overestimates the shear stress, while the DCM gives an underestimation. A combined use of both DCM and EDM could give an envelope of the actual shear values.

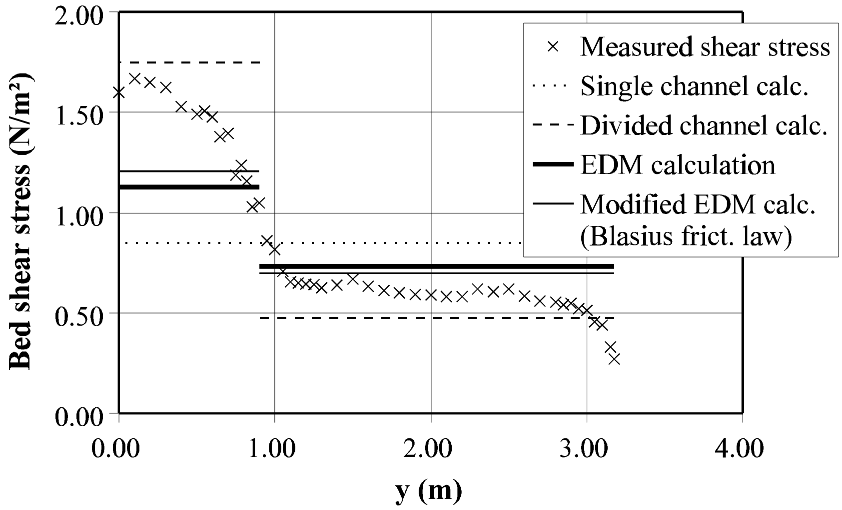

Figure 4.7 : Bed shear stress distribution : calculation against FCF test 020501 data

The discrepancy exhibited by the EDM was investigated further as it could be due to the use of a wrong friction model. From the experimental data, it can effectively be seen that the FCF operates in smooth turbulent conditions (Myers and Brennan 1990; Ackers 1991) while the EDM was developed using Manning equation which is strictly only suitable for rough turbulent flow. A new version of the EDM was thus tested, using Darcy-Weisbach friction law.

A modified Blasius friction law (Ackers 1991) is used to get the Darcy-Weisbach f value :

$$f = 0.2\,\mathbf{Re}^{-0.2} \tag{4.19}$$

where **Re** is the Reynolds number of the flow, defined as **Re** = $4UR/\nu$ with R and ν standing respectively for the section hydraulic radius and the kinematic viscosity of the water. Used in Darcy-Weisbach law (2.36), this expression gives a "Manning look-alike" relation between mean velocity U, friction slope S_f, section geometry and roughness :

$$U = \sqrt{\frac{8g}{f}}\, R^{1/2}\, S_f^{1/2} = \sqrt{\frac{8g}{0.2\left(4UR/\nu\right)^{-0.2}}}\, R^{1/2}\, S_f^{1/2} \tag{4.20}$$

or

$$U = R^{2/3}\left[\left(\frac{4}{\nu}\right)^{1/9}\left(\frac{8\,g}{0.2}\right)^{5/9} S_f^{1/18}\right] S_f^{1/2} = k\ R^{2/3}\ S_f^{5/9} \tag{4.21}$$

where k becomes the roughness parameter.

With this friction law, new expressions of EDM χ_i ratios are easily developed. The calibration gives a ψ^t value close to the one obtained from Manning law and the new corresponding bed shear stress distribution is plotted on Figure 4.7. This does not significantly improve the approximation of the shear stress versus the experimental data but it proves that the EDM can be generalised to other friction models than the Manning law.

Two reasons for the EDM relative failure to predict the bed shear stress could be suggested : (1) an error in estimating the subsection discharges; and (2) the influence of the velocity distribution. On one hand, the discharge distribution between subsections as calculated by the EDM presents some small discrepancies with measured data (Figure 4.5), although the overall performance is rather satisfactory. On the other hand, the relation between bed shear stress and velocity is not linear but quadratic (2.38). Therefore, it is clear that, for non-uniform velocity distribution as observed in each subsection, the square of the subsection mean velocity will differ from the mean value of the local velocity square. This could also partly explain the discrepancy between local and subsection-averaged bed shear stress.

4.6 Calibration of geometrical-exchange parameter y^g

After calibration for uniform and prismatic flows, the Exchange Discharge Model was tested against available non-prismatic flow data for calibration of the geometrical exchange parameter ψ^g. Meandering channel data were not used as they imply bend effects that could interfere with the geometrical transfer process investigated. Two sets of experiments were finally selected that present a rectilinear main channel skewed to rectilinear floodplains. The first one comes from the FCF Series A (Elliott and Sellin 1990) with two different skewing angles. The second one is at a smaller scale and presents a narrower main channel but data are available for both smooth and rough floodplains (Jasem 1990). For this calibration, the value of the turbulent exchange parameter ψ^t is assumed to remain constant at $\psi^t = 0.16$, as the two types of exchanges are modelled independently, even if their effects are finally combined.

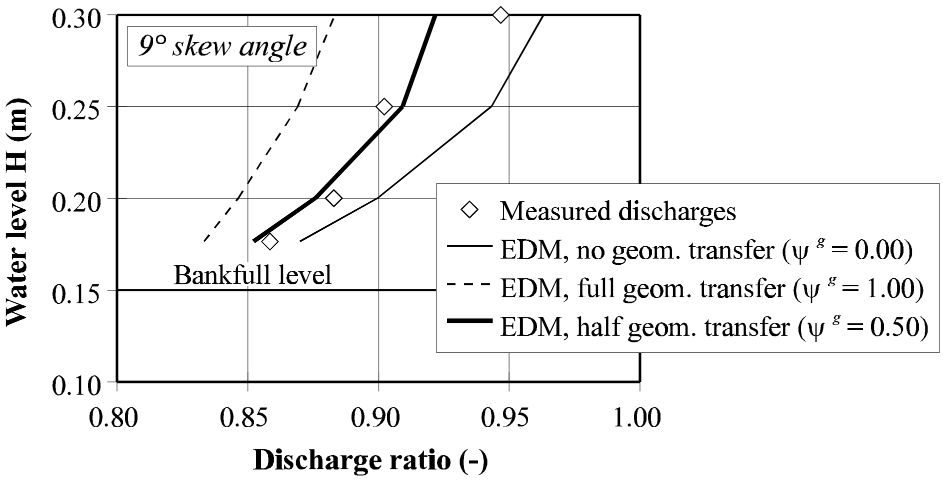

Figure 4.8 : Discharge in skewed channels : EDM calculation against FCF data (Elliott and Sellin 1990), discharges expressed as fraction of the discharges computed by the DCM

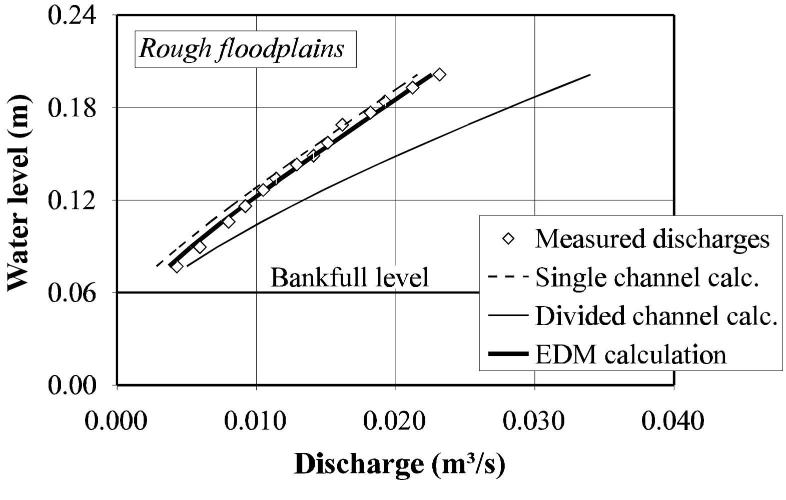

Figure 4.9 : Discharge in skewed channels : calculation against Jasem's data (1990)

Figure 4.8 presents the stage-discharge data for one of FCF data, where the discharges are normalised for legibility with respect to the DCM computed discharges. It shows that the standard EDM for prismatic flows ($\psi^t = 0.16$, $\psi^g = 0$) overestimates the discharge, whereas taking the geometrical transfer discharge into account without correction factor ($\psi^t = 0.16$, $\psi^g = 1$) increases the head losses and leads to a discharge underestimation. After some adjustments, the best agreement was obtained by taking into account half the geometrical transfer discharge ($\psi^t = 0.16$, $\psi^g = 0.5$). It is presumed that this factor is due to the modelling of the velocity profile transverse evolution as 3 discrete values rather than gradually varied, leading then to an overestimation of the momentum transfer.

The model, with this geometrical exchange correction factor $\psi^g = 0.5$ was tested against Jasem's data (Figure 4.9). Due to the too narrow main channel, for the smooth floodplains case, the compound channel acts as a single one : SCM, DCM and EDM give all the same correct result and their comparison is not significant. In the rough floodplains case, the complete Exchange Discharge Model gives satisfactory results and its prediction fits well the measured discharges.

The use of a same value of ψ^t in the non-prismatic and in the prismatic cases could be questioned. Indeed, the geometrical transfer could affect the turbulent structures that generates the turbulent exchange. For the smallest geometrical transfer, probably both processes coexist, although this should be verified through additional experimental measurements. Therefore, it seems acceptable to use the whole value of the turbulent exchange, with $\psi^t = 0.16$. For larger geometrical transfer, all the turbulent exchange is certainly cancelled out. In this case, the turbulent exchange discharge becomes thus negligible with regard to the geometrical transfer discharge, no matter what value is selected for ψ^t. As an illustration, typical values of the ratio between the transfer discharge q^g and the turbulent exchange discharge q^t can be computed for the FCF skewed-channel experiments reported on Figure 4.8. For the lower water depth (H = 0.175 m), this ratio is in the range 0.50 .. 1.00, and both exchange processes probably exist; while, for the larger water depth (H = 0.30 m), the ratio is larger than 10, and the turbulent exchange is now negligible.

Finally, it should be noted that the calibration of the geometrical correction factor $\psi^g = 0.5$ was only done for geometries with a maximum skew angle of 9° between main channel and floodplains, while larger angles are often observed in the field. Further experimental comparisons are thus needed to validate this calibration for larger skew angle. Nevertheless, the following case study indicates that good results could probably be obtained, even for a meandering channel.

4.7 Case study : River Sambre, Belgium

Up to now, the Exchange Discharge Model proved to give good results when used for a stage-discharge or derived prediction. Here, it is tested in its additional head loss form (4.17) for water profile computation, with the correction applied individually to each cross-section. For this purpose, the EDM was included in a water profile computation software called AXERIV, previously developed at UCL under the name CADRIV (Zech et al. 1988). This software is based on the standard step-method for solving the Bernoulli equation (French 1985) and is thus very similar to most of the usual commercial packages, like for example HEC-Ras (*HEC* 1998).

The upgraded AXERIV software was tested for a 4 km meandering reach of River Sambre, Belgium (Figure 4.10). Grassland floodplains which extend on both sides of the main channel were flooded several times during the last years. The river is partly regulated by dams, and there is no pseudo-uniform flow possible due to control by a downstream weir : a gauging curve can only be obtained from complete water profile computations. Accurate geometric data (with cross-section profiles known at intervals of about 100 m, including floodplains) are available. Eighteen flood events were recorded for both inbank and overbank flows. For each of them, discharge was measured together with upstream and downstream water depths.

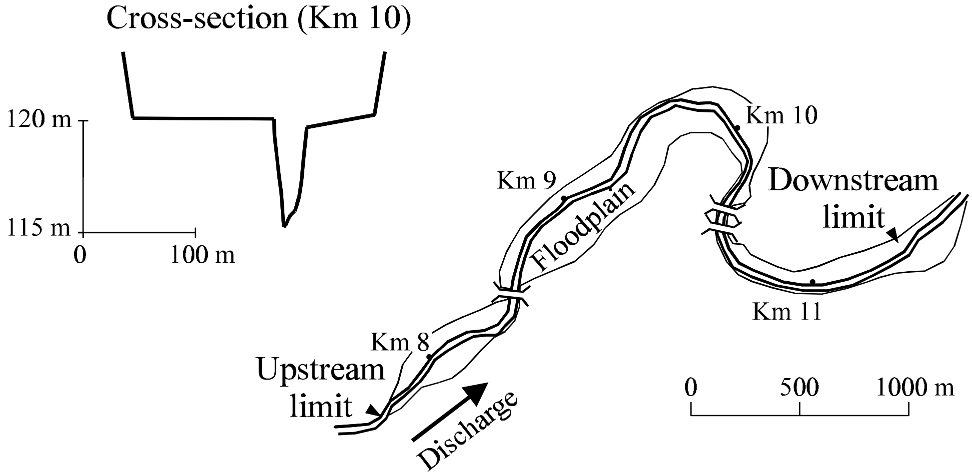

Figure 4.10 : River Sambre, Belgium : plan view of channel and floodplains, typical cross-section

These data were used to get an accurate and realistic calibration of the river roughness parameters, in order to be able to estimate discharge values and flooding of floodplains for future flood events. As no intermediate water levels were recorded along the reach, global roughness coefficients were estimated for the whole reach : one for the main channel and one for both floodplains. Both roughness coefficients are taken constant with flow depth and are not affected by seasonal variation as all the recorded floods only occurred in winter.

For each gauged discharge, a water profile was computed from the corresponding measured downstream depth and tentative roughness coefficients. The upstream computed water level was then compared to the measured one. For inbank gauged flows (discharge less than 100 m³/s), the fitting between computed upstream level and measured data gives a main-channel Manning's roughness coefficient of $n_c = 0.026$.

Overbank flow calculations were then performed in the same way to get the value of the roughness coefficient for the floodplains. Three different methods were used : the Single Channel Method, the Divided Channel Method (using HEC-Ras) and the Exchange Discharge Model. They are synthesised on Figure 4.11 : each gauged discharge presents its specific downstream water level, the upstream calculated levels are shown compared to the measured values. Manning roughness coefficients obtained from calibration are reported in Table 4.3.

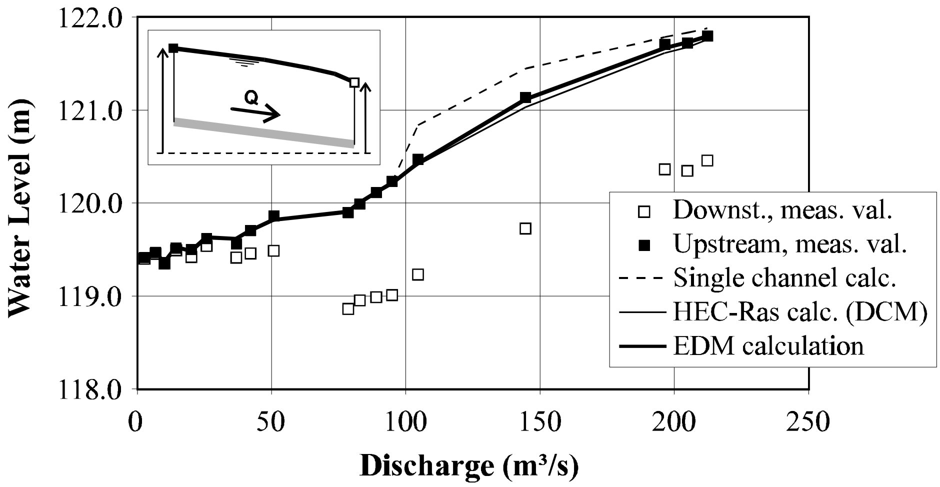

Figure 4.11 : Water-profile computation in River Sambre, Belgium. Measured downstream water levels, measured and computed upstream water levels (lines between points are only drawn for figure legibility)

Table 4.3 : Manning roughness coefficients used for water-profile computation in River Sambre

Method	Main channel : n_c	Floodplain : n_f
SCM	0.026	0.026
DCM	0.026	0.100
EDM	0.026	0.031

The results first demonstrate that it is no more possible to use the SCM with the same roughness value as in the main channel, as the energy slope (difference between up- and downstream levels) is over-estimated for low overflow. HEC-Ras (DCM) gives better results, as the energy slope evolution is better estimated. Nevertheless, computations with various floodplains roughness coefficients show that its value can vary in the range $n_f = 0.100 .. 1.000$ which are quite unrealistic when compared to the character of the floodplains as observed in the field.

Finally, the Exchange Discharge Model gives the best results : the correlation between measured and computed energy slope is very good. An accurate floodplains roughness coefficient can be estimated as $n_f = 0.031$, which is coherent with field observations on grasslands. The head loss distribution along the reach length for a given profile (Q = 205 m³/s) shows that the additional loss due to interaction can represent up to 25 % of the total losses (Figure 4.12).

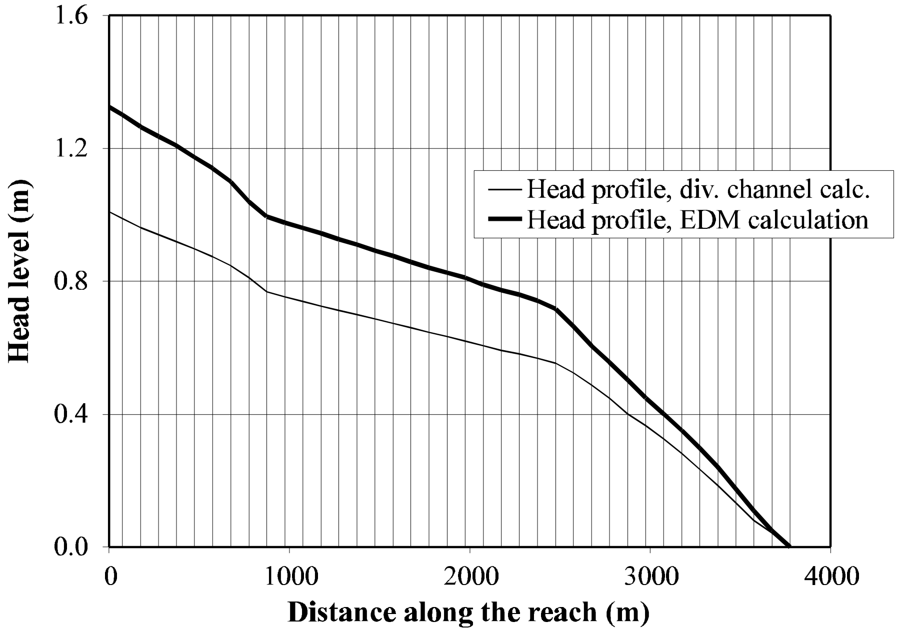

Figure 4.12 : Head loss distribution along the reach of River Sambre, for the discharge Q = 205 m³/s : friction loss evaluated by the DCM and additional loss evaluated by the EDM

In order to check the assumed mean value of $\psi^t = 0.16$ after calibration, a small sensitivity analysis was performed. A 15 % reduced value of $\psi^t = 0.13$ was tested and the floodplain roughness was estimated with the EDM in the same way as previously. As the additional loss decreases, the friction one has to increase and the floodplains roughness coefficient becomes $n_c = 0.032$, which is only 3 % higher and still coherent with field observations. It proves that the EDM sensitivity to his ψ^t value is not too high and that its calibration does not necessarily need to be improved for practical application.

4.8 Extension of the EDM to unsteady flow

4.8.1 Momentum transfer in unsteady flow

As seen above, the EDM proved to produce satisfactory results for steady flow computation in both prismatic and non-prismatic compound channels. Similarly, good results could thus be expected for unsteady flow computation. However, when unsteady flow occurs, additional mass transfer between main channel and floodplains are observed, due to the filling or emptying of the floodplains, following water level variations. This additional mass transfer generates an additional momentum transfer that should be taken into account. The present paragraph investigates the significance of this effect, through an extension of the EDM that considers this geometrical transfer discharge due to unsteady flow.

The extension of the Exchange Discharge Model to unsteady flow is thus founded on two assumptions : (1) the friction slope S_f can be estimated in the same way as the friction slope in steady flow; and (2) the additional geometrical transfer q^{gu} due to unsteady flow generates a momentum transfer in the same way as the other exchange discharges q^t and q^g considered formerly. The first assumption enables the estimation of the friction slope required in the one-dimensional Saint-Venant equation (4.6) on the basis of a uniform-flow equation like the Manning's one. The EDM additional loss is similarly added to the friction term of the Saint-Venant equation. The second assumption simply states the momentum transfer is equal to the multiplication of the velocity difference with the sum of three exchange discharges : (1) the turbulent exchange q^t; (2) the steady-flow geometrical transfer q^g; and (3) the so-called unsteady-flow geometrical transfer q^{gu} resulting from the additional geometrical transfer.

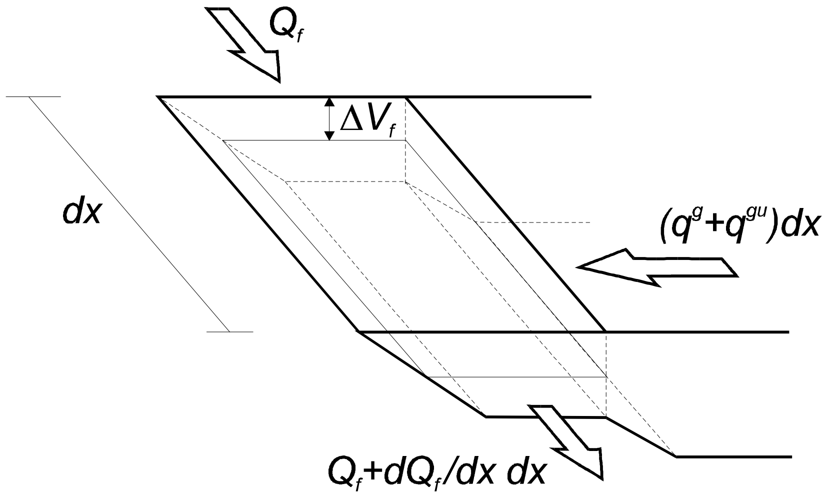

Figure 4.13 : Volume conservation for a floodplain reach during unsteady flow

The value of this unsteady geometrical transfer discharge q^{gu} can be found from the mass balance written for a floodplain reach (subsection *f*) during a time interval Δt (Figure 4.13)

$$\begin{aligned}\Delta V_f &= B_f\, dx \Delta H \\ &= \int_t^{t+\Delta t} \left(Q_f + \left(q^g + q^{gu}\right)dx - Q_f - \frac{\partial Q_f}{\partial x} dx \right) dt \end{aligned} \tag{4.22}$$

where ΔV_f and ΔH are the variation of the water volume in the floodplain and of the water level in the channel, during the time interval Δt; B_f is the mean width of the floodplain; dx is the length of the reach; and Q_f is the floodplain discharge.

The time interval Δt is then defined short enough to assume that q^g and q^{gu} are constant, and that the discharge Q_f varies linearly, during the interval. The integration of (4.22) leads after simplifications to

$$\left(q^{g}+q^{gu}\right)\Delta t = B_f\,\Delta H + \frac{1}{2}\left(\left.\frac{\partial Q_f}{\partial x}\right|_t + \left.\frac{\partial Q_f}{\partial x}\right|_{t+\Delta t}\right) \tag{4.23}$$

Given the definition of q^g by (4.11), at the time t, (4.23) becomes

$$\left(q^{gu}\right)\Delta t = B_f\,\Delta H + \frac{1}{2}\left(\left.\frac{\partial Q_f}{\partial x}\right|_{t+\Delta t} - \left.\frac{\partial Q_f}{\partial x}\right|_t\right) \tag{4.24}$$

and we finally get the value of the unsteady geometrical transfer discharge q^{gu}

$$q^{gu} = B_f\,\frac{\partial H}{\partial t} + \frac{1}{2}\frac{\partial}{\partial t}\left(\frac{\partial Q_f}{\partial x}\right) \tag{4.25}$$

showing that the water entering or leaving the floodplain ($B_f\,\partial H/\partial t$) comes either from the main channel (q^{gu}), or from the upstream reach of the floodplain ($\partial/\partial t\ (\partial Q_f/\partial x)$).

The distribution between both supplying sources will depend on the relative flood wave celerity. For floodplains acting only as storage volume, the floodplain discharge Q_f is equal to zero and, according to (4.25), the water level increase on the floodplain results only from a filling by the main channel. If the floodplain conveyance is not negligible, the floodplain discharge will also lightly contribute to the volume increase. For example, it counts for 5 to 10 % of the feeding in the test case presented in the next part.

4.8.2 Flood wave simulations

This extended EDM model was incorporated in a one-dimensional unsteady flow computational model solving the Saint-Venant equations by an explicit predictor-corrector McCormack scheme (Garcia-Navarro and Saviron 1992). In this numerical scheme, the unsteady geometrical transfer discharge q^{gu} is easy to estimate : while a first value of q^{gu} for the predictor step is given as a result of the previous time step, a second one is then evaluated using the water levels produced by the predictor-step, before processing to the corrector step.

Numerical simulations were performed for comparison with the experimental data of Tominaga et al. (1995). Their test flume was 11.5 m long, with a 0.20-m width main channel flanked by two 0.20-m width symmetrical floodplains. The main-channel depth was 59 mm and the bed slope was fixed at $S_0 = 0.001$. The measurement section was located 7.5 m downstream from the entrance. A controlled flood wave was imposed upstream, with discharge increasing linearly from 3 to 20 l/s. The time to reach the flood peak was either $T_p = 60$ s or $T_p = 120$ s. The downstream end of the channel was a control section. As no roughness value was published, the present computations are performed with an estimated roughness coefficient equals to $n_c = n_f = 0.010$, corresponding to the perspex walls of the flume. These values seem to be confirmed by the correct prediction of the water level, in steady-flow condition, just before the begining of the flooding.

Figure 4.14 presents the water level evolution in the measurement section, for the hydrograph with peak time T_p = 60 s. Three simulations where performed : one with the classical DCM, one with the steady-flow EDM (including turbulent q^t and steady geometrical q^g exchanges), and the last one with the unsteady-flow EDM (also including unsteady geometrical exchange q^{gu}). The rising stage is well estimated by the three models. For the falling stage, all three methods slightly underestimate the water level, and the unsteady EDM gives the best prediction.

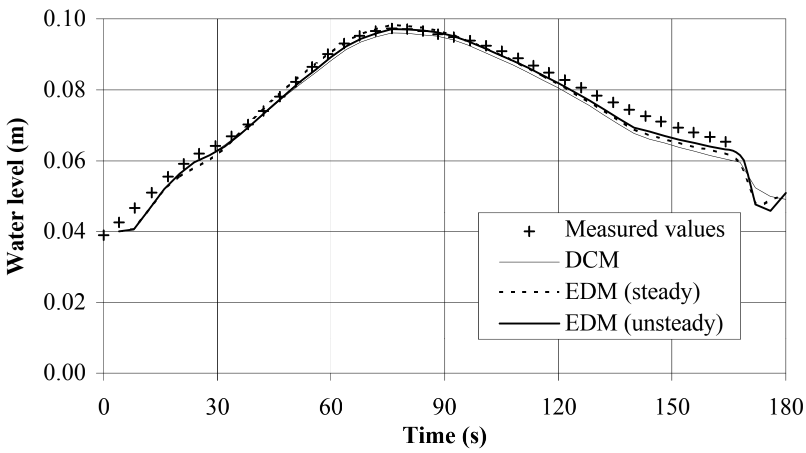

Figure 4.14 : Water level evolution with time (T_p = 60s)

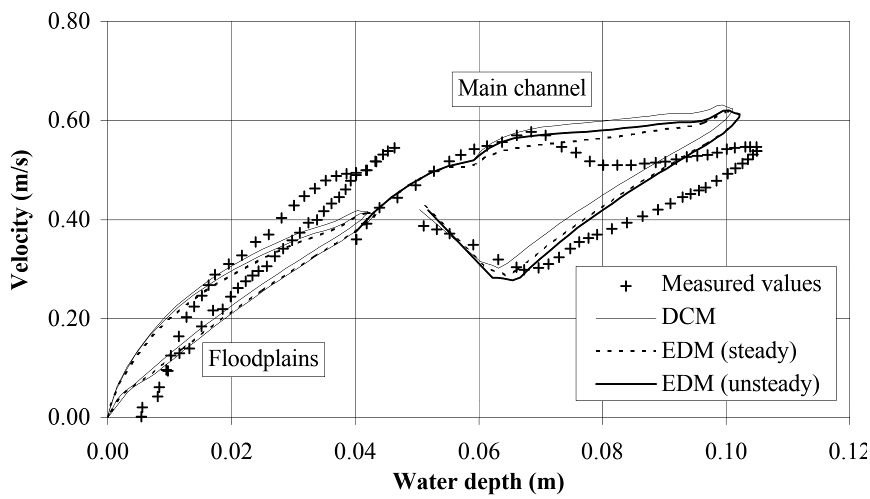

Figure 4.15 : Velocity-stage loop curve (T_p = 120s)

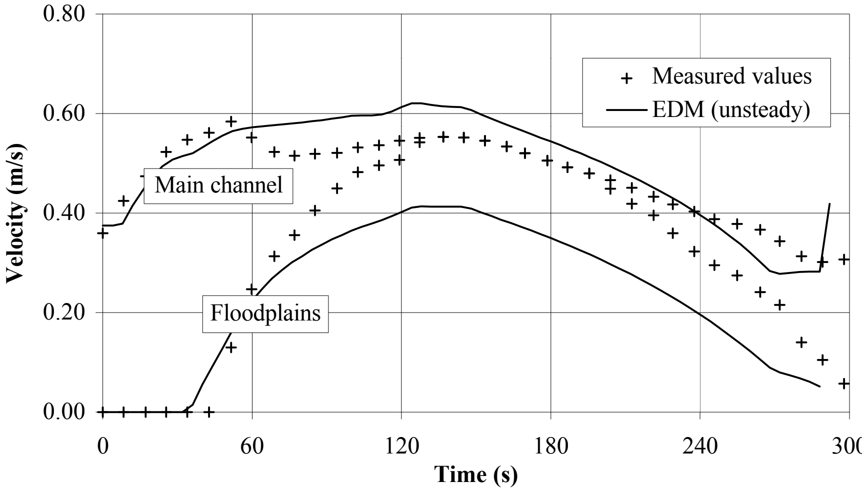

Figure 4.16 : Subsection velocities evolution with time (T_p = 120s)

Figure 4.15 presents velocity-water level loop curves for both main channel and floodplain. All the three methods present curves of similar aspect when compared to experimental data but fail to model it accurately. One explanation is to be found in Figure 4.16 which presents measured and computed velocities as a function of time, showing that the computed one does not match the measurements. Indeed, during such a short flood event in a rather short flume, it is possible in the experiments that the flow does not reach a velocity distribution corresponding to the uniform flow, whereas the computation always assumes such uniform-flow velocity distribution.

4.8.3 Additional head loss analysis

The evolution according to the time of the friction slope S_f and of the additional head loss S_a is presented on Figure 4.17. During the stage rise, the discharge increase is relatively greater than the rise of the water level and of the corresponding conveyance. As a result, the friction slope is higher than the channel bottom slope $S_0 = 0.001$. It is only later, during the recession, that the discharge decrease leads to lower friction. This may explain the loop shape of the velocity-stage curves of Figure 4.15. The friction-slope peak at 170 s corresponds to the end of floodplain emptying : as the momentum transfer suddenly disappears, the water level decreases and the friction slope arises.

The evolution of additional losses is easier to explain when referring to Figure 4.18 that presents the discharge exchanged through the interface between the main channel and a floodplain. As the floodplains in the actual case are not so wide, the turbulent exchange discharge q^t is significantly higher than the geometrical ones. It should be noted that its maximum value, higher than 1 l/s/m, is not negligible compared to the peak value of the total channel discharge of 20 l/s.

The steady-flow geometrical transfer discharge q^g is negative during the flooding, as the floodplain conveyance decreases downward. Indeed, since the channel discharge increases according to the time, the water profile is rather steep at the downstream end of the channel, leading to a downward decreasing water depth on the floodplains. During the recession, the profile will be more parallel to the channel bottom and the steady-flow geometrical transfer will reduce to zero.

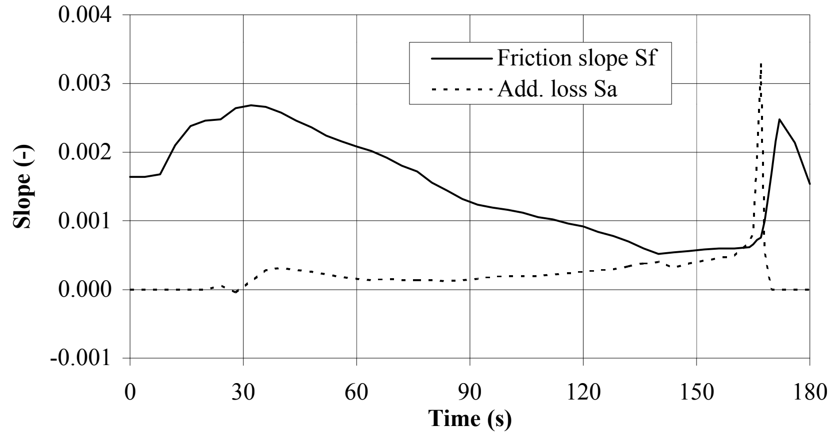

Figure 4.17 : Friction slope and additional loss evolution with time (T_p = 60s)

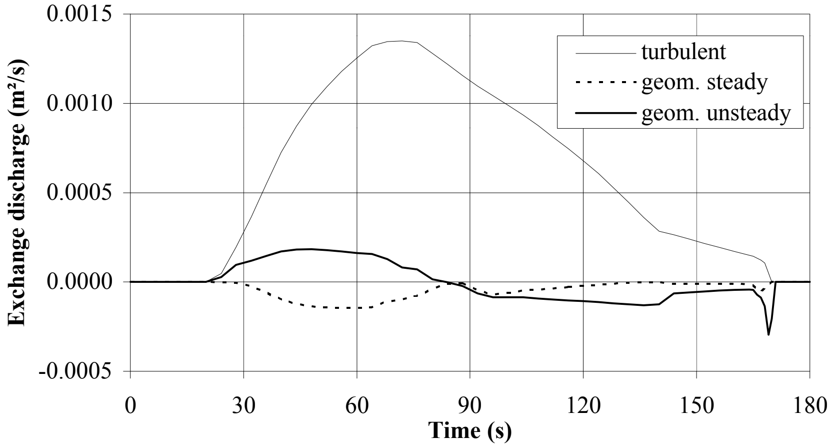

Figure 4.18 : Exchange discharges evolution with time (T_p = 60s)

The geometrical transfer discharge q^{gu} due to unsteadiness is positive toward the floodplains during the rising stage as the water level is increasing. For this particular example, it approximately counterbalances the steady-flow geometrical transfer, resulting in a sum near zero. For this reason, the additional loss from the unsteady EDM computation is lower than from the steady-flow model, giving lower water profiles due to lower total head losses (Figure 4.14). During the stage recession, the floodplains are emptying (with a maximum discharge just when flow is leaving floodplains, at 165 s), the geometrical transfer due to unsteadiness is negative and the associated momentum transfer slows down the main channel, corresponding to higher additional loss (Figure 4.17), with a peak when water is completely leaving the floodplains.

From these results, one can conclude that the extended EDM for unsteady flow seems to reproduce appropriately existing phenomena : during flooding, the momentum transfer increases the floodplains discharge and does not interfere with main channel. During recession, it enlarges the main-channel losses in such a way that floodplains emptying may be delayed.

However, one should point out that the hydrographs experimentally investigated by Tominaga et al. (1995) are maybe unrealistically steep when considering natural rivers. If we assume that Tominaga et al. flume is a scale representation of a 20-m wide main channel, using a Froude similitude, the corresponding discharges and peak times are respectively Q = 300 .. 2000 m^3/s and T_p = 10 or 20 minutes. Excepted maybe in urban area, the peak time in natural rivers is several order of magnitude longer. The unsteady-flow transfer discharge is thus expected to be also several order of magnitude lower in natural rivers. Accordingly, the corresponding momentum transfer can be neglected in most of the cases, and has to be strictly considered only when dealing with rapidly growing floods.

4.9 Summary of the method (steady flow case)

4.9.1 Discharge Computation

For computing the discharge Q as a function of water depth (stage-discharge curve), required data are : (1) The channel cross-section; (2) the mean bottom slope S_0; and (3) an estimation of the Manning roughness coefficients n_i for each subsection.

The following steps have to be carried out :

1. For the given water depth H, estimate the corresponding cross-section geometrical parameters for each subsection : area A_i, hydraulic radius R_i, conveyance K_i ($=A_i R_i^{2/3}/n_i$), and bank level h_i.

2. If applicable (non-prismatic flow), estimate the rate of change of the conveyances of the floodplains $\kappa_{ij}\, dK_f/dx$ as described by equation (4.12).

3. Compute ratio χ_i values by solving equation (4.14) with a value of ψ^t = 0.16 and ψ^g = 0.5, using the procedure described in Appendix 2 : solve equations (A2.13) and (A2.12) for auxiliary variable X_i by Newton-Raphson method and then get χ_i from equation (A2.9).

4. Compute the discharge Q by equation (4.15).

A numerical example of such a calculation is given in Appendix 2.

4.9.2 Energy Slope Calculation

For estimating an energy slope S_e as a function of water depth (water profile computation), required data are : (1) The discharge Q; (2) the channel cross-section; and (3) an estimation of the Manning roughness coefficients n_i for each subsection.

The following steps have to be carried out :

1. For the given water depth H, estimate the corresponding cross-section geometrical parameters for each subsections : area A_i, hydraulic radius R_i, conveyance K_i ($=A_i R_i^{2/3}/n_i$), and bank level h_i.

2. Estimate the rate of change of the conveyances of the floodplains $\kappa_{ij}\ dK_f/dx$ as described by equation (4.12).

3. Compute ratio χ_i values by solving equation (4.14) with a value of $\psi^t = 0.16$ and $\psi^g = 0.5$, using the procedure described in Appendix 2 : solve equations (A2.13) and (A2.12) for auxiliary variable X_i by Newton-Raphson method and then get χ_i from equation (A2.9).

4. Compute the global ratio χ value by equation (4.18).

5. Compute the correct energy slope S_e by equation (4.17).

4.10 Conclusion

A new model of main channel to floodplain interaction in compound channels so-called the Exchange Discharge Model has been presented in this chapter. The momentum transfer is estimated as the product of the velocity difference at the interface by the discharge exchanged through this interface due to turbulence. The turbulent exchange discharge is estimated by a model analogous to a mixing length model including a proportionality factor ψ^t which is found to be reasonably constant from comparison with experimental data.

The Exchange Discharge Model improves the stage-discharge prediction for experimental data and natural data if compared to the classical Single Channel and Divided Channel Methods. Its accuracy is similar to Ackers' Method but the model presents the advantage to be a physically-based model without numerous parameter fitting. It is also as accurate as the Lateral Distribution Method for natural rivers and rather better for experimental flume, when no specific calibration are used.

For non-prismatic flows, the Exchange Discharge Model is extended by taking into account, in the momentum transfer, a mass transfer corresponding to the geometrical change. The EDM supplies then satisfactory stage-discharge results for the skewed channel case tested, providing that a reduction coefficient $\psi^g = 0.5$ is applied to the geometrical transfer discharge. This reduction can not be completely explained on basis of the existing experimental data. More experimental data, as developed in Part III, are therefore needed.

Lastly, the momentum transfer is formulated in the Exchange Discharge Model as an additional head loss, thus enabling practical water-profile computations. The proposed model can be easily implemented in most of the commonly-used software packages. Tested for a case study on River Sambre in Belgium, the model gave correct flow predictions when used with realistic roughness coefficient values held constant for all water depths. This was not the case with the widely-used HEC-Ras software (that uses the Divided Channel Method).

A extension of the EDM for unsteady flow is also proposed, taking into account the additional unsteady-flow geometrical transfer discharge and the corresponding momentum transfer. The computational results obtained using this extension seem to reproduce appropriately some of the basic flow processes measured experimentally. It should be pointed out that this unsteady-flow geometrical transfer discharge is only significant when dealing with sudden events in urban areas, presenting rapidly growing discharge. Its effect can be neglected when considering more natural river conditions.

As a conclusion, the proposed EDM, which yields accurate results for both prismatic and non-prismatic cases, and which is easy to use, even in water-profile computations, seems to meet the objectives of developing a new theoretically founded method for compound channel discharge estimation. However, the proposed model raises new questions regarding : (1) the validity of the turbulent exchange discharge model; and (2) the significance of both calibration parameters. These points will be further investigated in the next two parts of this work. In Part II, modelling of the periodical turbulent structures generating the turbulent exchange discharge will be performed, and a tentative model of these structures, enabling a better understanding of the parameter ψ^t significance, will be proposed. In Part III, experimental measurements of the geometrical transfer discharge and corresponding momentum transfer will be performed in a compound channel with symmetrically narrowing floodplains, enabling further discussion of this transfer.

Part II

Turbulent exchange

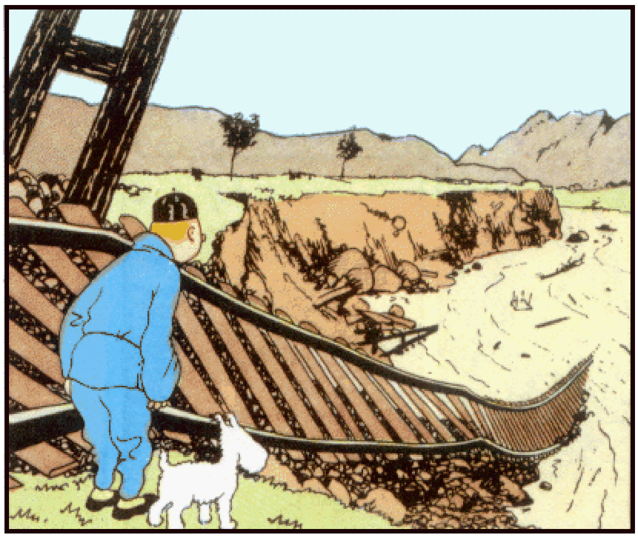

A flood on the Yang-Tse River,
in Hergé (1946), Le Lotus Bleu

Chapter 5
Periodical turbulent structures in compound channels : State of the art

5.1 Introduction

When developing the Exchange Discharge Model in Chapter 4, a so-called turbulent exchange discharge was defined at the interface between main-channel and floodplain. This turbulent exchange discharge, and the associated momentum transfer, may allow to model the effect of the large periodical structures observed at the surface of a compound-channel flow (Figure 5.1) on the stage-discharge relation. The turbulent exchange was defined as being proportional to the interface area and to the velocity difference between subsections. The proportionality factor ψ^t was said to be similar, in some degree, to a kind of mixing length.

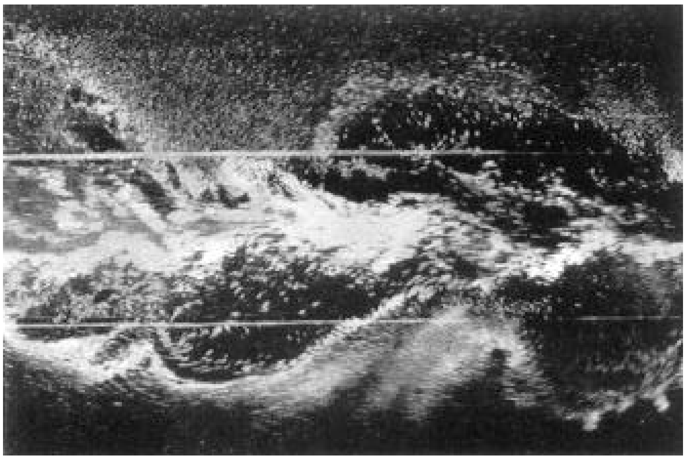

Figure 5.1 : Large periodical structures at the surface of a compound-channel flow (Sellin 1964)

The purpose of the second Part of this work is therefore to investigate further this exchange discharge concept and to clarify the significance of the ψ^t parameter. At first, the periodical structures will be further investigated using new experimental measurements, hydrodynamic stability analysis and numerical computations. Using those results, a qualitative description of the observed large vortices will be proposed, together with a tentative modelling of the corresponding exchange discharge and momentum transfer.

As an introduction, this brief chapter will review some significant previous works regarding these periodical structures. The findings relevant to the present work will be highlighted.

5.2 Experimental observations

As quoted in Chapter 1, Sellin (1964) was the first to report the observation of large-scale turbulent structures at the surface of a compound channel (Figure 5.1). Using aluminium powder scattered on the water surface and a camera moving downstream at constant velocity, he highlighted the presence of large vortices, whose vertical axis are located near the interfaces between main channel and floodplains. By analysing the pictures, the distances between adjacent vortex centres were estimated. The frequency distribution of these distances – or wave length – showed a clear peak for a wave-length value that equals twice the main-channel width, for this particular channel geometry.

Alavian and Chu (1985) also investigated experimentally the vortex structures in an experimental compound-channel flow. They performed an hydrodynamic stability analysis of the parallel shear flow corresponding to the measured velocity profiles. Analysing the neutral stability curves, as a function of the bottom-friction coefficient, they showed that the latter has a stabilising effect on the flow.

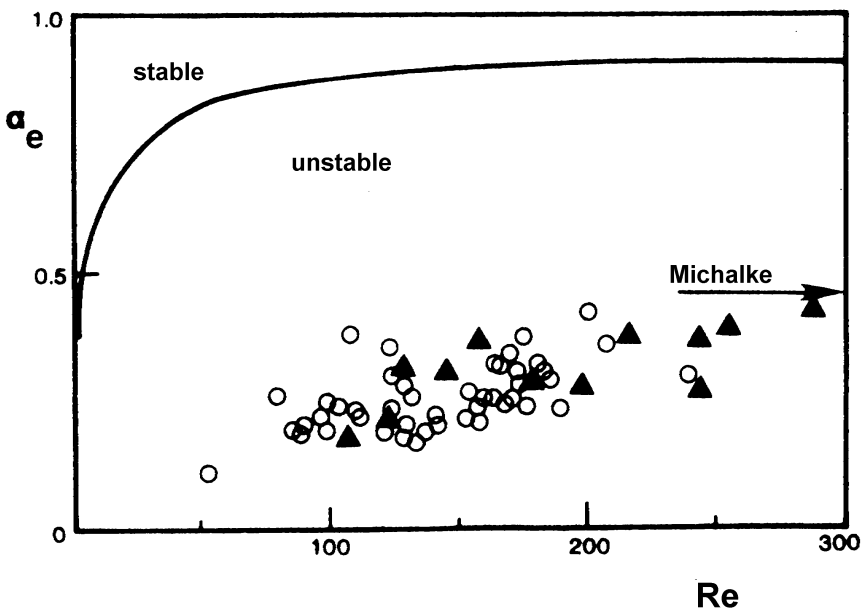

Figure 5.2 : Measured wave number α of large eddies, as a function of Reynolds number (Tamai et al. 1986)

Tamai et al. (1986) achieved systematic measurements for several compound geometries, in both open-channel and closed-channel flow. The vortex wave lengths were recorded through hydrogen-bubble wire flow-visualisation techniques; and, as in Sellin's experiments, a clear periodicity was observed. With reference to hydrodynamic stability analysis, they suggested that the observed wave length could correspond to the most rapidly amplified perturbation of the mean flow. Indeed, for increasing Reynolds number, Figure 5.2 shows that the measured wave-number of the large eddies tends towards the wave number of the most amplified perturbation for inviscid flow, as computed by Michalke (1964) – see below.

Similar experiments were performed by Meyer and Rehme (1994), but for air flow in a closed duct presenting a kind of compound-channel shape. Using Laser-Doppler Anemometry (LDA), they also identified clear periodical structures. The length scale of large eddies was found to be geometry-dependent, but almost independent of the mean velocity.

Fukuoka and Watanabe (1995, 1997) particularly investigated the influence on the turbulent structures of a vegetation-covered area located just at the interface between the main channel and the floodplain. They achieved vortices wave-length measurements in a laboratory flume. Additionally, they observed similar vortices at the surface of an actual river, using aerial photography.

Using Particle Imaging Velocimetry (PIV) together with LDA, Nezu and Nakayama (1997) were able to give a more complete description of the tri-dimensional flow structures in a compound channel (Figure 5.3). Their experiments highlighted time-discontinuities of the helical secondary-currents previously observed through time-averaged LDA measurements (Tominaga and Nezu 1991), as quoted in Chapter 1. The resulting intermittent upward flows along the main-channel bank have therefore strong interaction with the horizontal vortices observed at the interface.

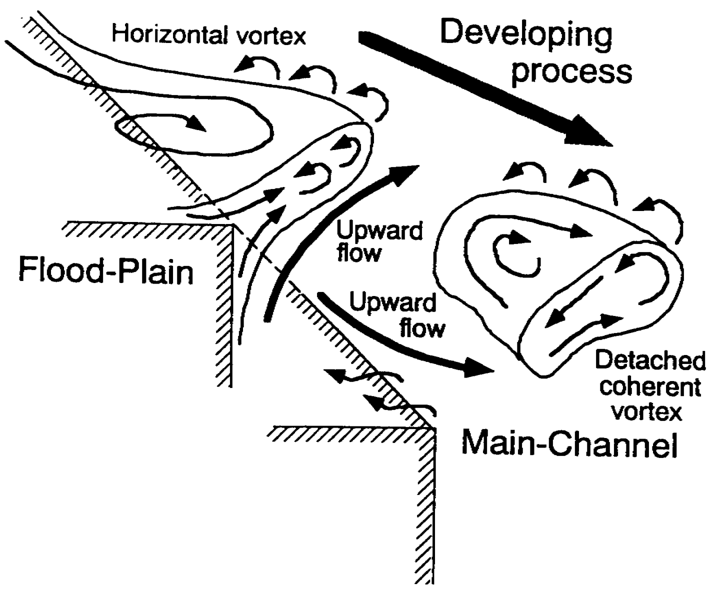

Figure 5.3 : Two- and tri-dimensional flow structures in a compound channel (Nezu and Nakayama 1997)

Using similar PIV techniques, Lukowicz and Köngeter (1999) also investigated the development of the horizontal vortices at the interface. They showed that, in some degree, the vortex shape could be described by an Oseen-vortex equation. This point will be further developed in Chapter 10, where the Oseen-vortex equation will be presented and compared with some results from the present work.

5.3 Modelling of periodical structures

5.3.1 Hydrodynamic stability analysis

As quoted in the previous paragraph, several authors used hydrodynamic stability analysis in order to get information on the development of horizontal vortices. The main purpose of such an analysis is to determine whether a small perturbation of a given flow (the so-called basic flow) will grow up (instability) or will be damped (stability); and, as a function of selected parameters depicting the basic flow, to define neutral stability curves, separating stable and unstable flows. In the compound-channel case, the basic flow to be considered is a parallel shear flow, for which general results are already well documented (Drazin and Reid 1981). A more complete presentation of the hydrodynamic stability analysis of a parallel shear flow will be given in Chapter 7, with application to compound channels; while some significant previous works are already mentioned here.

Tamai et al. (1986) suggested that the vortex wave length could correspond to the wave length of the most rapidly amplified perturbation in the mean flow. However, they only referred to the early works of Michalke (1964) who analysed the stability of a general two-dimensional parallel shear flow, on the basis of the two-dimensional Navier-Stokes equations. Further information could thus be gathered from extended analysis considering the complete shallow-water equations, including the bed friction.

Such an analysis, already suggested by Alavian and Chu (1985), was fully developed by Chu et al. (1991), for an inviscid flow ($Re \to \infty$). Chu et al. considered either a depth or a bed-friction transverse variation, that generates a basic flow whose velocity profile is modelled either by a hyperbolic-tangent function (mixing-layer flow) or by a hyperbolic-secant function (jet flow) (Figure 5.4). Assuming a rigid water surface, they developed an extended stability-analysis equation and investigated temporally growing perturbations. Their results showed the stabilising effect of the bottom friction : for a friction coefficient high enough, and for a bed level variation smooth enough (weak shearing), the flow becomes stable for any perturbation wave-length.

Fukuoka and Watanabe (1995, 1997) also considered bed-friction effects, but using a non-linear stability analysis, limited to the second order mode. They obtained a very good agreement with their experimental results for channel with vegetation-covered area at the interface between subsections.

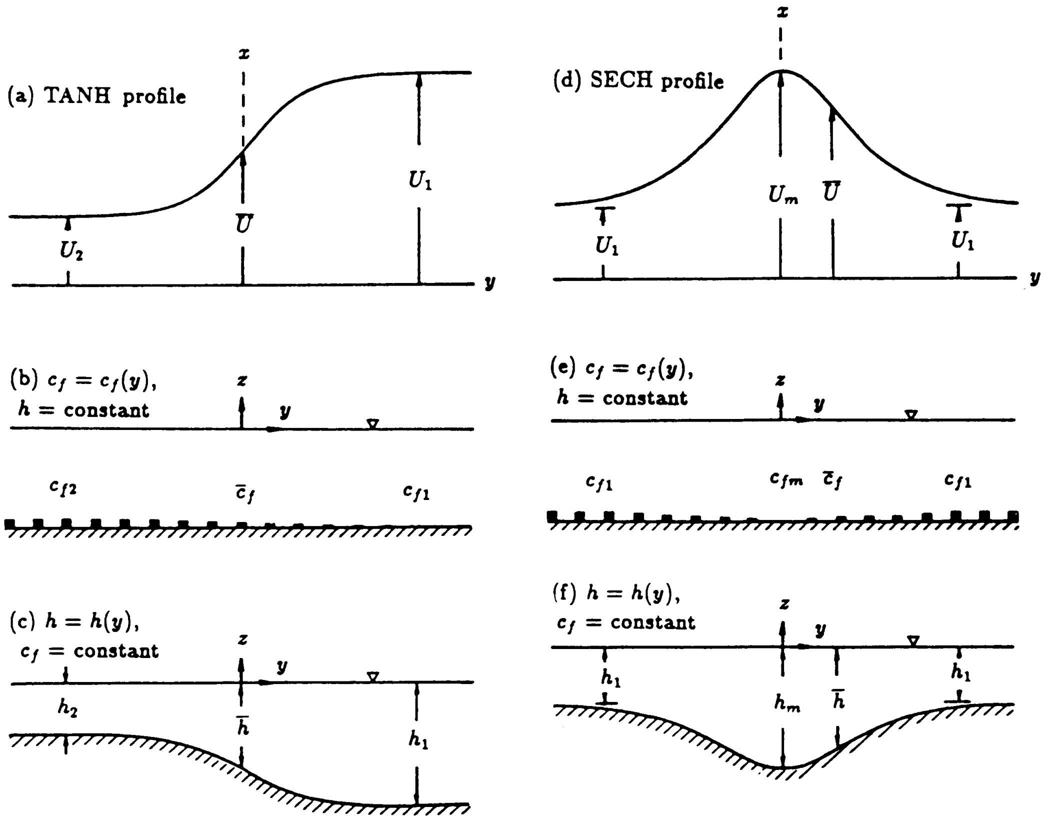

Figure 5.4 : Geometries and velocity profiles analysed by Chu et al. (1991) : the velocity profiles are created either by varying friction coefficient (b, e), or by varying depth (c, f)

Modelling the instabilities of wakes (such as an island wake), Chen and Jirka (1997) included the viscosity effect in their analysis. However, the stability results became almost independent of the viscosity variations as soon as Reynolds number are larger than Re = 10^3. On the other hand, the bed-friction stabilising effect was again highlighted. In addition, Chen and Jirka considered not only temporal growing of the perturbations but also spatial growing, in such a way that the flow does no more need to be considered as periodical in space.

Experimental investigation and instability analysis of the spatial growth of a single mixing-layer in a compound channel has been performed by Chu and Babarutsi (1988) and by van Prooijen and Uijttewaal (2001). These observations show that, due to the mixing-layer confinement by river walls, a maximum value of the vortex wave-length exists, and vortices merging is limited to a certain extend.

A last improvement of the analysis is proposed by Ghidaoui and Kolyshkin (1999). They performed a stability analysis for shallow-water flow, that allows water-surface level variation, in opposition to the rigid-lid assumption previously used. They showed that the classical rigid-lid assumption tends to overestimate the instability domain extension; while the wave length corresponding to the most amplified perturbation seems to remain constant.

Research by Chu et al., Chen and Jirka, Ghidaoui and Kolyshkin, etc. clearly improved the stability analysis results. Nevertheless, they mostly focused on the neutral curve determination which is classically the main target of such an analysis; while, for the present work, following Tamai et al., the determination of the wave length corresponding to the most amplified perturbation should be the main objective. This latter point will thus be the aim of Chapter 7. Chu et al.'s equations will be used for that purpose, as it has been showed that the bed-friction effect was dominating, compared to the viscosity and to the water-level variations.

5.3.2 Numerical computation

As quoted in Chapter 1, many authors attempted to model numerically the flow in a compound channel (Krishnappan and Lau 1986; Keller and Rodi 1988; Naot et al. 1993a; etc.). However, most of them used time-averaged modelling; or, even when using Large Eddy Simulation (Thomas and Williams 1995), they only analysed time-averaged results. Only a few authors performed unsteady modelling and investigated the periodical structures in a compound channel or in a partly-vegetated channel generating a similar shear layer.

Nadaoka and Yagi (1998) developed such unsteady simulations, using a depth-averaged model called SDS-2DH. This model represents explicitly the large horizontal vortices due to the transverse shearing; while the small-scale turbulence effect is implicitly modelled through an eddy-viscosity corresponding to the so-called "Sub-Depth-Scale turbulence". When applied to a partly-vegetated channel case, large horizontal vortices actually developed; and the resulting velocity profile and velocity variations were satisfactorily reproduced, when compared with experimental data. The additional shear-stress due to the corresponding momentum transfer was of the same order of magnitude as the shear-stress due to the sub-depth-scale turbulence. In similar numerical experiments, Ikeda (1999) found that large-eddy shear-stress could even stands for 75 % of the whole shear stress.

Tri-dimensional numerical experiments by Hosoda et al. (1998) should also be pointed out, as they modelled the development of both helical secondary-currents and large horizontal-vortices in a compound channel, using an Unsteady-RANS model. Their results correspond, at least qualitatively, to available observations of these structures (such as in Nezu and Nakayama 1997).

However, in the present work, Nadaoka and Yagi model will be preferred as it is based on a depth-averaged modelling, which is much simpler to implement than a 3-D model as the Hosoda et al. one Moreover, it seems that this depth-averaged model has not been applied to compound channels before. Full developments and results will thus be presented in Chapter 8.

Chapter 6
Experimental measurements of periodical structures

6.1 Introduction : experimental set-up

As pointed out in the previous Chapter, few measurements of periodical structures are available for flow in compound channels. New experimental measurements were therefore initiated, with two main objectives : (1) obtain a complete data set, giving information on the periodical structures, but also including stage-discharge curves and velocity profiles; and (2) benefit from new measurement techniques, such as Particle Tracking Velocimetry (PTV), to investigate not only the structure in itself, as done by Nezu and Nakayama (1997), but also its periodicity characteristics. The measurements were performed for an asymmetric compound-channel cross section (Figure 6.1), in such a way that a unique shear layer will be observed at the interface between the main-channel and the single floodplain.

The asymmetric cross section has been constructed with coated plywood in the UCL compound-channel flume. This flume is basically 10-m long, 1.20-m wide (only 0.80 m of the available width were used in the present experiments), and is set to a bottom slope $S_0 = 0.99 \times 10^{-3}$. It is supplied upstream through a 2-m length stilling tank and has a downstream 1-m length outlet tank, with an adjustable weir. The total available discharge is 30 l/s. Classical measuring devices include an electromagnetic flowmeter, for the discharge; an automatic point gauge installed on a trolley, for the water levels; and a Pitot tube, for the velocities. Further details on both equipment and measuring procedures are available in Appendix 3.

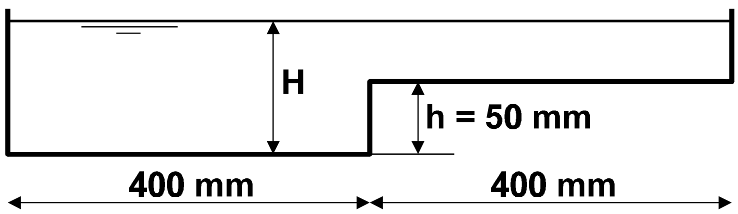

Figure 6.1 : Cross section of the experimental asymmetric compound channel

Observations of the turbulent structures were performed using a Particle-Tracking Velocimetry (PTV) system : the flow free-surface was seeded with floating tracers, whose successive positions were recorded using a digital camera (Figure 6.2). Post-processing of the recorded images included the identification of the tracers and the reconstruction of their trajectories; while further analysis enabled the detection of the periodical structures and an estimation of their wave length.

This Chapter will first present classical measurements performed in the asymmetric compound section : (1) stage-discharge curve, necessary for setting a uniform-flow water depth in the following experiments; and (2) velocity profiles, required for comparison with the velocity profiles from the PTV measurements. The PTV technique and results are then presented. Lastly, some tentative point-measurements of the velocity temporal variations are reported, using an Acoustic Doppler Probe.

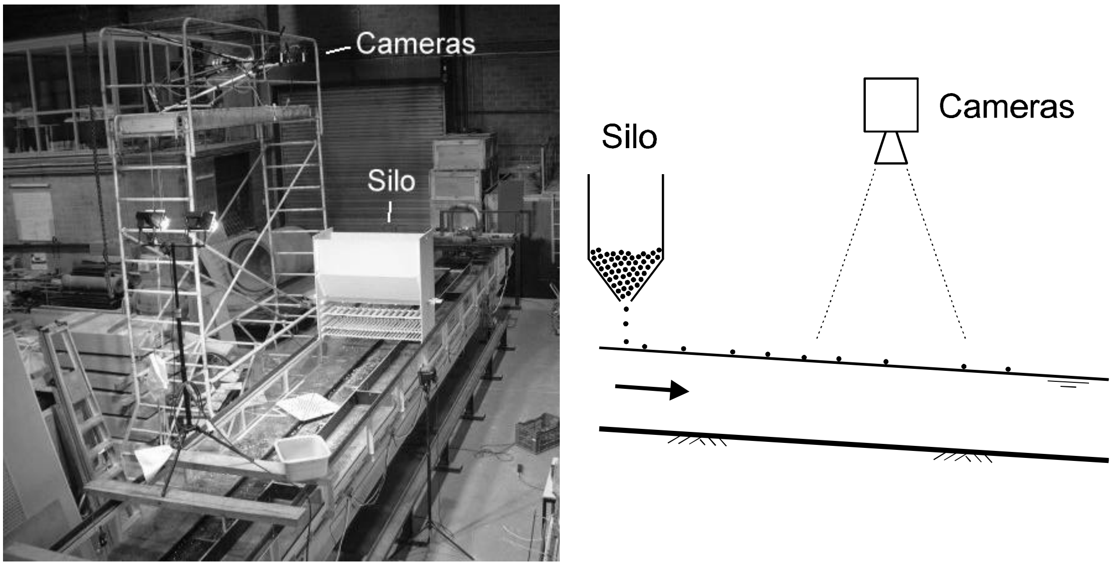

Figure 6.2 : Experimental set-up for Particle Tracking Velocimetry

6.2 Stage-discharge curv e

The stage-discharge curve is obtained from water-depth measurements, in uniform-flow conditions. As detailed in Appendix 3, the uniform flow for a given discharge is achieved by adjusting the downstream water level, until the water profile is parallel to the channel bed. The stage-discharge curve for the asymmetric compound-channel cross-section (Figure 6.1) is plotted on Figure 6.3.

For comparison, the stage-discharge curve is also computed using the EDM. A Manning roughness coefficient equal to n = 0.0107 s/m$^{1/3}$ is selected for both main channel and floodplain. This value is obtained from isolated main-channel stage-discharge measurements (see Chapter 11), and no further fitting is required, demonstrating again the validity of the EDM.

For further experiments, four discharge values are selected, covering relative depth H_r in the range 0.10 .. 0.40 (Table 6.1). Relative depth less than H_r = 0.10 would also be of interest, as it is expected that the shear layer is strongest at the lower floodplain depth, due to the increase of the velocity difference between main channel and floodplain.

However, when the main-channel water depth is less than H = 54 mm, measurement becomes almost impossible on the floodplain, due to too low local water depth ($H - h$ = 4 mm) : the Pitot tube diameter is larger than the water depth; while PTV tracers enter in contact with the bed and do not float anymore. On the other hand, relative depths higher than H_r = 0.40 are less interesting for the present investigation. Indeed, the velocity gradient reduces and the shear layer weakens. Tri-dimensional structures become dominant in such a way that the horizontal vortices have a lower influence. At such depths, the section starts to behave again as a single channel.

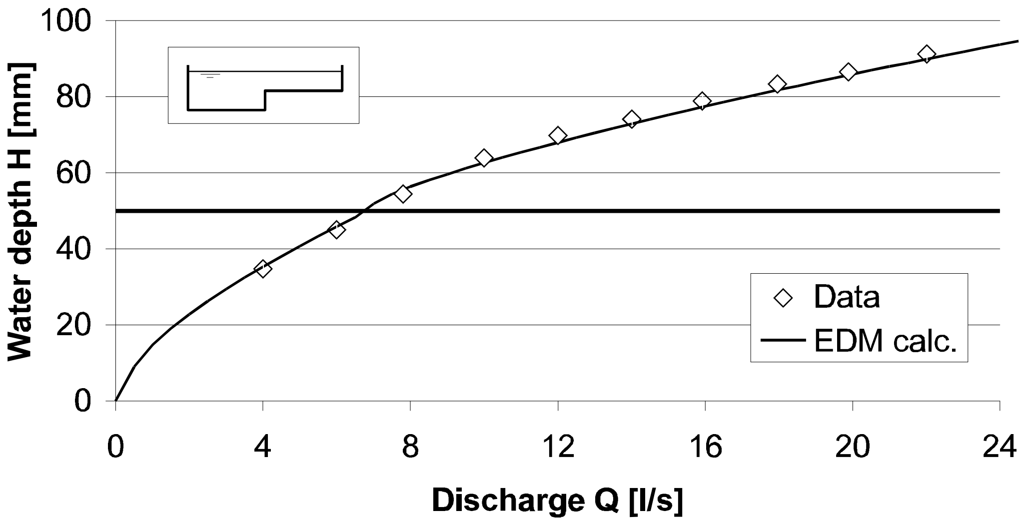

Figure 6.3 : Stage-discharge curve, asymmetric compound channel : measured and computed values

Table 6.1 : Selected discharges and water depths for further experiments

Case	Q (l/s)	H (mm)	H_r
LCA 08	7.8	54.4	0.10
LCA 10	10.0	63.9	0.23
LCA 12	12.0	68.8	0.30
LCA 16	15.9	78.9	0.38

6.3 Velocity profiles : Pitot-tube measurements

For the four selected uniform-flow cases (Table 6.1), velocity measurements are performed using a Pitot tube. The main measurement section is located at the station x = 7 m in the flume, although measurements are also performed in other sections for control purposes. The typical measurement lattice is depicted on Figure 6.4. It includes 11 vertical lines, with 5 to 7 points on each line in the main channel, depending on the water depth; and with 1 to 3 points in the floodplain.

A typical distribution of the velocity longitudinal component *u* is given on Figure 6.5, for the LCA 10 case (Q = 10 l/s) at x = 7 m. Although the measurement mesh is dense enough to get accurate depth-averaged velocities, it is not sufficient to get detailed observation on flow features such as the surface-velocity decrease due to helical secondary currents. However, at this stage, the velocity difference between main channel and floodplain is already clearly seen; while the momentum transfer due the shear layer also appears : velocities in the floodplain are clearly increased near the interface, and slightly decreased in the main channel.

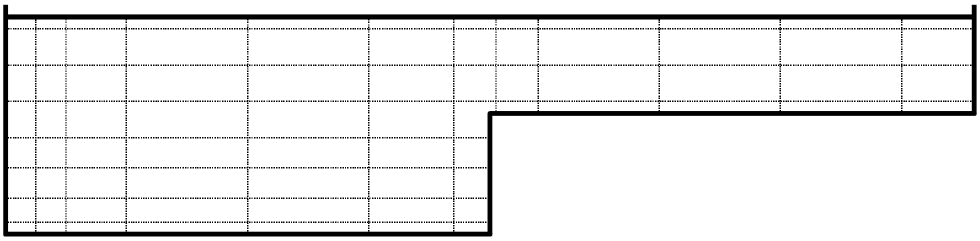

Figure 6.4 : Typical measurement mesh for Pitot tube

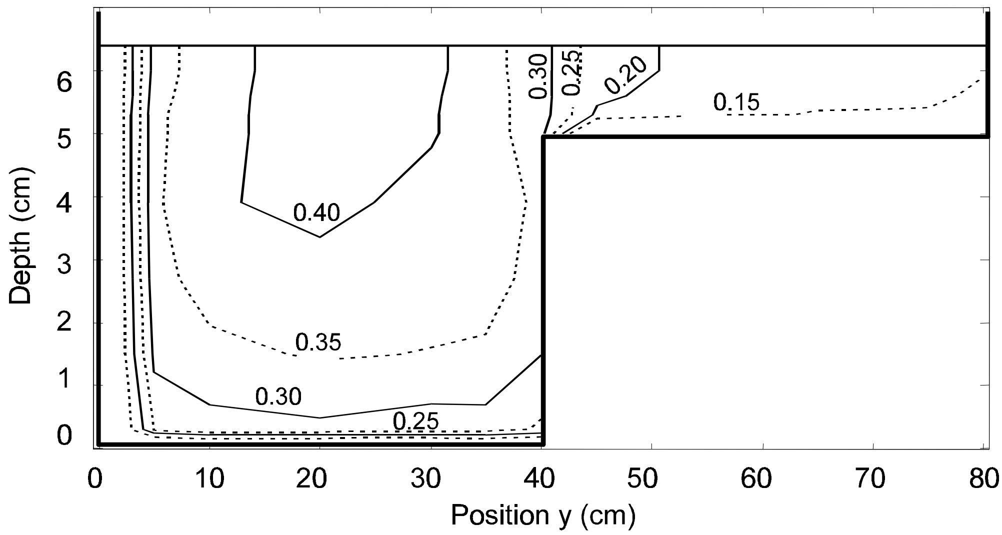

Figure 6.5 : Longitudinal velocity u distribution, LCA 10, x = 7 m

The depth-averaged velocities U are then estimated from the local measurements, and the resulting profile are given on Figure 6.6. The profiles at x = 7 m present the typical shape of a compound-channel flow : the velocity is higher in the main channel than in the floodplain; and, due to momentum transfer, the velocity gradient is smoothed at the interface, with a local velocity reduction in the main channel and a local velocity increase in the floodplain. When the discharge and water depth increase, the velocity increases slightly in the main channel and significantly in the floodplain, resulting in a reduction of the velocity difference.

From the velocity profile measurements at successive stations (see LCA 10 on Figure 6.6), one can wonder if the uniform-flow condition is effectively achieved. Indeed, although the water surface profile is parallel to the channel bottom, at the point-gauge measurement precision, the velocity profile clearly evolves along the channel, with velocity increasing in the main channel and decreasing in the floodplain. As a result, the discharge distribution between subsections changes also according to the position, as shown by Figure 6.7.

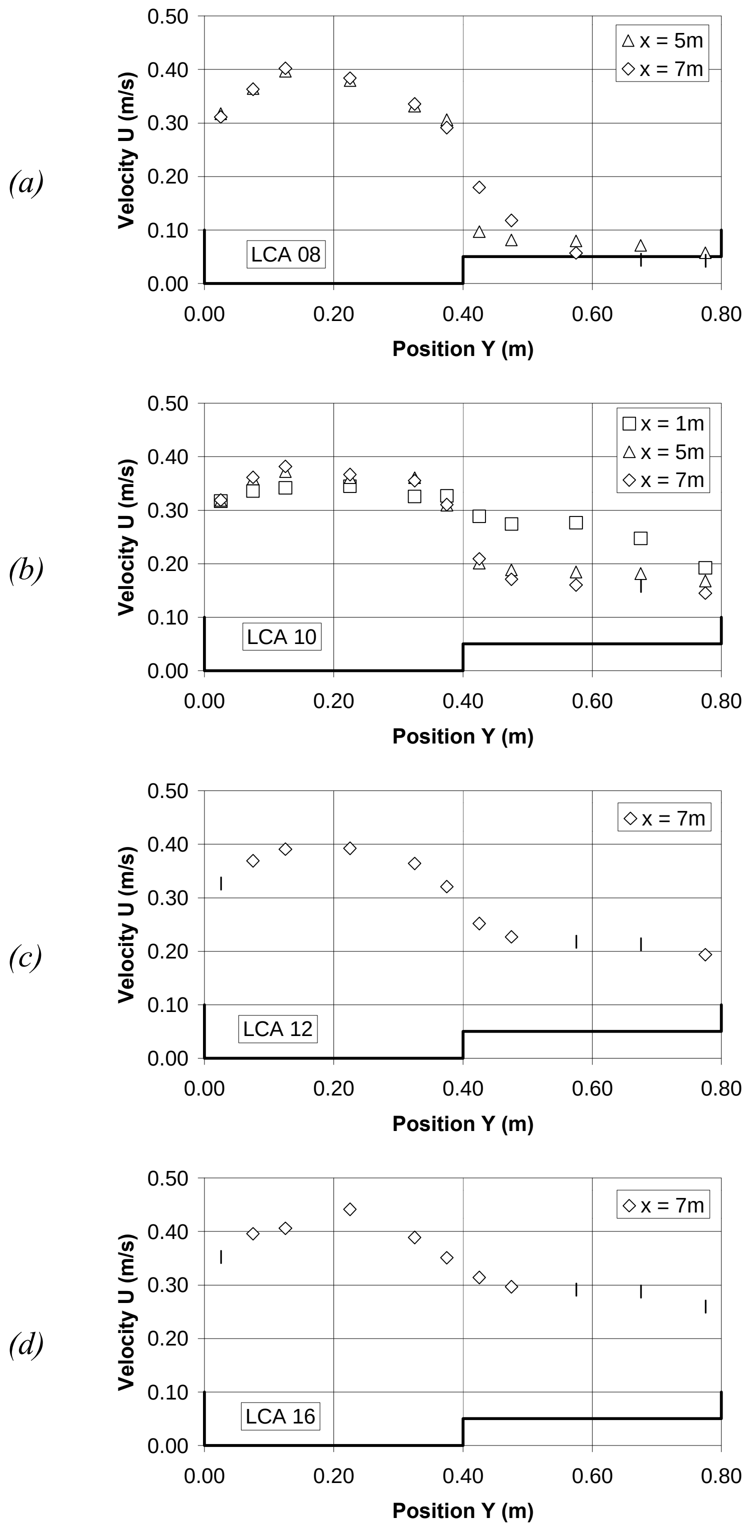

Figure 6.6 : Pitot-tube measurements : depth-averaged velocity profiles

It is presumed that this effect is due to an ill-conditioned upstream condition in the flume. Indeed, it is observed that the flow enters the flume with an almost uniform velocity, resulting in an over-discharge in the floodplain. The flow then has to adapt its distribution towards uniform-flow distribution, generating accordingly a small mass transfer from the floodplain to the main channel. However, this flow-distribution change seems not large enough to affect the parallelism between the water profile and the bed, at least in respect of the measurement device accuracy.

A better flow distribution could be obtained either by using a longer flume, or by modifying the inlet tank arrangement. Whereas the first solution is not possible for the existing facility, the second one has not been used in the present work, due to a lack of time. It is then assumed that, in the measurement section at x = 7 m, the flow is close enough from uniform-flow condition to get valuable observations of periodical turbulent structures. Indeed these structures are expected to have a growth rate large enough. As a result, their shape should be not much influenced by the inlet conditions. They depend thus mainly on the geometry of the flume and on the overall velocity difference, which, in the measurement section, corresponds almost to uniform-flow condition.

A similar ill-conditioning of the upstream velocity distribution is expected for the three other cases (LCA 08, LCA 10 and LCA 16), although detailed measurements were not performed. Only for the LCA 08 case, an additional velocity profile was measured at x = 5 m (Figure 6.6a). This profile shows clear discrepancies with the profile at x = 7 m, due probably to the upstream-distribution ill-conditioning, but also to a lower measurement accuracy in this section. Indeed, the water depth on the floodplain ($H - h$ = 4.4 mm) is close to the Pitot-tube diameter (4 mm), in such a way the latter perturbs quite significantly the flow, and thus the measurement accuracy. Moreover, with such small water depth, the flow is very sensitive to small discontinuities of the channel bed, such as the joints between the plywood plates, located at x = 2, 4, 6 and 8 m.

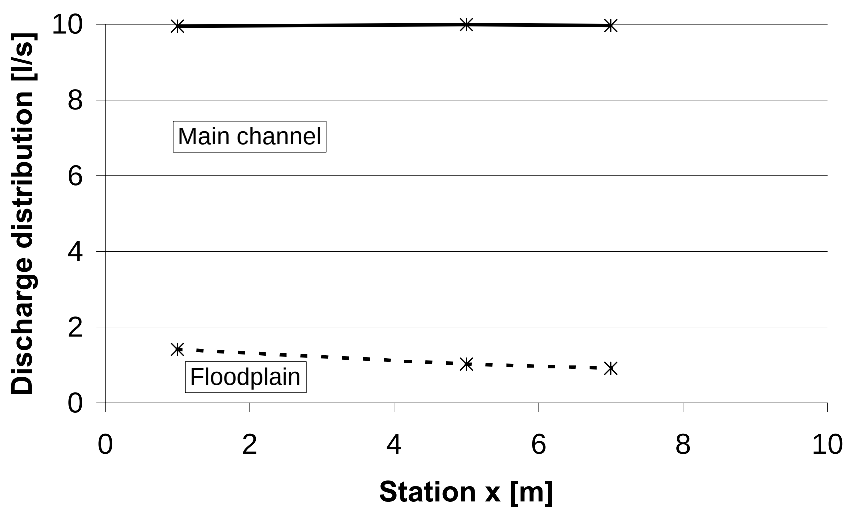

Figure 6.7 : LCA 10 : evolution of the discharge distribution along the channel

For further analysis and comparison, the shear-layer widths l_s have been estimated from the above velocity profiles. This estimation is obtained by fitting to the measured depth-averaged profiles an hyperbolic-tangent function, similar to the profiles whose stability will be investigated in the next Chapter :

$$U(y) = U_m + U_s \ \mathrm{TANH}\left(\frac{y_{infl} - y}{l_s} \right) \tag{6.1}$$

where U_m is the velocity at the inflexion point y_{infl}; U_s is half the difference between maximum and minimum velocity; and l_s is the estimated shear-layer width.

These shear-layer widths are summarised in Table 6.2. Large scatter is observed, partly due to the low number of measurement points available on the velocity profile. However, from the estimates at x = 7 m, it seems that the medium discharges have a finer shear layer. The larger shear-layer width for Q = 8 l/s could be due to the larger velocity difference between both subsections, but also to the lower measurement accuracy on the floodplain. At the largest discharge (Q = 16 l/s), the larger value of the shear-layer width may be due to a weaker shear layer whose limits are more difficult to locate accurately. Lastly, it should be pointed out that the estimated shear-layer widths correspond to developed flow, including the vortices smoothing effect on the velocity profile; and not to an unperturbed basic flow as will be defined in the Stability Analysis (see Chapter 7).

Table 6.2 : Shear-layer width l_s [m] estimated from the Pitot-tube measurements

	LCA 08	LCA 10	LCA 12	LCA 16
x = 5 m	0.039	0.037	-	-
x = 7 m	0.100	0.057	0.067	0.090

6.4 Particle-Tracking Velocimetry process

The surface-velocity field of the investigated flow is measured using a Particle-Tracking Velocimetry (PTV) system. The PTV system used in the UCL laboratory has been initially developed for dense granular-flow observation, by Capart et al. (2001), but has also been used in the past for surface velocimetry, using floating tracers (Devriendt et al. 1998). It is based on the analysis of a sequence of images depicting the displacements of the tracers dispersed on the flow surface.

The succession of operations for this analysis process is :

1. Identification of particle centres on each image;
2. Matching of particles between successive images;
3. Reconstruction of the particle trajectories and estimation of the particle velocities.

These operations will be further explained below.

As shown by Figure 6.2, the pictures are obtained from cameras set about 4 m above the flow surface. Two coupled digital cameras were used, each of them having a resolution of 256 × 256 pixels, in such a way the image size equals 512 × 256 pixels. A typical image, from the LCA 08 sequence, is given on Figure 6.8. One pixel on the image equals 3.35 mm, and the frame rate is 25 Hz. Each sequence is 40-s long, and counts 1000 images.

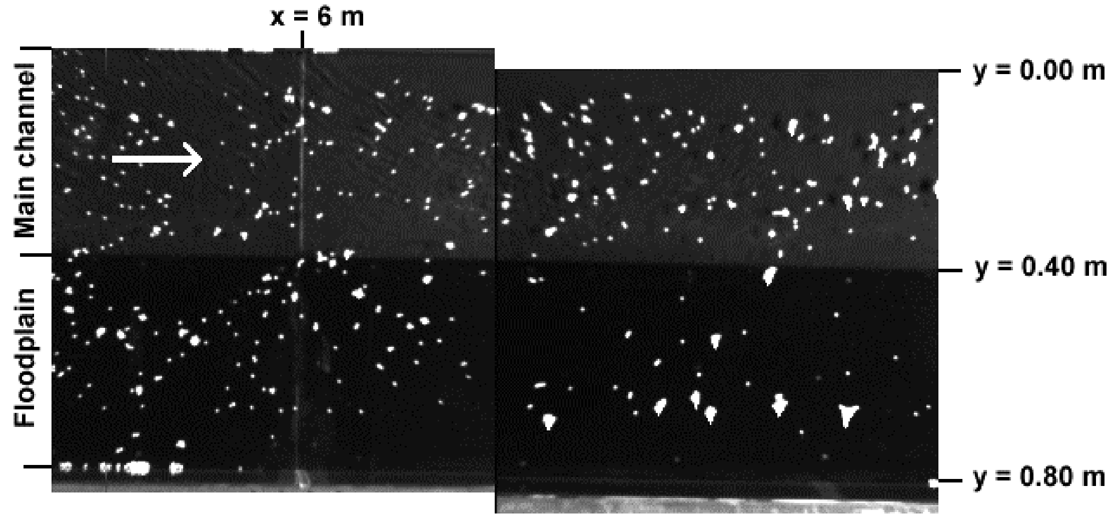

Figure 6.8 : LCA 08, typical image of the floating tracers

The floating tracers are expanded-polystyrene (EPS) pearls, with a diameter 4-6 mm. These EPS pearls were selected for several reasons : (1) their floating ability; (2) their white colour that contrasts well with the dark flume bottom; (3) their size, larger than a pixel, and resulting thus in good visibility on the images, but also small enough to follow the local flow velocity; and (4) their availability at low cost. However, as many floating particles, due to their light weight, these pearls are subject to the surface-tension effect and tend to agglomerate in clusters. This clustering effect partly reduces the number of discernible particles and therefore the precision of the measurement, although the identification algorithm can separate the clusters into individual particles. The clusters are most noticeable in the downstream area of slow-moving flows, and thus mainly in the LCA 08 case, where the slowest velocity is observed (see the clusters in the floodplain on Figure 6.8). Some tedious adjustment of the particle spreading at the flow surface are thus necessary in the begin of each run, in order to get the highest tracer density with as few clusters as possible.

Once the image sequence is archived, the analysis begins. Prior to the identification of the particles, two successive filterings are operated : (1) a low-pass filter; and (2) a high-pass filter. The low-pass filter is used for smoothing the image and eliminating parasitic light spots, due to for example lighting reflections on surface waves. The high-pass filter then enables to highlight the high-contrast areas corresponding to white particles on dark flume bottom, even if the primitive lighting of the picture area is uneven. From such a filtered image, the identification algorithm implemented by Capart. et al. (2001) locates the particles with a subpixel accuracy of about ¼ pixel size.

Next step is the identification of a particle position on successive images. Capart et al. (2001) developed therefore a robust matching method based on the Voronoï diagram : for a set of points in a plane, the Voronoï construction designates the splitting of the plane into polygonal regions (or "cells") such that each polygon encompasses the region of the plane which is nearest to one given point than to any other point. It has been found that such a Voronoï diagram for a set of particles is only weakly deformed when the particles move with the flow, in such a way it is a good and robust indicator for particle matching (Figure 6.9). In the present experiments, the particles are much more sparse than in a granular flow and such a robust algorithm is probably not necessary. However, it was found easier to use this analysis tool as it was already available and operational.

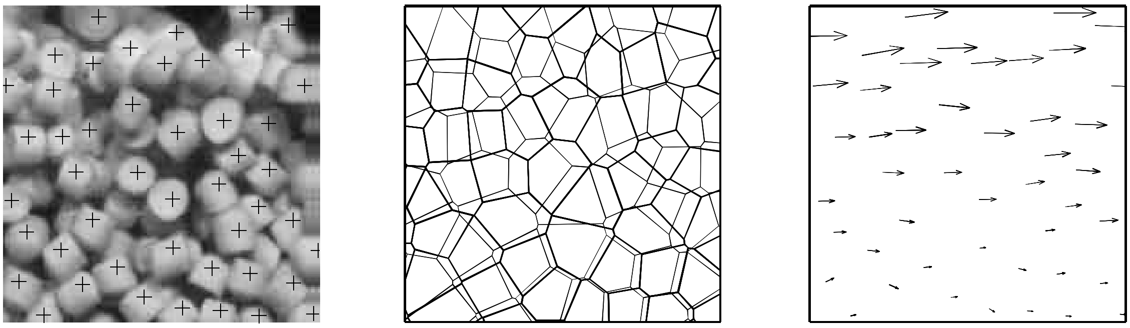

(a) (b) (c)

Figure 6.9 : Voronoï matching algorithm : (a) image of a granular flow, with identified particles; (b) Voronoï diagrams for two successive images; and (c) displacement vectors (Capart et al. 2001)

In addition to the matching step, some filtering is performed, in order to eliminate possible mismatches. Trajectories are then constructed by following particles through the entire image sequence, and velocities are calculated as the ratio of the distance between two successive positions of the particle and the time interval between the two corresponding images.

The results analysis will then be performed on the basis of both time-averaged velocity profiles and instantaneous velocity fields. The time-averaged velocity profiles will enable comparison and cross-validation with Pitot-tube measurements; while some information on the flow structures will already be gathered. The instantaneous velocity fields analysis will take advantage of all the possibility offered by this measurement technique. The velocity fields will be interpolated on a regular grid, for identifying periodical variations. The trajectories, based on actual particle positions, will lastly be investigated in a moving frame, in order to highlight the vortex structures.

6.5 Velocity profiles : PTV results

Time-averaged velocity profiles are extracted from the surface-velocity field obtained by PTV : 20 intervals are defined in the transverse direction y; all the velocities corresponding to tracers located in one interval are then averaged, in time and in x-wise direction; and the velocity standard-deviations in each interval are also estimated. Figure 6.10 gives the velocity longitudinal- and transverse-component (U, V) profile for the LCA 08 case (Q = 8 l/s). Velocity intervals equal to one time the standard deviation are also plotted, giving an indication of the amplitude of the velocity variations.

The profiles of the longitudinal component of the velocity (Figure 6.10) are quite similar to those gathered from Pitot-tube measurement (see Figure 6.6). The velocity difference between main channel and floodplain is clearly depicted. The effect of the momentum transfer is observed near the interface, where the floodplain velocity increases while the main-channel velocity decreases, resulting in a velocity-profile smoothing. Logically, the PTV-measured velocity is higher than the depth-averaged Pitot-measured velocity, as the bottom velocity is lower than the surface one. However, when considering only the measurement points nearest to the free surface, the Pitot-measured velocity compares more adequately with the PTV-measured velocity (Figure 6.11).

Further information can be gathered from the analysis of the profile of the velocity transverse component (Figure 6.10). The transverse component is positive in the first half of the main channel (y < 0.20 m), and negative in the second half (0.20 < y < 0.40 m), indicating that, at the surface, the water flows towards the main-channel centre line. This result hints to the existence of secondary-current cells in the main channel, in accordance with previous observations (Tominaga and Nezu 1991, see Figure 1.5). Negative transverse velocity is also observed in the floodplain (y > 0.40 m). This probably does not indicate helical secondary currents as in the main channel, but seems to be a consequence of the ill-conditioned upstream discharge-distribution already quoted above (§ 6.3). This means that a geometrical transfer could still exist around x = 7 m. This point will be further investigated in the next paragraph.

Finally, the standard deviation of the velocity transverse-component (Figure 6.10) also gives interesting indication on the flow behaviour. Indeed, this standard deviation is noticeably larger in the interface area (0.40 < y < 0.50 m), showing that the transverse-velocity variation amplitude is larger in this area, probably as a result of horizontal vortices development.

Figure 6.12 gives the surface-velocity profile for the four tested cases. When compared with the LCA 08 case, similar observations are obtained for the three other cases, at least for part of the conclusions regarding : (1) the velocity difference between subsections; (2) the momentum transfer influence on the velocity longitudinal-component profile; and (3) the development of secondary-current cells in the main channel, as depicted by the velocity transverse-component profile. On the other hand, two of the LCA-08 conclusions are no longer valid : (1) the geometrical transfer seems less marked in the transverse velocity profile; and (2) the larger standard deviation of the transverse velocity is no more observed at the interface. The latter point indicates maybe weaker vortices; or, at least, weaker information on these vortices, as will be discussed in the next paragraph.

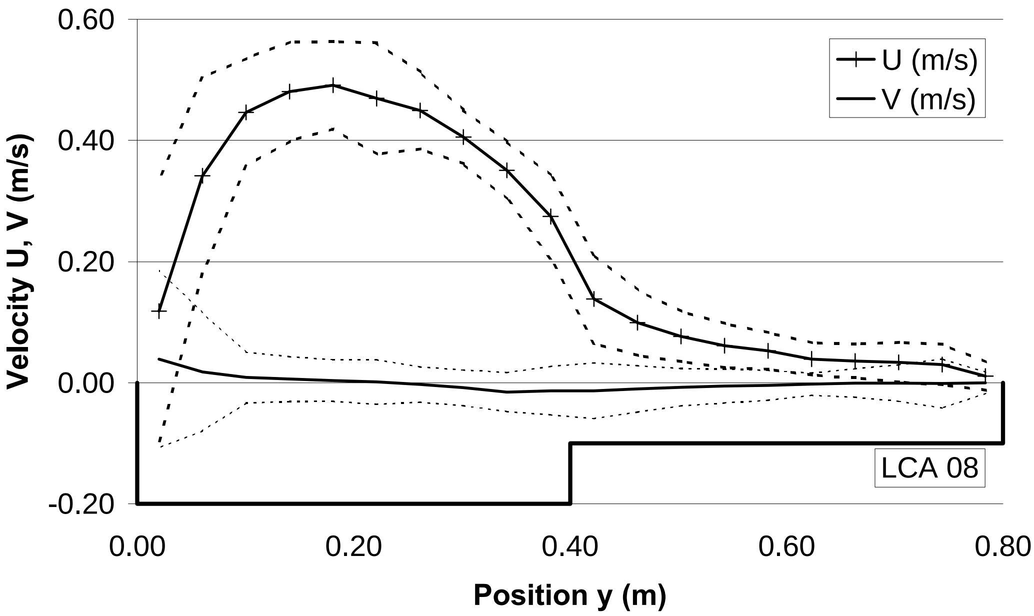

Figure 6.10 : LCA 08 : Profiles of the longitudinal and transverse components of the surface velocity, obtained by PTV measurements. Dotted lines indicate a one standard-deviation interval around the measured velocity. Positive transverse velocity flows towards increasing y

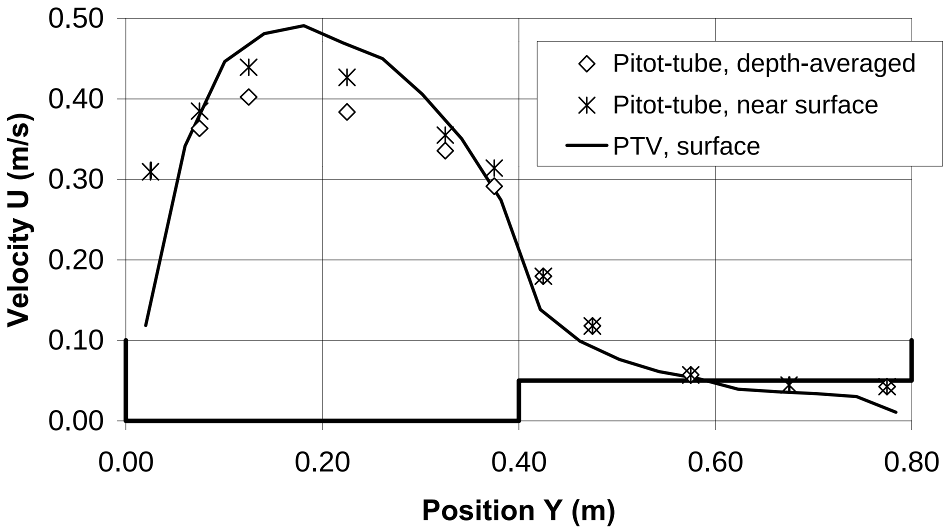

Figure 6.11 : LCA 08 : longitudinal surface-velocity profile, PTV and Pitot-tube measurement

The repeatability of the velocity profile measurements has been checked for the LCA 12 case. Using two sequences of images, taken at different time, two velocity profiles were estimated. It has been found that both profiles superposed perfectly, giving therefore some further confidence in the measurement accuracy.

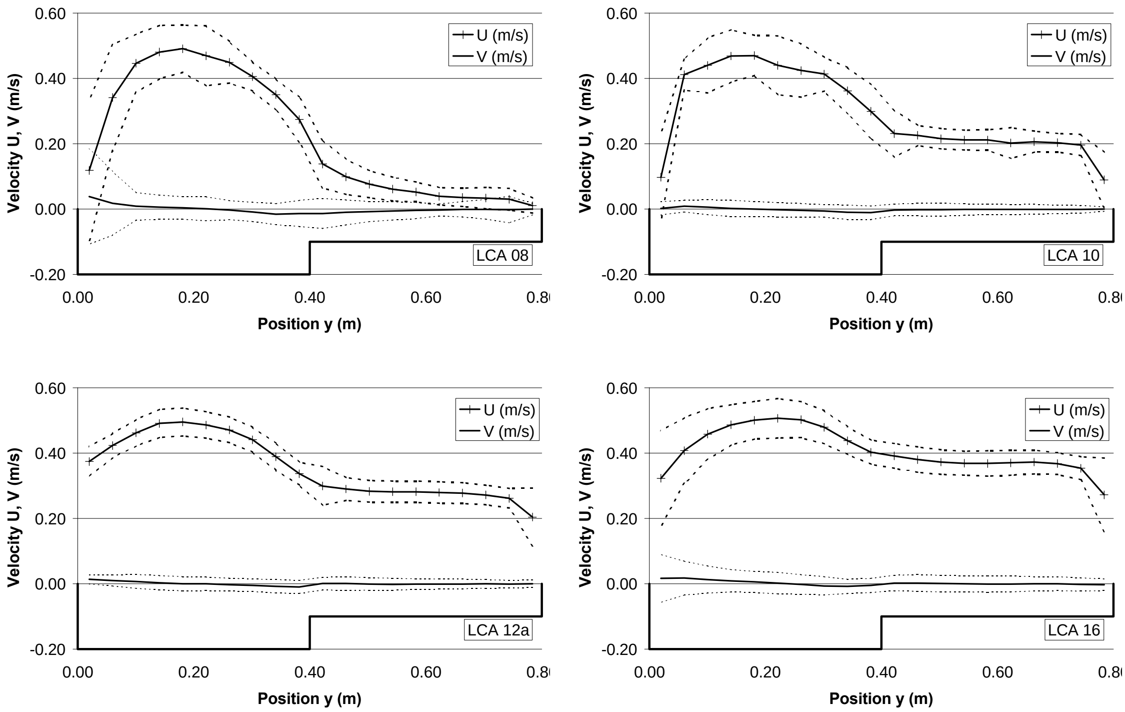

Figure 6.12 : Longitudinal and transverse surface-velocity profiles, PTV measurements

6.6 Periodical structures analysis

6.6.1 LCA 08 case

An instantaneous velocity field for LCA 08 case is plotted on Figure 6.13. As in the time-averaged velocity profile (Figure 6.10), the velocity is higher in the main channel (y < 0.40 m) than in the floodplain (y > 0.40 m). In the floodplain, some tendencies can be observed from the velocity transverse-component variations. For x < 6 m, a current develops towards the main channel. This current corresponds to the negative time-averaged transverse velocities observed previously on the floodplain (Figure 6.10). It could be due to the mass transfer generated by the ill-conditioned upstream discharge distribution. Another explanation could be the presence of a joint at x = 6 m (see Figure 6.8) : this joint creates a small bump on the flume bottom. Although this bump height is less than 1 mm, it is significant when compared to the 4.4 mm water depth on the floodplain. This second explanation of the observed mass transfer could also justify the fact that the latter disappears when x > 6 m.

Another interesting feature of the velocity field on the floodplain (Figure 6.13), for x > 6 m, is the alternation of positive and negative transverse velocity components in the x-wise direction, that could already indicate the presence of vortex structures. However, these structures are generally more easily identified on a vorticity field. The velocity field is therefore interpolated towards a regular grid (25×25 mm), using the linear interpolation function available in Matlab software. Indeed, although it is also possible to compute a vorticity field from the irregular mesh corresponding to the actual particles position, this computation is more computer-time consuming, and has been found to be too sensitive to the density of the particles. The vorticity Ω is estimated as

$$\Omega = \frac{\partial U}{\partial y} - \frac{\partial V}{\partial x} \tag{6.2}$$

The vorticity field corresponding to the velocity field from Figure 6.13 is plotted on Figure 6.14. Positive vorticity is observed in the boundary layer corresponding to the left bank of the main-channel (y < 0.15 m), and negative vorticity occurs in the shear layer at the interface (0.30 m < y < 0.50 m), corresponding to the velocity gradient. In the shear layer, some spots of higher vorticity amplitude exist (y = 5.7, 6.0 and 6.4 m), indicating the probable presence of vortices. When considering a sequence of vorticity-field plots, these spots are roughly observed to move in the flow direction. However, due to the particle density, the accuracy of the vorticity plots is not enough to clearly identify these structures throughout the whole image sequence. Therefore, the periodic features of these structures can not be estimated with this method.

An alternative method is therefore used, based on the velocity transverse-component analysis near the interface area. Indeed, when periodical vortices exist at the interface, this velocity transverse-component is expected to presents alternating positive and negative values. Figure 6.15 gives the transverse velocity variation with time, at x = 6.30 m. This graph shows the existence of periodical oscillations corresponding to the expected periodical vortices. A Fourier analysis enables to identify a clear peak in the spectrum for a period T = 3.63 s (Figure 6.16).

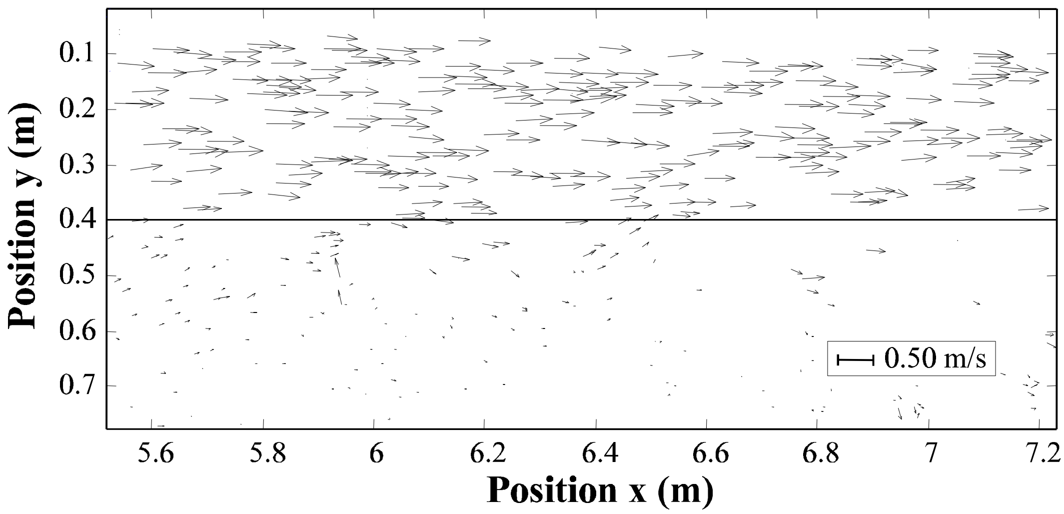

Figure 6.13 : LCA 08, instantaneous surface-velocity field

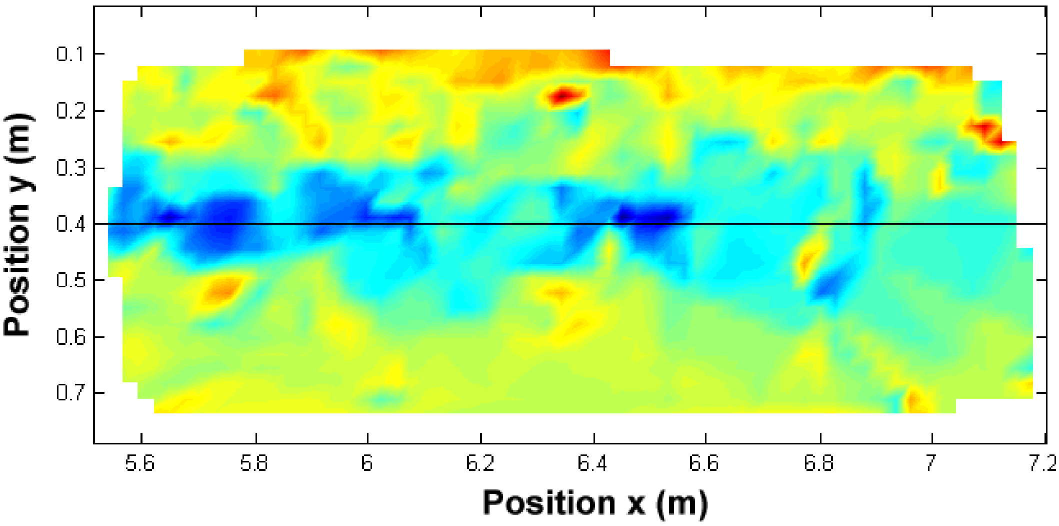

Figure 6.14 : LCA 08, vorticity field. Positive vorticity is in red and negative vorticity is in blue.

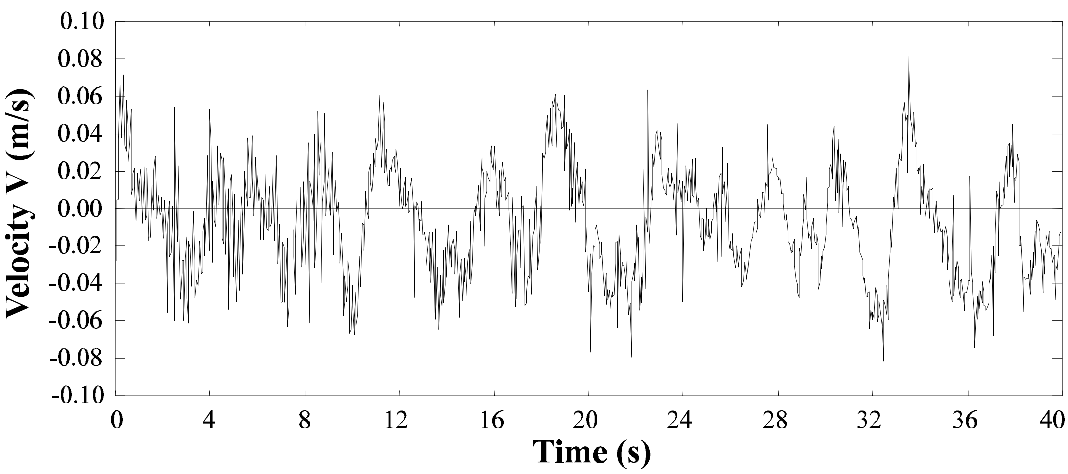

Figure 6.15 : LCA 08, transverse velocity V variation with time, near the interface (y = 0.44 m; x = 6.30 m)

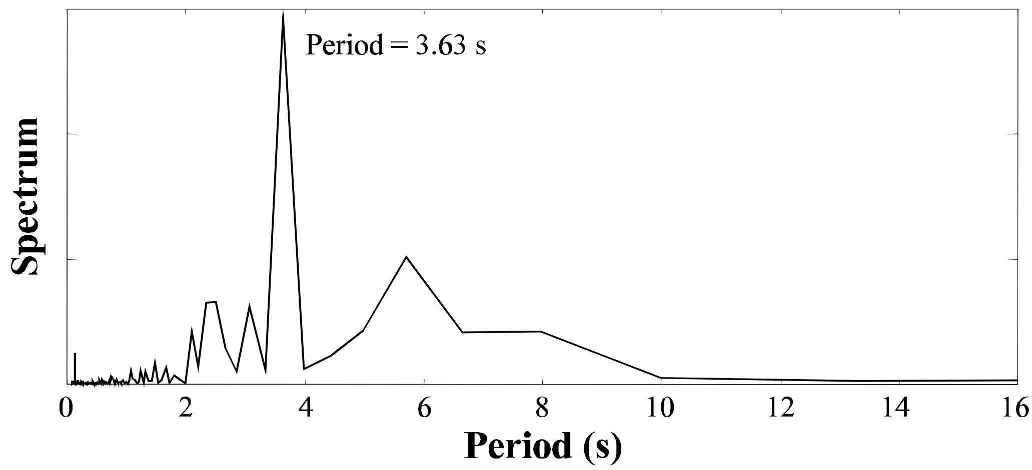

Figure 6.16 : LCA 08, transverse velocity V : spectral analysis (y = 0.44 m; x = 6.30 m)

In order to improve this vortex period assessment, the previous analysis is extended to all the interface points along the image-frame length. Figure 6.17 gives the velocity variation for all the points of the regular grid at y = 0.44 m. This transverse position has been chosen close to the interface, but not at the interface itself (y = 0.40 m), where the transverse velocity is less clearly identified due to the presence of higher velocity flow in the main channel, and, also, due to the lower density of particles. The latter can be explained by the presence of the main-channel helical secondary-currents that were identified previously from the time-averaged velocity profiles. As these helical secondary-currents create a surface flow towards the main-channel axis, the particles in the main channel tends to accumulate around this centre axis, as will be depicted by the trajectories plot (Figure 6.19).

The transverse-velocity variation plot on Figure 6.17 shows again the alternation of positive and negative velocities. It also shows that, for y < 6 m, only positive transverse velocities are observed, as pointed out on the instantaneous velocity field (Figure 6.13). This gives credit to the mass-transfer explanation founded on the influence of the joint at y = 6 m. A Fourier analysis of the transverse-velocity variation is then performed for each station x, and the calculated spectrum are given on Figure 6.18. As for the x = 6.30 m station, a clear peak is observed at T = 3.63 s on most of the image-frame length.

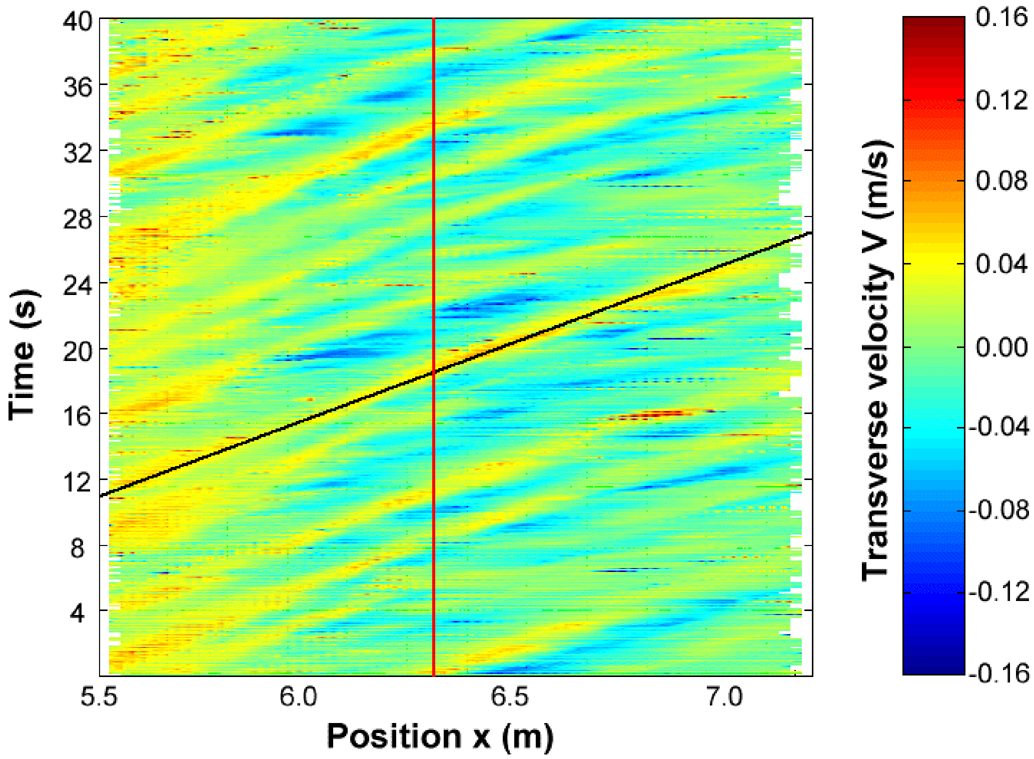

Figure 6.17 : LCA 08, transverse velocity V variation with time, near the interface (y = 0.44 m). The red line indicates the x = 6.30 m station (Figure 6.15). The black line is one structure track.

Another result can be obtained from the analysis of Figure 6.17. Indeed, the transverse velocities are found to vary with time at a given station, but also to vary with space at a given time, indicating the presence of a row of vortices in the shear layer. The pattern of diagonals depicting higher and lower transverse velocities corresponds thus to the displacement of the vortex structures with regard to the time. The vortex celerity can then be estimated from the slope of such a diagonal, as the one outlined in black on Figure 6.17 :

$$c = \frac{\Delta x}{\Delta t} = \frac{1.72 \text{ m}}{16 \text{ s}} = 0.1075 \text{ m/s} \tag{6.3}$$

This celerity is clearly lower than the longitudinal velocity at the interface (Figure 6.10), indicating that the vortices move at the floodplain velocity, and that their centres are therefore probably located more on the floodplain itself than on the interface. On the other hand, from this vortex celerity c = 0.11 m/s and from the vortex period T = 3.63 s, one also gets an estimation of the vortex wave length $\lambda = T\,c$ = 0.39 m.

Using the vortex-celerity value, it is now possible to plot the particle trajectories in a frame moving at this vortex celerity. Vortices can clearly be identified from Figure 6.19 and Figure 6.20 that show these trajectories. As inferred from the celerity value, the vortex centres are located on the floodplain. This observation is in accordance with the location of the standard-deviation peak on the time-averaged transverse-velocity plot (Figure 6.10). It also explains why the velocity plots were more clear when taken in the floodplain than just at the interface (as for Figure 6.15).

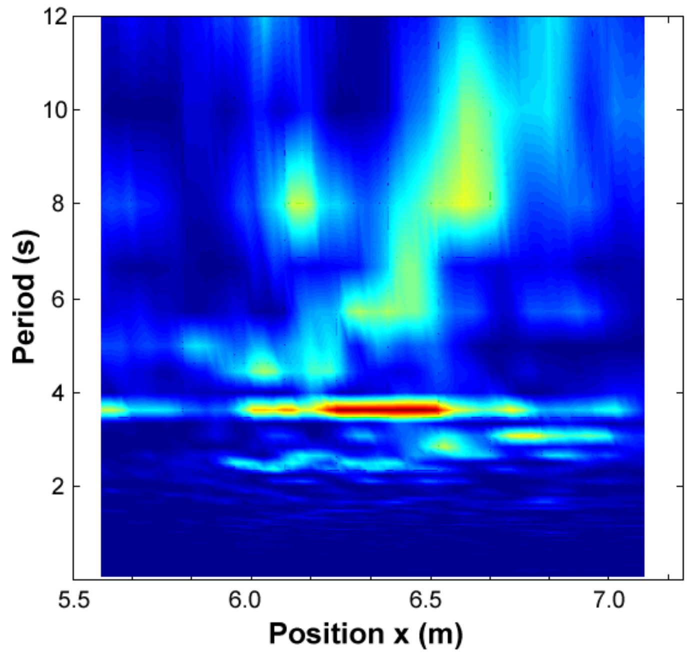

Figure 6.18 : LCA 08, transverse velocity V : spectral analysis (y = 0.44 m). High spectrum-density is plotted in red.

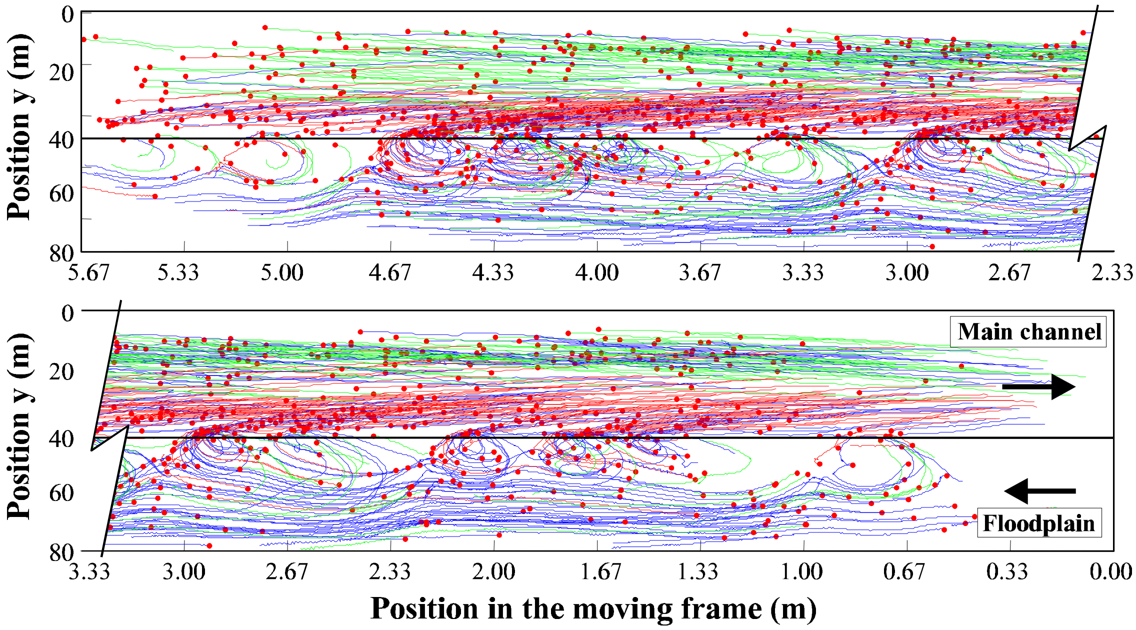

Figure 6.19 : LCA 08 : particle trajectories, in a frame moving at the velocity c = 0.11 m/s. Abscissa 0 of the moving frame corresponds to the right end of the image frame at the begin of the sequence. Red points indicate the initial point of a trajectory. Green and red lines stand for particles whose displacement are mainly towards respectively right or left bank..

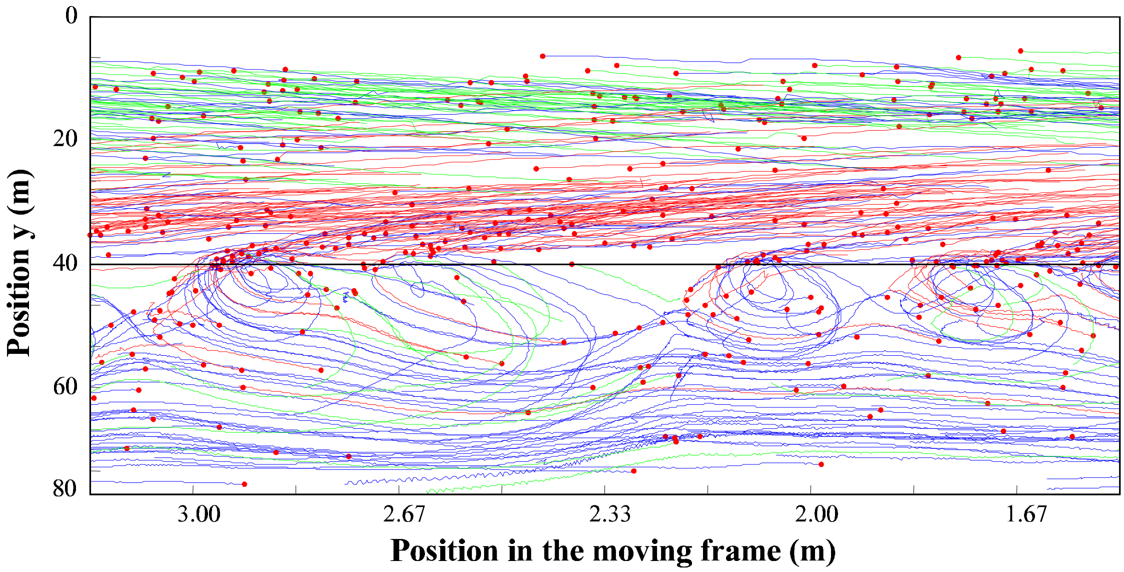

Figure 6.20 : LCA 08 : particle trajectories, in a frame moving at the velocity c = 0.11 m/s. Close-up vue.

It should be pointed out that this observation could be an artefact due to the choice of the moving-frame velocity : only the particles moving at the same velocity have their trajectories perpendicular to the interface and produce an apparent vortex pattern.

However, when the moving-frame velocity differs from the vortex celerity c, it has been observed that no clear structures appear.

From the trajectories picture, one can also estimate a vortex wave-length. From neighbouring-vortices observation, the latter seems to be in the range $\lambda = 0.33 .. 0.50$ m; while an overall survey identifies around 12 vortices in the interval $0.67 < x < 5.67$ m, giving thus $\lambda \approx 0.42$ m. Both estimates are found almost in accordance with the value $\lambda = 0.39$ m calculated from vortex celerity c and period T values.

Lastly, as already pointed out in previous analysis, the effect of the helical secondary currents is clearly seen on Figure 6.19, where the concentration of the particles in the main-channel centre is obvious.

6.6.2 Other cases analysis

Similar analysis are performed for case LCA 10, 12 and 16, but with lower quality results. Reasons for this relative failure could be as follow : (1) when the relative depth H_r increases, the velocity gradient and the shearing reduce, in such a way that the horizontal turbulent structures become weaker; (2) as the velocity increases, a given structure will be observed for a shorter time in the image frame and will thus be more difficult to identify; and (3) also due to higher velocity, the helical secondary currents will be stronger in the main channel, withdrawing more particles from the interface area, and reducing thus the measurement precision in the area of main interest.

Results are given in Table 6.3 for the four cases investigated. As explained just above, the results quality decreases when the discharge and water depth increase : first, the vortices are less discernible on the trajectory plot, i.e. for all cases except LCA 08. Then, for larger discharges, no more clear peak can be identified on the Fourier analysis of the transverse velocity at the interface : for LCA 12, depending on the station x considered, two peaks could be pointed out; while for LCA 16, the signal is too noisy to identify any peak. On the other hand, transverse-velocity plots similar to Figure 6.17 show positive and negative velocities alternation for all the cases, although more noisy; and a perturbation celerity c can always be estimated.

Table 6.3 : Periodical turbulent structures characteristics, PTV measurements

Case	Period T [s]	Celerity c [m/s]	Interface velocity $U_{(y = 0.40\text{ m})}$ [m/s]	Wave length λ [m]
LCA 08	3.63	0.108	0.206	0.39
LCA 10	2.35	0.238	0.265	0.56
LCA 12	2.35 or 4.40	0.286	0.318	0.67 or 1.26
LCA 16	-	0.343	0.397	-

The analysis of the available results shows that the wave length λ tends to increase with the water depth. This observation could be explained by the reduction of the bed-friction influence, according to the growing water depth : the turbulent structures can then develop larger in the transverse direction; and, consequently, could have larger overall size. The perturbation celerity *c* also increases with the water depth, as a result of the mean-velocity increase; but, in all the cases, it is found lower than the interface velocity. Lastly, the period *T* decreases with increasing discharge : this could also be explained by the higher mean velocity, as the structures move faster in front of a fix observer.

6.7 Additional ADV velocity measurements

Some tentative additional instantaneous local velocity-measurements are performed using a Sontek Acoustic Doppler Velocimetry probe. The particular 2D-3D side-looking probe-configuration used (Figure 6.21) enables the measurement of both longitudinal and transverse velocity-component at a rate of 25 Hz, as soon as the local water depth is larger than 2 cm. For water depth larger than 5 cm, all the three velocity components are available. However, the latter case will not be achieved in the present experiments, as the area of interest is located just above bank level. On the other hand, not all the 2D measurements will be satisfactory, as it is observed that the flow is strongly affected by the presence of the probe.

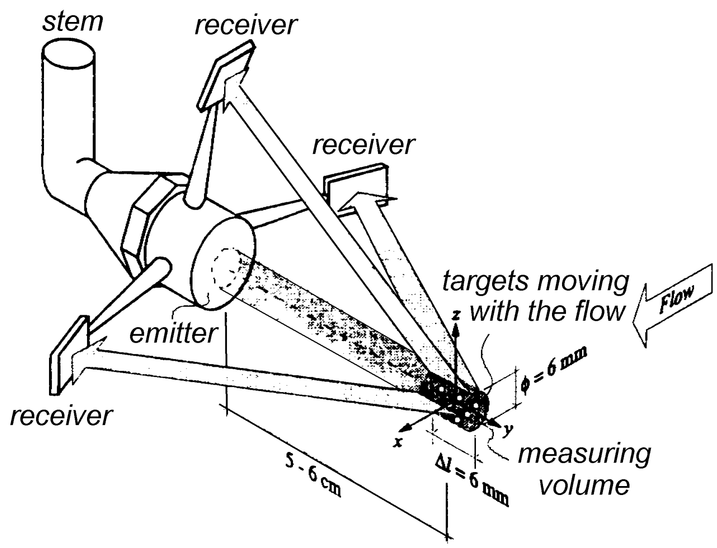

Figure 6.21 : Sontek 2D-3D side-looking ADV probe

The most interesting measurement points are those located near the interface. Figure 6.22 shows that measurements are performed at Δy = 5 cm intervals in main channel, and also in floodplain, when water depth is sufficient. The probe is always located outside the interface area, in order to limit the disturbance of the flow and of the turbulent structures. When this condition is achieved, the time-averaged longitudinal velocities are satisfactorily close to those measured with the Pitot-tube.

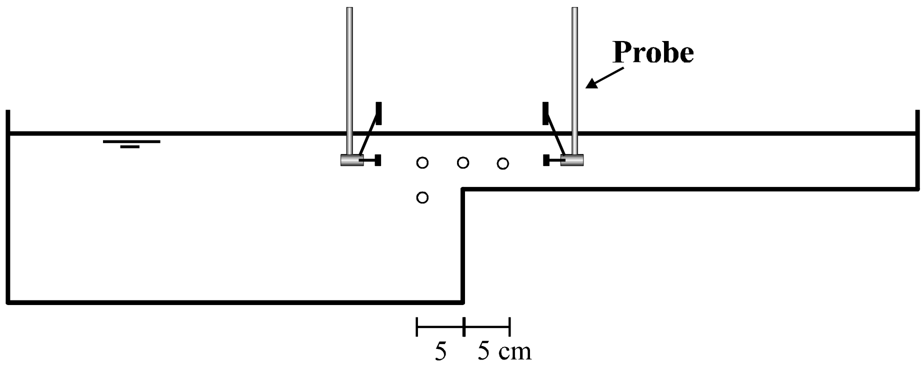

Figure 6.22 : ADV measurements, typical measurement points

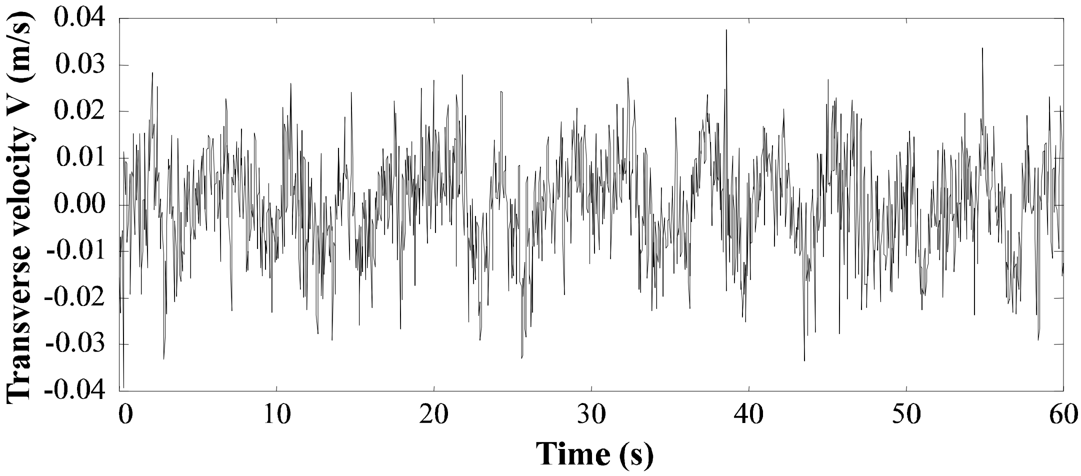

Figure 6.23 : LCA 08, transverse velocity variation at the interface,
x = 7 m, y = 0.40 m, z = 50 mm

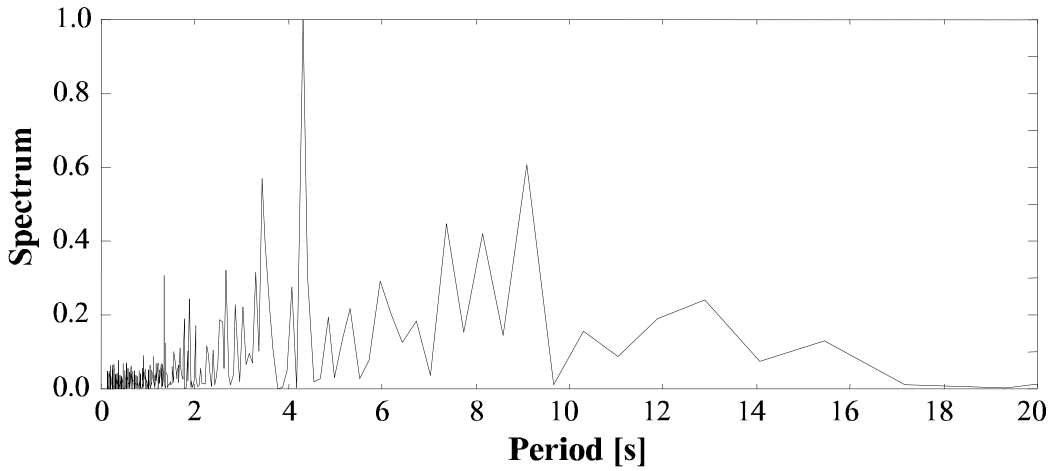

Figure 6.24 : LCA 08, spectral analysis of the transverse velocity-component at the interface, x = 7 m, y = 0.40 m, z = 50 mm

Figure 6.23 gives a typical transverse-velocity plot for LCA 08 case, just above main-channel bank level. Oscillations due to the periodical structures can clearly be identified. The spectral analysis for a 160 s long time period is given in Figure 6.24, in which a peak can be identified for a period $T = 4.3$ s. The velocity measurements at the other stations are similarly analysed and peak periods are also estimated when the measurements are not too noisy. The turbulent-structures period is finally found to be in the range $T = 3.9$ .. 4.3 s. Although slightly larger, this period is close to the one obtained from the PTV measurements analysis.

The three other cases are similarly investigated. Although the results are generally more scattered when the water depth increase, some tentative period estimates can be extracted (Table 6.4). The period interval obtained is generally too large to give some conclusion. One can only observe that the period values are in the same range for the ADV measurements than for the PTV ones; and, as already observed from the PTV values, the period tends to reduce when discharge and water depth increase.

Table 6.4 : Periodical turbulent structures period : ADV measurements

Case	T_{ADV} [s]	T_{PTV} [s]
LCA 08	3.9 .. 4.3	3.63
LCA 10	1.5 .. 3.9	2.35
LCA 12	1.5 .. 1.8	2.35 or 4.40
LCA 16	0.6 .. 0.9	-

6.8 Conclusion

Measurements of the flow in an asymmetric compound-channel section have been presented. Classical measurements with a Pitot tube show the existence of the velocity gradient between the main-channel and the floodplain. The surface-velocity field has also been investigated using a PTV technique. When considering time-averaged velocities, the velocity gradient is also identified; while, from the transverse-component analysis, one infers the existence of secondary-current cells in the main-channel. When considering the standard deviation of this velocity transverse-component, it is clear, at least for the lowest water depth investigated, that the exchange is more important at the interface between main channel and floodplain.

The analysis of the instantaneous velocity field obtained from the PTV measurements allows the identification of the vortices at the interface. Some characteristics of these periodical structures have been estimated : period T, celerity c and wave-length λ (see Table 6.3). For increasing discharge, the celerity c and wave-length λ increase, while the period T decreases. In all the cases, the vortex centres are located on the floodplain.

An additional result is the identification of some points to be improved in order to get better measurements when planning a further experimental campaign. Due to the secondary-current cells in the main-channel, the surface tracers tends to concentrate on the main-channel centre line and to leave the area of interest : the experimental set-up should take this phenomena into account, at least by spreading the tracers on the water surface as close as possible to the image frame. The second point to be improved is the discharge distribution at the flume entrance : due to this ill-conditioned upstream condition, a mass transfer from the floodplain to the main channel occurs on the whole channel length, and perturb the observations, as the flow is not as perfectly uniform as it could be expected.

Another point to be investigated further is the spatial development of the shear-layer perturbation. Indeed, when measuring in only one section, one assumed that the perturbation has reached a stationary state in this measurement section. However, according to further analytical and numerical investigations in next Chapters, it would be useful to observe the growth of the shear-layer perturbation, in order to see if the wave length of vortices remains constant along the channel length, or if the vortices merge. Actually, it could be expected that, due to the presence of the walls, or even due to the bed friction, some constrain exists that limit the maximum wave length of the vortices during their spatial growth, but this point has to be verified experimentally.

Chapter 7
Hydrodynamic stability analysis of a shear layer

7.1 Introduction

When attempting to analyse the large vortices observed at the interface between the main channel and a floodplain of a compound channel, an accurate understanding of the process of vortex generation is of primary importance. As already pointed out, these vortices are generated by the shearing at the interface between subsections, as a result of the velocity gradient. The physical mechanism governing their development is the so-called Kelvin-Helmholtz instability.

This Kelvin-Helmholtz instability process is described e.g. by Drazin and Reid (1981, p. 14). Let us consider the basic two-dimensional flow of incompressible inviscid fluids in two horizontal parallel infinite streams of opposite velocities (Figure 7.1). This flow constitutes a very simplified model for mixing-layer situations, such as stratified flow or compound-channel flow. In this simplified situation, all the vorticity is concentrated in the vortex sheet separating the two flows of opposite velocities.

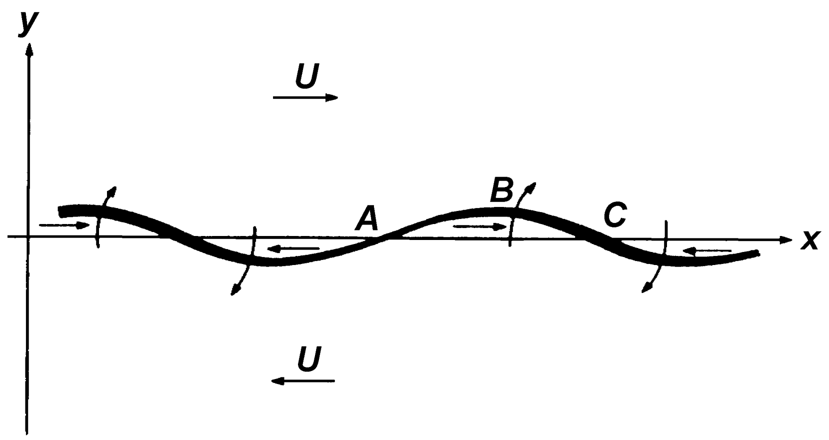

Figure 7.1 : Kelvin-Helmholtz instability : growth of a sinusoidal disturbance of a vortex sheet. The positive vorticity is normal to the paper, and the local strength of the sheet is represented by the thickness of the sheet. The curved arrows indicate the directions of the self-induced movement of the vorticity in the sheet, and show (1) the accumulation of vorticity at points like C; and (2) the general rotation about points like C, which together lead to exponential growth of the disturbance (Drazin and Reid 1981)

Let now consider an initial disturbance which slightly displaces the sheet so that its elevation becomes sinusoidal. As, in an inviscid fluid, each vortex line is carried with the fluid and induces a rotating flow, positive vorticity will be swept away from points like A towards points like C (Figure 7.1). As a result, the vorticity accumulated at C will induce clockwise velocities around this point and thereby amplify the sinusoidal displacement of the vortex sheet; leading to an exponential growth of the disturbance, so long as the disturbance remains small enough not to significantly change the basic flow; and to the development of individual vortices located on the initial shear layer.

Hydrodynamic Stability Analysis provides mathematical tools for analysing and modelling these Kelvin-Helmholtz instabilities, as well as more complex similar situations. In a hydrodynamic stability analysis, one first defines a basic flow, satisfying general flow equations like the Navier-Stokes or the Shallow-water ones. The purpose of the analysis in then to determine if this basic flow will remain stable when exposed to a small perturbation. The investigated perturbation also satisfies the flow equations and is generally assumed to be a periodical function. Adding the perturbation function to the basic flow, one can then simplify the flow equations to a differential equation, whose solution finally enables to determine whether the perturbation will grow up (instability) or will be damped (stability), as a function of its wave length.

In the present work, the basic flow whose stability will be investigated is a parallel shear flow, either corresponding to a mixing layer, in the asymmetric compound-channel case, or to a jet flow, in the symmetric compound-channel case. The stability of these flows will be described by using either the Rayleigh equation, for inviscid flows, or the Orr-Sommerfeld equation, for viscid flows. These classical equations will be developed hereafter, and then they will be extended to take into account the bed friction that appears in the Shallow-water equations. As the neutral stability curves (limit between stable and unstable flow) obtained from these equations have been widely investigated previously, the present work will focus only on the most amplifying perturbations. Indeed, Tamai et al. (1986) suggested that the observed vortices correspond to these most amplifying perturbations and, accordingly, that their wave length should be the same.

7.2 The Rayleigh equation

The Rayleigh equation describes the stability of a parallel flow subjected to a periodic perturbation, in an inviscid fluid ($\mathbf{Re} \to \infty$). The so-called parallel flow is a basic flow where the velocity components are all parallel to the streamwise x direction, corresponding e.g. to some stratified flow, to mixing-layer or to jet flow. The Rayleigh equation is founded on the two-dimensional Navier-Stokes equations, i.e. the tri-dimensional Navier-Stokes equations (2.1) where the third velocity component w in the z-direction is assumed equal to zero, z being indifferently a vertical or an horizontal direction. A fundamental hypothesis is also the linearization of the equations, assuming that the perturbations are small enough to neglect the terms resulting from a product of two perturbation components. The following development is largely inspired from Betchov and Criminale (1967), and from Drazin and Reid (1981).

The two-dimensional Navier-Stokes equations write

$$u_x + v_y = 0 \tag{7.1a}$$

$$u_t + u\,u_x + v\,u_y + p_x/\rho = X + \upsilon\left(u_{xx} + u_{yy}\right) \tag{7.1b}$$

$$v_t + u\,v_x + v\,v_y + p_y/\rho = \upsilon\left(v_{xx} + v_{yy}\right) \tag{7.1c}$$

where, compared to (2.1), the continuity equation (7.1a) multiplied respectively by u and v has been subtracted to the momentum equations (7.1b) and (7.1c). The partial derivatives are now designed by indices, for the sake of conciseness. In these equations, $u(x,y,t)$ and $v(x,y,t)$ are the velocity components in the x- and y-directions respectively; $p(x,y,t)$ is the pressure; X is the mass force; and υ is the fluid viscosity.

For the given external force X and boundary conditions, it is assumed that the equations (7.1) admit a steady solution, with a flow parallel to the x-direction, that constitutes the basic flow (U, V, P) :

$$U = U(y), \quad V = 0, \quad P = P(x) \tag{7.2}$$

where the pressure P only vary in the x-direction (a pressure gradient in the y-direction would generate a non-zero transverse velocity V, which is incompatible with the parallel-flow hypothesis). The Rayleigh equation will be developed for this general basic flow, while its particular shape will be specified later for each case to be studied (e.g. for a TANH(y) function describing the velocity profile in an asymmetric compound channel).

The actual flow is then obtained by addition of the steady basic flow (U, V, P) and an unsteady perturbation (u', v', p') :

$$u = U(y) + u'(x,y,t) \tag{7.3a}$$

$$v = v'(x,y,t) \tag{7.3b}$$

$$p = P(x) + p'(x,y,t) \tag{7.3c}$$

The perturbation is assumed to be small compared to the basic flow. As already pointed out, the purpose of the present analysis is to estimate the variation of the amplitude of this perturbation with time, and thus to determine wheter it will grow up or be damped.

The so-defined actual flow (7.3) is also a solution of the flow equations (7.1). Writing these flow equations (7.1) for this actual flow (7.3), and subtracting the same flow equations (7.1) written for only the basic flow (7.2), one gets

$$u'_x + v'_y = 0 \tag{7.4a}$$

$$u'_t + U\,u'_x + u'u'_x + v'U_y + v'v'_y + p'_x/\rho = \upsilon\left(u'_{xx} + u'_{yy}\right) \tag{7.4b}$$

$$v'_t + U\,v'_x + u'v'_x + v'\,v'_y + p'_y/\rho = \upsilon\left(v'_{xx} + v'_{yy}\right) \tag{7.4c}$$

The perturbation being small, the products of two perturbation components in (7.4) are assumed negligible (linearization of the equations) :

$$u'_x + v'_y = 0 \tag{7.5a}$$

$$u'_t + U\,u'_x + v'U_y + p'_x/\rho = \upsilon\left(u'_{xx} + u'_{yy}\right) \tag{7.5b}$$

$$v'_t + U\,v'_x + p'_y/\rho = \upsilon\left(v'_{xx} + v'_{yy}\right) \tag{7.5c}$$

The resulting equations are then easier to solve, as they are now linear for the perturbation components constituting their unknowns. As a result, the perturbation evolution can be described by a sum of periodical solutions of (7.5). These solutions will be periodical both in time and in x-direction (main direction of the flow). They will be written as the real part of complex exponential functions :

$$u'(x,y,t) = \mathbf{u}(y)\, e^{i\alpha(x-ct)}, \quad v'(x,y,t) = \mathbf{v}(y)\, e^{i\alpha(x-ct)}, \quad p'(x,y,t) = \mathbf{p}(y)\, e^{i\alpha(x-ct)} \tag{7.6}$$

where $\mathbf{u}(y)$, $\mathbf{v}(y)$ and $\mathbf{p}(y)$ are complex functions defining the shape of the perturbation in the y-direction; c is the perturbation celerity; and α is the perturbation wave number :

$$\alpha = \frac{2\pi}{\lambda} \tag{7.7}$$

where λ is the perturbation wave length.

Both wave number α and celerity c are complex numbers, in such a way that their imaginary part implies an exponential growth (or damping) of the perturbation. The imaginary part of c generates a temporal growth of the perturbation; while the imaginary part of α also generates a spatial growth of the perturbation (e.g. a wake instability behind a fixed body, such as the Karman vortex street).

In the present work, one will focus on temporal growth of the perturbation, as one consider turbulent structures in uniform flow, far from any up- or downstream boundary conditions. The wave number α is thus imposed to be a positive real number, while the celerity is complex : $c = c_r + \mathrm{i}\, c_i$. The product αc_i defines the perturbation growth rate. Indeed, from (7.6), one gets (Riahi 2000, p. 49) :

$$\alpha c_i = \frac{1}{u'}\frac{\partial u'}{\partial t} \tag{7.8}$$

For a growth-rate positive value, the perturbation (7.6) will grow up exponentially; while it will be damped for a growth-rate negative value. Lastly, $\alpha c_i = 0$ indicates neutral stability.

Using the perturbation definition (7.6) in the equations (7.5), the latter reduce to a system of ordinary differential equations :

$$i\alpha \mathbf{u} + \mathbf{v}_y = 0 \tag{7.9a}$$

$$i\alpha\,(U-c)\,\mathbf{u} + U_y\,\mathbf{v} + i\alpha\,\mathbf{p}/\rho = \upsilon\,(\mathbf{u}_{yy} - \alpha^2\,\mathbf{u}) \tag{7.9b}$$

$$i\alpha\,(U-c)\,\mathbf{v} + \mathbf{p}_y/\rho = \upsilon\,(\mathbf{v}_{yy} - \alpha^2\,\mathbf{v}) \tag{7.9c}$$

In the last part of this development, the viscosity terms will be neglected, assuming a large Reynolds number (inviscid flow hypothesis : **Re** $\rightarrow \infty$). The equations (7.9) will be used in their complete form when developing the Orr-Sommerfeld equation (see § 7.4.1).

The pressure component **p** of the perturbation can be eliminated from (7.9), by deriving (7.9b) with regard to y, replacing $\mathbf{p}_y$ in (7.9c), and subtracting (7.9a) multiplied by U_y :

$$i\alpha \mathbf{u} + \mathbf{v}_y = 0 \tag{7.10a}$$

$$\mathbf{u}_y = \frac{i}{\alpha}\left(\frac{U_{yy}}{U-c} + \alpha^2\right)\mathbf{v} \tag{7.10b}$$

The Rayleigh equation is finally obtained by deriving (7.10a) with respect to y, and replacing $\mathbf{u}_y$ in (7.10b)

$$\mathbf{v}_{yy} = \left(\frac{U_{yy}}{U-c} + \alpha^2\right)\mathbf{v} \tag{7.11}$$

This equation defines an eigenvalue problem. Having defined appropriate boundary conditions, one has to find pairs of eigenvalues (α, c) for which an eigenfunction **v** exists. This eigenfunction **v** has to be a solution of the Rayleigh equation (7.11) and to satisfy these boundary conditions. The computed pairs of eigenvalues will then define the stability and instability area of the flow, according to the sign of the resulting growth rates αc_i.

7.3 Analysis of an inviscid shear layer

7.3.1 Velocity profile and boundary conditions

Using the Rayleigh equation (7.11), one can now investigate the stability of a single shear layer, separating two semi-infinite areas where the flow is parallel to the shear layer. The basic-flow velocity profile is modelled by an hyperbolic tangent function (Figure 7.2) :

$$U^* = U_m^* + U_s^* \ \mathrm{TANH}\ (y^*/l_s^*) \tag{7.12}$$

where U_m^* is the mean velocity; 2 U_s^* is the difference between the maximum and the minimum velocities, measured far from the shear layer area; and l_s^* is a measure of the shear-layer width. The star designates dimensional values. Indeed, for a general analysis, one prefers to use dimensionless values of velocity and length, obtained by using U_s^* and l_s^* as scaling factors, respectively :

$$U = U^*/U_s^* \quad \text{and} \quad y = y^*/l_s^* \tag{7.13}$$

The values of the scaling factors can be defined as a function of the dimensional values describing the velocity profile (Chu et al. 1991) :

$$U_s^* = (U_2^* - U_1^*)/2 \tag{7.14a}$$

$$l_s^* = U_s^* \left(\frac{dU^*}{dy} \right)^{-1}_{y^*=0} \tag{7.14b}$$

where l_s^* is estimated as a function of the slope of the velocity profile (7.12) at its inflexion point ($y^* = 0$), where this slope is maximum.

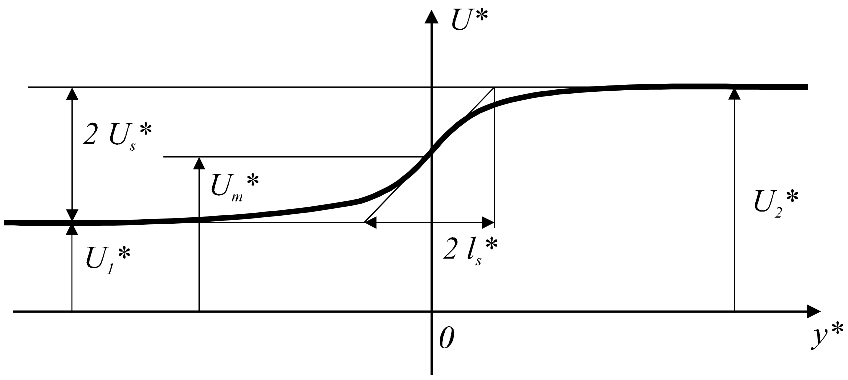

Figure 7.2 : Velocity profile for a shear layer flow, modelled by a TANH(y) function

Using these scaling factor definitions, the dimensionless velocity profile finally writes

$$U = U_m + \mathrm{TANH}\ (y) \tag{7.15}$$

When studying the temporal growth of the disturbance, the mean velocity U_m can be set equal to zero, without loss of generality. This means that the reference used is then a Lagragian reference, corresponding to an observer moving at the flow mean velocity. With regard to the Rayleigh equation (7.11), one can notice that this reference change will only affect the real part of the wave celerity c_r, from which the mean velocity U_m value should be subtracted.

Lets now consider the Rayleigh equation (7.11) far from the shear layer. The term $U_{yy}/(U\text{-}c)$ becomes negligible in comparison with the α^2 term, as the velocity U tends to a constant value. Approximate solutions are thus

$$\mathbf{v}(y) = A_1\, e^{\alpha y} + A_2\, e^{-\alpha y}, \qquad \text{for } y >> 0 \tag{7.16a}$$

$$\mathbf{v}(y) = A_3\, e^{\alpha y} + A_4\, e^{-\alpha y}, \qquad \text{for } y << 0 \tag{7.16b}$$

where A_1, A_2, A_3 and A_4 are constants.

As the shear layer is the only perturbation source, the perturbation v' has to disappear when moving far from it. This implies that A_1 and A_4 must be equal to zero. With such values of the constants, the solutions (7.16) define the boundary conditions for the eigenvalue problem.

7.3.2 Simulation results

The so-defined eigenvalue problem can be solved numerically, using the basic trial and error procedure described by Betchov and Criminale (1967). For a given value of the wave number α, a tentative value of the wave celerity c is set. The Rayleigh equation (7.11) is then integrated, for example between $y = -3$ and $y = 3$ (where $U(y = \pm 3) = \pm 0.995$ and $U_{yy} = \pm 0.020$, see (7.15)). The boundary condition (7.16b) is used as initial condition in $y = -3$. The value of the eigenfunction $\mathbf{v}(3)$ found at $y = 3$ is compared with the boundary condition (7.16a), and the value of c is adapted until the eigenfunction $\mathbf{v}(y)$ matches both its boundary conditions (7.16a) and (7.16b). This numerical solution is further explained in Appendix 4.

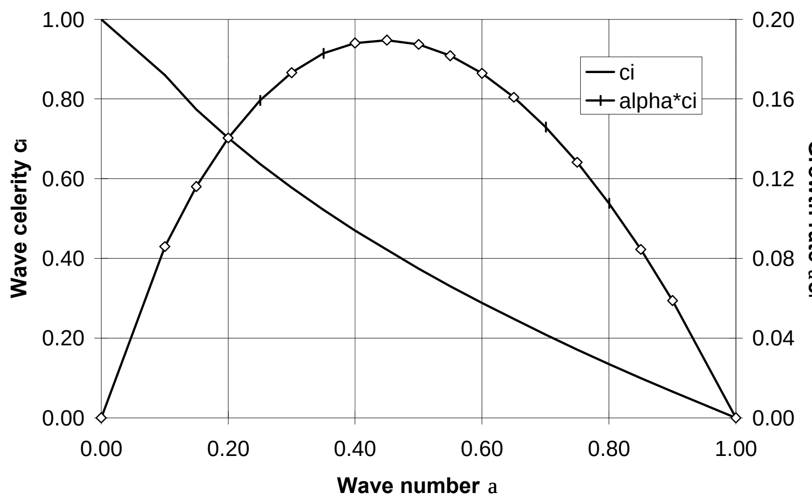

Figure 7.3 : Eigenvalues of the Rayleigh equation, for a velocity profile U = TANH(*y*)

Table 7.1 : Eigenvalues of the Rayleigh equation, for a velocity profile U = TANH(y)

α	c_i	$\alpha\, c_i$	α	c_i	$\alpha\, c_i$
0.000	1.0000	0.0000	0.500	0.3749	0.1874
0.100	0.8598	0.0860	0.600	0.2882	0.1729
0.200	0.7019	0.1404	0.700	0.2086	0.1460
0.300	0.5775	0.1733	0.800	0.1346	0.1077
0.400	0.4705	0.1882	0.900	0.0654	0.0588
0.445	**0.4262**	**0.1897**	1.000	0.0000	0.0000

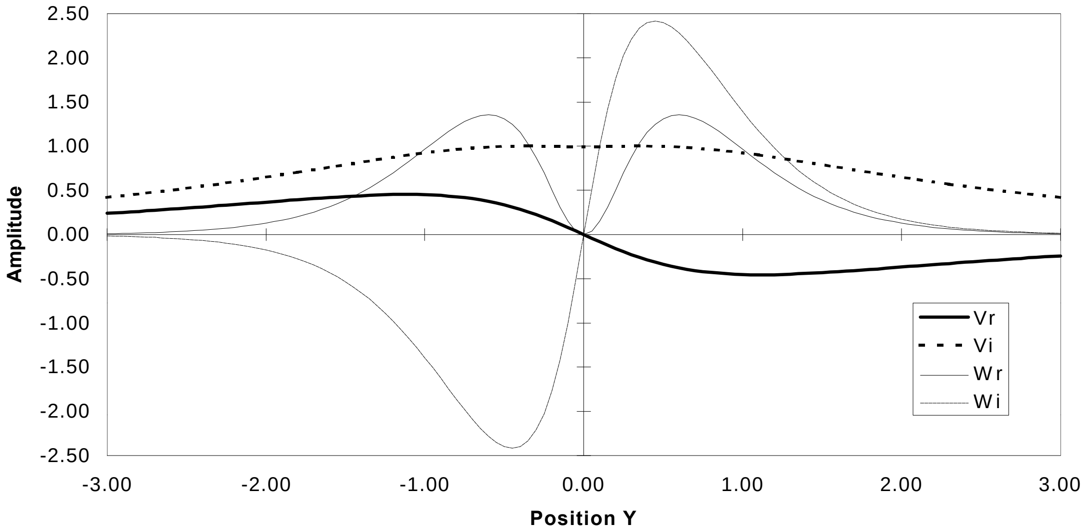

Figure 7.4 : Eigenfunction **v**(y) *for the maximum growth rate* ($\alpha = 0.445$), *and corresponding vorticity function* $\omega(y)$

Eigenvalues of the Rayleigh equation, for a hyperbolic-tangent function velocity profile, were first computed by Michalke (1964). These values are plotted on Figure 7.3 and summarised in Table 7.1. The maximum growth rate (7.8) equals $\alpha\, c_i = 0.1897$ and is obtained for the wave number $\alpha = 0.445$. Both real and imaginary part of the complex eigenfunction **v**(y) are given on Figure 7.4. Used with the periodical perturbation definition (7.6), this eigenfunction depicts the additional velocity field due to the perturbation. The eigenfunction **u**(y) is obtained from the derivative of the eigenfunction **v**(y), using (7.10a).

The vorticity field of the studied flow consists of both the basic flow and the perturbation vorticity :

$$\omega = \Omega\,(y) + \omega'(x, y, t) \tag{7.17}$$

The basic flow vorticity $\Omega(y)$ corresponds to the vortex sheet used as simplified model when investigating the Kelvin-Helmholtz instability

$$\Omega(y) = \left(\frac{\partial V}{\partial x} - \frac{\partial U}{\partial y}\right) = -\frac{\partial \,\mathrm{TANH}(y)}{\partial y} = -\mathrm{SECH}(y)^2 \tag{7.18}$$

while the additional vorticity $\omega'(x,y,t)$ due to the perturbation can be expressed as a periodical function, obtained from the eigenfunction **u** and **v**

$$\begin{aligned} \omega' &= \frac{\partial v'}{\partial x} - \frac{\partial u'}{\partial y} \\ &= \mathrm{w}(y)\, e^{\mathrm{i}\alpha(x-ct)} = \left(\mathrm{i}\alpha\mathbf{v} - \mathbf{u}_y\right) e^{\mathrm{i}\alpha(x-ct)} \end{aligned} \tag{7.19}$$

where the derivative of $\mathbf{u}(y)$ is obtained from $\mathbf{v}(y)$ by (7.10b). Both real and imaginary parts of the complex eigenfunction $\mathrm{w}(y)$ are given on Figure 7.4.

The complete vorticity field (7.17) is given on Figure 7.5, again for $\alpha = 0.445$. In this figure, the adimensional time has been set equal to $t = 0$. However, this does not mean that no perturbation exists, as, from a mathematical point of view, the perturbation growth starts at $t = -\infty$. From a physical viewpoint, the initial time t_0 should be selected to fit the initial perturbation amplitude : $\mathbf{v}_0 = \mathbf{v}\, e^{-\mathrm{i}\alpha c t_0}$.

From Figure 7.5, it is clear that the vorticity field is affected by the perturbation. For the non-perturbed basic flow, the maximum amplitude of the vorticity $\omega(y)$ was equally located on the axis $y = 0$, with a maximum absolute value of $|\omega|_{max} = 1$. Once the perturbation has developed, the flow presents periodical structures. Pair of vorticity peaks are found alternately on both sides of the shear layer. When the perturbation will further develop, one can expect that the vorticity peaks in such a pair will interact together and, finally, merge in a unique vortex, leading thus to the vortices pattern observed experimentally. However, this merging process implies further growth of the perturbation, that can not be captured by the present linear analysis, as the linearization used in the development of Rayleigh equation is no longer valid.

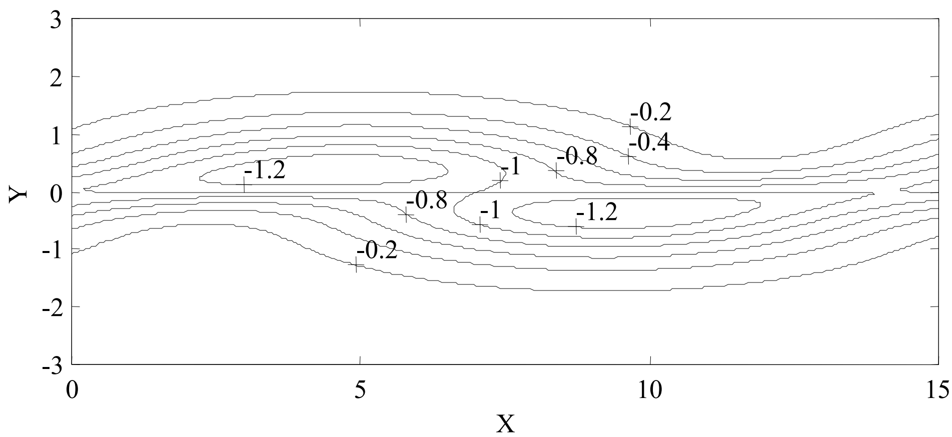

Figure 7.5 : TANH(y) *velocity profile : disturbed vorticity field,* $\alpha = 0.445$

A clue of the weakness of this linear analysis can also be seen in the maximum vorticity evolution. Indeed, as quoted by Michalke (1965a), the vorticity transport is governed by Helmholtz equation, which writes for a two-dimensional flow

$$\frac{D\omega}{Dt} = \frac{\partial \omega}{\partial t} + u\frac{\partial \omega}{\partial x} + v\frac{\partial \omega}{\partial y} = 0 \tag{7.20}$$

This means that, in such a flow, no vorticity source exists and the total vorticity remains constant along its trajectory. For this particular case, the vorticity maximum was $|\omega|_{max} = 1$ for the unperturbed flow, whereas it is now $|\omega|_{max} > 1.2$ (see Figure 7.5), which is in contradiction with Helmholtz equation (7.20).

Developing a non-linear stability analysis, limited to the third order, Michalke (1965a) obtained a perturbed-flow vorticity maximum closer to the unperturbed one. In the perturbed-flow vorticity field, the two iso-vorticity lines corresponding to the maximum of the unperturbed-flow vorticity were found closer to each other in the non-linear analysis than in the linear analysis. From this observation, Michalke concluded that, using higher order analysis, the maximum vorticity line would remain unique and only roll-on, in a vortex row aligned with the shear layer axis (Figure 7.6). It should be pointed out that, unlike the vorticity field, the maximum growth rate and the related wave number ($\alpha = 0.445$) seem not to be affected by this extension to a non-linear analysis.

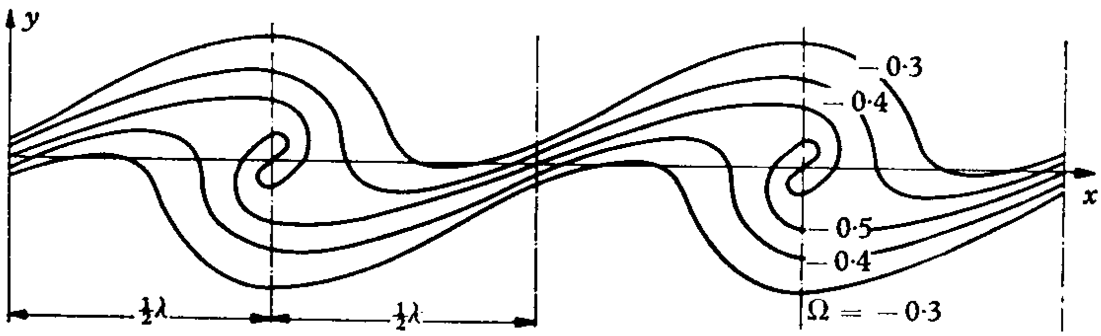

Figure 7.6 : Vorticity field, extrapolation from a non-linear analysis (Michalke, 1965a)

Using a complex value for α and a real one for c, Michalke (1965b) also investigated the spatial development of a perturbation of the hyperbolic-tangent-function basic flow. The maximum growth rate is obtained for a wave number $\alpha_r = 0.403$ slightly lower than in the temporal growth analysis. The perturbation growth is rather fast : starting from an initial perturbation whose amplitude equals 0.0005 of the unperturbed flow maximum velocity, the whole development of a vortex is obtained in only 2 wave lengths (using a linear analysis).

This last result is not relevant for comparison with the numerical experiences in Chapter 8, where only temporal growth will be studied, using periodical boundary conditions. On the other hand, one can expect that such spatial growth of the perturbation occurred in the physical experiments (see Chapter 6). Although the wave number giving the maximum growth rate differs slightly between both cases, comparisons remain possible between the spatial growth observed experimentally and the temporal growth as investigated in this Chapter and numerically modelled in Chapter 8. The large calculated growth rate also gives confidence in the fact that fully developed vortices were observed in the experiments. However, only a non-linear analysis could tell if the observed vortices still have the initial wave length or have merged together in larger one. This point will be further discussed in § 7.7.2, where the UCL experimental results are compared with the present stability analysis.

7.4 Viscous flow analysis

7.4.1 The Orr-Sommerfeld equation

The effect of viscosity on the linear stability analysis results will be briefly described in this paragraph, for the classical hyperbolic-tangent function velocity profile (7.15). The stability of such a viscous parallel flow is depicted by the Orr-Sommerfeld equation. The latter is obtained from the flow equations (7.9) expressed for periodical perturbations (7.6). Similarly to the Rayleigh equation development, the pressure **p** and the **u** are successively eliminated from the equations (7.9), and the Orr-Sommerfeld equation finally writes (Betchov and Criminale 1967), using a non-zero viscosity υ :

$$(U-c)(\mathbf{v}_{yy}-\alpha^2\mathbf{v})-U_{yy}\mathbf{v}=-\frac{\mathrm{i}\upsilon}{\alpha}(\mathbf{v}_{yyy}-2\alpha^2\mathbf{v}_{yy}+\alpha^4\mathbf{v}) \tag{7.21}$$

This equation is now a fourth order differential equation; and it effectively reduces to the Rayleigh equation (7.11) when the viscosity υ is neglected.

The boundary conditions for a hyperbolic-tangent function basic flow are obtained as for the Rayleigh equation : far from the shear layer, the second derivative of the velocity profile U_{yy} becomes negligible. For $y > 3$, the Orr-Sommerfeld equation (7.21) admits a solution

$$\mathbf{v}(y)=\sum_{n=1}^{4}A_n e^{p_n y} \tag{7.22}$$

where the p_n values are obtained by replacing **v** in (7.21) by its value (7.22) :

$$\begin{aligned} p_1 &= \alpha & p_2 &= -\alpha \\ p_3 &= \alpha\left(1+\mathrm{i}\frac{U-c}{\upsilon\alpha}\right)^{1/2} & p_4 &= -\alpha\left(1+\mathrm{i}\frac{U-c}{\upsilon\alpha}\right)^{1/2} \end{aligned} \tag{7.23}$$

where U is estimated at $y = 3$ ($U \approx 1$). The decay of the perturbation when y grows implies that $A_1 = A_3 = 0$.

Similarly, for $y < -3$, the solution of the Orr-Sommerfeld equation (7.21) has the form

$$\mathbf{v}(y) = \sum_{n=1}^{4} B_n e^{q_n y} \tag{7.24}$$

where the q_n values are

$$\begin{aligned} q_1 &= \alpha & q_2 &= -\alpha \\ q_3 &= \alpha\left(1 - \mathrm{i}\frac{U-c}{\upsilon\alpha}\right)^{1/2} & q_4 &= -\alpha\left(1 - \mathrm{i}\frac{U-c}{\upsilon\alpha}\right)^{1/2} \end{aligned} \tag{7.25}$$

where U is now estimated at $y = -3$ ($U \approx -1$). One has $B_2 = B_4 = 0$ as the perturbation decays far from the shear layer.

With these boundary conditions, the Orr-Sommerfeld equation (7.21) defines a new eigenvalue problem that can be solved numerically, as done for the Rayleigh equation. Details on the solution procedure are given in Appendix 4.

7.4.2 The viscous shear-layer

The Orr-Sommerfeld equation eigenvalues are presented for 3 viscosity values ($\upsilon = 0.100$, 0.050 and 0.020), corresponding to Reynolds number **Re** = 10, 20 and 50; where the Reynolds number is defined for the shear layer, using as velocity and length scale the velocity difference U_s* and the shear-layer width l_s* respectively :

$$\mathbf{Re} = \frac{U_s^* l_s^*}{\upsilon} \tag{7.26}$$

The wave-celerity eigenvalues c_i and the growth rates αc_i are given respectively on Figure 7.7 and Figure 7.8, as a function of the wave number α, with reference to the inviscid flow results previously obtained. The eigenvalues corresponding to the maximum growth rate are summarised in Table 7.2. From these results, it is clear that the viscosity has a stabilising effect on the shear layer. As the wave celerity decreases, the growth rate also decreases. It even becomes lower than zero, reducing the wave-number interval in which the flow is unstable. The maximum growth rate is also obtained for a lower wave number, when the viscosity increases, giving a larger perturbation wave length λ (7.7).

The stabilising effect due to the viscosity can be explained by the resulting increased diffusion, that has a smoothing effect on the velocity profile, and thus on the perturbation. This diffusion process is clearly depicted by the vorticity field (Figure 7.9) : the vorticity peak values decrease with lower Reynolds number. Similarly, the two vorticity peaks observed on both sides of the shear layer in the inviscid case are less distinct when the viscosity increases. Nevertheless, the viscosity increase does not lead to the merging of these two peaks, which can only be captured by a non-linear analysis.

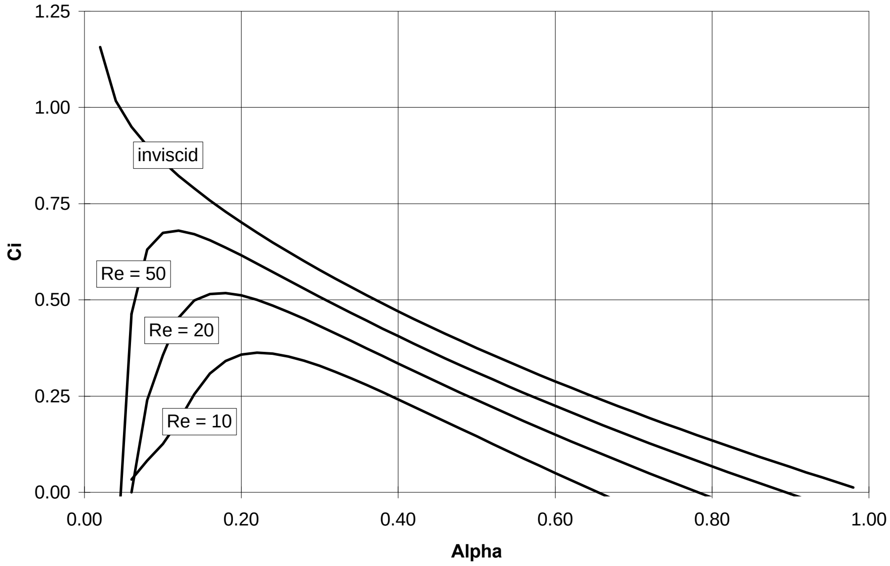

Figure 7.7 : Viscous shear layer : wave celerity, according to the viscosity

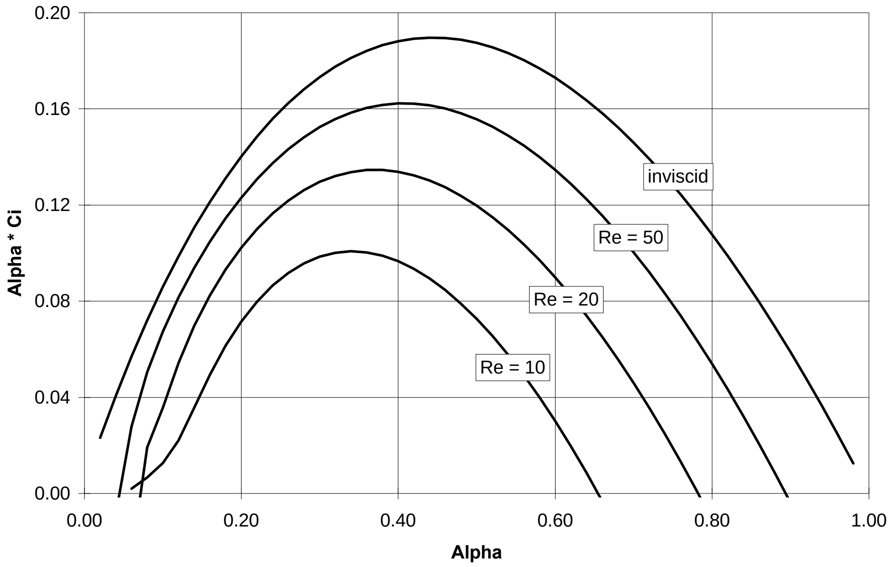

Figure 7.8 : Viscous shear layer : perturbation growth rate, according to the viscosity

Table 7.2 : Eigenvalues of the Orr-Sommerfeld equation, at maximum amplification

Re	υ	α	c_r	c_i	αc_i
10	0.100	0.3410	0.0196	0.2955	0.1008
20	0.050	0.3710	0.0047	0.3630	0.1347
50	0.020	0.4080	-0.0001	0.3979	0.1624
∞	0	0.4450	0.0000	0.4262	0.1897

Inviscid
($\mathbf{Re} \to \infty$)

Re = 50

Re = 20

Re = 10

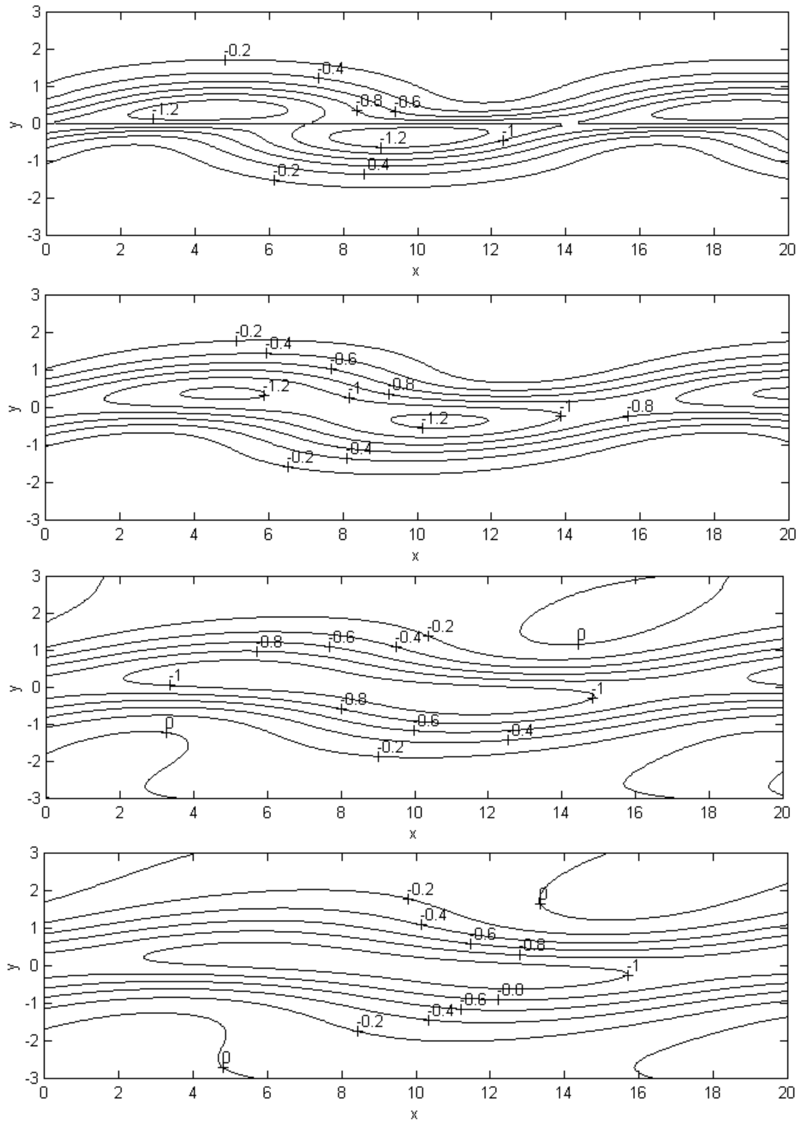

Figure 7.9 : Viscous shear layer : vorticity field,
at maximum amplification, according to the viscosity

Although the previous results show that the viscosity has a significant effect on the instability of the shear layer, it is also clear that this effect reduces rapidly with increasing Reynolds number : for a Reynolds number as low as **Re** = 50, the results are already very close to the inviscid analysis results. The shear-layer Reynolds numbers of the experiments related in the previous Chapter are in the range **Re** = 10000, when computed with the molecular viscosity $\upsilon = 10^{-6}$ m^2/s : the corresponding flows can thus considered as inviscid for further analysis, similarly to previous studies (e.g. Chen and Jirka 1997).

7.5 Extension for shallow-water flow

7.5.1 Extension of the Rayleigh equation for bed friction

Results from the previous paragraphs indicate that, regarding the wave length of the vortices that will develop, an inviscid linear analysis can provide interesting results, even if limited to the simulation of a perturbation temporal-growth. Only if the vortices shape is to be investigated, a non-linear analysis should be required. On the other hand, in the whole analysis, it has been assumed that the velocity profile was generated by appropriate mass-force field or boundary conditions. For the practical cases to be investigated in this work, the governing equations are no more the two-dimensional Navier-Stokes equations, but the Shallow-water equations. This means that the velocity profile will now be governed by both the cross-section shape and the bed friction. In order to investigate how the stability results are affected by these effects, the Rayleigh equation will now be extended to shallow-water flow, according to Chu et al. (1991)

Chu et al. (1991) proposed to develop a stability equation from the Shallow-water or Saint-Venant equations (2.33). A rigid-lid approximation is used, assuming that the water level remains constant with time, although small pressure variations are allowed, due to the perturbation. Using the partial derivative notation defined in § 7.2, the Shallow-water equations write now

$$(uH)_x + (vH)_y = 0 \tag{7.27a}$$

$$u_t + u\, u_x + v\, u_y + g\,(z_w)_x = -\frac{c_f}{H} u\sqrt{u^2+v^2} \tag{7.27b}$$

$$v_t + u\, v_x + v\, v_y + g\,(z_w)_y = -\frac{c_f}{H} v\sqrt{u^2+v^2} \tag{7.27c}$$

where H is the local water depth, variable with y, but constant with x and t, according to the rigid-lid assumption; z_w is the water level; and c_f is the friction factor, defined by (2.40). The notations u and v are adopted for the depth-averaged longitudinal and transverse components of the velocity, not to be confused with the basic flow notation U and V.

The basic flow, parallel to the x-direction, is expressed by

$$U = U(y), \quad V = 0, \quad Z_w = Z_w(x) \tag{7.28}$$

where the water level only vary with x, due to the rigid-lid assumption. This basic flow has to satisfy (7.27b) :

$$g\,(Z_w)_x = -\,g\,S_{0x} = -\,\frac{c_f}{H}\,U^2 \tag{7.29}$$

where S_{0x} is the channel bed slope. This condition (7.29) shows that the longitudinal velocity U only depends on the energy slope, equal to the bed slope in uniform-flow condition, on the local water depth H and on the friction factor c_f.

The actual flow in the channel is then obtained by the addition of the steady basic flow (U, V, Z_w) and an unsteady perturbation (u', v', z_w'), as in the Rayleigh equation development :

$$u = U(y) + u'(x,y,t) \tag{7.30a}$$

$$v = v'(x,y,t) \tag{7.30b}$$

$$z_w = Z_w(x) + z_w'(x,y,t) \tag{7.30c}$$

Replacing the variables in the flow equations (7.27) by their values (7.30), simplifying with the basic flow (7.29), and neglecting the perturbation product terms (linearization hypothesis), one gets

$$\left(u'H\right)_x + \left(v'H\right)_y = 0 \tag{7.31a}$$

$$u'_t + U\,u'_x + v'\,U_y + g\,(z_w')_x = -\,2\frac{c_f}{H}U\,u' \tag{7.31b}$$

$$v'_t + U\,v'_x + g\,(z_w')_y = -\,\frac{c_f}{H}U\,v' \tag{7.31c}$$

Assuming periodical values for the perturbation, as in (7.6), the flow equations become

$$\mathrm{i}\alpha\mathbf{u} + \mathbf{v}_y + H_y/H\,\mathbf{v} = 0 \tag{7.32a}$$

$$-\,\mathrm{i}\alpha c\,\mathbf{u} + \mathrm{i}\alpha U\,\mathbf{u} + U_y\,\mathbf{v} + \mathrm{i}\alpha\,g\,\mathbf{z_w} = -\,2\frac{c_f}{H}U\,\mathbf{u} \tag{7.32b}$$

$$-\,\mathrm{i}\alpha c\,\mathbf{v} + \mathrm{i}\alpha U\,\mathbf{v} + g\,(\mathbf{z_w})_y = -\,\frac{c_f}{H}U\,\mathbf{v} \tag{7.32c}$$

The water level component $\mathbf{z_w}$ of the perturbation can be eliminated from (7.32), by deriving (7.32b) with regard to y, replacing $(\mathbf{z_w})_y$ in (7.32c), and subtracting (7.32a) multiplied by U_y :

$$\mathbf{v}_y = -\,\mathrm{i}\alpha\mathbf{u} - H_y/H\,\mathbf{v} \tag{7.33a}$$

$$\left(\mathrm{i}\alpha(U-c)+2\frac{c_f}{H}U\right)\mathbf{u}_y$$
$$=-\left(2\frac{c_f}{H}U\right)_y\mathbf{u}-\left(\alpha^2(U-c)+U_{yy}-\frac{U_yH_y}{H}-\mathrm{i}\alpha\frac{c_f}{H}U\right)\mathbf{v} \tag{7.33b}$$

Although it would be possible to eliminate the **u** values in (7.33b) using (7.33a), the system of two equations will be used in its present form, in order to keep a more legible mathematical expression. It should be pointed out that, when the friction coefficient c_f and the bed-level variation H_y equal zero, the equations (7.33) reduce to (7.10), giving simply the classical Rayleigh equation. The boundary-conditions definition and the numerical solution of (7.33) are similar to the ones already described for the Rayleigh equation.

Looking forward to study a velocity profile defined by the classical hyperbolic-tangent function and in accordance with (7.29), Chu et al. (1991) used either a continuously variable friction [$c_f \approx (\mathrm{TANH}(y))^{-2}$, constant value of H], or a variable water depth [$H \approx (\mathrm{TANH}(y))^{-2}$, constant value of c_f], as depicted on Figure 5.4. However, in the present study, one seeks to analyse the flow stability in a channel with a piece-wise cross-section (Figure 7.10), corresponding to the classical laboratory flumes. The velocity profile will nevertheless be approximated by an hyperbolic-tangent function (7.15), for further comparison with classical results presented above. One assumes therefore that the velocity profile (7.29) defined according to the channel geometry is smoothed by viscosity, even though this viscosity is neglected in the stability analysis.

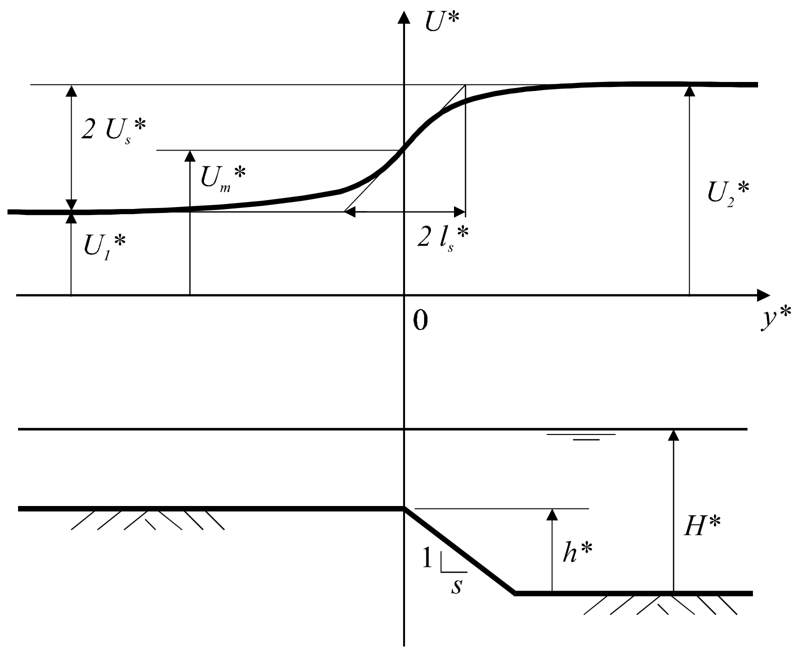

Figure 7.10 : Velocity profile for a shear layer flow, modelled by a TANH(y) function, in a piece-wise cross section

In the present case, the mean velocity U_m in the hyperbolic-tangent velocity profile (7.15) can no longer be set equal to zero. Indeed, its value will affect the result through the bed friction terms in (7.27) which are proportional to U^2. On the other hand, the scaling factor U_s* and l_s* are defined according to (7.14).

7.5.2 Influence of the bed friction

First results are computed for a channel with vertical main-channel banks ($s = 0$). However, the friction on the vertical wall is neglected in the equations (7.33), together with the derivative H_y, in order to avoid the resulting discontinuity in the solution. Although this approximation is questionable (see next paragraph), this allows a first investigation of the sensitivity of the solution to the bed friction and will enable comparison with previous results from § 7.3. The Manning friction law is used. The length scale is set equal to the main-channel depth (l_s* = H*), and the relative water depth is equal to $H_r = 0.5$.

The wave celerity c and growth rate αc_i are shown on Figure 7.11 and Figure 7.12, according to the wave number α, for several friction factor values. The values corresponding to the maximum amplification are summarised in Table 7.3. The bed friction is found to have a stabilising effect, as observed by Chu et al. (1991) : the perturbation growth rate reduces when the friction factor increases, and the wave-number interval for which the flow is unstable reduces accordingly. Unlike the growth rate, the wave number giving the maximum amplification is not or slightly affected by the friction increase.

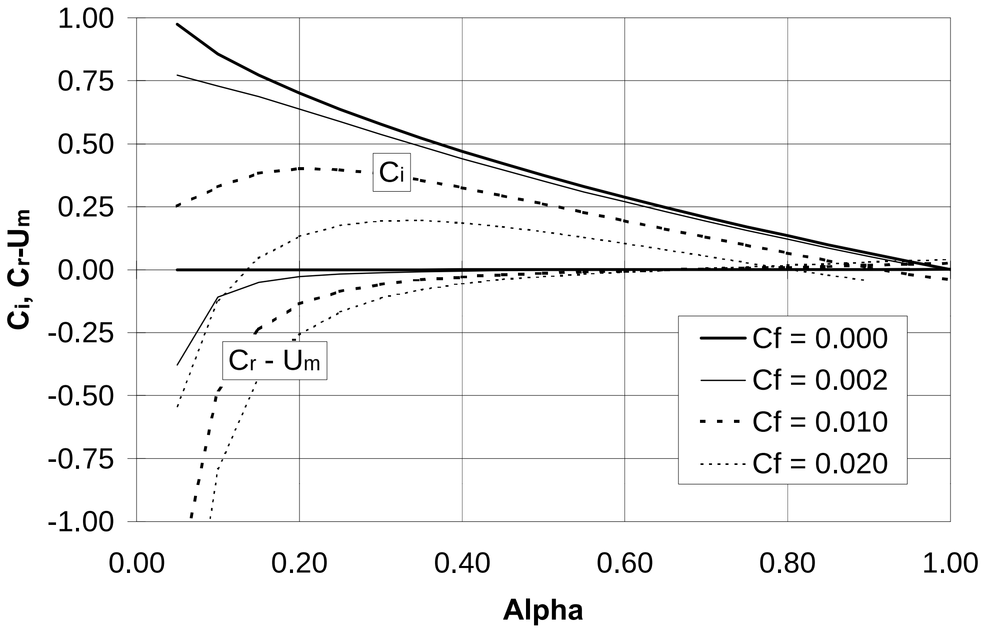

Figure 7.11 : Wave celerity c, according to the friction factor c_f

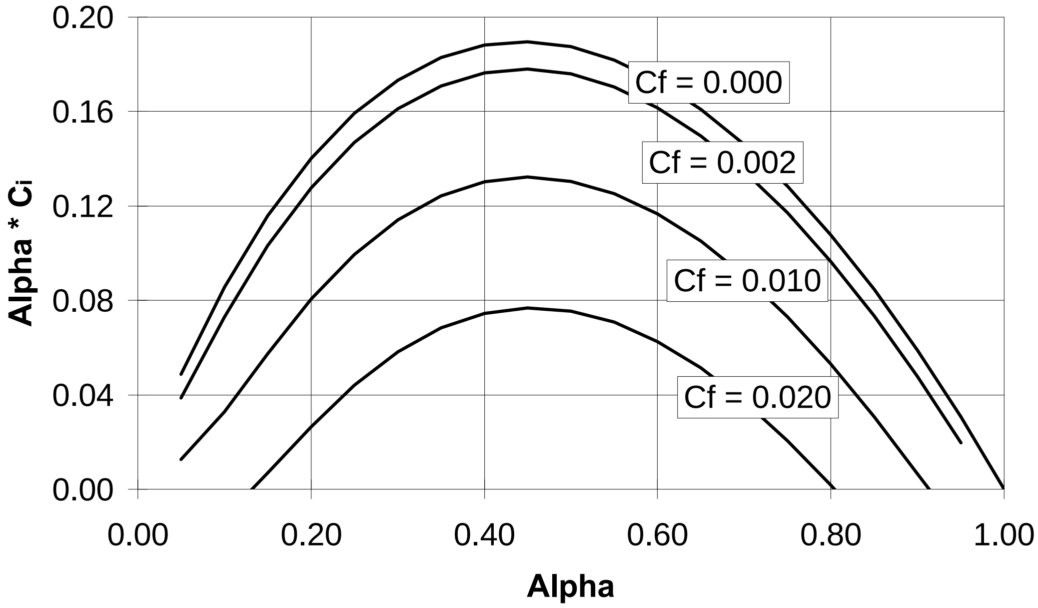

Figure 7.12 : Growth rate αc_i, according to the friction factor c_f

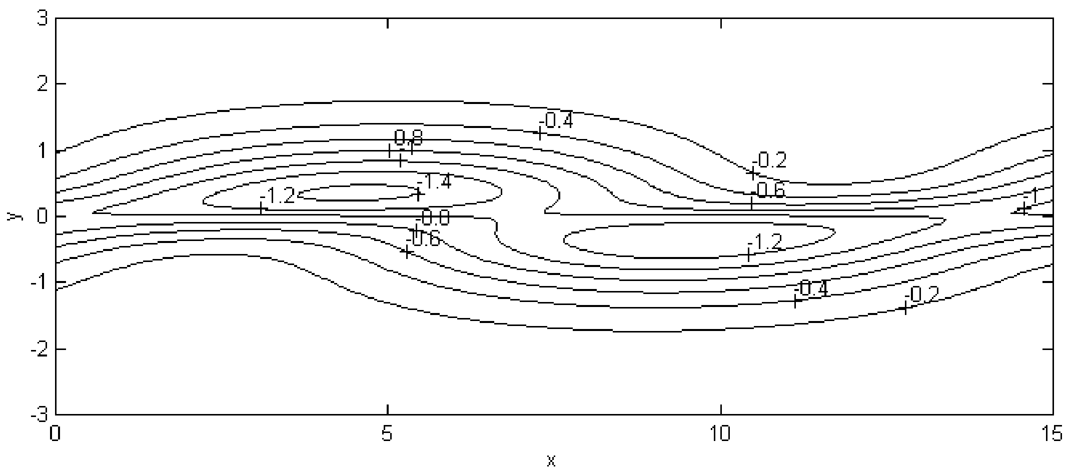

Figure 7.13 : Vorticity field at the maximum amplification, $c_f = 0.02$

Table 7.3 : Wave celerity and wave number at maximum amplification, according to the friction factor c_f

c_f	α	c_r - U_m	c_i	$\alpha\, c_i$
0.000	0.445	0.0000	0.4262	0.1897
0.002	0.450	-0.0039	0.3955	0.1780
0.010	0.450	-0.0198	0.2937	0.1322
0.020	0.455	-0.0378	0.1690	0.0769

A last result to be pointed out is the decrease of the value of the real part of the wave celerity c_r. For the lower wave-numbers, this real part is less than the basic-flow velocity at the interface U_m : this means that the perturbation moves with a velocity equal to the velocity somewhere on the floodplain ($U < U_m$); and, therefore, that its mass centre is shifted on the floodplain ($y < 0$). This effect could indicate a slowing down of the flow due to the friction on this floodplain. However, this effect has almost disappeared at the wave number corresponding to the maximum amplification. Indeed, Figure 7.13 shows the vorticity field at the maximum amplification, for $c_f = 0.02$, and indicates only a small asymmetry, with a higher vorticity in the main-channel area ($y > 0$).

7.5.3 Influence of the channel geometry

A first parameter investigated is the bank slope s, with s = 1 and s = 2 values. The length scale is still $l_s^* = H^*$; the relative depth is 0.5; and the friction parameter equals $c_f = 0.002$. The ratio between the shear-layer width 2 l_s^* and the bank width $s\ h^*$ equals therefore 4 and 2 respectively.

The growth rates are given on Figure 7.14, and the eigenvalues corresponding to the maximum amplification are summarised in Table 7.4. When comparing the s = 1 case with the s = 2 case, it is clear that a steeper bank implies a less stable flow : the flow is unstable for a larger interval of wave number and the maximum growth rate is also larger. The wave number corresponding to the maximum amplification is also slightly larger. For both cases, the real part of the wave celerity c_r is smaller than the interface velocity U_m, indicating as previously a shifting of the vortex centres to the floodplain.

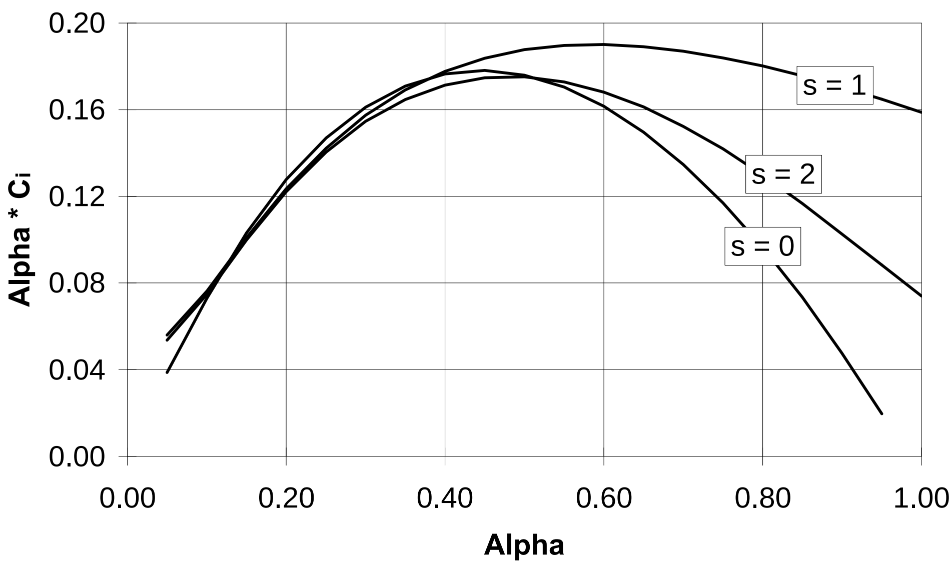

Figure 7.14 : Growth rate αc_i, according to the bank slope s (c_f = 0.002)

Table 7.4 : Wave celerity and wave number, according to the bank slope s ($c_f = 0.002$)

s	α	$c_r - U_m$	c_i	$\alpha\, c_i$
0	0.450	-0.0039	0.3955	0.1780
1	0.590	-0.3034	0.3221	0.1901
2	0.480	-0.2902	0.3653	0.1753

One should expect that the solution of the vertical-bank case ($s = 0$) is in continuity with the solutions of both previous cases. However, the vertical-bank case is more stable and present less shifting to the floodplains. This is probably due to some approximations made in its solution. The friction on the internal vertical bank was indeed neglected, together with the derivative of the water depth at this vertical bank. Accordingly, this last result should be considered circumspectly.

The second parameter to be investigated is the effect of the walls that constrain the perturbation development. For that purpose, a new boundary condition for the perturbation eigenfunction $\mathbf{v}(y)$ is introduced, simply stating that

$$\mathbf{v}(y_{wall}) = 0 \tag{7.34}$$

where y_{wall} is the position of the wall (Betchov and Criminale 1967).

Two first simulations are performed with respectively one and two walls, at $y_{wall} = -3$ or 3. The friction is neglected ($c_f = 0$) and the bank slope set equal to 0. The computed wave celerity c and growth rate αc_i are given, according to the wave number α, on Figure 7.15 and Figure 7.16. The growth rates corresponding to the maximum amplification are summarised in Table 7.5.

When only one wall exists, one observes a non-symmetry of the perturbation, and the real part of the wave celerity is affected ($c_r - U_m \neq 0$) : the vortices do not travel at the interface velocity U_m anymore. When symmetric walls are considered, this effect disappears.

In both cases, the growth rates are lower than in the unconfined case, mainly for the lower wave number α. Indeed, the presence of the walls inhibits partly the vortices development. This phenomena is enhanced for the longer wave length λ (i.e. smaller wave number α), as the unconfined vortex diameter would be larger than the existing distance between the walls. However, this effect is less present for the medium wave numbers, corresponding to the maximum growth rates. The maximum amplification is therefore obtained for wave numbers close to the unconfined-case one; while only the growth rate is lower.

The constraining effect of the walls increases when the distance between the walls reduces. Indeed, smaller wave-length vortices (or larger wave number) will be affected. As shown by Table 7.5, for walls settled at $y_{wall} = -2$; 2, the maximum growth rate drops to $\alpha c_i = 0.0948$; while the corresponding wave number is not modified.

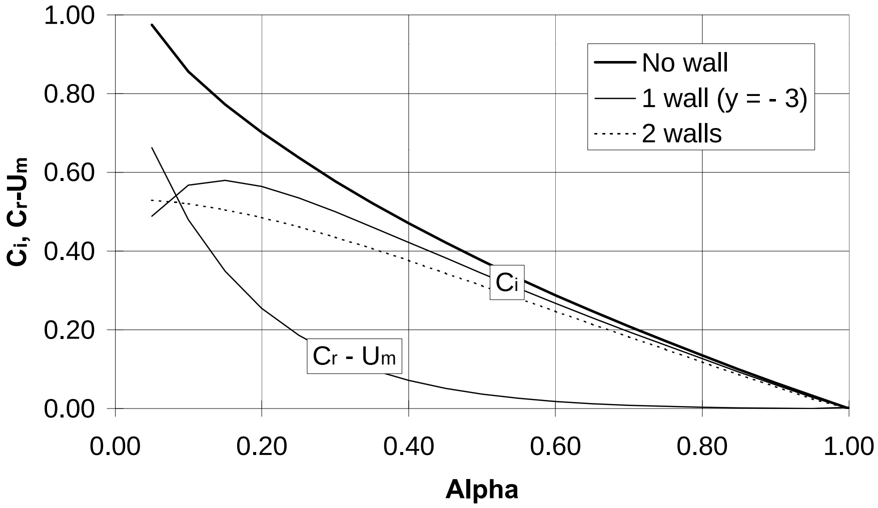

Figure 7.15 : Wave celerity c according to the numbear of walls ($c_f = 0$)

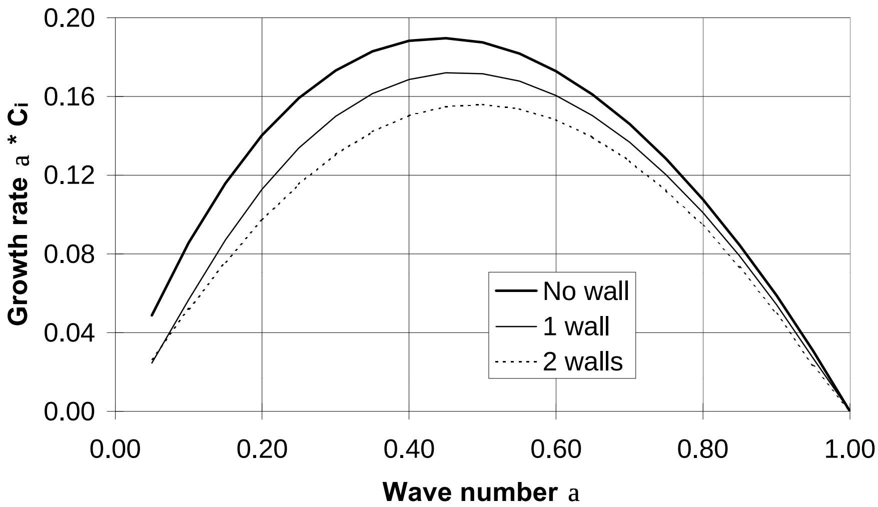

Figure 7.16 : Growth rate αc_i, according to the number of walls ($c_f = 0$)

Table 7.5 : Wave celerity and wave number, according to the number of walls

Number of wall	α	$c_r - U_m$	c_i	$\alpha\, c_i$	
0	0.445	0.0000	0.4262	0.1897	$c_f = 0.000$
1	0.470	0.0451	0.3667	0.1723	"
2	0.490	0.0000	0.3185	0.1560	"
2	0.485	0.0000	0.1954	0.0948	$y_{wall} = - 2; 2$
2	0.495	-0.0016	0.2901	0.1436	$c_f = 0.002$

When bed friction is taken into account, similar results are observed, and the conclusions of the previous paragraph regarding the bed-friction influence are verified : the maximum growth rate reduces, while the wave number increases only slightly.

Although not investigated further in this Chapter, one expects that the constraining effect of walls on a confined flow will be further enhanced when a non-linear stability analysis is considered. Indeed, due to the non-linear effects, small vortices tend to merge together into larger ones. In the case of confined flow, the further development of these larger vortices is constrained by the wall. This effect will be clearly demonstrated in the numerical simulations presented in the next Chapter. On the other hand, this means also that, even if merging process occurs in experimental conditions, there could be a kind of maximum vortex size observable for each given channel geometry.

7.6 Analysis of a symmetric compound channel flow

7.6.1 Classical results : jet flow

When symmetrical compound channels are considered, two parallel shear layers will be observed corresponding to the two interfaces between the main channel and each floodplain. This situation roughly corresponds to a jet flow, of which the stability has been investigated by many authors (see Betchov and Criminale 1967; Drazin and Reid 1981). The basic flow for a jet is classically represented by a hyperbolic-secant-square function (Bickley jet) :

$$U = \mathrm{SECH}^2(y) \tag{7.35}$$

As the velocity tends towards zero, far from the jet, the perturbation will also decay and the boundary conditions can be expressed similarly to the hyperbolic-tangent case (7.16).

When solving the Rayleigh equation for such a velocity profile (7.35), two distinct eigenvalues of the wave celerity c are found for a range of wave number α (Figure 7.17). This means that two modes of instability exist for the jet flow : (1) Mode I is called the even mode, as its eigenfunction $\mathbf{v}$ is symmetric; and (2) Mode II, called the odd mode, as its eigenfunction $\mathbf{v}$ is antisymmetric. The resulting vorticity fields are depicted on Figure 7.18 : accordingly, the instability modes are also respectively quoted as sinuous and varicose modes.

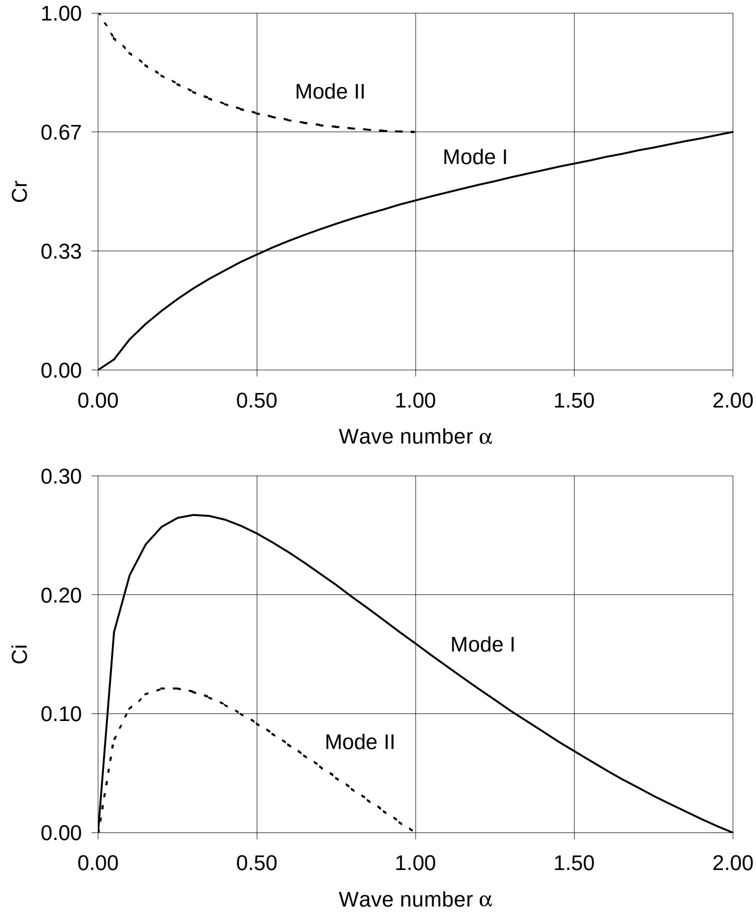

Figure 7.17 : Jet flow, wave celerity c according to wave number α

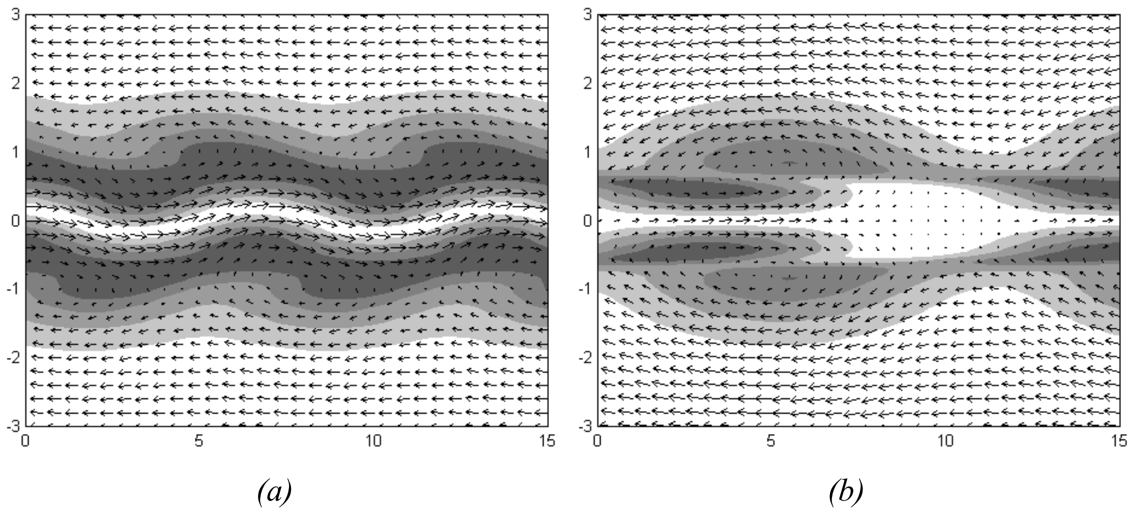

Figure 7.18 : Jet-flow instability modes : vorticity and velocity fields.
(a) Mode I : Even or Sinuous mode; and (b) Mode II : Odd or Varicose mode
(velocities are plotted in a moving frame)

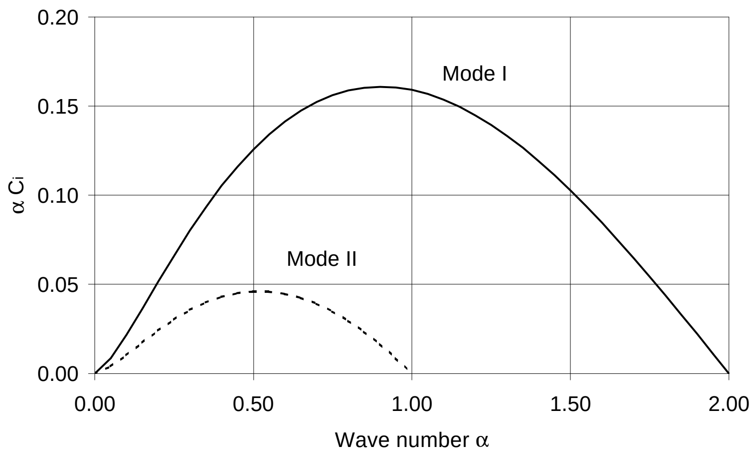

Figure 7.19 : Jet flow stability : growth rate αc_i *for both instability modes*

Table 7.6 : Jet-flow stability : eigenvalues and growth rate at maximum amplification

Mode	α	c_r	c_i	αc_i
I – sinuous	0.902	0.451	0.178	0.161
II – varicose	0.518	0.715	0.089	0.046

The growth rates αc_i of the perturbation are given on Figure 7.19 for both instability modes. In all cases, the sinuous mode I is found to be more unstable than the varicose mode II. This can easily be understood when considering the velocity field depicted by Figure 7.18 : the longitudinal velocity variations in the varicose mode are much larger than in the sinuous mode; and such a perturbation is therefore more difficult to obtain from the basic flow. It can also be observed from Figure 7.17 that, for both modes, the real part of the wave celerity c_r tends to $c_r = 2/3$ for a growing wave number α. This particular value of c_r, which corresponds to the neutral stability, equals the basic-flow velocity at its inflexion points. This means also that, when the varicose mode is considered, the vortices move faster than the velocity at the interface, and slower than this velocity when the sinuous mode is considered. The eigenvalues and growth rates for the maximum amplification are summarised in Table 7.6.

7.6.2 Adapted velocity profile

Whereas the hyperbolic-secant-square function (7.35) fits well the velocity profile of a jet flow, this function is no longer appropriated when studying symmetrical compound-channel flow. Figure 7.20 shows a typical velocity profile for such a flow (Wallingford FCF 020501 case, Knight 1992). It is clear that this velocity profile presents two shear layers steeper and more separated than in the classical Bickley jet. In order to study the actual compound-channel flow stability, an appropriate function should be used for basic-flow modelling. In the present work, it is proposed to use the sum of two hyperbolic-tangent functions, with a shifted abscissa :

$$U = \frac{U^*}{U_s^*} = \frac{U_m^*}{U_s^*} + \frac{1}{2}\left[\mathrm{TANH}\left(\frac{y^* + y_{shift}^*}{l_s^*}\right) + \mathrm{TANH}\left(\frac{-y^* + y_{shift}^*}{l_s^*}\right)\right] \tag{7.36}$$

The shifting factor y_{shift}^* is chosen in order to normalise the jet width : for each shear-layer width l_s^*, its value is selected in such a way that the distance between both inflexion points of the velocity profile equals 1.

The Rayleigh equation is solved for the velocity profile (7.36), with several values of the shear-layer width l_s^*. Figure 7.21 presents the corresponding stability results, where the wave number α is multiplied by the shear-layer width l_s^*, as the scaling factor is now the shifting factor y_{shift}^*. This results show that, when the shear-layer width reduces, the mode I (sinuous) becomes more stable, while the mode II (varicose) is more unstable. Indeed, the distance between both shear layers increases and their interaction decreases : the velocity variations observed on Figure 7.18b for the varicose instability mode of the Bickley jet are therefore less important, and this mode can develop more easily.

For shear-layer widths l_s^* less than 0.50, the two instability modes are found almost indistinguishable. The maximum amplification is obtained for a corrected wave number in the range $\alpha l_s^* = 0.438$ .. 0.461, which is close to the wave number at maximum amplification for the TANH(y) velocity profile : $\alpha = 0.445$ (Table 7.1). This means that, for such widths, both shear layers could behave almost independently; and results from single shear-layer analysis may be applicable.

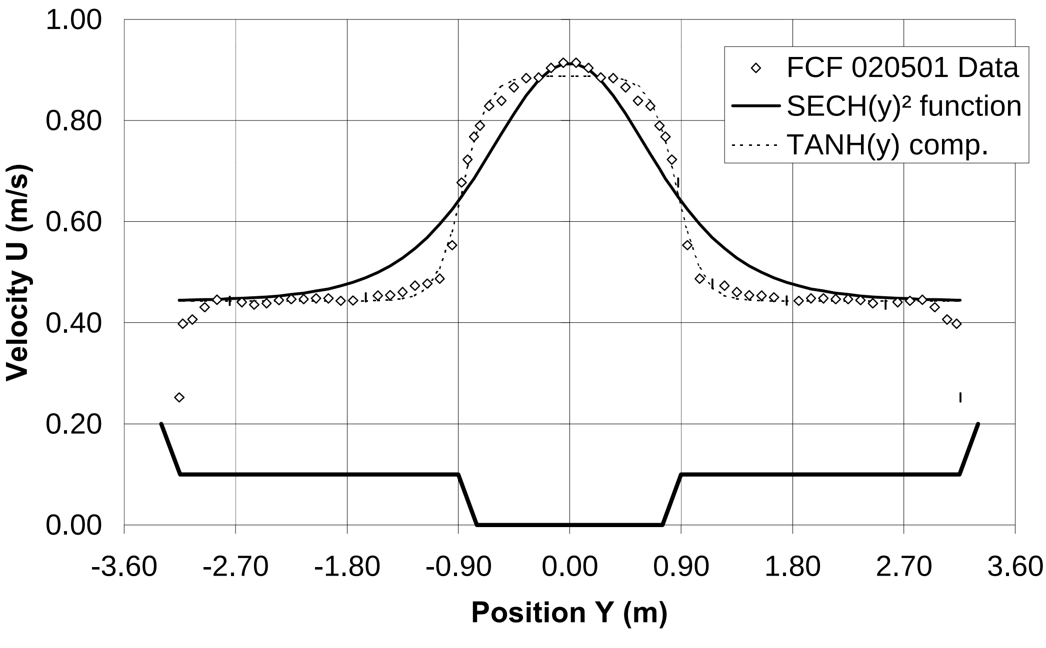

Figure 7.20 : FCF 020501, velocity profile compared to a SECH(y)^2 *function*

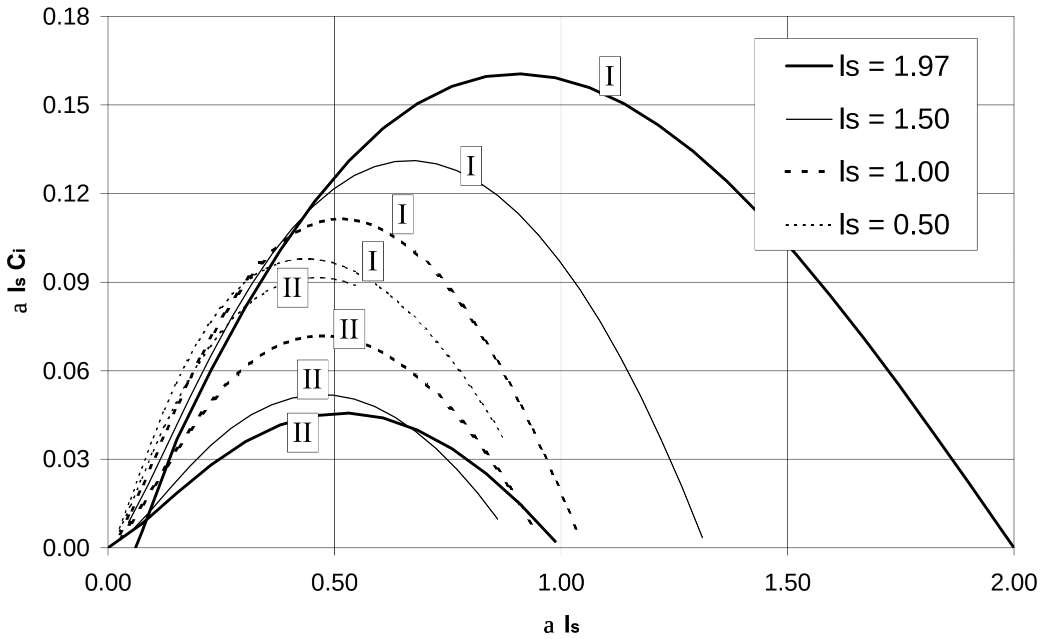

Figure 7.21 : Symmetric-jet stability, for adapted velocity profiles.
I *stands for mode I (sinuous); and* II *for mode II (varicose).*
l_s = 1.97 corresponds to the SECH(y)^2 *function*

It should be pointed out that similar results were obtained by Michalke and Schade (1963), from stability analysis of piece-wise trapezoidal velocity profile, presenting also a reduction of the ratio between the shear-layer and the jet width.

These results are quite interesting, as actual velocity profiles in compound channels present such steep shear-layers. Typically, for the FCF 020501 velocity profile plotted on Figure 7.20, the ratio of the shear-layer and the jet widths equals 0.20, in such a way that both shear layers are almost independent. One can therefore benefit from all the observations previously obtained for the single shear-layer, including the influence of bed friction and geometry.

7.7 Applications

7.7.1 FCF Series 06 (single shear layer)

In the paragraph 7.5, the influence of friction and geometry parameters on the stability-analysis results has been reviewed. This stability analysis will now be particularised to a given geometry, to be investigated numerically in the next Chapter. Indeed, whereas one expects that the non-linear effects taken into account by the numerical simulation will affect the final results, due to vortices merging, the first part of the instability development will remain in the linear-assumption domain and comparison between the numerical results and the present analysis will be valuable.

The geometry selected for this single shear-layer analysis is the asymmetric compound-channel case investigated in the Flood Channel Facility Series 06 tests (Knight 1992), where the main channel is bordered by a unique floodplain. For this geometry, accurate velocity profiles were measured, enabling comparison with the numerical simulation results. Unfortunately, neither for the present Series 06, nor for other experiments in the FCF, estimation of the periodical-structures wave length are available : maybe such an estimate could be gathered from the raw LDA velocity measurements made in several geometries (see e.g. Knight and Shiono 1990), but it seems that nobody has already published such results.

The relevant parameters of the FCF Series 06 geometry are as follow. The main channel is 1.65 m width (y_{wall}* = 1.65 m), and has a h* = 0.15-m height bank, with a bank slope s = 1. The floodplain is 2.25 m width (y_{wall}* = - 2.25 m). Investigated water depths in the main channel are in the range H* = 0.16 .. 0.30 m (Table 7.7). The friction factor c_f is estimated from the Manning roughness-coefficient value n = 0.01106 s/m$^{1/3}$ (see § 8.2.2). The basic-flow parameters are estimated from numerically-computed unperturbed velocity profiles (see Chapter 8), by fitting an hyperbolic-tangent function (7.12) (Table 7.7). Indeed, the measured velocity profiles can not be used as basic flows, as they already present enlarged shear layers, due to the perturbation development.

The extended Rayleigh equation (7.33) is integrated for the given geometry and basic flows; and the eigenvalues corresponding to the maximum amplification are summarised in Table 7.8. The maximum amplification is obtained for wave numbers in the range α = 0.653 .. 0.766, with the smallest wave number α (or larger wave length λ) observed at the largest depth H*. The growth rates αc_i are larger for the small depths. This could be explained by a higher shear in these cases, due to the higher velocity difference between subsections. In all the cases, the wave celerity c_r is lower than the flow velocity at the interface U_m, indicating that the vortices move at a velocity closer to the floodplain velocity.

Table 7.7 : FCF Series 06 : water depth and velocity profile characteristics (dimensional values)

Label	H* [m]	U_m* [m/s]	U_s* [m/s]	l_s* [m]
060101	0.15826	0.483	0.346	0.029
060201	0.16505	0.524	0.332	0.047
060301	0.17619	0.583	0.313	0.081
060401	0.18836	0.641	0.296	0.118
060501	0.19793	0.683	0.285	0.149
060601	0.21348	0.748	0.269	0.199
060701	0.24781	0.879	0.243	0.313
060801	0.30185	1.064	0.214	0.499

Table 7.8 : FCF Series 06 : growth rate and wave celerity at the maximum amplification

Label	α	c_i	$\alpha\, c_i$	c_r - U_m
060101	0.766	0.269	0.206	- 0.377
060201	0.744	0.282	0.210	- 0.360
060301	0.734	0.287	0.210	- 0.356
060401	0.722	0.290	0.210	- 0.349
060501	0.712	0.293	0.208	- 0.344
060601	0.695	0.296	0.206	- 0.333
060701	0.663	0.298	0.198	- 0.307
060801	0.653	0.274	0.179	- 0.263

In order to investigate the results sensibility to the length scale l_s*, two additional tests are done for the 060501 case, with l_s* = 0.100 and 0.200. Indeed, as the bank height and the wall positions have fixed dimensional values, their adimensional values will change according to l_s* and will affect the analysis results. The wave number and growth rate at maximum amplification are summarised in Table 7.9. It is found that the wave-number value is clearly affected by the length scale l_s*, with the lowest value corresponding to the smallest length scale. An additional result concerns the dimensional wave length λ* of the vortices, which is significantly affected by the change of length scale, not so much due to the wave-number change, but simply due to scaling change.

For the sake of further comparison with numerical results, the velocity and vorticity field of the perturbed flow are plotted on for FCF 060501 case (l_s* = 0.149 m). Pairs of vorticity peaks are clearly identified on both sides of the interface (y* = 0 m); while a vorticity discontinuity is also observed at this interface, due to the bed level angular point. The velocity field, plotted in a frame moving at the interface velocity U_m, shows noticeable vortices, located on the interface.

Table 7.9 : FCF 060501 : growth rate, wave celerity and wave length at maximum amplification

l_s* [m]	α	c_i	$\alpha\, c_i$	c_r - U_m	λ* [m]
0.100	0.674	0.316	0.213	- 0.306	0.932
0.149	0.712	0.293	0.208	- 0.344	1.315
0.200	0.736	0.276	0.203	- 0.371	1.707

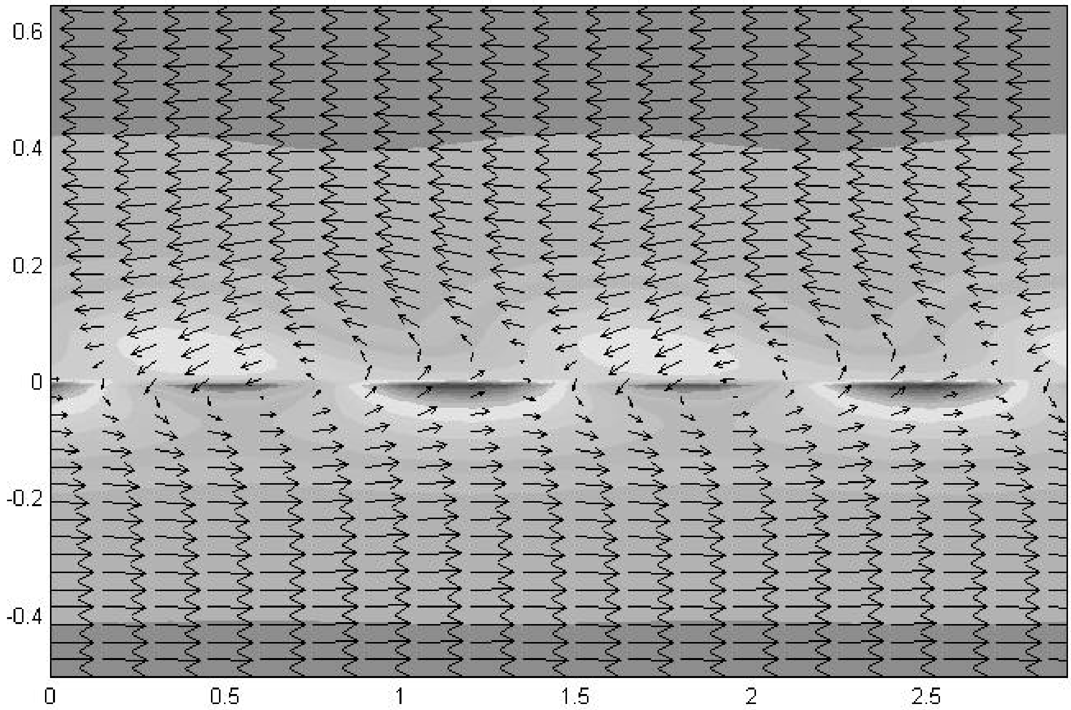

Figure 7.22 : FCF 060501 : velocity (arrows) and vorticity (grey scale) field of the perturbed flow, at maximum amplification (x- and y-position axis are in dimensional values)

Lastly, it should be pointed out that the Reynolds numbers (7.26) corresponding to the investigated basic flow are in the range **Re** ≈ 50, unlike the previous estimation from § 7.4.2. Indeed, in the present case, a turbulent viscosity $\upsilon_t \approx 10^{-3}$ m^2/s is used for the velocity-profile computations (see Chapter 8). As a consequence, and according to § 7.4.2 results, one can expect a small reduction of the actual wave-number and growth-rate values, compared to the inviscid-analysis values given in Table 7.8.

7.7.2 UCL flume (single shear layer)

Similar calculations are performed for the UCL flume with an asymmetric floodplain. For this data set, experimental values of vortex wave-length are available for several cases, as seen in the previous Chapter. The geometry of the channel is given by Figure 6.1, and the investigated test cases are summarised in Table 6.1. The basic-flow parameters (Table 7.10) are again estimated from numerically-computed unperturbed velocity profiles (see Chapter 8), by fitting an hyperbolic-tangent function (7.12). For solving the extended Rayleigh equation, one uses a value of the bank slope equal to s = 1, as it has been found above (§ 0) that taking s = 0 and neglecting simultaneously the friction on the vertical bank could lead to an underestimation of the wave number at the maximum amplification.

The wave number and growth rate at the maximum amplification are given in Table 7.11. The wave numbers are now in the range α = 0.65 .. 0.85, while the growth rate are in the same range as for the FCF Series 06. The wave celerity c_r is again lower than the flow velocity at the interface U_m, indicating that the vortices move at a velocity close to the floodplain velocity : this result is in accordance with the experimental observations.

Table 7.10 : UCL flume : water depth and velocity profile characteristics (dimensional values)

Label	H_r	H^* [mm]	U_m^* [m/s]	U_s^* [m/s]	l_s^* [m]
LCA 08	0.10	54.4	0.249	0.159	0.040
LCA 10	0.23	63.9	0.311	0.138	0.052
LCA 12	0.30	68.8	0.308	0.163	0.054
LCA 16	0.38	78.9	0.342	0.158	0.062

Table 7.11 : UCL flume : growth rate and wave celerity at the maximum amplification, calculated and measured vortex wave length

Label	α	c_i	$\alpha\, c_i$	c_r - U_m	λ^* calc. [m]	λ^* meas. [m]
LCA 08	0.841	0.212	0.177	-0.473	0.299	0.39
LCA 10	0.722	0.274	0.198	-0.365	0.453	0.56
LCA 12	0.681	0.292	0.199	-0.327	0.498	0.67 – 1.26
LCA 16	0.643	0.309	0.199	-0.284	0.606	-

Lastly, the dimensional wave-length λ^* of the perturbations are calculated from the wave-number values, and compared to the experimental values, when available (Table 7.11). Both values are found to compare rather satisfactorily : for each case, both calculated and measured wave-lengths have close values, although the measured one is in all cases around 30 % larger than the calculated one (when the experimental value of $\lambda^* = 0.67$ m is considered for LCA 12). Moreover, the variation of the wave-length according to the discharge is similar for calculated and measured values.

Several causes could explain the underestimation of the vortex wave-length by the stability analysis, when compared to the measurements : (1) the linear analysis assumption; (2) the influence of the bank slope value s; or (3) an experimental error. In a non-linear analysis, vortices are allowed to merge together and to grow up to larger wave length. However, the ratio between experimental and calculated wave lengths indicates that, if such growing occurs, it is rapidly stopped, probably as a result of the constraining of the flow by the channel banks. Secondly, a wrong estimation of the vortices wave-length could be due to the treatment of the main-channel vertical bank. Indeed, results from § 0 indicate that similar differences between the wave numbers can be obtained when varying the bank slope in the interval $s = 0 .. 2$. Lastly, as pointed out in Chapter 6, a mass transfer exists between subsections, due to the upstream discharge-distribution ill-conditioning. The periodical structures could thus be affected due to this mass-transfer and its effect on the velocity profile : as quoted in Chapter 6 conclusion, further experimental investigations are required to observe the vortices development along the channel length.

7.7.3 Sellin's data (double shear layer)

The last geometry investigated is the flume used by Sellin, for which vortex wave-length measurements are available (Sellin 1964). Sellin's flume is 0.456-m wide, with a bed slope of S_0 = 0.00085 (Figure 7.23). From the uniform-flow experiments reported in his paper for an isolated single channel, the flume roughness can be estimated as equal to n = 0.0064 s/m$^{1/3}$. As quoted in Chapter 5, Sellin measured that the vortex wave-length equals twice the main-channel width, that means λ^* = 228 mm. This wave length was observed for a water depth around H^* = 52 mm, and corresponds to the vortices on Figure 5.1.

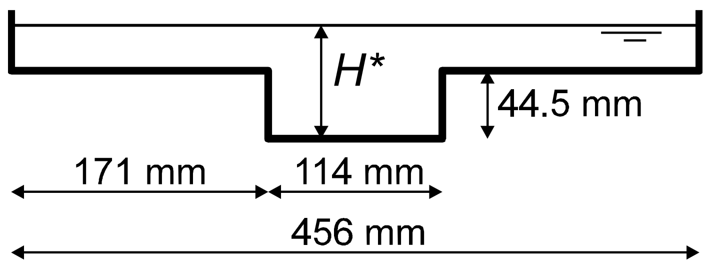

Figure 7.23 : Sellin flume geometry

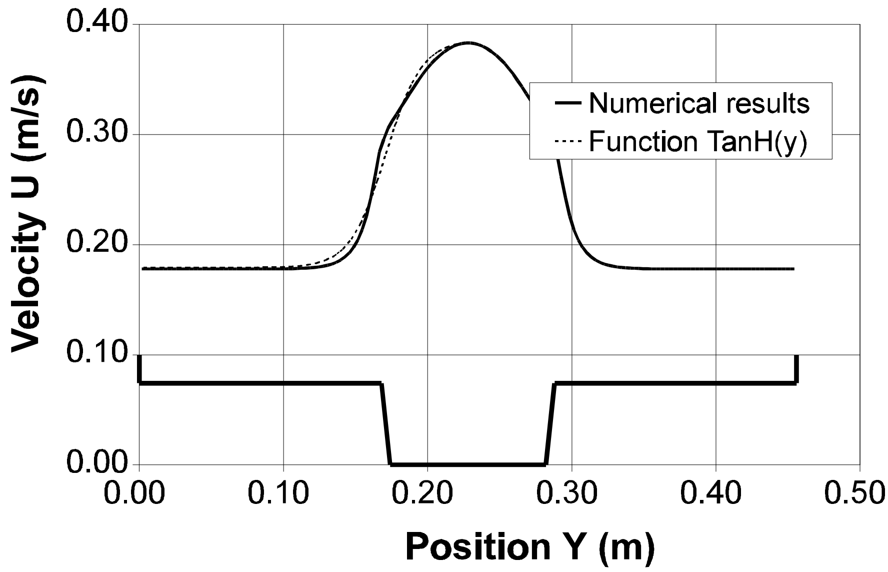

Figure 7.24 : Sellin flume : computed velocity profile and TANH *function.*

The basic flow is again estimated from a numerically-computed unperturbed velocity profile (see Chapter 8). This velocity profile is given of Figure 7.24. When fitting an hyperbolic-tangent function to one of the shear layers, this shear-layer width can be estimated as l_s^* = 24.7 mm. This width is less than a quarter of the main-channel velocity-profile width (distance between the two inflexion points), and, according to the analysis in § 0, the stability of the basic flow can be investigated by considering only one shear layer, rather than a jet-flow profile.

As for the UCL flume, a bank slope equal to $s = 1$ in used for this analysis. The maximum growth rate equals $\alpha c_i = 0.217$ and is obtained for a wave number $\alpha = 0.719$. The corresponding wave length equals $\lambda^* = 216$ mm and agrees very well with the experimental estimation of $\lambda^* = 228$ mm. It should be noticed that, according to this result, the vortices observed by Sellin still have the initial wave-length of the most amplified perturbation. This could indicate that, in this case, the perturbation was not significantly affected by non-linear effects and that no vortices merging occurred, as if the perturbation lateral development was constrained on one side by the floodplain bank and, on the other side, by the main-channel symmetry axis.

7.8 Conclusions

The various stability analysis quoted and developed in this Chapter give some more insight into the initial perturbation development in the shear layer at the interface between a main channel and a floodplain. Such analysis provide values of the wave number α, and of the wave length λ, for which the perturbations will grow the fastest. For cases where non-linear effects and merging phenomena can be neglected, these wave lengths are expected to match the vortices wave-lengths observed in compound channels.

Two parameters have been found to affect significantly these preferential wave lengths, namely the bed friction and the cross-section geometry. Other parameters were investigated but showed lower influence : the viscosity and the wall effect. When non-linear effects are not considered, perturbation temporal-growth, as investigated here, and spatial-growth, not considered in this work, gave rather similar wave length for the maximum amplification. For symmetrical compound channels, when the main channel is wide enough, when compared to the shear-layer width, both shear layers were found to behave almost independently.

Several computations were performed for actual geometries. Wave number α and wave length λ at the maximum amplification were estimated for (1) the FCF Series 06 (asymmetrical channel); (2) the UCL experiments as described in the previous Chapter; and (3) Sellin's experiments (symmetrical channel). The FCF results will solely be used for the validation of the numerical simulation in next Chapter, as no periodical-structures wave-length estimations are available in this data set.

When compared with the UCL measurements, the stability analysis seems to underestimate the vortex wave-length, although similar variations according to the water depth are observed. This could be due to vortex merging and growing processes, occurring in the experiments, but not taken into account by the linear stability analysis. However, either the treatment of the bank slope in the calculations, or the experimental imperfections due to the ill-conditioned upstream discharge distribution, could also explain this discrepancy. For Sellin's experiments, a very good matching has been obtained between measured and estimated wave lengths. This would clearly indicate that no merging occurred between vortices in the shear layers of this channel, due to the main-channel small width.

From both these comparisons, one can conclude that the stability analysis produces satisfactory results, at least in cases where the linear assumption remains valid; and that no vortex merging actually occurred, due to geometrical constraining.

Chapter 8
Numerical modelling of periodical structures in a compound-channel flow

8.1 Introduction : SDS-2DH numerical model

As quoted above, the Part II of the present work is dedicated to the modelling of periodical turbulent structures, such as large vortices with vertical axis, which were identified by several authors at the interface between the main channel and a floodplain of a compound channel (see Chapter 5), and for which new measurements are also reported in Chapter 6. Indeed, these horizontal vortices are expected to be responsible of the momentum transfer observed between subsections, as modelled by the EDM (see Chapter 4). The Chapter 7 has shown that an hydrodynamic stability analysis could help in predicting the initial development of such periodical structures. However, non-linear effects, not taken into account in the stability analysis, are responsible for further growth and development of the turbulent structures. The purpose of this Chapter is thus to extend the analysis, through the use of a numerical model that will account for all non-linear effects.

As the phenomena to be investigated is mainly two-dimensional, a depth-averaged model will be preferred to a complete three-dimensional model solving the Navier-Stokes equations, in order to limit the programming complexity and the computational cost. The model that will be used is the so-called SDS-2DH model by Nadaoka and Yagi (1998). This model, whose principle will be described below, produces indeed satisfactory results when modelling horizontal vortices due to transverse shearing in partly-vegetation-covered channels. The model had not been applied to compound-channel geometry yet; but it was expected that it could produce similarly good results.

According to Nadaoka and Yagi (1998), the turbulence structure of a shallow-water flow is characterised by the coexistence of 3D turbulence, having length scales less than the water depth, and horizontal two-dimensional eddies with much larger length scales. As a result, the spectral structure of such a flow can be depicted as on Figure 8.1 : a first peak corresponds to the horizontal 2D vortices generated by the transverse shearing. In this area, an inverse cascade of spectral energy can be observed, due to processes like vortex pairing; while a direct attenuation also exists, due to dissipation by bottom friction. A part of this dissipated energy may be supplied to 3D turbulence, at higher wave-number α; while bottom friction may also directly provide 3D turbulent energy.

The SDS-2DH model is then defined according to this flow structure (Nadaoka and Yagi 1998) : the large horizontal vortices are computed explicitly, using the shallow-water equations (2DH) that includes transverse-shearing terms; while the small-scale 3D turbulence is implicitly modelled as "Sub-Depth Scale turbulence" (SDS). The Sub-Depth Scale turbulence effect on the depth-averaged flow is taken into account through an eddy viscosity $\upsilon_t = \upsilon_{SDS}$. The latter is estimated by using the one-equation turbulence model *k-l* (see § 2.4.3) : the length scale l_d is assumed to be proportional to the water depth H (2.49 : $l_d = \xi H$); while a depth-averaged transport equation is used for the turbulent kinetic energy k (2.46a). Indeed, as the 2D vortices generate part of the 3D turbulence, it is suggested that 3D turbulent kinetic energy could be transported accordingly by the 2D structures.

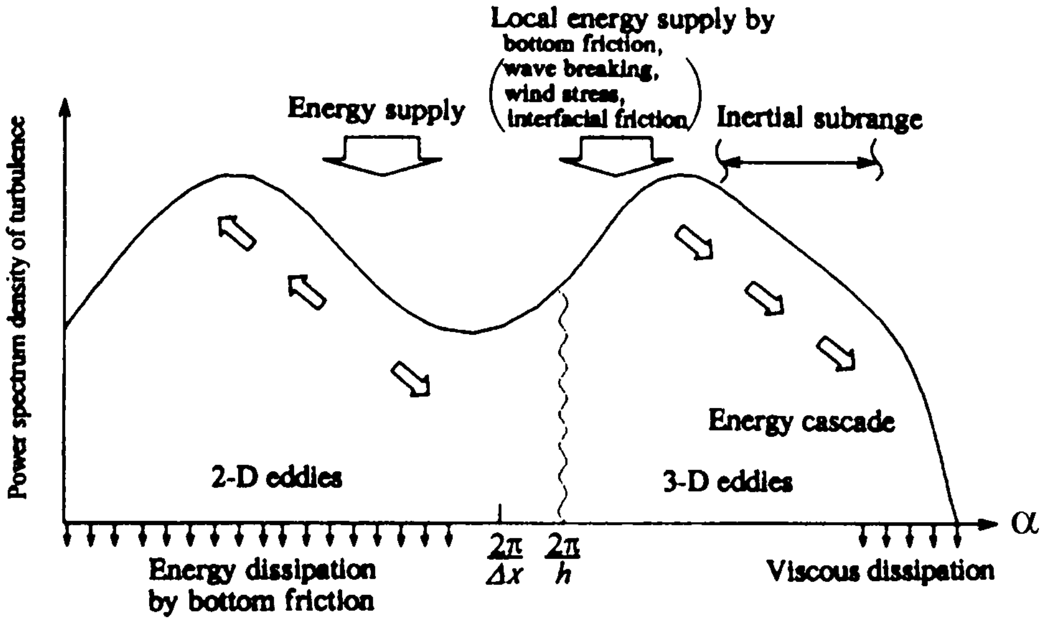

Figure 8.1 : Turbulent energy spectrum in a depth-averaged flow with a shear layer, according to Nadaoka and Yagi (1998)

This proposed SDS-2DH model is somewhat difficult to categorise with reference to classical model types. Its principle is similar to Large Eddy Simulation (LES), or even Very Large Eddy Simulation (VLES), according to the length scales to be modelled. Indeed, similarly to the SDS-2DH model, LES and VLES models solve explicitly the large turbulence scales, while the smaller scales are modelled implicitly, using a so-called subgrid model (Ferziger and Peric 1996). However, when the grid size reduces, LES results tend towards the results obtained from a Direct Navier-Stokes (DNS) simulation, in which all turbulence scales are modelled, from the larger one to the smaller one, that corresponds to molecular dissipation. This means that, when decreasing the grid size, an LES subgrid model will converge towards molecular viscosity. From a strict viewpoint, the SDS-2DH model thus can not be considered as LES since, for smaller grid size, it will not converge to molecular viscosity. There are two reasons for that : (1) the model is based on a transport equation of the kinetic-energy; and (2) it is based on a depth-averaging hypothesis. Most likely this will not jeopardise the results obtained with this model, as the smaller scales to be explicitly computed are much larger than the scales at which molecular dissipation occurs; but it remains a weakness from the theoretical point of view.

On the other hand, as the *k-l* turbulence model used in the SDS-2DH model is based on a Reynolds averaging of the velocities and on Reynolds shear stresses, it could be categorised as a Reynolds-Averaged Navier-Stokes (RANS) simulation (Ferziger and Peric 1996). Such a RANS simulation basically considers a steady flow, in which a time-averaged (i.e. Reynolds averaged) velocity $\bar{u}$ can be isolated from its fluctuating value $u = \bar{u} + u'$ (see Figure 8.2a) :

$$\bar{u} = \frac{1}{T_a} \int_{t_0 - T_a/2}^{t_0 + T_a/2} u \, dt \tag{8.1}$$

where t_0 is a reference time; and T_a is the time interval on which the averaging is performed. From a mathematical point of view, this interval T_a length should tend towards infinity; but, from a practical point of view, it will be long enough, as soon as it is much greater than the typical-fluctuation time-scale T_s :

$$T_s << T_a \tag{8.2}$$

The effects of the turbulence is then accounted through Reynolds-averaged shear stresses $\tau_{ij} = -\rho\, \overline{u_i' u_j'}$ (2.41), and a turbulence model as the ones detailed in Chapter 2.

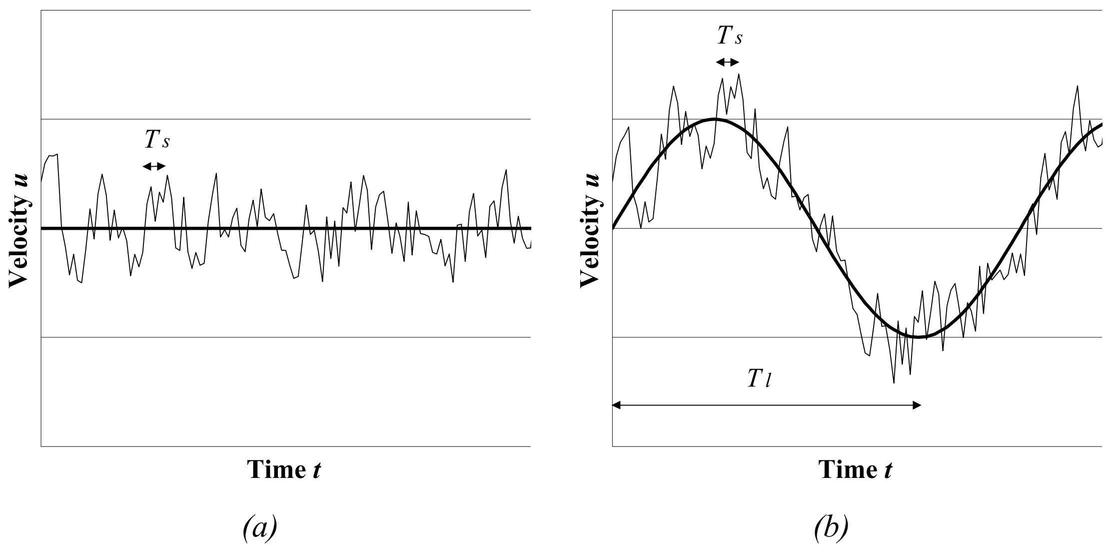

Figure 8.2 : RANS methods, time-averaging of the velocity : (a) steady RANS; and (b) unsteady RANS (fine line : actual velocity u, bold line : averaged velocity $\bar{u}$)

However, in the present SDS-2DH simulations, unsteady velocities are considered, as the large-scale turbulence is computed explicitly. Consequently, this model is of the

Unsteady Reynolds-Averaged Navier-Stokes (URANS) kind. This means that the velocities are no more averaged on a time interval T_a tending towards infinity, but on a time interval that is short enough for still capturing explicitly the large-scale structures of time-scale T_l (see Figure 8.2b) :

$$\bar{u}(t) = \frac{1}{T_a} \int_{t-T_a/2}^{t+T_a/2} u \, dt \tag{8.3}$$

with

$$T_s << T_a << T_l \tag{8.4}$$

The effect of the small-scale turbulence is then accounted through Reynolds-averaged shear-stress models similar to the ones used in RANS simulations.

The validity of the URANS modelling will rely on the condition (8.4) : indeed, in order to define a Reynolds-averaged velocity that encompasses all the small-scale fluctuations and that varies according to the large-scale structures, the latter have to be several order of magnitude larger than the small-scale fluctuations ($T_s < 10^{-4}\ T_l$). Following Nadaoka and Yagi, it is expected that, for the considered depth-averaged shear flow, this condition is satisfied, as the observed vortices are quite large, but also as part of the small-scale 3D turbulence is already averaged through the depth-averaging. However, when planning further works, it would be interesting to investigate the actual turbulence spectrum of a compound-channel flow, in order to verify Nadaoka and Yagi assumption; while the use of the Sub-Depth Scale model, instead of a subgrid model as in classical LES, should also be questioned.

The Saint-Venant equations, including the SDS-2DH model, are solved with a MacCormack scheme, for a staggered grid, as described in Appendix 1. Several compound-channel test-cases will then be investigated in the present Chapter : (1) an asymmetrical geometry from the Wallingford Flood Channel Facility (FCF Series 06); (2) Sellin (1964) experiments in a symmetrical cross-section; and (3) the asymmetrical cross-section tested in the UCL flume (see Chapter 6). A detailed presentation of the FCF 06 simulations will be given, including comparison with the stability-analysis results and with the measured-velocity profiles. Comparison with Sellin and UCL data will then focus on the actual periodical-structures size and shape. An analysis of the additional shearing due to the horizontal vortices will be given in Chapter 10.

8.2 FCF Series 06 simulations : values of the parameters

8.2.1 Geometry and mesh size

The FCF 06 cross section is given on Figure 8.3 : the main-channel-bottom width equals 1.50 m, the bank height is h = 0.15 m, the bank slope is s_c = 1, and the floodplain-bottom width is 2.25 m. The flume length is 57 m, and the longitudinal bed slope equals $S_0 = 1.027 \times 10^{-3}$. The investigated water depth and discharge are summarised in Table 8.1 (Knight 1992).

Three different node spacing will be used : (1) 0.15×0.15 m^2; (2) 0.05×0.05 m^2; and (3) 0.03×0.03 m^2. The node positions are defined in such a way that, in the interface area ($1.65 < y < 1.80$ m), the bed level values in the staggered grid are specified exactly on the cross-section ridges (see Figure 8.3). The outside banks ($y < 0$ m and $y > 4.05$ m) are not modelled but are replaced by vertical walls, in such a way that no mesh adaptation is required when varying the water depth H. It is expected that this approximation will not affect the periodical-structures modelling, as the walls influence on the shear-layer is mostly limited to a constraining effect. In the longitudinal direction, the whole flume length (57 m) will be included in the computational domain, in a first stage; while further tests will be performed for a shorter length (19 m), in order to reduce the computational time. The domain sizes are summarised in Table 8.2.

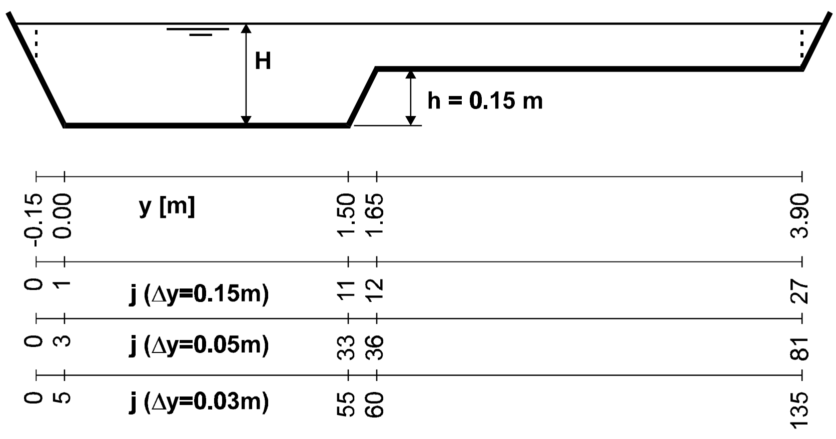

Figure 8.3 : FCF 06, cross-section and mesh definition (j identifies the mesh indices in the transverse direction)

A free-slip condition is used at the boundary walls; while a cyclic condition is used between the downstream and the upstream boundaries. The computation is initiated from an unperturbed uniform-flow. The computer rounding errors are then allowed to grow in such a way that vortices may appear and develop for the most amplifying wave number. In a typical run, this vortex-generation process will take about 50000 computing steps. An estimate of the maximum time steps Δt is given in Table 8.2, according to the condition (A1.18) defined in Appendix 1. The proportionality factor ξ linking the SDS-turbulence length-scale l_d to the water depth H (2.49) is set equal to

$\xi = 0.2$. Nadaoka and Yagi (1998) suggested a value of $\xi = 0.1$, but the latter was found to produce unstable simulations in several cases.

Table 8.1 : FCF 06, investigated water depths and discharges (Knight 1992)

Case	Relative depth H_r	Water depth H	Discharge Q
060101	0.05	0.158 m	0.224 m^3/s
060201	0.10	0.165 m	0.238 m^3/s
060301	0.15	0.176 m	0.265 m^3/s
060401	0.20	0.188 m	0.293 m^3/s
060501	0.25	0.198 m	0.343 m^3/s
060601	0.30	0.213 m	0.395 m^3/s
060701	0.40	0.248 m	0.593 m^3/s
060801	0.50	0.302 m	0.929 m^3/s

Table 8.2 : Mesh characteristics, computational domain sizes and estimated maximum time steps

Mesh size	Flume 57-m length	Flume 19-m length	Max. time step Δt
0.15×0.15 [m²]	380×27	-	0.0360 [s]
0.05×0.05 [m²]	1140×81	380×81	0.0107 [s]
0.03×0.03 [m²]	1900×135	-	0.0057 [s]

8.2.2 Roughness coefficient

The roughness-coefficient value has to be carefully estimated in these simulations. Indeed, as already discussed when developing the Lateral Distribution Method (Chapter 3), one attempts to estimate accurately both the velocity and the bed shear-stress values, which are linked together by the roughness coefficient. This means that the actual roughness coefficient, corresponding exactly to the bed material, should be used. Otherwise, fitting the roughness-coefficient value, in order to predict correctly the velocity profile, would jeopardise the bed shear-stress estimation. Indeed, such a fitted roughness coefficient would also include the effect of additional losses due to secondary currents.

The FCF bed is made of smoothed concrete. Its Manning roughness coefficient is estimated on the basis of single-channel experiments, with water depth varying in the range $H = 0$ .. 0.30 m (FCF Series 04 and FCF Series IB, see Knight 1992). As the computations will be performed using a two-dimensional model, the local water-depth H is used in the Manning equation (1.3) instead of the hydraulic radius R :

$$U = \frac{1}{n} H^{2/3} S_0^{1/2} \tag{8.5}$$

Local Manning n values are then estimated from 12 velocity profiles, measured at different water depths in the FCF single channel. The resulting Manning-coefficient profiles are given on Figure 8.4. Most of the computed values are in the range n = 0.010 .. 0.012 s/m$^{1/3}$. The smallest roughness is observed above the inclined channel bank (y > 0.75 m), and the highest roughness is observed just besides this bank (0.60 < y < 0.75 m). This can be explained by the transverse shearing in this area. The flow accelerates near the walls and decelerates just besides, resulting in the observed roughness variations. Neglecting the values too close of the walls (y > 0.825 m), an averaged Manning-roughness coefficient is found equal to n = 0.01106 s/m$^{1/3}$.

A validation of this Manning-coefficient value is possible by testing the relation between the velocity U and the bed shear-stress τ_b. The latter can be expressed as a function of the velocity U by using its definition (2.27) written for a uniform flow (S_{fx} = S_0), and by replacing the slope S_0 value using Manning equation (8.5) :

$$\tau_b = \rho g\, H\, S_0 = \rho g \frac{n^2 U^2}{H^{1/3}} \tag{8.6}$$

The roughness values n calculated according to (8.6), from the velocity U and the bed shear-stress τ_b measurements (Knight 1992), are plotted on Figure 8.5 for the FCF 060501 case. The so-calculated roughness coefficients are found in good agreement with the previous estimate of n = 0.01106 s/m$^{1/3}$.

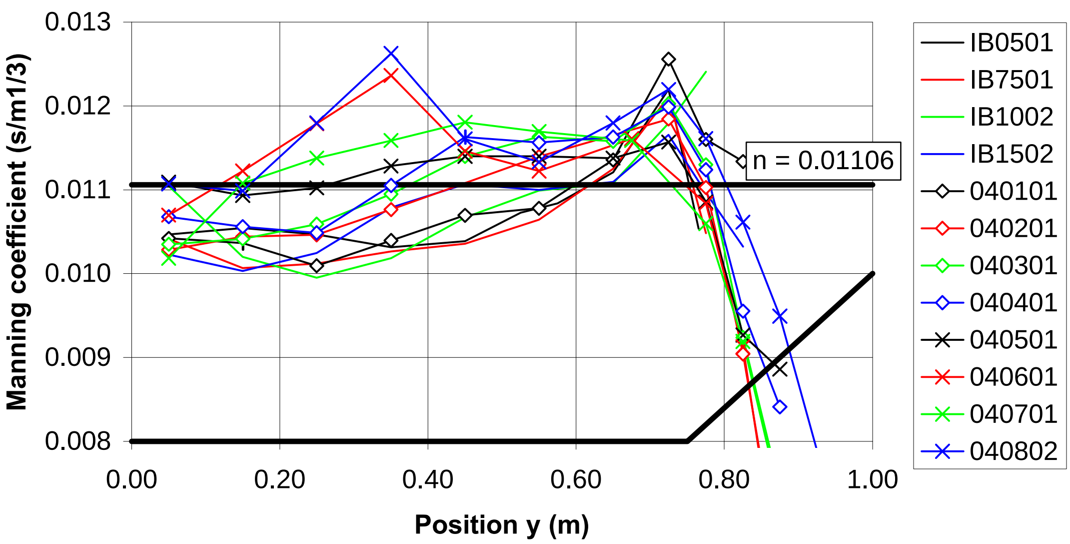

Figure 8.4 : Manning roughness-coefficient, estimated values from velocity profiles (FCF IB and FCF 04, half section)

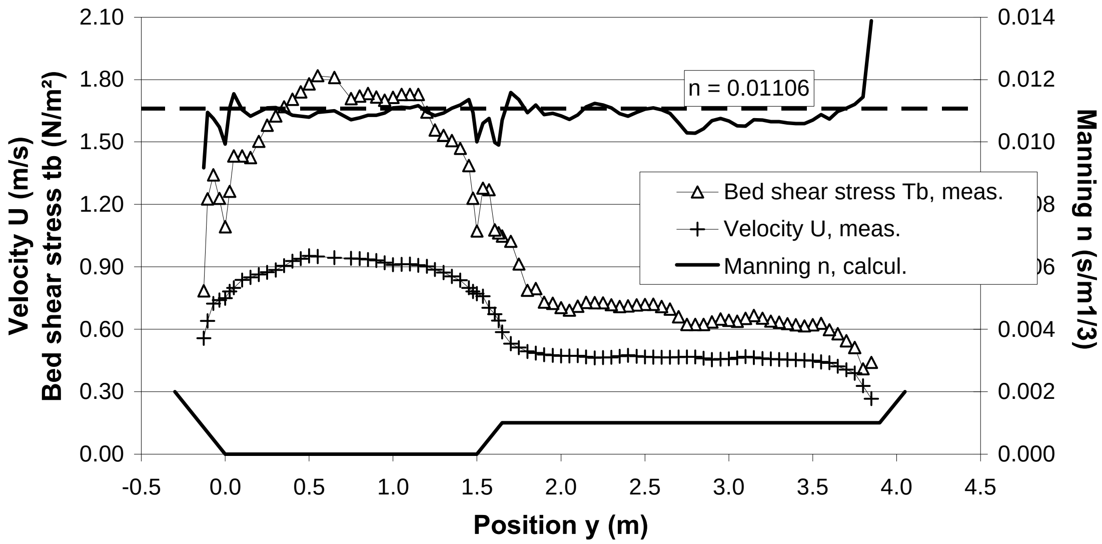

Figure 8.5 : FCF 060501, Manning roughness coefficient n calculation, from velocity U and bed shear-stress τ_b measurements

8.3 Typical-simulation analysis : FCF 060501 case

8.3.1 Unperturbed-flow velocity profile

The FCF 060501 case (H_r = 0.25, see Table 8.1) will be studied as a typical case, in order to investigate in some details the main features of the SDS-2DH model results (Bousmar and Zech 2000). Other cases will then be explored in § 8.4, which presents a short sensibility analysis of the computational results to several parameters. Prior to the description of the periodical turbulent-structures development, the unperturbed-flow velocity profile is also shortly commented, as it has been used as basic flow in the previous Chapter (see § 7.7.1).

The unperturbed-velocity profile is obtained by solving the Saint-Venant equations, with the appropriate shear-stress model, on a simplified mesh having the same width as the one used for the complete simulation, but with a length limited to 4 nodes in the longitudinal direction. In this way, thanks to the cyclic boundary condition, unperturbed uniform-flow conditions are easily obtained, without having to program a specific method of the LDM type.

Unperturbed-velocity profiles are given on Figure 8.6, computed on the 0.05×0.05 m^2 mesh, with a roughness value n = 0.01106 s/m$^{1/3}$ and the *k-l* equations of the SDS-2DH model. Similarly to classical results, the velocity is underestimated on the floodplain and slightly overestimated in the main channel, as the actual roughness coefficient has been used and as no momentum-transfer mechanism is modelled. This result is also not surprising, as one of the purposes of this chapter is precisely to improve such velocity-profile computations through the modelling of periodical turbulent structures.

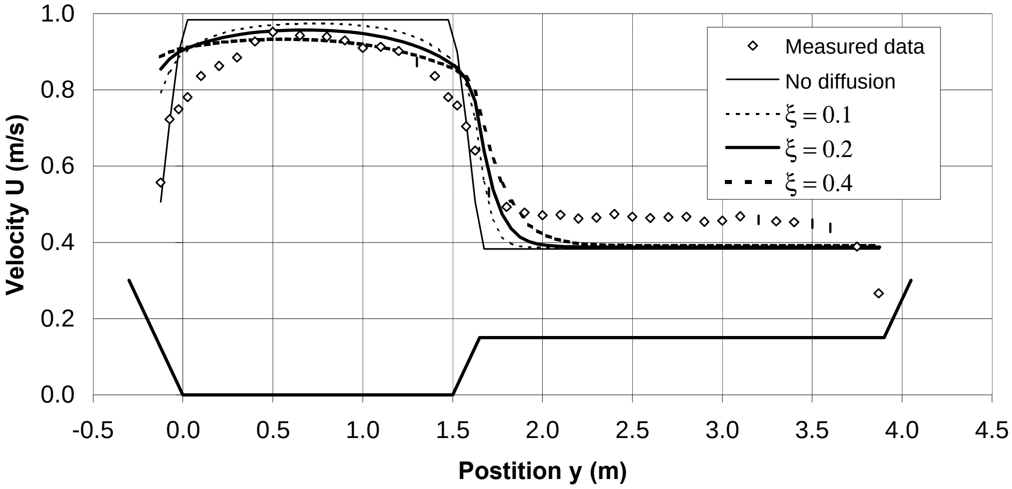

Figure 8.6 : FCF 060501, unperturbed-flow velocity U profiles, SDS-2DH turbulence model, influence of the ξ factor

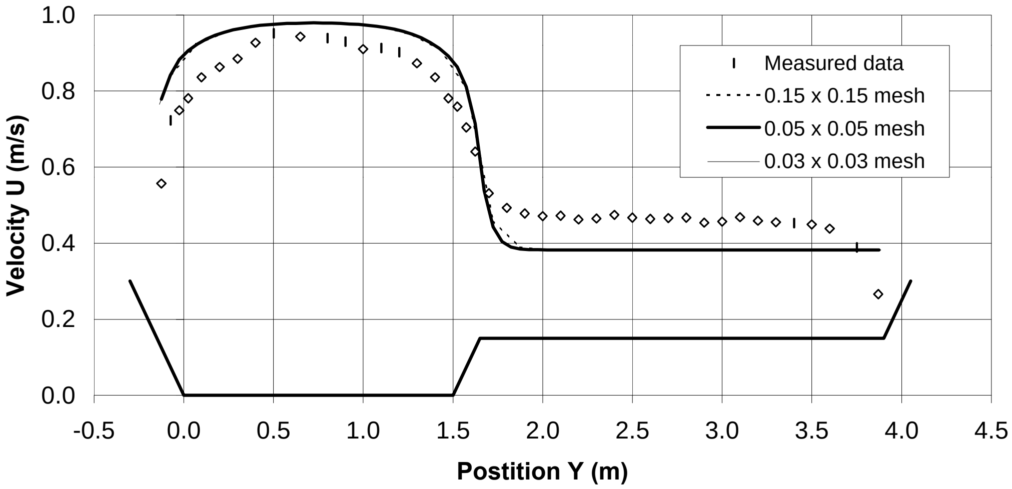

Figure 8.7 : FCF 060501, unperturbed velocity U profiles, SDS-2DH turbulence model (ξ = 0.2), influence of mesh size

Results on Figure 8.6 are given for several different values of the parameter ξ that links the SDS-turbulence length scale l_d to the water depth H. As the shear stresses τ_{ij} are directly proportional to this factor ξ, the velocity profile is logically affected by its value : smoother profiles are observed for larger ξ values. Consequently, the shear-layer width l_s* of the unperturbed-flow velocity profile varies accordingly and could thus influence the results of the stability-analysis, as well as the wave length of the periodical structures in the numerical simulations. This point will be shortly discussed in the sensitivity analysis.

Another interesting result is the mesh size influence on the unperturbed velocity profile (Figure 8.7). While some minor discrepancies are observed near the interface, between the velocity profiles computed with the 0.15×0.15 m^2 mesh and with the 0.05×0.05 m^2 mesh; the profile computed with the 0.03×0.03 m^2 mesh is not discernible from the 0.05×0.05 m^2 one. This indicates that, when considering the unperturbed-flow velocity profile, the use of the 0.05×0.05 m^2 mesh is sufficient.

In order to assess the value of the basic-flow parameters for the hydrodynamic stability analysis performed in the previous Chapter, a hyperbolic-tangent function (7.12) is fitted on the floodplain ($y > 1.65$ m) to the velocity profile computed with $\xi = 0.2$ and a 0.05×0.05 m^2 mesh (Figure 8.8). Indeed, in this area, no geometrical effect, such as the bank transverse slope, affects the velocity. According to this fitting, the velocity scale equals $U_s^* = 0.285$ m/s, and the shear-layer width equals $l_s^* = 0.149$ m, as quoted in Table 7.7.

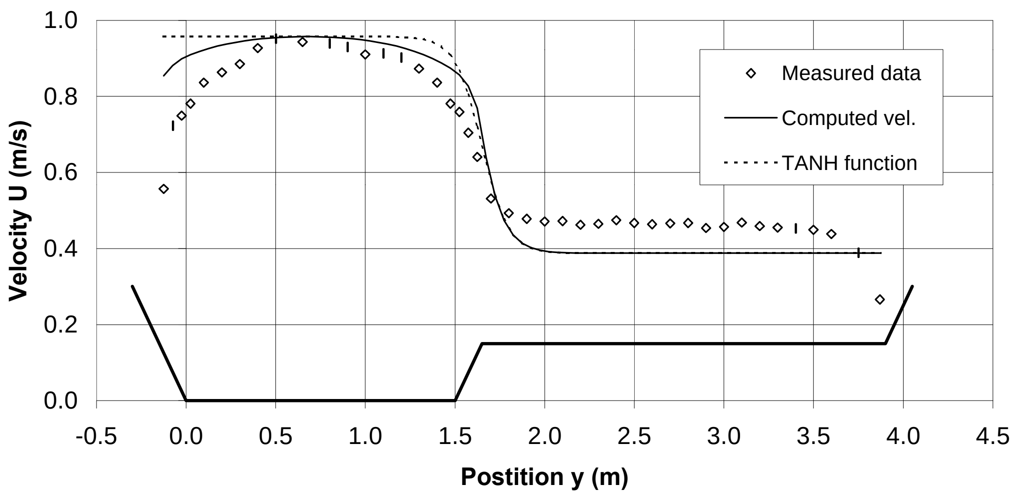

Figure 8.8 : FCF 060501, unperturbed velocity U profiles, fitting of a TANH function

8.3.2 Perturbation development

The SDS-2DH model is now applied to the whole 0.05×0.05 m^2 mesh, and the rounding errors are allowed to grow up. The time step is set equal to $\Delta t = 0.0025$ s, and the simulation is run until $t = 300$ s. The perturbation apparition and growth is depicted by Figure 8.10 and Figure 8.11. Figure 8.10 gives the velocity field between $t = 100$ s and $t = 175$ s, in a frame moving at the interface velocity; and Figure 8.11 gives the vorticity field, between $t = 100$ s and $t = 275$ s, for a larger window. The superposition of both velocity and vorticity fields is given on Figure 8.9, at the time $t = 150$ s.

The flow evolution can be described as follow : at the time t = 100 s, no perturbation is visible and the velocity field is still uniform. The shear layer reduces to a vortex sheet, located at the interface between main channel and floodplain. The instability appears in the time interval t = 100 .. 125 s. At t = 125 s, vortices are clearly identified in the velocity field; the vortex sheet is oscillating, on the whole channel length, and already tends to break into separate vortices. From t = 125 s to t = 150 s, the vortices develop more and extend transversally, increasing consequently the shear-layer width. After t = 150 s, the initial vortices are completely developed, and begin to merge together into larger ones. This merging process can be clearly identified at t = 175 s. After a while, however, the merging process stops and the vortices size remains approximately constant with reference to the time. This indicates probably that the vortices have reach their maximum size, and that any further growth or merging is constrained by the channel walls, that limit the transverse vortex development.

It can be observed that the velocity field observed before vortices merging matches at least qualitatively the velocity field obtained from the stability analysis (Figure 7.22); whereas, as expected, the numerical vorticity field is more convincing, as it presents only one vorticity peak per vortex, instead of two in the stability analysis results.

The evolution of the perturbation can similarly be observed on the transverse velocity V plot at the interface between main channel and floodplain (Figure 8.12). Before t = 110 s, the velocity remains constant, and no perturbation is visible. From t = 110 s to t = 130 s, a periodic variation appears, that grows exponentially, according to the stability analysis predictions. Then, the variation amplitude becomes constant, as if the vortices development was temporarily stopped, probably due to the stabilising effect of the bed friction and of the viscosity due to the SDS model. However, as from t = 150 s, and mostly t = 170 s, the velocity period increases step by step, indicating the begin of the vortices merging.

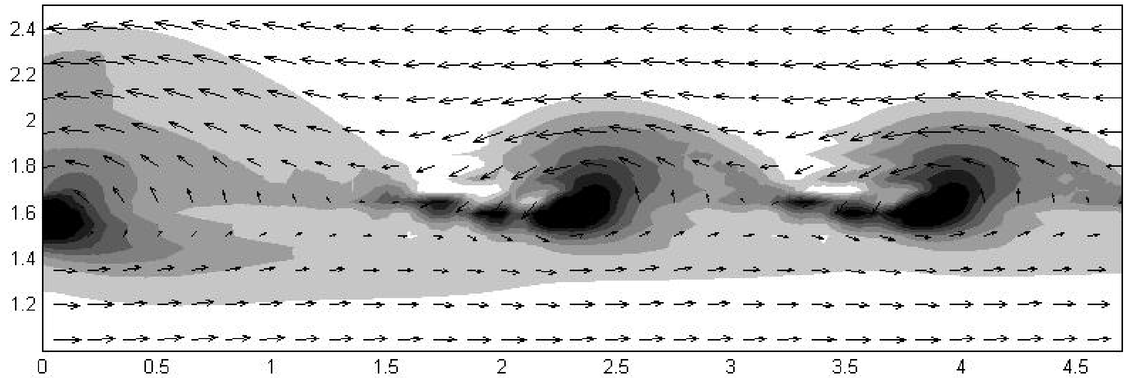

Figure 8.9 : FCF 060501, vorticity and velocity field in a moving frame, at t = 150 s (only a part of the computational domain is shown)

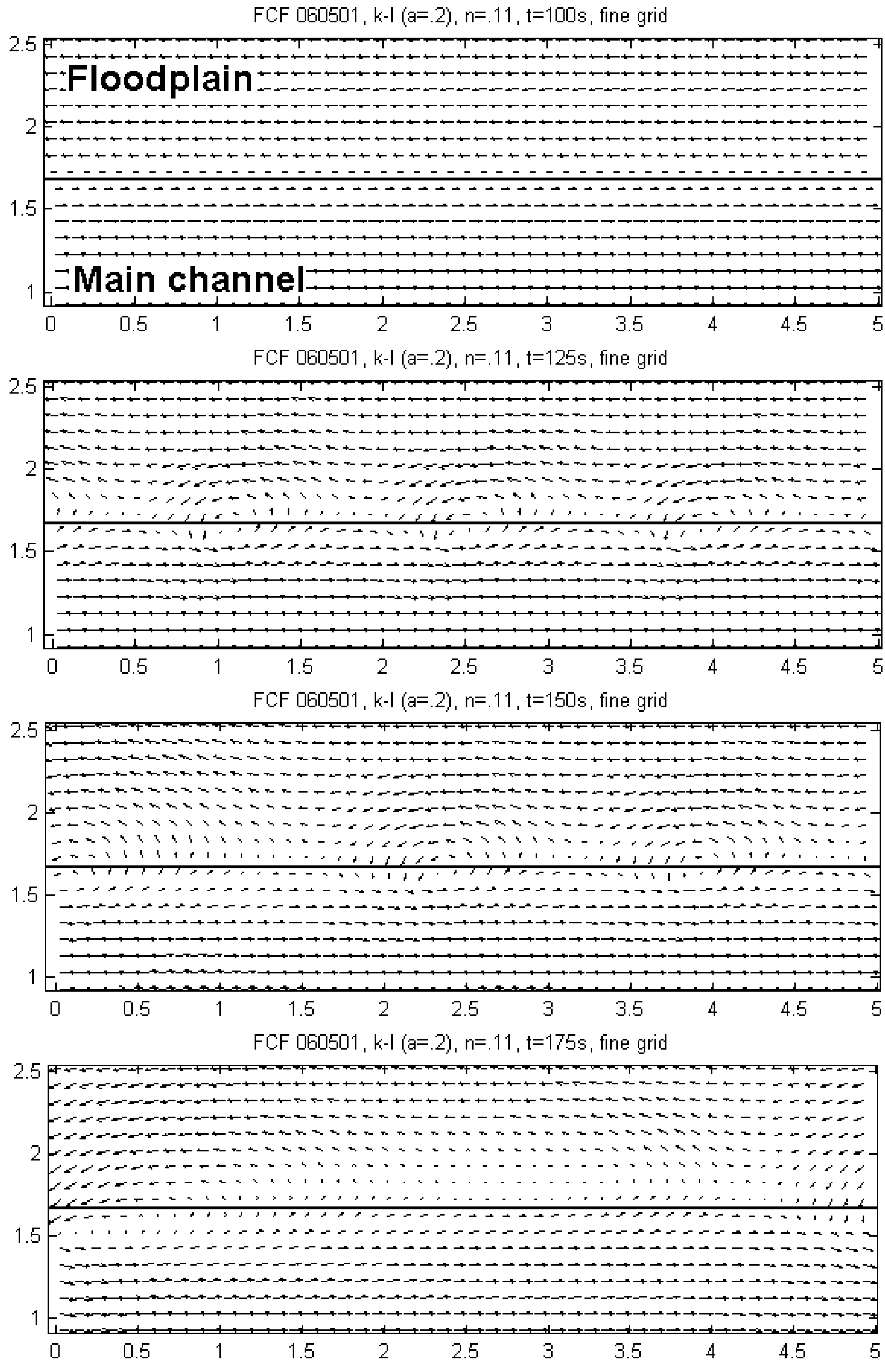

Figure 8.10 : FCF 060501, velocity field in a moving frame (only a part of the 57-m length computational domain is shown, the position y reference is shifted of 0.15 m, in comparison with Figure 8.3)

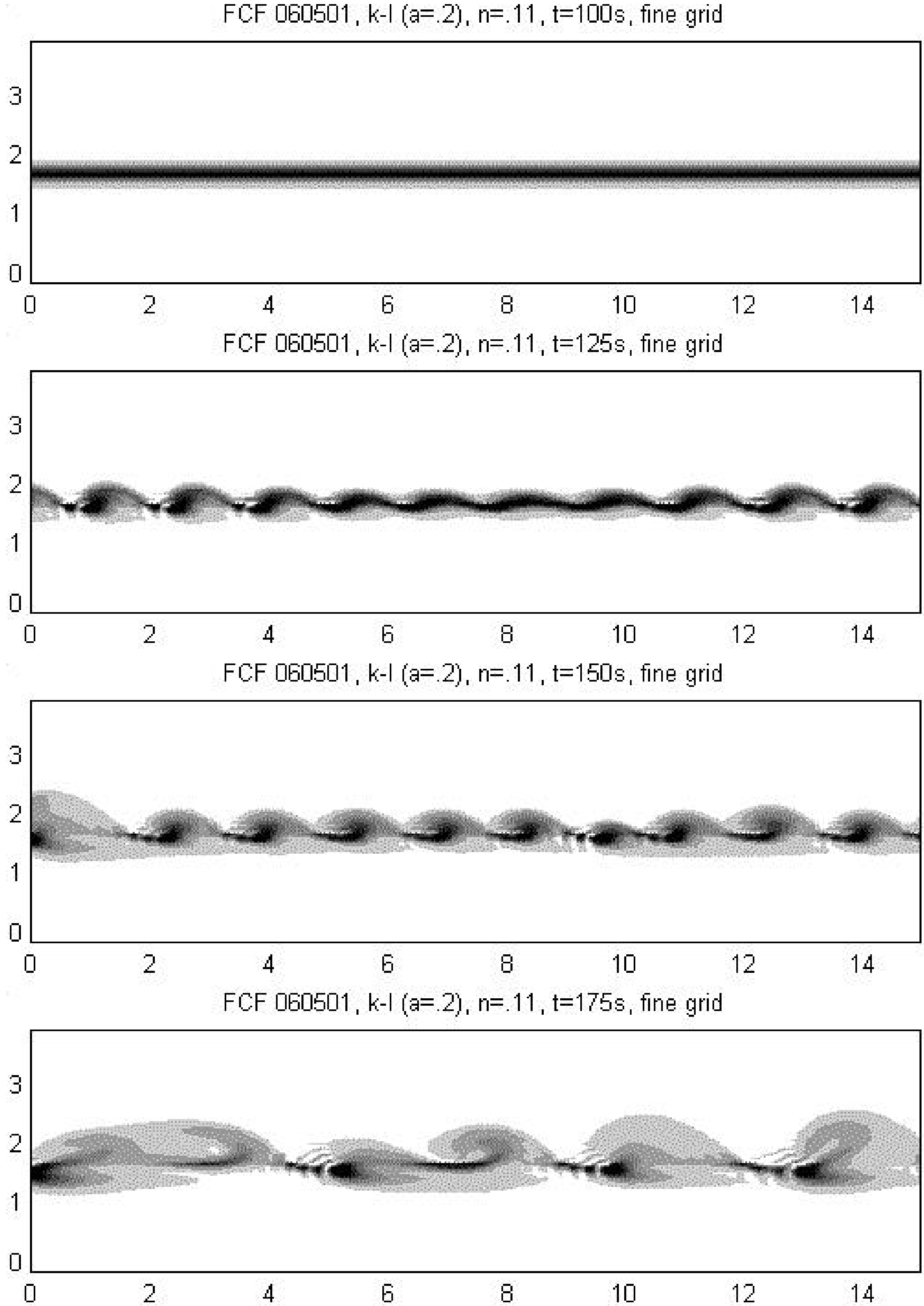

Figure 8.11 : FCF 060501, vorticity field
(only a part of the 57-m length computational domain is shown)

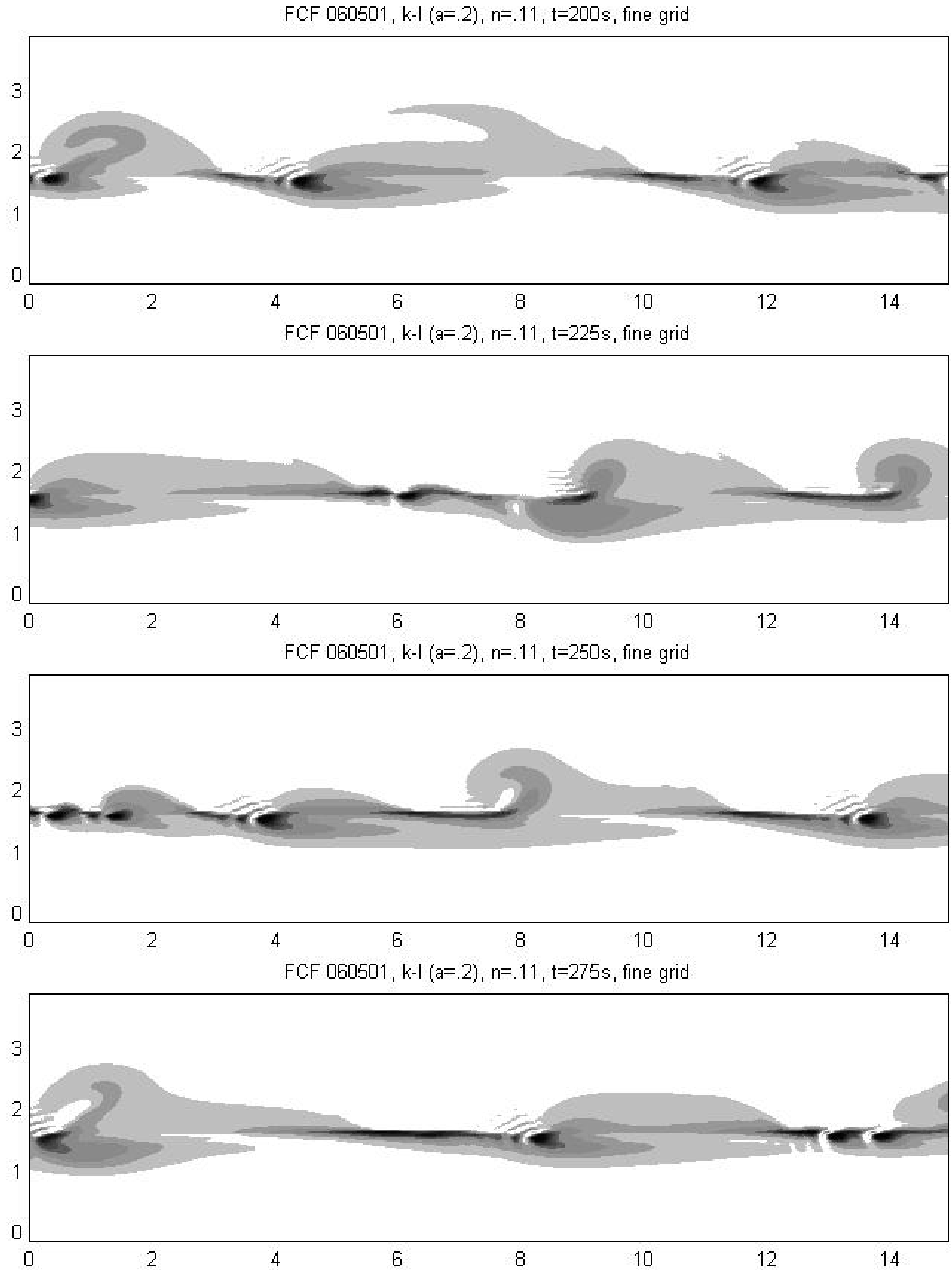

Figure 8.11 (continued)

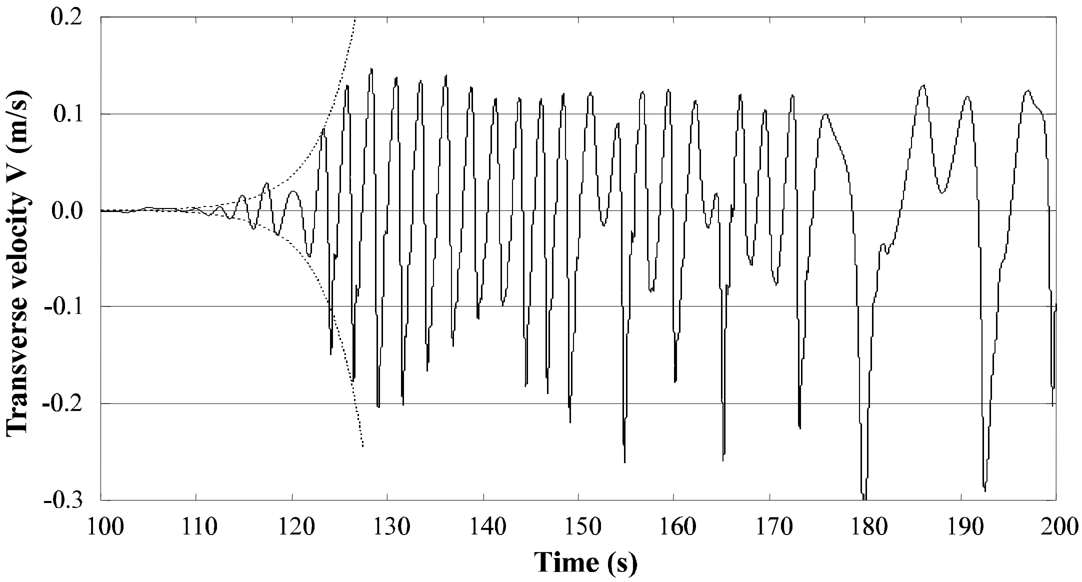

Figure 8.12 : FCF 060501, transverse velocity V evolution, at the interface (y = 1.65 m)

8.3.3 Vortices characteristics

As the numerical-simulation results agree at least qualitatively with the hydrodynamic-stability-analysis predictions, some quantitative values will be extracted for further comparison, namely the wave length and the growth rate of the vortices.

The perturbation growth rate is estimated by fitting an exponential function $ae^{\theta t}$ to the transverse velocity V plot on Figure 8.12, where a is a constant and θ is the dimensional growth rate, whose value is found equal to $\theta = 0.256\ \mathrm{s}^{-1}$. The wave length of the vortices is obtained from a Fourier analysis of the transverse velocity V longitudinal profile, along the interface. At $t = 125$ s, a clear peak is observed in the spectrum at $\lambda = 1.46$ m (Figure 8.13). This value is in accordance with the first estimate one could get from the analysis of the vorticity plot at the same time (Figure 8.11). At $t = 175$ s, the spectrum is less clear, and several peaks corresponding to the merged vortices can be identified. The transverse velocity V variation with time (Figure 8.12) is also investigated in the time interval t = 100 .. 200 s, and the spectrum peak is observed for a period $T = 2.56$ s (Figure 8.14). Accordingly, the vortices celerity c can finally be estimated as

$$c = \frac{\lambda}{T} = \frac{1.46\ \mathrm{m}}{2.56\ \mathrm{s}} = 0.57\ \mathrm{m/s} \tag{8.7}$$

These perturbations characteristics can be compared with the predictions by the stability analysis (see Table 7.8), provided the appropriate scaling factor are used (see § 8.3.1) : $l_s^* = 0.149$ m for the lengths, $U_s^* = 0.285$ m/s for the velocities, and $t_s^* = l_s^* / U_s^* =$ 0.522 s for the time. As shown by Table 8.3, the difference between the wave-length values is not greater than 10 %, indicating a rather good matching between both results. For both stability analysis and numerical simulation, the wave celerity values are also close. As the interface velocity equals $U_m = 0.64$ m/s, in both cases, the celerity values denote that the vortex centres are shifted towards the floodplain. The larger difference between the growth-rate values is probably due to the difficulty to define it accurately from the numerical results; but also to non-linearity and viscosity effects in the numerical simulations.

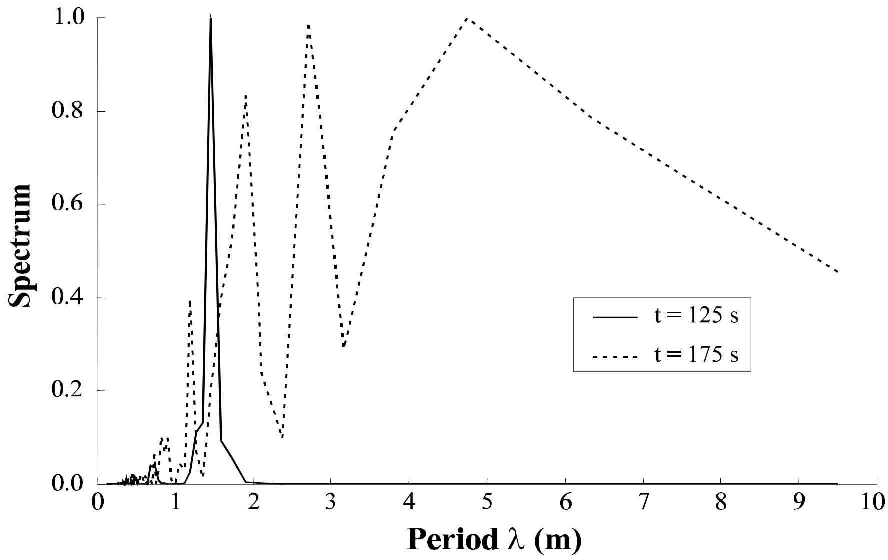

Figure 8.13 : FCF 060501, transverse velocity spectral analysis, at t = 125 s and 175 s

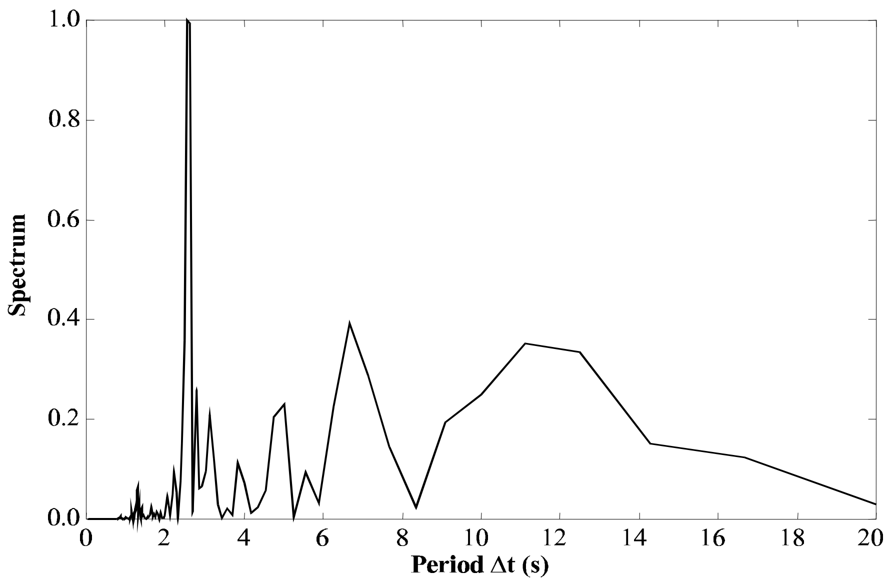

Figure 8.14 : FCF 060501, transverse velocity spectral analysis, at the interface, in the time interval t = 100 .. 200 s

Table 8.3 : FCF 060501, vortices characteristics

	Wave length λ	Wave celerity c	Growth rate αc_i
Stability analysis	1.31 m	0.59 m/s	0.208
Numerical simulation	1.46 m	0.57 m/s	0.134

8.3.4 Velocity and bed shear-stress profiles

The longitudinal-velocity U and bed shear-stress τ_b profiles are given on Figure 8.15 and Figure 8.16 respectively, before and after the perturbation development. Due to the growth of the vortices, the shearing increases, and the shear-layer becomes wider, resulting in smoothed profiles in the interface area. These smoothed profiles seem to match the measured data better than the profiles of the unperturbed flow, at least in the interface area; and the enlarged shear-layer width is closer to the observed value. This would indicate that the SDS-2DH model computes appropriately the momentum transfer due to the horizontal vortices.

However, on the floodplain, at a distance from the interface, the velocity and bed shear-stress are no longer affected by the perturbation, and the model underestimates their values. Assuming that the roughness estimation from § 8.2.2 is correct, this indicates that the SDS-2DH model misses some shearing on the floodplain. The missing additional shearing could originate from the helical secondary-currents, that are expected to be the main source of momentum transfer on the floodplains (Knight and Shiono 1996). Indeed, such currents are not taken into account in the present simulation with a depth-averaged model. The next Chapter will present an attempt to model their effects through the use of dispersion terms in the Saint-Venant equations, as suggested in Chapter 2.

On the other hand, the profiles inaccuracy near the left main-channel bank ($y < 0.50$ m) are probably due to the combined use of a vertical wall and of a free-slip condition. This results in an underestimation of the shearing in this area and in an overestimation of the velocity and bed shear stress.

Finally, the water-level variations during the simulation of the perturbation development are given on Figure 8.17. An horizontal transverse profile of the water level has been used as initial condition. As shown by Figure 8.17a, before the perturbation development (at t = 100 s), a 2 mm level difference is observed between the main channel and the floodplain. This difference is due to the velocity difference between both subsections. The numerical model manages to get an horizontal specific-energy profile rather than an horizontal water level. When the perturbation amplifies, the averaged water level still presents a transverse level difference but the profile is smoothed, due to the shear-layer enlargement. Moreover, as shown by Figure 8.17b, significant periodic longitudinal variations of the water depth are observed. The minimum water depths correspond to depressions in the vortices centre. These water-level variations constitute an inconsistency with the hydrodynamic stability analysis, where a rigid-lid assumption was used for the water surface (§ 7.5.1), and could also explain part of the discrepancies observed when comparing the results of these two methods (Table 8.3).

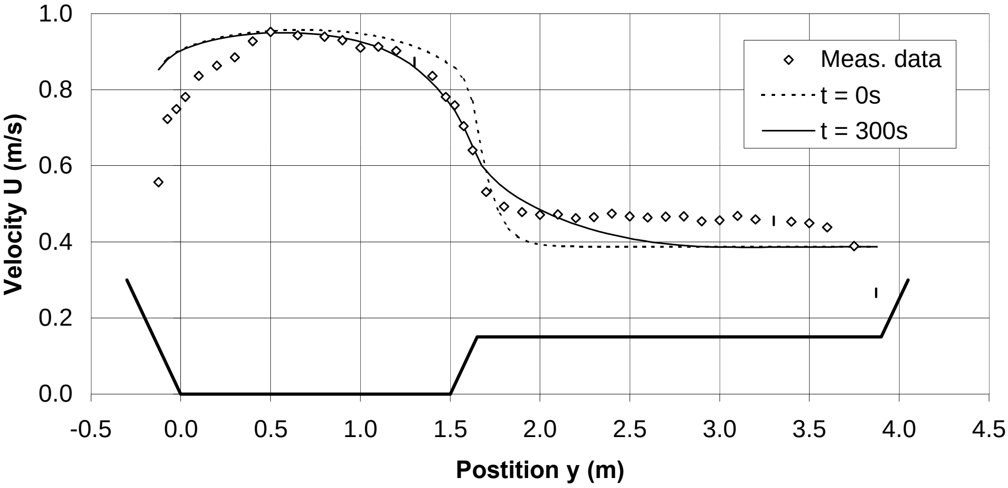

Figure 8.15 : FCF 060501, longitudinal-velocity U profile, before (t = 0 s) and after (t = 300 s) perturbation development

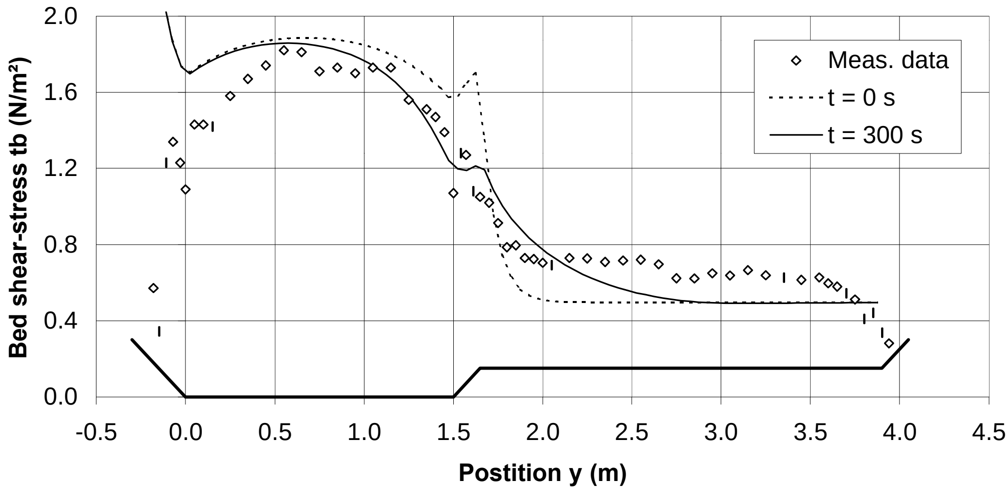

Figure 8.16 : FCF 060501, bed shear-stress τ_b profile, before (t = 0 s) and after (t = 300 s) perturbation development

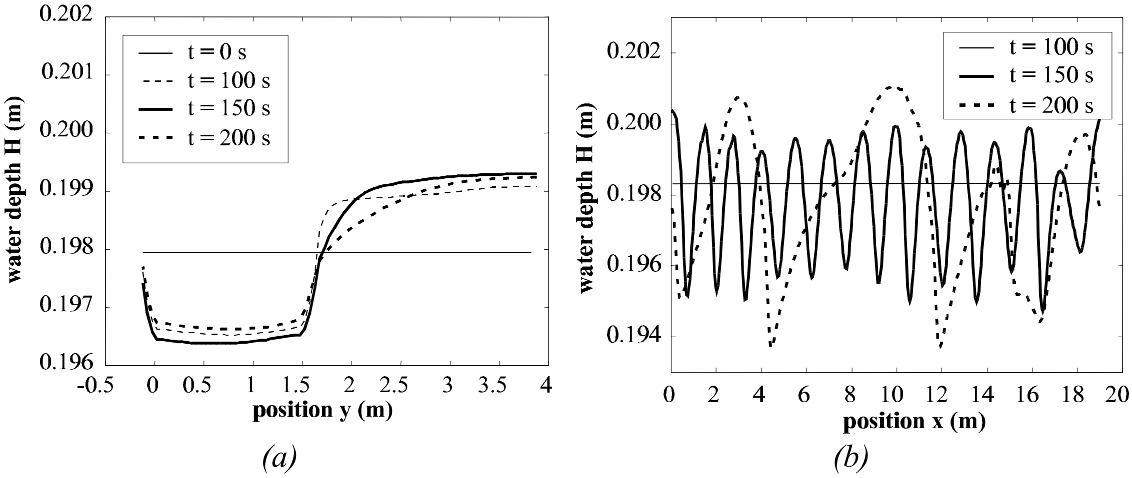

Figure 8.17 : FCF 060501, water depth variations during perturbation development : (a) transverse profile (values averaged along x); (b) longitudinal profile at the interface

8.4 Sensitivity analysis, for the FCF 06 simulation

8.4.1 Mesh resolution

A first parameter to be investigated in this sensibility analysis is the mesh resolution. The three mesh sizes quoted in Table 8.2 are successively tested. For the 0.15×0.15 m^2 and the 0.03×0.03 m^2, the perturbation development is almost similar to the one observed for the 0.05×0.05 m^2 case, as described in previous paragraph. However, the time at which the perturbation appears is significantly larger for the coarser mesh (Table 8.4).

The vorticity field before vortices merging is given on Figure 8.18. From this Figure, it is clear that the 0.15×0.15 m^2 mesh is too coarse to provide satisfactory results (Figure 8.18a). For the two finer meshes, a similar vortex shape is obtained, although the 0.05×0.05 m^2 mesh presents some vorticity unevenness, for example at $x = 9$ m. This could also indicate that, to some extend, this mesh is also too coarse.

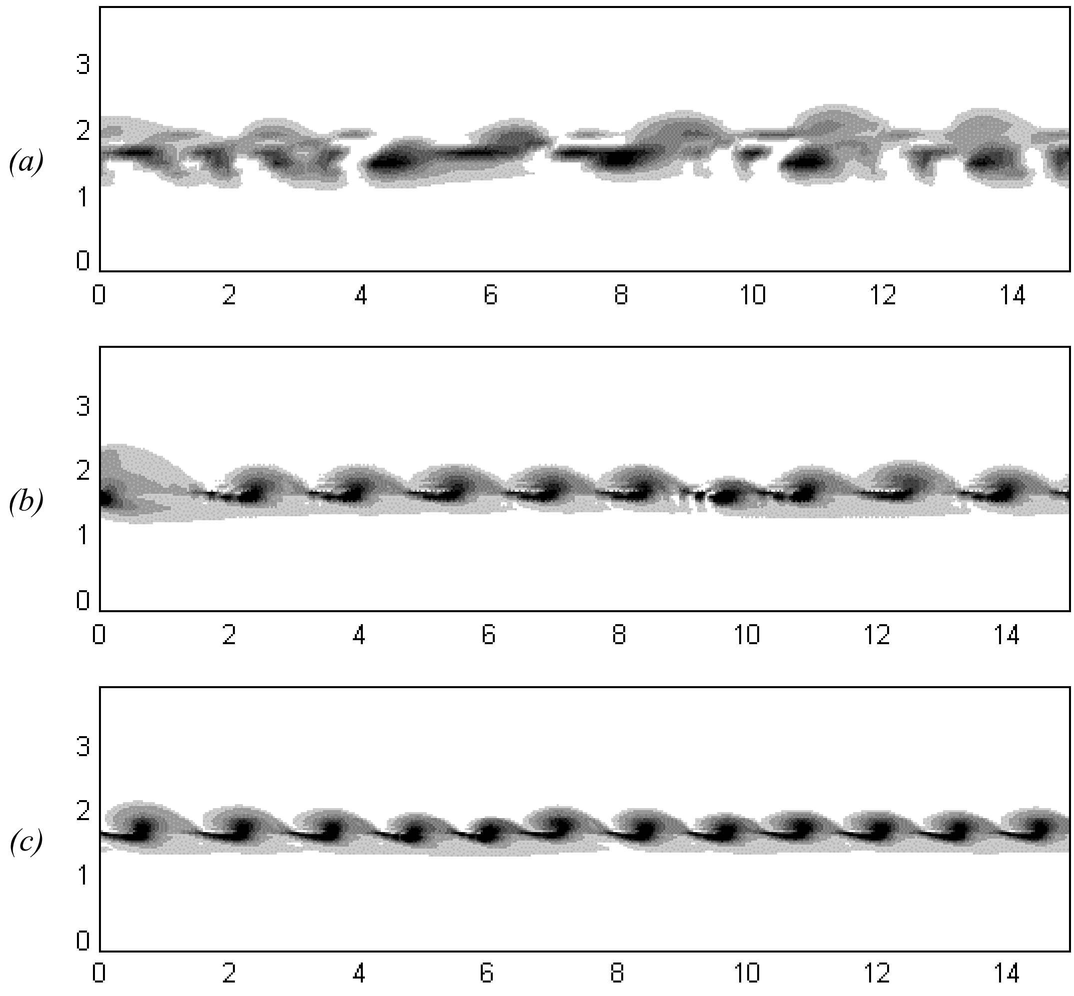

Figure 8.18 : FCF 060501, vorticity field before vortices merging (part of the computational domain) : (a) 0.15 ´ 0.15 m^2 mesh, t = 200 s; (b) 0.05 ´ 0.05 m^2 mesh, t = 150 s; and (c) 0.03 ´ 0.03 m^2, t = 125 s

Table 8.4 : FCF 060501, mesh size influence on the perturbation development

Mesh size	Development time	Wave length λ	Growth rate αc_i
0.15×0.15 m²	180 s	1.96 m	0.092
0.05×0.05 m²	110 s	1.46 m	0.134
0.03×0.03 m²	110 s	1.27 m	0.130

Table 8.5 : FCF 060501, mesh Reynolds numbers $\mathbf{Re}_m$

Mesh size	Averaged value	Main channel	Interface (peak value)	Floodplain
0.15×0.15 m²	132	55	308	200
0.05×0.05 m²	44	18	93	65
0.03×0.03 m²	26	11	55	40

Some indications on the mesh resolution can be gathered from the mesh Reynolds number

$$\mathbf{Re}_m = \frac{(|U| + |V|)\Delta x}{\upsilon_t} \tag{8.8}$$

where Δx is the mesh size and $\upsilon_t = \upsilon_{SDS}$ is the turbulent viscosity used in the calculation (see e.g. Peyret and Taylor 1983). This mesh Reynolds number indicates the ratio between the convection and the dissipation scales. When its value is less than $\mathbf{Re}_m < 4$ (for two-dimensional computations), the mesh is fine enough to capture explicitly all the scales involved in the flow, as the convection processes are modelled from the largest scale to the dissipation scale. When the mesh Reynolds-number value is higher, part of the smaller turbulent structures will not be captured by the simulation.

Estimations of the mesh Reynolds numbers for the three cases investigated are given in Table 8.5. This shows clearly that, for all the cases, their is a mesh under-resolution, in such a way that part of the smaller-scale structures are indeed not captured. This observation is in accordance with the simulation principle as presented in § 8.1. However, for the coarser mesh, the mesh Reynolds number is so high that even the largest structures are not captured adequately. In order to achieve a mesh Reynolds number $\mathbf{Re}_m = 4$, corresponding to a resolution high enough to capture all the structures, one should use a grid size in the range 0.003×0.003 m^2.

As such a mesh has 100 times more nodes than the 0.03×0.03 m^2 one, this would lead to a prohibitive calculation time. Indeed, the simulation for the 0.03×0.03 m^2 mesh already took around 400 CPU-hours on a 120 Mhz processor (HP Exemplar SPP1600). Probably the simulation speed could be improved by introducing a random noise in the initial conditions, instead of relying on the growth of rounding errors. However, since one is also interested by the process of vortex merging, which also takes some time to develop, this would only reduce the computation time by 40-50 %.

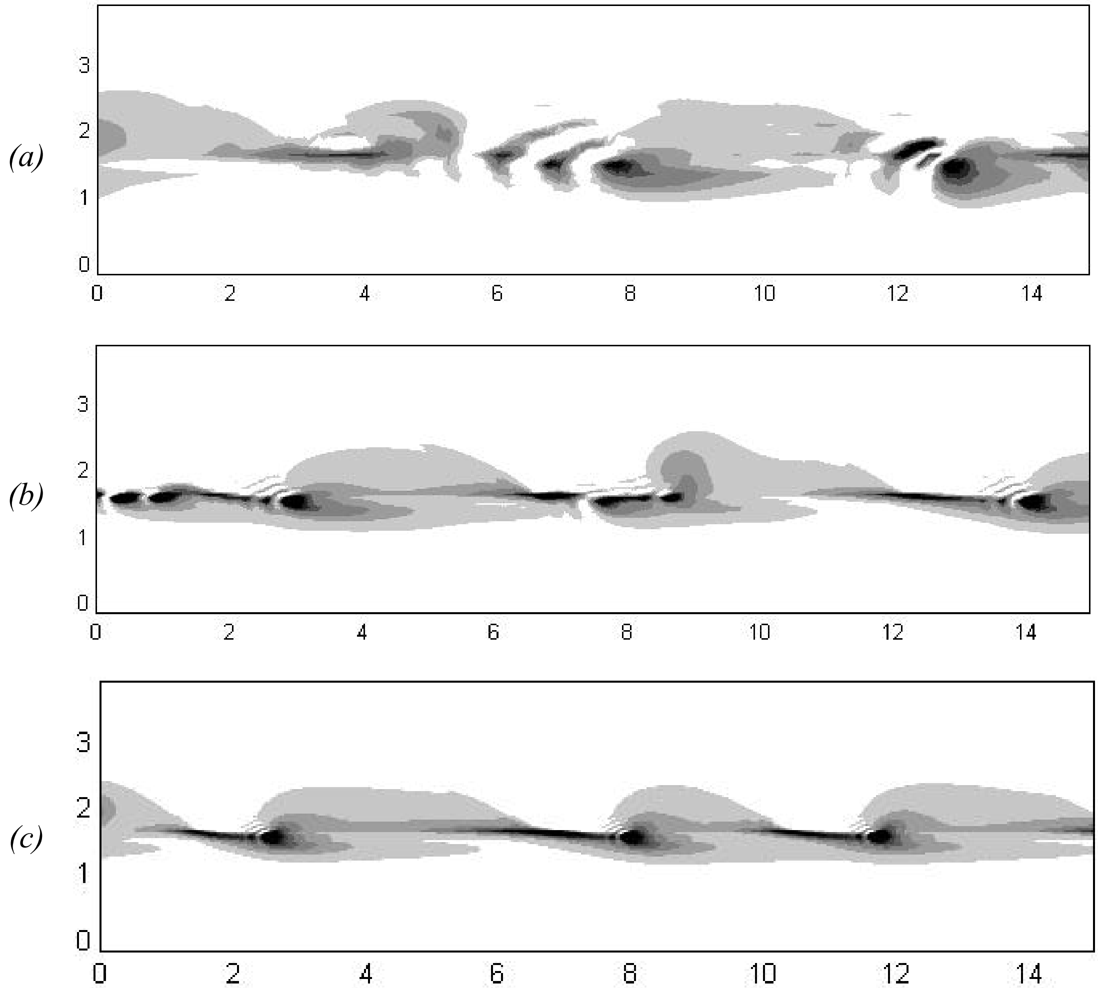

Figure 8.19 : FCF 060501, vorticity field after vortices merging, t = 300 s (part of the domain) : (a) 0.15 ´ 0.15 m^2 mesh; (b) 0.05 ´ 0.05 m^2 mesh; and (c) 0.03 ´ 0.03 m^2

After the merging of vortices, similar observations can be made (Figure 8.19) : the mesh under-resolution clearly affects the 0.15×0.15 m^2 mesh vorticity field, while the two finer mesh present almost similar vorticity fields. This latter point is of great interest as it is expected that such merged vortices will actually be observed in compound channels. Accordingly, no significant difference is observed between the time-averaged velocity profiles corresponding to these two finer mesh resolutions. Probably no further difference would be observed for a simulation performed using the ideal 0.003×0.003 m^2 mesh proposed above.

Anyway, one should also keep in mind that the development of large-scale structures remains the main focus of this work. Therefore, one has to compromise between the mesh resolution and the computation time. Accordingly, further simulations have been performed using the 0.05×0.05 m^2 mesh. Indeed, the mesh refinement did not affect the velocity profile results, and it should also be noted that the vortex wave length and growth rate did not change significantly between this selected mesh resolution and the finer 0.03×0.03 m^2 mesh (Table 8.4).

8.4.2 Computational-domain length

Another parameter that could influence the simulation results is the computational-domain length L. Indeed, when the perturbation develops, the vortex wave length must be a divisor of this domain length, due to the cyclic boundary condition. On the other hand, it is interesting to reduce this length, in order to limit the computation time. Several simulations were thus performed to investigate this domain-length influence : (1) for the whole FCF flume length (L = 57 m); (2) for a third of this length (L = 19 m); and (3) for additional smaller length (with decrements of ΔL = 0.5 m).

The computed vortex wave lengths λ are summarised in Table 8.6. All the computed values are in the range λ = 1.375 .. 1.462 m. It can be observed that, when the domain length L reduces the number of vortices changes in such a way that the vortex wave length remains as close as possible to the one for the maximum amplification. However, no significant variations of the growth-rate value are observed between the tested domain length. Accordingly, a domain length equal to L = 19 m is selected for the further investigations, leading to a maximum possible error of 6 % on the vortex wave-length estimation.

Table 8.6 : FCF 060501, computational-domain length L influence of the vortex wave length λ and on the number of vortices observed in the domain. Smaller and larger divisors indicate the wave length that would be obtained by decreasing or increasing the number of vortices by 1

Domain length L	Wave length λ	Nbr. of vortices	Smaller divisor	Larger divisor
57.0 m	1.462 m	39	1.500 m	1.425 m
19.0 m	1.462 m	13	1.583 m	1.357 m
18.5 m	1.423 m	13	1.542 m	1.321 m
18.0 m	1.385 m	13	1.500 m	1.286 m
17.5 m	1.458 m	12	1.591 m	1.346 m
17.0 m	1.417 m	12	1.546 m	1.308 m
16.5 m	1.375 m	12	1.500 m	1.269 m

8.4.3 Water depth

The influence of the water depth H in investigated by simulating the 8 cases tested in the FCF 06 Series (see Table 8.1). According to the typical simulation from § 8.3, the following parameters are used throughout all the cases : (1) SDS-2DH model with $\xi = 0.2$; (2) $0.05 \times 0.05\ m^2$ mesh, on a 19-m length domain; (3) time step $\Delta t = 0.0025$ s; and (4) roughness coefficient $n = 0.01106\ s/m^{1/3}$, according to § 8.2.2. The unperturbed-flow velocity-profile characteristics are summarised in Table 7.7.

As shown by Figure 8.20, the vorticity field presents significant differences when the water depth varies. Comparing the H = 0.198 m and H = 0.248 m cases (Figure 8.20b and c), one observed that the vortex wave length and transverse expansion enlarge with the depth, as the stabilising effect due to the friction on the floodplain bottom decreases. On the other hand, considering the H = 0.165 m case (Figure 8.20a), as the wave length reduces when the water depth decreases, the mesh resolution becomes too low and the vorticity field presents unevenness, as with the 0.15×0.15 m^2 mesh at H = 0.198 m (Figure 8.18a).

These first observations are confirmed when performing spectral analysis as in § 8.3.3. The vortex wave length λ, growth rate αc_i and celerity c are summarised in Table 8.7. Both the wave length and the celerity are found to increase according to the water depth H, while the results are less clear regarding the growth rate, probably due to the larger inaccuracies involved in its estimation (by fitting an exponential curve).

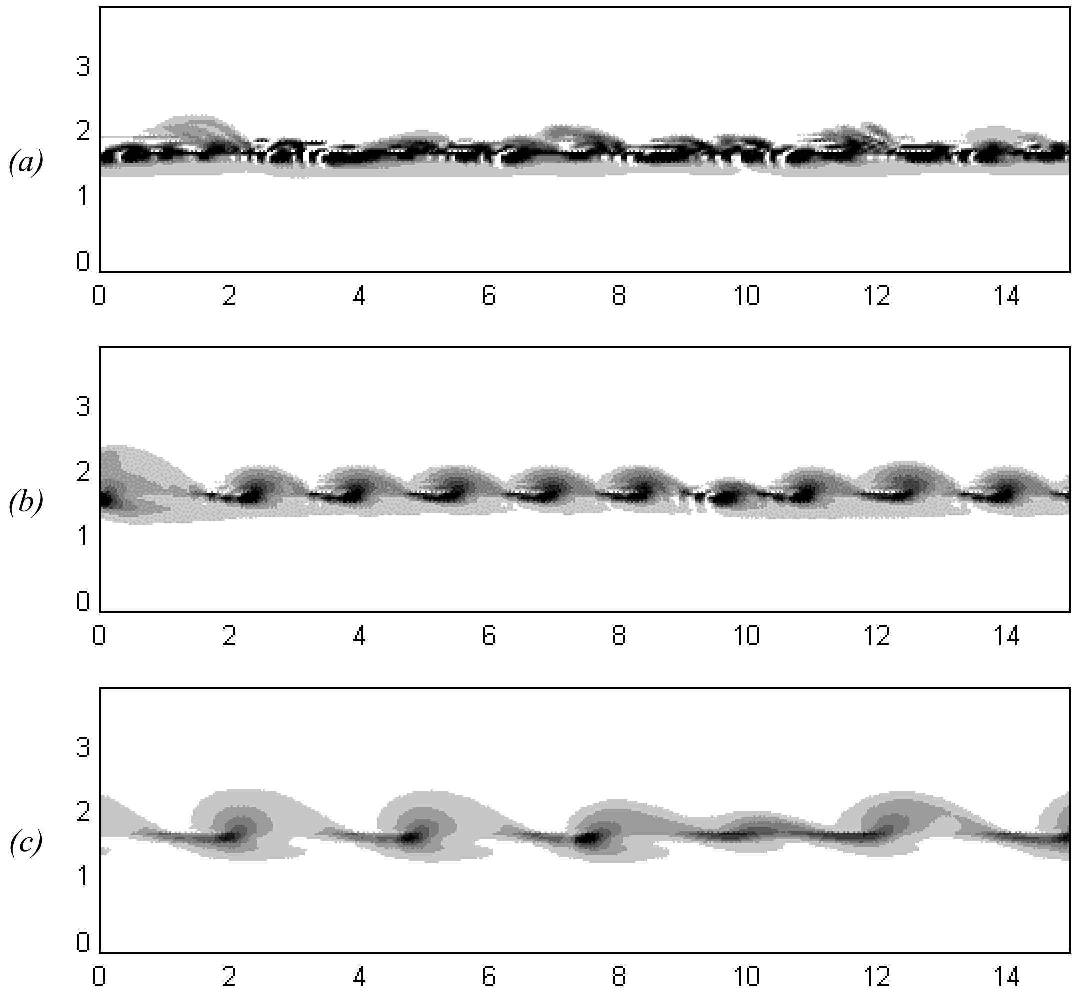

Figure 8.20 : FCF 06, vorticity field before vortices merging (part of the computational domain) (a) FCF 060201, H = 0.165 m, t = 100 s; (b) FCF 060501, H = 0.198 m, t = 150 s; and (c) FCF 060701, H = 0.248 m, t = 125 s

Table 8.7 gives also the comparison between the numerical results and the stability-analysis results. The wave lengths, λ, are poorly estimated by the numerical model for the lower water depths, maybe due to the low mesh resolution; while the values match together almost perfectly for the larger water depths, where the mesh resolution is better when compared to the vortex size (Figure 8.21). As already pointed out, the growth rate αc_i values estimated from the numerical simulations present much scattering. However, they are found in the same range as the values from the stability analysis (Figure 8.22).

Lastly, the vortex celerity c values computed numerically and by the stability analysis agree very well together (Figure 8.23). This result is not surprising, as this celerity depends strongly on the interface velocity U_m, whose value estimated from the numerical simulation is imposed as a basic flow for the stability analysis. On the other hand, for both estimations, the vortex celerity is found to be lower than this interface velocity, indicating again that the vortex centres are shifted to the floodplains.

Table 8.7 : FCF Series 06, vortex characteristics, numerical computation and stability analysis

Case	Wave length λ (numerical)	Wave length λ (stab. anal.)	Growth rate αc_i (numerical)	Growth rate αc_i (stab. anal.)	Celerity c (numerical)	Celerity c (stab. anal.)
060101	0.463 m	0.238 m	0.018	0.206	0.11 m/s	0.35 m/s
060201	0.864 m	0.397 m	0.074	0.210	0.33 m/s	0.40 m/s
060301	1.000 m	0.693 m	0.151	0.210	0.46 m/s	0.47 m/s
060401	1.462 m	1.027 m	0.176	0.210	0.53 m/s	0.53 m/s
060501	1.462 m	1.315 m	0.134	0.208	0.57 m/s	0.59 m/s
060601	1.900 m	1.799 m	0.171	0.206	0.65 m/s	0.65 m/s
060701	2.941 m	2.966 m	0.127	0.198	0.88 m/s	0.80 m/s
060801	4.750 m	4.801 m	0.136	0.179	1.01 m/s	1.00 m/s

In a second stage, the velocity U and the bed shear-stress τ_b profiles corresponding to the flow after vortex merging are compared with the available measurements from the FCF (Figure 8.24 and Figure 8.25). As observed in the FCF 060501-case analysis (§ 8.3.4), the additional shearing due to the vortex development in the shear layer tends to improve the velocity and the bed shear-stress predictions in the interface area.

For the lower water depths (H_r = 0.05 .. 0.15) both velocity and bed shear stress are accurately modelled on the floodplain. In the main-channel, the velocity is partly underestimated (y < 1 m), whereas the bed shear-stress value is correct. This could be due either to an erroneous roughness-coefficient value, or to the approximations made when modelling the bank. The hypothesis of an erroneous roughness-coefficient seems however improbable, as the ratio of the velocity and the bed shear stress is correctly reproduced in the other parts of the section and in all the other geometries.

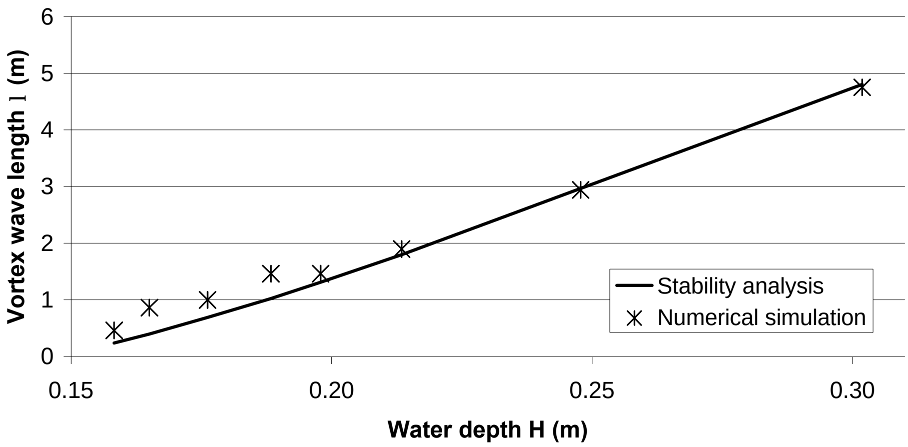

Figure 8.21 : FCF 06, vortex wave length λ according to the water depth H : numerical-simulation and stability-analysis results

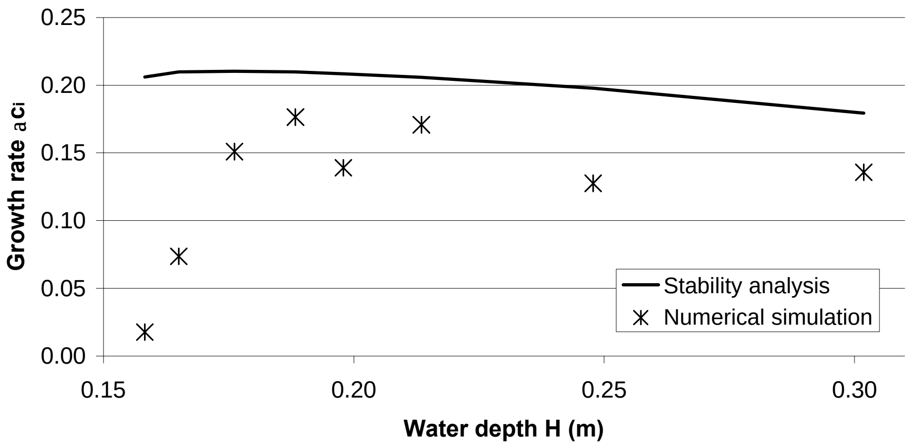

Figure 8.22 : FCF 06, vortex growth rate αc_i according to the water depth H : numerical-simulation and stability-analysis results

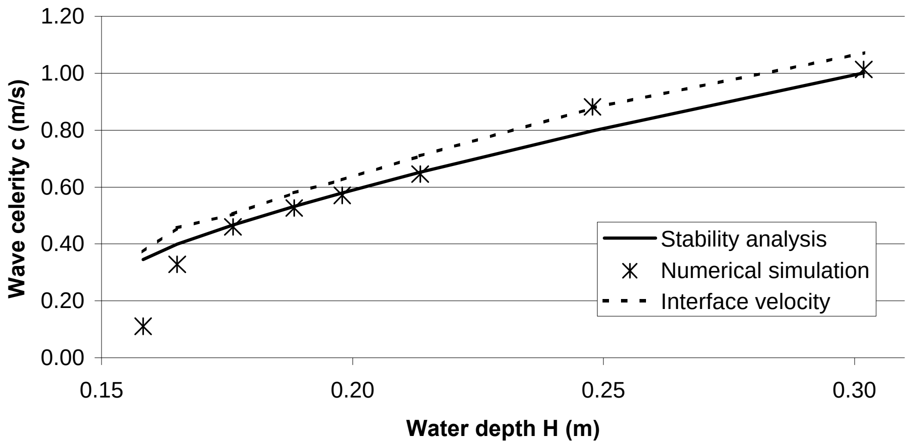

Figure 8.23 : FCF 06, vortex celerity c according to the water depth H : numerical-simulation and stability-analysis results

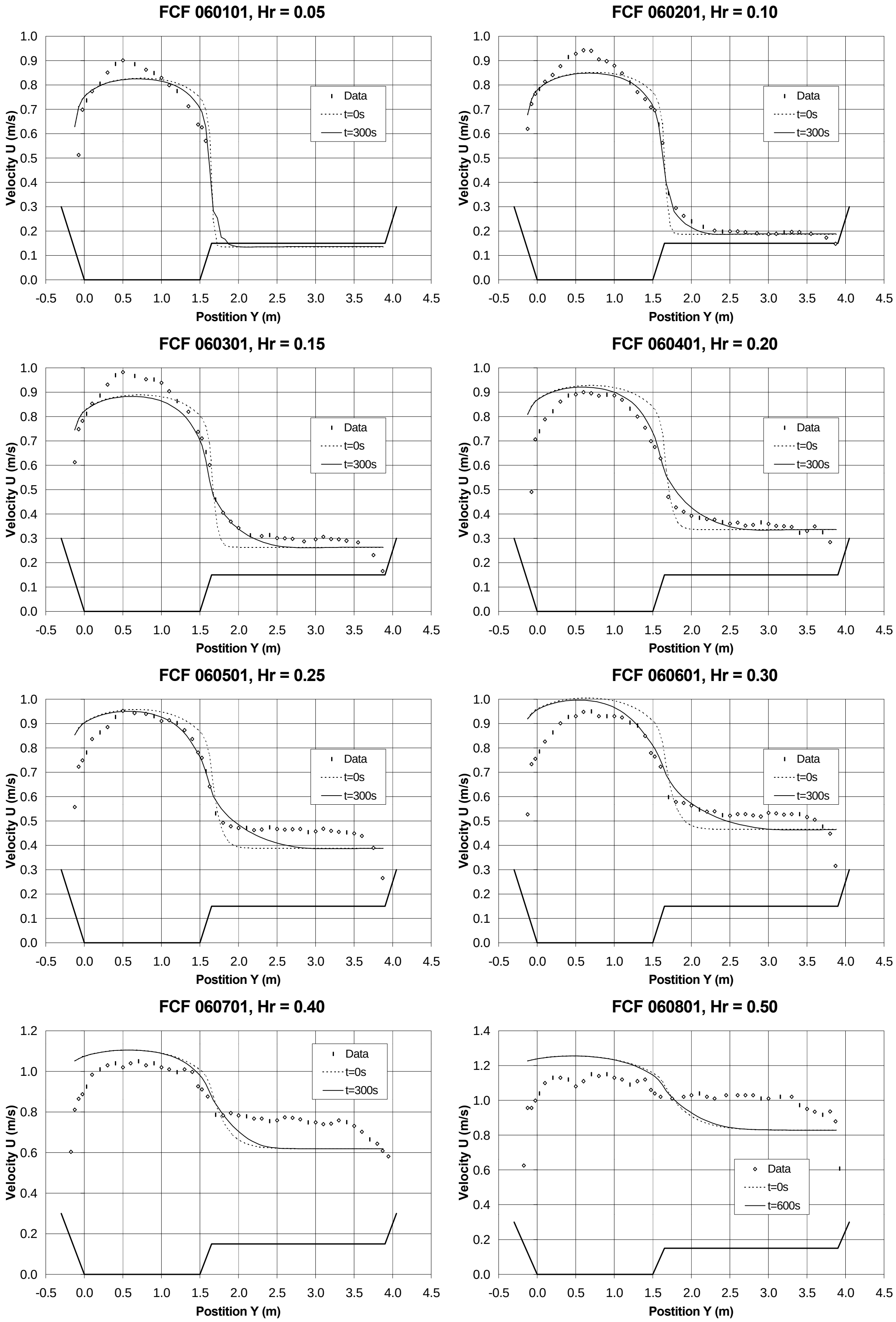

Figure 8.24 : FCF 06, velocity profiles : experimental data and numerical results (before vortices development, t = 0 s, and after vortices merging, t = 300 s)

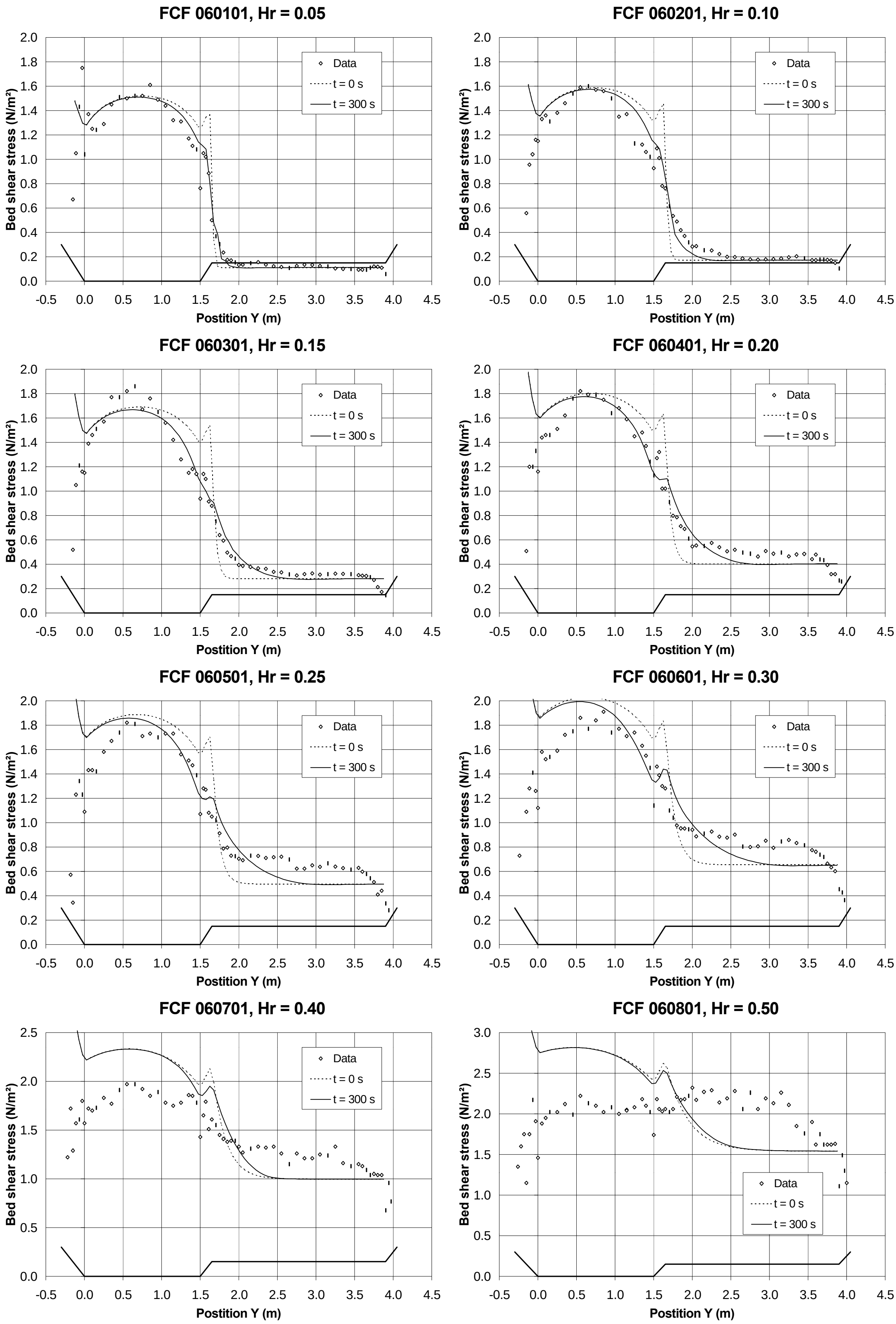

Figure 8.25 : FCF 06, bed shear-stress profiles : experimental data and numerical results (before vortices development, t = 0 s, and after vortices merging, t = 300 s)

For middle water depths (H_r = 0.20 .. 0.30), the conclusions are similar to the observations for the FCF 060501 case. Both the velocity and the bed shear stress are underestimated on the floodplain, probably due to the development of helical secondary currents, not modelled in the present simulation. In the main channel, the velocity is correctly estimated near the interface; while it is now overestimated near the left bank, as the shearing on the latter in neglected by the free-slip condition used.

For the higher water depths (H_r = 0.40 .. 0.50), the velocity and the bed shear stress are clearly underestimated on the floodplain and overestimated in the main channel. Indeed, for the FCF 060801 case (H_r = 0.50), the measured velocity profile is almost flat, indicating that the channel behaves now almost as a single channel. Such a behaviour implies obviously the development of significant tri-dimensional structures that are not captured by the present two-dimensional simulation.

The influence of the vortices modelling on a two-dimensional simulation results has thus been explored for a range of water depths and compared with experimental results. From this comparison, one can conclude that the modelling of the vortices improves to some extent the modelling of velocity and bed shear-stress profiles for lower water depths ($H_r \leq 0.30$); although a modelling of the helical secondary-currents is probably necessary for further improvement of the result in the floodplain area. For the larger water depths ($H_r \geq 0.40$), the secondary-currents and the associated tri-dimensional structures become dominant, and the horizontal vortex development does no longer affect the flow significantly.

8.4.4 Influence of other parameters

The influences of the roughness-coefficient and ξ-parameter on the numerical results were tested through some additional simulations. The main effect of these parameters is a modification of the shear-layer width of the unperturbed-velocity profile. The perturbation growth rate and the vortex wave length are affected accordingly.

Rather than proceeding further with such an analysis of the influence of the SDS-2DH turbulence-model parameters, it is probably more interesting to investigate the use of other turbulence models, and to test a true LES model on this problem. However, such further developments are out of the scope of the present work.

8.5 Sellin's flume simulation

A simulation is now performed for the flume geometry used by Sellin (Bousmar and Zech 2001c). As described in § 7.7.3 and Figure 7.23, this flume has a symmetric compound cross-section, 456-mm wide, with 44.5 mm-high floodplains. Although no velocity-profile measurement was published for this flume, this geometry is still of interest since an estimate of the wave length of the observed vortices is provided (λ = 228 mm, see Chapter 5), for a water depth $H \approx 52$ mm.

Numerical simulations are performed using a 3 × 3 mm^2 mesh (1000 × 152 nodes), a time step $\Delta t = 0.001$ s, a SDS-2DH parameter $\xi = 0.1$, and an roughness-coefficient value $n = 0.0064$ s/m$^{1/3}$. The latter may seem rather low. However, it has been fitted on the basis of the uniform-flow experiments in single channel reported by Sellin (1964). As the vertical main-channel banks can not be depicted in the numerical mesh, oblique banks are used, with a slope $s = 0.13$ (a bank is represented by 3 nodes). The roughness-coefficient value is artificially increased to $n = 0.0300$ s/m$^{1/3}$ for these nodes, in order to reproduce the additional bed shear existing on the bank, when compared with an horizontal bottom. The corresponding velocity profiles (unperturbed and perturbed) are given on Figure 8.26.

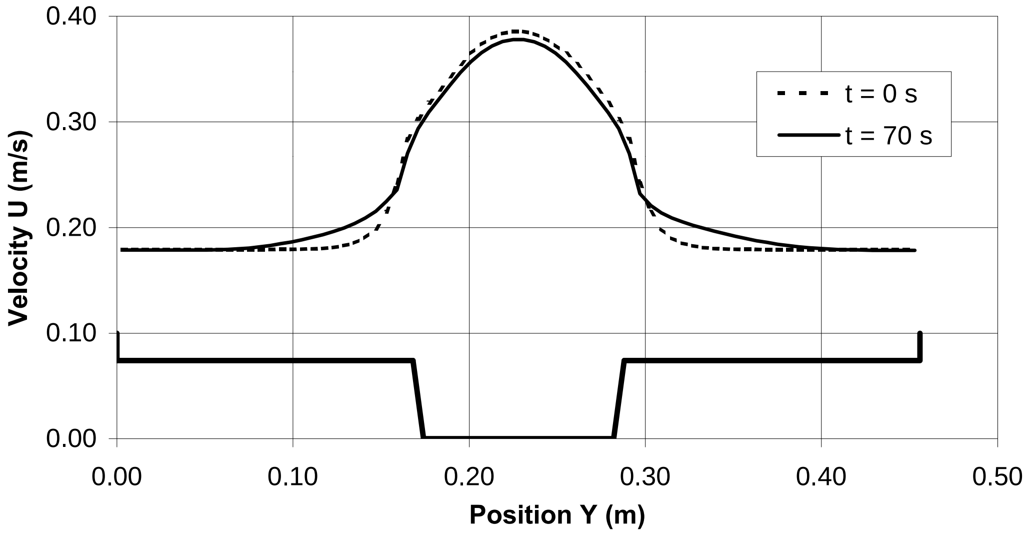

Figure 8.26 : Sellin's flume, numerical velocity profile, before and after perturbation growth

The perturbation growth is depicted on Figure 8.27, which shows the vorticity and velocity fields, at different times. The perturbation appears around t = 30 s and grows until t = 50 s. Then, vortex merging occurs until t = 70 s. Table 8.8 gives a comparison of the vortices characteristics observed experimentally, estimated with the stability analysis, and computed from the present simulation. For the latter, the vortex wave length before vortex merging is used (at t = 50 s). Indeed, it is found that, with this value, the three available results agree surprisingly well together : the wave length λ estimated by the stability analysis is within 5 % of the measured one, and the numerical result within 10 %. For both cases, the wave celerity is lower than the interface velocity U_m = 0.28 m/s, indicating a shifting of the vortices towards the floodplains, as observed experimentally (see Figure 5.1).

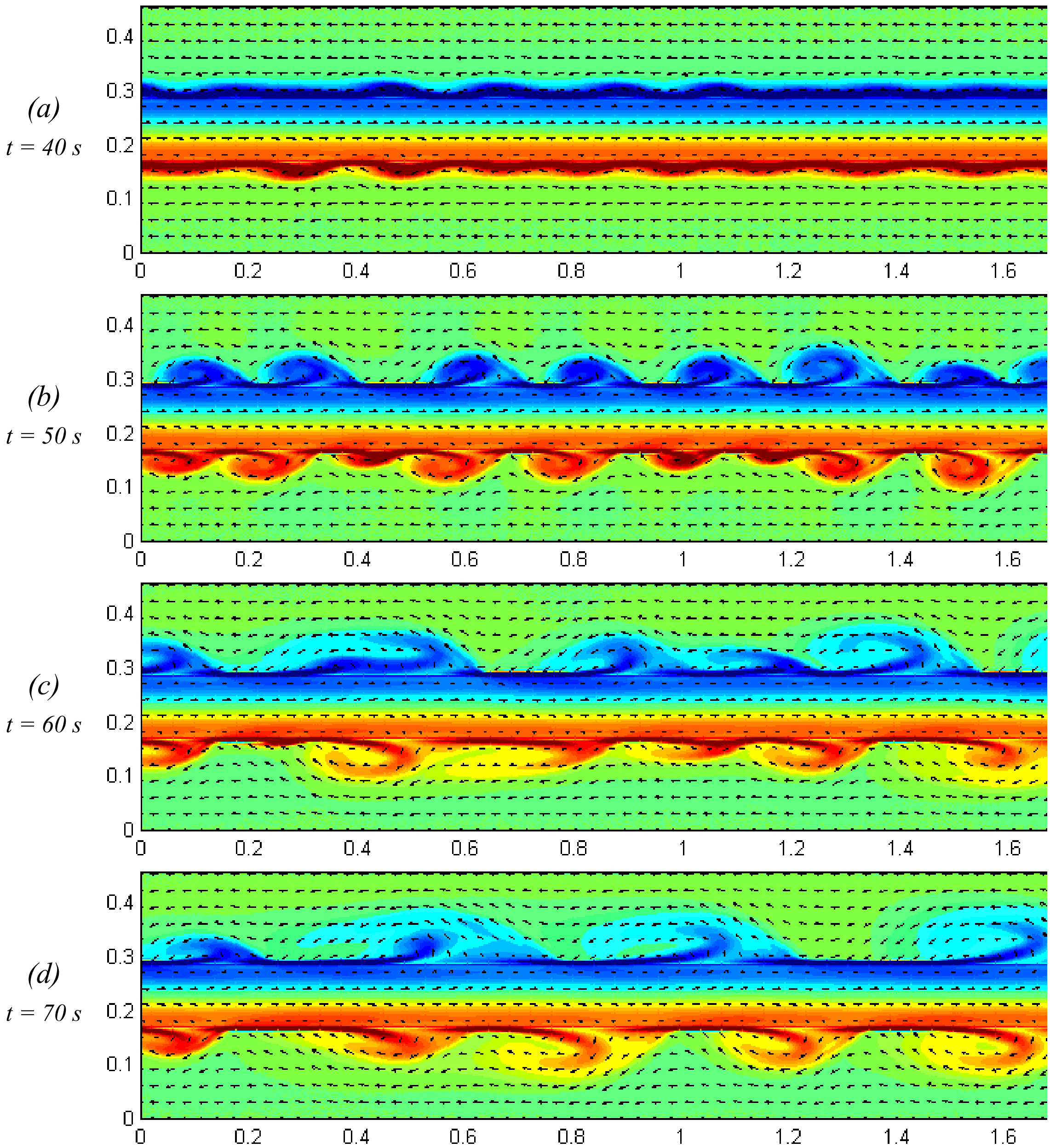

Figure 8.27 : Sellin's flume, vorticity and velocity field, according to SDS-2DH simulation

Table 8.8 : Sellin's flume, vortices characteristics

	Wave length λ	Growth rate αc_i	Wave celerity c
Experimental	228 mm	-	-
Stability analysis	216 mm	0.217	0.23 m/s
Numerical simulation (before merging, t = 50 s)	250 mm	0.113	0.22 m/s

8.6 UCL flume simulations

Lastly, simulations were performed for the asymmetric compound-channel geometry investigated in the UCL flume (Chapter 6). The simulation parameters are : a $10 \times 10\ \text{mm}^2$ mesh (500×80 nodes); a time step $\Delta t = 0.0025$ s; a SDS-2DH parameter $\xi = 0.1$; and an roughness-coefficient value $n = 0.0107\ \text{s/m}^{1/3}$. As for Sellin's flume, the vertical wall between the main channel and the floodplain is depicted by an inclined wall, with a slope $s = 0.2$ (the bank is here represented by 2 nodes). The roughness-coefficient value is artificially increased to $n = 0.0317\ \text{s/m}^{1/3}$ for these nodes, in order to reproduce the additional bed shear existing on the sloping bank. The roughness coefficient is also increased on the channel side banks, in order to moderate the free-slip condition effect. The unperturbed-flow velocity profiles are given on Figure 8.28, and their characteristics are summarised in Table 7.10.

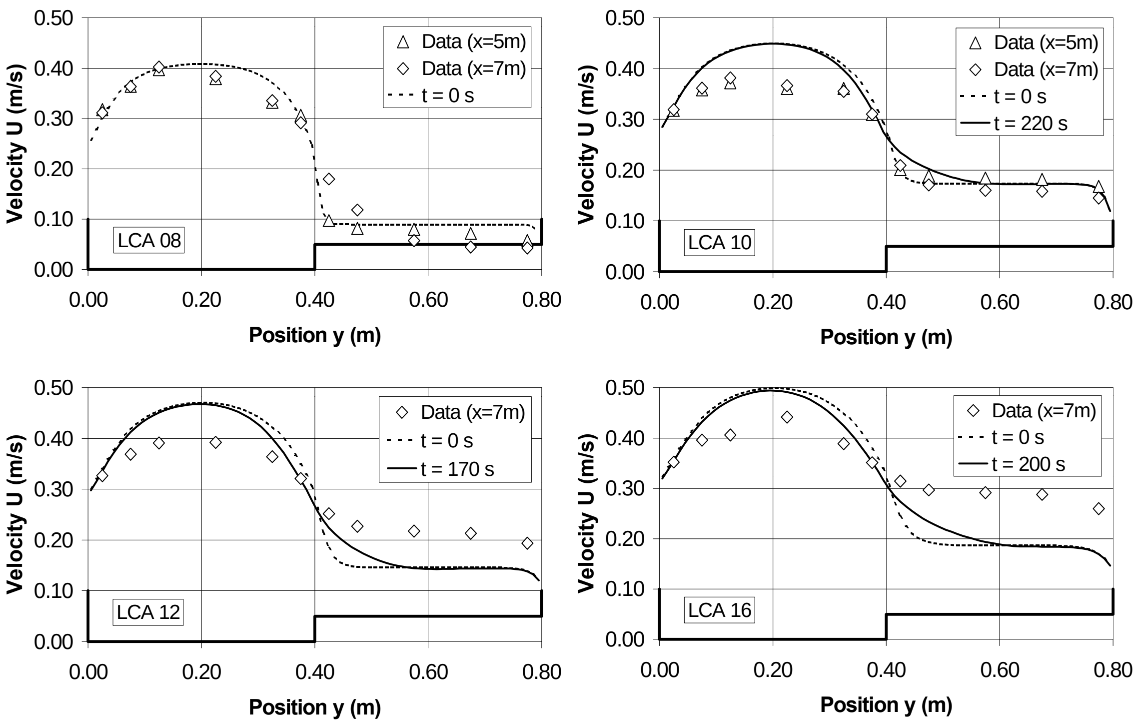

Figure 8.28 : UCL flume, measured and computed velocity profiles

Conclusions similar to the ones for FCF 06 can be made regarding the velocity-profile variation according to the water depth H : the velocity prediction is improved in the shear-layer area; while, for the larger discharges, the velocity remains underestimated on the floodplain. However, in this case, the measured data is also questionable, as an ill-conditioned upstream discharge distribution has been reported in Chapter 6.

A typical vorticity field evolution is given on Figure 8.29, for the LCA 10 case (H_r = 0.23). For this particular case, the vortices appears at t = 160 s, and the merging starts around t = 180 s. As for previous simulations, it is observed that the vortices develop mainly in the floodplain, although some vorticity field oscillations are also observed in the main channel at t = 200 s. Similar plots are obtained for the LCA 12 and LCA 16 cases. On the other hand, no clear vortices were identified in the LCA 08 simulation results, even when using a refined 5 × 5 mm^2 mesh. Probably this failure may be attributed to the low mesh resolution.

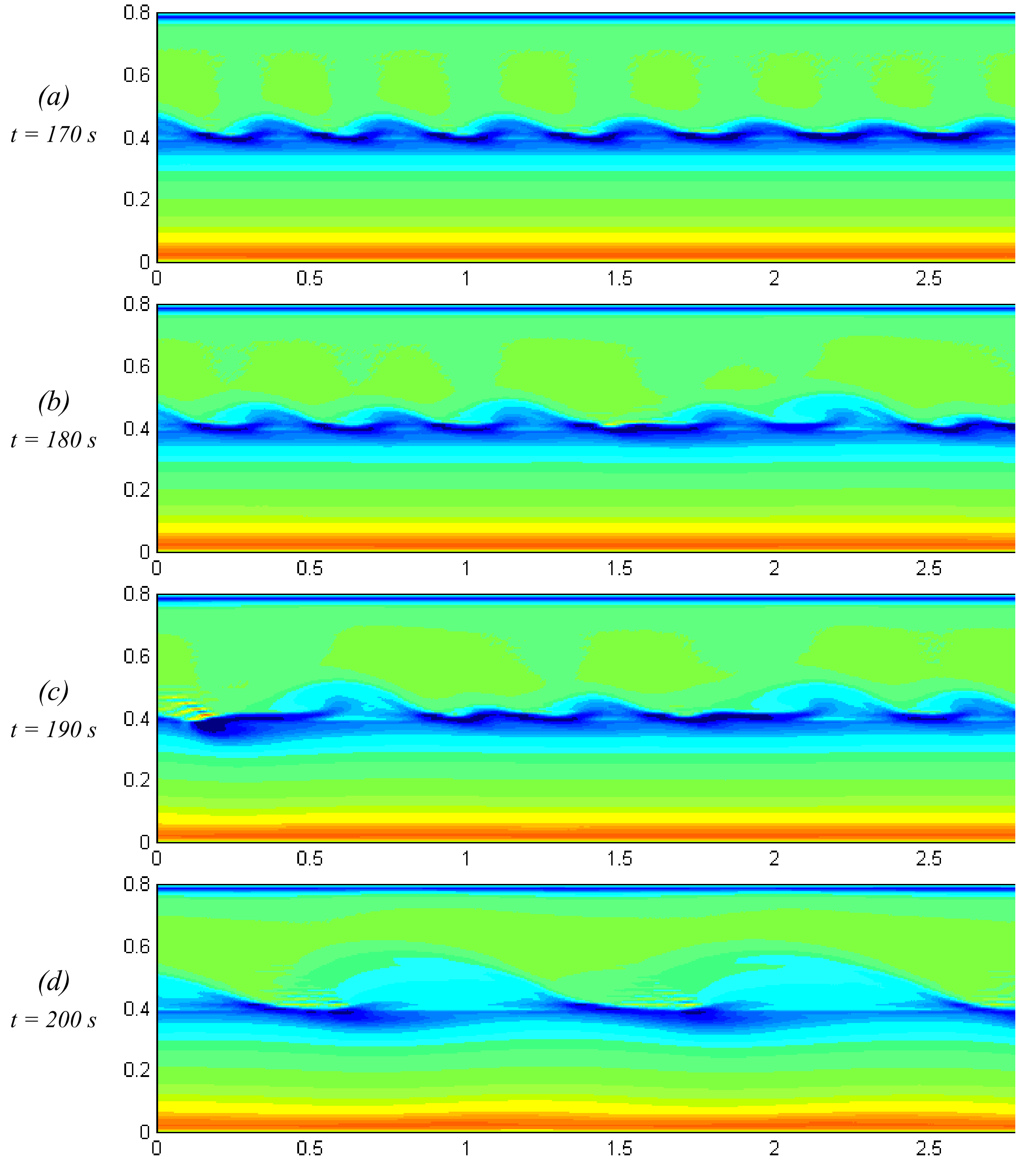

Figure 8.29 : UCL flume, LCA 10 case, vorticity field according to the numerical simulation (floodplain is above the shear layer (y > 0.40 m), and main channel is below (y < 0.40 m))

The vortex wave lengths λ, estimated before vortex merging, are reported in Table 8.9 and Figure 8.30, for comparison with the experimental values and with the stability-analysis estimates. Some scattering is observed between the three estimates, as the numerical values are 30 % lower than the measured ones. However, a similar tendency is observed for the three sets of values, with the vortices wave length increasing according to the water depth. For the LCA 10 case, the vortices wave length λ = 0.71 m, obtained after vortices merging is also reported. This value is found to be larger than the experimental one, indicating either an erroneous estimate, either a not fully developed flow perturbation.

Table 8.9 : UCL flume, comparison of the estimated vortices wave lengths λ (m)

Case	H_r	Experimental λ	Stability anal. λ	Numerical λ
LCA 08	0.10	0.39	0.30	-
LCA 10	0.23	0.56	0.45	0.38 (0.71)
LCA 12	0.30	0.67 – 1.26	0.50	0.45
LCA 16	0.38	-	0.61	0.71

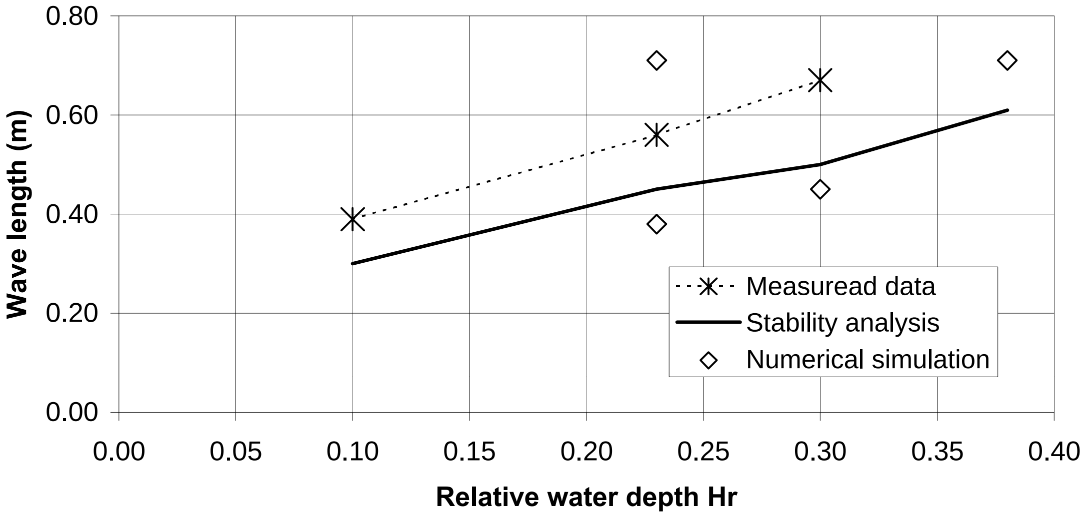

Figure 8.30 : UCL flume, comparison of the estimated vortices wave lengths λ

This last comparison validates the numerical approach only partially. Probably better results could be obtained with a more refined grid. Repeating similar tests with a true LES turbulence model would also be helpful. However, the remarks formulated in the conclusion of Chapter 6 regarding the possible experimental weaknesses should also be taken into account before rejecting definitely one or the other model.

8.7 Conclusion

The numerical simulations with the SDS-2DH model of Nadaoka and Yagi (1998) are possibly based on a questionable hypothesis. Indeed, this model operates according to a LES principle (compute explicitly the larger turbulence scales and model the smaller ones) but uses a URANS method (transport equation for the kinetic energy).

Nevertheless, several significant results are obtained with this method : (1) the vortex development in the shear layer is qualitatively reproduced; (2) the vortex wave length estimated before vortex merging agrees satisfactorily with prediction of the hydrodynamic stability analysis; (3) the same vortex wave length before merging agrees very well with the measured wave length from Sellin's experiments, and, to a lower extend, with the UCL measurements; and (4) due to the vortex development, the computed velocity and bed shear-stress profiles are improved in the interface are, when compared to FCF measurements.

On the other hand, two key questions remain unanswered : (1) the influence of the merging process; and (2) the underestimation of the floodplain velocity.

It as been suggested that the latter point is due to the helical secondary currents that exist in the channel but are not taken into account by the depth-averaged modelling. This point will be further investigated in the next Chapter, by adding the dispersion terms in the Saint-Venant equations in order to model the additional momentum transfer due to these currents.

Regarding the merging process, in the Chapter 7 on the stability analysis, it was suggested that, due to non-linear effects, vortices in the shear layer would merge together to form larger ones. Such merging processes are indeed observed in the numerical results; and, due to the flow constraining by the channel walls, the flow stabilises for some maximum merged-vortex wave length. However, when compared with the available experimental results, bearing also in mind the measurement accuracy, it seems that the observed vortices would better match with the non-merged vortices in the numerical simulation than with the merged ones. It should be pointed out that this result agrees with the observations of Tamai et al. (1986). In this case, the measured wave lengths of vortices were also close to the characteristics of non-merged vortices, estimated by linear stability analysis, indicating thus that no merging would have occurred (see Figure 5.2).

It is unfortunately impossible to give a definitive explanation for this last result, as it could be due either to an experimental error, or to a numerical problem. Accordingly, two suggestions could be proposed for further work. First, as already noticed in Chapter 6 conclusions, new experimental investigations should not only focus on the characteristics of developed vortices, but also on the development process itself, by observing the flow along the whole channel length starting from the inlet tank, in order to distinguish a possible merging process. Secondly, the choice of the Nadaoka and Yagi's numerical model should be questioned, and maybe a true LES model should be adopted. Additionally, the mesh resolution should also be improved in some cases, keeping of course in mind the computation time. Lastly, simulations of the spatial growth of the perturbations, instead of the temporal growth, could lead to better results in the comparisons with the experimental results, although such simulations require more complex boundary conditions than the cyclic condition used in this work.

Chapter 9
Secondary-currents modelling through dispersion terms

9.1 Introduction

In the previous Chapter, a depth-averaged numerical model, including Sub-Depth Scale turbulence, was applied for compound-channel flow modelling. Results from this SDS-2DH model reproduced well the development of the vortices with vertical axis at the interface between main channel and floodplains. The effect of these vortices in terms of momentum transfer was evidenced by its influence on the transverse profile of the depth-averaged longitudinal velocity component. Nevertheless, even if the velocity predictions around the interface were clearly improved, the velocity on the floodplains remained underestimated away from the interface (Figure 8.15).

The easiest way to overcome this underestimation would be to decrease the roughness coefficient on the floodplains. Unfortunately this would lead to an underestimation of the bottom shear stress, for which an accurate prediction is also of interest for the river engineer. In fact, the discrepancy between measured and computed velocities has to be explained by the presence of helical secondary currents (Shiono and Knight, 1996). These currents transfer a part of the momentum transversally and are accordingly expected to increase the velocity on the floodplains if taken into account in the numerical simulations. Of course, such secondary currents can be modelled thoroughly only by 3D modelling. But their effect can also be introduced in depth-averaged modelling, through the addition of a secondary-current or a dispersion term. Such an example of a secondary-current term is given by the Shiono and Knight LDM (3.14).

In this Chapter, after a short review of the present knowledge on secondary-currents origins, the values of the parameters of the dispersion model proposed in § 2.5 are estimated. Then the influence of the dispersion terms on the velocity profile is explored in conjunction with the effect of large vortices, as obtained in the numerical simulations of the previous Chapter.

9.2 Origin of secondary currents

As pointed out in § 2.5, several sources of secondary currents can be identified, depending on the flow conditions (Table 9.1) : (1) the secondary currents of Prandtl's first kind are driven by centrifugal forces in curved channels (see e.g. Chang, 1988); and

(2) the secondary currents of Prandtl's second kind are due to turbulence anisotropy in prismatic channels (Nezu and Nakagawa, 1993). For prismatic compound-channel flow, the anisotropy of turbulence due to the presence of the re-entering corner also generates Reynolds stresses as well as corresponding secondary currents (Tominaga and Nezu, 1991).

Table 9.1 : Sources of secondary currents

Curved channel	Narrow channel ($B < 2\,H$)	Wide channel ($B > 2\,H$)	Compound channel
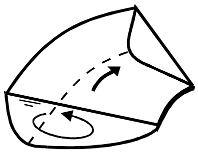	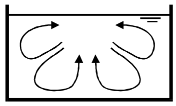	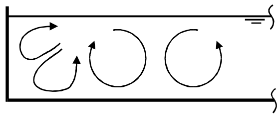	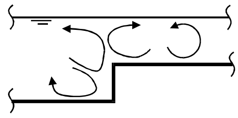
Centrifugal forces	Anisotropy of turbulence, due to walls, corner effect.	Anisotropy of turbulence, due to bed and/or flow perturbations	Anisotropy of turbulence, due to walls, corner effects
$\bar{v}_{\max} \approx 0.30\,\bar{u}$	$\bar{v}_{\max} \approx 0.03\,\bar{u}$	$\bar{v}_{\max} \approx 0.03\,\bar{u}$	$\bar{v}_{\max} \approx 0.04\,\bar{u}$

The turbulence-anisotropy effect can be explained by using the transport equation for the longitudinal vorticity Ω. The latter is obtained from the Navier-Stokes equations (2.1), written for uniform steady flow, by deriving the *y*- and the *z*-wise momentum equation according to *z* and *y*, respectively, and by subtracting one resulting equation from the other (Nezu and Nakagawa 1993) :

$$\bar{v}\frac{\partial\Omega}{\partial y}+\bar{w}\frac{\partial\Omega}{\partial z}=\frac{\partial^2}{\partial y\partial z}\left(\overline{w'^2}-\overline{v'^2}\right)+\left(\frac{\partial^2}{\partial y^2}-\frac{\partial^2}{\partial z^2}\right)\overline{v'w'}+\upsilon\nabla^2\Omega \tag{9.1}$$

with $$\Omega=\frac{\partial\bar{v}}{\partial z}-\frac{\partial\bar{w}}{\partial y} \tag{9.2}$$

where $\bar{v}$ and $\bar{w}$ are the Reynolds averaged velocities; v' and w' are the velocity fluctuations; $\overline{v'w'}$ is a Reynolds stress; and υ is the molecular viscosity.

According to Nezu and Nakagawa (1993), the convection terms (left-hand part of 9.1) and the diffusion term (last term in the right-hand side) can be assumed to be negligible with regard to the generation and Reynolds stress terms (first and second terms in the right-hand side). The vorticity equation (9.1) then reduces to

$$\left(\frac{\partial^2}{\partial y^2}-\frac{\partial^2}{\partial z^2}\right)\overline{v'w'}=\frac{\partial^2}{\partial y\partial z}\left(\overline{v'^2}-\overline{w'^2}\right) \tag{9.3}$$

This shows clearly that the turbulence anisotropy (difference between $\overline{v'^2}$ and $\overline{w'^2}$) due to the channel geometry generates the Reynolds stresses. The latter will then produce longitudinal vorticity and secondary currents. In order to solve (9.3), a model for the generation term has to be adopted; while the Reynolds stress is developed according to the Boussinesq model (2.41) :

$$-\overline{v'w'} = \upsilon_t \left(\frac{\partial \overline{w}}{\partial y} + \frac{\partial \overline{v}}{\partial z} \right) \tag{9.4}$$

For a narrow channels (width $B \leq 2 \times$ water depth H), Ikeda (1981) proposed the following model for the generation term, assuming a periodic distribution of the bed shear-stress τ_b :

$$\frac{\overline{v'^2} - \overline{w'^2}}{U^{*2}} = \frac{\tau_b}{\tau_{b,\ averaged}} \left(1 - \frac{z}{H} \right) = \left(1 + \delta \cos\left(\frac{ky}{H} \right) \right) \left(1 - \frac{z}{H} \right) \tag{9.5}$$

where $\tau_{b,averaged}$ is the width-averaged value of τ_b; U^* is the averaged shear velocity; and δ and k are parameters. Solving (9.3) with this model (9.5) shows that the dominating secondary currents are obtained for $k = \pi$. The corresponding velocity field is given by

$$\frac{\overline{v}}{U^*} = \frac{6\delta}{\kappa\pi^3} \sin\left(\frac{\pi\, y}{H} \right) \left[2\cos\left(\frac{\pi\, z}{H} \right) - \pi \left(2\frac{z}{H} - 1 \right) \sin\left(\frac{\pi\, z}{H} \right) \right] \tag{9.6a}$$

$$\frac{\overline{w}}{U^*} = \frac{6\delta}{\kappa\pi^3} \cos\left(\frac{\pi\, y}{H} \right) \left[\left(2\frac{z}{H} - 1 \right) \cos\left(\frac{\pi\, z}{H} \right) + 1 \right] \tag{9.6b}$$

where κ is the Karman constant. Such an idealised velocity field is given by Figure 9.1. However, in actual channels, due among other things to the effect of the walls, the velocity field will be more complex and a "corner effect" will be observed : two superposed secondary-current cells are observed in each channel half section (Figure 9.2). An upstream current is observed near the wall and a downstream one exists in the channel centre; while the cell corresponding to Ikeda's model is pushed back in the bottom area. As a result of the downstream current in the channel centre, the maximum longitudinal velocity is no more observed at the free surface, but at some distance below this surface.

In wider channels (width $B > 2 \times$ water depth H), secondary-current cells are still observed, although the walls can only influence the flow in a part of the channel width. It is expected that the turbulence anisotropy that generates the secondary currents is due to small perturbations, either in the flow itself, or on the channel bed (Nezu and Nakagawa 1993). The secondary currents in a wide channel generally appear in counter-rotating pairs, and the cell width is approximately equal to the water depth H.

In compound channels, additional turbulence anisotropy is due to the re-entering corner at the interface between main channel and floodplain, as observed by Tominaga and

Nezu (1991) and depicted on Figure 1.5. This additional anisotropy reinforces the upward current along the main-channel bank, in such a way that stronger secondary currents are observed in this subsection. In the floodplain, similar secondary-current cells are observed near the interface, and are expected to be present on the whole subsection width. Unfortunately, available detailed measurements on the floodplain are generally limited in extension to an area close to the interface.

For all the considered cases, it can be concluded that the secondary-current generation processes are controlled by the main flow anisotropy. As a consequence, the transverse velocity component $\bar{v}$ will be proportional to the longitudinal component $\bar{u}$ (see Table 9.1). Another observation of interest is that the secondary-current cell width is generally of the same range as the water depth H; and that the idealised velocity field computed by Ikeda can be a good first approximate of the secondary-current cells, at least in the wide channels. The corresponding velocity profile will therefore be used to calibrate the dispersion model proposed in § 2.5.

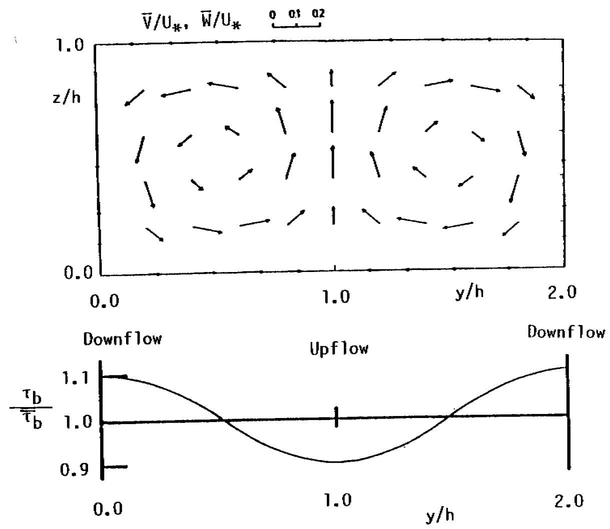

Figure 9.1 : Idealised secondary currents, in a narrow prismatic channel, according to Ikeda's model (9.6) (Nezu et Nakagawa, 1993)

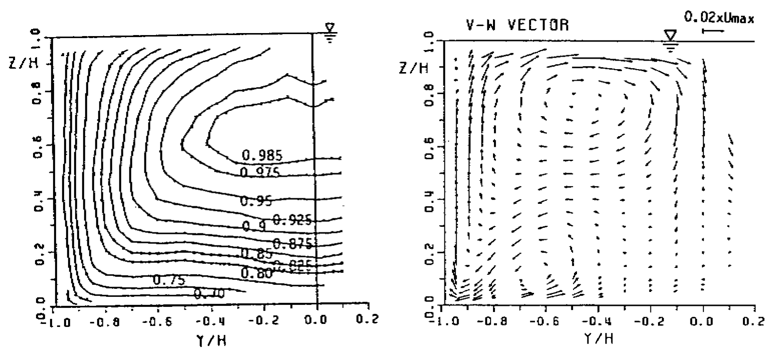

Figure 9.2 : Narrow prismatic channel, corner effect on the longitudinal and transverse velocity fields (Nezu and Nakagawa 1993)

9.3 Dispersion-model calibration

As the longitudinal velocities $\bar{u}$ are proportional to their depth-averaged value U, and as results from the previous paragraph indicate that the transverse component $\bar{v}$ is also proportional to this depth-averaged value, it has been proposed that the dispersion terms are proportional to the square of the depth-averaged velocity U (2.52) :

$$\int_{z_b}^{z_w} \left(\bar{u}-U\right)^2 dz = \chi_{uu} U^2 H\,,\quad \int_{z_b}^{z_w} \left(\bar{u}-U\right)\left(\bar{v}-V\right) dz = \chi_{uv} U^2 H$$

$$\text{and} \quad \int_{z_b}^{z_w} \left(\bar{v}-V\right)^2 dz = \chi_{vv} U^2 H \tag{9.7}$$

where χ_{uu} ,χ_{uv} and χ_{vv} are defined as the dispersion coefficients.

The value of the so-defined dispersion coefficients should ideally be deduced either from theoretical considerations or from experimental data. A theoretical estimation can be obtained by assuming a classical logarithmic profile for the longitudinal velocity component $\bar{u}$ (Nezu and Nakagawa 1993) :

$$\bar{u} = \frac{U*}{\kappa} \ln\left(\frac{z\,U*}{\upsilon}\right) + A \tag{9.8}$$

where the constant values are chosen according to Schoemaker (1991), who calibrated a roughness function for the FCF flume : $\kappa = 0.41$ and $A = 0.375$. The Ikeda profile (9.6a) is used for the transversal component $\bar{v}$ (Figure 9.3), with the abscissa y and the δ parameter values chosen to get the maximum velocity approximately equal to $\bar{v}_{max} \approx 0.04\,U$ (according to Table 9.1). Indeed, the absolute values of the coefficients χ_{uv} and χ_{vv} are expected to be maximum at the secondary-current cell centres, as $\bar{v}$ is maximum there, and to be null between two adjacent cells.

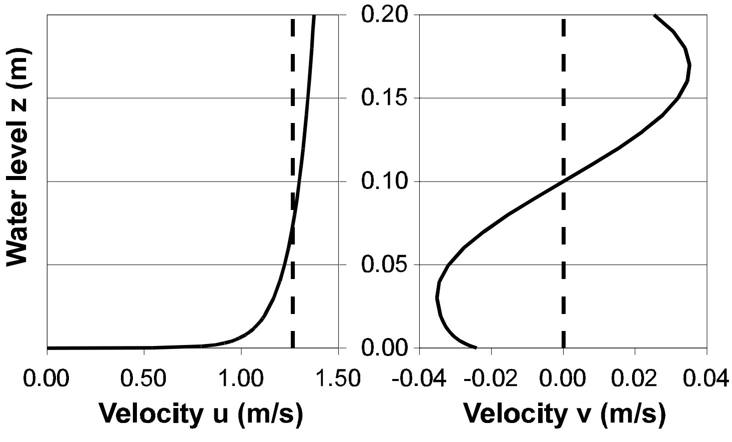

Figure 9.3 : Typical vertical profiles of local longitudinal and transverse velocity components, for a wide channel, with H = 0.2 m and U = 0.045 m/s.*

The dispersion terms are found to be rather independent of the water depth. Their estimation for $H = 0.20$ m is given in Table 9.2. According to the ratio between the longitudinal and the transverse velocities, the χ_{uu} value is one order of magnitude larger than the values of the χ_{uv} and χ_{vv} coefficients.

A second estimation of the dispersion-coefficient values can be obtained from experimental data, in this case from the Flood-Channel-Facility (FCF) data set (Knight, 1992), as the latter is also used for results comparison. This data set provides LDA measurements of $\bar{u}$ and $\bar{v}$ values at several locations in the main channel and on the floodplains, for about 10 different geometries or water depths. Unfortunately, few points are available on each vertical on the floodplains (from 1 to 4), and the measurements have to be used carefully as the experimenters faced probe orientation problems that could lead to inaccurate values of $\bar{v}$ (Shiono and Knight 1991).

The velocity products $(\bar{u}-U)^2$, $(\bar{u}-U)(\bar{v}-V)$ and $(\bar{v}-V)^2$ are estimated at each available point of each vertical, and dispersion-coefficient values are obtained from (9.7). The integration in (9.7) is made using the trapezoid rule. For that purpose, the values of the velocity products at the free-surface are assumed equal to their values at the highest point on the vertical (constant extrapolation); while the values at the bed are set equal to the values at the lowest available point. Such an approximation appears as rather crude. However, due to the few points available, a theoretical velocity profile, such as (9.8) or (9.6a), can not be fitted more accurately to the data to be integrated.

Figure 9.4 gives the so-estimated dispersion-coefficient profiles. For the χ_{uu} coefficient (Figure 9.4a), almost constant values are obtained in the main channel, with $\chi_{uu} \approx 0.0080$ ($y < 0.75$ m). More scattering is observed above the main-channel bank ($0.75 < y < 0.90$m); while the floodplain values are lower : $\chi_{uu} \approx 0.0020$ ($y > 0.90$ m). These lower floodplain values are probably due to the fewer measurement points available on each vertical; as 4 points per vertical are available only for the FCF 080501 and FCF 100501 cases. In these cases, the χ_{uu} coefficients are found slightly larger and it is expected that their values could equal $\chi_{uu} \approx 0.0080$ if enough measurement points were available. Consequently, this constant value $\chi_{uu} = 0.0080$ will be assumed on the whole-channel width.

Keeping in mind this inaccuracy of the estimated coefficients for the floodplain, the two other dispersion coefficients χ_{uv} and χ_{vv} can be investigated (Figure 9.4b and c). Their values are found to present a linear growth from the main channel central axis to the interface with the floodplain; and equal maximum values are obtained for all the tested geometries. These coefficients then present a linear decrease through the floodplain, but with more scattering, probably due again to the fewer number of points available on each vertical. A unique secondary-current cell, extending on the whole channel width, could be expected from such a coefficient profile, although this seems not realistic in regard to the width-to-depth ratio.

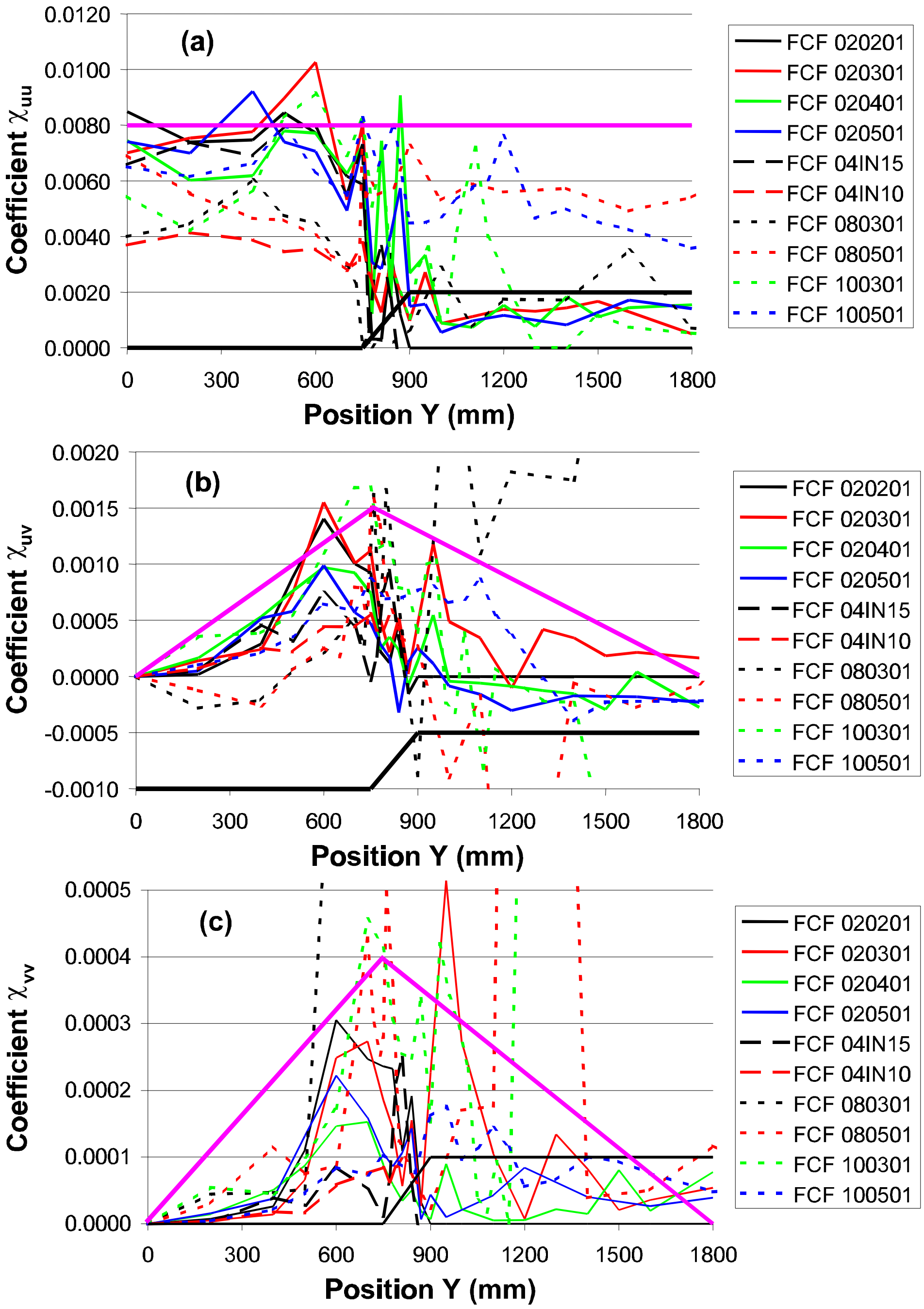

Figure 9.4 : Dispersion coefficients estimated from the LDA measurements in the FCF (part of the section)

Table 9.2 : Estimated maximum values for the dispersion coefficients

	χ_{uu}	χ_{uv}	χ_{vv}
Theoretical (log law and Ikeda)	0.0077	0.0014	0.0005
Experimental (FCF)	0.0080	0.0015	0.0004

The dispersion coefficient values (or maximum values) are synthesised in Table 9.2, for both theoretical calculation and experimental estimation. In spite of all the inaccuracies involved in these estimations (simplified secondary-current model and sparse measurements), both set of coefficients are found to be almost equal, giving some confidence in their estimated value.

9.4 Numerical results

Numerical simulations are performed for the asymmetrical geometry of the FCF 060501 case, previously investigated using the SDS-2DH model (§ 8.3). In this case, numerical simulations showed that the velocity-profile prediction is improved in the interface area, when accounting for the horizontal vortices generated in the shear layer. On the other hand, at a distance from the interface, the floodplain velocity was underestimated. As the actual roughness coefficient value of $n = 0.01106\ \mathrm{s/m^{1/3}}$ was used (according to § 8.2.2), it was concluded that this velocity difference was due to the helical secondary-current effect. The present simulation enables thus to validate this explanation, by using simultaneously the SDS-2DH model for the horizontal vortices and the dispersion terms for the helical secondary currents (Bousmar and Zech 2001a).

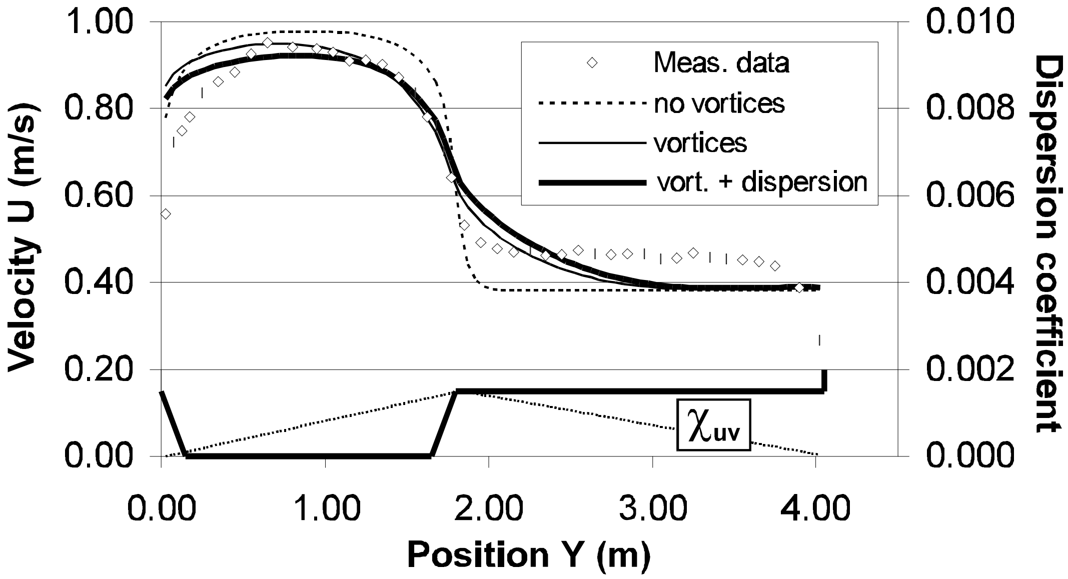

Figure 9.5 : FCF 060501, velocity profiles : for common simulation, with SDS-2DH only, and with SDS-2DH and dispersion (theoretical values of the dispersion coefficients)

Figure 9.5 shows the computed velocities compared with the experimental data for the flow without vortices (common simulation) and with vortices, thanks to the SDS-2DH model. As already noticed, taking into account the vortices effect improves clearly the velocity prediction in the shear-layer area. But, as already pointed out, the transverse extension of the influence of vortices is not large enough for increasing sufficiently the computed velocities. Moreover, as already said, changing the roughness-coefficient value to make the floodplain velocities more exact would damage the accuracy of the bed shear-stress prediction.

On Figure 9.5, the results of a similar simulation are also depicted, now including the dispersion terms, with dispersion-coefficient values as deduced previously : constant $\chi_{uu} = 0.0080$, linearly variable χ_{uv} and χ_{vv}, with maximum values $\chi_{uv} = 0.0015$ and $\chi_{vv} = 0.0005$ (see Table 9.2). Although not sufficient, the effect of the dispersion terms is perceptible, mainly in the shear-layer area.

The dispersion-term effect can be better explained by considering the x-wise momentum equation (2.53b). Assuming a uniform steady flow, this equation reduces to a form similar to the LDM and expresses the balance of four terms : (1) the bottom slope $S_0 = -\partial z_w/\partial x$; (2) the friction slope S_{fx}; (3) the turbulent shear stress τ_{xy} (corresponding to the SDS-2DH model); and (4) the dispersion term :

$$g\,S_0 = g\,S_{fx} - \frac{1}{H}\frac{\partial}{\partial y}\left(H\frac{\tau_{xy}}{\rho}\right) + \frac{1}{H}\frac{\partial}{\partial y}\left(\chi_{uv}U^2H\right) \tag{9.9}$$

In this balance, the momentum available through the bottom slope S_0 is mainly dissipated by the friction slope S_{fx}, while the shear stress due to turbulence and the dispersion can either dissipate or produce momentum. As the longitudinal velocity U is proportional to the square root of the friction slope, due to the use of Manning equation (2.35), the weight of the term S_{fx} in (9.9) will define the velocity profile.

In the main-channel area, for a velocity quite constant along y, the positive gradient of χ_{uv} leads to a positive value of the dispersion term. There is an additional dissipation, the friction slope reduces and, as shown by Figure 9.5, the computed velocity is lowered accordingly. On the floodplain, a negative gradient of χ_{uv} allows to add momentum and to increase slightly the velocity. Nevertheless, it is clear that the dispersion-coefficient values estimated a priori are too small to improve significantly the velocity prediction.

According to these comments, Figure 9.6 and Figure 9.7 show, for velocity and bed shear stress respectively, the results of a trial-and-error fitting of the dispersion coefficient χ_{uv}. To obtain an accurate velocity value, it was necessary to use dispersion-coefficient value varying between $\chi_{uv} = -0.0100$ and $\chi_{uv} = 0.0020$, thus up to 6 times greater than the theoretical one. Such large values are in fact needed in order to get a sufficient gradient of χ_{uv} on the floodplain and, accordingly, a sufficient value of the dispersion term in (9.9). Nevertheless, even if this fitted dispersion-coefficient value gives an accurate modelling of the velocity, it is difficult to explain in term of physical process. Indeed, it would correspond to a unique secondary-current cell on the floodplain, which is unrealistic when considering its width-to-depth ratio; as for such a width to depth ratio, numerous cells with a width comparable to the water depth ($H = 0.05$ m) would have been expected.

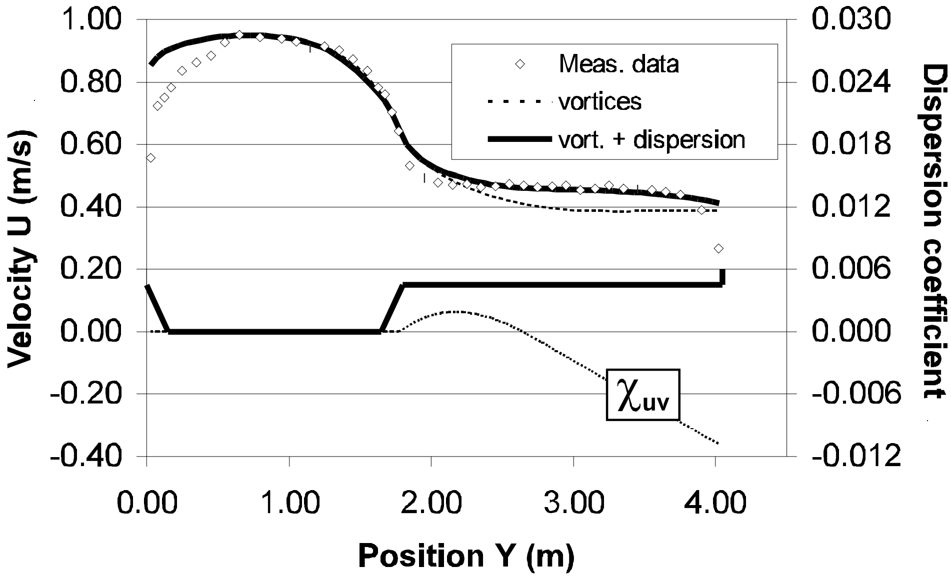

Figure 9.6 : FCF 060501, velocity profile : dispersion with optimised-coefficient values

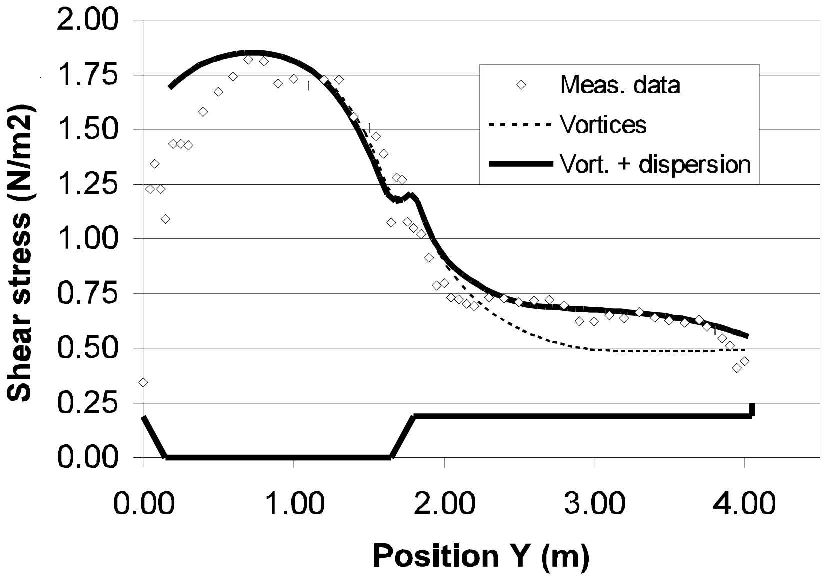

Figure 9.7 : FCF 060501, bed shear-stress profile : dispersion with optimised-coefficient values

9.5 Conclusion

The influence of the helical secondary currents on the floodplain velocity in a compound-channel flow can be simulated by the use of dispersion terms. A similar calibration of the dispersion model proposed in § 2.5 is obtained using either theoretical relations or experimental measurements. However, an adapted calibration of the dispersion coefficient is required to produce an accurate modelling of both velocity and bed shear-stress profiles; and the so-fitted dispersion coefficients are difficult to explain in term of turbulence structures.

It should be pointed out that Shiono and Knight (1991) obtained a quite similar result when developing their secondary-current term Γ for the Lateral Distribution Method (see Chapter 3). Indeed, along both main-channel and floodplain width, they observed a linear variation of the depth-averaged value of the velocity product in the right-hand side of the LDM equation (3.8). They suggested accordingly to use a constant value Γ for the derivative of this product.

According to the developments in Chapter 3, for a uniform flow, both secondary-current term in the LDM and dispersion term in the Saint-Venant equations should represent the effect of the same phenomena [see (3.8), (3.14), (3.17) and (9.7)] :

$$\Gamma = \frac{\partial}{\partial y}\left\{H\left(\rho \bar{u}\bar{v}\right)_d\right\} = \rho \frac{\partial}{\partial y}\int_{z_b}^{z_w}\left(\bar{u}-U\right)\left(\bar{v}-V\right)dz = \rho \frac{\partial}{\partial y}\left(\chi_{uv}U^2H\right) \tag{9.10}$$

Using the optimised value of the dispersion coefficient χ_{uv} (Figure 9.6), a Γ value can thus be estimated for the FCF 060501 case. This value is almost constant on the floodplain, where $\Gamma_f = -0.063$. For comparison, Shiono and Knight (1991) obtained a value of $\Gamma_f = -0.123$ for the FCF 020501 case (symmetrical channel with same water depth and floodplain width as FCF 060501); while Knight and Abril (1996) obtained a value of $\Gamma_f = -0.119$ for the same case. As the other parameters of the simulations (roughness and turbulent friction) are not exactly the same, it can be concluded that both dispersion and LDM values of Γ match satisfactorily together. On the other hand, in the shear-layer area, the value of Γ calculated from the dispersion coefficient (9.10) does no more fit with Knight and Abril estimation, but, in this case, the momentum transfer due to the horizontal vortices is already taken into account through the periodical-structures modelling by the SDS-2DH model.

Finally, one can conclude that modelling the secondary currents through the use of dispersion terms produces results quite similar as the one obtained by using of a secondary-current term Γ in the LDM, as suggested by to Shiono and Knight (1991). However, the physical meaning of the dispersion term is easier to analyse. Unfortunately, this analysis shows that the optimised dispersion coefficient used can not be interpreted in terms of secondary-current cells.

As a consequence, further works should still focus on the momentum-transfer mechanisms that exist on the floodplain and that could justify the observed velocity increase. Probably it could be useful to consider again this problem from an experimental viewpoint, with the particular objective of improving the description of the turbulence structures on the floodplain.

Chapter 10
Tentative modelling of the momentum transfer associated with the turbulent exchange

10.1 Introduction

The numerical results from two-dimensional simulations in Chapter 8 have shown that the horizontal vortices play an important part in the momentum transfer between main channel and floodplains, although the effect of secondary currents is also significant on the floodplain, as seen in Chapter 9. This last Chapter of the Part II will propose some exploratory suggestions that could help to understand this momentum transfer and to model it. These suggestions will also enable tentative links with the momentum-transfer modelling by the Exchange Discharge Model (EDM) developed in Chapter 4.

First of all, the additional shear stress due to the presence of the horizontal vortices will be estimated from the numerical results. Indeed, this additional shear stress is responsible for the momentum transfer between subsections. This shear stress will also be compared with models of eddy viscosity. Secondly, in parallel with this additional shear-stress analysis from a time-averaged viewpoint, the local-momentum balance will be investigated at some given time and the momentum-transfer process will be further highlighted. Lastly, a tentative modelling of the vortices, using a Oseen- (or gaussian-) vortex equation, will point out significant parameters, with reference to the momentum balance. These three analysis will be performed for the FCF 060501 case, already investigated in details in § 8.3.

10.2 Additional shear stress

The diffusion processes in the numerical simulations are controlled by two sources of transverse shearing : (1) the shear stress corresponding to small turbulence scales, estimated by the SDS-2DH model; and (2) the additional shear stress due to the large-scale structures. The SDS-2DH shear stress τ_S is estimated by the Boussinesq equation (2.42), with the eddy-viscosity value υ_S defined by equation (2.51). The large-scale-turbulence shear stress τ_L can be estimated through a Reynolds averaging of the velocity field. The averaged velocities $\overline{U}(y)$ and $\overline{V}(y)$ are obtained (1) by averaging the local velocities $U(x,y,t)$ and $V(x,y,t)$ along the channel length; and (2) by using ensemble averaging of the velocity field, given at several different times :

$$\overline{U}(y) = \frac{1}{nt}\sum_{nt}\left(\frac{1}{L}\int_L U(x,y,t)\,dx\right) \quad \text{and} \quad \overline{V}(y) = \frac{1}{nt}\sum_{nt}\left(\frac{1}{L}\int_L V(x,y,t)\,dx\right) \tag{10.1}$$

where L is the computational-domain length; and nt is the number of different times for which the ensemble averaging of the velocity field is processed. The fluctuations $U'(x, y, t)$ and $V'(x, y, t)$ are defined as

$$U'(x,y,t) = U(x,y,t) - \overline{U}(y) \quad \text{and} \quad V'(x,y,t) = V(x,y,t) - \overline{V}(y) \tag{10.2}$$

and the large-scale-turbulence shear stress τ_L can be estimated as a Reynolds shear stress :

$$\frac{\tau_L(y)}{\rho} = -\overline{U'V'} = -\frac{1}{nt}\sum_{nt}\left(\frac{1}{L}\int_L U'(x,y,t)\,V'(x,y,t)\,dx\right) \tag{10.3}$$

Both shear-stress values are plotted on Figure 10.1 for the FCF 060501 case, after the vortex-merging process. The averaging is performed for the L = 19 m computational domain, using the results at the times t = 350 s; 355 s .. 400 s. This figure clearly shows that the additional shear stress τ_L due to the horizontal vortices has a maximum value in the interface area (y = 1.65 m), corresponding to the momentum transfer between subsections.

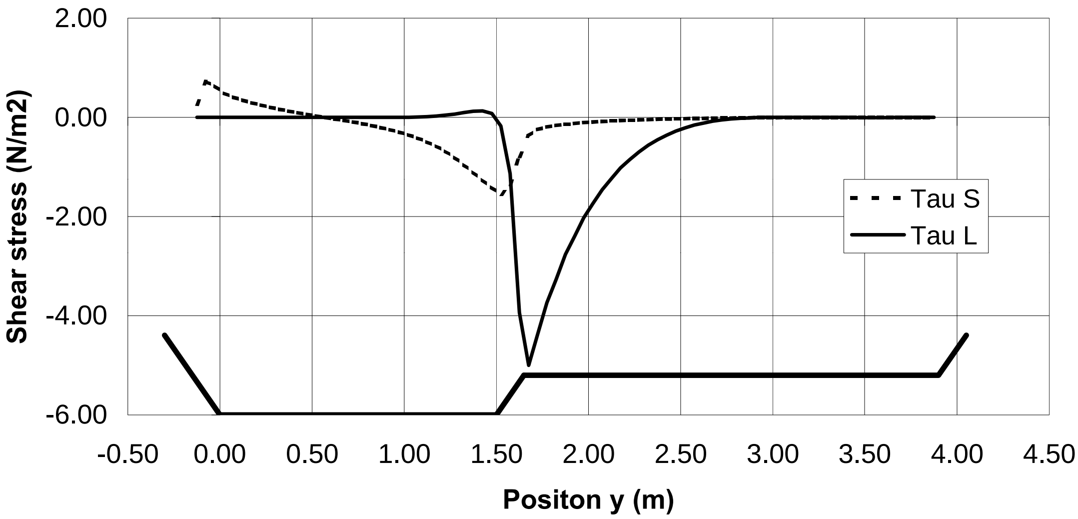

Figure 10.1 : FCF 060501, SDS-2DH τ_S and large-scale-turbulence τ_L shear-stress profiles

Table 10.1 : FCF 060501, shear-stress values at the interface (y » 1.65 m)

Apparent shear stress τ_a (experimental)	Small-scales shear stress τ_S (SDS-2DH model)	Large-scales shear stress τ_L (10.3)
8.93 N/m^2	1.55 N/m^2	5.00 N/m^2

The observation of this important additional shear stress in the interface area can be related with the concept of an apparent shear stress τ_a, defined on the vertical division line between subsections, as presented in § 1.3. A value of the apparent shear stress τ_a = 8.9 N/m^2 was estimated from the FCF 060501 measurements, on the basis of the momentum balance of the subsections (Knight 1992). Adding the additional large-scales shear stress τ_L to the small-scales shear stress τ_S, the total shear at the interface in the numerical simulations is found in the same range as this experimental value (Table 10.1).

From the large-scales-turbulent stress τ_L profile, it is also possible to compute the value of the actual eddy viscosity υ_L corresponding to these large structures, using the Boussinesq eddy-viscosity definition (2.41) :

$$\upsilon_L = \frac{-\overline{U'V'}}{\partial \overline{U} / \partial y} \tag{10.4}$$

This large-structures eddy viscosity υ_L is given on Figure 10.2, according to the velocity gradient $\partial \overline{U} / \partial y$ plotted on Figure 10.3, together with the viscosity υ_S defined by the SDS-2DH model. This actual eddy viscosity presents its largest value in the interface area, where the vortices are the most developed. The υ_L profile unevenness at y = 0.50 m and y = 3.25 m correspond to velocity-gradient values close or equal to zero. They are not significant in the present analysis, as they are out of the shear-layer area.

The large-scale eddy-viscosity υ_L profile presents some shape similarities with the velocity-gradient profile. It is therefore interesting to test the validity of the Prandtl mixing-length model (2.44) that links both these values :

$$\upsilon_L = l_m^2 \left| \frac{\partial \overline{U}}{\partial y} \right| \tag{10.5}$$

The estimated values of the mixing-length l_m are given on Figure 10.4. Only the significant values, located in the shear-layer area, are plotted. The mixing-length l_m presents two plateau's : the first in the main-channel (1.00 < y < 1.50 m) and the second in the floodplain (1.65 < y < 3.00 m). This could indicate that the mixing-length model is, at least, partially appropriate for the present problem : indeed, the transition between both plateau's corresponds to the main-channel bank, where the bed level is not constant. As Prandtl's mixing length is defined for a general two-dimensional flow, it can not account for the water-depth change occurring in the present case. However, the ratio between the two plateau values is not in accordance with the corresponding water-depth ratio H_r = 0.25.

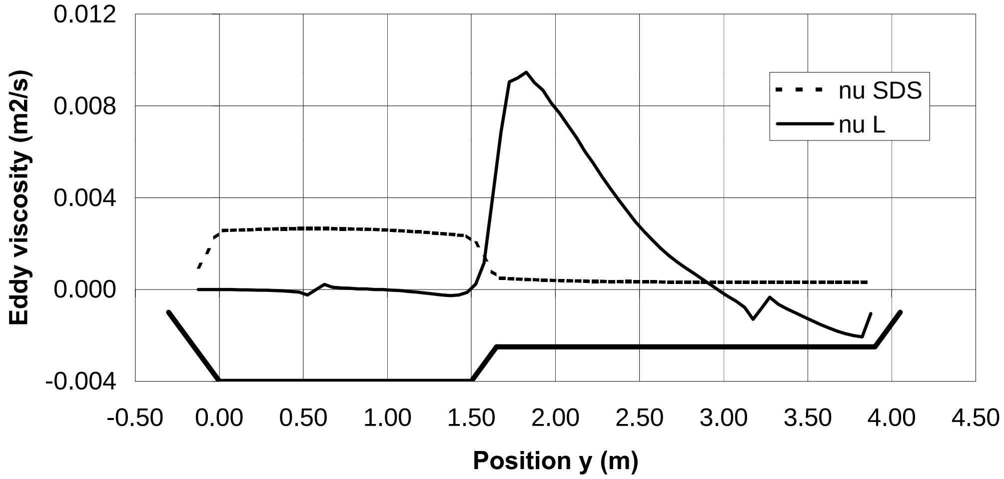

Figure 10.2 : FCF 060501, SDS-2DH υ_S and large-scale-turbulence υ_L viscosity

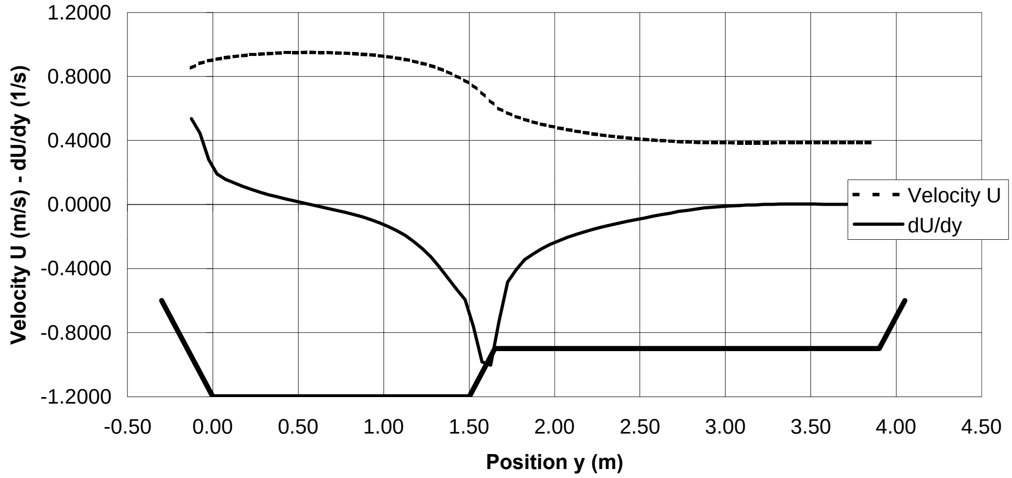

Figure 10.3 : FCF 060501, averaged longitudinal-velocity $\overline{U}$, and velocity gradient

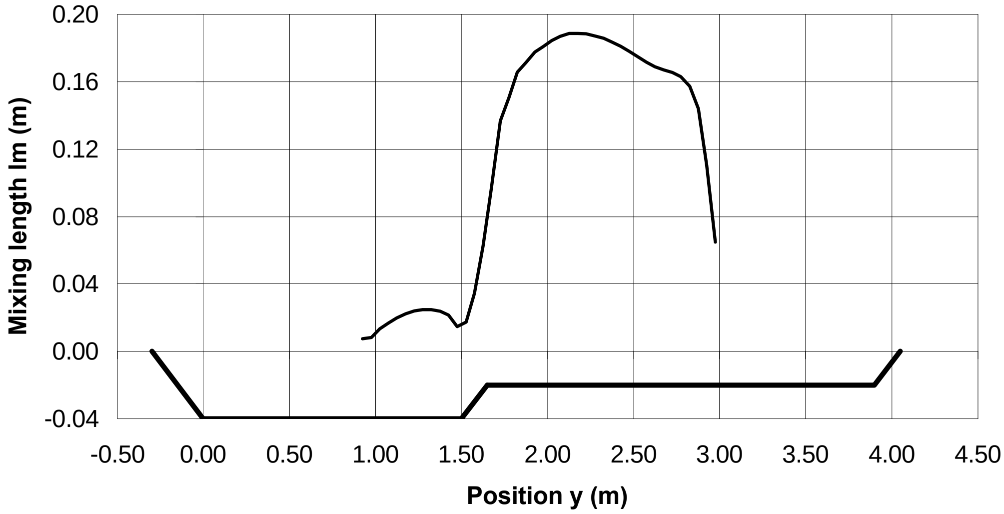

Figure 10.4 : FCF 060501, Prandtl mixing-length l_m profile

This last observation could be due to the effect of the large value of the SDS-viscosity υ_S when compared to the υ_L value (Figure 10.2). A further simulation is thus tentatively performed, starting from the already perturbed velocity field, but using now a constant SDS-viscosity $\upsilon_S = 0.25 \times 10^{-3}$ m^2/s, which is a tenth of the maximum υ_S value observed in the main channel for the previous simulation. The resulting large-scale-turbulence shear stress τ_L and mixing length l_m are given respectively on Figure 10.5 and Figure 10.6.

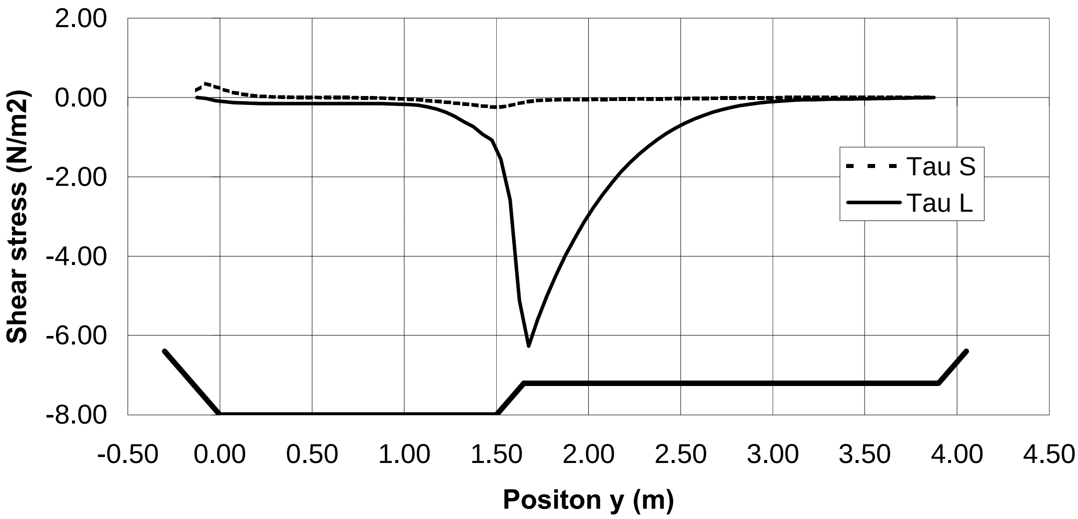

Figure 10.5 : FCF 060501, simulation with constant υ_S : SDS τ_S and large-scale-turbulence τ_L shear-stress profiles

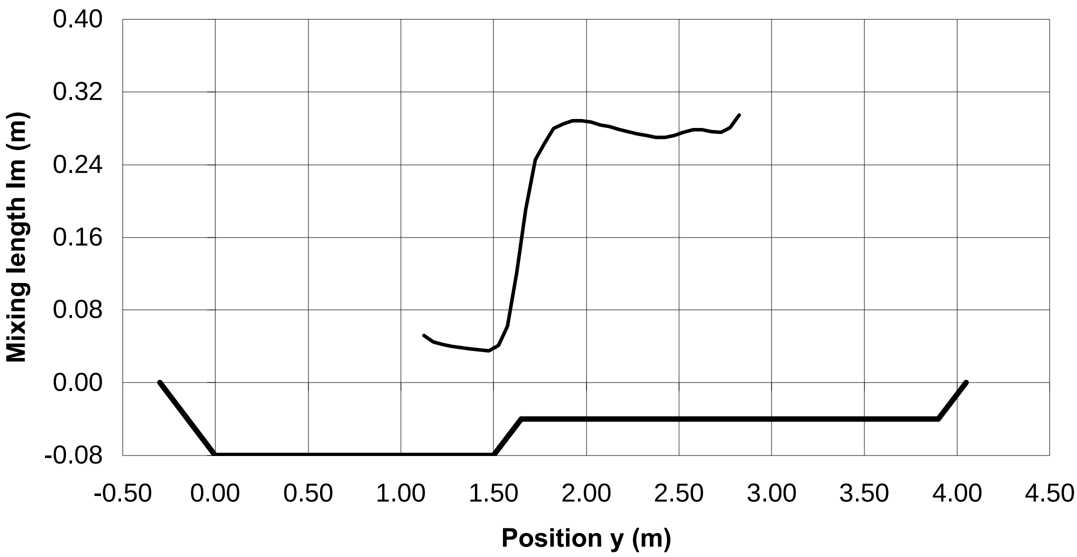

Figure 10.6 : FCF 060501, simulation with constant υ_S : Prandtl mixing-length l_m profile

Observations similar to the ones for the variable-viscosity simulation can be made. The additional shear-stress τ_L peak is observed in the interface area, and is now one order of magnitude larger than the SDS shear stress τ_S. It should also be pointed out that this shear-stress τ_l profile appears as very skewed. It is not symmetric, as in a classical shear layer, probably due to the water-depth variation across the interface. Regarding the mixing-length l_m values, two plateau's are again obtained, respectively in the main channel and in the floodplain. For this simulation, the transition between both values is smoother. The plateau values l_m are also around twice larger than the ones obtained with the larger SDS viscosity. However, their ratio does not match better with the water-depth ratio H_r.

A last clue of the possible validity of the mixing-length model is to be found in the mixing-length l_m value. Indeed, the latter is expected to be closely linked with the large turbulent-structures scale (Liggett 1994). In the present case, the mixing-length value on the floodplain equals $l_m = 0.28$ m, which is found at least in the same range as the shear-layer width $l_s* = 0.50$ m estimated after the vortex merging.

10.3 Momentum balance

The momentum-transfer process will now be further explored through the local balance of the momentum flow in each subsection. This balance is established on the basis of the Saint-Venant x-wise momentum equation (2.29), written in the conservative form. In the present analysis, the bed and friction slopes are assumed to be in equilibrium, and the diffusion terms (SDS turbulence) are neglected. The main-channel momentum-flow $M_c(x)$ in a given section is obtained by transverse integration of the momentum flow along the main-channel width :

$$M_c = \rho \int_{mc} \left(U^2 H + \tfrac{1}{2} g H^2 \right) dy \tag{10.6}$$

The momentum-flow variation DM_c is obtained by deriving M_c with regard to the channel length x, and by adding the temporal derivative of UH :

$$\begin{aligned} DM_c &= \frac{\partial}{\partial x}\left[\rho \int_{mc} \left(U^2 H + \tfrac{1}{2} g H^2 \right) dy \right] + \rho \int_{mc} \left(\frac{\partial}{\partial t}(UH) \right) dy \\ &= \rho \int_{mc} \left(\frac{\partial}{\partial x}\left(U^2 H + \tfrac{1}{2} g H^2 \right) + \frac{\partial}{\partial t}(UH) \right) dy \end{aligned} \tag{10.7}$$

The floodplain momentum-flow $M_f(x)$ and its variation DM_f are defined similarly, performing the integration along the floodplain width. According to the x-wise momentum equation, one gets finally the following balance :

$$\rho UVH = -DM_c = DM_f \tag{10.8}$$

where ρUVH equals the local shear force acting on the vertical division line at the interface. Its length-averaged value corresponds to the large-scale-turbulence shear stress τ_L (10.3), multiplied by the water-depth H.

Thanks to the cyclic boundary condition used in the simulations, it is possible to analyse the momentum-flow variations along the channel length at a given time. Such an analysis is similar to an analysis of the temporal variation of the momentum flow, for a pseudo-steady flow corresponding to the vortices development at the time investigated. Figure 10.7 gives the spatial variation of the momentum-flow at t = 150 s, when vortices are developed but not yet merged together (see Figure 8.11). This graph shows first that the balance (10.8) is actually verified. The small discrepancies observed are due to neglected slope terms and SDS-turbulence shear.

Figure 10.7 depicts the alternation of positive and negative transverse shearing, corresponding to the oscillating turbulent-exchange discharge suggested by the EDM. In fact, this illustrates that the momentum-transfer mechanism is not governed by an explicit net momentum transfer. The total momentum available remains almost constant (see Table 10.2), but, as suggested by Figure 10.8, a part of the main-channel momentum is temporarily transferred to the floodplain, between vortices (B); while the main-channel presents its maximum momentum flow only at stations corresponding to the vortex centres (C). As a result, the averaged momentum flow is decreased in the main-channel and increased on the floodplain.

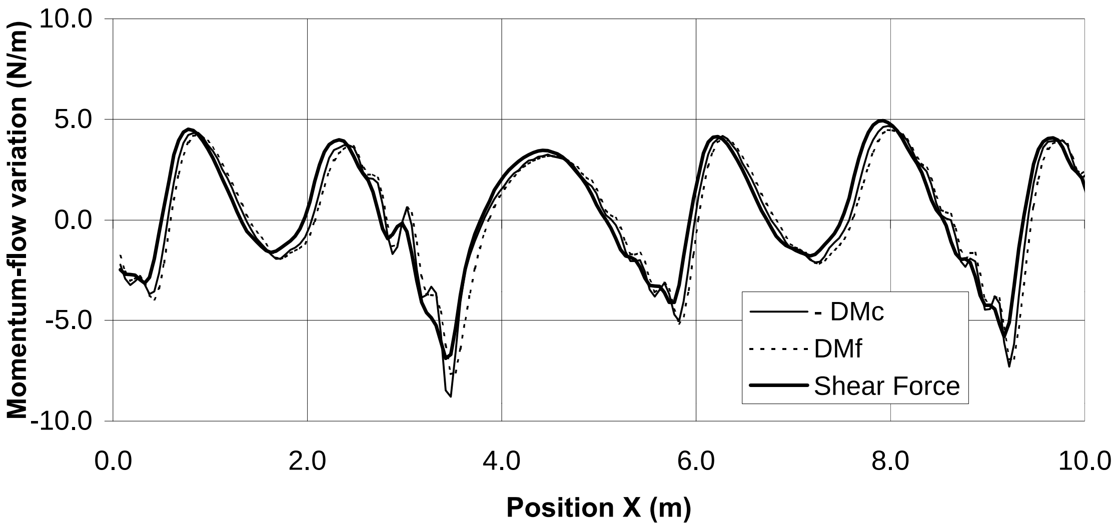

Figure 10.7 : FCF 060501, momentum-flow variations along channel length, t = 150 s (part of the channel length, a positive value indicates an increasing floodplain momentum)

This explanation is further validated by Table 10.2 that presents the momentum-flow values in each subsection and in the whole channel at some given times. The length-averaged values show first that, in accordance with classical explanations of the momentum transfer in a compound channel, the momentum flow decreases in the main-channel when vortices develop, while it increases on the floodplain, resulting however in a reduction of the total channel momentum. Secondly, the local values at vortex centre and between vortices show the alternation of increased and decreased momentum flow, as described above (Figure 10.8), while the total momentum remains almost constant for a given time.

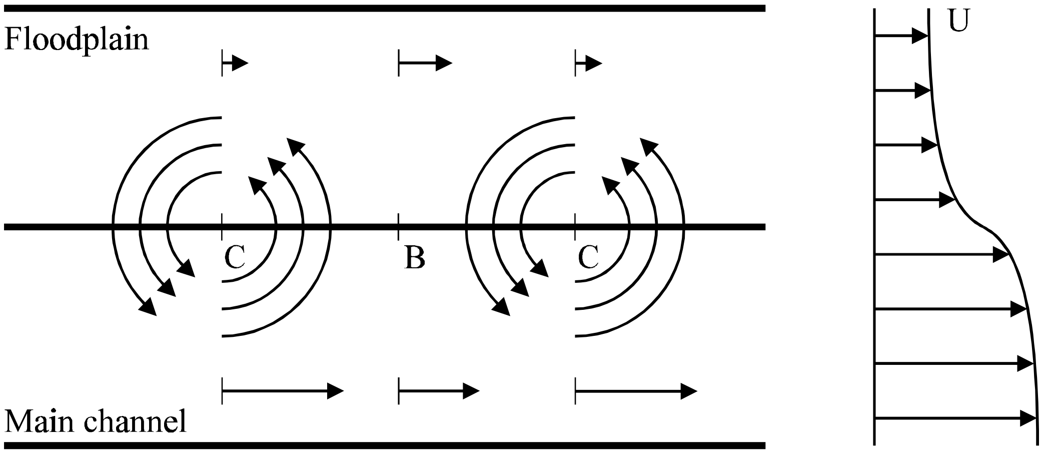

Figure 10.8 : Schematic view of the supposed momentum transfer mechanism

Table 10.2 : FCF 060501, subsection momentum-flow values

Time t (s)	Location	M_c (N)	M_f (N)	$M_c + M_f$ (N)
0	Averaged	**598.8**	**43.3**	**642.1**
125	Averaged	**593.9**	**44.9**	**638.8**
	At vortex centre	595.1	43.5	638.6
	Between vortices	592.5	46.5	639.0
150	Averaged	**589.7**	**46.1**	**635.8**
	At vortex centre	592.4	42.1	634.5
	Between vortices	586.1	50.1	636.2
300	Averaged	**578.7**	**47.1**	**625.8**
	At vortex centre	585.0	39.3	624.3
	Between vortices	572.7	54.7	627.4

10.4 Vortex model

As suggested in the previous paragraph, the momentum transfer mechanism is closely linked with the vortex behaviour. Indeed, the longitudinally-averaged transverse shear force $\tau_L H$ depends on the local shear force ρUVH; and the latter depends on the vortex-circulation $\Gamma = \int r\,v\,d\theta$, where v stands now for the tangential velocity at a distance r from the vortex centre. As pointed out in Chapter 5, Lukowicz and Könteger (1999) showed that the shape of the vortices they observed in compound channel can be approximated by an Oseen-vortex equation. The shape of vortices obtained in the present simulations will be similarly compared with the Oseen equation, and its links with the general parameters of the flow will be shortly discussed.

The equation describing the Oseen vortex, or Gaussian vortex, is obtained by the integration of the two-dimensional Navier-Stokes momentum equation, written for cylindrical coordinates, assuming an axial symmetry and neglecting the gravity effect (Truckenbrodt 1968) :

$$\frac{\partial v}{\partial t} = \upsilon \left(\frac{\partial^2 v}{\partial r^2} + \frac{1}{r}\frac{\partial v}{\partial r} - \frac{v}{r^2} \right) \tag{10.9}$$

where r is the distance from the symmetry centre; and $v(t, r)$ is the tangential velocity. The radial velocity equals zero, due to the axial symmetry assumption. Integrating (10.9), one gets the vortex velocity distribution as a function of the distance to the vortex centre

$$v(t,r) = \frac{\Gamma_\infty}{2\pi r}\left[1 - \exp\left(-\frac{r^2}{r_t^2}\right)\right] \quad \text{with} \quad r_t^2 = 4\upsilon\,(t_0 + t) \tag{10.10}$$

where Γ_∞ is the circulation at $r = \infty$; r_t is a radius scale; and t_0 is an initial time.

The corresponding circulation profile is given by

$$\Gamma = 2\pi v(t,r) = \Gamma_\infty \left[1 - \exp\left(-\frac{r^2}{r_t^2}\right)\right] \tag{10.11}$$

For small radii $r < r_t$, the Oseen vortex behave like a rigid body, and the velocity and circulation increase accordingly (Figure 10.9). For the large radii $r > r_t$, the Oseen vortex behave like a potential vortex : the circulation remains constant $\Gamma \rightarrow \Gamma_\infty$, and the velocity decreases asymptotically to zero. In an unconstrained situation, the radius scale r_t will grow with time and the vortex will develop accordingly.

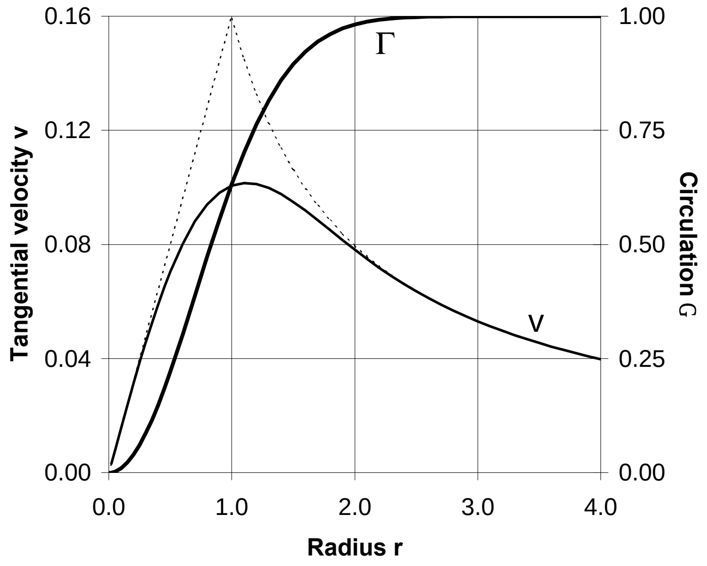

Figure 10.9 : Oseen vortex, velocity v and circulation Γ profiles, for $\Gamma_\infty = 1$ and $r_t = 1$

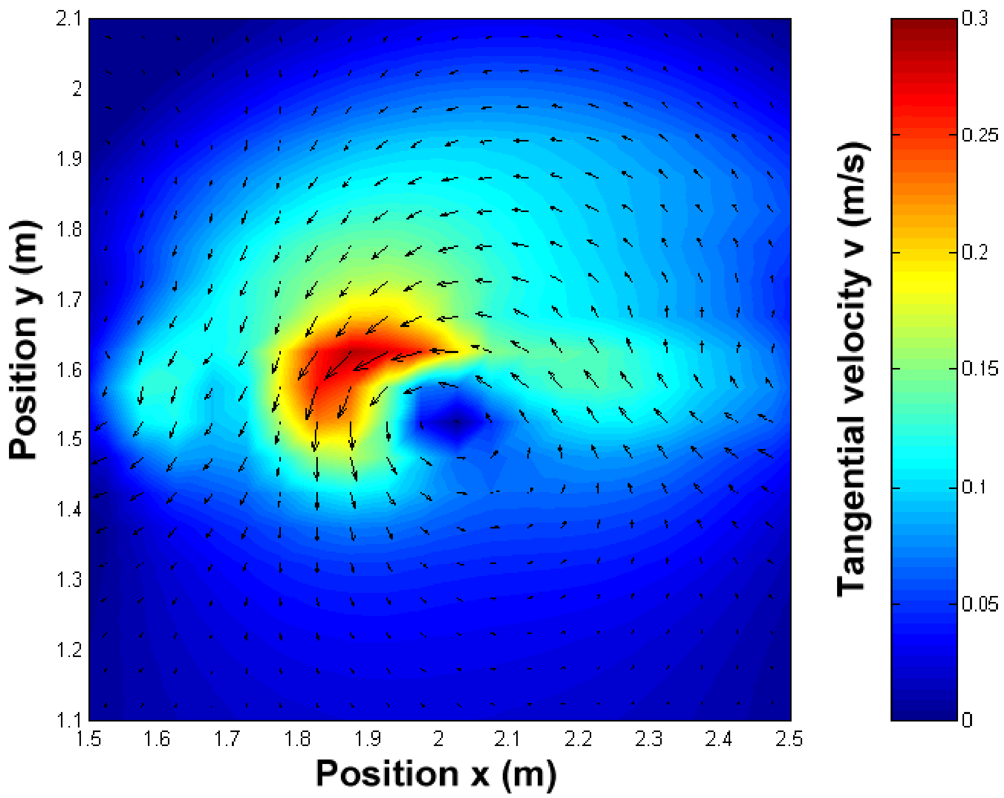

Figure 10.10 : FCF 060501 case, t = 150 s, unit-discharge-fluctuation field (U'H, V'H) and intensity of the tangential velocity v (part of the domain)

In the present case, it is suggested that the vortices observed in a compound-channel flow can be approximated by Oseen vortices, linearly superposed to the averaged flow. Figure 10.10 shows such a vortex from the FCF 060501 simulation, at t = 150 s, where the fluctuations (U', V') of the velocities are given by (10.2), and where the velocities are multiplied by the water depth H, in order to depict more clearly the continuity through the interface between subsection. Although the plotted vortex do not present a perfect axial symmetry, its shape agree approximately with the Gaussian vortex, with a rigid-body centre and a decrease of the tangential velocity at a further distance.

For further analysis, vortex-circulation profiles are given on Figure 10.11, at the time t = 125 s and t = 150 s, the latter corresponding to the vortex plotted on Figure 10.10. The vortex-circulation estimated with the Oseen equation (10.11) agrees well with the numerically computed one, as far as appropriate values of the circulation Γ_∞ and of the radius scale r_t are used. For radii larger than r = 0.50 m, the quality of the matching between both profiles decreases, as the numerically-simulated vortices are limited in space, due to other adjacent vortices and to the walls, whereas the Oseen vortex develops in an infinite space.

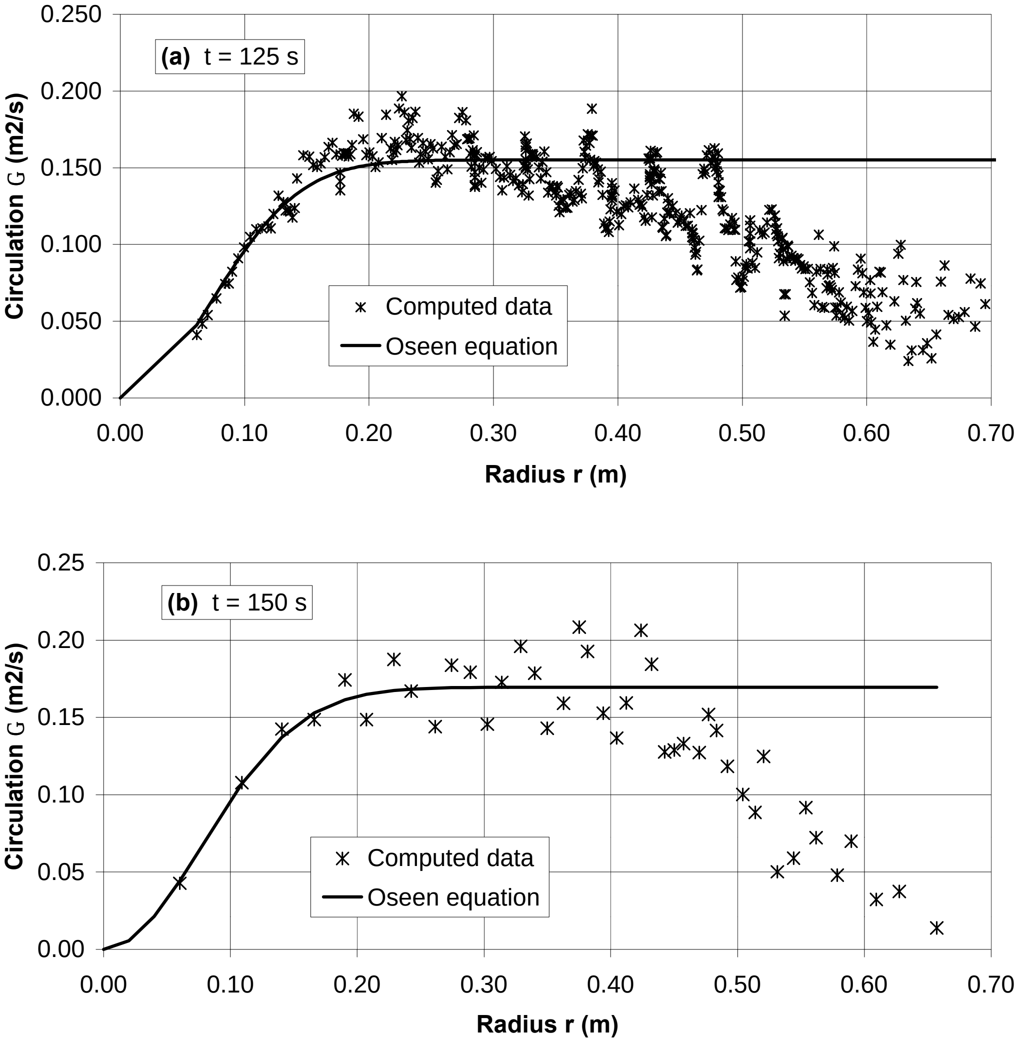

Figure 10.11 : FCF 060501, vortex circulation : computed values and Oseen equation

Table 10.3 : Oseen vortices, characteristic values, compared to the averaged flow

	Length scale	Circulation scale
Oseen equation, $t = 125$ s	$r_t = 0.10$ m	$\Gamma_\infty = 0.16$ m^2/s
Oseen equation, $t = 150$ s	$r_t = 0.11$ m	$\Gamma_\infty = 0.17$ m^2/s
Averaged flow $\overline{U}$, $t = 150$ s	$l_s{*} = 0.27$ m	$2\pi\, l_s{*}\, U_s{*} = 0.48$ m^2/s

The Oseen-equation parameter Γ_∞ and r_t values are summarised in Table 10.3. Due to the vortex development, the values at $t = 150$ s are slightly larger than at $t = 125$ s. These values are compared with typical values from the averaged-flow profile $\overline{U}(y)$. Indeed, it can be expected that the observed vortices are closely linked to the flow in which they develop. The typical length scale for the averaged flow is the shear-layer width $l_s{*}$, which is almost three times larger than the vortex-radius scale r_t. This shear-layer width could be linked with the radius $3r_t$ where the Oseen-vortex circulation has reach the value Γ_∞ (see Figure 10.11), meaning that, outside this area, the flow could be dominated by the averaged flow. On the other hand, it could also be suggested that the vortex circulation is proportional to the velocity difference $2U_s{*}$ between the main channel and the floodplain, at least when considering the driving of the rigid-body part of the vortex. However, a first comparison between the actual circulation and an estimation based on both length and velocity scale $l_s{*}$ and $U_s{*}$ is not convincing.

10.5 Conclusion

When developing the EDM, it has been assumed that the momentum transfer corresponding to the turbulent-exchange discharge q^t (4.10) can be expressed as

$$q^t \Delta U = \psi^t \, \Delta U \left|\Delta U\right| \left(H - h_f\right) \tag{10.12}$$

where ΔU is the velocity difference between main-channel and floodplain. This expression was founded on a model analogous to a mixing-length model.

The analyses in the present Chapter have shown that, when considering a two-dimensional modelling, the mixing-length model was indeed appropriate for depicting the momentum transfer, and that the estimated mixing length could probably be linked to a certain extend with the shear-layer width. The momentum-transfer mechanism in itself has also been depicted through momentum-balance analysis, showing the effect of the actual alternation of the direction of the flow through the interface. This effect is similar to the EDM-supposed oscillating turbulent-exchange discharge. Lastly, some vortex characteristics have been investigated, through a comparison with the Oseen-vortex equation. This showed again that the velocity difference between subsection and the shear-layer width are significant parameters. Regarding the EDM, whereas the velocity difference is explicitly used in the momentum transfer expression (10.12), the shear-layer width is expected to be linked with the ψ^t parameter, which was already identified as a mixing-length-related parameter (see Chapter 4).

All the presented results should obviously be extended to other test cases, in order to identify possible relations between the quoted parameters. However, before performing these additional analyses, the weaknesses of the two-dimensional numerical model should be corrected. Among these weaknesses, the main point to handle is probably the SDS-turbulence model, as it has been showed that using a lower υ_S value could strongly influence the estimation of the large-scale-turbulence shearing.

Nevertheless, these results already tend to indicate an appropriate modelling by the EDM of the momentum-transfer mechanism due to horizontal vortices. However, whereas the EDM has proved to give accurate results for whole-cross-section discharge, some weakness regarding the subsection discharge prediction was also reported in Chapter 4. According to the present results, the cause of this failing is not to be looked for in the vortex modelling. Probably the secondary-current effect investigated in Chapter 9 could justify partly this problem, as nothing in the EDM can handle this phenomena.

Part III

Geometrical transfer

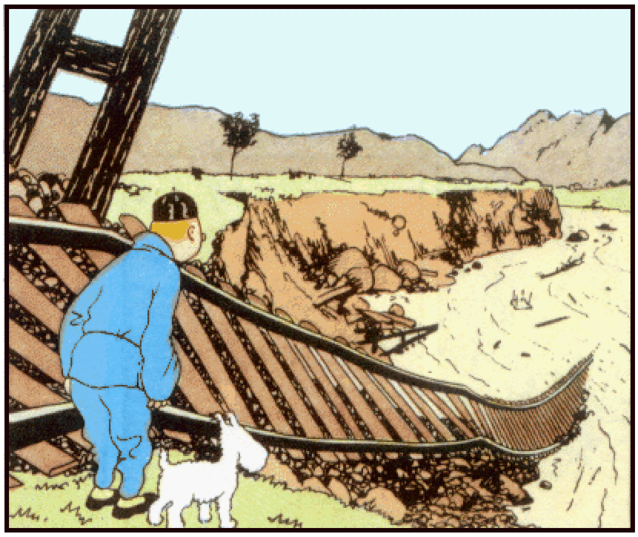

A flood on the Yang-Tse River,
in Hergé (1946), Le Lotus Bleu

Chapter 11
Flow in non-prismatic compound channels : State of the art

11.1 Introduction

When developing the Exchange Discharge Model in Chapter 4, a so-called geometrical-transfer discharge was defined at the interface between main-channel and floodplain, in addition to the turbulent-exchange discharge already investigated in Part II of this work. This geometrical-transfer discharge results from cross-section-area changes on the channel length, when floodplains width varies due either to the main-channel meandering, or to a valley constriction. Through the associated momentum transfer, the EDM attempts to model the effect on the stage-discharge relation of such a mass transfer between subsections.

The purpose of the third Part of this work is therefore to investigate further this geometrical-transfer concept and to clarify the significance of the ψ^g parameter used in its modelling. New experiments have been specifically designed for that purpose : flow measurements are performed in a symmetrical compound channel with narrowing floodplains, rather than in a meandering compound channel as in most of the previous studies dealing with non-prismaticity. Indeed, in such a geometry, the effect of mass transfer can be clearly highlighted, without additional curvature effects as in a meandering case.

After a short state-of-the-art supplement given in this Chapter, new experimental results will be presented for the novel geometry suggested above. These results will be used to validate both the extended Lateral Distribution Method proposed in Chapter 3, and the EDM. Lastly, one will shortly present and discuss some additional measurements made in a prismatic channel where geometrical transfer occurs due to the flow non-uniformity near a control section.

11.2 Flow in a meandering compound channel

11.2.1 Experimental observations

Toebes and Sooky (1967) performed some of the first experiments on meandering compound channels. They investigated the stage-discharge relationship for several geometries and measured a higher conveyance-reduction in meandering channels than in prismatic channel, due to the stronger interaction between the floodplains and the sinuosity of the main channel. They also observed that, for the overbank-flow case, the helical flow in the main-channel meanders rotates in the opposite direction compared to the inbank-flow case, due to floodplain water crossing over the main-channel.

The large scale Wallingford Flood Channel Facility (FCF) enabled the investigation of a complete set of meandering compound channels geometries (Sellin et al. 1993). These experiments again highlighted a conveyance reduction that increases with the main-channel sinuosity. Nevertheless, this sinuosity effect decreases with increasing water depth on the floodplain, as the floodplain flow becomes predominant. The secondary-current pattern was also depicted more accurately (Figure 11.1). In the crossover fraction of the main channel, floodplain water plunges into the main channel, reaching the channel bottom around its centre line; while in bend apex, a part of main-channel water is ejected towards the downstream floodplain. In both areas, strong mass transfer were thus observed, with corresponding momentum transfer. Using Laser-Doppler Anemometer measurements in a smaller flume, Shiono and Muto (1998) have confirmed the previous observations and shown the predominance of the horizontal shearing in the generation of secondary currents.

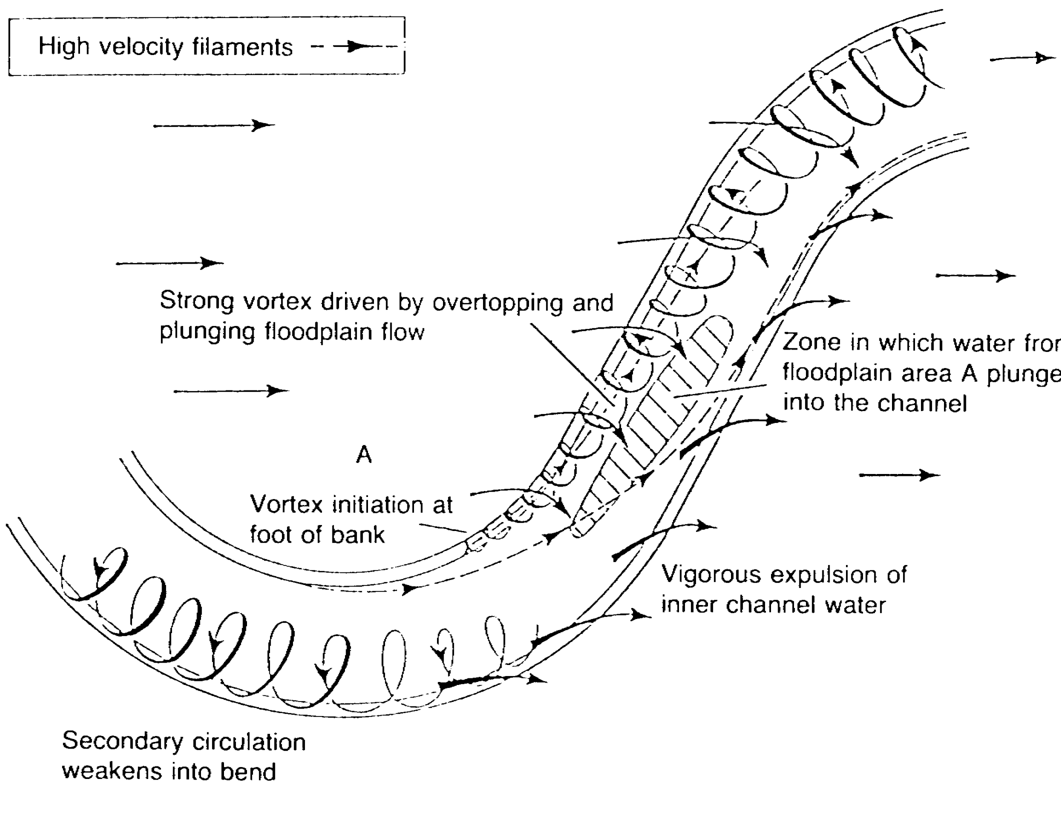

Figure 11.1 : Flow structure in a meandering compound channel (Sellin et al. 1993)

11.2.2 Skewed compound channels

A second set of experiments related to mass transfer was performed in the FCF for the simplified geometry given on Figure 11.2, where a straight main-channel is skewed to a straight floodplain (Elliott and Sellin 1990). The same kind of experiments has also been performed at a smaller scale by Jasem (1990). In both cases, the main effects of the mass transfer due to skewness were clearly identified : (1) the velocity decreases in the main channel, due to the inflow of slower water from the narrowing floodplain; (2) the velocity increases on the enlarging floodplain, due to the inflow of faster main-channel water; (3) the total conveyance decreases; and (4) a momentum transfer is associated to the mass transfer, and has been quantified as an apparent shear stress at the interface. The development of a helical secondary-current was also observed, presenting a similar shape as in the meandering case, with a plunging zone around the centre line of the main channel.

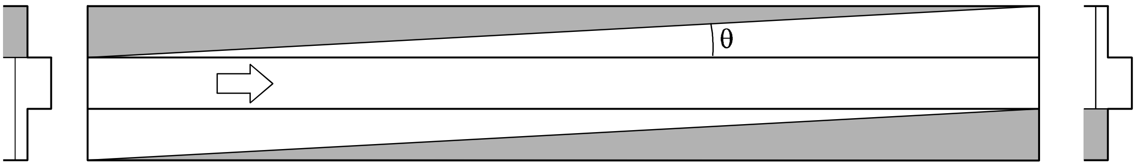

Figure 11.2 : Typical skewed channel geometry, as investigated by Elliott and Sellin (1990) and Jasem (1990)

11.2.3 Calculation advances

Using the FCF meandering-channel results, Greenhill and Sellin (1993) developed an adapted version of the Divided Channel Method (DCM), dedicated to meandering channel modelling. In the classical DCM for prismatic channels, the compound-channel cross-section is divided by vertical division lines into three sub-sections (Figure 1.1), and the total discharge is then calculated as the sum of the 3 subsections discharges computed separately. In their method, Greenhill and Sellin propose a cross-section division adapted to meandering channels, using an horizontal division line at the main-channel bank level (Figure 11.3). This results in the following subsections : (1) the inbank part of the main-channel, (2) the floodplain within the meander-belt width, and (3) the floodplain outside the meander belt. Moreover, the length of the division lines between both floodplains parts is added to the wetted perimeter of the floodplain subsection 2 in order to decrease its hydraulic radius and to reduce its conveyance, as a substitute to the momentum effect of the mass transfer. Although this method proved its accuracy against FCF data, some of its parameters, like the meander-belt width or the inbank depth, could be difficult to estimate for natural rivers.

Ervine et al. (1993) used the same approach of an adapted DCM to analyse FCF data, but without developing a computational strategy. They defined the ratio F^* between the actual measured discharge and the discharge evaluated by the adapted-DCM. A low value of this ratio F^* indicates a high momentum transfer. Such low F^* values are observed (1) when channel sinuosity increases; (2) when the main-channel aspect ratio reduces (width to depth ratio); and (3) when the meander-belt width increases compared to the total floodway width.

Shiono et al. (1999) recently proposed an empirical formula, based on a quite large set of data. This formula gives good results on the tested data but, like most of empirical formulae, could be difficult to apply to other situations. Lastly, Ervine et al. (2000) developed a new version of the Lateral Distribution Method, as presented in Chapter 3, equation (3.15). This LDM includes a secondary-current term taking into account transverse velocities in the cross-section of a meandering compound-channel; but, again, it requires a parameter that has to be empirically estimated.

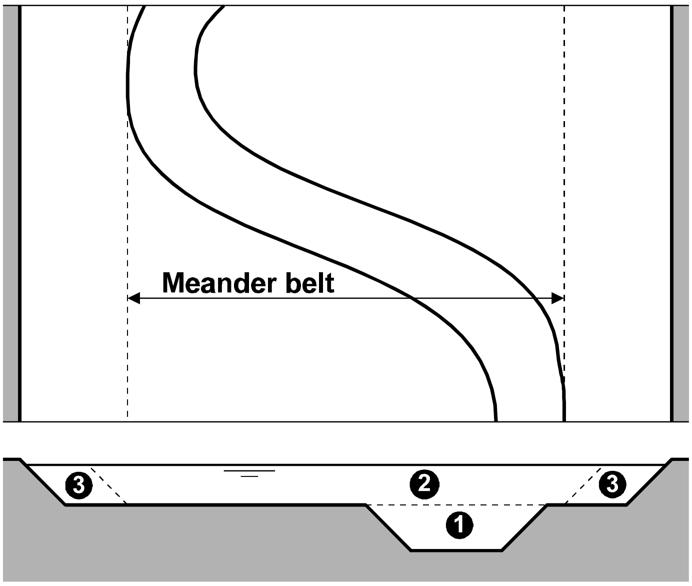

Figure 11.3 : DCM modification by Greenhill and Sellin (1993) : definition of subsections and of the meander belt.

Chapter 12
Experimental measurements of the flow in a symmetrically narrowing compound channel

12.1 Introduction

As detailed in Chapter 1 and 11, both prismatic and meandering compound-channels geometries have been extensively investigated in laboratory flumes. While several computational methods have been successfully developed for prismatic channels (see Chapter 1), fewer methods have been proposed for meandering channels. These methods (presented in § 11.2.3), are either empirical or not fully compatible with the prismatic channel ones, as they use subsection divisions dedicated to meandering geometry. One of the difficulties linked with the interpretation of meandering channel experiments and with the subsequent development of computational methods is the superposition of mass transfer and effects of secondary currents due to curvature.

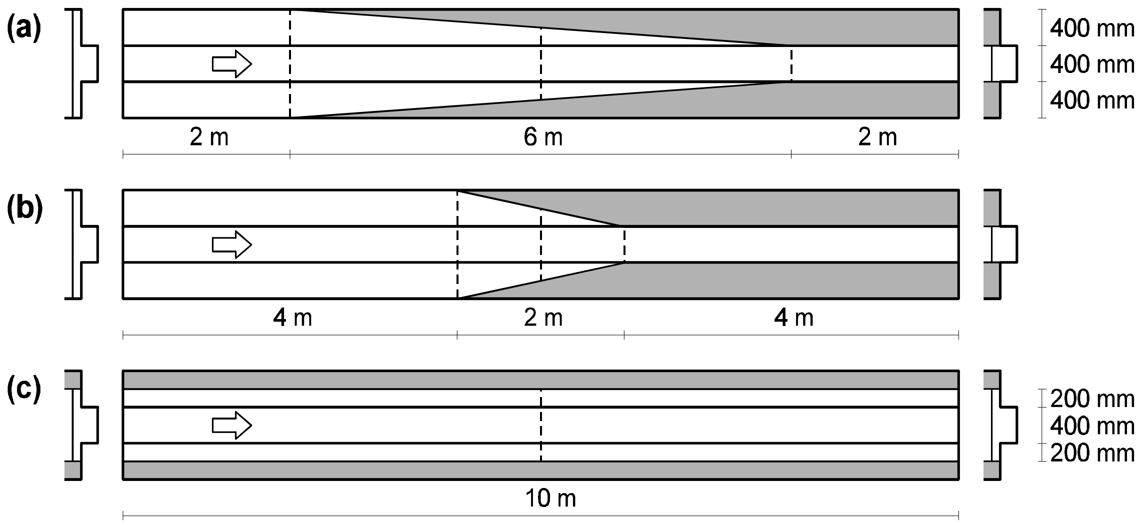

Figure 12.1 : Plan view and typical cross-section of the tested geometries; (a) 6-m length narrowing floodplains; (b) 2-m length narrowing floodplains; and (c) prismatic channel with 200-mm width floodplains.

The present Chapter investigates therefore a simplified configuration with a straight main-channel, flanked by two symmetrical narrowing floodplains (Figure 12.1). It is expected that, due to the decrease of floodplains width, a mass transfer will occur from floodplain to main channel, that is similar to the one observed in a meandering channel of, at least, small sinuosity. On the other hand, thanks to the symmetry of the studied geometries, the secondary currents generated in the main-channel will affect weakly the momentum balance between floodplains and main channel, and will probably develop less than in a meandering channel.

From the experiments, the flow structure will be depicted in details, the mass transfer will be evaluated, and the momentum balance between floodplains and main channel will be estimated quantitatively. A second set of experiments is performed in a prismatic compound channel, enabling the comparison between the flows in a similar cross-section, with and without mass transfer. This comparison will highlight the additional head loss due to this mass transfer, which will be found to be significant with regard to the frictional losses. Lastly, these results will then be used in next Chapters to validate the extension of the LDM proposed in Chapter 3 for non-prismatic geometry; and the geometrical-transfer modelling in the EDM. The additional head loss computed by the EDM will be compared with the measured one.

12.2 Experimental set-up

Experiments were performed in the UCL compound-channel flume already depicted in Chapter 6. This flume is 10-m long and 1.20-m wide, with a bottom slope set at $S_0 = 0.99 \times 10^{-3}$, and a maximum available discharge Q = 30 l/s. A complete description of this facility and of its equipment is given in Appendix 3.

A symmetrical compound cross-section was build in this flume using coated plywood, with two floodplains 400-mm width and 50-mm high (Figure 12.1). Movable vertical plywood embankments were used to form the different channel planform geometries : (1) main-channel only; (2) prismatic symmetrical compound channel with 200-mm width (Figure 12.1c) or 400-mm width floodplains; (3) non-prismatic symmetrical compound channel with floodplains narrowing from 400-mm to 0-mm width on a 6-m length (converging angle $\theta = 3.8°$: Figure 12.1a) or on a 2-m length (converging angle $\theta = 11.3°$: Figure 12.1b).

Detailed flow measurements were performed in the narrowing geometries, for several discharges and water depth (Wilkin and Jacquemart 2001; Bousmar et al. 2001). For each given discharge, the downstream water level was adjusted, using the tailgate, in such a way that the backwater profile reaches a given water depth in the central cross section [x = 5 m], where the floodplain width is 200 mm. For 3 selected relative water depth $H_r = (H\text{-}h)/H$ = 0.2; 0.3 and 0.5 in this central cross section, this will enable the comparison of the velocity distribution between similar cross-section geometries but with different discharges and mass-transfer rates. For comparison, detailed velocity distributions were also measured for uniform flows in the prismatic channel with 200 mm-width floodplains, at the same relative depths. Table 12.1 summarises all the tests performed.

Table 12.1 : Experimental cases : geometries and discharges Q tested for the given relative water depth H_r at x = 5 m

Geometry	Q [l/s] for $H_r = 0.2$	Q [l/s] for $H_r = 0.3$	Q [l/s] for $H_r = 0.5$
Floodplains narrowing from 400 to 0 mm in 6 m	10.0	10.0; 12.0	12.0; 16.0; 20.0
Floodplains narrowing from 400 to 0 mm in 2 m	10.0	10.0; 12.0	12.0; 16.0; 20.0
Prismatic, floodplains 200 mm width	9.9	13.4	27.6

For each test in narrowing-floodplains geometries, both water levels and velocities were measured at selected locations. Water levels were recorded along the main-channel centre line and along transverse profiles. Velocities and velocity directions were measured in 4 cross sections (Figure 12.1) : (1) the channel entrance [$x = 0$ m]; (2) the entrance of the narrowing reach [$x = 2$ or 4 m, for the 6- or 2-m narrowing length, respectively]; (3) the central cross section, where the relative depth is imposed [$x = 5$ m]; and (4) the end of the convergence [$x = 8$ or 6 m].

As explained in Appendix 3, water levels were measured using an automatic point gauge meter mounted on a trolley above the flume. The gauge absolute precision is 0.1 mm but, due to small surface oscillations, the actual precision is estimated to 0.2 mm when water is flowing. Velocities were measured using a Pitot tube connected to a low differential pressure manometer. The overall accuracy is estimated to be better than 2 %, by comparison between the discharge obtained by integration of the local velocity measurements and the discharge measured using the electromagnetic flowmeter. The velocity directions were measured using a home-made vane, with an absolute precision of 0.5 °. This precision is rather low, regarding the small transverse velocity components observed in the main-channel, where direction measurements should thus be considered from a qualitative viewpoint. However, on the floodplains, the transverse velocity components are greater and the relative measuring precision is increased.

The roughness coefficient for the flume was estimated using 11 discharge measurements for uniform flows in the isolated main channel, established by adjusting the downstream level using the tailgate. The Manning roughness coefficient for the plywood was found to be equal to $n = 0.0107$ m/s$^{1/3}$. The discharges in uniform flow were also measured for the two prismatic compound channels and a very good fitting was obtained between the measured discharge and the ones computed by the EDM without any further roughness-value adjustment (Figure 12.2). This provides an additional validation of the EDM, for prismatic compound-channel flow.

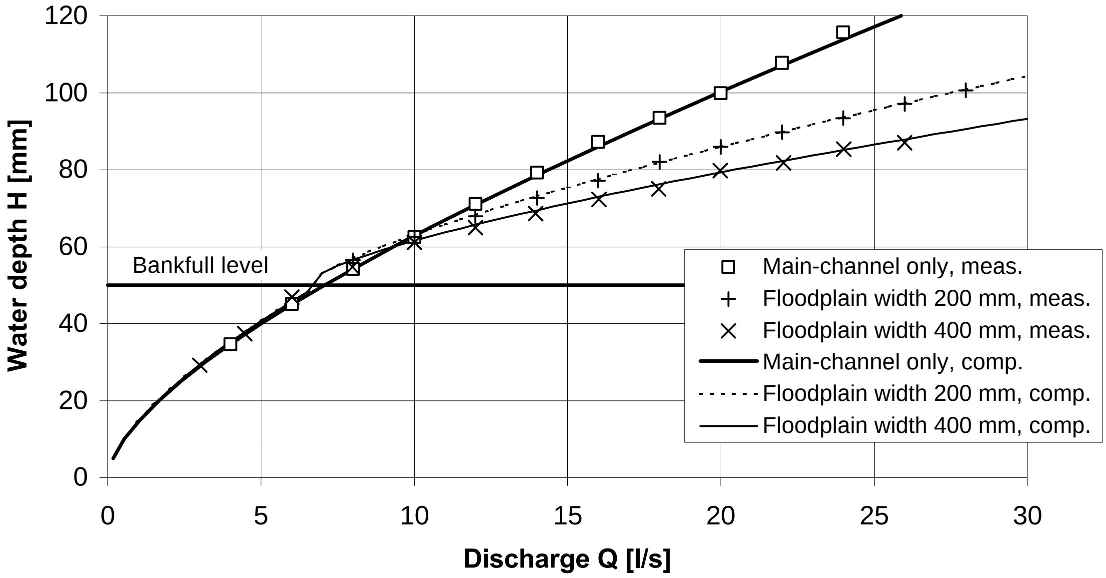

Figure 12.2 : Uniform flow in main-channel only and in prismatic compound channel (floodplain width = 200 or 400 mm) : measured data and EDM-computed values

12.3 Experimental results : flow description

The longitudinal water profiles measured for the case of 2-m long contraction are plotted on Figure 12.3. Specific flow behaviour can already be identified for the 3 successive parts of the geometry. In the upstream prismatic part of the channel ($0 < x < 4$ m), the water depth remains constant or increases slightly for the highest discharge (M1 profile) as the flow increases its specific energy before entering the constricting reach. In the constricting reach ($4 < x < 6$ m), there is a plunging profile, as the flow is accelerated. The water level slope increases logically for an increasing discharge at a given water depth; or for a decreasing water depth at a given discharge (M2-kind profile). In the downstream prismatic reach (where only main-channel flows, $6 < x < 10$ m), there is either a M1 or a M2 profile, depending on the level imposed by the tailgate. The scattering of some profiles is due to cross-waves generated by the angle between the contracting and the prismatic sections. These cross-waves are more apparent for the M2 than for M1 profiles. Similar observations are obtained for case of 6-m long contraction.

Transverse water profiles were also measured but, in no case, significant level differences were observed between the main-channel and the floodplains, with regard to the measurement accuracy (± 0.2 mm).

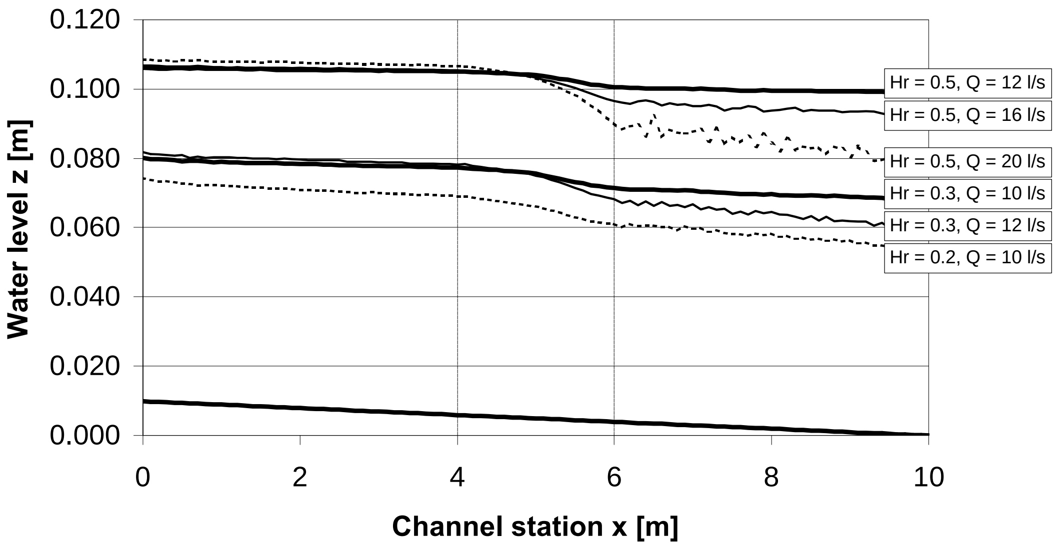

Figure 12.3 : Measured water profiles, 2-m length narrowing case. Tailgate is adjusted in such a way that the water level at station x = 5 m remains constant for a given H_r

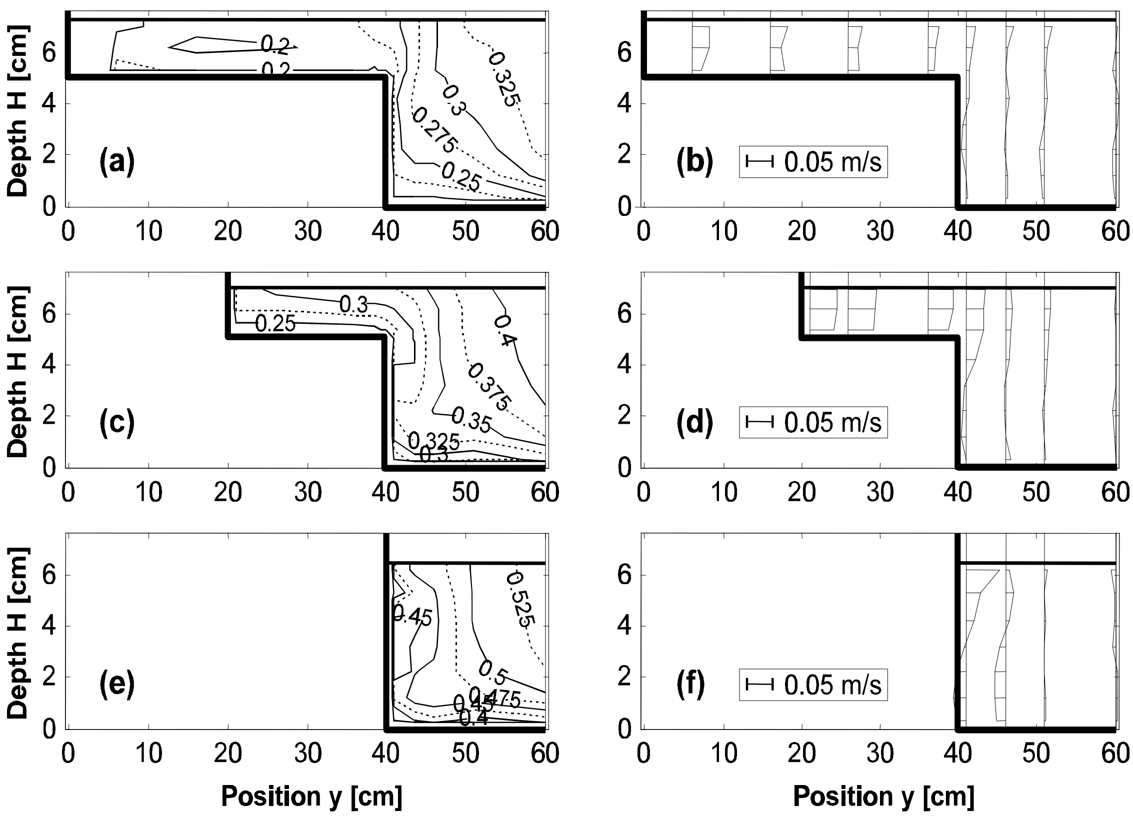

Figure 12.4 : Velocity distribution on half-channel width, 2-m length narrowing case, H_r = 0.3, Q = 12 l/s : (a, c, e) longitudinal velocity components (m/s); (b, d, f) transverse velocity components (m/s); (a-b) x = 4 m; (c-d) x = 5 m; (e-f) x = 6 m

The distribution of longitudinal and transverse velocity components is given on Figure 12.4 for 3 cross-section (x = 4, 5 and 6 m) of the 2-m length narrowing case, for relative depth $H_r = 0.3$ at $x = 5$ m and discharge $Q = 12$ l/s. This shows clearly the effects of the contraction : (1) the maximum velocity increases along the channel, as the cross-section area decreases; (2) the flow on the floodplain presents a transverse component towards the main-channel, corresponding to the water forced to leave the floodplain; (3) as a result, there is locally a slight decrease of the longitudinal velocity component in the main-channel, near the interface, due to the inflow of slower water from the floodplain; (4) the transverse component of the velocity, above the bank level, develops until the main-channel centre line (this mass transfer enables the modification of the flow distribution); and (5) in cross-section planes, this surface current seems to generate a secondary current cell in the inbank part of the main-channel. Similar observations are obtained for the other cases.

The depth-averaged longitudinal-velocity profiles for the same case is given in Figure 12.5. Again the flow acceleration is clearly depicted and, although the difference between maximum and minimum velocity does not change in value, the ratio of this difference to the maximum velocity is decreasing. Indeed, to ensure the mass balance depicted by the continuity equation (4.2) when the floodplain width decreases, the velocity has to increase in the downstream part of the floodplain, while another part of the discharge is transferred to the main-channel. The velocities are plotted in plan view on Figure 12.6, where depth-averaged values have been computed separately for velocities measured respectively above and below the bank-top level. The flow direction on the floodplains is obviously forced by the embankment angle. This direction is also observed in the downstream cross-section, for the velocities at the limit of the floodplain. In the main-channel, the separation of the velocities above and below bank-top level highlights the development of a secondary current cell driven by the floodplain transverse velocities. The slight outwards component of the bottom velocity in the downstream section confirms this secondary flow.

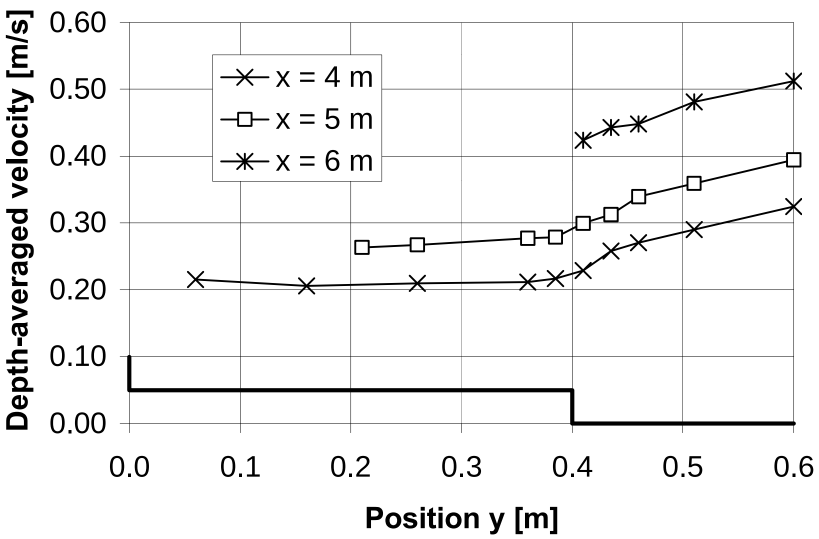

Figure 12.5 : Depth-averaged velocity profiles, 2-m length narrowing case, $H_r = 0.3$, $Q = 12$ l/s

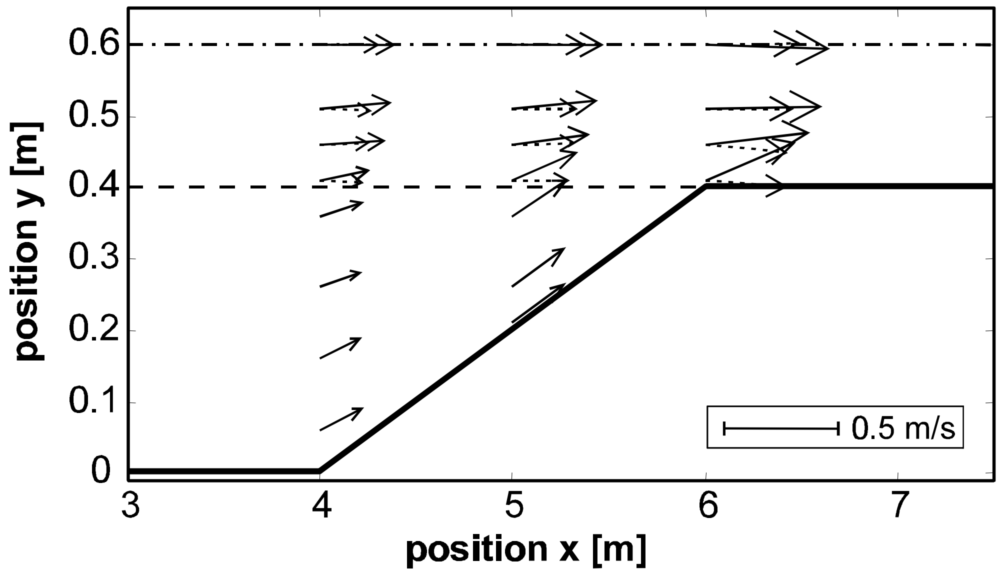

Figure 12.6 : Plan view of depth-averaged velocities, 2-m length narrowing case, H_r = 0.3, Q = 12 l/s : above bank level (solid arrows) and below bank level (dotted arrows)

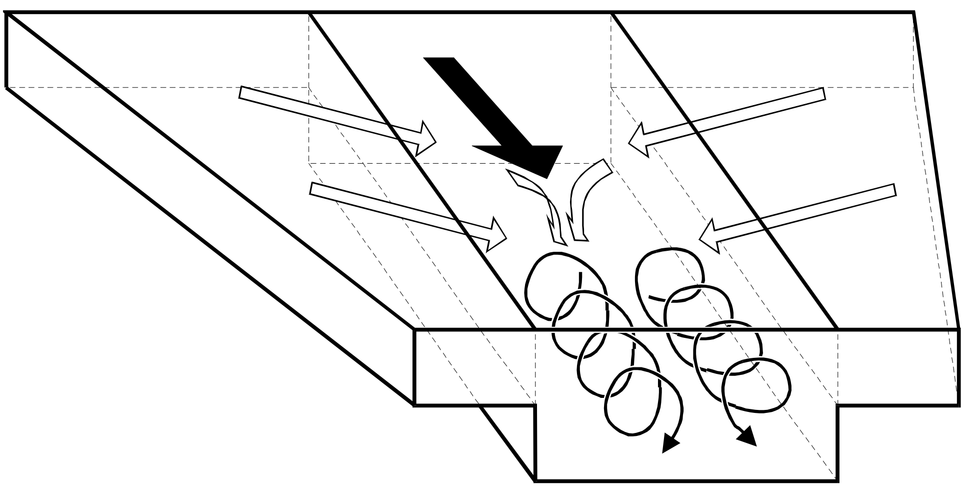

Figure 12.7 : Schematic view of the flow structure in a compound channel with narrowing floodplains

All these observations on the flow structure are synthesised on Figure 12.7 : (1) due to the narrowing floodplains, a transverse current is forced from the floodplain to the main-channel; (2) this current enters the main-channel and, due to symmetry, plunges to the channel bottom around the centre-line; and (3) as a result, a helical flow is generated in the inbank part of the main-channel, rotating back from the centre-line at the bottom to the channel bank. This flow structure is found to be very similar to the one observed in meandering channel, as described in the Chapter 11 (Figure 11.1). Only the effect of sinuosity is of course not observed here. It gives thus confidence in the fact that the constriction case could supply information about the meandering case and that the related model developments could have a wider validity.

12.4 Discharge distribution

The mass transfer between floodplains and main-channel is of primary importance in the development of the observed secondary currents and of the subsequent momentum transfer. The mass transfer can be estimated from the evolution of the discharge distribution along the channel, as plotted on Figure 12.8 for the 6-m length narrowing test cases. It is observed that, for a given geometry and a given relative depth H_r in the central section, the curves corresponding to different total discharges are superposed. This shows that the discharge distribution is almost independent of the total discharge, and, consequently, of the overall frictional losses.

This observation should be compared with the water profiles plotted on Figure 12.3. For a given geometry and a given water depth in the central section, the upstream water level does not change significantly according to the total discharge and, thus, the respective cross-sectional areas of the floodplain and of the main-channel subsections do not change with the discharge, between the entrance and central cross-sections. This indicates once again that the discharge distribution in the converging channel is mainly governed by the geometry and is relatively independent of the frictional losses.

The velocity distributions given in Figure 12.9 for several configurations with a relative depth of $H_r = 0.5$ confirm the similarity between the given flows. While the velocity amplitude depends on the total discharge and, thus, on the frictional losses; neither this total discharge, nor the related frictional losses, nor the floodplain converging angle influence significantly the velocity and discharge distribution. In the three plotted cases the local deceleration of the main-channel velocity near the interface is observed due to the floodplain inflow. The velocity fields present the same aspect and relative intensity. The fact that the velocity distribution does not depend of the friction is of prime interest, when developing a model of the flow. It gives confidence in the EDM estimation of an additional head loss S_a governed by the geometry, whose amplitude is proportional to the frictional losses (see Chapter 4, equation 4.8).

Some further information can be gathered from the discharge distribution evolution given by Figure 12.8 : (1) For a lower water depth, the mass transfer will be lower, as the initial floodplain discharge is also lower; (2) the floodplain discharge evolution seems linear for the lower water depths, while, for higher water depth ($H_r = 0.5$) the mass transfer in the second half of the converging reach ($x > 5$ m) is higher than that in the first ($x < 5$ m). The latter observation is found in accordance with the increased water-level slope at the end of the converging section (Figure 12.3).

From Figure 12.8, it is also observed that a small mass transfer exists before entering the converging reach ($x < 2$ m). Although the flow could indeed anticipate the mass transfer that will occur in the converging reach, just as it increases its specific energy before the contraction, this mass transfer is more probably a bias due to an erroneous discharge distribution forced at the flume entrance, as observed in the asymmetric channel experiments in Chapter 6. The discharge distribution tends towards uniform-flow distribution in the prismatic reach, but this section is not long enough therefore.

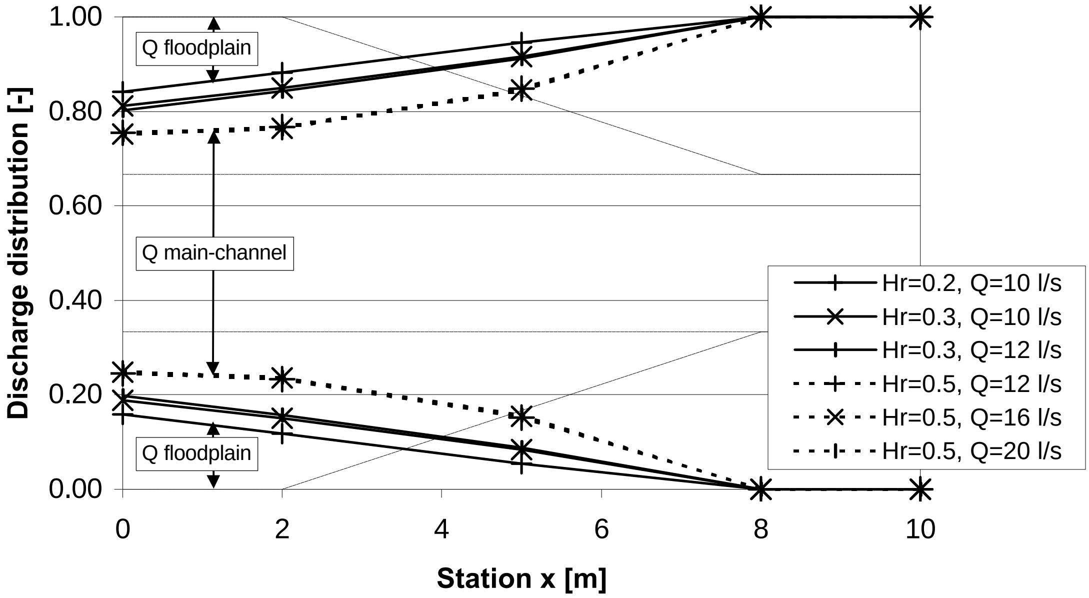

Figure 12.8 : Discharge distribution between subsections, 6-m length narrowing case

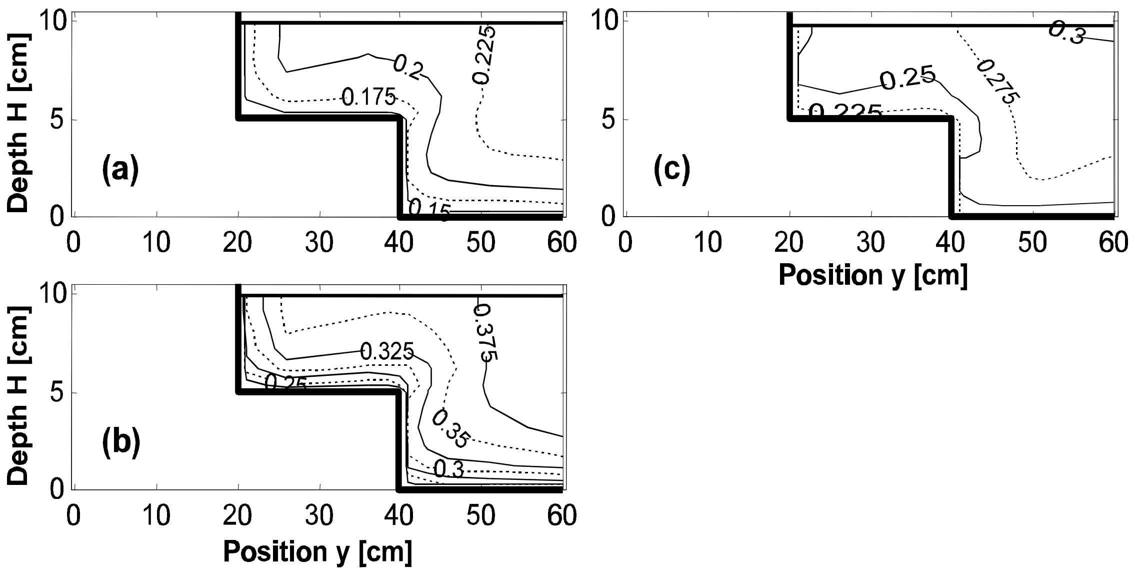

Figure 12.9 : Longitudinal velocity distributions (m/s) at x = 5 m, with H_r = 0.5 : (a) 6-m length case, Q =12 l/s; (b) 6-m length case, Q = 20 l/s; and (c) 2-m length case, Q = 16 l/s

Lastly, the discharge distributions for the converging-floodplains cases, at *x* = 5 m, can be compared with the discharge distribution in the reference prismatic cases (Figure 12.10), as the cross-section geometry is the same for all cases at this station. The discharge distribution is found to be roughly the same for converging geometry and for the equivalent prismatic geometry.

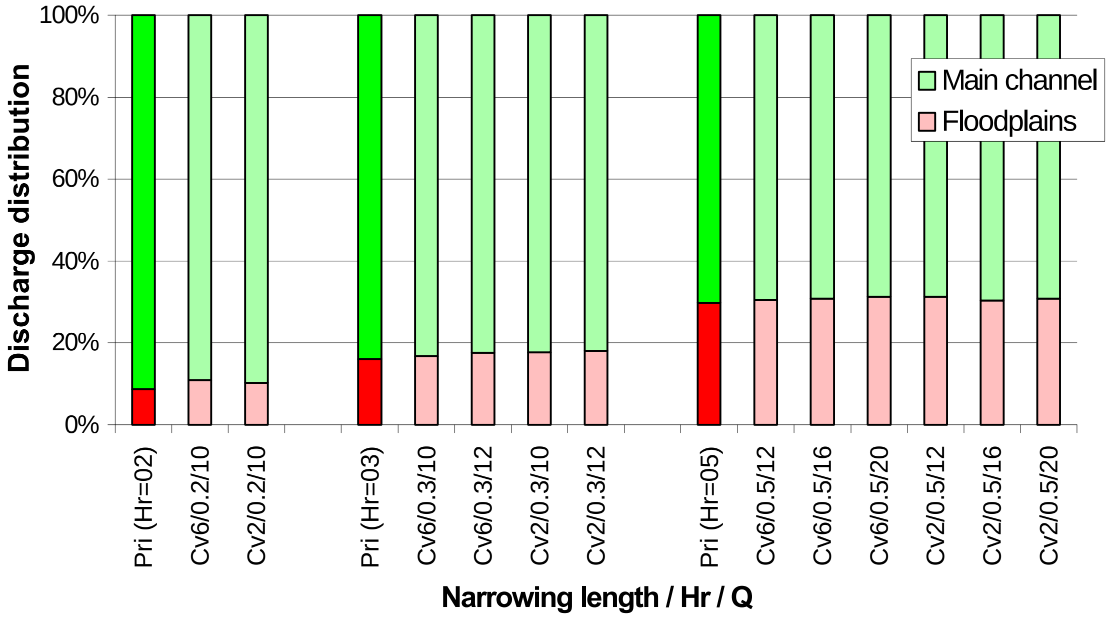

Figure 12.10 : Discharge distribution between subsections at x = 5 m.
Cv6 and Cv2 stand respectively for 6-m and 2-m narrowing cases (dotted bars);
Pri stands for the prismatic reference-case (plain colour bars)

However, one should point out that the measured discharge distribution is not exactly the same in the converging and in the prismatic cases. The floodplain discharge is always slightly larger in the converging case than in the prismatic one. As detailed in Table 12.2, this larger discharge fraction on the floodplains is mainly observed for the lower water depths (H_r = 0.2; 0.3), with a discharge ratio between floodplains and main channel up to 25 % larger for the converging case, when compared to the prismatic one, at H_r = 0.2. This could be due either to the ill-conditioned upstream discharge-distribution as quoted above; or to the fact that, in a non-prismatic channel, the flow does not adapt instantaneously its discharge distribution to the actual cross-section geometry, but needs some distance for this adaptation.

The possible correspondence between discharge distributions is of first interest, as one-dimensional flow modelling usually assumes that the friction loss in a given section is equal to the loss in an equivalent prismatic reach for a uniform flow having the same hydraulic radius and averaged velocity (French 1985) : accordingly, such an assumption implies also for the discharge distribution to be the same in the actual section and in the corresponding prismatic reach. Due to the ill-conditioned upstream discharge-distribution in the experiments, this assumption can unfortunately not be definitely validated. Further experiments, with a corrected inlet condition, would therefore be required.

Table 12.2 : Discharge distribution between subsection for the narrowing-floodplain cases, compared to the prismatic reference case (Pri)

Case (length / H_r / Q)	Total discharge Q_{tot} [l/s]	Main-channel discharge Q_{mc} [l/s]	One floodplain discharge Q_{fp} [l/s]	Floodplain discharge ratio 2 * Q_{fp} / Q_{tot} [%]
Pri (Hr=02)	9.95	9.09	0.43	0.087
Cv6/0.2/10	9.98	8.89	0.54	0.109
Cv2/0.2/10	10.00	8.98	0.51	0.102
Pri (Hr=03)	13.42	11.26	1.08	0.161
Cv6/0.3/10	9.92	8.26	0.83	0.167
Cv6/0.3/12	11.95	9.85	1.05	0.176
Cv2/0.3/10	9.98	8.20	0.89	0.178
Cv2/0.3/12	11.99	9.82	1.08	0.181
Pri (Hr=05)	27.57	19.35	4.11	0.298
Cv6/0.5/12	12.01	8.35	1.83	0.305
Cv6/0.5/16	15.84	10.96	2.44	0.308
Cv6/0.5/20	19.65	13.49	3.08	0.313
Cv2/0.5/12	12.00	8.25	1.88	0.313
Cv2/0.5/16	15.94	11.11	2.42	0.303
Cv2/0.5/20	20.01	13.84	3.09	0.309

12.5 Momentum analysis

Using the available experimental data, the momentum fluxes in and between floodplain and main-channel are evaluated; and the momentum balance is checked according to the momentum equation (4.3), where all the terms are grouped in the left hand member, for a steady flow :

$$\frac{\partial}{\partial x}\left(\rho A U^2\right)+\rho g A\frac{\partial H}{\partial x}-\rho g A S_0+\rho g A S_f+\left(\rho q_{out}U-\rho q_{in}u_l\right)=0 \qquad (12.1)$$

Figure 12.11 gives these results for typical cases. The momentum are computed respectively for (1) one floodplain; (2) half the width of the main-channel; and (3) half the width of the whole cross-section. The momentum gradients are estimated at three location of the converging reach, by discrete finite difference between the available cross-sectional data : (1) at the first quarter of the narrowing reach [x = 3.5 m or 4.5 m, for the 6-m and 2-m long narrowing cases respectively]; (2) at the middle [x = 5 m]; and (3) at the last quarter [x = 6.5 m or 5.5 m]. The frictional losses are estimated using either S_f from the Manning equation (4.1) for the subsections, or S_e from the EDM relation (4.17) for the whole section, which is justified by the rather good results obtained by this method for the stage-discharge estimations in the present study (Figure 12.2).

For each case, the sum of all the terms of momentum equation (12.1) is given. Considering it also includes the experimental data inaccuracies, this balance error is found to be relatively low. It is observed that the highest errors are associated with the highest discharge and smaller water depth. Regarding the influence of the discharge, even if the absolute error increases, it should be pointed out that the error weight seems to be quite constant when compared with the other terms of the balance.

The discharge $Q = 12$ l/s, for a relative water depth $H_r = 0.3$ at $x = 5$ m, in the 6-m length narrowing case (Figure 12.11a), will be analysed as a typical case. Regarding the whole channel balance, we observe that the friction slope $\rho g A S_f$ is not exactly balanced by the bottom slope - $\rho g A S_0$. The latter is slightly higher, as the flow is not uniform and as the actual water level is greater than the normal depth that would be observed in a prismatic channel with the same cross-section, bottom slope and discharge. The balance is obtained thanks to both the convection term $\partial\left(\rho A U^2\right)/\partial x$ and the pressure term $\rho g A \partial H/\partial x$. The convection term has a positive value, due to the acceleration in the convergence; and the negative value of the pressure term indicates a plunging water profile; while the increase of absolute value of both terms along the channel is in accordance with the increased water level slope observed on the water profile (Figure 12.3). These convection and pressure terms are up to twice larger than the slope-terms - $\rho g A S_0$ and $\rho g A S_f$; while their difference, that is one order of magnitude smaller, equilibrates the slope terms difference $\rho g A(S_f - S_0)$. This shows already that the convection phenomena are not negligible when compared to the friction and have thus to be taken into account when attempting to evaluate the momentum equilibrium.

The same balance is observed in the main-channel, although the convection term has increased with the pressure term. The equilibrium is now only obtained by taking into account the momentum transfer term - $\rho q_{in} u_L$ due to the inflow from the floodplain which has almost the same weight as the slope terms.

In the floodplain balance, the momentum transfer term $\rho q_{out} U$ has the same weight than in the main-channel, while all other terms are significantly lower. As a result, the lateral flow is the main term in the momentum equilibrium for the floodplain. The negative value of the convection term can be explained by the cross-sectional area reduction for the narrowing floodplains, which exceeds the influence of the acceleration.

Other useful information can be gathered from comparison with the other cases given on Figure 12.11. For the 2-m length narrowing case (Figure 12.11b), the converging angle is three times the converging angle of the 6-m length case. As a result, the longitudinal convection, lateral flow and pressure terms are observed to be around three times their values for the 6-m length case, while the friction and bottom slope terms are not affected.

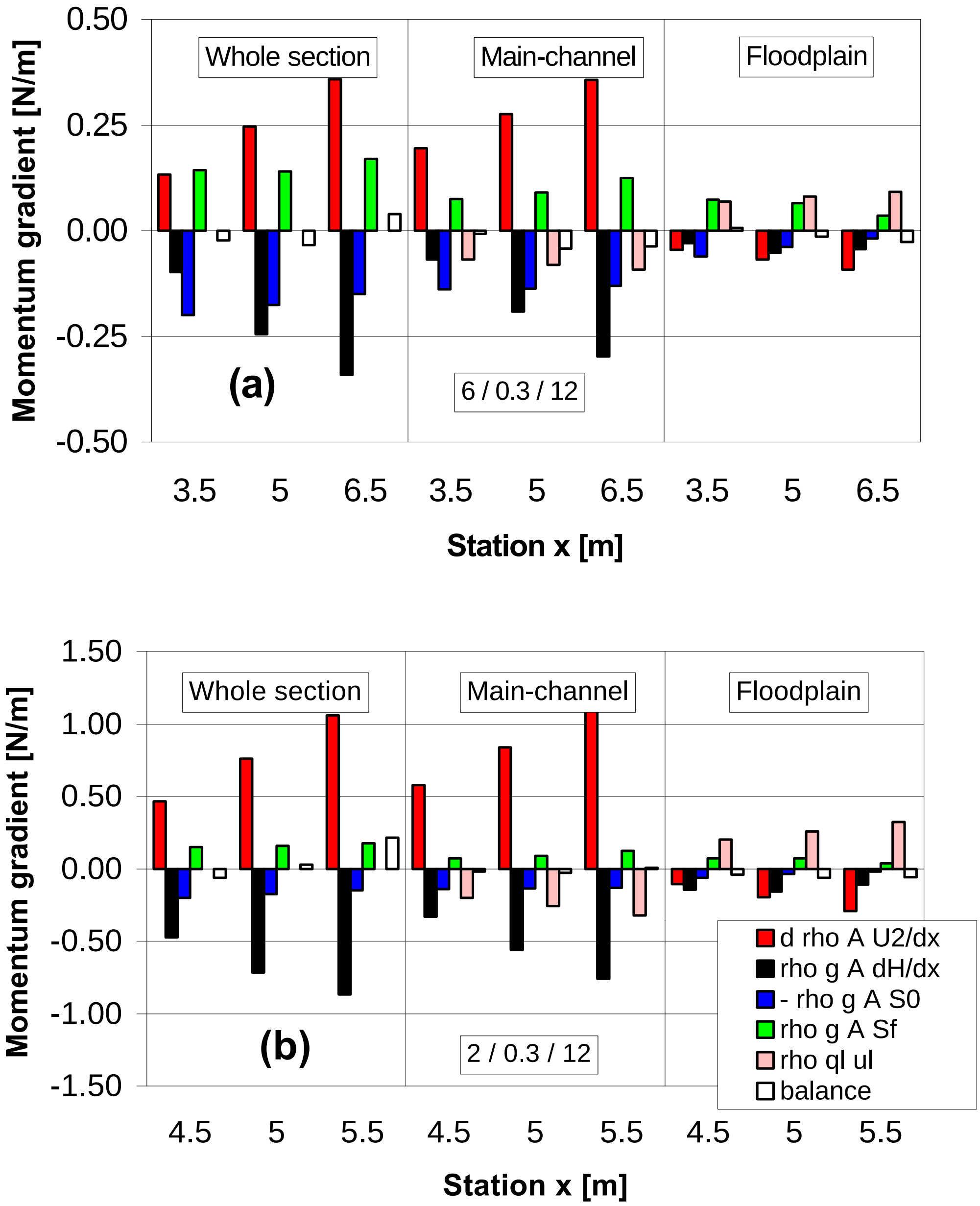

Figure 12.11 : Momentum balance, according to momentum equation (12.1) :
(a) 6-m length case, $H_r = 0.3$, $Q = 12$ l/s; (b) 2-m length case, $H_r = 0.3$, $Q = 12$ l/s;
(c) 6-m length case, $H_r = 0.5$, $Q = 12$ l/s; (d) 6-m length case, $H_r = 0.5$, $Q = 20$ l/s.
'rho ql ul' stands either for $-\rho q_{in} u_L$ (main-channel) or for $\rho q_{out} U$ (floodplain).

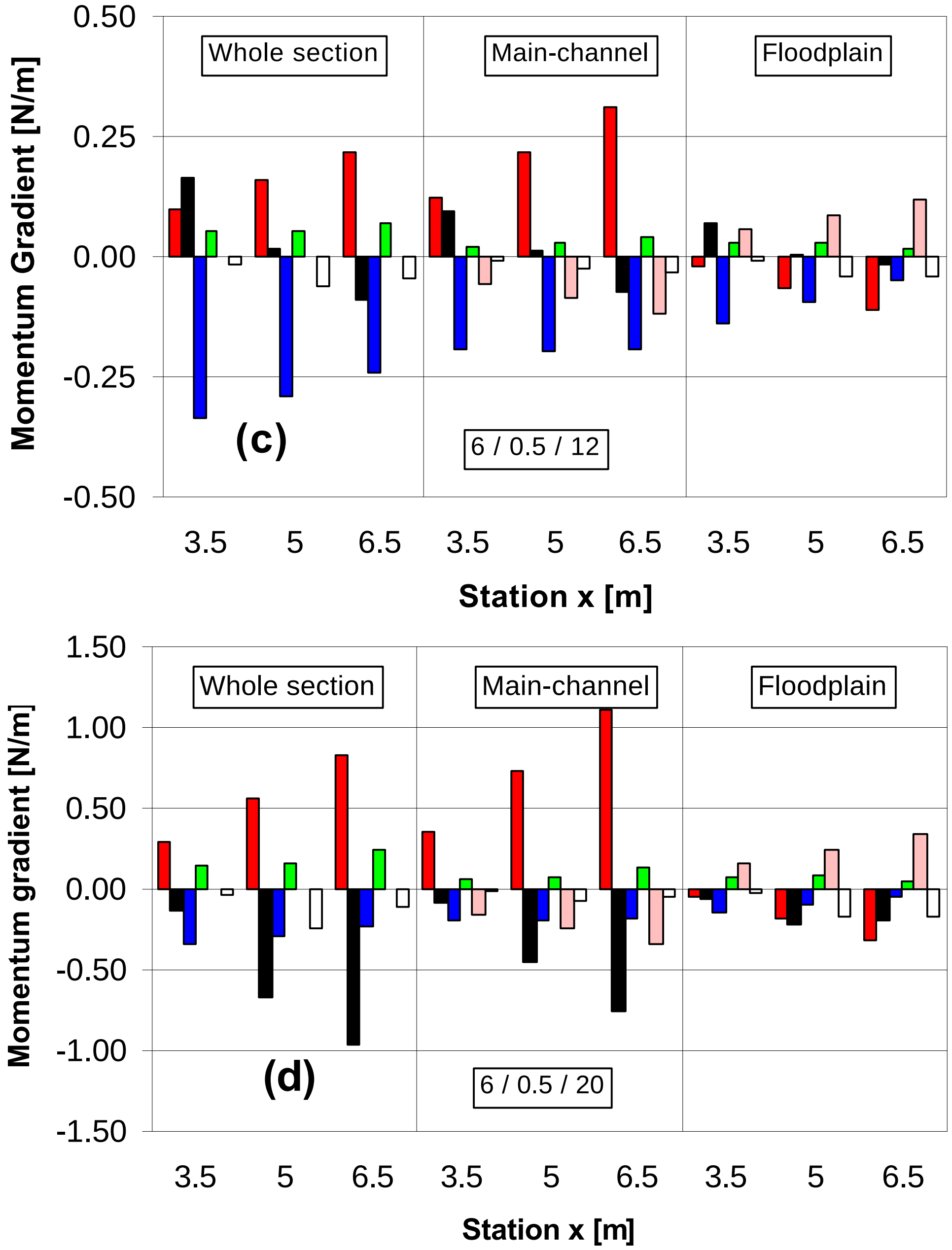

Figure 12.11 (continued)

For the same discharge, but with higher water depth $H_r = 0.5$ (Figure 12.11c), due to slower velocities, the convection term decreases slightly compared to the case $H_r = 0.3$ (Figure 12.11a). The pressure term becomes positive in the first part of the converging section, according with the observation that the water-surface slope is less than the bottom slope in this part of the channel. This special behaviour could be explained by the rather high downstream level imposed to the water profile. Due to the higher cross-sectional area available, the friction term reduces and the bottom slope term increases. When the discharge increases to $Q = 20$ l/s, for the same water depth (Figure 12.11d), all the convection, pressure and friction terms increase according to the discharge, while the bottom slope term remains the same. However, even for this high discharge, the flow is clearly dominated by the convection and not by the friction, and the lateral flow terms remain significant in the balance.

12.6 Head loss analysis

In order to estimate the contribution of the mass and corresponding momentum transfer to the total head loss, the latter has been estimated from the water profile measurements and compared to the frictional losses estimated from the prismatic-channel experiments, where no geometrical transfer is expected. The head profile (Figure 12.12) is approximated by adding to the water profile the kinetic energy $\alpha U^2/2g$ computed with the mean velocity (total discharge divided by the whole cross-section area). For computational convenience, the Coriollis coefficient α has been taken equal to 1. These head values have been checked locally, in the four cross-sections where detailed velocity measurements are available and no significant discrepancies have been found. The head loss at $x = 5$ m is then given by the slope of the curve fitting the energy profile.

For estimating the friction loss S_f, we use the Manning equation (4.1), which requires the knowledge of conveyance K. The latter is estimated from the tests in the prismatic channel with 200-mm-wide floodplains (Figure 12.1c), where uniform flow prevails, in such a way that, for these tests, the friction loss S_f equals the bed slope S_0.

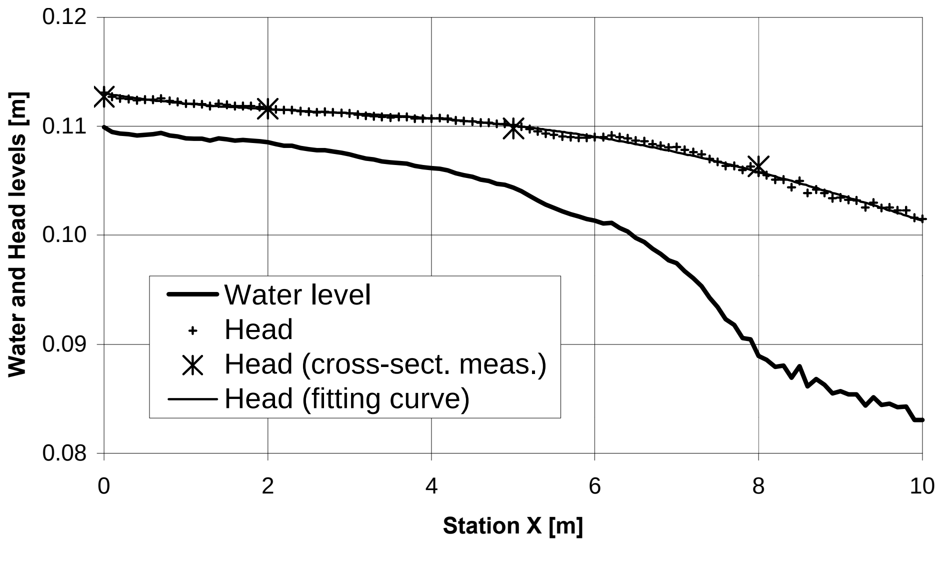

Figure 12.12 : Water and energy profile, 6-m length case, $H_r = 0.5$, $Q = 20$ l/s

The total head loss S_e and the friction loss S_f are given on Figure 12.13 for all the tested cases. It is clearly observed that the total head loss is greater than the friction loss. This difference demonstrates the significance of the additional loss S_a due to the mass and momentum transfer induced by the geometrical changes. The difference increases with the converging angle, while the ratio between this difference and the friction slope S_f

remains constant for an increasing discharge Q at a given water depth H_r. This shows that the additional loss increases with the mass transfer but also remains proportional to the whole discharge. As a conclusion, the additional loss ratio $\chi = S_a/S_f$ is mainly driven by geometrical parameters and thus by convection phenomena, as it is independent of the discharge. EDM results also represented on Figure 12.13 will be discussed in Chapter 14.

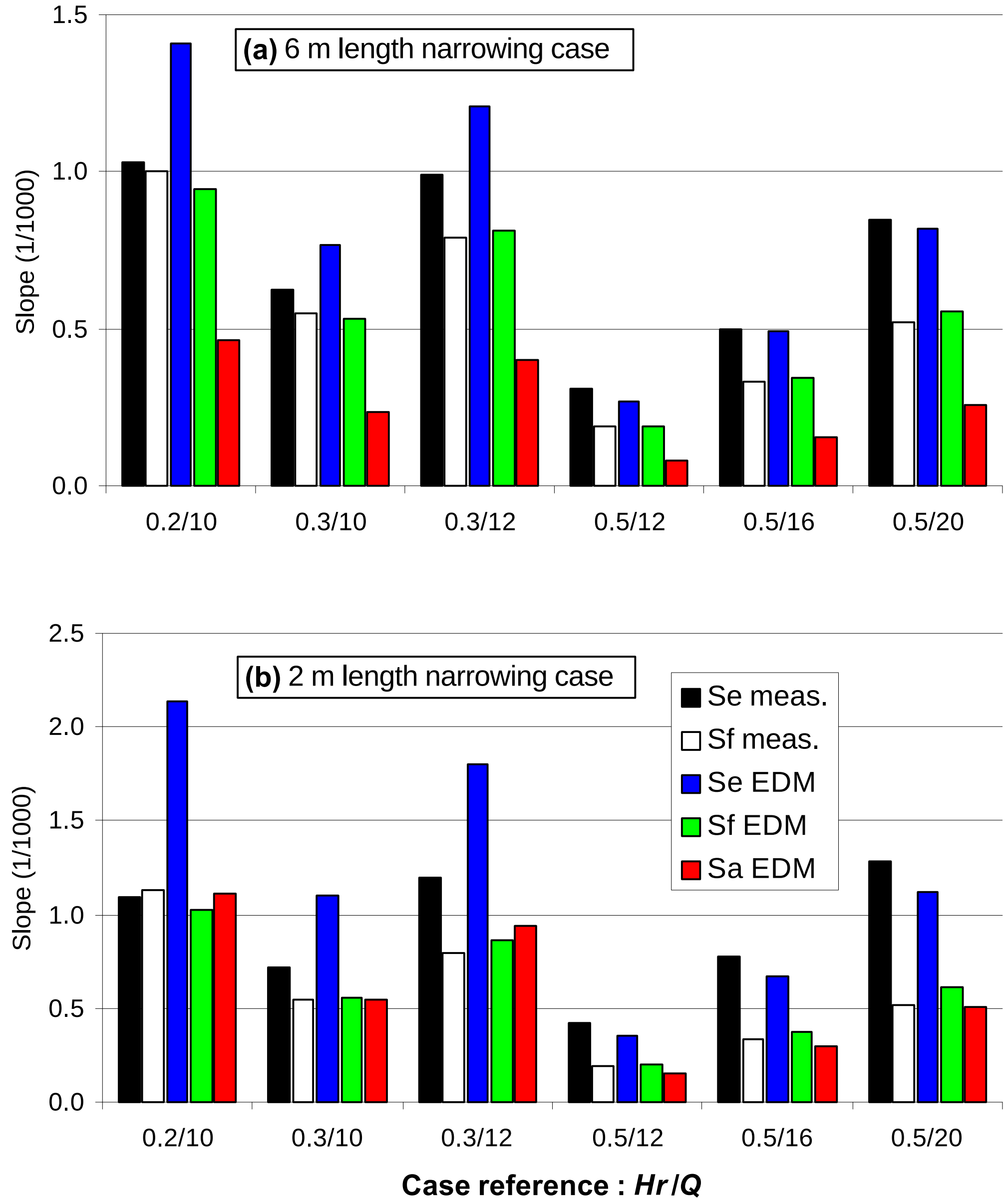

Figure 12.13 : Head loss S_e, friction loss S_f and additional loss S_a. Experimental and EDM-computed values

12.7 Conclusion

Experimental results have been presented for the flow in a compound channel with symmetrically narrowing floodplains. Water profiles and velocity distribution have been measured. The flow structure is found to be similar to the one observed in meandering compound channels : the floodplain-width change induces a mass transfer towards the main-channel. A transverse current is then observed in the upper part of the main-channel, plunging to the channel bottom around its centre line and generating an helical current in the inbank part of the channel.

The significance of the momentum transfer associated with the mass transfer has been highlighted, in terms of momentum balance for the floodplains and for the main-channel, but also in terms of additional head loss for the whole cross-section. This additional head loss increases according to the water depth, to the converging angle and to the discharge. However, its ratio to friction loss is independent of the discharge, indicating that the additional loss is mainly driven by geometrical aspects.

These observations give confidence in one of the main assumptions made during the EDM development, which states that the ratio between additional loss and friction slope in only driven by cross-section geometry, and not by discharge. The validity of the EDM for geometrical-transfer modelling will be further investigated in Chapter 14.

Chapter 13
Extension of the Lateral Distribution Method for a non-prismatic geometry

13.1 Introduction

Using the experimental measurements from Chapter 12, the proposed extension of the Lateral Distribution Method (LDM) for a non-prismatic geometry (3.20) will be applied and discussed in the present Chapter :

$$\rho g H S_e + \frac{\partial}{\partial y}\left(\rho\lambda\sqrt{\frac{gn^2}{H^{1/3}}}H^2 U\frac{\partial U}{\partial y}\right) - \frac{\rho g n^2}{H^{1/3}}\sqrt{1+S_{0y}^2}\,U^2 = \Gamma + \rho\kappa H U\frac{\partial U}{\partial y} \tag{13.1}$$

where S_e is the energy slope; Γ is the secondary-current term defined by Shiono and Knight; and $\kappa = V/U$ is the ratio between transverse and longitudinal components of the velocity

As explained in Chapter 3, this extended LDM (13.1) intends to take into account the effects of the flow non-prismaticity on the depth-averaged velocity profile by : (1) using the actual energy slope S_e, instead of the bed slope S_0; and (2) defining an adapted secondary-current term, which accounts for the mass-transfer and which is proportional to the ratio κ between transverse and longitudinal components of the velocity.

The complete two-dimensional model will also be used in this Chapter, in order to verify the relative weight of the different terms in the extended LDM equation. This 2D model solves the Saint-Venant equations, using a MacCormack scheme for a curvilinear grid, as detailed in Appendix 1.

Four narrowing-floodplain test cases are selected from Chapter 12 for further analysis. These cases, together with the prismatic-channel reference cases are summarised in Table 13.1. Three cases from the 6-m long contraction series have been selected, covering both water-depth and discharge variations; while a fourth case from the 2-m long contraction series will be used to investigate the influence of the converging angle θ variation. In Table 13.1, the energy-slope estimates S_{e1D} are the one obtained in § 12.6 from the one-dimensional water profile (see Figure 12.12); while the ratio κ estimation will be discussed below.

Table 13.1 : Parameters of the experiments to be modelled

Case	Converging angle θ [°]	Water depth at $x = 5$ m [mm]	Discharge Q [l/s]	Estimate of the energy slope S_{e1D}	Estimate of the ratio $\kappa_{fp} = V/U$	Estimate of the ratio $\kappa_{mc} = V/U$
Cv6/05/20	3.8	100	20	0.84×10^{-3}	0.07	0.01
Cv6/05/12	3.8	100	12	0.31×10^{-3}	0.07	0.01
Cv6/03/12	3.8	71.5	12	0.99×10^{-3}	0.07	0.01
Cv2/05/20	11.3	100	20	1.29×10^{-3}	0.20	0.06
Pri05	Prismatic	100	27.6	0.99×10^{-3}	0.00	0.00
Pri03	Prismatic	71.5	13.5	0.99×10^{-3}	0.00	0.00

13.2 Prismatic channel simulations

Simulations were first performed for the two reference situations Pri05 and Pri03, using the helical secondary-current term Γ; and setting $S_e = S_0 = 0.99 \times 10^{-3}$ and $\kappa = 0$ as the flow is uniform and in a prismatic channel. The computed velocity profiles are plotted on Figure 13.1 and Figure 13.2. The Manning roughness coefficient is set at $n = 0.0107$ s/m$^{1/3}$, according to the calibration performed using isolated main-channel flow data (§ 12.2). A good fitting between measured and computed velocities is obtained with $\lambda = 0.05$; $\Gamma_{mc} = 0.30$ and $\Gamma_{fp} = -0.10$ for the Pri05 case; and $\Gamma_{mc} = 0.20$ and $\Gamma_{fp} = -0.05$ for the Pri03 case. The dimensionless eddy viscosity λ value is slightly lower than the usual ones, maybe due to the smaller scale of the flume. However, Knight and Abril (1996) have shown that this parameter influence was small compared to the secondary-current parameter Γ. The latter presents values closer to the usual ones.

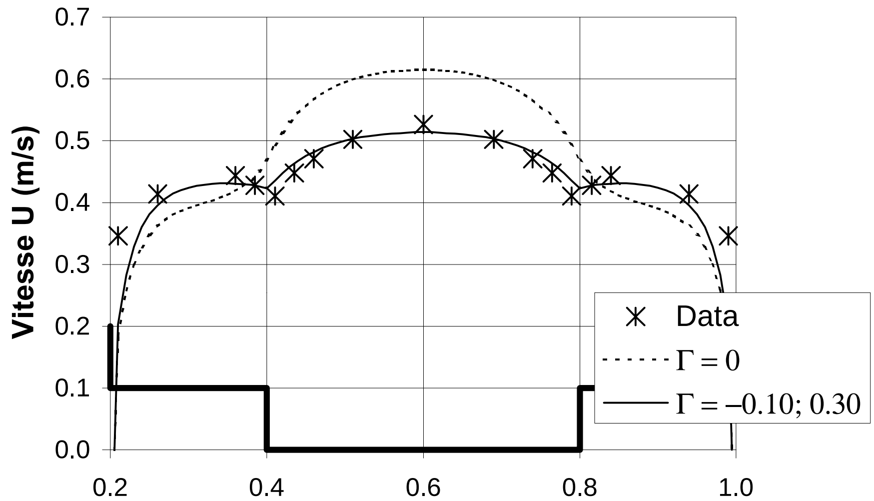

Figure 13.1 : Pri05 case, measured and LDM-computed velocity profiles

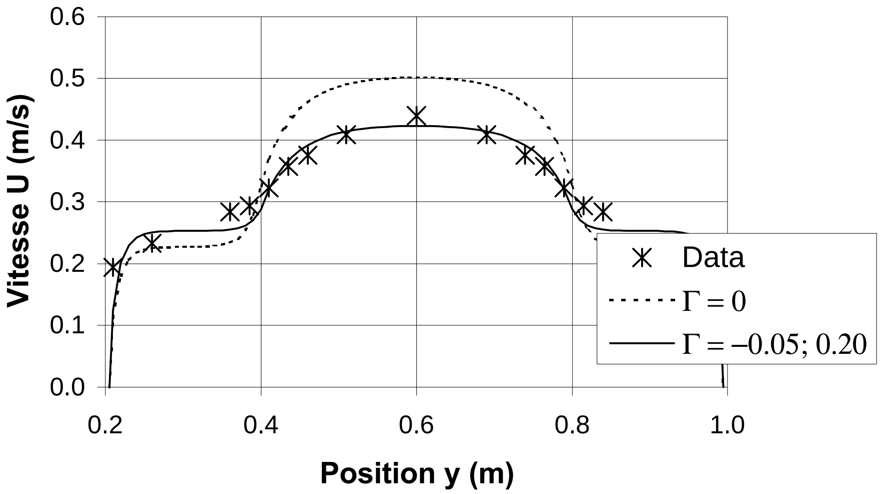

Figure 13.2 : Pri03 case, measured and LDM-computed velocity profiles

13.3 Extended-LDM simulations

The velocity ratio $\kappa = V/U$ on the floodplains can be estimated either from actual measurements, or a priori from the channel geometry. Indeed, if the direction of the flow is assumed to be parallel to the converging embankments, the velocity ratio κ equals the tangent of the converging angle θ (Table 13.1). For comparison, actual ratio κ values obtained from the experimental data are plotted of Figure 13.3. For the larger discharge cases (Q = 20 l/s : Cv6/05/20 and Cv2/05/20), the measured κ values are close to the estimated one, at least along the embankments. The κ value on the floodplain decreases when approaching the main-channel, probably indicating a gradual alignment of the velocities with the main-channel axis.

For the lower discharge cases (Q = 12 l/s : Cv6/05/12 and Cv6/03/12), the measured κ values are lower than the estimated one. This could be the consequence of a lower mass transfer rate between the floodplains and the main-channel. However, the evolution of the discharge distribution between floodplain and main-channel is the same for the Cv6/05/20 and Cv6/05/12 cases, as show by Figure 12.8, indicating that the mass transfer rate is the same. A cause for this discrepancy is thus probably the rather low precision (0.5 °) of the micro-vane used for measuring the local velocity direction (see § 12.2 and Appendix 3). Indeed, it has been pointed out that this angle measurement is probably meaningful, from a quantitative viewpoint, only for the larger velocities and angles, which is the case for Cv6/05/20 and, mainly, Cv2/05/20.

For the main-channel, as the water depth increases, the transverse velocity and the κ ratio are lower than in floodplains, for a same mass transfer. The transverse velocity is also expected to decrease linearly towards the main-channel axis, due to the channel symmetry. However, for simplicity, a constant value of κ will be used in a first stage. Indeed, as the longitudinal velocity gradient $\partial U / \partial y$ tends to zero in the vicinity of the main-channel axis, an error on the κ value will not jeopardise the simulation results. The values of $\kappa_{mc} = 0.01$ and $\kappa_{mc} = 0.06$ will be used respectively for the Cv6 and Cv2 series. These values correspond to the maximum κ values experimentally observed in the main-channel, near the interface with the floodplains, where the full mass transfer enters the main-channel.

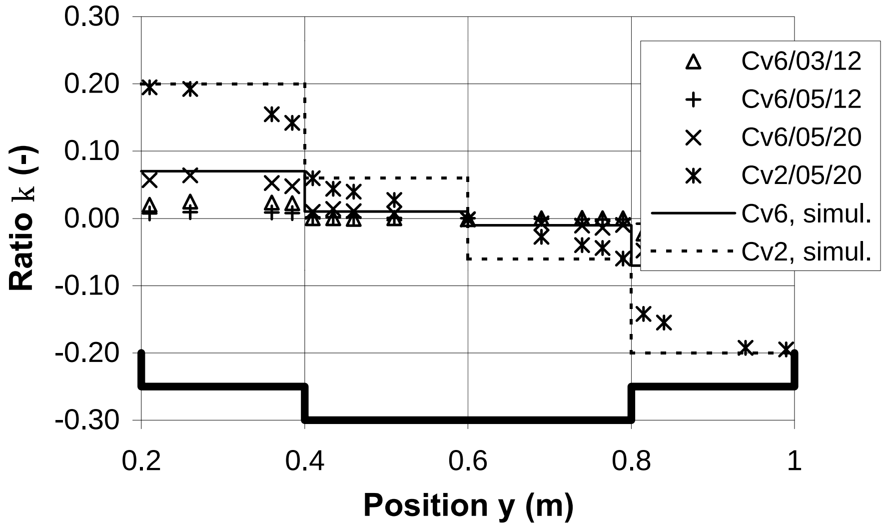

Figure 13.3 : Ratio κ : measured values, and values used for simulations

Extended-LDM results for non-prismatic channels are first presented for the Cv6/05/20 case (Figure 13.4). Simulation is initially performed with the classical LDM (3.10), without any secondary current. Both main-channel and floodplains velocities are clearly overestimates. A second attempt, using the Shiono and Knight secondary-current term Γ (3.14), as calibrated for the reference situation with the same water depth (Pri05) : this gives lower velocities, but again overestimated. Probably a better fitting would be possible by adjusting the Γ values, but it would miss physical meaning. It should also be pointed out that, as the Γ term encompasses the velocity value, its value will not remain constant when varying the bed or the energy slope, contrarily to the roughness *n* and to the adimensional eddy viscosity λ, which are independent of the velocity.

The results of the extended LDM (16), without Γ, are also presented on Figure 13.4. The computed velocities are clearly underestimated on the floodplain, and slightly overestimated in the main-channel. The transverse velocity gradient $\partial U / \partial y$ is found to be too large, probably since the mass-transfer secondary-current term induces too much shearing. Adjusting the ratio κ value would reduce this shearing, but it would also lead to unrealistically low values of κ. It could also be conjectured that setting the velocity equals to zero at the wall, as imposed by the no-slip condition, could have a major influence on the whole profile, due to this increased shear.

The influence of the boundary condition is therefore tested. The results are improved when using a free-slip condition instead of the no-slip condition (Figure 13.5), but not decisively : indeed, the velocity remains underestimated on the floodplains and overestimated in the main channel. A further improvement could be obtained by using simultaneously both helical Γ and mass-transfer κ currents : it was indeed observed that the mass-transfer generates significant helical currents, at least in the main-channel (see § 12.3). For that purpose, the value of Γ is, in a first stage, selected as equal to the one calibrated for the reference case. The velocities are now correctly estimated in the middle of the main-channel but remain underestimated on the floodplains.

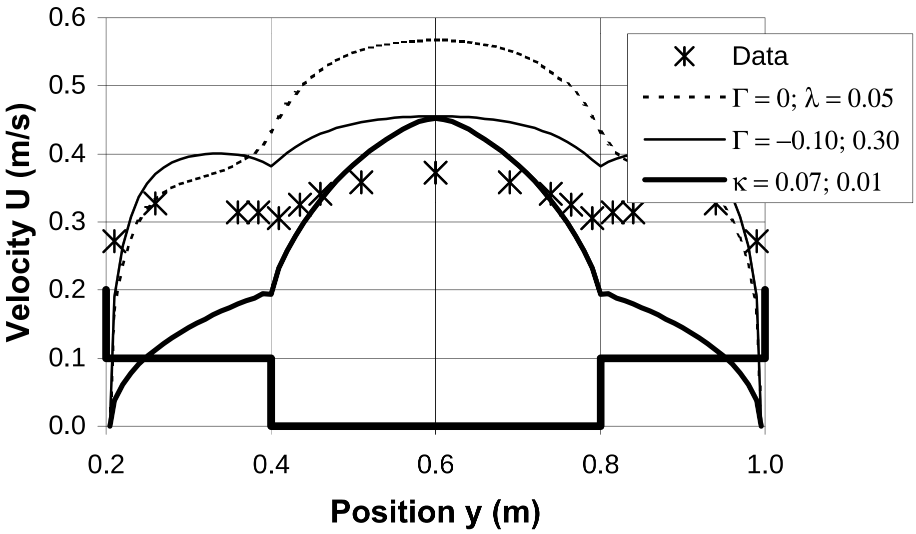

Figure 13.4 : Cv6/05/20 case : longitudinal-velocity profile. Measured and LDM-computed values : influence of the secondary-current model (λ = 0.05)

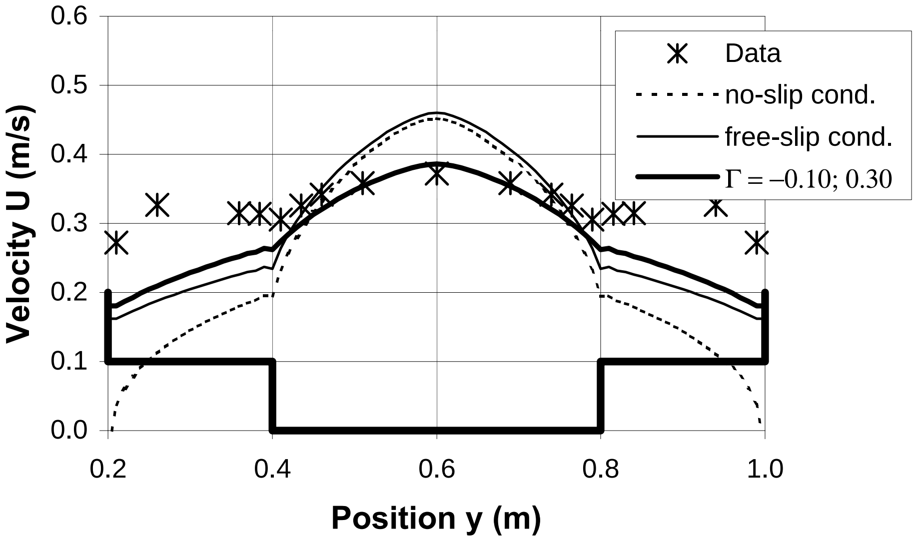

Figure 13.5 : Cv6/05/20 case : longitudinal-velocity profile. Measured and Extended-LDM-computed values : influence of the boundary condition ($\lambda = 0.05$; $\kappa_{fp} = 0.07$; $\kappa_{mc} = 0.01$)

Similar results were obtained for the other converging channel cases. Better adjustment would be possible by tuning the parameters, but this tedious fitting is beyond the scope of the present study, as it would jeopardise the physical meaning of these parameters. Before any fitting of this kind, a full two-dimensional simulation is developed. It is expected that this simulation will enable to investigate the relative weight of all the terms of the LDM equation (13.1). This could help to identify the causes of the poor results of this extended LDM, when compared with the measured velocities.

13.4 Two-dimensional modelling

13.4.1 Numerical model

The Saint-Venant equations (2.33) are solved numerically, using a finite difference model and a Mac-Cormack scheme, as detailed in Appendix 1. The size of the curvilinear boundary-fitted mesh is 201 × 31 nodes, respectively in the channel longitudinal and transverse directions. A no-slip condition is used along the wall and a symmetry condition is used at the channel axis. The Manning roughness-coefficient local value n_{2D} is estimated in order to get an actual roughness equals to $n_{1D} = 0.0107$ s/m$^{1/3}$ in each channel subsection. Indeed, as the friction slope computation is based on the water depth H rather than on the actual hydraulic radius R, a corrected value of the roughness coefficient has to be used : $n_{2D} = n_{1D}\ (H/R)^{2/3}$. According to the flume geometry, for a mean water-depth $H = 0.10$ m in the main channel, the roughness coefficient equals $n_{mc} = 0.0124$ s/m$^{1/3}$ in the main-channel, and $n_{fp} = 0.0114$ s/m$^{1/3}$ in the floodplains. An eddy viscosity proportional to the shear velocity U^* is used (2.43), with $\lambda = 0.1$; and the dispersion terms are neglected. The measured upstream unit discharge q and downstream water level H are used as boundary conditions. The simulation is allowed to run until the maximum water-level and velocity variations between two time step are lower than a given limit (typically 10^{-6} m and 10^{-6} m/s).

Typical results for the Cv6/05/20-case simulation are given on Figure 13.6. The mass transfer from the floodplain to the main channel is well depicted by the velocity field; while the water level decreases, due the flow acceleration, in accordance with the downstream-imposed water level.

Detailed results are given on Figure 13.7. The water-depth longitudinal profile (Figure 13.7a) and the longitudinal-velocity U profiles (Figure 13.7b) are correctly simulated, when compared with the measured data. The computed transverse-velocities V (Figure 13.7c) present more deviation from the data, mainly at the 2-m station (entrance of the converging section) and at the 8-m station (end of the converging section). This could be due to : (1) the inaccurate velocity-direction measurements, as quoted previously; (2) the ill-conditioned upstream discharge-distribution, although the latter has been taken into account in the upstream boundary condition; or (3) to some actual geometry unevenness (e.g. at the joint between 2 bottom plywood plates) that was not incorporated in the numerical model. Indeed, it should be noted that no joint is present at the 5-m station, where the transverse-velocity profile is satisfactorily computed.

A last result of interest is the specific energy of the flow, given on Figure 13.8. This specific energy e, or head is computed as :

$$e = z + \frac{1}{2g}\left(U^2 + V^2\right) \tag{13.2}$$

The specific energy plot on Figure 13.8 is in accordance with the previous results : as the water level transverse slope equals zero (Figure 13.6), the specific-energy transverse variation matches the longitudinal-velocity U profile (Figure 13.7b). However, this result is surprising, as it is usually expected that the specific energy presents a horizontal transverse profile, and that the velocity is oriented according to the largest head gradient. Maybe this behaviour could be due to the no-slip condition used at the wall. This condition generates losses near the wall, that are not taken into account by the specific energy definition (13.2). Due to lack of time, this point has not been further investigated in the present work, as all other results were satisfactory, but it should be handled in a next study.

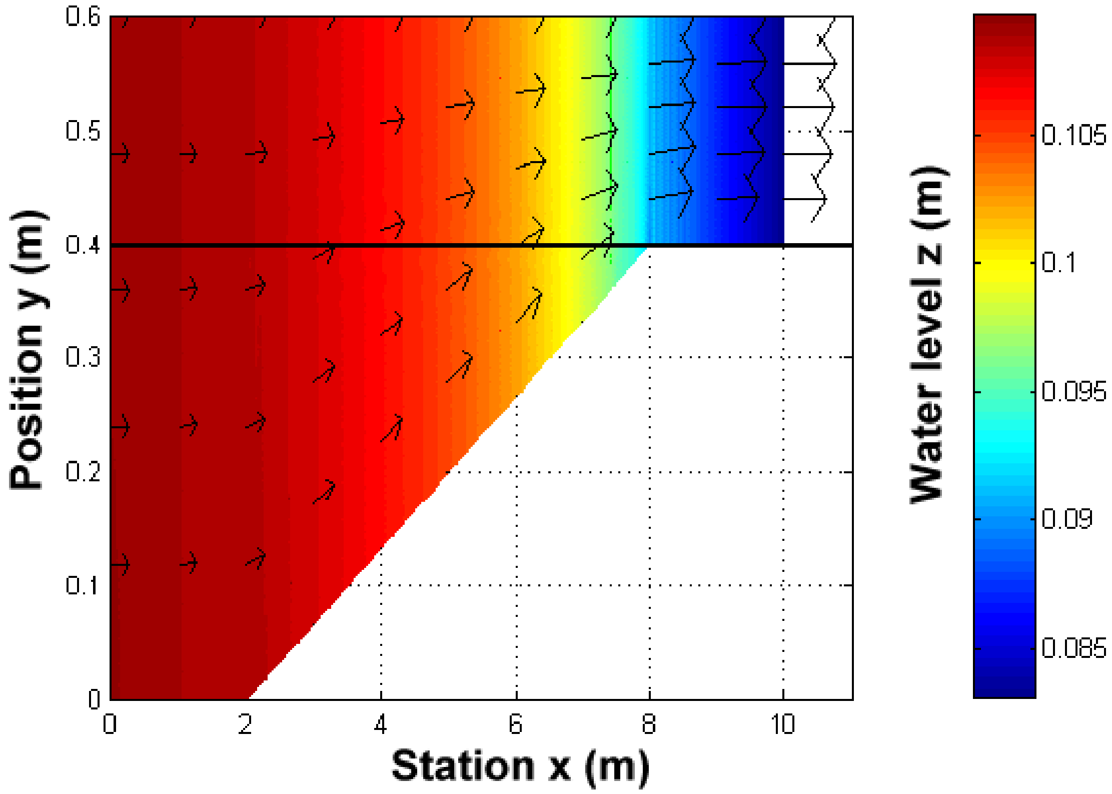

Figure 13.6 : Cv6/05/20 case, two-dimensional model results : water level z and velocity field (for half a section)

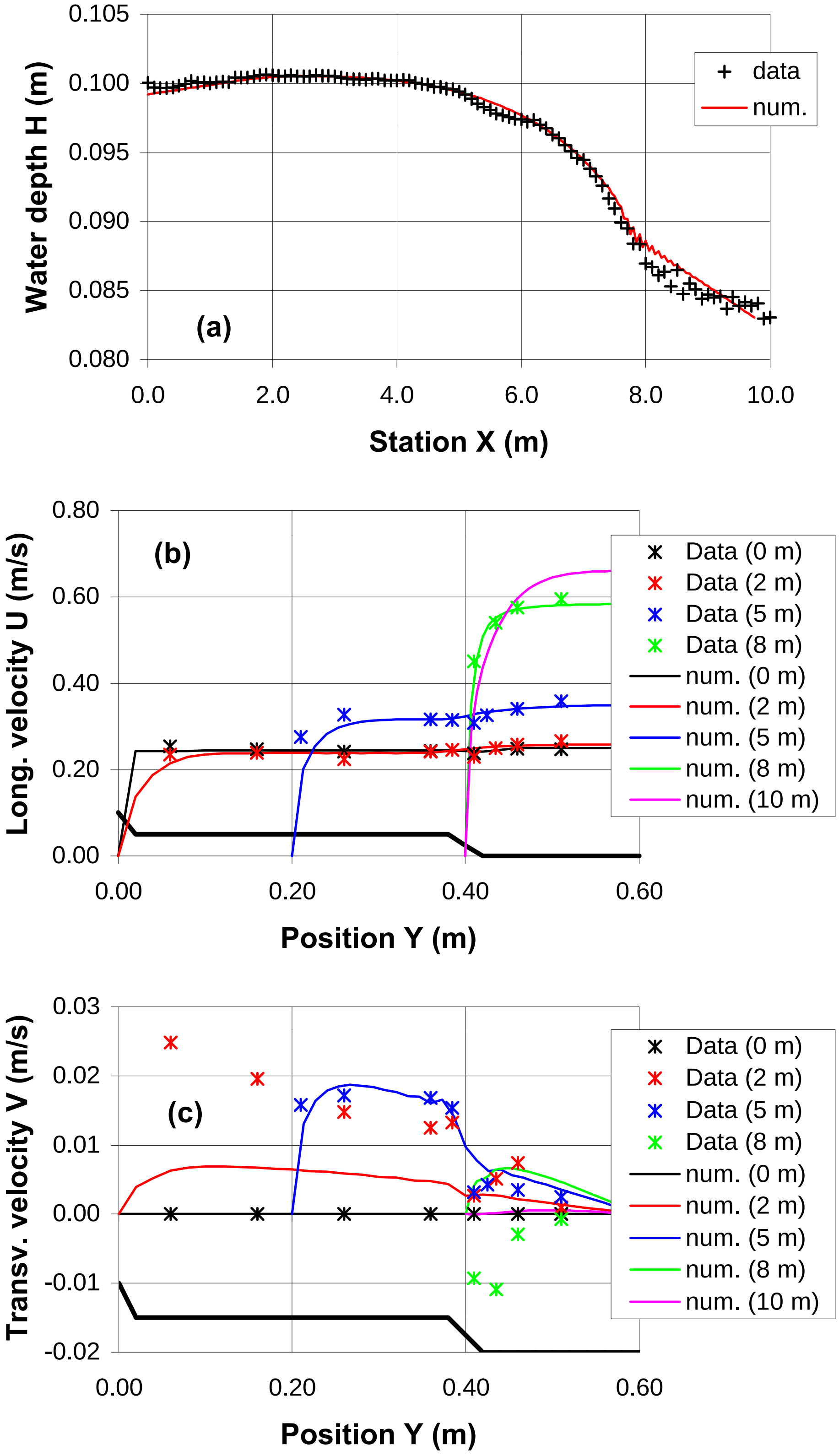

Figure 13.7 : Cv6/05/20 case, two-dimensional model : (a) Water-depth H longitudinal profile; (b) longitudinal velocity U profiles (for half a section); and (c) transverse velocity V profiles (for half a section)

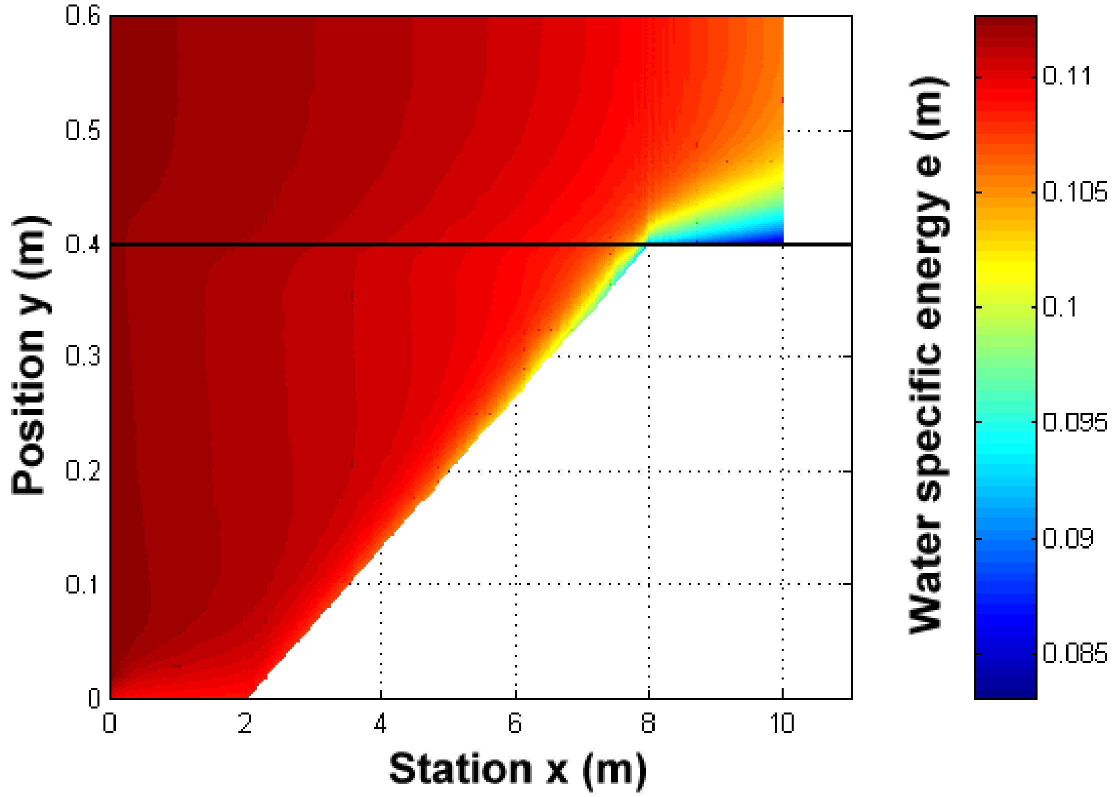

Figure 13.8 : Cv6/05/20 case, two-dimensional model results : specific energy e

13.4.2 Momentum balance

Using the two-dimensional simulation results, the weights of the terms of the *x*-momentum equation (2.33b) are evaluated at several locations. This will enable further comparison with the extended LDM equation (13.1). For analysis purpose, (2.33b) is presented in a non-dimensional form, by dividing it by $\rho g H$:

$$\frac{U}{g}\frac{\partial U}{\partial x}+\frac{\partial H}{\partial x}-S_{0x}+S_{fx}+\frac{V}{g}\frac{\partial U}{\partial y} -\frac{1}{\rho g H}\frac{\partial}{\partial x}\left(H\,\tau_{xx}\right)-\frac{1}{\rho g H}\frac{\partial}{\partial y}\left(H\,\tau_{xy}\right)=-\frac{1}{g}\frac{\partial U}{\partial t} \tag{13.3}$$

where the temporal derivative $\partial U/\partial t$ is expected to be equal to zero, as the solution is obtained for a permanent flow. This term is therefore written in the right-hand side of (13.3), in order to be compared to the summation of all the other terms, that corresponds to the balance error. According to the computation convergence criteria, its absolute value should be less than 2.5×10^{-3} (with $\Delta t = 0.004$ s)

The weight of the different terms of (13.3) are plotted on Figure 13.9 for three stations (x = 2; 5; and 8 m) and several transverse position y. At all the location investigated, the balance error is found smaller than expected.

General observations can be gathered from the $x = 5$ m station balance (Figure 13.9b). As expected, the acceleration ($U/g\ \partial U/\partial x$) and pressure ($\partial H/\partial x$) terms are no more negligible in regard of the bottom slope ($-S_{0x}$). On one hand, the acceleration term is positive excepted near the wall, indicating that the flow is accelerating. At the wall, a negative acceleration term is observed, corresponding to a flow deceleration. Indeed, due to the obstruction by the wall, the flow direction has to change from streamwise to transverse, towards the main channel. The transverse velocity component increases, while the longitudinal component decreases, in accordance with the continuity equation. On the other hand, the negative pressure term is in accordance with the water-level decrease. The next main term in the balance is the friction slope (S_{fx}), which is larger on the floodplains, due to the lower water depth.

However, near the wall and near the interface between the main channel and the floodplain, the transverse convection ($V/g\ \partial U/\partial y$) – corresponding to the mass-transfer secondary-current – is locally larger, and even dominant in the momentum balance, as a result of the combined effect of the large transverse velocity V and of the large gradient of longitudinal velocity U. Except in these same area of large velocity gradient, the transverse eddy friction τ_{xy} remains low; while the longitudinal eddy friction τ_{xx} is always negligible, as expected.

The same results are observed at the $x = 8$ m station (Figure 13.9c), with a larger acceleration and a greater water depth slope; while, at the $x = 2$ m station (Figure 13.9a), the acceleration are lower and the water depth is still increasing, indicating that the flow is still accumulating energy before entering the converging section (M1 profile).

It should be pointed out that those results are roughly in accordance with the similar momentum balance, previously computed from the experimental data (Figure 12.10). However, the transverse variation of all the terms is more clearly depicted by the present analysis, as the numerical results are available with a finer resolution than the experimental ones.

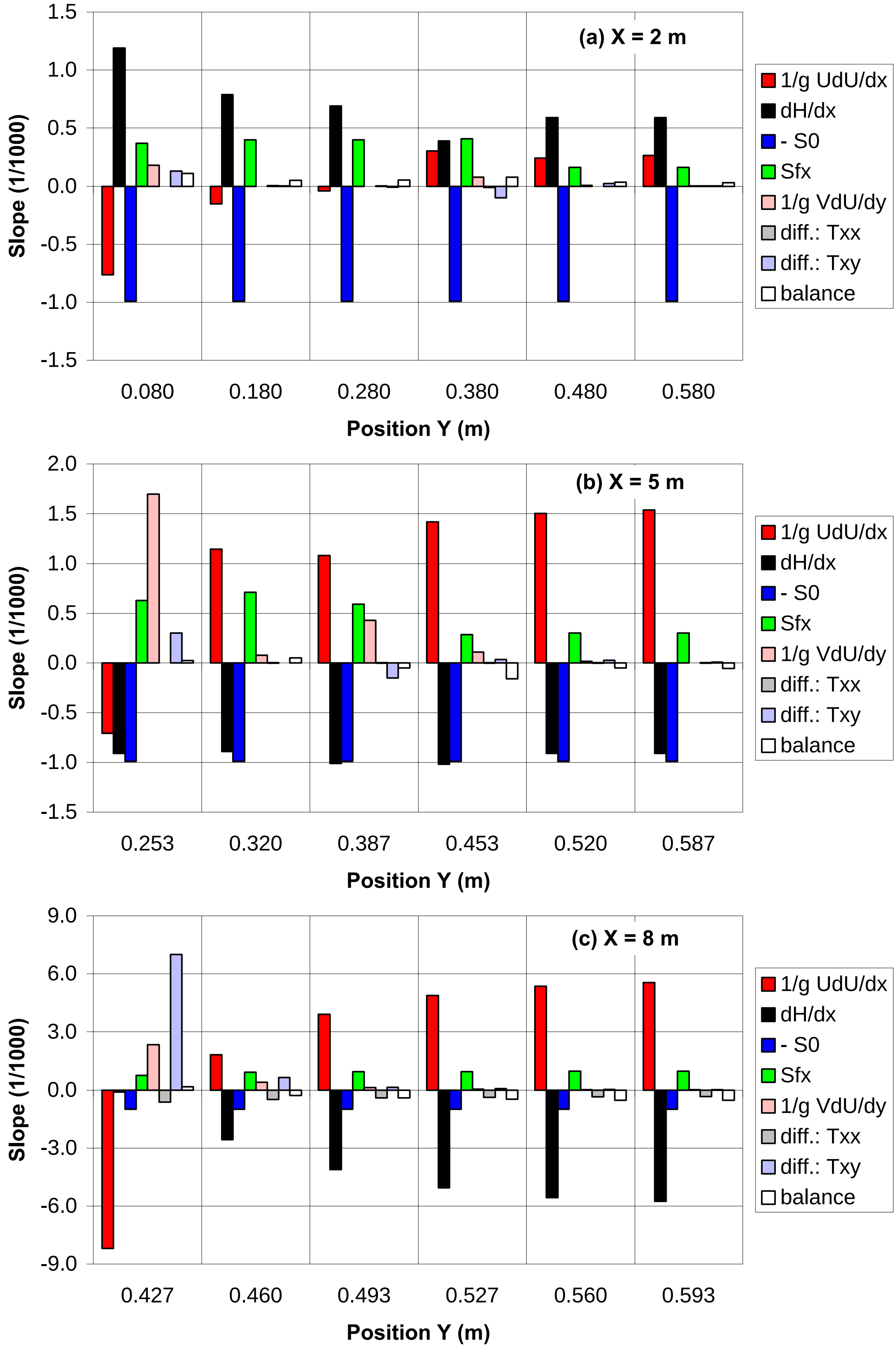

Figure 13.9 : Cv6/05/20 case, momentum balance (13.3) for half a section, according to two-dimensional numerical results : (a) x = 2 m station; (b) x = 5 m station; and (c) x = 8 m station

13.5 Improvement of the Extended LDM

The momentum balance (Figure 13.9) and the specific energy plot (Figure 13.8) presented above enable a further discussion of the extended LDM (13.1). This demonstrates clearly that, as assumed when developing this equation in Chapter 3, the longitudinal shear-stress τ_{xx} is indeed negligible, while the acceleration and pressure terms have to be taken into account. Nevertheless, it shows also that the latter are not constant along the channel width, in such a way that the longitudinal energy slope S_e can no more be estimated as a one-dimensional energy slope S_{e1D}. This is notably the case near the wall.

The longitudinal energy slope $S_{e2D}(y)$ estimated locally from the two-dimensional model is given on Figure 13.10 for the Cv6/05/20 case, at the $x = 5$ m station. While this slope is slightly lower than the one-dimensional S_{e1D} one in the main-channel; it is several times larger near the walls, as a consequence of the longitudinal-velocity U deceleration. As a consequence, using the one-dimensional energy slope S_{e1D} in the whole channel leads to a momentum balance deficit near the wall and, accordingly, the velocity decreases erroneously, as observed above.

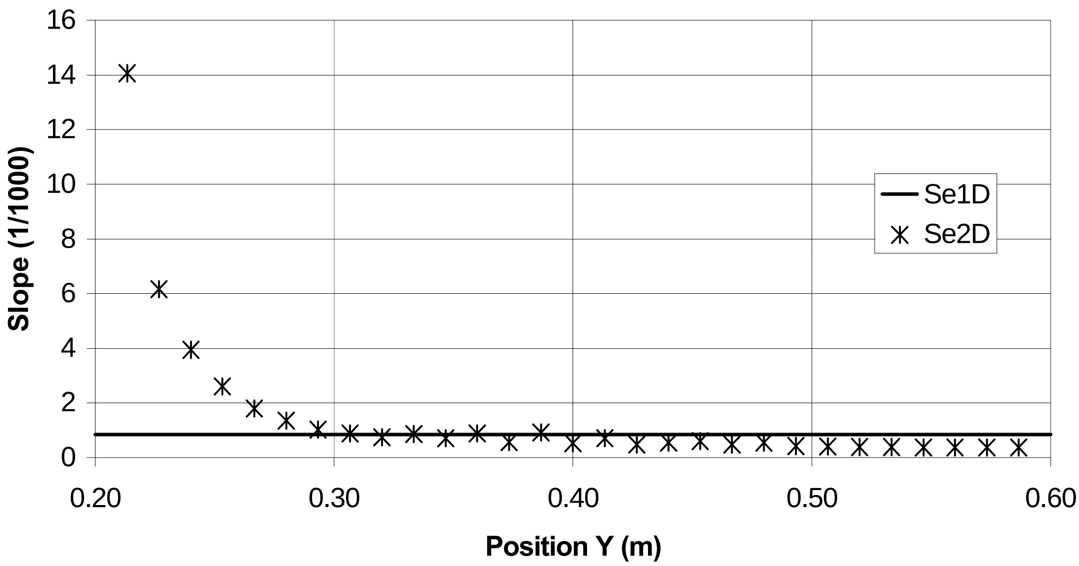

Figure 13.10 : Cv6/05/20, longitudinal energy slope $S_{e2D}(y)$ for half a section, as estimated from the two-dimensional model results

At last, a corrected simulation of the extended LDM is thus performed using the local energy slope $S_{e2D}(y)$ estimated from the two-dimensional model, and the results are given by Figure 13.11 for the four selected test-cases, with different water depths, discharges and converging angles. Using the a priori estimated values of κ (Table 13.1) and $\Gamma = 0$, a noticeably accurate fitting is obtained between the computed and the measured velocities, when compared to the previous attempts. As the roughness coefficient n was not adjusted, it is expected that the bottom shear stress profile would be also correctly modelled, even if it was not measured for this particular data set, and if comparison are therefore not possible.

From the latter, it can be concluded that it is possible to use the extended LDM with physically meaningful parameters values, although it requires also a accurate estimate of the local energy slope that is not always available. Using previous version of the LDM, it was also possible to get an accurate fitting, as far as enough data was provided for empirical calibration of the LDM parameters; which made it uncomfortable for a purely predictive use. The extended method presented here also requires extra data, but enables a better understanding of the parameters meaning. In this way, it is considered as a step forward for compound-channel flow modelling and understanding.

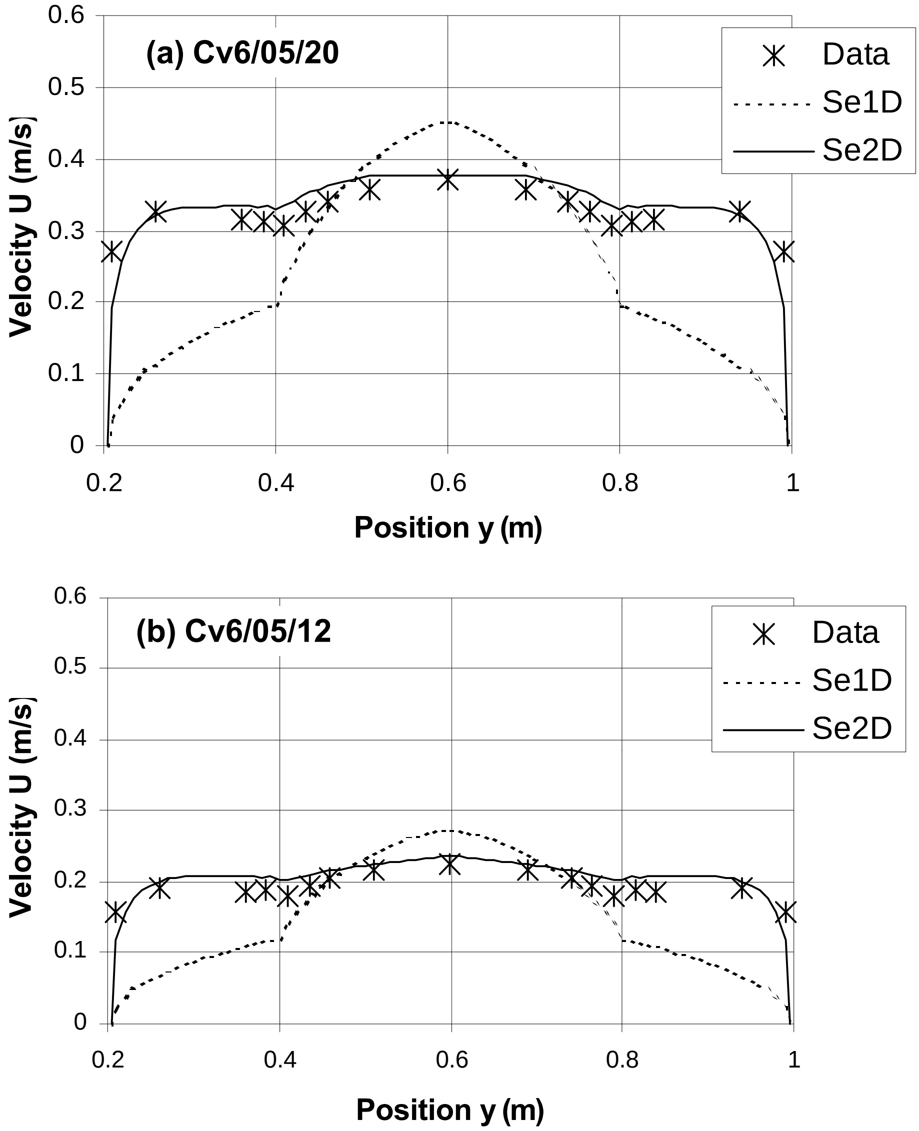

Figure 13.11 : Measured and Extended-LDM computed – using S_{e2D} (y) – velocity profiles : (a) Cv6/05/20 case; (b) Cv6/05/12 case; (c) Cv6/03/12 case; and (d) Cv2/05/20 case. $\lambda = 0.05$; $\Gamma = 0$; κ according to Table 13.1

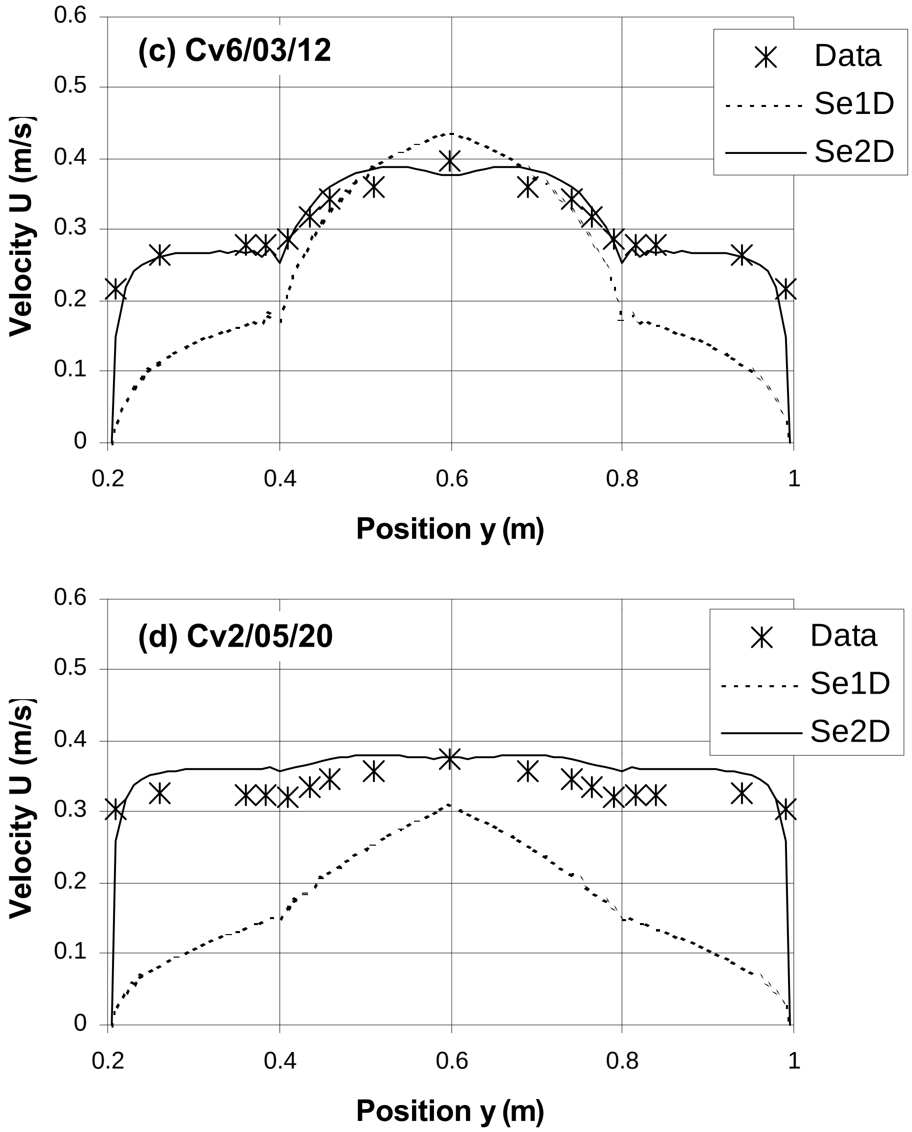

Figure 13.11 (continued)

13.6 Conclusion

The present Chapter has investigated the application of the LDM to flow in non-prismatic channels : experimental results from Chapter 12 have been compared with the results of the extension of the LDM to non-uniform flow proposed in Chapter 3.

In this extended LDM, the energy slope is used instead of the bed slope. This energy slope is computed as the sum of the acceleration, pressure and bottom-slope terms. A new secondary-current term is also defined, corresponding to the mass transfer due to non-prismaticity. This term is estimated according to the ratio κ between the transversal and longitudinal depth-averaged velocity components. This ratio κ value is found to depend mainly of the continuity equation and, as a consequence, of the channel geometry. It is assumed to have a constant value in each channel subsection.

First simulations were performed by using a one-dimensional approximate of the energy slope S_{e1D}, and by estimating a priori the parameter values. No fitting of the latter was allowed. Unsatisfactory results were obtained from these simulations. Results of a complete two-dimensional modelling demonstrated that : (1) the acceleration and pressure terms are indeed not negligible; and (2) the energy slope is not constant along the channel width, due to the decrease of the velocity longitudinal-component, in the vicinity of the wall.

Using the actual distribution of longitudinal energy slope $S_{e2D}(y)$ along the channel width, instead of the one-dimensional estimate, correct velocity-profiles predictions are obtained. Although this energy slope distribution is uneasy to assess, the other parameters of the proposed extended LDM have interesting properties, when compared with the calibration process of secondary-current models previously developed for the LDM : (1) they have a clear physical meaning; (2) they can be a priori estimated; and (3) they are relevant for non-prismatic flow modelling.

Chapter 14
Validation of the EDM for non-prismatic compound channels

14.1 Water-profile computations

In this short Chapter, the experimental results from Chapter 12 will be used for further validation of the Exchange Discharge Model (EDM), presented in Chapter 4. The particular geometry tested will enable to investigate the geometrical transfer process and the ψ^g factor significance.

Water profile computations are therefore performed with the EDM, using the AXERIV software (Bousmar and Zech 1999a). For each case, the measured water depth is used as downstream condition, while the measured discharge gives the upstream condition. The roughness coefficient is set equal to $n_c = n_f = 0.0107$ s/m$^{1/3}$, according to single-channel measurements from Chapter 12. Measured and computed water profiles are then compared for several conditions : (1) using DCM; (2) using EDM without mass transfer ($\psi^g = 0$); and (3) using EDM with entire mass transfer ($\psi^g = 1$).

Typical results are plotted on Figure 14.1, for four selected cases. Both the DCM and the EDM without mass transfer underestimate the head losses and the resulting water levels in all cases. The EDM with mass transfer gives better results, provided a $\psi^g = 1$ value is used, contrarily to the former calibration that gave $\psi^g = 0.5$ (see Chapter 4).

The largest discrepancy between measured and EDM computed water-profiles is obtained in the upstream and converging reaches of the 6-m length case, with $H_r = 0.5$ and $Q = 20$ l/s (Figure 14.1b). However, for this particular case, noticeable cross-waves are observed in the downstream prismatic section, in such a way the downstream water-level condition, to be used in the computation, is more difficult to assess. As the computed water-profile parallels well the measured one, it is expected that, with a slightly corrected downstream condition, both profiles could coincide. A lower discrepancy is also observed for the 2-m length case, with $H_r = 0.5$ and $Q = 12$ l/s, but only in the upstream prismatic reach (Figure 14.1d). This discrepancy, less than 1 mm, is supposed to a consequence of the ill-conditioned upstream discharge-distribution, that generates extra losses on the floodplains, not taken into account by the numerical modelling.

The specific-energy profiles on Figure 14.1 present also interesting features. Although the EDM-computed water-profiles ($\psi^g = 1$) match the measured ones, the corresponding specific-energy profiles are not consistent with the measurements for all the investigated cases. For the lower water level ($H_r = 0.2$, Figure 14.1c), the measured specific-energy seems better estimated by the DCM; while its value is correctly modelled by the EDM ($\psi^g = 1$) only for the higher water depth ($H_r = 0.5$, Figure 14.1b and d).

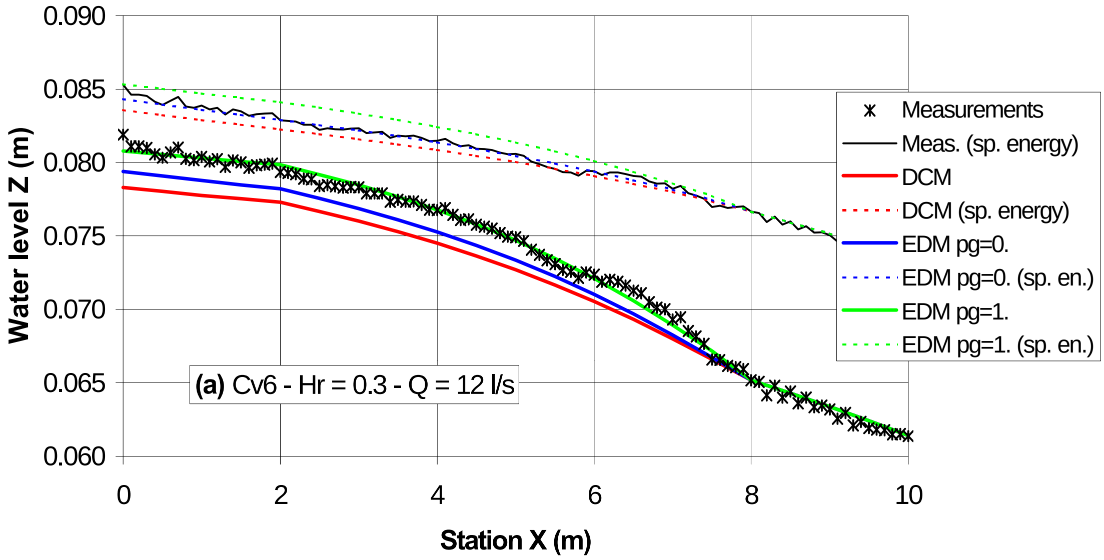

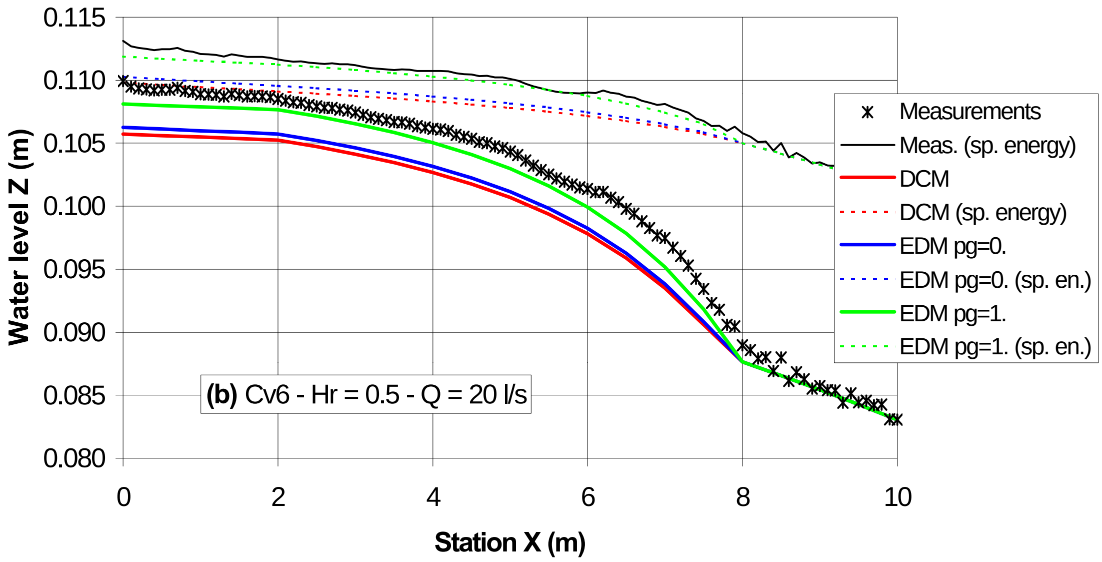

Figure 14.1 : Water-level and specific-energy profiles, measured and computed values : (a) 6-m length case, $H_r = 0.3$, $Q = 12$ l/s; (b) 6-m length case, $H_r = 0.5$, $Q = 20$ l/s; (c) 2-m length case, $H_r = 0.2$, $Q = 10$ l/s; and (d) 2-m length case, $H_r = 0.5$, $Q = 12$ l/s

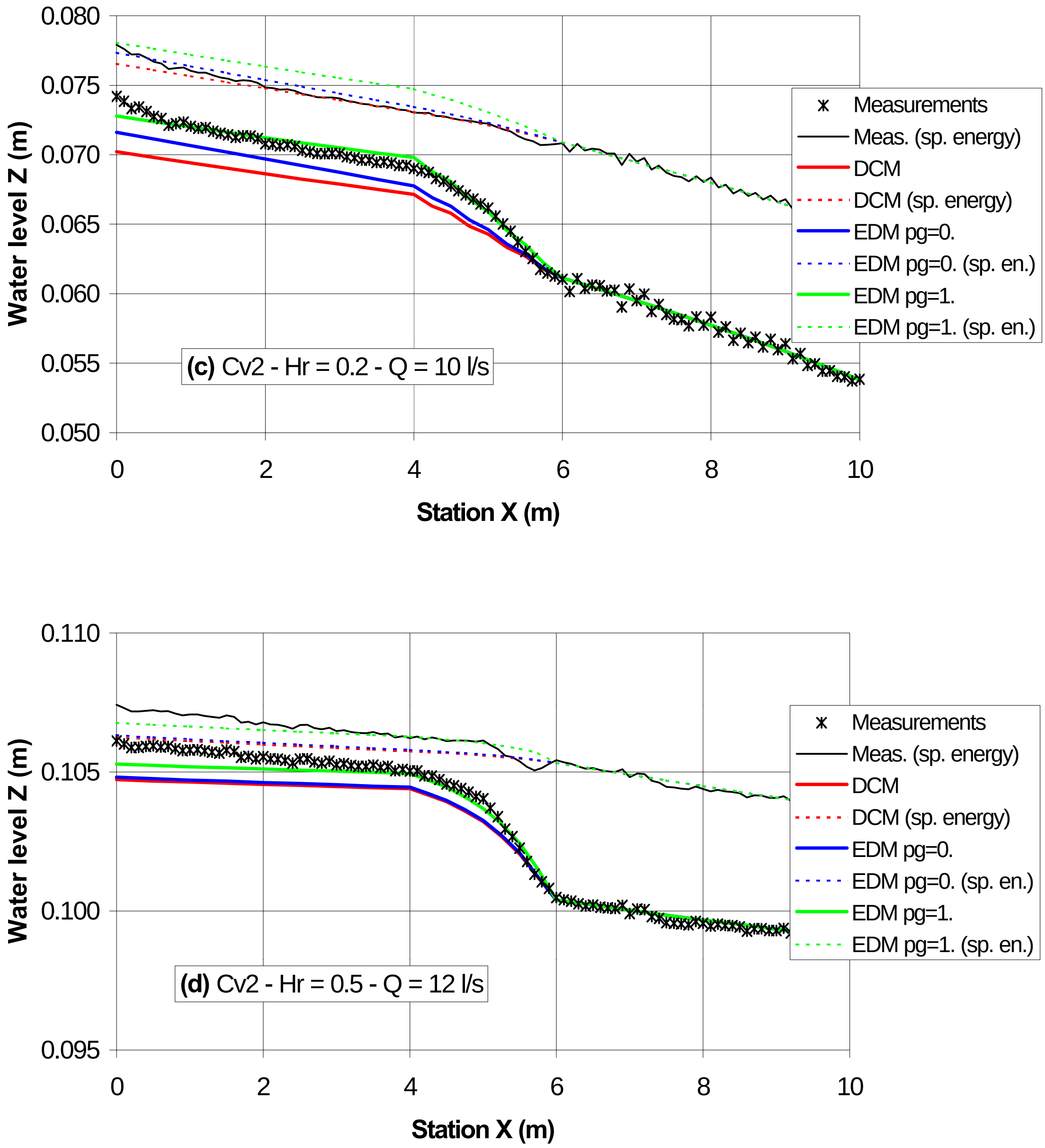

Figure 14.1 (continued)

This observation is probably due to a difference in the specific-energy profile calculation. Indeed, the specific-energy is computed as the sum of the water level z and the kinetic energy $\alpha U^2/2g$: for computational convenience, the measured values were estimated using a Coriollis coefficient α taken equal to 1 (see § 12.6); while an estimate of its actual value is used in the EDM calculation. Due to the larger velocity differences at lower water depths (H_r = 0.2 .. 0.3), the difference between the actual α value and 1 is also larger, and could explain the observed gap between measured and computed specific-energy for these cases.

14.2 Discharge distribution

As shown by Figure 14.2, the computed discharge distribution differs from the measured one, probably partly due to the ill-conditioned upstream discharge distribution in the experimental cases quoted above. Indeed, while the computed discharge distribution remains constant in the upstream prismatic section, the measured one evolves and progressively approaches the EDM one.

However, as depicted by Figure 14.3, the EDM seems also to underestimate slightly the floodplain discharge, when compared with the prismatic-reference case data, contrary to previous observation in Chapter 4, where EDM overestimated the floodplain discharge (Figure 4.5). Due to this floodplain-discharge underestimation by the EDM, but also to the ill-conditioned upstream distribution, the measured floodplain discharge is larger than the computed one, and, accordingly, the mass transfer in the converging reach is higher in the experiments. As a result, the observed momentum transfer increases also. This could explain why the momentum transfer has also to be intensified in the computation, through the use of a higher ψ^g value than expected, in order to fit the measurements

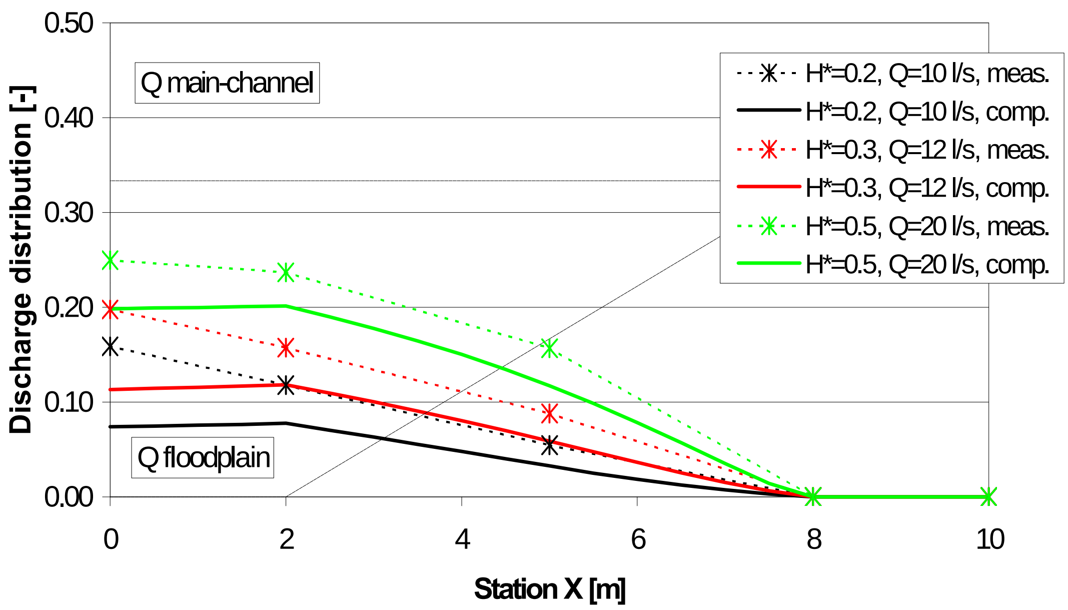

Figure 14.2 : 6-m length case, discharge distribution between subsections (half a channel). Experimental and EDM-computed values (ψ^g = 1)

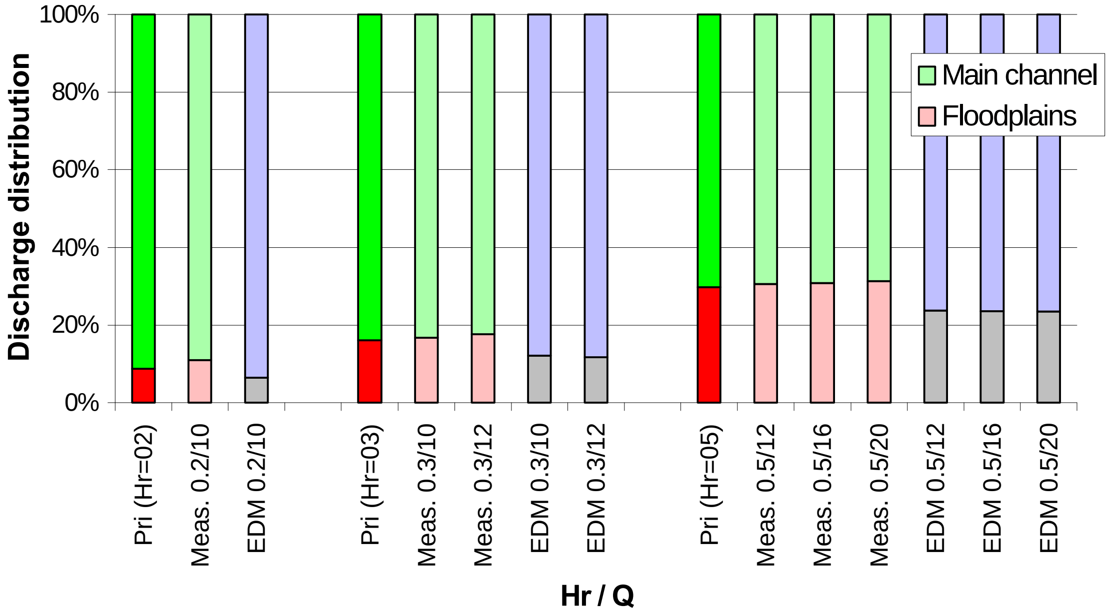

Figure 14.3 : Discharge distribution between subsections at x = 5 m. Experimental (prismatic reference-case and 6-m length converging-case) and EDM-computed values ($\psi^g = 1$)

Given the ψ^g higher value, the inaccurate discharge distribution seems not affect further the computed water profile (Figure 14.1). Indeed, in the upstream area, the water level is higher than the uniform depth given on Figure 12.2. As a result, the friction slope S_f is small and errors in its estimation only slightly affects the water profile. In the converging reach, although the computed and measured discharge distributions are different, their evolutions are parallel and, thanks to the higher ψ^g, the resulting momentum transfers are also similar, leading to a relatively small error on the computed water profile. In the downstream reach, the whole discharge flows in the main-channel and the upstream discharge distribution exerts no more influence.

14.3 Head loss analysis

To conclude this validation, the computed total head loss S_e, friction loss S_f and additional loss S_a are compared on Figure 14.4 with the experimental values from Figure 12.13, for all the tested cases. For all the cases, the friction loss is accurately modelled (error generally less than 5 % for the 6-m length narrowing case, and less than 10 % for the 2-m case). The total loss, and thus the additional loss, is overestimated for the lower water depth (H_r = 0.2 and 0.3), mainly for the higher converging angle (2-m length narrowing case); while it is correctly estimated for the higher water depth (H_r = 0.5).

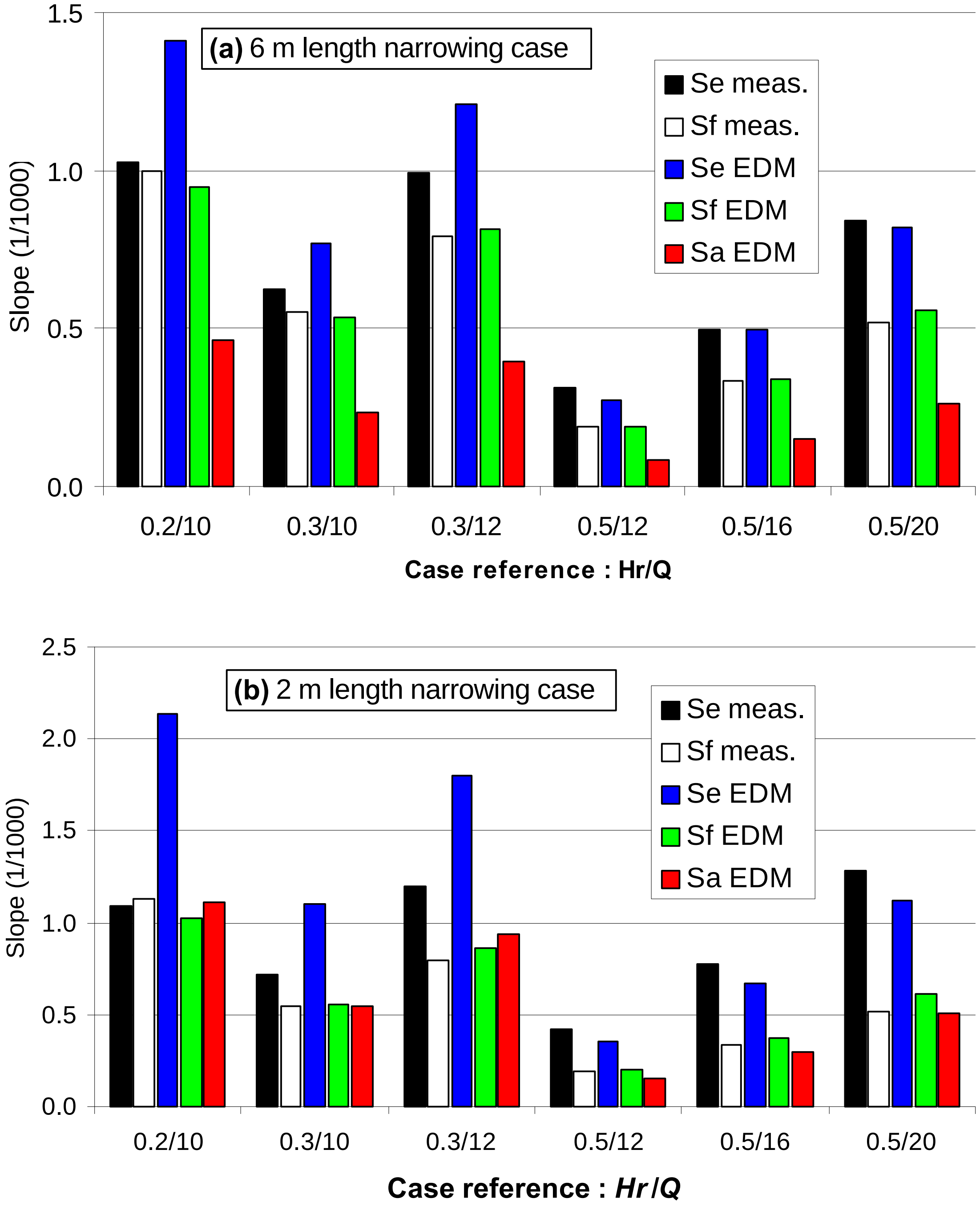

Figure 14.4 : Head loss S_e, friction loss S_f and additional loss S_a, experimental and EDM-computed values ($\psi^g = 1$)

However, as the water profiles were properly modelled for almost all these cases, it is likely that this error has only an influence on a small length of the profile computation and does not affect the whole result. On the other hand, the good results obtained for the friction loss and, in several cases, for the total head loss, give confidence in an appropriate additional loss modelling by the EDM.

14.4 Conclusion

Comparison are presented between the experimental data and computations using the EDM. The EDM-predicted discharge distribution does not fit with measurements, but the latter are influenced by a questionable upstream set-up. Taking this into account through the use of a higher ψ^g value, the computed water profiles fit well the measurements; and friction loss and total head loss are properly estimated, at least for the higher water depths.

A conclusion of this Chapter is thus an improved validation of the EDM. Unfortunately, due to the ill-conditioned upstream discharge distribution, no definitive calibration of the ψ^g coefficient can be supplied. Further experimental data are thus still required, with a more appropriate upstream discharge distribution. On the other hand, symmetrically enlarging floodplains should also be investigated, in order to study the mass transfer from the main channel to the floodplains.

Chapter 15
Additional experimental results and EDM validation : Flow near critical depth

15.1 Introduction

In the previous Chapter, the validity of the EDM has been investigated for the modelling of the momentum transfer due to the geometrical mass-transfer in a non-prismatic channel. The geometrical-transfer effect will now be explored in an ever more simple geometry, but with still more complicated flow features : a prismatic compound channel is considered, with a control section as downstream boundary condition. As the water level reduces when approaching this control section, the discharge distribution varies accordingly, and strong geometrical transfers between floodplains and main channel are observed. Due to the water-level decrease, the main-channel water depth will even become lower than the bank height, despite the fact that water can still flow on the floodplains. This results in two-dimensional features of the water-surface (transverse slope) that have to be taken into account.

The two-dimensional numerical model developed in this work could probably provide interesting information on this particular situation. However, due to a lack of time and of measured data, it has been chosen to restrict the present investigation to one-dimensional modelling. Two main objectives will be considered : (1) assess the possible limit of validity of such an approach; and (2) test once more the EDM validity. After a short state-of-the-art review on critical flow in compound channels, some experimental results will be presented and compared to EDM computations (Bousmar and Zech 1999b).

15.2 Critical flow in a compound channel : state of the art

In compound channels, two critical depths can be observed for some cross sections. Blalock and Sturm (1981) first observed experimentally two minima in the specific-energy curve (Figure 15.1a). In order to calculate the two corresponding critical depths, they calculated the specific-energy values, using for the kinetic energy value $\alpha U^2/2g$ a Coriollis coefficient α estimation based on the DCM discharge distribution. According to Blalock and Sturm, for an increasing water depth H (due e.g. to a bed slope S_0 decrease, at a constant discharge Q), the first critical depth is below the bank level and corresponds to the transition from super- to subcritical flow in the main channel (Figure 15.1b). At the beginning of overbanking, supercritical flow appears in floodplains while flow remains subcritical in the main channel. The second critical level is then above the bank level and corresponds to the depth where flow changes from super- to subcritical in the floodplains. Strong two-dimensional aspects are observed in the flow between those two depth (Blalock and Sturm, 1983).

Those two-dimensional features were confirmed by Yuen and Knight (1990) who observed super- and subcritical flow in a same cross-section for a given water depth. Due to the momentum transfer, the velocity in the floodplains is higher in the interface zone : an higher Froude number is thus observed in this zone, which is the last to become subcritical. Yuen and Knight measured a relative inaccuracy of Blalock and Sturm's critical-depth estimation, as the latter neglects the momentum transfer between subsections. Sturm and Sadiq (1996) observed, at critical depths, lower water levels in the main channel than in the floodplains, invalidating locally the one-dimensional flow modelling. Nevertheless, by direct integration of an adapted gradually varied flow equation, using a corrected Froude number, they obtained good agreement of computed water profiles with experimental data, for depths quite close to the critical ones.

The purpose of the current Chapter is to enlarge such comparisons with experimental data. For water-profile computation, the Standard Step Method will be used, using the AXERIV Software (Bousmar and Zech 1999a) as it is closer to the methods found in commercial package.

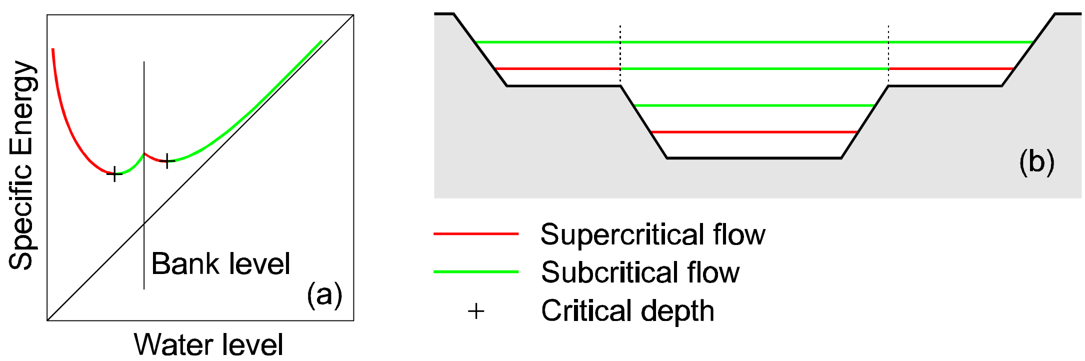

Figure 15.1 : Flow transitions in a compound channel : (a) specific energy curve, (b) location of super- and subcritical flow in subsections

15.3 Experimental results

Measurements were performed in the UCL compound-channel flume (see Appendix 3). As quoted above, the prismatic geometry is tested, with two symmetrical floodplains 400-mm wide, extending on the whole channel width (Figure 15.2). The longitudinal bed slope is set to $S_0 = 0.85 \times 10^{-3}$. The weir is completely lowered, in order to have a control section near the flume downstream-boundary, with water falling in the outlet tank at the station $x = 10$ m.

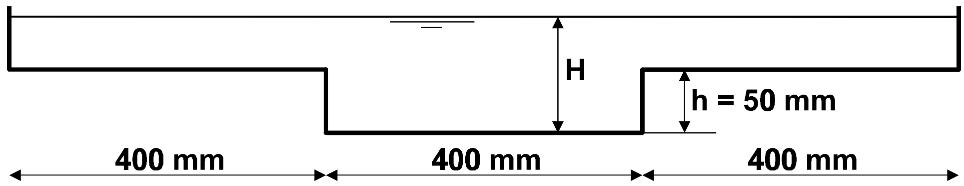

Figure 15.2 : Cross section of the experimental symmetrical compound channel

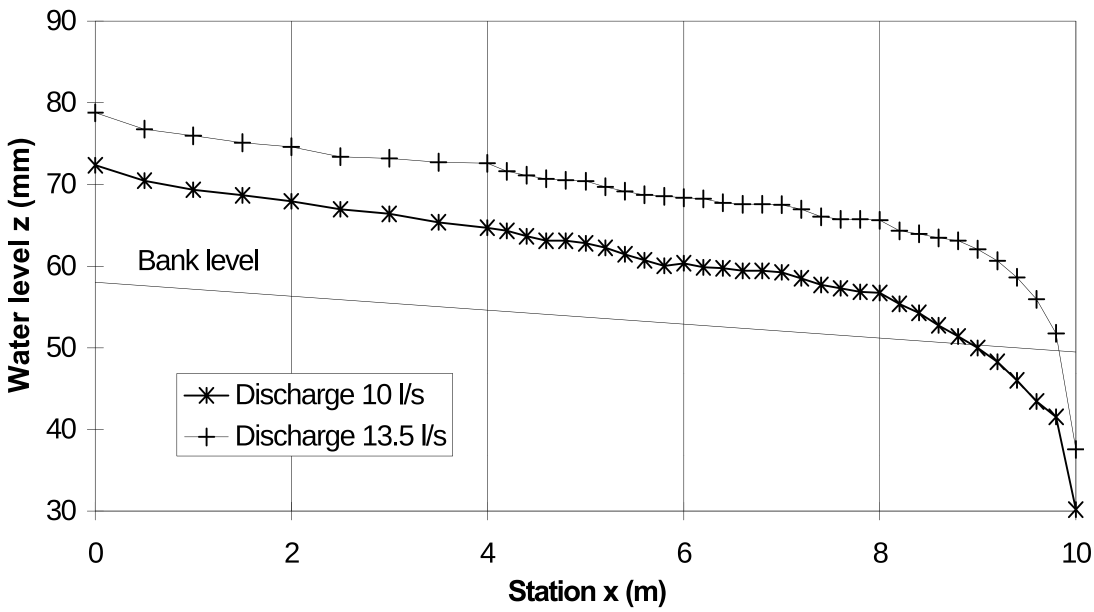

Figure 15.3 : Measured water profiles, along the centre line of the main channel

Two measured water profiles are presented, for discharges Q = 10.0 l/s and Q = 13.5 l/s (Figure 15.3 and Figure 15.4). For the 10.0 l/s discharge, the downstream limits of the flooded area in the floodplains were at station x = 8.5 m on the right floodplain and at x = 9.5 m on the left one (see Figure 15.5). In this case, the last wet half-meter was almost still water retained by surface tension on the plywood. For the 13.5 l/s discharge, the floodplains were flooded till the downstream control section. Figure 15.3 gives the water profiles measured along the centre line of the main channel. Irregularities in the profiles are due to channel bed irregularities, this sensibility to geometry could be explained by the proximity to the critical depth.

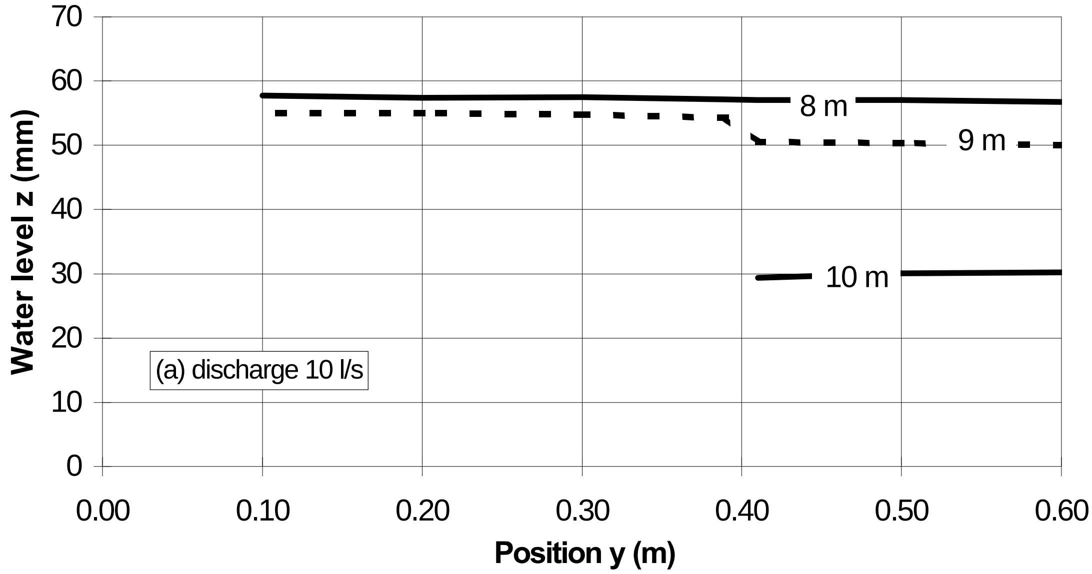

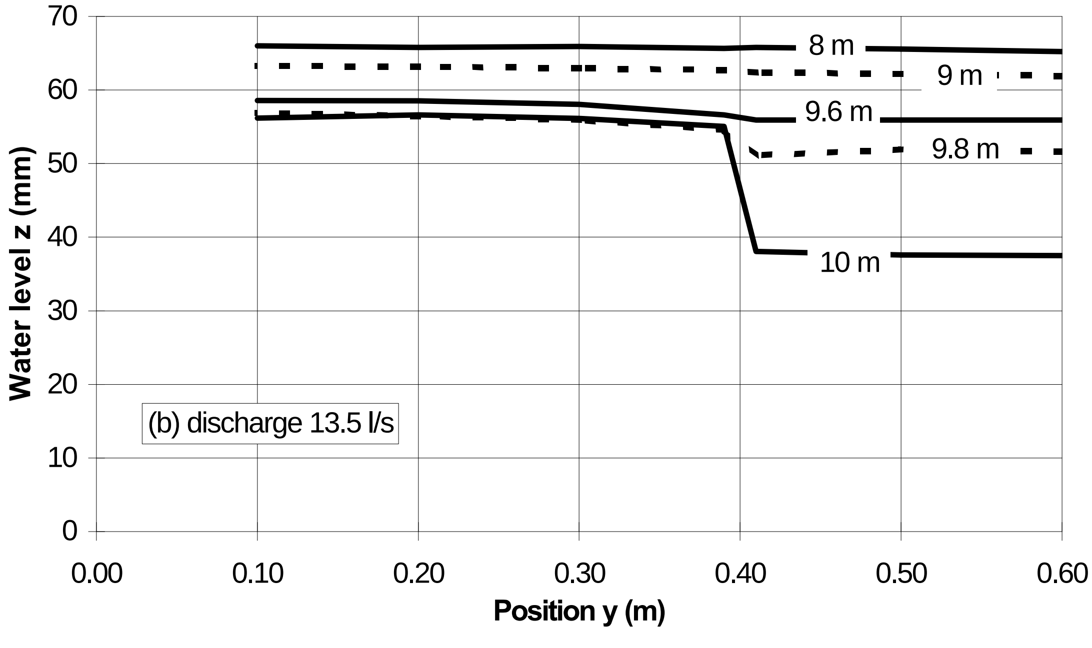

Figure 15.4 : Transverse water profiles at given stations : (a) Q = 10 l/s; and (b) Q = 13.5 l/s (for half a section)

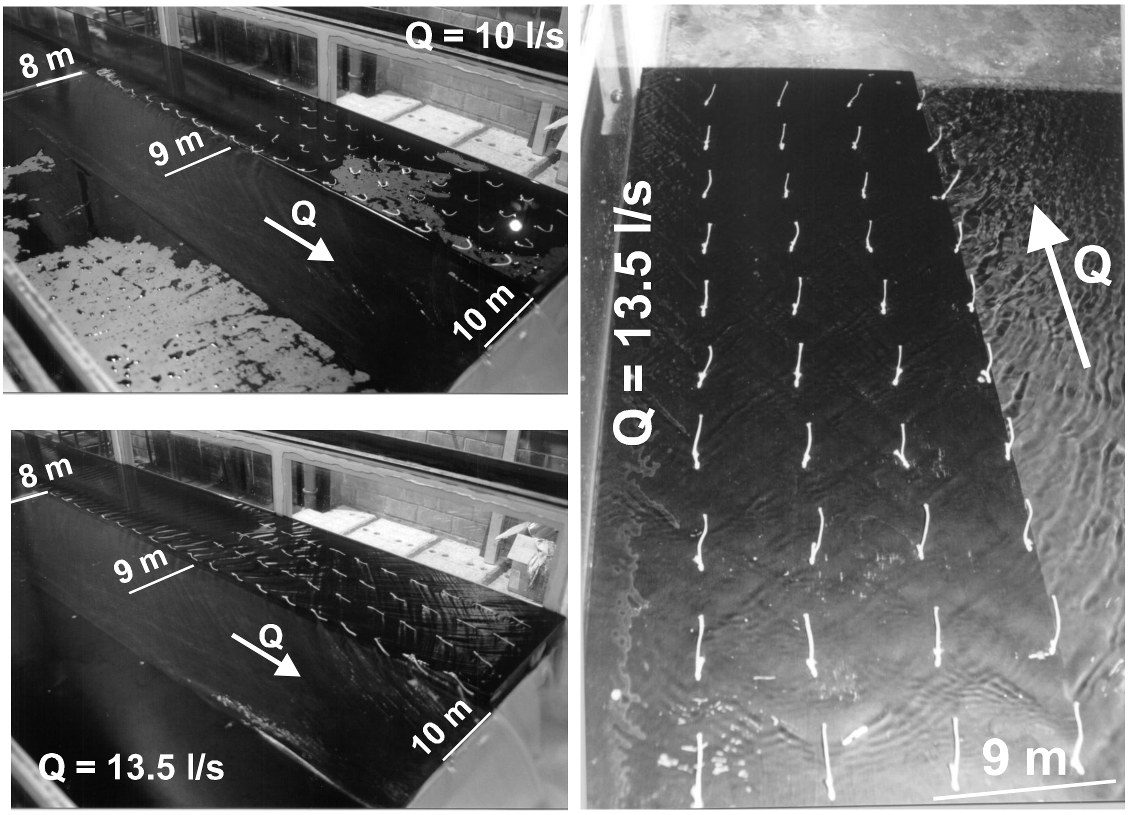

Figure 15.5 : Photographs of the outlet section at Q = 10 l/s and Q = 13.5 l/s

Figure 15.4 shows level differences in the profile across the channel similar to the ones observed by Sturm and Sadiq (1996). These differences are observed in the last meter of the 13.5 l/s profile, with water level falling under the bank level, and in the last 1.5 m of the 10 l/s profile, where the floodplains are emptying into the main channel. In these areas, an important lateral velocity component from floodplains to main channel was observed (Figure 15.5).

15.4 Critical-depth analysis

For a 10 l/s discharge, the analysis of the specific energy curve (Figure 15.6) according to Blalock and Sturm predicts a unique critical depth in the main channel at 39.9 mm. The measure of a water depth of 30.2 mm, at the outlet section, and of 41.5 mm, 0.20 m upstream from the outlet (see Figure 15.3), confirms this prediction. The critical depth is thus located a few centimetres upstream from the outlet edge.

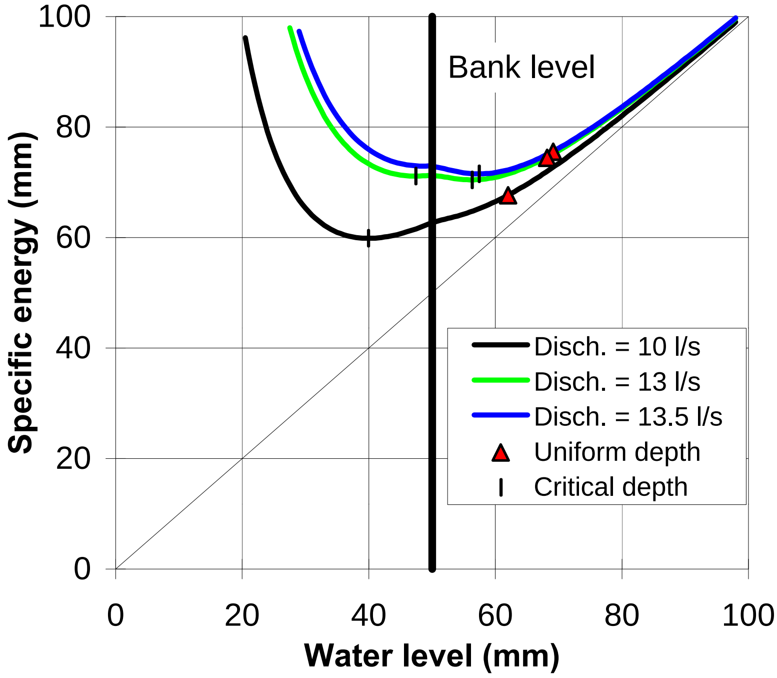

Figure 15.6 : Specific energy curve, calculated for discharges of 10, 13 and 13.5 l/s

For the 13.5 l/s discharge, the two downstream levels of the water profile in the main channel are measured at 51.6 and 37.5 mm while the same sections in the floodplain both present a 56.0 mm depth (see Figure 15.4b). The critical depth is computed as unique at 57.4 mm, and seems thus overestimated. As it was proposed by Yuen and Knight (1990), this could be explained by a wrong estimation of the specific energy, the computation of which neglects the momentum transfer influence. Indeed, for a slightly smaller discharge (13 l/s), a double critical depth appears, at 47.4 and 56.3 mm (Figure 15.6). Actually, the transition between a double and a unique critical depth is thus not so clear, due to the absence of two-dimensional aspects in the model.

15.5 Water-profile computations

Water profiles were computed using a classical resolution of the one-dimensional steady-flow Bernoulli equation by the Standard Step Method (French, 1985). The computations were performed with : (1) the Single Channel Method (SCM); (2) the Divided Channel Method (DCM); and (3) the Exchange Discharge Model (EDM), with a value of $\psi^g = 0.5$, as calibrated in Chapter 4. As the standard step method is unable to compute profiles crossing the critical depth, the downstream water level fixed for computation was chosen as the last measured point of the water profile above the computed critical depth. The cross-sections of the flume were carefully measured to model also the water surface irregularities. In order to get accurate simulations, even in steep water-slope areas near the critical depths, an interval of 0.20 m between cross-sections was selected.

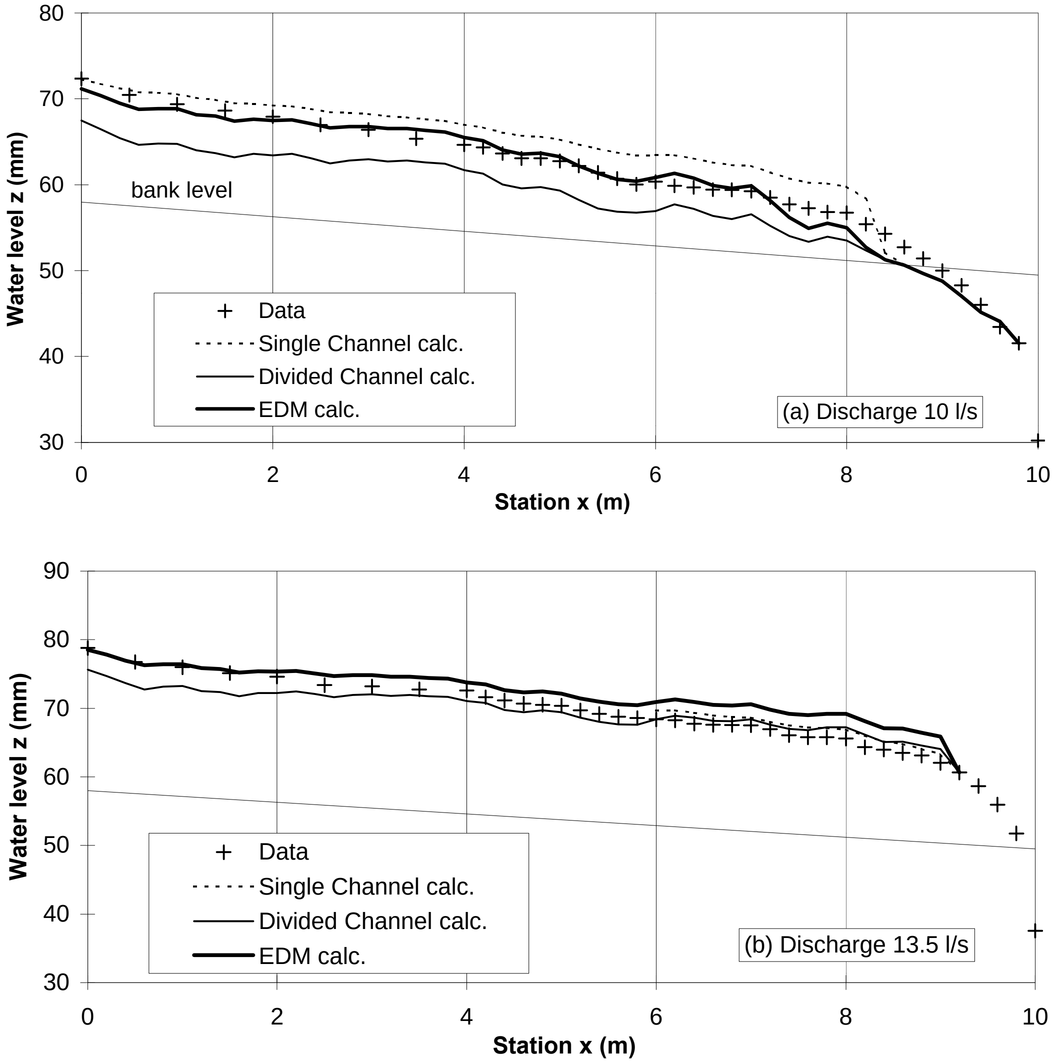

Figure 15.7 : Measured and computed water profiles, computation starting from critical depth : (a) Q = 10 l/s; and (b) Q = 13.5 l/s

For the 10 l/s discharge (Figure 15.7a), EDM clearly produces the best results with a quite accurate simulation of the surface irregularities. The results can be improved only in the downstream area. It could be due to the closeness of the control section and to the subsequent influence of vertical velocities at this point; but also to two-dimensional flow features, just upstream of this control section. A better agreement can be obtain if the downstream condition is taken, for example, 1 m upstream from the outlet (Figure 15.8a). In this case, the agreement of the EDM is very good compared to the measurement precision, even for the 3 downstream metres of the flume. The generally better results of the EDM proves its ability to model accurately the sudden conveyance reduction and the resulting water-slope increase that occurs when water just exceeds the bank level, generating the momentum transfer.

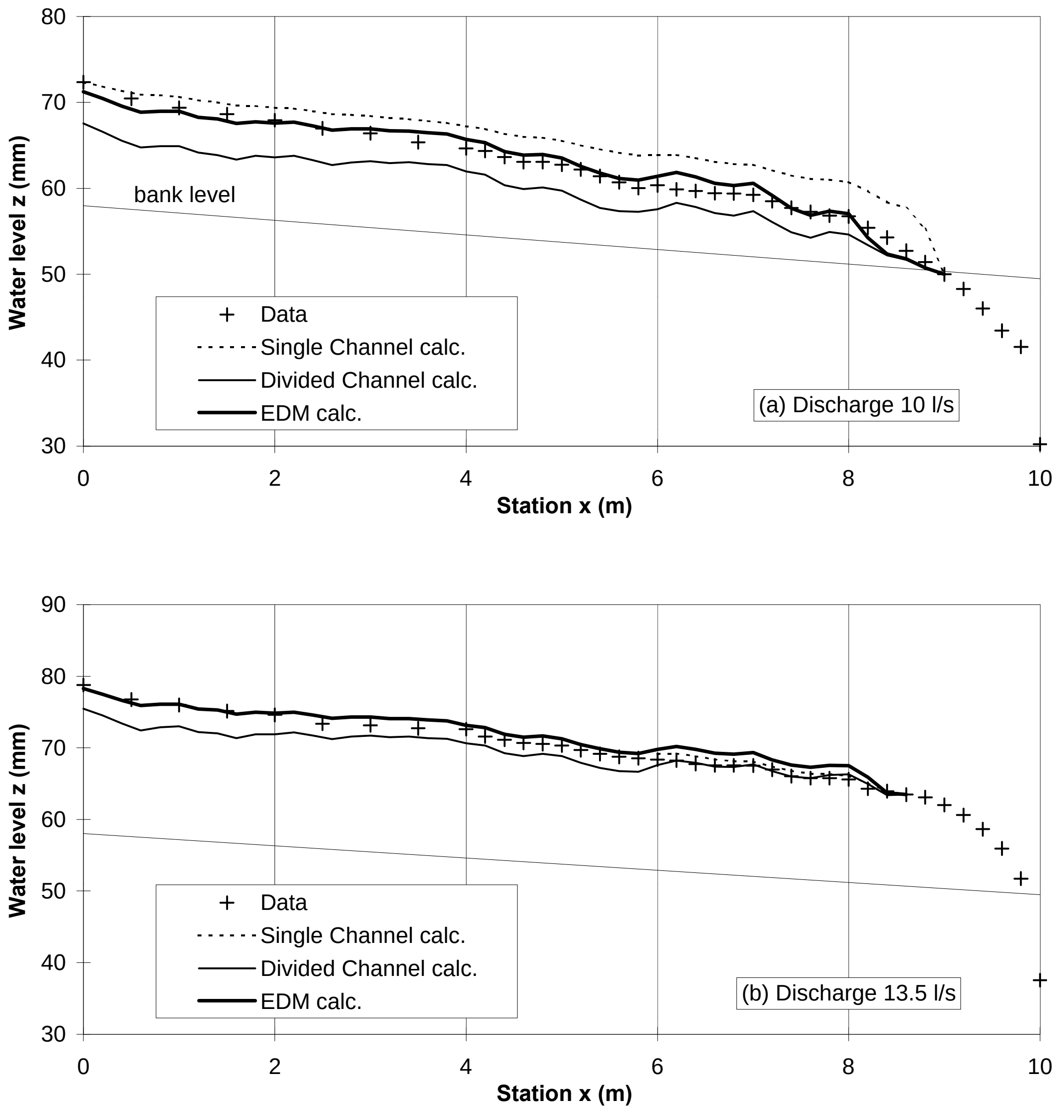

Figure 15.8 : Measured and computed water profiles : (a) Q = 10 l/s, computation starting from x = 9 m; and (b) Q = 13.5 l/s, computation starting from x = 8.6 m

For the 13.5 l/s discharge (Figure 15.7b), none of the 3 methods gives directly satisfactory results. The SCM is clearly inapplicable as the profile computation is cut off at 6 m section, due to a local rise of the critical depth (the latter also computed by SCM), that thus intersects the water profile. Only the EDM seems to model accurately the upstream part of the profile, where the latter approaches the uniform depth. Slightly better results for the downstream area can again be obtained by taking the downstream condition at a greater distance from the outlet (Figure 15.8b), upstream of the two-dimensional flow area. The small distance between the water profile and the critical-depth profile, along almost the whole channel, could explain the difficulty to get better results for this discharge

15.6 Conclusion

Two water profiles were measured in a compound channel with a control section as downstream condition. In both cases, two-dimensional components appeared on the water surface near the critical depth. It is found that specific-energy curve analysis, performed according to Blalock and Sturm (1981) fails in estimating accurately the critical depth above floodplains level, probably because the momentum transfer between subsections is not taken into account.

Using the EDM, an accurate modelling of the upstream part of the water profile is made possible. On the other hand, none of the tested methods succeed in modelling the profile in areas adjacent to critical depth, probably due to the observed two-dimensional characteristics. Better results are only obtained when the downstream condition is imposed at some distance upstream of the control section, where the flow surface is again one-dimensional. In this case, the EDM gives again the best results, when considering the whole length of the computed water profile.

In order to improve this analysis, velocity measurements should be made in the downstream part of the flume. This would enable the mapping of the Froude number of the flow, and, accordingly, the exact location of the critical sections in both main channel and floodplains. Using such observations, critical-depth estimations could at least be validated; while a better assessment of the one-dimensional model limits would be facilitated.

Conclusion

1. Summary of the results

In the present work, the flow in a compound channel has been investigated using theoretical, experimental and numerical modelling. A one-dimensional model, the Exchange Discharge Model (EDM), has been proposed as a general framework for flow modelling and analysis. The momentum-transfer mechanisms in prismatic and non-prismatic channels have been deeply explored. Consequently, the first part of this conclusion will summarise the most significant results of this research work; while the second part will propose some improvement possibilities that could constitute objectives for further studies.

The Exchange Discharge Model takes into account the momentum-transfer effect on the channel conveyance through an additional head loss, to be added to the friction loss estimated by the classical Divided Channel Method. The momentum transfer is therefore modelled as proportional to the discharges exchanged through the interface between the main channel and the floodplain, and to the velocity difference between both subsections. Two sources of exchange discharges are identified : (1) a turbulent-exchange discharge, due to the large-scale horizontal vortices that develops in the shear layer at the interface; and (2) a geometrical-transfer discharge, due to the mass transfer that occurs in non-prismatic channels, or in non-uniform flow conditions.

Using the EDM, the actual channel-roughness values can be adopted, and only two additional parameters (ψ^t and ψ^g) have to be assessed. It has been found that, in a first approximation, constant values could be given to both parameters. With these values, the EDM-predicted discharges match measured data with a better accuracy than the classical Single Channel and Divided Channel Methods, and with the same accuracy as the Ackers and the Lateral Distribution Methods. Water profiles are accurately calculated by the EDM. The prediction of the flow distribution between subsection is also improved, but with a lower accuracy than for the total discharge estimation.

The turbulent-exchange process has been investigated experimentally, analytically and numerically. Using experimental velocity-field measurements obtained by a PTV technique, an analysis method has been developed to identify periodical-structures characteristics. The vortex wave lengths obtained from the experiments, from a linear hydrodynamic stability analysis and from a numerical simulation, are found in fairly good agreement. However, the influence of the vortices-merging process could not be definitively evaluated : indeed, it seems that the experimentally-observed vortex wave lengths match better with the wave lengths estimated before than after vortices merging in the numerical simulation, whereas, one should expect that vortices merging actually occurs in the experiments.

Additionally, it has been found that the presence of the vortices improves the numerically-predicted velocity profiles, at least in the shear-layer area; while the computed velocity remains underestimated on the floodplain, probably due to the secondary-currents effect. A detailed analysis of the shear stress at the interface and of the related momentum-transfer process tends to indicate that the effect of the large horizontal vortices is adequately modelled by the EDM; and that the EDM weakness regarding the flow-distribution prediction could also be imputed to the secondary-currents effect.

On the other hand, the geometrical-transfer process has been investigated experimentally, through flow measurements in a compound channel with symmetrically narrowing floodplains, for which no curvature-driven currents should be observed, when compared to the meandering geometries investigated by previous authors. Nevertheless, it has been observed that secondary currents driven by the geometrical transfer are quite similar to the currents previously depicted in the cross-over area of a meandering compound channel.

When comparing measurements performed in the same cross section and with the same water depth but with a different discharge, it has been noticed that the flow distribution does not depend on the total discharge, but only on geometrical parameters. Accordingly, this validated the assumption made during the EDM development, that the ratio between the additional loss due the geometrical transfer and the friction loss is independent from the whole-channel discharge.

When compared with the water profile measurements, the EDM gave satisfactory results, although an increased value of the ψ^g parameter had to be used. This need for an increased ψ^g value has been imputed to an underestimation of the floodplain discharge by the numerical simulation : as a result, the mass transfer reduced and the ψ^g value had to be increased in order to get an unmodified geometrical momentum transfer. Two reasons for this floodplain-discharge underestimation were suggested : (1) the effect of an ill-conditioned upstream discharge distribution; and (2) the erroneous flow-distribution estimation by the EDM.

Lastly, some reflections were proposed regarding the secondary-current modelling in the Lateral Distribution Method (LDM), and attempting to improve the physical meaning of the parameters used in such models. On one hand, the helical secondary currents observed in prismatic channels were investigated using a dispersion-term modelling : results similar to the one of the Shiono and Knight LDM were obtained, but the dispersion coefficients used therefore had no physical meaning in term of secondary-currents pattern. On the other hand, a tentative extension of the LDM for non-prismatic channels was proposed, replacing the bed-slope term by an energy-slope term, and defining a secondary-current term strictly proportional to the actual transverse velocity. Accurate results with this extended LDM were obtained only when a non-constant value of the energy slope across the channel width was considered.

2. Perspectives for further works

In the present work, the EDM has been validated for prismatic-channel modelling. Regarding non-prismatic geometries, it has only been tested for small mass-transfer rates : for a slightly-meandering river geometry in the River-Sambre test case, and for limited converging angles in the narrowing-floodplains experiments. It is expected that the EDM geometrical-transfer modelling is appropriate for larger mass-transfer rates. However, the EDM validation should be extended to such meandering compound channels with larger sinuosity, for example using data from the FCF Series B experiments (Sellin et al. 1993).

Promising results were obtained from the investigations of the periodical turbulent structures in the shear layer between the main channel and a floodplain. However, two weaknesses were identified : (1) the merging-process modelling, linked with the wall-constraining effect; and (2) the secondary-current effect on the floodplain velocity. Additionally, the numerical simulations would benefit of an improved Sub-Depth-Scale modelling, closer to an actual LES model.

In order to explore further the possible vortices merging, it could be useful to switch from the perturbation temporal-growth analysis to a spatial-growth analysis, that corresponds better to experimental conditions. This spatial growth could be observed experimentally by repeating the PTV measurements for several stations along the channel length; as far however as the inlet-tank configuration is adapted in order to correct the ill-conditioned upstream discharge-distribution observed in the experiments reported in Chapter 12. Whereas the extension of the stability analysis to perturbation spatial-growth should not be too difficult, the extension of the numerical simulations will require adapted upstream and downstream boundary conditions, enabling a random initial perturbation to be introduced in the computational domain.

On the other hand, new experimental observations of the secondary-currents development on the floodplains are necessary, in order to assess better their effect on the momentum balance. Whereas the horizontal vortices were rather easily captured using surface velocimetry, the identification of secondary-current cells probably requires the measurement of the instantaneous velocity field in a cross-section vertical plane. Such a measurement will be much more difficult, as the ratio between the longitudinal velocity and the transverse and vertical velocities is rather large. Accordingly, the tracers used for flow visualisation will move fast through a vertical observation plane, resulting in very small transverse displacements to be measured. Maybe a tri-dimensional stereoscopic particle-tracking method such as the one recently developed at the UCL (Spinewine et al. 2001) could provide some interesting results.

When investigating the geometrical-transfer process, the flow was experimentally studied in a novel geometry with symmetrically narrowing floodplains, providing interesting observations. Such experiments should be pursued with a corrected upstream discharge distribution, in order to reduce the incertitude regarding the actual discharge distribution in a non-prismatic reach, with reference to the corresponding discharge distribution in a prismatic reach with a similar cross-section. On the other hand, whereas the narrowing geometry enables the observation of a geometrical transfer from the floodplain to the main channel, the opposite geometrical transfer should also be investigated, using a compound channel with symmetrically enlarging floodplains.

As pointed out above, the EDM validation should be enlarged to the FCF meandering-channel geometries. If possible, analyses similar to the one made for the symmetric geometry should be performed, regarding the flow distribution in a non-prismatic geometry and in the corresponding prismatic reach, but also by estimating the actual mass-transfer rates.

Lastly, it could be interesting to enlarge this work to morphological processes associated with compound-channel flow. Indeed, it has been observed both experimentally (Benson et al. 1997) and in the field (Woo and Kim 1997) that sediment transport occurs from the main channel to the floodplains, resulting in large deposits on the floodplains. Such transport processes are certainly linked with the exchange discharges proposed in the EDM development. As a consequence, the EDM could constitute an interesting framework for modelling such phenomena.

Appendices

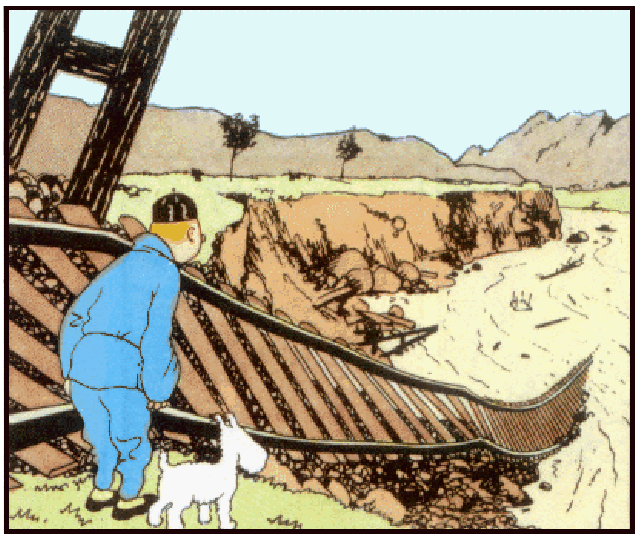

A flood on the Yang-Tse River,
in Hergé (1946), Le Lotus Bleu

References

Abida, H., and Townsend, R.D. (1994). "A model for routing unsteady flows in compound channels." *Journal of Hydraulic Research, IAHR*, 32 (1), 145-153.

Abril, J.B. (1995). "Numerical modelling of turbulent flow in compound channels by the finite element method." *Proc. 26th Congress of IAHR, Hydra 2000*, London, 5, 1-6.

Ackers, P. (1993). "Flow formulae for straight two-stage channels." *Journal of Hydraulic Research, IAHR*, 31 (4), 509-531.

Ackers, P. (1991). "Discussion on 4 papers of Journal of Hydraulic Research, 28 (2), 1990)." *Journal of Hydraulic Research, IAHR*, 29 (2), 263-271.

Ackers, P. (1992). "Hydraulic design of two-stage channels." *Proc. I.C.E., Water, Maritime and Energy*, 96 (4), 247-257.

Alavian, V., and Chu, V.H. (1985). "Turbulent exchange flow in shallow compound channel." *Proc. 21st Congress of IAHR*, Melbourne, 3, 446-451.

Asano, T., Hashimoto, H., and Fujita, K. (1985). "Characteristics of variation of Manning's roughness coefficient in a compound cross section." *Proc. 21st Congress of IAHR*, Melbourne, 6, 30-34.

Benson, I., Valentine, E.M., Nalluri, C., and Bathrust, J.C. (1997). "Flood Channel Facility : experiments in two-stage mobile boundary channels." *Proc. 27th Congress of IAHR*, San Francisco, B2, 949-954.

Bertrand, G. (1994). "Le calcul d'axes hydrauliques dans les rivières à plaines inondables." *Mémoire de Stage*, Ministère Wallon de l'Equipement et des Transports, D. 213, Chätelet, Belgium (in French).

Berz, G. (2000). "Flood disasters : lessons from the past - worries for the future." *Proc. 28th Congress of IAHR, Post congress volume*, Graz, Austria, 9-16.

Betchov, R., and Criminale, W.O. (1967). *Stability of parallel flows*. Academic, New York.

Bhattacharyya, N.N., and Bora, A.K. (1997). "Floods of the Brahmaputra river in India." *Water International, IWRA*, 22 (4), 222-229.

Blalock, M.E., and Sturm, T.W. (1981). "Minimum specific energy in compound open channel." *Journal of the Hydraulics Division, ASCE*, 107 (6), 699-717.

Blalock, M.E., and Sturm, T.W. (1983). "Closure of Minimum specific energy in compound open channel (Blalock, Sturm, 1981)." *Journal of the Hydraulics Division, ASCE*, 109 (3), 483-486.

Bousmar, D., and Zech, Y. (1999a). "Momentum transfer for practical flow computation in compound channels." *Journal of Hydraulic Engineering, ASCE*, 125 (7), 696-706.

Bousmar, D., and Zech, Y. (1999b). "Adequacy of one-dimensional flow modelling in compound channels near critical depth." *Proc. 28th Congress of IAHR*, Graz, Austria, CD-Rom proceedings.

Bousmar, D., and Zech, Y. (2000). "Depth-averaged large eddy simulation of the turbulence structures in a compound-channel flow." *Proc. Hydroinformatics'2000*, Iowa City, USA, CD-Rom proceedings.

Bousmar, D., and Zech, Y. (2001a). "Secondary-current impact on momentum transfer for compound channels flow modelling." *Proc. 29th Congress of IAHR*, Tsinghua University Press, Beijing, China, D1, 189-195.

Bousmar, D., and Zech, Y. (2001b). "Discussion of Two-dimensional solution for straight and meandering overbank flows, by D.A. Ervine, K. Babaeyan-Koopaei and R.H.J. Sellin, JHE, 2000, 126(9)." *Journal of Hydraulic Engineering, ASCE* (in press).

Bousmar, D., and Zech, Y. (2001c). "Periodic turbulent structures modelling in a symmetric compound channel." *Proc. 29th Congress of IAHR*, Tsinghua University Press, Beijing, China, D1, 244-249.

Bousmar D., Scherer R., and Zech Y. (1998). "One-dimensional unsteady flow computation in channels with floodplains." *Hydraulic Engineering Software VII*, Blain, ed., Computational Mechanics Publications, Southampton, U.K., 205-214.

Bousmar, D., Wilkin, N., Jacquemart, J.-H., and Zech, Y. (2001). "Experiments on overbank flow in symmetricaly narrowing floodplains." Submitted for publication in *Journal of Hydraulic Engineering, ASCE*.

Capart, H., Young, D.L., and Zech, Y. (2001). "Voronoï imaging methods for the measurement of granular flows." *Experiments in Fluid* (in press).

Cassells, J.B.C., Lambert, M.F., and Myers, R.W.C. (2001). "Discharge prediction in straight mobile bed compound channels." *Proc. Institution of Civil Engineers, Water and Maritime Engineering*, 148 (3), 177-188.

Chang, H.H. (1988). *Fluvial processes in river engineering*. John Wiley and Sons, New York.

Chaudhry, M.H. (1979). *Applied hydraulic transients*. Van Nostrand Reinhold, New York (2nd edition 1987).

Chaudhry, M.H. (1993). *Open-Channel Flow*. Prentice Hall, New Jersey.

Chen, D., and Jirka, G.H. (1997). "Absolute and convective instabilities of plane turbulent wakes in a shallow water layer." *Journal of Fluid Mechanics*, 338, 157-172.

Chu, V.H., and Babarutsi, S. (1988). "Confinement and bed-friction effects in shallow turbulent mixing layers." *Journal of Hydraulic Engineering, ASCE*, 114 (10), 1257-1274.

Chu, V.H., Wu, J.H., and Khayat, R.E. (1991). "Stability of transverse shear flow in shallow open channels." *Journal of Hydraulic Engineering, ASCE*, 117 (10), 1370-1388.

Devriendt, D., Douxchamps, D., Capart, H., Craeye, C., Macq, B., and Zech Y. (1998). "Three-dimensional reconstruction of a periodic free surface from digital imaging measurements." *Advances in Fluid Mechanics II*, M. Rahman, G. Comini, C.A. Brebbia, eds, Computational Mechanics Publications, Southampton, U.K., 203-212.

Dracos, T., and Hardegger, P. (1987). "Steady uniform flow in prismatic channel with flood plains." *Journal of Hydraulic Research, IAHR*, 25 (2), 169-185.

Drazin, P.G., and Reid, W.H. (1981). *Hydrodynamic stability*. Cambridge University Press, Cambridge.

Elliott, S.C.A., and Sellin, R.H.J. (1990). "SERC flood channel facility : skewed flow experiments." *Journal of Hydraulic Research, IAHR*, 28 (2), 197-214.

Ervine, A., Fuller, C., and Pender, G. (1997). "Sediment transport in a gravel bed channel during overbank flow." *Proc. 27th Congress of IAHR*, San Francisco, B2, 1031-1036.

Ervine, D.A., and Baird, J.I. (1982). "Rating curves for rivers with overbank flow." *Proc. Institution of Civil Engineers, Part 2*, 73, 465-472.

Ervine D.A., Babaeyan-Koopaei K., and Sellin, R.H.J. (2000). "Two-dimensional solution for straight and meandering overbank flows." *Journal of Hydraulic Engineering, ASCE*, 126 (9), 653-669.

Ervine, D.A., Willetts, B.B., Sellin, R.H.J., and Lorena, M. (1993). "Factors affecting conveyance in meandering compound flows." *Journal of Hydraulic Engineering, ASCE*, 119 (12), 1383-1399.

Ferziger, J.H., and Peric, M. (1996). *Computational methods for fluid dynamics*. Springer, Berlin.

French, R.H. (1985). *Open-channel hydraulics*. McGraw-Hill, New-York, USA.

Fukuoka, S., and Watanabe, A. (1995). "Horizontal flow structures in channels with dense vegetation clusters and the numerical analysis thereof." *Proc. 26th Congress of IAHR*, *Hydra 2000*, London, 1, 296-301.

Fukuoka, S., and Watanabe, A. (1997)."Horizontal structure of flood flow with dense vegetation clusters along main channel banks." *Proc. 27th Congress of IAHR*, San Francisco, B2, 1408-1413.

Garcia-Navarro, P., and Saviron, J.M. (1992). "McCormack's method for the numerical simulation of one-dimensional discontinuous unsteady open channel flow." *Journal of Hydraulic Research, IAHR*, 30 (1), 95-105.

Ghidaoui, M.S., and Kolyshkin, A.A. (1999). "Linear stability analysis of lateral motions in compound open channels." *Journal of Hydraulic Engineering, ASCE*, 125 (8), 871-880.

Ghosh, S.N., and Jena, S.B. (1971). "Boundary shear distribution in open channel compound." *Proc. Institution of Civil Engineers*, 49, 417-430.

Greenhill, R.K., and Sellin, R.H.J. (1993). "Development of a simple method to predict discharges in compound meandering channels." *Proc. Institution of Civil Engineers, Water Maritime and Energy*, 101 (1), 37-44.

Harlow, F.H., and Welsh, J.E. (1965). "Numerical calculation of time dependent viscous incompressible flow with free surface." *Phys. Fluids*, 8, 2182-2189.

HEC (1998). *HEC-RAS, River Analysis System, Hydraulics reference manual*. USACE, Hydrologic Engineering Center, Davis, Calif., USA.

Hirsch, C. (1988). *Numerical computation of internal and external flows*. John Wiley and Sons, Chichester, U.K.

Hollinrake, P.G. (1987). "The structure of flow in open channels, a literature survey. Vol. I" *Report SR96*, HR Wallingford, UK.

Hollinrake, P.G. (1988). "The structure of flow in open channels, a literature survey. Vol. II" *Report SR153*, HR Wallingford, UK.

Hollinrake, P.G. (1989). "The structure of flow in open channels, a literature survey. Vol. III" *Report SR209*, HR Wallingford, UK.

Hollinrake, P.G. (1990). "The structure of flow in open channels, a literature survey. Vol. IV" *Report SR227*, HR Wallingford, UK.

Hollinrake, P.G. (1992). "The structure of flow in open channels, a literature survey. Vol. V" *Report SR301*, HR Wallingford, UK.

Hosoda, T., Sakurai, T., Kimura, I., and Muramoto, Y. (1998). "Unsteady flows in compound open channels with horizontal vortices and secondary currents by means of non-linear k-epsilon model." *Flow modeling and turbulence measurements VII*, Tainan, Taiwan, 355-362.

Ikeda, S. (1981). "Self-formed straight channels in sandy beds." *Journal of the Hydraulics Division, ASCE*, 107 (4), 389-406.

Ikeda, S. (1999). "Role of lateral eddies in sediment transport and channel formation." *River Sedimentation*, Jayawardena, Lee and Wang, eds., Balkema, Rotterdam, 195-203.

Jasem, H.K. (1990). "Flow in two-stage channels with the main channel skewed to the flood plain direction." *PhD Thesis*, University of Glasgow.

Jayaratne, B.L., Tu, H., Tamai, N., and Kan, K. (1995). "Unsteady flow characteristics in compound channels with vegetated flood plains." *Proc. 26th Congress of IAHR, Hydra 2000*, London, 1, 379-384.

Keller, R.J., and Rodi, W. (1988). "Prediciton of flow characteristics in main channel/floodplain flows." *Journal of Hydraulic Research, IAHR*, 26 (4), 425-441.

Khatibi, R.H., Williams, J.J.R., and Wormleaton, P. (1997). "Identification problem of open-channel friction parameters." *Journal of Hydraulic Engineering, ASCE*, 123 (12), 1078-1088.

Knight, D.W., and Abril, B. (1996). "Refined calibration of a depth averaged model for turbulent flow in a compound channel." *Proc. Institution of Civil Engineers, Water, Maritime and Energy*, 118, 151-159.

Knight, D.W., and Demetriou, J.D. (1983). "Flood plain and main channel interaction." *Journal of the Hydraulics Division, ASCE*, 109 (8), 1073-1092.

Knight, D.W., and Hamed, M.E. (1984). "Boundary shear in symmetrical compound channel." *Journal of the Hydraulics Division, ASCE*, 110 (10), 1412-1430.

Knight, D.W., and Sellin, R.H.J. (1987). "The SERC flood channel facility." *Journal of the Institution of Water and Environmental Managment*, 1 (2), 198-204.

Knight, D.W., and Shiono, K. (1990). "Turbulence measurements in a shear layer region of a compound channel." *Journal of Hydraulic Research, IAHR*, 28 (2), 141-156.

Knight, D.W., and Shiono, K. (1996). "River Channel and flood plain hydraulics." *Floodplain processes*, M. Anderson, P. Bates and D. Walling, eds., Wiley and Sons, 139-181.

Knight, D.W., ed. (1992). "SERC Flood Channel Facility Experimental Data-Phase A." *Report SR314*, HR Wallingford, Wallingford, UK.

Knight, D.W., Shiono, K., and Pirt, J. (1989). "Prediciton of depth mean velocity and discharge in natural rivers with overbank flow." *Proc. Int. Conf. on Hydraulics and Environmental Modelling of Coastal, Estuarine and River Waters*, Falconer, R.A., Goodwin, P. and Matthew, R.G.S., eds., Gower Publishing, 419-428.

Knight et al. (2002). *Flow in compound channels*. IAHR monograph, IAHR, Madrid, Spain (in press).

Krishnappan, B.G., and Lau Y.L. (1986). "Turbulence modelling of flood plain flows." *Journal of Hydraulic Engineering, ASCE*, 112 (4), 251-266.

Lai, C. (1986). "Numerical modeling of unsteady open-channel flow." *Advances in hydroscience*, B.C. Yen, ed., Academic, London, 14, 161-333.

Lambert, M.F., and Myers., W.R. (1998). "Estimating the discharge capacity in straight compound channels." *Proc. Institution of Civil Engineers, Water, Maritime and Energy*, 130 (2), 84-94.

Lambert, M.F., and Sellin, R.H.J. (1996). "Discharge predicition in straight compound channels using the mixing length concept." *Journal of Hydraulic Research, IAHR*, 34 (3), 381-394.

Launder, B.E., and Spalding, D.B. (1974). "The numerical computation of turbulent flow." *Computer Methods in Applied Mechanics and Engineering*, 3, 269-289.

Liggett, J.A. (1994). *Fluid mechanics*. Mc Graw Hill, New-York.

Linsley, R.K., and Franzini, J.B. (1972). *Water-ressources engineering*. McGraw-Hill, New-York, USA.

Lotter, G.K. (1933). "Considerations on hydraulic design of channels with different roughness of walls." *Trans. All Union Scientific Research, Institute of Hydraulic Engineering*, Leningrad, 238-241 (in Russian).

Lukowicz, J.V., and Köngeter, J. (1999). "Coherent structures in compound open-channel flows : experimental investigation using DPIV." *Proc. 28th Congress of IAHR*, Graz, Austria.

Lyness, J.F., Myers, W.R.C., and Wark, J.B. (1997). "The use of different conveyance calculations for modelling flows in a compact compound channel." *Journal of the Institution of Water and Environmental Management*, 11 (5), 335-340.

Lyness, J.F., Myers, W.R.C., Cassells, J.B.C., and O'Sullivan, J.J. (2001). "The influence of planform on flow resistance in mobile bed compound channels." *Proc. Institution of Civil Engineers, Water and Maritime Engineering*, 148(1), 5-14.

Manning, R. (1889). "On the flow of water in open channels and pipes." *Trans. Institution of Civil Engineers of Ireland*, 20, 161-207.

Marchal, R., and Philippe, B. (1998). "Conception et réalisation d'un canal hydraulique à section composée. Modélisation de l'écoulement dans une rivière à plaines inondables." *Final study work*, Université catholique de Louvain, Louvain-la-Neuve, Belgium (in French).

Meyer, L., and Rehme, K. (1994). "Large scale turbulence phenomena in compound rectangular channels." *Experimental Thermal and Fluid Science*, 8, Elsevier Science, New-York, 286-304.

Michalke, A. (1964). "On the inviscid instability of the hyperbolic-tangent velocity profile." *Journal of Fluid Mechanics*, 19, 543-556.

Michalke, A. (1965a). "Vortex formation in a free boundary layer according to stability theory." *Journal of Fluid Mechanics*, 22, 371-383.

Michalke, A. (1965b). "On spatially growing disturbances in an inviscid shear layer." *Journal of Fluid Mechanics*, 23, 521-544.

Michalke, A., and Schade, H. (1963). "Zur Stabilität von freien Grenzschichten." *Ingenieur-Archiv*, 23, 1-23 (in German).

Myers, W.R.C. (1978). "Momentum transfer in a compound channel." *Journal of Hydraulic Research, IAHR*, 16 (2), 139-150.

Myers, W.R.C and Brennan, E.K. (1990). "Flow resistance in compound channels." *Journal of Hydraulic Research, IAHR*, 28 (2), 141-155.

Myers, W.R.C., and Elsawy, E.M. (1975). "Boundary shear in channel with flood plain." *Journal of the Hydraulics Division, ASCE*, 101 (7), 933-946.

Nadaoka, K., and Yagi, H. (1998). "Shallow-water turbulence modeling and horizontal large-eddy computation of river flow." *Journal of Hydraulic Engineering, ASCE*, 124 (5), 493-500.

Naot, D., Nezu, I., and Nakagawa, H. (1993a). "Hydrodynamic behavior of compound rectangular open channels." *Journal of Hydraulic Engineering, ASCE*, 119 (3), 390-408.

Naot, D., Nezu, I., and Nakagawa, H. (1993b). "Calculation of compound channel flow." *Journal of Hydraulic Engineering, ASCE*, 119 (12), 1418-1426.

Nezu, I., and Nakagawa, H. (1993). *Turbulence in open channel flows*. IAHR Monograph, Balkema Publishers, Rotterdam.

Nezu, I., and Nakayama, T. (1997). "Space-time correlation structures of horizontal coherent vortices in compound open-channel flows by using particle-tracking velocimetry." *Journal of Hydraulic Research, IAHR*, 35 (2), 191-208.

Nicollet, G., and Uan, M. (1979). "Ecoulements permanents à surface libre en lits composés." *La Houille Blanche*, 1, 21-30 (in French).

Peyret, R., and Taylor, T.D. (1983). "Computational methods for fluid flow." Springer-Verlag, New-York

Posey, C.J.F. (1967). "Computations of discharge including overbank flow." *Civil Engineering, ASCE*, 37 (4), 62-63.

Prinos, P., and Townsend, R.D. (1984). "Comparison of methods for predicting discharge in compound open channels." *Advances in Water Resources*, 7, 180-187.

Rastogi, A.K., and Rodi, W. (1978). "Predicitons of heat and mass transfer in open channels." *Journal of the Hydraulics Division, ASCE*, 104 (3), 397-420.

Rodi, W. (1980). *Turbulence models and their application in hydraulics : a state of the art review*. IAHR book publications, Delft.

Rouse, H., and Ince, S. (1954). *History of hydraulics*. La Houille Blanche, supplément, Paris.

Schoemaker, H.J. (1991). "Discussion on 4 papers of Journal of Hydraulic Research, 28 (2), 1990)." *Journal of Hydraulic Research, IAHR*, 29 (2), 259-262.

Sellin, R.H.J (1964). "A laboratory investigation into the interaction between the flow in the channel of a river and that over its flood plain." *La Houille Blanche*, 7, 793-802.

Sellin, R.H.J. (1995). "Hydraulic performance of a skewed two-stage flood channel." *Journal of Hydraulic Research, IAHR*, 33 (1), 43-64.

Sellin, R.H.J., Ervine, D.A., and Willetts, B.B. (1993). "Behaviour of meandering two-stage channels." *Proc. Institution of Civil Engineers, Water, Maritime and Energy*, 101, 99-111.

Shiono, K., Al-Romaih, J.S., and Knight, D.W. (1999). "Stage-discharge assessment in compound meandering channels." *Journal of Hydraulic Engineering, ASCE*, 125 (1), 66-77.

Shiono, K., and Knight, D.W. (1990). "Mathematical models of flow in two or multi stage straight channels." *Proc. Int. Conf. on River Flood Hydraulics*, Wiley and Sons, 229-238.

Shiono, K., and Knight, D.W. (1991). "Turbulent open channel flows with variable depth across the channel." *Journal of Fluid Mechanics*, 222, 617-646.

Shiono, K., and Muto, Y. (1998). "Complex flow mechanisms in compound meandering channels with overbank flow." *Journal of Fluid Mechanics*, 376, 221-261.

Smart, G.M. (1992). "Stage-discharge discontinuity in composite flood channels." *Journal of Hydraulic Research, IAHR*, 30 (6), 817-833.

Spinewine, B., Capart, H., Larcher, M., and Zech, Y. (2001). "Three-dimensional Voronoï imaging methods for the measurement of near-wall particulate flows." Submitted for publication in *Experiments in Fluids*.

Stephenson, D., and Kolovopoulos, P. (1990). "Effects of momentum transfer in compound channels." *Journal of Hydraulic Engineering, ASCE*, 116 (12), 1512-1522.

Sturm, T.W., and Sadiq, A. (1996). "Water surface profiles in compound channel with multiple critical depths." *Journal of Hydraulic Engineering, ASCE*, 122 (12), 703-709.

Tamai, N., Asaeda, T., and Ikeda, Y. (1986). "Study on generation of periodical large surface eddies in a composite channel flow." *Water Resources Research*, 22 (7), 1129-1138.

Thomas, T.G., and Williams, J.J.R. (1995). "Large eddy simulation of turbulent flow in an asymmetric compound channel." *Journal of Hydraulic Research, IAHR*, 33 (1), 27-41.

Toebes, G.H., and Sooky, A. (1967). "Hydraulics of meandering rivers with floodplains." *Journal of the Waterways and Harbour Division, ASCE*, 93 (2), 1053-1066.

Tominaga, A., and Nezu, I. (1991). "Turbulent structure in compound open channel flow." *Journal of Hydraulic Engineering, ASCE*, 117 (1), 21-41.

Tominaga, A., Liu, J., Nagao, M., and Nezu, I. (1995). "Hydraulic characteristics of unsteady flow in open channels with flood plains." *Proc. 26th Congress of IAHR, Hydra 2000*, London, 1, 373-378.

Tominaga, A., Nagao, M., and Nezu, I. (1994). "Experimental study on unsteady flow in open channels with flood plains." *Proc. of Symp. on Fundamentals and Advancements in Hydraulic Measurements and Experimentation, ASCE*, 396-405.

Troskolanski, A.T. (1962). *Théorie et pratique des mesures hydrauliques*. Dunod, Paris (in French).

Truckenbrodt E. (1968). *Fluid mechanik.* Springer Verlag, Berlin, (2nd edition 1980) (in German).

van Prooijen, B.C., and Uijttewaal, W.S.J. (2001). "Development of large turbulence structures in shallow mixing layers." *Proceedings of the 2001 International Symposium on Environmental Hydraulics*, Arizona (in press).

Wark, J.B., James, C.S., and Ackers, P. (1994). "Design of straight and meandering compound channels." *National River Authority RandD Report 13*, UK.

Wark, J.B., Samuels, P.G., and Ervine, D.A. (1990). "A practical method of estimating velocity and discharge in compound channels." *Proc. Int. Conf. on River Flood Hydraulics*, Wiley and Sons, UK, 163-172.

Watanabe A., and Fukuoka S. (2001). "Hydraulic characteristics of unsteady flows in meandering compound channels.." *Proc. 29th Congress of IAHR*, Tsinghua University Press, Beijing, China, D1, 83-89.

Wilkin, N., and Jacquemart, J.H. (2001). "Etude expérimentale et numérique des rivières à lit composé : écoulement au droit de rétrécissements progressifs des plaines d'inondation." *Final study work*, Université catholique de Louvain, Louvain-la-Neuve, Belgium (in French).

Woo, H., and Kim, W. (1997). "Floods of the Han river in Korea." *Water International, IWRA*, 22 (4), 230-237.

Wormleaton, P.R. (1988). "Determination of discharge in compound channels using the dynamic equation for lateral velocity distribution." *Proc. Int. Conf. on Fluvial Hydraulics, IAHR*, Budapest, Hungary.

Wormleaton, P.R., Allen, J., and Hadjipanos, P. (1982). "Discharge assessment in compound channel flow." *Journal of the Hydraulics Division, ASCE*, 108 (9), 975-994.

Wormleaton, P.R., and Merrett, D.J. (1990). "An improved method of the calculation for steady uniform flow in prismatic main channel/flood plain sections." *Journal of Hydraulic Research, IAHR*, 28 (2), 157-174.

Wormleaton, P.R., and Hadjipanos, P. (1985). "Flow distribution in compound channels." *Journal of Hydraulic Engineering, ASCE*, 111 (2), 357-361.

Yen, B.C. (1973). "Open-channel flow equations revisited." *Journal of Eng. Mech. Engineering, ASCE*, 99 (5), 979-1009.

Yen, B.C. (1992). "Dimensionally homogeneous Manning's Formula." *Journal of Hydraulic Engineering, ASCE*, 118 (9), 1326-1332.

Yen, B.C., Camacho, R., Kohane, R., and Westrich, B. (1985). "Signifiance of flood plains in backwater computation." *Proc. 21st Congress of IAHR*, Melbourne, 3, 439-445.

Yen, C.L., and Overton, D.E. (1973). "Shape effects on resistance in flood plain channels." *Journal of the Hydraulics Division, ASCE*, 99 (1), 219-238.

Yuen, K.W.H., and Knight, D.W. (1990). "Critical flow in a two stage channel." *Proc. Int. Conf. on River Flood Hydraulics*, Wiley and Sons, 267-276.

Yulistiyanto, B. (1997). "Flow around a cylinder installed in a fixed-bed open channel." *PhD Thesis*, EPFL, Lausanne.

Yulistiyanto, B., Zech, Y., and Graf, W.H. (1998). "Flow around a cylinder : shallow-water modeling with diffusion-dispersion." *Journal of Hydraulic Engineering, ASCE*, 124 (4), 419-429.

Zech, Y., Bertrand, G., and Vandestrick-Huberlant, B. (1988). "Computer Aided Design software in fluvial hydraulics : program CADRIV." *Proc. of Computer Methods and Water Resources 1st Int. Conf.*, Rabat, 4, 267-275.

Appendix 1
Numerical solution of the Saint-Venant equations

A1.1 Introduction

This appendix present the numerical methods used for solving the Saint-Venant equations, or shallow-water equations, (2.33) that have been developed in Chapter 2 :

$$\frac{\partial H}{\partial t}+\frac{\partial}{\partial x}(UH)+\frac{\partial}{\partial y}(VH)=0 \tag{2.33a}$$

$$\frac{\partial U}{\partial t}+U\frac{\partial U}{\partial x}+V\frac{\partial U}{\partial y}=-g\frac{\partial z_w}{\partial x}-gS_{fx}+\frac{1}{H}\frac{\partial}{\partial x}\left(H\frac{\tau_{xx}}{\rho}\right)+\frac{1}{H}\frac{\partial}{\partial y}\left(H\frac{\tau_{xy}}{\rho}\right) \tag{2.33b}$$

$$\frac{\partial V}{\partial t}+U\frac{\partial V}{\partial x}+V\frac{\partial V}{\partial y}=-g\frac{\partial z_w}{\partial y}-gS_{fy}+\frac{1}{H}\frac{\partial}{\partial x}\left(H\frac{\tau_{yx}}{\rho}\right)+\frac{1}{H}\frac{\partial}{\partial y}\left(H\frac{\tau_{yy}}{\rho}\right) \tag{2.33c}$$

where the friction terms S_{fx} and S_{fy} are given by (2.35); and the turbulent shear stress are modelled using the Boussinesq assumption (2.42). The dispersion terms are here neglected, for the sake of conciseness : their development using the finite-difference method would be similar to the development of the other terms considered in this appendix.

As quoted in the conclusion of Chapter 2, two numerical models are used in this work for solving the Saint-Venant equations. Both are classical finite-difference models, based on a MacCormack integration scheme, insuring second order precision in both space and time. The first one is written using a staggered mesh; while the second model is written using a curvilinear collocated mesh. The staggered mesh is used for uniform-flow modelling in Part II, and the collocated mesh is used for non-prismatic channel modelling in Part III.

This Appendix 1 presents briefly both finite-difference models, the MacCormack scheme with the related stability criterion, and the boundary conditions.

A1.2 Discrete approximation using a staggered mesh

The first spatial discretisation makes use of a staggered "marker-and-cell" (MAC) mesh (Harlow and Welsh 1965), slightly adapted for shallow-water flow modelling. In such a mesh, the velocities U and V are defined for positions situated at a middle distance between the points where the bed level z are defined (Figure A1.1). In addition to the classical MAC mesh, proposed for compressible-flow modelling, bed-level values z_b need also to defined, as shallow-water flow is here considered. These values z_b are given for points located at the centre of squares formed by 4 points where the water-level value z is defined. This location enables an easy estimation of the bed level value at any point of interest (z, U, V) using a linear interpolation. Such a staggered mesh provides a good coupling between the velocities and the water depth, insuring a very good mass and momentum conservation during the resolution (Ferziger and Peric 1996) : this condition is indeed required for the uniform-flow modelling with cyclic boundary condition, to be performed in the second part of this work.

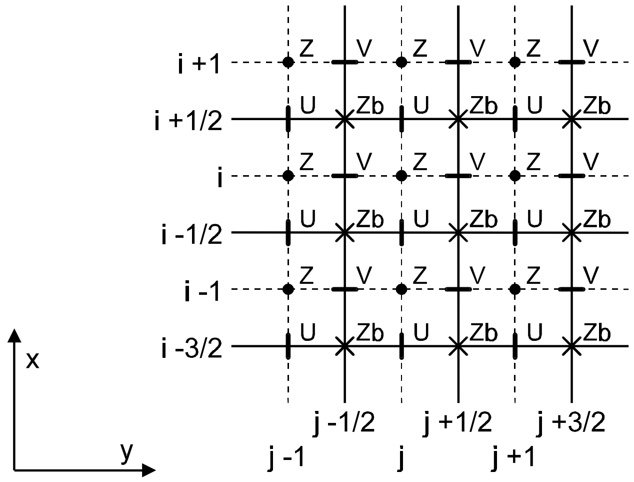

Figure A1.1 : Staggered "MAC" mesh definition, for shallow-water flow modelling

In order to facilitate the programming, the fractional indices from Figure A1.1 are replaced by entire values as depicted by Figure A1.2, where points with the same indices are grouped in shadowed areas. Additionally, the values of the viscosity υ_t, and of the turbulent kinetic energy k are defined at the same locations as the water level z.

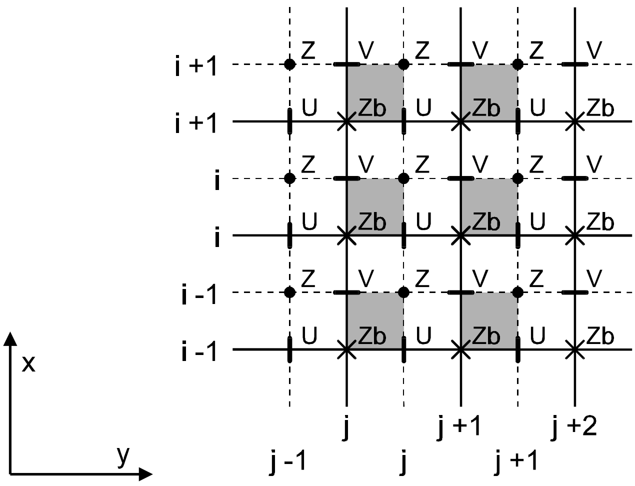

Figure A1.2 : Staggered MAC mesh, nodes numbering with entire indices

Each equation from (2.33) is then discretised with a computational molecule centred on the location where the value varying with the time is defined : on the water-level z definition point for the continuity equation (2.33a) and for the turbulent kinetic energy transport equation (2.46a); on the longitudinal-velocity U definition point for the x-momentum equation (2.33b); and on the transverse-velocity V definition point for the y-momentum equation (2.33c).

The first order derivatives in the momentum equations are written using in alternation a forward and a backward difference operator, corresponding respectively to the predictor and the corrector steps of the MacCormack scheme (see below). The first order derivatives in the continuity equation and the second order derivatives (diffusion terms) are written using centred difference operator. When the value of a variable is needed on a point different of its definition point, this value is interpolated from adjacent values.

Accordingly, the discretised continuity equation (2.33a) writes at the node (i, j) :

$$\frac{\partial z_{ij}}{\partial t} + \frac{1}{\Delta x}\left(H^U_{i+1,j} U_{i+1,j} - H^U_{ij} U_{ij}\right) + \frac{1}{\Delta y}\left(H^V_{i,j+1} V_{i,j+1} - H^V_{ij} V_{ij}\right) = 0 \tag{A1.1}$$

where H^U_{ij} and H^V_{ij} stands for interpolated values of the water-depth, at the definition points of U and V :

$$H^U_{ij} = \frac{1}{2}\left(z_{i-1,j} + z_{ij}\right) - \frac{1}{2}\left(z_{bij} + z_{bi,j+1}\right) \tag{A1.2a}$$

$$H^V_{ij} = \frac{1}{2}\left(z_{i,j-1} + z_{ij}\right) - \frac{1}{2}\left(z_{bij} + z_{bi+1,j}\right) \tag{A1.2b}$$

and where the temporal derivative $\partial H_{ij} / \partial t$ becomes $\partial z_{ij} / \partial t$, as the bed level z_b remains constant. The computational molecule of (A1.1) is given on Figure A1.3.

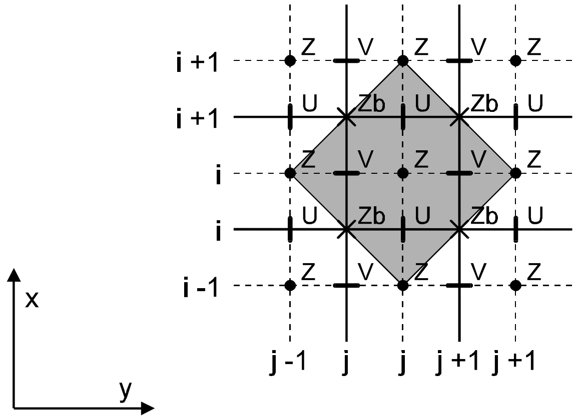

Figure A1.3 : Staggered MAC mesh, computational molecule for the continuity equation (A1.1)

The momentum equations (2.33b) and (2.33c), with the shear-stress definition (2.42) are discretised in a similar way. Their computational molecules are given on Figure A1.4. For the predictor step (forward difference operator), these equations write :

$$
\begin{aligned}
&\frac{\partial U_{ij}}{\partial t}+\frac{1}{\Delta x}U_{ij}\left(U_{i+1,j}-U_{ij}\right)+\frac{1}{\Delta y}V_{ij}^{m}\left(U_{i,j+1}-U_{ij}\right)= \\
&\quad -\frac{1}{\Delta x}g\left(z_{ij}-z_{i-1,j}\right)-gS_{fxij} \\
&\quad +\left(\frac{1}{\Delta x}\right)^{2}\frac{1}{H_{ij}^{U}}\left[2H_{ij}^{Z}\upsilon_{tij}\left(U_{i+1,j}-U_{ij}\right)-2H_{i-1,j}^{Z}\upsilon_{ti-1,j}\left(U_{ij}-U_{i-1,j}\right)\right] \\
&\quad +\frac{1}{\Delta x}\frac{1}{H_{ij}^{U}}\left[\frac{2}{3}H_{ij}^{Z}k_{ij}-\frac{2}{3}H_{i-1,j}^{Z}k_{i-1,j}\right] \\
&\quad +\left(\frac{1}{\Delta y}\right)^{2}\frac{1}{H_{ij}^{U}}\left[H_{i,j+1}^{B}\upsilon_{ti,j+1}^{m}\left(U_{i,j+1}-U_{ij}\right)-H_{ij}^{B}\upsilon_{tij}^{m}\left(U_{ij}-U_{i,j-1}\right)\right] \\
&\quad +\frac{1}{\Delta x.\Delta y}\frac{1}{H_{ij}^{U}}\left[H_{i,j+1}^{B}\upsilon_{ti,j+1}^{m}\left(V_{i,j+1}-V_{i-1,j+1}\right)-H_{ij}^{B}\upsilon_{tij}^{m}\left(V_{ij}-V_{i-1,j}\right)\right]
\end{aligned}
\tag{A1.3a}
$$

$$
\begin{aligned}
&\frac{\partial V_{ij}}{\partial t}+\frac{1}{\Delta x}U_{ij}^{m}\left(V_{i+1,j}-V_{ij}\right)+\frac{1}{\Delta y}V_{ij}\left(V_{i,j+1}-V_{ij}\right)= \\
&\quad -\frac{1}{\Delta y}g\left(z_{ij}-z_{i,j-1}\right)-gS_{fyij} \\
&\quad +\frac{1}{\Delta x.\Delta y}\frac{1}{H_{ij}^{V}}\left[H_{i+1,j}^{B}\upsilon_{ti+1,j}^{m}\left(U_{i+1,j}-U_{i+1,j-1}\right)-H_{ij}^{B}\upsilon_{tij}^{m}\left(U_{ij}-U_{i,j-1}\right)\right] \\
&\quad +\left(\frac{1}{\Delta x}\right)^{2}\frac{1}{H_{ij}^{V}}\left[H_{i+1,j}^{B}\upsilon_{ti+1,j}^{m}\left(V_{i+1,j}-V_{ij}\right)-H_{ij}^{B}\upsilon_{tij}^{m}\left(V_{ij}-V_{i-1,j}\right)\right] \\
&\quad +\left(\frac{1}{\Delta y}\right)^{2}\frac{1}{H_{ij}^{V}}\left[2H_{ij}^{Z}\upsilon_{tij}\left(V_{i,j+1}-V_{ij}\right)-2H_{i,j-1}^{Z}\upsilon_{ti,j-1}\left(V_{ij}-V_{i,j-1}\right)\right] \\
&\quad +\frac{1}{\Delta y}\frac{1}{H_{ij}^{V}}\left[\frac{2}{3}H_{ij}^{Z}k_{ij}-\frac{2}{3}H_{i,j-1}^{Z}k_{i,j-1}\right]
\end{aligned}
\tag{A1.3b}
$$

where the values of $S_{fx\,ij}$ and $S_{fy\,ij}$ are estimated using (2.35), with respectively the velocity values (U_{ij}, V_{ij}^{m}) and (U_{ij}^{m}, V_{ij}); H_{ij}^{Z} and H_{ij}^{B} stands for interpolated values of the water-depth, at the definition points of z and z_b :

$$H_{ij}^{Z}=z_{ij}-\frac{1}{4}\left(z_{bij}+z_{bi,j+1}+z_{bi+1,j}+z_{bi+1,j+1}\right) \tag{A1.4a}$$

$$H_{ij}^{B}=\frac{1}{4}\left(z_{ij}+z_{i,j-1}+z_{i-1,j}+z_{i-1,j-1}\right)-z_{bij} \tag{A1.4b}$$

and where the values U_{ij}^m, V_{ij}^m and υ_{tij}^m are defined as the mean of the four neighbouring values, respectively at the definition points of V, U and z_b :

$$U_{ij}^m = \frac{1}{4}\left(U_{ij} + U_{i,j-1} + U_{i+1,j} + U_{i+1,j-1}\right) \tag{A1.5a}$$

$$V_{ij}^m = \frac{1}{4}\left(V_{ij} + V_{i,j+1} + V_{i-1,j} + V_{i-1,j+1}\right) \tag{A1.5b}$$

$$\upsilon_{tij}^m = \frac{1}{4}\left(\upsilon_{tij} + \upsilon_{ti,j-1} + \upsilon_{ti-1,j} + \upsilon_{ti-1,j-1}\right) \tag{A1.5c}$$

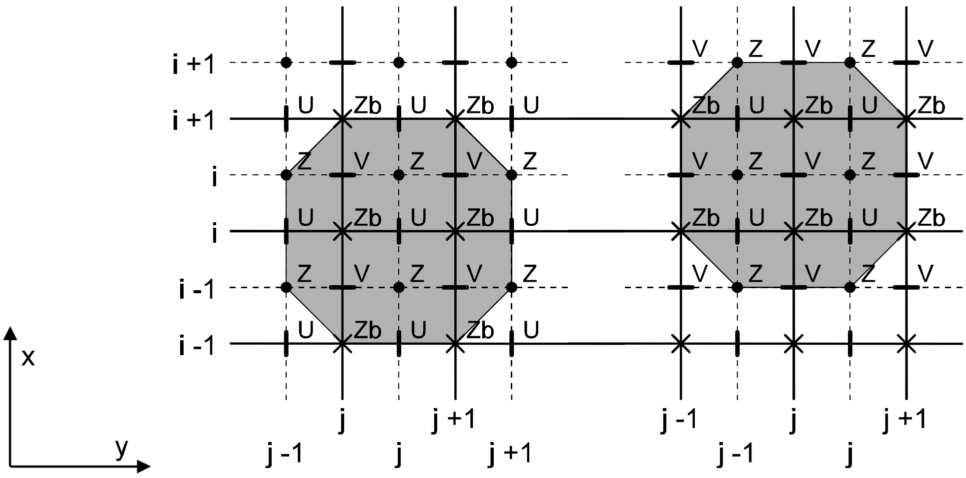

Figure A1.4 : Staggered MAC mesh, computational molecules for the momentum equations (A1.3)

The discretisation of the turbulent kinetic-energy transport equation (2.46a) is obtained similarly, centred on the z point, with a computational molecule larger than the continuity-equation one, due to the term P_h, which writes :

$$\begin{aligned} P_{hij} = \upsilon_{tij} \Bigg\{ & 2\left(\frac{1}{\Delta x}\left(U_{i+1,j} - U_{ij}\right)\right)^2 + 2\left(\frac{1}{\Delta y}\left(V_{i,j+1} - V_{ij}\right)\right)^2 \\ & + \left[\frac{1}{2\Delta y}\left(\frac{U_{i,j+1} - U_{i+1,j+1}}{2} - \frac{U_{i,j-1} - U_{i+1,j-1}}{2}\right)\right. \\ & \left.+ \frac{1}{2\Delta x}\left(\frac{V_{i+1,j} - V_{i+1,j+1}}{2} - \frac{V_{i-1,j} - V_{i-1,j+1}}{2}\right)\right]^2 \Bigg\} \end{aligned} \tag{A1.6}$$

A1.3 Discrete approximation using a curvilinear collocated mesh

The second spatial discretisation makes use of a curvilinear collocated mesh. As the mesh is collocated, some continuity and surface-instability problems will be faced, when compared with the staggered mesh. However, the curvilinear mesh is required in order to perform computations with boundary-fitted mesh for the non-prismatic geometries investigated in the third part of this work. Indeed, it turned out to be too difficult to build this curvilinear mesh using a staggered finite-difference formulation, at least in the frame of this work.

As depicted on Figure A1.5, the curvilinear mesh is defined in the (x, y) space, with the U and V velocities aligned with the x and y directions; and it is linked through a transformation function to a rectangular grid in the (ξ, η) space. The derivatives in the (x, y) space are expressed in the (ξ, η) space by a variable change (Ferziger and Peric 1996). For example, the derivatives of the velocity U are now written in the (ξ, η) space :

$$\begin{pmatrix} \dfrac{\partial U}{\partial x} \\ \dfrac{\partial U}{\partial y} \end{pmatrix} = \mathbf{J}^{-1} \times \begin{pmatrix} \dfrac{\partial U}{\partial \xi} \\ \dfrac{\partial U}{\partial \eta} \end{pmatrix} = \begin{pmatrix} \dfrac{\partial U}{\partial \xi}\dfrac{\partial \xi}{\partial x} + \dfrac{\partial U}{\partial \eta}\dfrac{\partial \eta}{\partial x} \\ \dfrac{\partial U}{\partial \xi}\dfrac{\partial \xi}{\partial y} + \dfrac{\partial U}{\partial \eta}\dfrac{\partial \eta}{\partial y} \end{pmatrix} \tag{A1.7}$$

where $\mathbf{J}$ is the Jacobian matrix of the transformation function that links the curvilinear and the rectangular meshes

$$\mathbf{J} = \begin{pmatrix} \dfrac{\partial x}{\partial \xi} & \dfrac{\partial x}{\partial \eta} \\ \dfrac{\partial y}{\partial \xi} & \dfrac{\partial y}{\partial \eta} \end{pmatrix} = \begin{pmatrix} \dfrac{x_{i+1,j} - x_{i-1,j}}{2} & \dfrac{x_{i,j+1} - x_{i,j-1}}{2} \\ \dfrac{y_{i+1,j} - y_{i-1,j}}{2} & \dfrac{y_{i,j+1} - y_{i,j-1}}{2} \end{pmatrix} \tag{A1.8}$$

where the values of the partial derivatives in the Jacobian matrix have been expressed using centred difference operators.

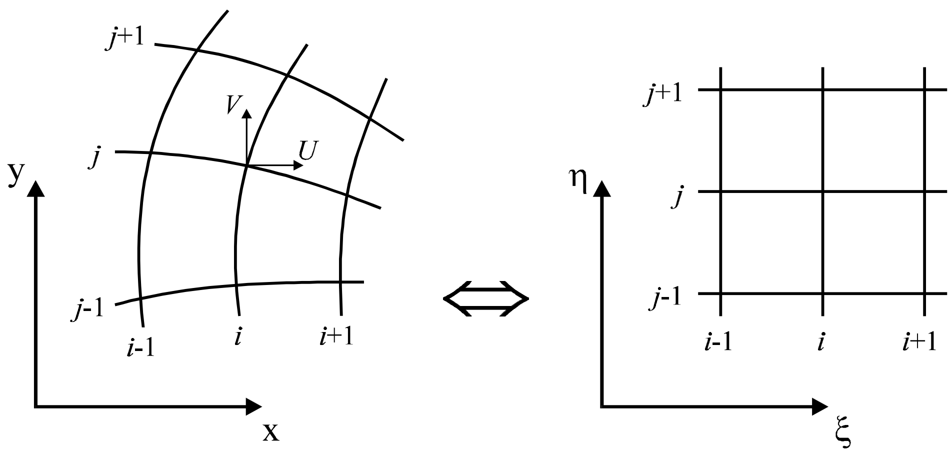

Figure A1.5 : Curvilinear mesh definition

The Saint-Venant equations (2.33) are discretised as for the staggered mesh, using here for all the first order derivatives a forward or a backward difference operator, respectively for the predictor and the corrector steps of the MacCormack scheme. The

Jacobian matrix **J** (A1.8) is estimated at the points where the equation is solved. Centred difference operators are used for the second order derivatives.

A1.4 MacCormack integration scheme

Whereas the spatial derivatives have now been developed as a function of discrete values of the variables, using finite-difference operators, the temporal derivative in each equation still needs to be discretised. A MacCormack scheme is used for that purpose. It will be presented here for the general equation

$$\frac{\partial \varphi}{\partial t} = F(t) \tag{A1.9}$$

where φ is the variable to be time integrated; and $F(t)$ is the value of the other terms of the equation, estimated at the time t, using the discrete approximation of the spatial derivatives.

The MacCormack scheme is a two-steps explicit integration scheme (Chaudhry 1993) between time n and time $n + 1$. In the first step (predictor step), the value of F is estimated at the time n, as in an explicit Euler scheme :

$$\frac{\partial \varphi}{\partial t} = \frac{\varphi^* - \varphi^n}{\Delta t} = F^n \qquad \text{or} \qquad \varphi^* = \varphi^n + \Delta t\ F^n \tag{A1.10}$$

where φ^* is the first estimate of the variable φ value at the time $n + 1$.

In the second step (corrector), the value of F is estimated at the time *, using the value φ^* estimated by the predictor step. As this value is an estimate of the variable value at the time $n + 1$, this step is similar to an implicit Euler scheme, although the computation remains here explicit :

$$\frac{\partial \varphi}{\partial t} = \frac{\varphi^{**} - \varphi^n}{\Delta t} = F^* \qquad \text{or} \qquad \varphi^{**} = \varphi^n + \Delta t\ F^* \tag{A1.11}$$

where φ^{**} is a second estimate of the variable φ value at the time $n + 1$.

The variable value at the time $n + 1$ is finally given by the mean value of φ^* and φ^{**}, corresponding to a trapezoidal scheme, without implicit computations :

$$\varphi^{n+1} = \frac{1}{2}\left(\varphi^* + \varphi^{**}\right) = \varphi^n + \Delta t\ \frac{1}{2}\left(F^n + F^*\right) \tag{A1.12}$$

In order to simplify the programming, the definition (A1.11) of φ^{**} can be replaced by the following expression, similar to the φ^* definition (A1.10)

$$\varphi^{**} = \varphi^* + \Delta t\ F^* \tag{A1.13}$$

Accordingly, the φ value at the time $n + 1$ writes :

$$\varphi^{n+1} = \frac{1}{2}\left(\varphi^n + \varphi^{**}\right) = \frac{1}{2}\left(\varphi^n + \varphi^* + \Delta t\, F^*\right) = \varphi^n + \Delta t\ \frac{1}{2}\left(F^n + F^*\right) \qquad \text{(A1.14)}$$

which is similar to (A1.12).

This scheme provides second-order accuracy in time, which means that the truncation error due to the discretisation is proportional to $(\Delta t)^2$. In order to get also a second order accuracy in space, one needs to use forward and backward difference operators in alternation for the spatial derivations, as noted in the previous paragraphs.

As the MacCormack scheme is an explicit scheme, its numerical stability is ensured only when the time step satisfies some given criterion. For a one-dimensional purely advective flow ($\upsilon_t = 0$), the stability criterion is given by the Courant-Friedrichs-Lewy (CFL) condition (Chaudhry 1993) :

$$\left(U \pm c\right)\frac{\Delta t}{\Delta x} \le 1 \qquad \text{(A1.15)}$$

where $c = \sqrt{gH}$ is the celerity of a tiny wave on the flow surface. When the flow is purely diffusive, the stability condition for a one-dimensional flow is given by

$$r = \frac{\upsilon_t\ \Delta t}{\left(\Delta x\right)^2} \le \frac{1}{2} \quad \text{for } \mathbf{Re}_m < 2 \qquad \text{(A1.16a)}$$

$$r = \frac{\upsilon_t\ \Delta t}{\left(\Delta x\right)^2} \le \frac{2}{\mathbf{Re}_m^2} \quad \text{for } \mathbf{Re}_m \ge 2 \qquad \text{(A1.16b)}$$

where $\mathbf{Re}_m = U\,\Delta x / \upsilon_t$ is the mesh Reynolds number (Peyret and Taylor 1983).

For an advective and diffusive one-dimensional flow, both conditions (A1.15) and (A1.16) combine together, and Peyret and Taylor (1983) propose the following condition :

$$r \le \frac{1}{2 + \mathbf{Re}_m} \quad \text{or} \quad \Delta t \le \frac{\left(\Delta x\right)^2}{2\upsilon_t + U\ \Delta x} \qquad \text{(A1.17)}$$

Finally, for a two-dimensional flow, Yulistiyanto (1997) developed the following condition, which is an extension of (A1.17) :

$$\Delta t \le \frac{1}{\dfrac{U + \sqrt{gH}}{\Delta x} + \dfrac{V + \sqrt{gH}}{\Delta y} + \dfrac{2\upsilon_t}{\left(\Delta x\right)^2} + \dfrac{2\upsilon_t}{\left(\Delta y\right)^2}} \qquad \text{(A1.18)}$$

A1.5 Boundary conditions

Several boundary conditions have to be imposed : on the wall (free-slip or no-slip condition), and at the upstream and downstream boundaries (cyclic condition, or imposed depth or discharge). In the case of the staggered mesh, it is convenient to define fictitious nodes (Figure A1.6), where the variable values are fixed in such a way that the evolution of the variables at a computational node near the boundary can be estimated as at any other inner node.

Figure A1.6 indicates the nodes where fictitious values have to be ascribed for a wall-condition definition. The first variable is the transverse velocity, whose value equals zero, as no flow is possible through the wall :

$$V_{j=0} = 0 \tag{A1.19}$$

Accordingly, the water-surface slope in the direction normal to the wall equals also zero. This gives the value of the water level $z_{j=-1}$ at the fictitious node :

$$\left(\frac{\partial z}{\partial y}\right)_{wall} = \frac{z_{j=0} - z_{j=-1}}{\Delta y} = 0 \quad \text{or} \quad z_{j=-1} = z_{j=0} \tag{A1.20}$$

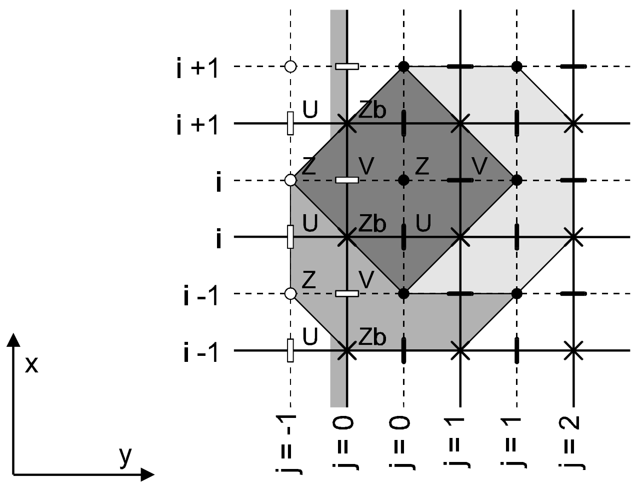

Figure A1.6 : Staggered mesh, definition of fictitious nodes (j=-1) for boundary treatment, with the computational molecules for the inner nodes

The longitudinal-velocity $U_{j=-1}$ value can be prescribed using either a free-slip, either a no-slip condition. In the free-slip condition, the velocity gradient through the wall is assumed to equal zero. Consequently, the velocity value at the fictitious-node is obtained similarly to the water level (A1.20) :

$$\left(\frac{\partial U}{\partial y}\right)_{wall} = \frac{U_{j=0} - U_{j=-1}}{\Delta y} = 0 \quad \text{or} \quad U_{j=-1} = U_{j=0} \tag{A1.21}$$

For the no-slip condition, one has to assign a null-velocity value at the wall, whereas the fictitious node where one can fix a value is behind the wall. The value $U_{j=-1}$ at this fictitious node is obtained thanks to Taylor-series developments (Peyret and Taylor 1983) that give

$$U_{j=-1} = \frac{1}{3}\left(U_{j=1} - 6U_{j=0} + 8U_{wall}\right) \tag{A1.22}$$

where $U_{wall} = 0$ is the velocity at the wall.

When using the cyclic boundary condition for the upstream and downstream boundaries, the velocities values at the fictitious nodes are simply copied from the corresponding inner node at the other end of the computational domain. Only the water-level values require a special treatment. Indeed, due to the bed slope, in a uniform flow, the water level z at the upstream end of the flume is higher than at the downstream end, while the water depth H remains constant (Figure A1.7). As a consequence, the water level at a fictitious node (e.g. at the upstream end of the domain) writes

$$z_{i=-1} = z_{i=imax} + \Delta z_b \tag{A1.23}$$

where *imax* is the indices of the downstream-section nodes; and Δz_b is the bed-level difference between the upstream and the downstream end of the domain.

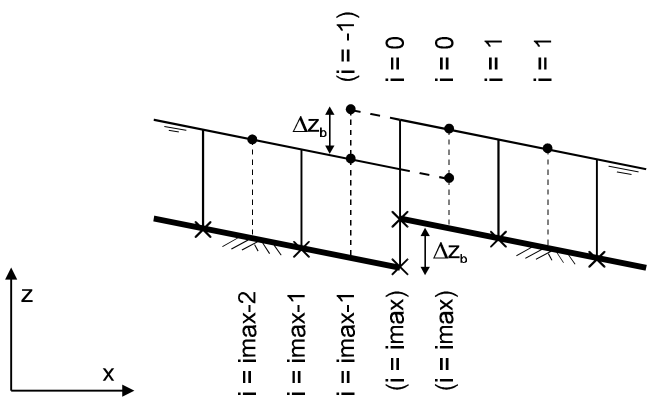

Figure A1.7 : Cyclic boundary condition, bed-level correction

For the curvilinear mesh, the boundary conditions are defined almost similarly, although the variable values are now ascribed on the boundary nodes themselves. At the walls, instead of the transverse velocity V, the velocity normal to the direction of the local boundary is set equal to zero. On the other hand, as a given discharge and a given water depth have to be used respectively as upstream and downstream conditions, a classical characteristics method is used to link the variable values at the boundary with the values at the adjacent inner node (Chaudhry 1993).

Appendix 2
Practical solution of the Exchange Discharge Model

A2.1 Introduction

In order to use the Exchange Discharge Model (EDM) presented in Chapter 4, the ratios χ_i of the additional loss S_a and the friction slope S_f have to be estimated, by solving the system of equations (4.14) :

$$\chi_1 = \frac{1}{gA_1}\left[\psi^t\,(H - h_1)\left(\frac{R_2^{2/3}}{n_2}\left(\frac{1+\chi_1}{1+\chi_2}\right)^{1/2} - \frac{R_1^{2/3}}{n_1}\right) + \psi^g\,\kappa_{21}\,\frac{dK_1}{dx}\right] \cdot \left[\frac{R_1^{2/3}}{n_1} - \frac{R_2^{2/3}}{n_2}\left(\frac{1+\chi_1}{1+\chi_2}\right)^{1/2}\right] \tag{4.14a}$$

$$\begin{aligned}\chi_2 = \frac{1}{gA_2}\Bigg\{&\left[\psi^t\,(H - h_1)\left(\frac{R_2^{2/3}}{n_2}\left(\frac{1+\chi_1}{1+\chi_2}\right)^{1/2} - \frac{R_1^{2/3}}{n_1}\right) + \psi^g\,\kappa_{12}\,\frac{dK_1}{dx}\right]\\ &\cdot\left[\frac{R_2^{2/3}}{n_2}\left(\frac{1+\chi_1}{1+\chi_2}\right)^{1/2} - \frac{R_1^{2/3}}{n_1}\right]\left(\frac{1+\chi_2}{1+\chi_1}\right)\\ &+\left[\psi^t\,(H - h_3)\left(\frac{R_2^{2/3}}{n_2}\left(\frac{1+\chi_3}{1+\chi_2}\right)^{1/2} - \frac{R_3^{2/3}}{n_3}\right) + \psi^g\,\kappa_{32}\,\frac{dK_3}{dx}\right]\\ &\cdot\left[\frac{R_2^{2/3}}{n_2}\left(\frac{1+\chi_3}{1+\chi_2}\right)^{1/2} - \frac{R_3^{2/3}}{n_3}\right]\left(\frac{1+\chi_2}{1+\chi_3}\right)\Bigg\}\end{aligned} \tag{4.14b}$$

$$\chi_3 = \frac{1}{gA_3}\left[\psi^t\,(H - h_3)\left(\frac{R_2^{2/3}}{n_2}\left(\frac{1+\chi_3}{1+\chi_2}\right)^{1/2} - \frac{R_3^{2/3}}{n_3}\right) + \psi^g\,\kappa_{23}\,\frac{dK_3}{dx}\right] \cdot \left[\frac{R_3^{2/3}}{n_3} - \frac{R_2^{2/3}}{n_2}\left(\frac{1+\chi_3}{1+\chi_2}\right)^{1/2}\right] \tag{4.14c}$$

When the channel is a straight symmetrical one with uniform flow, this non-linear system of 3 equations with 3 variables simplifies and an analytical solution can be found. For the general problem, a numerical solution procedure has to be used. Both these solutions will be presented in this Appendix, together with a numerical example.

A2.2 Symmetrical Case : analytical solution

In a symmetrical channel with uniform flow, the following simplifications can be applied to the equations (4.14) : (1) The geometrical transfer terms $\kappa_{ij}\, dK_i/ds$ disappear; and (2) some geometrical parameters are symmetrical : $A_1 = A_3$, $R_1 = R_3$, $n_1 = n_3$ and $h_1 = h_3$. As a consequence, the floodplain χ_i ratios are also equal : $\chi_1 = \chi_3$; and the system of 3 equations (4.14) reduces to 2 equations :

$$\chi_1 = \frac{-\psi^t\,(H - h_1)}{g\,A_1}\left(\frac{R_2^{2/3}}{n_2}\left(\frac{1+\chi_1}{1+\chi_2}\right)^{1/2} - \frac{R_1^{2/3}}{n_1}\right)^2 \qquad \text{(A2.1a)}$$

$$\chi_2 = \frac{2\,\psi^t\,(H - h_1)}{g\,A_2}\left(\frac{R_2^{2/3}}{n_2}\left(\frac{1+\chi_1}{1+\chi_2}\right)^{1/2} - \frac{R_1^{2/3}}{n_1}\right)^2 \left(\frac{1+\chi_2}{1+\chi_1}\right) \qquad \text{(A2.1b)}$$

Assuming that the main-channel velocity is higher than the floodplain one, the solutions of the system must satisfy the following conditions :

$$-1 < \chi_1 \le 0 \qquad \text{(A2.2a)}$$

$$0 \le \chi_2 \qquad \text{(A2.2b)}$$

$$\frac{1}{(1+\chi_1)^{1/2}}\,\frac{R_1^{2/3}}{n_1} \le \frac{1}{(1+\chi_2)^{1/2}}\,\frac{R_2^{2/3}}{n_2} \qquad \text{(A2.2c)}$$

meaning that : (1) The floodplain velocity is accelerated due to the momentum transfer from the main channel (A2.2a); (2) the main channel velocity is reduced (A2.2b); and (3) the floodplains velocities remain slower than the main channel one (A2.2c).

If we define an auxiliary variable X as

$$X = \left(\frac{1+\chi_1}{1+\chi_2}\right)^{1/2} \qquad \text{(A2.3)}$$

the system (A2.1) finally reduces to one equation :

$$X^2 = \frac{1+\chi_1}{1+\chi_2} = \frac{1 - \dfrac{\psi^t\,(H - h_1)}{g\,A_1}\left(\dfrac{R_2^{2/3}}{n_2}X - \dfrac{R_1^{2/3}}{n_1}\right)^2}{1 + \dfrac{2\,\psi^t\,(H - h_1)}{g\,A_2}\left(\dfrac{R_2^{2/3}}{n_2}X - \dfrac{R_1^{2/3}}{n_1}\right)^2\left(\dfrac{1}{X}\right)^2} \qquad \text{(A2.4)}$$

which is a quadratic equation with 2 possible solutions :

$$X = \frac{p\,\dfrac{R_1^{2/3}}{n_1}\dfrac{R_2^{2/3}}{n_2} + \sqrt{\left(p\,\dfrac{R_1^{2/3}}{n_1}\dfrac{R_2^{2/3}}{n_2}\right)^2 - \left(p\left(\dfrac{R_2^{2/3}}{n_2}\right)^2 + 1\right)\left(p\left(\dfrac{R_1^{2/3}}{n_1}\right)^2 - 1\right)}}{1 + p\left(\dfrac{R_2^{2/3}}{n_2}\right)^2} \qquad \text{(A2.5)}$$

with p defined as

$$p = \left(\frac{2}{g\,A_2} + \frac{1}{g\,A_1}\right)\psi^t\,(H - h_1) \qquad \text{(A2.6)}$$

The positive sign is selected for the square root term in (A2.5) as only this root satisfy the conditions (A2.2) rewritten as

$$0 < X \leq 1 \qquad \text{(A2.7a)}$$

$$\frac{R_1^{2/3}}{n_1}\frac{n_2}{R_2^{2/3}} \leq X \qquad \text{(A2.7b)}$$

The final solution of the system (4.14) for a uniform flow in a symmetrical and prismatic channel is thus :

$$\chi_1 = \chi_3 = \frac{-\psi^t\,(H - h_1)}{g A_1}\left(\frac{R_2^{2/3}}{n_2}X - \frac{R_1^{2/3}}{n_1}\right)^2 \qquad \text{(A2.8a)}$$

$$\chi_2 = \frac{2\,\psi^t\,(H - h_1)}{g\,A_2}\left(\frac{R_2^{2/3}}{n_2}X - \frac{R_1^{2/3}}{n_1}\right)^2\left(\frac{1}{X}\right)^2 \qquad \text{(A2.8b)}$$

where X is given by (A2.5), with a p value defined by (A2.6).

Although such a solution for a prismatic symmetrical channel is of limited practical applicability, it has been useful for computations relative to typical experimental-flume geometries, when fitting the ψ^t parameter value.

A2.3 General Case : numerical solution

To get a numerical iterative solution of the system (4.14) for the general case, we first define three auxiliary variables :

$$X_i = \left(1+\chi_i\right)^{1/2}, \qquad i = 1, 2, 3 \tag{A2.9}$$

The system (4.14) becomes :

$$X_1^2 - 1 = \frac{1}{gA_1}\left[\psi^t\,(H\text{ - }h_1)\left(\frac{R_2^{2/3}}{n_2}\frac{X_1}{X_2} - \frac{R_1^{2/3}}{n_1}\right) + \psi^g \kappa_{21}\frac{dK_1}{ds}\right] \cdot \left[\frac{R_1^{2/3}}{n_1} - \frac{R_2^{2/3}}{n_2}\frac{X_1}{X_2}\right] \tag{A2.10a}$$

$$\begin{aligned} X_2^2 - 1 = \frac{1}{gA_2}\Bigg\{ & \left[\psi^t\,(H\text{ - }h_1)\left(\frac{R_2^{2/3}}{n_2}\frac{X_1}{X_2} - \frac{R_1^{2/3}}{n_1}\right) + \psi^g \kappa_{12}\frac{dK_1}{ds}\right] \\ & \cdot \left[\frac{R_2^{2/3}}{n_2}\frac{X_1}{X_2} - \frac{R_1^{2/3}}{n_1}\right]\left(\frac{X_2}{X_1}\right)^2 \\ & + \left[\psi^t\,(H\text{ - }h_3)\left(\frac{R_2^{2/3}}{n_2}\frac{X_3}{X_2} - \frac{R_3^{2/3}}{n_3}\right) + \psi^g \kappa_{32}\frac{dK_3}{ds}\right] \\ & \cdot \left[\frac{R_2^{2/3}}{n_2}\frac{X_3}{X_2} - \frac{R_3^{2/3}}{n_3}\right]\left(\frac{X_2}{X_3}\right)^2 \Bigg\} \end{aligned} \tag{A2.10b}$$

$$X_3^2 - 1 = \frac{1}{gA_3}\left[\psi^t\,(H\text{ - }h_3)\left(\frac{R_2^{2/3}}{n_2}\frac{X_3}{X_2} - \frac{R_3^{2/3}}{n_3}\right) + \psi^g \kappa_{23}\frac{dK_3}{ds}\right] \cdot \left[\frac{R_3^{2/3}}{n_3} - \frac{R_2^{2/3}}{n_2}\frac{X_3}{X_2}\right] \tag{A2.10c}$$

and must satisfy the following conditions, assuming again that the velocities in the main channel are higher than in the floodplains :

$$0 < X_1 \le 1; \quad 1 \le X_2 \quad \text{and} \quad 0 < X_3 \le 1 \tag{A2.11a}$$

$$\frac{1}{X_1}\frac{R_1^{2/3}}{n_1} \le \frac{1}{X_2}\frac{R_2^{2/3}}{n_2} \quad \text{and} \quad \frac{1}{X_3}\frac{R_3^{2/3}}{n_3} \le \frac{1}{X_2}\frac{R_2^{2/3}}{n_2} \tag{A2.11b}$$

Equations (A2.10a) and (A2.10c) can be seen as quadratic equations respectively of X_1 and X_3 : extracting the roots and selecting the appropriate ones (only the X_{1+} and X_{3+} roots satisfy the condition given by (A2.11b)), after simplifications, we get an expression of X_1 and X_3 as a function of X_2 :

$$X_1 = \frac{1}{2} X_2 \frac{1}{X_2^2 + \frac{\psi^t\,(H\text{ - }h_1)}{gA_1}\left(\frac{R_2^{2/3}}{n_2}\right)^2} \left(2\frac{\psi^t\,(H\text{ - }h_1)}{gA_1}\frac{R_1^{2/3}}{n_1}\frac{R_2^{2/3}}{n_2} \right.$$
$$- \frac{\psi^g\,\kappa_{21} dK_1/ds}{gA_1}\frac{R_2^{2/3}}{n_2} \tag{A2.12a}$$
$$+ \left\{ \left[4\frac{\psi^t\,(H\text{ - }h_1)}{gA_1} + \left(\frac{\psi^g\,\kappa_{21}\,dK_1/ds}{gA_1}\right)^2 \right] \left(\frac{R_2^{2/3}}{n_2}\right)^2 \right.$$
$$\left.\left. + 4X_2^2 \left[1 - \frac{\psi^t\,(H\text{ - }h_1)}{gA_1}\left(\frac{R_1^{2/3}}{n_1}\right)^2 + \frac{\psi^g\,\kappa_{21} dK_1/ds}{gA_1}\frac{R_1^{2/3}}{n_1} \right] \right\}^{1/2} \right)$$

$$X_3 = \frac{1}{2} X_2 \frac{1}{X_2^2 + \frac{\psi^t\,(H\text{ - }h_3)}{gA_3}\left(\frac{R_2^{2/3}}{n_2}\right)^2} \left(2\frac{\psi^t\,(H\text{ - }h_3)}{gA_3}\frac{R_3^{2/3}}{n_3}\frac{R_2^{2/3}}{n_2} \right.$$
$$- \frac{\psi^g\,\kappa_{23} dK_3/ds}{gA_3}\frac{R_2^{2/3}}{n_2} \tag{A2.12b}$$
$$+ \left\{ \left[4\frac{\psi^t\,(H\text{ - }h_3)}{gA_3} + \left(\frac{\psi^g\,\kappa_{23} dK_3/ds}{gA_3}\right)^2 \right] \left(\frac{R_2^{2/3}}{n_2}\right)^2 \right.$$
$$\left.\left. + 4X_2^2 \left[1 - \frac{\psi^t\,(H\text{ - }h_3)}{gA_3}\left(\frac{R_3^{2/3}}{n_3}\right)^2 + \frac{\psi^g\,\kappa_{23} dK_3/ds}{gA_3}\frac{R_3^{2/3}}{n_3} \right] \right\}^{1/2} \right)$$

Using these expressions in equation (A2.10b), we finally get a single function of X_2 that has to be equal to zero :

$$F(X_2) = F\left(\frac{X_1}{X_2}, \frac{X_3}{X_2}, X_2\right) = 0$$
$$= 1 - X_2^2 + \frac{1}{gA_2}\left\{ \left[\psi^t\,(H\text{ - }h_1)\left(\frac{R_2^{2/3}}{n_2}\frac{X_1}{X_2} - \frac{R_1^{2/3}}{n_1}\right) + \psi^g\,\kappa_{12}\frac{dK_1}{ds} \right] \right.$$
$$\cdot \left[\frac{R_2^{2/3}}{n_2}\frac{X_1}{X_2} - \frac{R_1^{2/3}}{n_1} \right]\left(\frac{X_2}{X_1}\right)^2 + \left[\psi^t\,(H\text{ - }h_3)\left(\frac{R_2^{2/3}}{n_2}\frac{X_3}{X_2} - \frac{R_3^{2/3}}{n_3}\right) \right. \tag{A2.13}$$
$$\left. \left. + \psi^g\,\kappa_{32}\frac{dK_3}{ds} \right] \cdot \left[\frac{R_2^{2/3}}{n_2}\frac{X_3}{X_2} - \frac{R_3^{2/3}}{n_3} \right]\left(\frac{X_2}{X_3}\right)^2 \right\}$$

as X_1/X_2 and X_3/X_2 are defined as functions of X_2 by equations (A2.12).

The value of X_2 can finally be found using a Newton-Raphson resolution of equation (A2.13), with an initial value of X_2 = 1. Getting the value of X_2 as a function of the cross-section geometrical parameters, we finally obtain the values of the χ_i ratios from the X_i definition (A2.9).

A2.4 Numerical example

As an example, the EDM calculation of a compound-channel discharge is applied for the particular case of the test 020501 in Wallingford FCF. The geometrical data of the section are given by Knight (1992) (see Figure 1.1) : main-channel half width b = 0.75 m; section half width B = 3.15 m; bank level above channel bottom h = 0.15 m; bank slope s_c = 1. The bottom slope is $S_0 = 1.027 \times 10^{-3}$ and the Manning roughness coefficients can be estimated at $n_c = 0.010$ s/m$^{1/3}$ and $n_f = 0.010$ s/m$^{1/3}$.

The calculation is done according to the steps presented in the summary of the method (§ 4.9.1), with a water level in test 020501 equal to H = 0.198 m, using, for the sake of generality, the numerical solution presented in § A2.3.

1. As the channel is symmetrical, parameters will be equal for both floodplains. The computed subsection areas are $A_1 = A_3 = 0.1091\ \mathrm{m}^2$ and $A_2 = 0.3338\ \mathrm{m}^2$; the hydraulic radii are $R_1 = R_3 = 0.047$ m and $R_2 = 0.174$ m; the subsection conveyances are $K_1 = K_3 = 1.421\ \mathrm{m}^3/\mathrm{s}$ and $K_2 = 10.384\ \mathrm{m}^3/\mathrm{s}$; and the bank level are $h_1 = h_3 = 0.15$ m .

2. There is no geometrical transfer discharge so that $dK_f/ds = 0$.

3. The numerical solution of (4.14) is calculated by the Newton-Raphson method, according to § A2.3. For the first iteration, a value X_2 = 1 is assumed. With that value, equations (A2.12) give $X_1/X_2 = X_3/X_2 = 0.6947$ and equation (A2.13) gives $F(1) = 0.7007$. The derivative of $F(X_2)$ is estimated numerically :

$$\frac{dF(X_2)}{dX_2} = \frac{F(X_2 + 0.001) - F(X_2)}{0.001} = -2.5765 \tag{A2.14}$$

   and the correction to X_2 is given by the Newton-Raphson method :

$$dX_2 = -\frac{F(X_2)}{dF(X_2)/dX_2} = 0.2719 \tag{A2.15}$$

   A second iteration is thus carried out with X_2 = 1.2719. At the end of the third iteration, we get X_2 = 1.2452; $X_1/X_2 = X_3/X_2 = 0.6464$ and $F(X_2) = 2 \times 10^{-3}$. The corresponding χ_i values are $\chi_1 = \chi_3 = -0.3521$; and $\chi_2 = 0.5506$ (A2.9). These values are found equal to those computed by the analytical solution up to the fourth digit.

4. The corrected conveyance are estimated by equation (4.16) : $K_1{*} = K_3{*} = 1.765\mathrm{m}^3/\mathrm{s}$ and $K_2{*} = 8.339\mathrm{m}^3/\mathrm{s}$; and the discharge is finally given by equation (4.15) : $Q = 0.3804\ \mathrm{m}^3/\mathrm{s}$.

This discharge computed by the EDM is found to be close to the measured one Q = 0.3832 m^3/s. The discharge computed by the SCM would have been Q = 0.3396 m^3/s; and by the DCM, Q = 0.4239 m^3/s. This proves once again the efficiency and accuracy of the EDM.

Appendix 3
UCL flume : experimental set-up

A3.1 Flume description

In order to support the experimental part of this work, a new compound-channel flume has been specifically build in the UCL Laboratory (see Marchal and Philippe 1998). This flume is 1.20-m wide, and its overall length equals 14 m (Figure A3.1 and Figure A3.2). This length comprises : (1) a 10-m long measurement section, with a coated-plywood bottom; (2) a 2-m long inlet tank; and (3) a 2-m long outlet tank. The bed slope is variable in the interval $S_0 = 0$ .. 0.03, thanks to a pair of coupled adjustment jacks. In order to facilitate this adjustment process, the flume has been build on a unique frame.

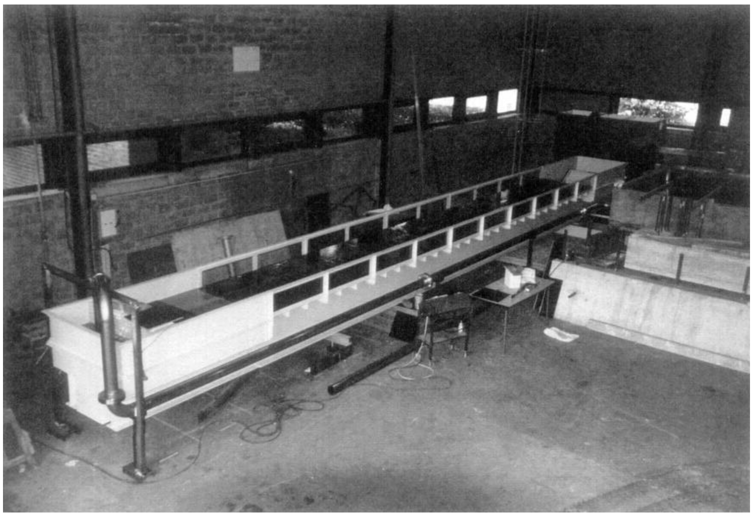

Figure A3.1 : UCL compound-channel flume, general view

The discharge is supplied through an upstream reservoir with constant level (see Figure A3.2), in such a way that an accurate discharge control is possible, independently from the pump working. Flow rate in the interval $Q = 0$ .. 30 l/s is available, and discharge measurement is operated by an electromagnetic flowmeter. Several equipment are used in order to still the flow at the supply-pipe end and in the inlet tank : (1) a coco-fibres mat, wrapped around the pipe; (2) a honeycomb screen, ensuring parallel flow; and (3) a vertical contraction, for the transition to the measurement section (Figure A3.3). It is thought that this contraction design could be related with the ill-conditioned upstream discharge distribution observed in Chapter 6 and Chapter 12. The downstream level is controlled through an adjustable weir.

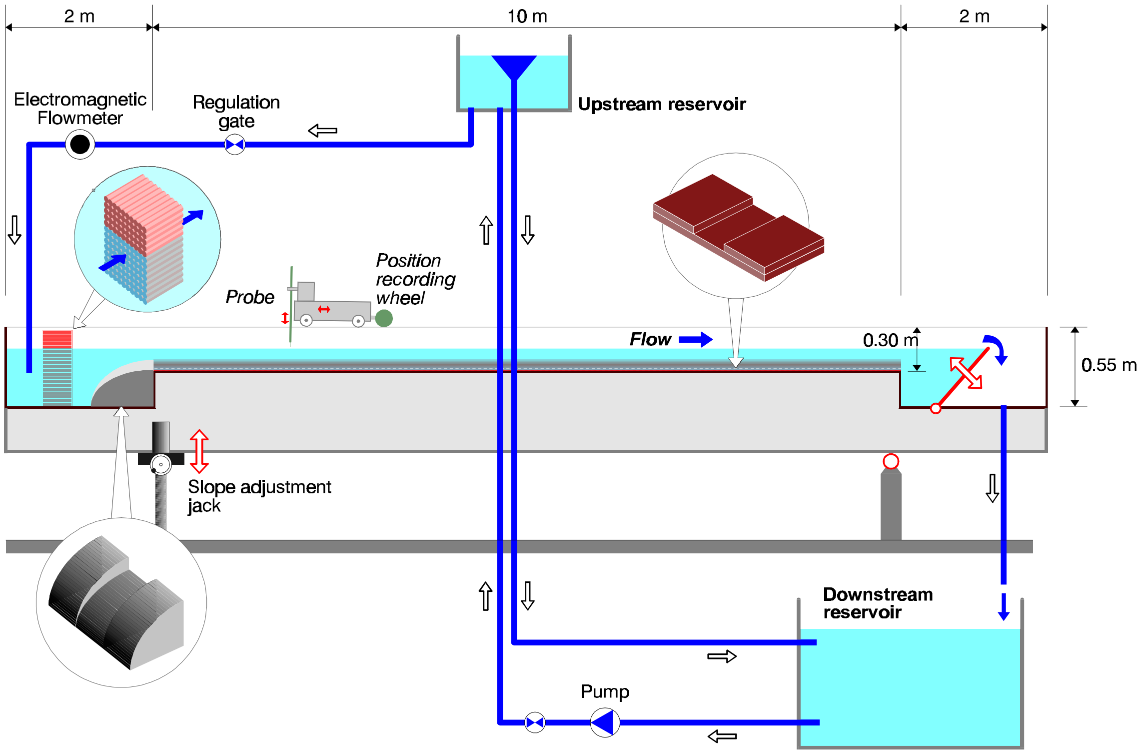

Figure A3.2 : UCL compound-channel flume

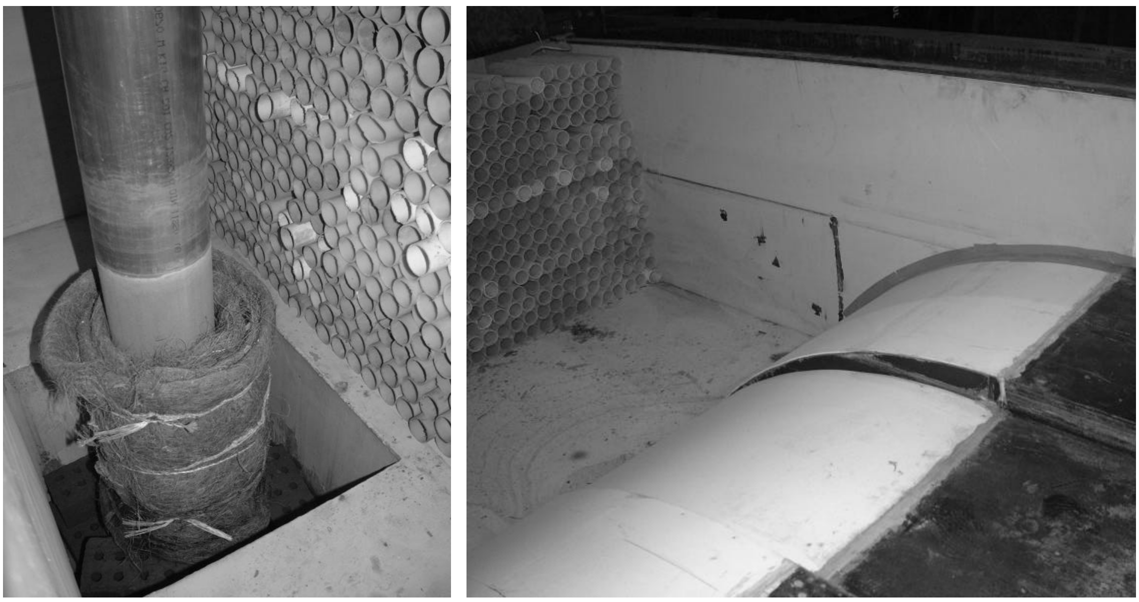

(a) (b)

Figure A3.3 : Inlet tank, stilling devices and vertical contraction

A two-directional measurement trolley is fixed above the flume. Both its *x*- and *y*-wise positions are recorded automatically.

A3.2 Measuring devices

The classical measuring devices used during this work are summarised in Table A3.1. The performed measurements include : (1) discharge; (2) level (bed and water); (3) velocity; and (4) velocity direction. As already quoted, the discharge is measured with an electromagnetic flowmeter, with a 0.5 % precision.

The levels were measured using either an electronic or an automatic height gauge, both mounted on the measurement trolley. The electronic height gauge is used with a sharp-ended stem. Its absolute precision is 0.01 mm. However, due to water surface oscillations, the measurements accuracy is expected to be limited to 0.10 mm. The automatic point gauge is a Water-Level Follower (WAVO), from Delft Hydraulics (Figure A3.4). Its functioning is based on a vibrating needle that is automatically maintained at the water-surface level. As the vibrating needle is suspended at the end of a chain, great care is required when moving the trolley, in order to limit its pendulum movements.

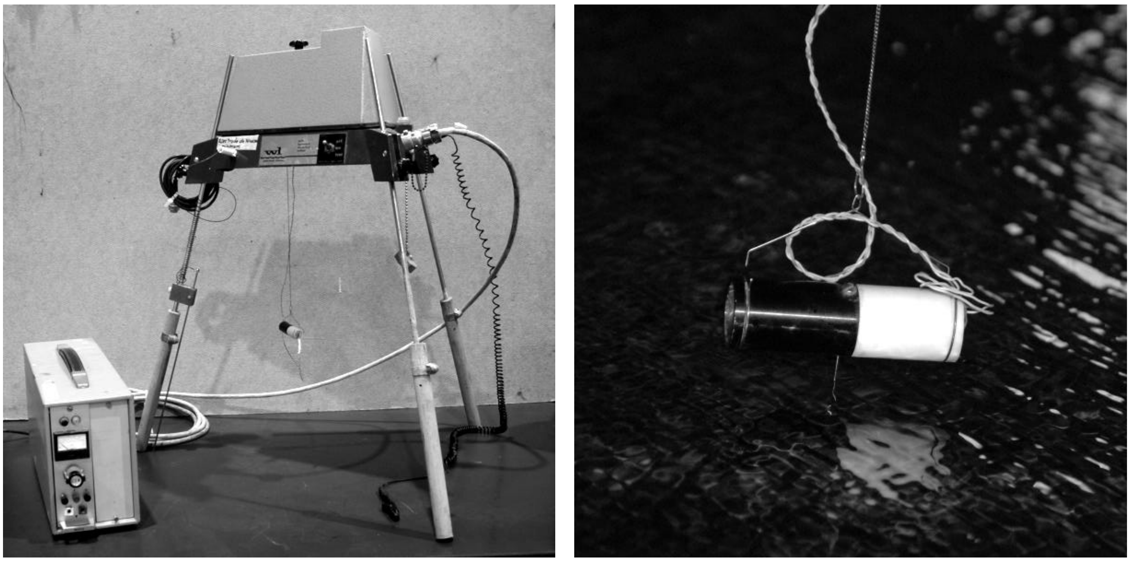

(a) *(b)*

Figure A3.4 : Water-Level Follower (WAVO) : (a) general view; and (b) close-up of the vibrating-needle device

Velocities are measured by a 4-mm diameter Pitot tube, connected to a low differential pressure manometer. Classically, the velocity U is estimated as

$$U = \phi \sqrt{\frac{2\left(p_d - p_s\right)}{\rho}} \tag{A3.1}$$

where p_d and p_s are respectively the dynamic and the static flow pressures, recorded through the axial and the lateral holes of the Pitot tube; ρ is the specific mass of water; and ϕ is a correction factor. This ϕ factor accounts for the differences between the actual and the idealised flow lines along the Pitot-tube head, and for the corresponding losses

(Troskolanski 1962). For the present tube, its value has been experimentally estimated at $\phi = 0.90$. By comparison of the averaged velocity field and the actual discharge, measured by the electromagnetic flowmeter, the velocity-measurement accuracy is estimated to be around 2 %. It has been noted that a careful adjustment of the zero reading from the pressure manometer is necessary to get accurate measurements of low velocities. This adjustment is performed by by-passing the Pitot tube and connecting both entries of the manometer to a still-water vase.

Table A3.1 : Measuring devices used in the UCL flume

Device	Producer [serial number]	Measurement range	Measurement precision [estimated]
Electromagnetic flowmeter "Magmaster"	ABB Kent-Taylor [V 11632 / 5 / 6]	0 .. 100 l/s	0.5 %
Electronic height gauge "HDS-20M"	Mitutoyo [0001830]	0 .. 250 mm	0.01 mm [0.10 mm]
Automatic height gauge "Water-Level Follower"	Delft Hydraulics [WAVO – 73 W 166]	0 .. 100 mm	0.10 mm [0.20 mm]
Pitot tube, 4 mm diameter	Airflow	..	[2 %]
Differential manometer "LPM 9481"	Druck [16612]	-10 .. 10 mbar	0.1 %
Micro vane	UCL	0 .. 30 °	[0.5 °]

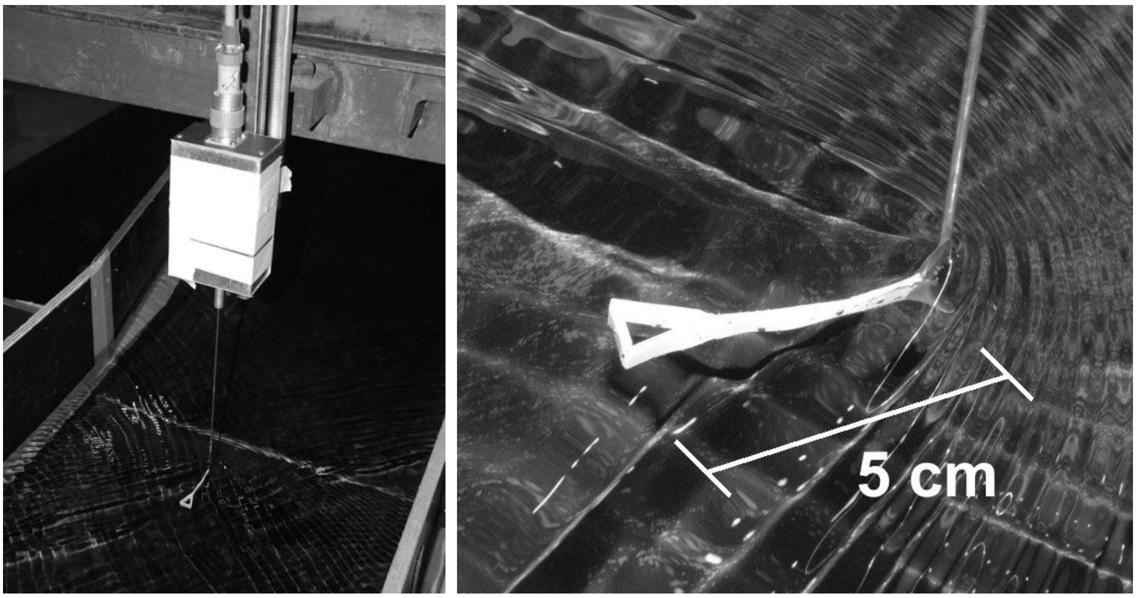

(a) *(b)*

Figure A3.5 : Micro vane, for velocity direction measurement

The velocity-direction measurements are performed using a UCL-made micro vane (Figure A3.5). This micro vane is 5 cm long and 0.5 cm height. Its end has a fishtail shape, in order to increase its sensibility for the lowest transverse velocities. The micro vane is fixed on a low-friction rotational-displacement transducer for automatic reading purpose. Due to some difficulty encountered during the micro-vane construction, it is not perfectly symmetric. As a result, its zero fitting is unfortunately uneasy, in such a way that the measurement precision is estimated to be not better than 0.5 °.

A3.3 Measuring procedures

A3.3.1 Bed slope

In order to measure the flume bed slope, the downstream weir is set at its highest position and the measurement section is filled up with still water (Q = 0 l/s). The water depth H is then recorded as several stations, using the electronic height gauge : at each location, the zero reading is set for the bottom level, and the horizontal water level is measured accordingly. A linear regression through the measured points gives finally the requested bed slope S_0.

A3.3.2 Water profile

Water profiles are measured using the WAVO mounted on the trolley, which is pushed by hand on the whole channel length. During this travelling, one measurement per 10 cm is recorded. In each case, the profile is also measured during the return travel, in order the validate the measurement.

Two corrections are necessary for a proper use of the WAVO data : (1) a reference level has to be set; and (2) the WAVO local level depends on the trolley rails and has to be corrected accordingly. The reference level is fixed on the central axis of the flume bottom, at the downstream end of the measurement section, corresponding to its lowest point.

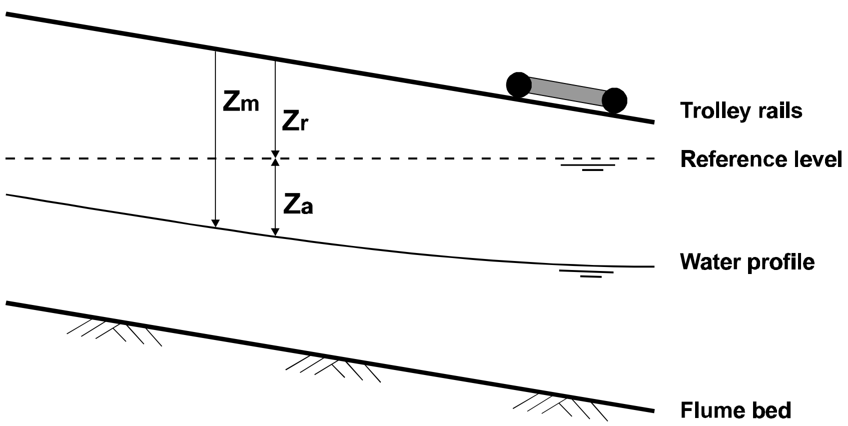

Figure A3.6 : Level measurement correction, according to the trolley rails level

The second adjustment is necessary as the WAVO measures a water level z_m relative to its actual position on the trolley rails (Figure A3.6); whereas one is interested by the actual water level z_a relative to a horizontal reference plane. This actual level z_a is obtained by subtracting to the measured level z_m a previously-recorded measurement of the rails position z_r, relative to a reference plane. This correction value z_r is obtained by setting an horizontal water level, as for the bed slope measurement, and by recording the water profile using the present procedure.

The stage-discharge relation can finally be measured by setting uniform flows for a range of discharges. The uniform flow condition is obtained by adjusting the downstream tailgate level until the measured water profile is found parallel to the flume bottom. It is expected that this process gives the uniform water-depth value with an accuracy equal or better than 0.20 mm.

A3.3.3 Velocity distribution

Velocities in a cross-section are recorded according to a given measurement mesh. This mesh density is decided according to the measurement purpose : when only the discharge distribution is of interest, 4 or 5 points are fixed at different levels on 4-5 vertical in the main-channel, and 1 to 3 points are fixed on 4-5 verticals in each floodplain. This mesh density is only increased (up to 10 points on a vertical in the main-channel) when one is also interested in the detailed flow structure. When a symmetric cross-section is investigated, the measurements are generally limited to half a section.

The local velocities are then depth-averaged (using a trapezoid-integration rule), and an estimate of the discharge is obtained by a second integration on the section width. This discharge estimate is compared with the actual discharge measured by the electromagnetic flowmeter, and the resulting error is uniformly distributed over the local measurements.

A transverse velocity is obtained as the product of the corresponding longitudinal velocity, measured with the Pitot-tube, and the tangent of the velocity direction, measured with the micro-vane. According to the difficulty encountered for setting the zero reading, an estimate of the resulting error is given by the depth-averaged transverse velocity at the channel axis, which is expected to equal zero in a symmetric cross-section. This error is again uniformly reported on all the direction measurements.

In order to facilitate the experimental work, most of the measurements procedures described above have been implemented in a data acquisition program "HydroCAP", written using the Labview software from National Instruments. This program enables an automatic recording and formatting of the measurements made using the WAVO, the Pitot tube and the micro vane.

Appendix 4
Hydrodynamic Stability Analysis : Numerical solution of the eigenvalue problem

A4.1 Inviscid shear layer

The eigenvalue problem to be solved for the inviscid shear-layer stability analysis (§ 7.3) is defined on one hand by the Rayleigh equation (7.11), or by its predecessor system (7.10) :

$$\mathbf{v}_y = - i\alpha\, \mathbf{u} \tag{7.10a}$$

$$\mathbf{u}_y = \frac{i}{\alpha}\left(\frac{U_{yy}}{U-c} + \alpha^2\right)\mathbf{v} \tag{7.10b}$$

where the velocity U profile is defined by the hyperbolic-tangent function (7.15)

$$U = U_m + \mathrm{TANH}\,(y) \tag{7.15}$$

and, on the other hand, by the boundary conditions (7.16) :

$$\mathbf{v}(y) = A_2\, e^{-\alpha y} \qquad \text{for } y >> 0 \tag{7.16a}$$

$$\mathbf{v}(y) = A_3\, e^{\alpha y} \qquad \text{for } y << 0 \tag{7.16b}$$

In order to solve this problem, one seeks for pairs of eigenvalues (α, c) for which an eigenfunction exists. A basic trial-and-error procedure is used for that purpose (Betchov and Criminale 1967). The solution steps are as follow :

1. Set a value for the wave number α (positive real number, $0 < \alpha$), for which the problem will be solved,
2. Set a tentative value for the wave celerity c (complex number, $c = c_r + i\, c_i$),
3. From a pair of values (**u**, **v**) defined according to one of the boundary conditions, compute the eigenfunctions **u** and **v** by numerical integration of the Rayleigh equation, using e.g. a Runge-Kutta method of 4th order (see below, § A4.3),
4. Compare the eigenfunctions values with the boundary condition at the other end of the integration interval, and correct the c value accordingly, until the eigenfunctions match the boundary condition,
5. Repeat the same procedure for other wave-number α values.

As the Rayleigh equation (7.11) is a second-order differential equation, it is necessary to use the auxiliary variable **u** in order to reduce the problem to the pair of first-order equations (7.10), that can be solved by the Runge-Kutta method.

In the present case, the integration is performed on the interval -3 < y < 3, with a step $\Delta y = 0.01$. At the boundary, the condition (7.16) can be rewritten :

$$\mathbf{v}_y = \alpha\,\mathbf{v} \qquad \text{for } y \ll 0 \tag{A4.1a}$$

$$\mathbf{v}_y = -\,\alpha\,\mathbf{v} \qquad \text{for } y \gg 0 \tag{A4.1b}$$

or, replacing $\mathbf{v}_y$ by **u**, according to (7.10a) :

$$\mathbf{v} + \mathrm{i}\,\mathbf{u} = 0 \qquad \text{for } y \ll 0 \tag{A4.2a}$$

$$\mathbf{v} - \mathrm{i}\,\mathbf{u} = 0 \qquad \text{for } y \gg 0 \tag{A4.2b}$$

The integration starts form (A4.2a) at y = - 3. As the differential equations are homogeneous, the initial variables can be defined with an arbitrary factor. For example, one can use **v** = 1 + i 0 and **u** = 0 + i 1, that satisfy the condition (A4.2a). The integrated eigenfunction will have to satisfy the condition (A4.2b) at y = 3.

An automatic search of the c value for which the eigenfunction satisfies this boundary condition (A4.2b) is performed by defining the corresponding target function $F(c)$:

$$F(c) = \mathbf{v}(3) - \mathrm{i}\,\mathbf{u}(3) \tag{A4.3}$$

where **v** and **u** are the eigenfunction obtained by the Runge-Kutta integration. One looks then for the c value for which this target function equals zero.

Using a plausible initial value for c, the solution can be obtained by a Newton-Raphson method in a few iterations. As both the target function $F(c) = F_r + \mathrm{i}\,F_i$ and the unknown $c = c_r + \mathrm{i}\,c_i$ are complex, one has in fact to solve a system of two equations with two unknowns. The increments Δc_r and Δc_i to be added to c_r and c_i are chosen in such a way that the target function F equals zero for $c + \Delta c$. Using the Taylor development for $F(c + \Delta c)$ as a function of $F(c)$ and its partial derivatives, one gets

$$\Delta c_r = \frac{\dfrac{\partial F_r}{\partial c_i} F_i - \dfrac{\partial F_i}{\partial c_i} F_r}{\dfrac{\partial F_r}{\partial c_r}\dfrac{\partial F_i}{\partial c_i} - \dfrac{\partial F_r}{\partial c_i}\dfrac{\partial F_i}{\partial c_r}} \quad \text{and} \quad \Delta c_i = \frac{\dfrac{\partial F_i}{\partial c_r} F_r - \dfrac{\partial F_r}{\partial c_r} F_i}{\dfrac{\partial F_r}{\partial c_r}\dfrac{\partial F_i}{\partial c_i} - \dfrac{\partial F_r}{\partial c_i}\dfrac{\partial F_i}{\partial c_r}} \tag{A4.4}$$

where the partial derivatives are estimated as

$$\frac{\partial F}{\partial c_r} = \frac{F(c + dc_r) - F(c)}{dc_r} \quad \text{and} \quad \frac{\partial F}{\partial c_i} = \frac{F(c + \mathrm{i}\,dc_i) - F(c)}{dc_i} \tag{A4.5}$$

where dc_r and dc_i are small increments; and $F(c+dc_r)$ and $F(c+\mathrm{i}\,dc_i)$ are evaluated by two additional Runge-Kutta integrations of the Rayleigh equation (7.10), using the incremented celerity values.

For the inviscid shear layer defined by a hyperbolic-tangent function (7.15), one has $c_r = U_m$. Only the c_i value has then to be explored when seeking for the root of the target function. For other cases, including friction or geometry changes, the value $c_r = U_m$ is a good approximate to start the eigenvalue search.

Once the eigenvalues (α, c) and the eigenfunction $\mathbf{v}$ have been computed, one observes that the latter is symmetric in the complex plane, with reference to the $y = 0$ station. In order to facilitate the visualisation and the reading of this eigenfunction, it is common to multiply it by a given factor (corresponding to the arbitrary factor quoted above), in such a way that $\mathbf{v_r}$ is antisymmetric ($\mathbf{v_r}(0) = 0$) and $\mathbf{v_i}$ is symmetric.

A4.2 Viscous shear layer

In the case of the viscous shear layer, the eigenvalue problem is defined by the Orr-Sommerfeld equation (7.21)

$$(U-c)(\mathbf{v}_{yy}-\alpha^2\mathbf{v})-U_{yy}\mathbf{v}=-\frac{\mathrm{i}\upsilon}{\alpha}(\mathbf{v}_{yyy}-2\alpha^2\mathbf{v}_{yy}+\alpha^4\mathbf{v}) \qquad (7.21)$$

where, again, the velocity U profile is defined by the hyperbolic-tangent function (7.15); and by the boundary conditions (7.22-24) :

$$\mathbf{v}(y)=\sum_{n=1}^{4}A_n e^{p_n y} \quad \text{for } y \gg 0 \qquad (7.22)$$

where $A_1 = A_3 = 0$; and

$$\begin{aligned} p_1 &= \alpha & p_2 &= -\alpha \\ p_3 &= \alpha\left(1+\mathrm{i}\frac{U-c}{\upsilon\alpha}\right)^{1/2} & p_4 &= -\alpha\left(1+\mathrm{i}\frac{U-c}{\upsilon\alpha}\right)^{1/2} \end{aligned} \qquad (7.23)$$

And

$$\mathbf{v}(y)=\sum_{n=1}^{4}B_n e^{q_n y} \quad \text{for } y \ll 0 \qquad (7.24)$$

where $B_2 = B_4 = 0$; and

$$\begin{aligned} q_1 &= \alpha & q_2 &= -\alpha \\ q_3 &= \alpha\left(1-\mathrm{i}\frac{U-c}{\upsilon\alpha}\right)^{1/2} & q_4 &= -\alpha\left(1-\mathrm{i}\frac{U-c}{\upsilon\alpha}\right)^{1/2} \end{aligned} \qquad (7.25)$$

The Orr-Sommerfeld equation (7.21) is again integrated by the Runge-Kutta method, in the present case, from $y = 3$ to $y = -3$. For this purpose, one defines the auxiliary variables $\mathbf{v}_y$, $\mathbf{v}_{yy}$ and $\mathbf{v}_{yyy}$; and one sets values for the wave number α and the viscosity υ.

However, an additional difficulty is faced when dealing with the initial-conditions choice for this integration, as the ratio A_4/A_2 between both part of the boundary condition (7.22) is unknown. This constitutes therefore an additional unknown to be solved, together with the celerity c. On the other hand, two target functions are also available, as one seeks to get $B_2 = B_4 = 0$ in (7.24). The problem will be solved through two integration passes, with different values for A_2 and A_4, and by taking benefit from the linearity of the equation (Betchov and Criminale 1967).

For the first pass, one sets $A_2 = 1$ and $A_4 = 0$. Accordingly, the initial condition for the integration is given by (7.22) written at $y = 3$:

$$\begin{aligned} &\mathbf{v}(3) = e^{-3\alpha} && \mathbf{v}_{yy}(3) = \alpha^2 e^{-3\alpha} \\ &\mathbf{v}_y(3) = -\alpha e^{-3\alpha} && \mathbf{v}_{yyy}(3) = -\alpha^3 e^{-3\alpha} \end{aligned} \tag{A4.6}$$

For the second pass, one sets $A_2 = 0$ and $A_4 = 1$. The initial condition is obtained similarly.

For each integration pass, using the Runge-Kutta method, one gets the values of the variables $\mathbf{v}$, $\mathbf{v}_y$, $\mathbf{v}_{yy}$ and $\mathbf{v}_{yyy}$ at $y = -3$. Deriving three times the boundary condition (7.24), the resulting system of four equations can be solved for the four unknowns B_n :

$$B_1 = \frac{-e^{-\alpha y}}{2\alpha\left(q_3^2 - \alpha^2\right)}\left(\mathbf{v}_{yyy} + \alpha\mathbf{v}_{yy} - q_3^2\mathbf{v}_y - \alpha q_3^2\mathbf{v}\right) \tag{A4.7a}$$

$$B_2 = \frac{e^{\alpha y}}{2\alpha\left(q_3^2 - \alpha^2\right)}\left(\mathbf{v}_{yyy} - \alpha\mathbf{v}_{yy} - q_3^2\mathbf{v}_y + \alpha q_3^2\mathbf{v}\right) \tag{A4.7b}$$

$$B_3 = \frac{e^{-q_3 y}}{2q_3\left(q_3^2 - \alpha^2\right)}\left(\mathbf{v}_{yyy} + q_3\mathbf{v}_{yy} - \alpha^2\mathbf{v}_y - \alpha^2 q_3\mathbf{v}\right) \tag{A4.7c}$$

$$B_4 = \frac{-e^{q_3 y}}{2q_3\left(q_3^2 - \alpha^2\right)}\left(\mathbf{v}_{yyy} - q_3\mathbf{v}_{yy} - \alpha^2\mathbf{v}_y + \alpha^2 q_3\mathbf{v}\right) \tag{A4.7d}$$

where q_3 is defined by (7.25).

As the Orr-Sommerfeld equation (7.21) is linear, the final values of B_2 and B_4 are obtained for any arbitrary values of A_2 and A_4 by superimposing results obtained from the above integrations :

$$B_2 = A_2\,(B_2)_{\mathrm{I}} + A_4\,(B_2)_{\mathrm{II}} \tag{A4.8a}$$

$$B_4 = A_2\,(B_4)_{\mathrm{I}} + A_4\,(B_4)_{\mathrm{II}} \tag{A4.8b}$$

where indices I and II stands for B_n values obtained by the above integrations using respectively $(A_2, A_4) = (1,0)$ and $(A_2, A_4) = (0,1)$.

As the first target function writes $B_2 = 0$, using (A4.8a) the value of the ratio A_4/A_2 equals

$$\frac{A_4}{A_2} = -\frac{(B_2)_{\text{I}}}{(B_2)_{\text{II}}} \tag{A4.9}$$

Setting $A_2 = 1$ (as the solutions are given for an arbitrary factor, thanks to the equation homogeneity), and according to (A4.8b), the second target function $B_4 = 0$ writes now

$$B_4 = (B_4)_{\text{I}} - \frac{(B_2)_{\text{I}}}{(B_2)_{\text{II}}}(B_4)_{\text{II}} = 0 \tag{A4.10}$$

As for the inviscid shear layer, the Newton-Raphson method is use to find the value of the celerity c that cancels out this target function (A4.10).

The search process for the eigenvalue c and eigenfunction $\mathbf{v}$ of the Orr-Sommerfeld equation (7.21), for given values of the wave number α and of the viscosity υ, can be summarised as follow :

1. Set a tentative value for the wave celerity c (complex number, $c = c_r + \mathrm{i}\, c_i$),
2. Set the initial condition (A4.6) at $y = 3$, using $A_2 = 1$ and $A_4 = 0$,
3. Integrate the Orr-Sommerfeld equation (7.21) for the on the interval $y = 3$ .. -3, using the Runge-Kutta method,
4. Estimate the values of $(B_2)_{\text{I}}$ and $(B_4)_{\text{I}}$, according to the variables $\mathbf{v}$, $\mathbf{v}_y$, $\mathbf{v}_{yy}$ and $\mathbf{v}_{yyy}$ values at $y = -3$ by (A4.7b) and (A4.7d),
5. Repeat the same process, using $A_2 = 0$ and $A_4 = 1$ for the initial condition, in order to assess the values of $(B_2)_{\text{II}}$ and $(B_4)_{\text{II}}$,
6. Compute the value of the target function B_4 (A4.10) for the c value set in step 1, and correct this c value accordingly, using the Newton-Raphson method, until $B_4 = 0$.

A4.3 The Runge-Kutta method

The Runge-Kutta method is a numerical method aimed at the integration of a first-order differential equation (or a system of first-order differential equations), such as

$$\frac{d\varphi}{dy} = F(\varphi, y) \tag{A4.11}$$

where φ is the function to be integrated; and y is the integration variable. An initial condition has to be defined, for example giving the value of the function $\varphi = \varphi_0$ at $y = y_0$.

The Runge-Kutta integration method proceeds by steps for determining the φ values at distinct nodes (see e.g. Hirsch 1988). Let y_i be the position of a node where the value φ_i is already known, and y_{i+1} the position of a node where the value φ_{i+1} has to be calculated. Between these nodes, separated by the increment Δy, one has therefore to find the increment $\Delta\varphi$ such as $\varphi_{i+1} = \varphi_i + \Delta\varphi$. A first estimation of this increment value can be obtained by

$$\Delta\varphi^{\mathrm{I}} = \Delta y\ F(\varphi_i, y_i) \tag{A4.12}$$

The Runge-Kutta method is a fourth-order method : this means that the integration error is proportional to $(\Delta y)^4$. To obtain such a precision, four successive refinements of the increment estimation are necessary. The first estimation is given by (A4.12), and the three additional estimations are as follow :

$$\Delta\varphi^{\mathrm{II}} = \Delta y\ F\left(\varphi_i + \frac{\Delta\varphi^{\mathrm{I}}}{2}, y_i + \frac{\Delta y}{2}\right) \tag{A4.13a}$$

$$\Delta\varphi^{\mathrm{III}} = \Delta y\ F\left(\varphi_i + \frac{\Delta\varphi^{\mathrm{II}}}{2}, y_i + \frac{\Delta y}{2}\right) \tag{A4.13b}$$

$$\Delta\varphi^{\mathrm{IV}} = \Delta y\ F\left(\varphi_i + \Delta\varphi^{\mathrm{III}}, y_i + \Delta y\right) \tag{A4.13c}$$

The value of the function φ at $y = y_{i+1}$ is finally given by

$$\varphi_{i+1} = \varphi_i + \Delta\varphi = \varphi_i + \left(\frac{\Delta\varphi^{\mathrm{I}}}{6} + \frac{\Delta\varphi^{\mathrm{II}}}{3} + \frac{\Delta\varphi^{\mathrm{III}}}{3} + \frac{\Delta\varphi^{\mathrm{IV}}}{6}\right) \tag{A4.14}$$